

Waterford Institute *of* Technology

DEVELOPMENT OF INTERFEROMETRIC  
& SPECTROSCOPIC TECHNIQUES  
FOR HIGH-RESOLUTION  
SPECTRAL MEASUREMENTS ON  
FIBRE BRAGG GRATINGS

Volume I of II

by

Ronan O'Byrne

---

Submitted for the Degree of  
Doctor of Philosophy

to the

School of Science  
Waterford Institute of Technology

---

Supervisors:

D. A. Flavin<sup>1</sup>, Dr. C. Keary<sup>1</sup>, Dr. P.J. Cregg<sup>1</sup> Dr. S. Sergeyev<sup>1,2</sup>  
& Prof. J. D. C. Jones<sup>3</sup>

<sup>1</sup>Waterford Institute of Technology, <sup>2</sup>Aston University, Birmingham, U.K.,  
<sup>3</sup>Heriot-Watt University, Edinburgh, U.K.

(Submitted to Waterford Institute of Technology, October 2013)

## Access to Thesis

Author: **Ronan O'Byrne** Student Number: **W20004473**

Thesis Title: **Development of interferometric & spectroscopic techniques for high-resolution spectral measurements on Fibre Bragg gratings**

In accordance with the **Copyright and Related Rights Act**, 2000, and **S.I. 427** of 2000 I agree that Waterford Institute of Technology, may, at their discretion, lend or copy the thesis detailed above upon request.

### Access rights to this thesis:

- |                                     |                                     |              |                                     |
|-------------------------------------|-------------------------------------|--------------|-------------------------------------|
| <input type="checkbox"/>            | Option 1: No restrictions on access | Print thesis | <input type="checkbox"/>            |
|                                     |                                     | eThesis      | <input type="checkbox"/>            |
| <input checked="" type="checkbox"/> | Option 2: Embargo details           | Print Thesis | <input checked="" type="checkbox"/> |
|                                     |                                     | eThesis      | <input checked="" type="checkbox"/> |
|                                     |                                     | Years        | Indefinitely                        |
|                                     |                                     | <u>2</u>     | <input type="checkbox"/>            |
|                                     |                                     | <u>2</u>     | <input type="checkbox"/>            |

### Supervisors:

We the supervisors, agree to the named thesis being made available under the conditions specified above.

Name: Dr. Claire Keary Dept: C. M. & P.

Signed: \_\_\_\_\_ Date: \_\_\_\_\_

Name: Dr. P.J. Cregg Dept: Engineering

Signed: \_\_\_\_\_ Date: \_\_\_\_\_

### Student:

I, the author, agree to the named thesis being made available under the conditions specified above and the terms specified in the **Waterford Institute of Technology eThesis Deposit Agreement**.

I confirm that the electronic copy mirrors the hard bound copy volume(s).

I confirm that the named thesis is my own work.

Name: Ronan O'Byrne Dept: C. M. & P.

Signed: \_\_\_\_\_ Date: \_\_\_\_\_

# Declaration

No part of the work described in this thesis, or the thesis itself, has been submitted as an exercise for a degree at this or any other institution.

The work herein has been performed entirely by the author.

---

Ronan O'Byrne.

October 2013

Dedicated to the memory of  
Dónal Flavin (R.I.P.)

# Acknowledgements

This thesis could not have been arrived at without the help and support of a great many people. I must begin with Dónal Flavin(R.I.P.), for giving me the opportunity to undertake this work, and for the loyalty, consideration and friendship he inspired in his colleagues and collaborators, who so generously took on the responsibility of my supervision. My thanks too to Dónal's family for their support at such a traumatic time for them, and since.

To Sergey Sergeev (W.I.T. and Aston University, UK), Claire Keary(W.I.T.), P.J. Cregg(W.I.T.), and Julian Jones(Heriot–Watt University, UK), I cannot express my gratitude nor the debt I owe for persevering with me this far. Your (seemingly boundless) patience, guidance and supervision have enabled me to get this work to completion. All errors that remain are solely my own.

I thank my colleagues in the Optics Research Group: John Rothwell, Kieran O'Mahoney, Dominic Murphy and Mohammad Alhourani for their warm welcome, ready support and advice; Frank O'Donnell for his kindness, consideration and advice, no matter when it was sought; and John Houlihan for his support.

I must also thank Dónal's other colleagues who formally and informally provided support and advice. Michael Brennan, Kieran Murphy, John O'Dwyer, Michael O'Keeffe, Padraig Kirwan, Paul O'Leary.

I gratefully thank Micheal O'hEigeartigh, Paul Barry and the staff of the School of Science Office for their support and expedience; Willie Donnelly and staff of the Research Office, for their kindness, good humour, patience and support throughout; Venie Martin and the Development Office for their support. Dealing with the difficult aftermath of Dónal's passing was greatly eased by their individual and collective efforts.

My sincere thanks to Frank Heraughty and the staff of Educational services for their very generous assistance and advice; the staff of Maintenance and facilities and the College Porters for their kindness, consideration and advice on countless occasions. Their efforts and assistance greatly aided the progression of my work.

My thanks to my collaborators Prof. David Nikogosyan and Stephen Slattery of UCC for their assistance, support and warm welcome when I visited their lab.

I thank Robert Maier and Bill McPherson of Heriot–Watt University for their

generosity and support, in providing advice and time; Prof. Ian Bennion of Aston University for his support and advice.

I thank Enterprise Ireland for their financial support via Enterprise Ireland commercialization fund, project code CFTD/04/330.

I thank Damien Foley for instilling in me my love of physics; Dr. H. M. Grimley for providing such an exceptional and memorable undergraduate laboratory experience; Tom Keenan and Norman Walsh for sharing their wealth of experience and personal management tricks.

Finally, I sincerely thank my mother, father and brother for their unstinting kindness, support and time, without which this work could not have happened.

# Publications

The work reported in this thesis has been presented at the following conferences:

1. R. P. O’Byrne, S. V. Sergeyev, D. A. Flavin, and D. N. Nikogosyan. **Strain Characterization of fiber Bragg gratings inscribed by high-intensity femtosecond UV pulses.** In A. Cutolo, B. Culshaw, and J. M. López-Higuera, editors, *Proceedings of the Third European Workshop on Optical Fibre Sensors*, volume 6619. SPIE, July 2007. ISBN: 9780819467614.
2. R. P. O’Byrne, S. V. Sergeyev, D. A. Flavin, S. A. Slattery, D. N. Nikogosyan, and J. D. C. Jones. **Comparison of depolarisation approaches for high resolution spectroscopic FBG measurements.** Oral presentation at Photon08 conference, Heriot–Watt University, UK.
3. R. P. O’Byrne and S. V. Sergeyev. **Application of pi-shifted short scan interferometry to remote sensing.** In Julian D. C. Jones, editor, *20th International Conference on Optical Fibre Sensors, Proc. SPIE*, volume 7503, page 75036R. SPIE, 2009.

and published in journal papers:

1. R. P. O’Byrne, S. V. Sergeyev, D. A. Flavin, S. A. Slattery, D. N. Nikogosyan, and J. D. C. Jones. **Anisotropic fiber bragg gratings inscribed by high-intensity femtosecond-uv pulses: manufacturing technology and strain characterization for sensing applications.** *IEEE Sens. J.*, 8(7):1256–1263, July 2008.
2. K. T. O’Mahoney, R. P. O’Byrne, S. V. Sergeyev, L. Zhang, and I. Bennion. **Short–Scan fiber interferometer for high-resolution Bragg grating array interrogation.** *IEEE Sens. J.*, 9(10):1277–1281, October 2009.

# Abstract

## Development of interferometric & spectroscopic techniques for high-resolution spectral measurements on Fibre Bragg gratings

by Ronan O'Byrne

This thesis reports the development of a custom Čzerny–Turner spectrometer, the SpectroBragg, which operates natively in the telecoms bands using an InGaAs photodiode array. The SpectroBragg's photodiode array enables the monitoring of  $\sim 70\text{nm}$  with  $\sim 1\text{ pm}$  accuracy with a sampling rate of 30 ms. The SpectroBragg is intended for use with fibre Bragg grating, FBG, sensors.

The strain characterisation of a novel anisotropic FBG, inscribed in Corning SMF–28 telecoms fibre, via a two–photon process at 264 nm is also reported. The two–photon process is more efficient at FBG inscription and the FBGs are structurally anisotropic in isotropic fibre. These FBGs combine the characteristics of high–birefringence fibre at the FBG with the transmission characteristics of SMF–28.

Demodulation systems, that have polarisation–sensitivity, behave as polarisation analysers producing an intensity modulation dependent upon the state of polarisation, affecting high–accuracy phase sensitive wavelength interrogation schemes.

In this thesis, two depolarisation approaches, a modified polarisation fixer system and a PDL balancing system, are examined as FBG signal depolarisers for anisotropic and isotropic FBG signals that are demodulated by the SpectroBragg spectrometer. The approaches are contrasted with the more traditional Lyot depolarisation system which is incorrectly specified.

Rayleigh scattering provides the fundamental minimum to signal attenuation, consisting of two components: incoherently and coherently scattered radiation. The scattered radiation, within the coherence length of a source signal, adds coherently, modifying the guided mode, and for a phase sensitive demodulation system, is recovered as phase noise.

In this thesis, the Hilbert transform technique, HTT, is used to analyse two–output,  $\pi$ –shifted interferograms from an all–fibre Michelson interferometer, to de-

modulate FBG signals, allowing for the recovery of interferograms not detectable with single-output interferograms. The Hilbert transform technique has been demonstrated to provide higher resolution wavelength determination than Fourier transform spectroscopy using shorter interferometer scans.

# Contents

<b>1</b>	<b>Introduction</b>	<b>V.I - 1</b>
1.1	Motivation for sensors . . . . .	V.I- 2
1.1.1	Fibre Sensors . . . . .	V.I- 4
1.2	Thesis Overview . . . . .	V.I- 5
1.2.1	Appendices . . . . .	V.I- 8
1.3	Notation . . . . .	V.I- 8
1.3.1	Tensor representation of quantities . . . . .	V.I- 8
1.3.2	Measurement terminology . . . . .	V.I- 9
1.4	References . . . . .	V.I- 9
<b>2</b>	<b>Literature Review</b>	<b>V.I - 12</b>
2.1	Introduction . . . . .	V.I- 12
2.1.1	Electromagnetic radiation . . . . .	V.I- 12
2.1.1.1	Quantum limits on resolution . . . . .	V.I- 13
2.1.1.2	Phase noise limitation . . . . .	V.I- 14
2.1.2	Wolf’s polarisation representation . . . . .	V.I- 16
2.1.2.1	Unified theory of coherence and polarisation . . . . .	V.I- 18
2.2	Optical fibres . . . . .	V.I- 22
2.2.1	Historical overview . . . . .	V.I- 22
2.2.1.1	Group and phase velocities, the cut-off frequency . . . . .	V.I- 23
2.2.2	Materials effects . . . . .	V.I- 25
2.2.2.1	Silica based Glass . . . . .	V.I- 25
2.2.2.2	Rayleigh scattering . . . . .	V.I- 28
2.2.3	Physical (optical) properties . . . . .	V.I- 32
2.2.4	Stress and Strain . . . . .	V.I- 37
2.2.4.1	Indicatrix . . . . .	V.I- 39
2.2.4.2	Photoelasticity . . . . .	V.I- 41
2.2.4.3	Stress/strain transfer to the fibre from surrounding material . . . . .	V.I- 43
2.2.4.4	Stress/strain effect on signal phase . . . . .	V.I- 43
2.2.5	Temperature . . . . .	V.I- 44

---

2.2.5.1	Thermal expansion . . . . .	V.I- 45
2.2.5.2	Thermo-optic effect . . . . .	V.I- 45
2.2.5.3	Temperature effect on signal phase . . . . .	V.I- 46
2.2.6	Strain & temperature cross-sensitivity . . . . .	V.I- 46
2.2.6.1	Ideal and realistic sensing systems . . . . .	V.I- 47
2.2.7	Magneto-optics: Faraday effect and Faraday rotation . . . . .	V.I- 48
2.2.8	Structural/wave guiding and material anisotropy . . . . .	V.I- 50
2.2.8.1	Twisting-induced (torsion) birefringence . . . . .	V.I- 52
2.2.8.2	Bending-induced birefringence . . . . .	V.I- 52
2.2.8.3	Induced birefringence application . . . . .	V.I- 54
2.2.8.4	PMF . . . . .	V.I- 55
2.2.8.5	Polarisation Dependent Loss . . . . .	V.I- 56
2.2.9	Optical fibre sensing . . . . .	V.I- 57
2.3	Fibre Bragg gratings . . . . .	V.I- 62
2.3.1	Historical overview . . . . .	V.I- 63
2.3.2	Photorefractive sensitivity mechanism . . . . .	V.I- 65
2.3.3	FBGs as sensors . . . . .	V.I- 67
2.3.3.1	Temperature sensitivity . . . . .	V.I- 68
2.3.3.1.1	Nonlinearities and 2 <sup>nd</sup> order effects . . . . .	V.I- 68
2.3.3.2	Strain sensitivity . . . . .	V.I- 69
2.3.3.2.1	Contracted notation . . . . .	V.I- 70
2.3.3.3	Isotropic and Anisotropic FBGs . . . . .	V.I- 72
2.3.3.4	Structural Health Monitoring . . . . .	V.I- 75
2.4	Demodulation systems . . . . .	V.I- 78
2.4.1	Optical subsystem . . . . .	V.I- 78
2.4.1.1	Diffraction gratings . . . . .	V.I- 80
2.4.1.2	Interferometry . . . . .	V.I- 80
2.4.1.3	Fabry-Perót interferometer . . . . .	V.I- 81
2.4.1.4	Two-beam interferometry . . . . .	V.I- 82
2.4.2	Fourier transform spectroscopy . . . . .	V.I- 85
2.4.2.1	Phase noise in interferometer . . . . .	V.I- 86
2.4.2.2	Polarisation-sensitivity . . . . .	V.I- 87
2.4.2.3	Thermal drift . . . . .	V.I- 88
2.4.2.4	Zero-OPD point . . . . .	V.I- 88
2.4.3	Receiver unit . . . . .	V.I- 89
2.4.3.1	Detector noise . . . . .	V.I- 89
2.4.3.1.1	Benefit of two differenced outputs: CMRR . . . . .	V.I- 90
2.4.3.2	Digitising noise . . . . .	V.I- 91

---

---

2.4.3.3	Relative intensity noise . . . . .	V.I- 91
2.5	Summary of theoretical background in the context of experimental work . . . . .	V.I- 92
2.6	References . . . . .	V.I- 94
<b>3</b>	<b>SpectroBragg characterisation</b>	<b>V.I - 122</b>
3.1	Introduction . . . . .	V.I- 122
3.2	Theory . . . . .	V.I- 123
3.2.1	Diffraction gratings . . . . .	V.I- 123
3.2.1.1	Grating equation . . . . .	V.I- 124
3.2.1.2	Grating Dispersion . . . . .	V.I- 126
3.2.1.3	Grating Free spectral range . . . . .	V.I- 127
3.2.1.4	Conical diffraction grating mounting . . . . .	V.I- 127
3.2.1.5	Ghosts & grating accuracy . . . . .	V.I- 127
3.2.1.6	Evanescent orders . . . . .	V.I- 128
3.2.1.7	Grating efficiency . . . . .	V.I- 128
3.2.2	Diffraction grating spectrometers . . . . .	V.I- 129
3.2.2.1	Čzerny–Turner mount . . . . .	V.I- 131
3.2.3	Super–resolution by signal analysis for SpectroBragg . . . . .	V.I- 133
3.2.3.1	Centroid approach . . . . .	V.I- 133
3.2.3.2	Non–linear regression curve fitting . . . . .	V.I- 133
3.2.3.3	Cubic Spline interpolation . . . . .	V.I- 135
3.2.3.4	Thresholding and noise . . . . .	V.I- 136
3.2.3.5	Alternative data selection method . . . . .	V.I- 136
3.2.4	Depolarising signal . . . . .	V.I- 137
3.2.4.1	Lyot depolariser . . . . .	V.I- 137
3.2.4.2	Polarisation scrambler . . . . .	V.I- 138
3.2.4.3	Talbot Bands and Channelled Spectra . . . . .	V.I- 138
3.3	Experimental apparatus/setup . . . . .	V.I- 140
3.3.1	Tec5 Array . . . . .	V.I- 141
3.3.2	Newport plane diffraction grating . . . . .	V.I- 142
3.3.3	Concave mirrors . . . . .	V.I- 144
3.3.4	Prism . . . . .	V.I- 146
3.3.5	SpectroBragg Apparatus construction . . . . .	V.I- 147
3.4	Results/Discussion . . . . .	V.I- 150
3.4.1	SpectroBragg Construction . . . . .	V.I- 150
3.4.1.1	SpectroBragg assembly angles . . . . .	V.I- 150
3.4.1.2	SpectroBragg wavelength angles . . . . .	V.I- 151
3.4.1.3	Evanescent orders . . . . .	V.I- 152

---

---

3.4.2	SpectroBragg Signal processing . . . . .	V.I- 154
3.4.2.1	Choice of algorithm . . . . .	V.I- 154
3.4.2.2	SpectroBragg data capture . . . . .	V.I- 155
3.4.3	Preliminary SpectroBragg work . . . . .	V.I- 155
3.4.3.1	Sub-picometre system resolution . . . . .	V.I- 163
3.4.4	Comparison of the SpectroBragg to contemporary spectrometers	V.I- 166
3.5	Conclusion . . . . .	V.I- 166
3.6	References . . . . .	V.I- 167
<b>4</b>	<b>Strain characterisation of novel anisotropic FBGs</b>	<b>V.I - 171</b>
4.1	Introduction . . . . .	V.I- 171
4.2	Theory . . . . .	V.I- 173
4.2.1	Isotropic and anisotropic FBGs . . . . .	V.I- 173
4.2.2	Inscribing anisotropic FBGs in isotropic fibre . . . . .	V.I- 174
4.2.3	Use of FBGs as sensors . . . . .	V.I- 175
4.2.4	Signal processing considerations . . . . .	V.I- 177
4.3	Experimental apparatus/setup . . . . .	V.I- 179
4.3.1	Strain characterisation approach . . . . .	V.I- 179
4.3.2	Fibre attachment approaches . . . . .	V.I- 180
4.3.3	Strain approach and attachment . . . . .	V.I- 180
4.3.4	Glass solder for attachment of fibre . . . . .	V.I- 181
4.3.5	Construction of the fibre mount . . . . .	V.I- 182
4.3.6	Attaching the fibre under test . . . . .	V.I- 184
4.3.7	Laboratory environmental conditions . . . . .	V.I- 186
4.3.8	Cautions on soldering the attachment . . . . .	V.I- 189
4.3.9	Recoated isotropic FBGs . . . . .	V.I- 189
4.3.10	Quasi-static strain apparatus . . . . .	V.I- 190
4.3.11	Dynamic strain characterisation apparatus . . . . .	V.I- 191
4.3.12	Adding a temperature reference FBG . . . . .	V.I- 195
4.4	Results & Discussion . . . . .	V.I- 197
4.4.1	Quasi-static strain characterisation results . . . . .	V.I- 197
4.4.2	Dynamic strain characterisation results . . . . .	V.I- 199
4.4.3	Results of strain-temperature discrimination work . . . . .	V.I- 208
4.5	Conclusion . . . . .	V.I- 211
4.6	References . . . . .	V.I- 213
<b>5</b>	<b>Polarisation mitigation approaches</b>	<b>V.I - 218</b>
5.1	Introduction . . . . .	V.I- 218
5.2	Theory . . . . .	V.I- 219
5.2.1	Depolarisation & polarisation mitigation approaches . . . . .	V.I- 219

---

---

5.2.1.1	Fibre Lyot depolariser . . . . .	V.I - 219
5.2.2	Fixing linear SOP as alternative . . . . .	V.I - 220
5.2.3	PDL . . . . .	V.I - 226
5.2.3.1	PDL balancing approach . . . . .	V.I - 226
5.3	Experimental apparatus/setup . . . . .	V.I - 229
5.3.1	Apparatus for generating polarisation changes . . . . .	V.I - 229
5.3.2	Depolarisation schemes . . . . .	V.I - 230
5.3.2.1	Apparatus for Lyot depolariser approach . . . . .	V.I - 230
5.3.2.2	Stationary Mach–Zehnder interferometer depolarisation/polarisation fixer . . . . .	V.I - 230
5.3.2.3	Approach employing Lefèvre polarisation controller . . . . .	V.I - 230
5.3.2.4	Apparatus for Circulator/Faraday mirror approach . . . . .	V.I - 232
5.3.2.5	Apparatus for PDL balancing approach . . . . .	V.I - 233
5.3.3	The SpectroBragg spectrometer as a polarisation–sensitive detector scheme . . . . .	V.I - 234
5.4	Results/Discussion . . . . .	V.I - 234
5.4.1	Comment on detection systems . . . . .	V.I - 234
5.4.2	Representing polarisation . . . . .	V.I - 234
5.4.3	Polarisation changes introduced by rotating FC/APC connector . . . . .	V.I - 236
5.4.4	Effect of SOP changes upon the SpectroBragg . . . . .	V.I - 239
5.4.4.1	Phase noise and the SpectroBragg . . . . .	V.I - 241
5.4.4.2	Quantifying the effect of the polarisation mitigation schemes . . . . .	V.I - 246
5.4.5	Summary of results . . . . .	V.I - 249
5.4.5.1	Lefèvre controller approach . . . . .	V.I - 250
5.4.5.2	Circulator/Faraday Mirror approach . . . . .	V.I - 255
5.4.5.3	PDL balancing approach . . . . .	V.I - 257
5.5	Conclusion . . . . .	V.I - 258
5.6	References . . . . .	V.I - 260
<b>6</b>	<b><math>\pi</math>–shift Interferometry with HTT</b>	<b>V.I - 262</b>
6.1	Introduction . . . . .	V.I - 262
6.2	Theory . . . . .	V.I - 264
6.2.1	Phase noise . . . . .	V.I - 265
6.2.2	Phase–shift interferometry . . . . .	V.I - 267
6.2.3	Interferogram recalibration . . . . .	V.I - 269
6.2.4	Hilbert Transform technique . . . . .	V.I - 271
6.3	Experimental apparatus/setup . . . . .	V.I - 272
6.3.1	Apparatus . . . . .	V.I - 273

---

---

6.3.2	Fibre stretcher driving voltage . . . . .	V.I - 275
6.3.3	Temperature experiment . . . . .	V.I - 276
6.3.4	NewFocus receiver configuration . . . . .	V.I - 277
6.4	Results and Discussion . . . . .	V.I - 278
6.4.1	Results . . . . .	V.I - 278
6.4.2	Analysis of interferograms . . . . .	V.I - 279
6.4.3	Peak Wavelength determination using centroid . . . . .	V.I - 290
6.4.4	Peak Wavelength determination using HTT . . . . .	V.I - 295
6.4.4.1	Refinement of HTT calculated values . . . . .	V.I - 298
6.4.5	Effect of window length upon recovered values . . . . .	V.I - 298
6.4.6	Centroid approach, different fixed lengths . . . . .	V.I - 300
6.4.7	Hilbert transform technique, different fixed lengths . . . . .	V.I - 304
6.4.8	Discussion . . . . .	V.I - 308
6.4.9	Tuneable-filter and bandpass filter . . . . .	V.I - 309
6.4.10	Side-peak structure . . . . .	V.I - 309
6.4.11	Optical Delay line . . . . .	V.I - 311
6.4.12	Long patch lead of fibre . . . . .	V.I - 312
6.4.13	PPLN Oven . . . . .	V.I - 312
6.5	Conclusion . . . . .	V.I - 313
6.6	References . . . . .	V.I - 315
<b>7</b>	<b>Summary and Conclusions</b>	<b>V.I - 319</b>
7.1	Overview . . . . .	V.I - 319
7.1.1	Chapter objectives . . . . .	V.I - 319
7.2	Summary of chapters . . . . .	V.I - 320
7.2.1	Chapter 3, the assembly and characterisation of the Spectro- Bragg . . . . .	V.I - 322
7.2.2	Chapter 4, the strain characterisation of novel anisotropic FBGs	V.I - 323
7.2.3	Chapter 5, examination of polarisation mitigation approaches	V.I - 324
7.2.4	Chapter 6, the use of $\pi$ -shift interferometry with the HTT to recover weak FBG signals . . . . .	V.I - 325
7.3	Future investigations . . . . .	V.I - 328
7.4	References . . . . .	V.I - 330
	<b>Notation</b>	<b>V.I - 343</b>

---

# List of Figures

2.1	Effect of phase noise, $\Delta\nu$ , on intensity from an interferometer with relative delay $\tau_0$ . Phase noise converts frequency fluctuations into intensity fluctuations. This figure is after Derickson [12]. . . . .	V.I - 15
2.2	Illustration of optical fibre. (a) Guiding core surrounded by a lower index cladding. A protective jacket provides mechanical protection, ease of handling and some isolation from environmental contaminants. (b) Cross-section of fibre with a propagating guided ray, coloured blue, $\theta_{in} > \theta_c$ ; and, a partially reflected, non-propagating lost ray, coloured red, $\theta_{in} < \theta_c$ . The boundary wave, $\theta_{in} = \theta_c$ is not shown. . .	V.I - 22
2.3	Two dimensional projection of Si—O—Si tetrahedra as triangles, in red. Bonds in (a) thermodynamic equilibrium crystal arrangement (quartz); (b) glass amorphous arrangement (fused silica). Two continuous random networks, CRNs, are indicated by green and blue loops. Direction arrows indicate loop as opposed to meaningful direction. After figure 5.3 of [63]. . . . .	V.I - 26
2.4	Attenuation spectrum for Corning SMF-28e and LEAF fibres. The peaks about $\sim 1380$ nm are OH absorption peaks. . . . .	V.I - 30
2.5	Incident light, $E_{inc}(\mathbf{r})$ , forward (blue) and backward (red) scattered by refractive index fluctuation scatterers. The length $L_{coh}$ is characteristic of the fibre, and is the length over which the phase undergoes a random walk of $2\pi^2$ radians. . . . .	V.I - 32
2.6	Linear inter-relationships of Electric field, $\underline{\mathbf{E}}$ , Magnetic field, $\underline{\mathbf{H}}$ , Stress, $\underline{\underline{\sigma}}$ , and Temperature $T$ on an extended Heckmann diagram, after figures 1.1 and 1.2 of [66]. Table 2.1 (page V.I - 35) contains the legend for clarity. . . . .	V.I - 33
2.7	Linear cross-coupled relationships of Electric field, $\underline{\mathbf{E}}$ , Magnetic field, $\underline{\mathbf{H}}$ , Stress, $\underline{\underline{\sigma}}$ , and Temperature $T$ from the extended Heckmann diagram of figure 2.6. . . . .	V.I - 34
2.8	Stresses acting on three orthogonal surfaces (after figure 2.4 of [100], and figure 5.1 of [101]). . . . .	V.I - 38

2.9	Shear deformation of one surface (after figure 2.7 of [100]). . . . .	V.I- 38
2.10	Ellipsoid of the indices, indicatrix, for a uniaxial material (after [102, 103]). $n_{or}$ and $n_{ex}$ are the ordinary and extraordinary refractive indices, respectively. . . . .	V.I- 39
2.11	Retardation plate delaying $E'_y$ with respect to $E'_x$ by $\Delta\Phi_B$ . . . . .	V.I- 41
2.12	Primary effect (green) and a secondary effect (purple), or paths, on $\underline{\mathbf{P}}$ , from a stimulus at $T$ . . . . .	V.I- 46
2.13	Strain–temperature plots for two sensors: (a) the ideal response and (b) a more realistic response. After [128, 129]. . . . .	V.I- 48
2.14	Optical effects from material in magnetic field. The Faraday effect rotates the incident (blue) about the axis of propagation, parallel to $\underline{\mathbf{H}}_{stat}$ , upon transmission. The Kerr rotation effect occurs on reflection. The quadratic Cotton–Mouton effect dominates in the transverse direction to $\underline{\mathbf{H}}_{stat}$ (green), where the Faraday effect disappears. . . . .	V.I- 49
2.15	Induced strain by bending a fibre: (a) The straight fibre, as used in §F.2 (page V.II F-3), with the fibre (dashed) and neutral (red) strain axis co-linear, and with orthogonal refractive indices: $n_{0x}$ and $n_{0y}$ ; (b) the fibre twisted through an angle $\theta$ about the fibre axis, rotates orthogonal axes $x$ and $y$ to $x'$ and $y'$ ; (c) the curved fibre (of radius $R$ ) with the neutral strain axis shifted radially outwards in the azimuthal direction defined by the plane containing both axes. (a) and (c) after figure VI.21 of [45], (b) after figure 1(a) [135]. . . . .	V.I- 53
2.16	Three fibre loop Lefèvre polarisation controllers. The QWP, HWP and QWP loops are placed at angles $\theta_{QWP_1}$ , $\theta_{HWP}$ and $\theta_{QWP_2}$ . to achieve the desired change in SOP from $\underline{\mathbf{E}}$ to $\underline{\mathbf{E}'}$ . After figure 9.71 [145], and figure 3(b) [144]. . . . .	V.I- 54
2.17	PMF types: Bow-tie, PANDA and elliptical jacket. After figure 8.7 [147]. . . . .	V.I- 56
2.18	Schematic FBG operation:(a) Sinusoidal refractive index variation, with period $\Lambda$ , (b) Longitudinal section of fibre with planes of $n_{eff}$ , (c) Phase matching condition matches $\underline{\mathbf{B}}$ , with distributed partial reflection from each plane $\underline{\mathbf{C}}$ to give reflected signal $\underline{\mathbf{D}}$ . . . . .	V.I- 62
2.19	FBG inscription techniques; (a) Interferometric UV inscription using glancing reflection from mirrors to generate interference pattern, (b) Diffraction grating inscription using a phase mask to produce $\pm 1$ orders which interfere. . . . .	V.I- 64
2.20	Graph showing the strong absorption peak of Ge–doped fused silica (after Adrian Dragomir <i>et al.</i> [213]). . . . .	V.I- 65

---

2.21	Diagram of different strains in material due to presence of sensors. The value $\underline{\underline{\epsilon}}_{\sigma_{\text{far}}}$ , is the intended measurand. The presence of the sensor causes a redistribution of stress (and hence strain), and in the vicinity of the fibre $\underline{\underline{\epsilon}}_{\sigma_{\text{near}}}$ is experienced. The cladding experiences $\underline{\underline{\epsilon}}_{\sigma_{\text{cl}}}$ which produces $\underline{\underline{\epsilon}}_{\sigma_{\text{FBG}}}$ , which is measured (after Van Steenkiste and Springer [96]). . . . .	V.I- 71
2.22	Writing plane asymmetry arising due to the fibre axis not coinciding with the focal plane (zero-OPD) of the inscribing UV radiation. . . .	V.I- 73
2.23	Uni-lateral writing asymmetry arising due to the absorption of the inscribing UV radiation as the UV flux traverses the fibre. . . . .	V.I- 73
2.24	Simulated inscription in PM fibre: two equal strength Gaussian FBG spectra are shifted relative to each other by $B_{\text{PMF}}$ , with one FBG at 1550 nm, and the other at 1549.9 nm. The resultant sum spectrum is shown in red, a flat-top profile. . . . .	V.I- 74
2.25	Intensity based FBG demodulation via (a) Edge filter, (b) scanning tuneable cavity filter, and (c) resonant cavity filter. After figure 8 of [193]. . . . .	V.I- 79
2.26	Fabry-Perót etalon where the incident beam is multiply reflected within the cavity, coherently superposing upon itself within its coherence length. . . . .	V.I- 81
2.27	Michelson interferometer providing two $\pi$ -shifted outputs. (a) The bulk optic Michelson and (b) the all-fibre equivalent. . . . .	V.I- 84
3.1	Diffraction grating orders, after figure 2.8(a) of [4] . . . . .	V.I- 125
3.2	Schematic of Čzerny-Turner for SpectroBragg. The reflected signal from the FBGs is collimated by the first mirror, diffracted onto the focusing mirror which concentrates the radiation onto the InGaAs array.	V.I- 130
3.3	Selecting angles to minimise aberrations in a Čzerny-Turner spectrometer. $R_1$ and $R_2$ are the radii of mirrors $M_1$ and $M_2$ , respectively.	V.I- 132
3.4	Talbot band effect: A phase delay is inserted into part of a beam illuminating a diffraction grating, e.g. by a glass slide, of thickness $d$ . The phase delay introduced between the two paths combines with the phase delay introduced by the diffraction grating to shift the relative phase difference by, (a) integer, $m$ , multiples of $\pm\pi$ , i.e. constructive interference; and (b) $\pm m\pi + \frac{\pi}{2}$ , i.e. destructive interference. (After Jahns <i>et al.</i> [35].) . . . . .	V.I- 139
3.5	InGaAs array mounting with USB controller unit. Inset shows array in housing. . . . .	V.I- 142

---

- 
- 3.6 The distance between the diffraction grating and  $M_2$ ,  $r$ , shown when plotted against diffraction grating grooves/mm and diffracted angle,  $\theta_d$ . The value of  $r$  is obtained by rearranging equation (K.27) (page V.II K-15) in terms of  $r$ . The constant blue area denotes complex (evanescent) diffracted angles. To obtain a smaller  $\theta_d$  a smaller number of grooves/mm is desirable. . . . . V.I- 143
- 3.7 Diffraction Grating polarisation efficiency curves for telecomms region, after Newport efficiency curves for 53\*-175H grating. ([http://gratings.newport.com/products/efficiency/effFrame.asp?sku=020\\$|53\\*-175H](http://gratings.newport.com/products/efficiency/effFrame.asp?sku=020$|53*-175H)) . . . . . V.I- 143
- 3.8 Block diagram of the SpectroBragg plan layout. The *FC/PC holder & mount* and *mirror*  $M_1$  are fixed relative to each other by the focal length,  $f_{M_1}$ , and angle  $\alpha$  (defined in figure 3.3, page V.I - 132). The *mirror*  $M_2$  and *InGaAs array* are fixed relative to each other by the focal length,  $f_{M_2}$ , and the angle  $\beta$  (figure 3.3). The diffraction grating has freedom to intercept the reflection from  $M_1$  along its path.  $M_2$  is restricted in the distance from the diffraction grating. The one area of overlap is highlighted by cross-hatching. . . . . V.I- 145
- 3.9 Schematic layout of the Čzerny–Turner spectrometer arrangement, due to diffracted angle of 1550 nm radiation. The numbers are as in figure 3.10. . . . . V.I- 148
- 3.10 The assembled SpectroBragg apparatus, emphasised against the associated apparatus.
- 1: AMA025/m platform with HFB003 FC/PC fibre holder,
  - 2: Collimating mirror KS2D,
  - 3: Diffraction grating mount,
  - 4: Focusing mirror KS2D,
  - 5: Photodiode array mount,
  - 6: KL02 kinematic positioner,
  - 7: Prism mount,
  - 8: Prism. . . . . V.I- 149
- 3.11  $\beta$  evaluated using the Rosendahl  $\cos^3$  equation, (3.18) (page V.I - 132), for four values of  $\alpha = \frac{\pi}{100}, \frac{\pi}{50}, \frac{\pi}{10}, \frac{\pi}{6}$ . . . . . V.I- 151
- 3.12 (a) Approximate graphical representation of the collimated spot overlap with the diffraction grating area. (b) Representation of overlap of the focusing mirror and the propagating diffracted first order,  $m = 1$  spots for wavelengths 1535 nm, 1550 nm and 1567 nm at the respective diffracted angles. . . . . V.I- 152
-

- 
- 3.13 Plot of propagating and evanescent diffracted angle against incident angle, for first order,  $m = 1$ . Diffraction gratings with 750 lines/mm and 1100 lines/mm with  $\lambda = 1550$  nm. . . . . V.I- 153
- 3.14 Plot of linear dispersion against incident angle, for first order,  $m = 1$ . Diffraction gratings with 750 lines/mm and 1100 lines/mm with  $\lambda = 1550$  nm. . . . . V.I- 154
- 3.15 Schematic arrangement to test temporal stability of the SpectroBragg and characterise linearity of local response. . . . . V.I- 156
- 3.16 Two telecomms–band lasers were used for the SpectroBragg calibration, 1534 nm and 1566 nm. Inset shows the different background voltages from the interlaced 256 arrays, for channel numbers 400 – 439.V.I- 156
- 3.17 SpectroBragg stability test, laser tuned from 1566.13nm to 1566.18nm in 10 pm steps. . . . . V.I- 158
- 3.18 SpectroBragg stability test, the reference traces of the 1534.08 nm laser. The colours correspond to traces in figure 3.17. . . . . V.I- 158
- 3.19 1566.13nm to 1566.18nm recalibrated by subtraction of corresponding 1534.08 nm data. . . . . V.I- 159
- 3.20 Recalibrated 1566.13 nm to 1566.18 nm data averaged, with corresponding standard deviations against set wavelength values. The oscillation about the linear fit is possibly as a result of backlash in the tuneable laser tuning dial. . . . . V.I- 160
- 3.21 Two telecomms lasers for the SpectroBragg calibration, 1534 nm and 1549 nm. Inset shows the different background voltages from the interlaced 256 arrays, for channel numbers 400 – 439. . . . . V.I- 161
- 3.22 1549.52nm to 1549.61nm recalibrated by subtraction of corresponding 1534.13 nm data. . . . . V.I- 161
- 3.23 Recalibrated 1549.52 nm to 1549.61 nm data averaged, with corresponding standard deviations against set wavelength values. . . . . V.I- 162
- 3.24 Schematic arrangement to determine the SpectroBragg sub–picometre resolution capability. . . . . V.I- 164
- 3.25 Strain steps of  $0.5 \mu\epsilon$  every 5 seconds. . . . . V.I- 164
- 3.26 Magnified view of figure 3.25, with differences  $(i - (i - 1))$  for index  $i$ . V.I- 165
- 4.1 Example profile of anisotropic FBG profile. The side lobe is not representative of the process and was specifically requested. Note the flat–top profile. . . . . V.I- 176
- 4.2 Typical profile of standard FBG. Note the Gaussian profile. . . . . V.I- 176
-

---

4.3	Plot of Gaussian( $\gamma = 2$ ) and Super-Gaussian ( $\gamma = 8$ ) profiles generated in Matlab. The generating function is $I(x, \sigma, \mu, \gamma) = Ae^{[-(\frac{x-\mu}{2\sigma})^\gamma]}$ , where $A$ is the maximum value of the function, $\mu$ is the mean value, $\sigma$ is the standard deviation and $\gamma$ is the super-Gaussian power $> 2$ [27]. $\gamma$ is related to the rapidity of the transition from maximum intensity to minimum intensity. . . . .	V.I- 179
4.4	Oz Optics circular glass solder preforms. . . . .	V.I- 181
4.5	Oz Optics oval ribbon glass solder preforms. . . . .	V.I- 181
4.6	Broken sections of ribbon solder facilitated rapid attachment of the fibre. . . . .	V.I- 182
4.7	Mount for soldering fibres. (a) Exploded view of fibre mount (parts CL5 clamp and BA2 base are Thorlabs catalogue labels); (b) Assembled mount, slide held by M6 bolt and rubber clamp; (c) Front clamp removed to show soldered fibre. . . . .	V.I- 183
4.8	Image of completed fibre mount, with two fibres soldered. . . . .	V.I- 184
4.9	Replacing the perspex cylinder with two half-cylinders. The two half-cylinders enabled faster replacing of broken fibres and proved safer for fibre handling. Hinges were not used. The increase on weight on the hinged side when in the open position would require extra bracing on the lower half to hold the weight. . . . .	V.I- 185
4.10	(a) Strain rig in elevation and plan view, (b) Isometric view of translation stage with mount, (c) Isometric view of perspex tube with RS2P4/M pillar posts, and aluminium block supports. . . . .	V.I- 188
4.11	Laser2000 supplied isotropic FBG, showing detail of the original and recoated section of fibre. . . . .	V.I- 189
4.12	Laser2000 supplied isotropic FBG, showing the non-uniformity of the recoating. . . . .	V.I- 189
4.13	Schematic diagram of apparatus used for EWOFS work. . . . .	V.I- 191
4.14	Schematic diagram of apparatus used for IEEE sensors paper work. . . . .	V.I- 192
4.15	Temporal response of co-anchored FBGs. Applying low tension to the FBGs during soldering prevents significant differences in slack. . . . .	V.I- 193
4.16	Image of the solder mount with two FBGs soldered. . . . .	V.I- 194
4.17	Close up image of soldered fibres. . . . .	V.I- 194
4.18	Modified Thorlabs PV40 oven placed within the perspex cylinder. . . . .	V.I- 195
4.19	Two FBGs to undergo applied strain with temperature reference placed in close proximity. . . . .	V.I- 195

---

---

4.20	Modified <i>Thorlabs</i> PV40 oven. (a) Schematic of PV40 oven (power cord not shown); (b) Exploded view of PV40, indicating the disassembly required; (c) End-plates replaced with Thermoflex foam insulation, adhered to PV40 top and lower sections by double sided adhesive, and a parallelepiped of insulation foam to occupy the cavity above the fibres where the PPLN crystal would sit; (d) modified PV40 reassembled. . . . .	V.I - 196
4.21	Strain response of anisotropic FBG. Slope of fit to data is $1.2601 \pm 0.00013 \text{ pm}/\mu\epsilon$ ( $0.8135 \times 10^{-6} \mu\epsilon^{-1}$ ). Also shown is the literature value ( $0.78 \times 10^{-6} \mu\epsilon^{-1}$ ) slope [9]. . . . .	V.I - 198
4.22	Residual of linear fit to data from 4.21. . . . .	V.I - 198
4.23	Apparent preservation of spectral profile, with original data inset. The inset shows the FBG reflection spectra for the anisotropic FBG at rest, with $340 \text{ m}\epsilon$ and with $680 \text{ m}\epsilon$ . The main figure shows the spectral profiles offset by their respective calculated centroids. The high degree of overlap suggests good spectral profile preservation. . . . .	V.I - 199
4.24	Example spectrum from the SpectroBragg spectrometer. The spectrometer's InGaAs array has 512 elements, covering approximately a $70 \text{ nm}$ window. Shown in the figure are Laser2000 telecomms FBGs at $1534 \text{ nm}$ and $1566 \text{ nm}$ ; and an anisotropic FBG at $1549 \text{ nm}$ . . . . .	V.I - 200
4.25	Calculated centroid for the anisotropic and isotropic FBGs under strain. The stability of the centroid value demonstrates the stability of the environmental enclosure. Inset is an example of low scale noise, replicated in time and profile by both FBGs. . . . .	V.I - 201
4.26	Plot of strain response for the anisotropic FBG over $0 - 265 \mu\epsilon$ . Strain response is $\sim 1.17 \pm 0.03 \text{ pm}/\mu\epsilon$ ( $0.75 \times 10^{-6} \mu\epsilon^{-1}$ ). The corresponding strain response of the isotropic FBG literature value ( $0.78 \times 10^{-6} \mu\epsilon^{-1}$ ) is also plotted [9]. . . . .	V.I - 202
4.27	Plot of residual to linear fit for anisotropic FBG. Note the double dipped 'w' shape of the residual, which is absent from the residual to the fit for the isotropic FBG, figure 4.29. . . . .	V.I - 202
4.28	Plot of strain response for the isotropic FBG over $0 - 265 \mu\epsilon$ . Strain response is $\sim 1.13 \pm 0.02 \text{ pm}/\mu\epsilon$ ( $0.74 \times 10^{-6} \mu\epsilon^{-1}$ ). The corresponding strain response of the isotropic FBG literature value ( $0.78 \times 10^{-6} \mu\epsilon^{-1}$ ) is also plotted [9]. . . . .	V.I - 203
4.29	Plot of residual to linear fit for isotropic FBG. . . . .	V.I - 203

---

4.30	Plot of strain response for the temperature reference isotropic FBG. Strain response is $\sim -0.013 \text{ pm}/\mu\epsilon$ ( $-0.0082 \times 10^{-6} \mu\epsilon^{-1}$ ), equivalent to a maximum temperature difference of $0.37^\circ\text{C}$ using the temperature response value of $10.7 \text{ pm}^\circ\text{C}^{-1}$ [2]. Inset shows the isotropic FBG literature strain response value ( $0.78 \times 10^{-6} \mu\epsilon^{-1}$ [9]). . . . .	V.I - 205
4.31	Plot of residual to linear fit for isotropic FBG. . . . .	V.I - 205
4.32	Plot showing every $50^{\text{th}}$ point in the cross-correlations of strained spectra with the unstrained spectrum, obtained by the OSA. The maxima indicate the position of best correlation. . . . .	V.I - 207
4.33	Plot showing every $4^{\text{th}}$ point of strained FBG spectra, offset by centroids. The zero-strain spectra is a continuous blue line, with the strained spectra overlaid. . . . .	V.I - 207
4.34	Plot of the centroid response to temperature changes of the three FBGs: (a) Isotropic (strain); (b) Anisotropic (strain); and (c) Isotropic (temperature reference). . . . .	V.I - 209
4.35	Plot of the spectral bandwidth response to temperature changes of three FBGs: (a) Isotropic (strain); (b) Anisotropic (strain); and (c) Isotropic (temperature reference). . . . .	V.I - 210
4.36	Plot of the percentage change in spectral bandwidth of three FBGs in response to temperature changes. . . . .	V.I - 211
5.1	Fibre Lyot pseudo-depolariser. The input SOP, $S_{in}$ , experiences a wavelength dependent rotation to produce $S_{out}$ , which occupies all orthogonal directions to the direction of propagation. . . . .	V.I - 220
5.2	Fixed output SOP via polarising stationary Mach-Zehnder interferometer. Input $\underline{S}_{in}$ is split into orthogonal linear SOPs $\underline{S}_{\parallel}$ and $\underline{S}_{\perp}$ . The half-waveplate, HWP, acts as a rotator to rotate $\underline{S}_{\perp}$ into $\underline{S}'_{\parallel}$ , in the same orientation as $\underline{S}_{\parallel}$ . $\underline{S}_{\parallel}$ and $\underline{S}'_{\parallel}$ are superposed to produce $\underline{S}_{out}$ . . . . .	V.I - 221
5.3	PDL compensation scheme using variable attenuator to balance losses in orthogonal SOPs. . . . .	V.I - 227
5.4	Balanced amplitudes in orthogonal components restricts SOPs to $S_2S_3$ great circle (in red). The term $\phi_{pr}$ , the phase retardation between the orthogonal components, is zero at $\pm S_2$ . . . . .	V.I - 228
5.5	Method for generation of polarisation changes to apparatus, achieved by rotating the FC/APC connector. . . . .	V.I - 229
5.6	Apparatus using the Lyot depolariser. . . . .	V.I - 230
5.7	Apparatus using the Lefèvre polarisation controller to change SOP to the orthogonal SOP, matching the SOP in the other arm, which is then superposed at the output. . . . .	V.I - 231

---

5.8	Apparatus consisting of polarising beam-splitter and balanced receiver, measures $S_1$ . . . . .	V.I - 232
5.9	Apparatus using Faraday Mirror and circulator to change SOP to the orthogonal SOP, matching the SOP in the other arm, which is then superposed at the output. . . . .	V.I - 232
5.10	Matching PDL in both SOP using variable attenuator. The output has equal intensities from both SOP, reducing intensity fluctuations due to polarisation changes. . . . .	V.I - 233
5.11	Poincaré sphere showing the angle, in blue, between data at $t_1$ and $t_2$ . . . . .	V.I - 235
5.12	Poincaré sphere of the SOPs produced by fibre rotation of anisotropic FBG signal. . . . .	V.I - 237
5.13	Poincaré sphere of the SOPs produced by fibre rotation of isotropic FBG signal. . . . .	V.I - 237
5.14	Poincaré sphere of the SOPs produced by fibre rotation of isotropic FBG signal, with profile rotated with respect to figure 5.13. . . . .	V.I - 238
5.15	Plot of the angle $\theta_\Delta$ between SOPs produced by fibre rotation of (a) the anisotropic FBG signal (figure 5.13) and (b) the isotropic FBG signal (figure 5.12). . . . .	V.I - 239
5.16	Demonstrating the sensitivity of the stationary Mach-Zehnder interferometer based systems to interference noise produced by vibrations at the ODL. Arrows indicate sections of no added polarisation noise. (a) shows the dihedral angle between subsequent SOPs and (b) shows the corresponding output of the SpectroBragg. . . . .	V.I - 242
5.17	The FFT of the SpectroBragg data with polarisation and interference noise. . . . .	V.I - 243
5.18	Plot of the standard deviation of the SpectroBragg data after FFT filtering of low frequency components. . . . .	V.I - 244
5.19	(a) shows the original SpectroBragg data (from figure 5.16) and (b) shows the filtered SpectroBragg data. . . . .	V.I - 244
5.20	Plot of ambiguous separation of low and high frequency components using the approach used to produce figure 5.18. . . . .	V.I - 245
5.22	Anisotropic FBG values for unfiltered and FFT filtered SpectroBragg data showing the intensity standard deviations for the applied SOP changes and background, from table 5.1(b) (page V.I - 248). . . . .	V.I - 251
5.23	Anisotropic FBG values for unfiltered and FFT filtered Polarimeter data showing the intensity standard deviations for the applied SOP changes and background, from table 5.1(b) (page V.I - 248). . . . .	V.I - 251

---

- 
- 5.24 Isotropic FBG values for unfiltered and FFT filtered SpectroBragg data showing the intensity standard deviations for the applied SOP changes and background, from table 5.1(b) (page V.I - 248). Unfiltered Circ. /FM value, 2.07, is off figure scale and listed. . . . . V.I - 252
- 5.25 Isotropic FBG values for unfiltered and FFT filtered Polarimeter data showing the intensity standard deviations for the applied SOP changes and background, from table 5.1(b) (page V.I - 248). . . . . V.I - 252
- 5.26 Anisotropic FBG values for unfiltered and FFT filtered SpectroBragg data showing the centroid standard deviations for the applied SOP changes and background, from table 5.1(c) (page V.I - 248). Anisotropic FBG unfiltered & FFT filtered Lyot values, 59.11 nm & 47.55 nm, are off figure scale and listed. . . . . V.I - 254
- 5.27 Isotropic FBG values for unfiltered and FFT filtered SpectroBragg data showing the centroid standard deviations for the applied SOP changes and background, from table 5.1(c) (page V.I - 248). . . . . V.I - 254
- 5.28 Ratios of the FFT filtered SpectroBragg  $\sigma_{\text{int.}}$  values (figures 5.22 (page V.I - 251) & 5.24 (page V.I - 252) to the FFT filtered Polarimeter  $\sigma_{\text{int.}}$  values (figures 5.23 (page V.I - 251) & 5.25 (page V.I - 252)) for the anisotropic and isotropic FBGs. . . . . V.I - 259
- 6.1 (a) Distributed sensing: the sensors are located distances from each other; (b) Remote sensing: The sensors are located closer together, but at a distance from the source and detector. . . . . V.I - 262
- 6.2 All-fibre three-output phase-shift interferometer arrangement. A  $3 \times 3$  coupler splits the incident light into three arms, each with 33% of the incident light. Upon reflection, the light exits the  $3 \times 3$  coupler and the  $\pi/3$  phase shifts are obtained. . . . . V.I - 269

6.3	Schematic arrangement of $\pi$ -shift apparatus. One FBG is placed in a Thorlabs PV40 PPLN oven where the temperature is changed to provide a changing signal. The FBGs are illuminated by a SLED, and the reflected FBG signals are passed with a high-coherence signal from a Thorlabs telecomms laser through $\sim 20$ km of Corning dispersion-shifted fibre. The signals are demodulated by an all-fibre interferometer based upon a Sifam $2 \times 2$ 50:50 coupler. A CIRC piezo-electric unit provides the changing optical path length in the scanning arm. The zero-OPD, balance point, of the interferometer is adjusted as necessary by an Oz Optics ODL650MC optical delay line. Newport Faraday mirrors compensate for birefringence induced difference in path length by reflecting light into the orthogonal state. The two-output or $\pi$ -shifted interferograms are captured by a NewFocus balanced receiver. The high-coherence reference signal is isolated by an Oz Optics tuneable filter or a JDS Uniphase (JDSU) bandpass filter and captured by a NewFocus receiver. . . . .	V.I - 272
6.4	Schematic arrangement of single receiver apparatus. The apparatus is identical to that shown in figure 6.3 except that the $\pi$ -shifted interferograms are not captured, instead only a single interferogram is captured by a NewFocus receiver. . . . .	V.I - 274
6.5	Sine and triangular waveforms, with limit lines at 20% and at 80%. . . . .	V.I - 275
6.6	Quintile histogram of waveforms shown in figure 6.5. . . . .	V.I - 276
6.7	Number of successfully retrieved separate interferograms for each temperature step. . . . .	V.I - 278
6.8	The spectra to be recovered, captured by an Ando AQ6317B OSA over 10 m of SMF-28 fibre. This spectrum was captured by an Ando AQ6317B optical spectrum analyser over 10 m of fibre, using 100 averages. Inset is an expanded view of the FBG spectra. . . . .	V.I - 279
6.9	Flowchart of the interferogram recalibration process. . . . .	V.I - 281
6.10	Flowchart of the Hilbert transform technique. . . . .	V.I - 282
6.11	The time base of a sample analytic signal with a linear fit. . . . .	V.I - 283
6.12	Residual to the linear fit to the sample interferogram's analytic signal. . . . .	V.I - 283
6.13	The spectrum of the captured reference interferogram. The non-linear sampling of the interferogram spreads the signal over several wavelengths. . . . .	V.I - 284
6.14	The recalibrated reference spectrum, which restores the spectral profile of the laser. The linear time base used permits the recalibration of the signal interferogram. Inset shows detail of laser base. . . . .	V.I - 284

---

6.15	Magnified view of the spectrum of the recalibrated signal spectrum of the FBG sensors. Side-peaks are to be observed symmetrically about the laser peak. The FBG signals locations are +3 and +5. . . . .	V.I - 285
6.16	Subset of the recalibrated spectrum used to suppress side-peaks. . . . .	V.I - 287
6.17	Recalibrated FBG sensor spectrum to suppress side-peak structure. The same view as shown in figure 6.15, with the same markers in place. . . . .	V.I - 287
6.18	Flowchart of the spectral side-peak suppression process. . . . .	V.I - 288
6.19	The recovered FBG spectra, using the two-output, $\pi$ -shifted interferogram and the single-output interferogram, (compare to figure 6.8 (page V.I - 279)). . . . .	V.I - 290
6.20	Centroid calculated wavelengths for the temperature signal FBG, using windows $2n_w + 1$ wide, for $n_w = 2, 3, 4$ . . . . .	V.I - 292
6.21	Centroid calculated wavelengths for the reference sensor FBG, using windows $2n_w + 1$ wide, for $n_w = 2, 3, 4$ . . . . .	V.I - 292
6.22	Temperature response of the sensor FBG, corrected against the reference FBG, to one standard deviation from centroid calculations. A linear and a quadratic fit are shown. Also plotted are the values obtained from using the literature value of $6.67 \times 10^{-6} \text{ }^\circ\text{C}^{-1}$ [41]. . . . .	V.I - 294
6.23	Plot of residuals to the fits to the data. . . . .	V.I - 294
6.24	Residual to the linear fit of the unwrapped phase of the high-coherence reference laser. . . . .	V.I - 296
6.25	Residual to the linear fit of the unwrapped phase of the sensor FBG. The black lines delimit a central part of the residuals, say 10%–80%, which has the smallest deviation from linearity . . . . .	V.I - 296
6.26	Temperature response of the sensor FBG, to one standard deviation, with windows $2n_w + 1$ wide, for $n_w = 4, 5, 6$ . A linear and a quadratic fit are shown. Also plotted are the values obtained from using the literature value of $6.67 \times 10^{-6} \text{ }^\circ\text{C}^{-1}$ [41]. . . . .	V.I - 297
6.27	Residual of the HTT of the sensor FBG for data in figure 6.26. . . . .	V.I - 297
6.28	Temperature response of the sensor FBG, to one standard deviation, using the HTT of the central portion of the unwrapped phases. . . . .	V.I - 299
6.29	Residual of the ratio of the HTT of the central portion of the unwrapped phases of the sensor FBG for data in figure 6.28. . . . .	V.I - 299
6.30	Centroid calculated wavelengths for the temperature signal FBG, using windows $2n_w + 1$ wide, for $n_w = 2, 3, 4$ . . . . .	V.I - 302
6.31	Centroid calculated wavelengths for the reference sensor FBG, using windows $2n_w + 1$ wide, for $n_w = 2, 3, 4$ . . . . .	V.I - 302

---

- 
- 6.32 Temperature response of the sensor FBG, corrected against the reference FBG, to one standard deviation from centroid calculations. A linear and a quadratic fit are shown. Also plotted are the values obtained from using the literature value of  $6.67 \times 10^{-6} \text{ }^\circ\text{C}^{-1}$  [41]. . . . V.I- 303
- 6.33 Plot of residuals to the fits to the data. . . . . V.I- 303
- 6.34 Centroid calculated wavelengths for the temperature signal FBG, using windows  $2n_w + 1$  wide, for interferogram length  $n_i = 4$ . . . . . V.I- 306
- 6.35 Centroid calculated wavelengths for the reference sensor FBG, using windows  $2n_w + 1$  wide, for interferogram length  $n_i = 4$ . . . . . V.I- 306
- 6.36 Temperature response of the sensor FBG, corrected against the reference FBG, to one standard deviation from centroid calculations. A linear and a quadratic fit are shown. Also plotted are the values obtained from using the literature value of  $6.67 \times 10^{-6} \text{ }^\circ\text{C}^{-1}$  [41]. . . . V.I- 307
- 6.37 Plot of residuals to the fits to the data. . . . . V.I- 307
- 6.38 Side-peak structure using different fibre stretcher scan rate (4 Hz as opposed to 10 Hz for data reported). Telecomms laser at 1551.52 nm. Side-peaks have not had second pass to reduce their magnitude in this plot. . . . . V.I- 310
- 6.39 Side-peaks obtained from a bulk interferometer (after O'Mahoney [9]) using a HeNe 632nm and the telecomms 1550nm onto a single receiver. The scan rate  $v_1$  was 10 kHz, and  $v_2$  was 20 kHz. . . . . V.I- 311

# List of Tables

2.1	Legend for variables in figure 2.6 (page V.I - 33). . . . .	V.I - 35
3.1	Newport specifications for SpectroBragg diffraction grating. . . . .	V.I - 144
3.2	Thorlabs specifications for SpectroBragg Mirrors. . . . .	V.I - 146
3.3	Mean calculated centroid wavelength, standard deviation and slope of linear fit to channel number against time plots for set wavelength data shown in figure 3.20. . . . .	V.I - 159
3.4	Mean calculated centroid wavelength, standard deviation and slope to linear fit of set wavelength data shown in figure 3.23. . . . .	V.I - 162
3.5	Comparison of the SpectroBragg spectrometer performance against Solar Laser Systems, Belarus, and Yokogawa, Japan. (1) Assuming 1 FBG per nm spacing. . . . .	V.I - 166
4.1	Laser2000 FBG specifications. . . . .	V.I - 190
4.2	Strain response values for the quasi-static and dynamic anisotropic FBG strain response experiments, with actual and idealised (i.e. would return literature value) strain steps. . . . .	V.I - 204
5.1	Combined summary of <b>(a)</b> correlation coefficient, $\rho_{\text{Int.}}$ , values for correlation between captured SpectroBragg intensity and calculated $\underline{\mathbf{S}}_{\text{SB}}$ ; <b>(b)</b> the FFT filtered and unfiltered (in parentheses) normalised standard deviations, $\sigma_{\text{Int.}}$ , for both SpectroBragg and polarimeter data; <b>(c)</b> the FFT filtered and unfiltered (in parentheses) standard deviation of centroid calculated wavelength, $\sigma_{\lambda_B}$ , for the anisotropic and isotropic FBGs. The values are for the data with applied SOP changes and without applied SOP changes (i.e. background); <b>(d)</b> the SpectroBragg intensity-centroid $\lambda_B$ correlation coefficient, $\rho_{\lambda_B}$ , as a measure of intensity's influence on $\lambda_B$ . . . . .	V.I - 248
6.1	The peak location of side-peaks shown in figure 6.15; The differences of these peaks from 1550 nm, ' $\Delta\lambda_{\text{peaks}}$ '; and the relative difference of each peak from its neighbouring peak, 'peak differences'. . . . .	V.I - 285

---

6.2	Average and standard deviation of captured linear power levels, as a percentage of the laser power, for the $\pi$ -shifted and single-output interferograms. The scaled total averaged noise level, $\text{noise}_{\text{total}}$ , and run-averaged noise level, $\text{noise}_{\text{ra}}$ , are presented, for comparison. . . . .	V.I - 289
6.3	Difference in power levels (dB) between the FBG peak levels and the total noise level, $\text{noise}_{\text{total}}$ , and run-averaged noise level, $\text{noise}_{\text{ra}}$ , for the $\pi$ -shifted and single-output interferograms. . . . .	V.I - 289
6.4	Table of normalised FBG thermal responses, $\frac{1}{\lambda_B} \frac{\delta\lambda_B}{\delta T}$ , for centroid windows of width = $2n_w + 1$ , with $n_w = 2, 3, 4$ and respective norm of residuals (pm) of linear fit for the temperature and reference FBGs shown in parentheses. . . . .	V.I - 291
6.5	Table of HTT approach FBG thermal responses, $\frac{1}{\lambda_B} \frac{\delta\lambda_B}{\delta T}$ , for Hamming windows of width = $2n_w + 1$ , with $n_w = 2, 3, 4$ and respective norm of residuals (pm) of linear fit for the temperature and reference FBGs. V.I -	298
6.6	Table of centroid approach FBG thermal responses, $\frac{1}{\lambda_B} \frac{\delta\lambda_B}{\delta T}$ , for rectangular windows of width = $2n_w + 1$ , with $n_w = 2, 3, 4$ and respective norm of residuals (pm) of linear fit for the temperature and reference FBGs. . . . .	V.I - 301
6.7	Table of temperature step size, beginning and final temperature (i.e. temperature range) which would return the centroid approach calculated FBG $\lambda_B$ values using the literature value of the normalised temperature response slope, $\frac{1}{\lambda_B} \frac{\delta\lambda_B}{\delta T} = 6.67(\times 10^{-6} \text{ } ^\circ\text{C}^{-1})$ , for $n_w = 2, 3, 4$ . V.I -	304
6.8	Table of HTT approach FBG thermal responses, $\frac{1}{\lambda_B} \frac{\delta\lambda_B}{\delta T}$ , for Hamming windows of width = $2n_w + 1$ , with $n_w = 13, 14, 15$ and respective norm of residuals (pm) of linear fit for the temperature and reference FBGs. V.I -	308
6.9	Table of temperature step size, beginning and final temperature (i.e. temperature range) which would give the HTT approach calculated FBG $\lambda_B$ values using the literature value of the normalised temperature response slope, $\frac{1}{\lambda_B} \frac{\delta\lambda_B}{\delta T} = 6.67(\times 10^{-6} \text{ } ^\circ\text{C}^{-1})$ , for $n_w = 13, 14, 15$ . . V.I -	308
7.1	After table 1 of [13]. Indication of modification of the <i>spectral density</i> , $S_W(\mathbf{r}, \omega)$ , <i>spectral DOP</i> , $\mathcal{P}_W(\mathbf{r}, \omega)$ , and <i>spectral DOC</i> , $\eta_W(\mathbf{r}_1, \mathbf{r}_2, \omega)$ , for types of devices used in this thesis, e.g. <i>polariser</i> , <i>retarder</i> , <i>rotator</i> and <i>absorber</i> , <i>focusing mirror</i> , <i>diffraction grating</i> , and <i>scattering medium</i> . . . . .	V.I - 321

---

# Chapter 1

## Introduction

---

James Clerk Maxwell combined the electric and magnetic fields under a single formalism, electromagnetism. Light usually refers to the visible range of the electromagnetic spectrum, between  $\sim 400 - 750$  nm. Electromagnetic radiation provides the energy for photosynthesis and electromagnetism describes the bonds with which molecules form. For humans, light is a significant means of discerning information about our environment. However, human vision uses only two aspects of electromagnetic radiation, the intensity and wavelength, being ordinarily insensitive to polarisation.

Controlling electromagnetic radiation for the purposes of communication has motivated many of the developments in our understanding of electromagnetic radiation. For politics and business the faster information can be reliably delivered, the better. The desire for faster and fuller long distance duplex communication has motivated semaphore tower networks, telegraph networks, radio networks, satellite communication networks and the modern optical fibre based telecommunications networks. New connections offering millisecond improvements can enable large financial gain for those with information ahead of the rest.

In the course of these developments, ubiquitous and open communications media, such as air, have been progressively replaced by more controllable media in the pursuit of increased speed, reliability and bandwidth. For example, the semaphore network could be interrupted by smoke, fog or heavy rain.

Optical fibres are very successful electromagnetic waveguides, carrying most of the world's telecommunications. Optical fibres have been developed to have minimum attenuation with minimum dispersion. The material and waveguide geometry impose fundamental limits upon the communications performance, as both the material and waveguide geometry change with their environment.

The disadvantageous environmental susceptibility that motivates improved communications can be recast as advantageous sensing capability. In particular, the environmental sensitivity of optical fibres has been used for sensing since the discovery of that environmental sensitivity.

The interaction of electromagnetic radiation with matter is of major importance. Electromagnetism is tensorial in nature, but is usually treated as vectorial (the trace of the tensor) as bianisotropy does exhibit itself usually. Quantum approaches are required for the most accurate description of these phenomena, but the classical approach is typically simpler and an adequate approximation for many applications. Understanding the interaction of electromagnetism with matter allows for the redirection, modification, focusing and ducting of propagating electromagnetic waves.

## 1.1 Motivation for sensors

Sensing can be defined as obtaining an otherwise inaccessible<sup>1</sup> property of interest which modifies another accessible and quantifiable property in a consistent manner (transduction), which is then interpreted, via an understanding of that consistent manner (transduction process) to reveal and quantify the inaccessible property of interest.

Sensing is of wide interest, most commonly for critical infrastructure, such as bridges and dams whose availability or failure can have substantial economic impact<sup>2</sup>. Many of these structures have reached, or are approaching, the end of their designed life span. Replacement costs are currently prohibitive, so the effective management of scheduled and emergency repairs, in addition to maximising non-destructive utilisation of these structures, requires the use of sensors to provide this information for management decisions.

The applications of novel materials, such as composite materials in aircraft or shipping, need to be monitored to ensure that the implemented design does not depart from predicted performance. Failure or advanced ageing of the structure can change the determination of the structure's value. Conversely, premature derating

---

<sup>1</sup>This may be due to cost or physical constraints.

<sup>2</sup>The I35 bridge over the Mississippi river in Milwaukee was built in 1967, as part of a nationwide infrastructure project, with many other bridges of similar construction and vintage [1, 2]. The bridge collapsed in 2007 killing 13 people. The bridge had carried  $\sim 140,000$  vehicles per day, and was an important part of the local infrastructure and economy. Other routes then had to bear the increased capacity, i.e. increased wear. In general there is the direct cost, such as reconstruction, and the indirect cost, from lost utility of the structure to be replaced [3]. The replacement I-35 bridge has had sensors attached to “*enable close behavioral monitoring for the bridge's life span.*” [4].

The short term costs of structure failure can be significant in terms of money and efficiency to the immediate economy, as business efficiency and productivity are impacted, e.g. the traffic that had used the bridge needed to use other, longer, routes.

or disposal of the structure may underestimate the attainable value of the structure. Historically, safety margins were added by the addition of extra materials [5], and structural health monitoring, SHM<sup>3</sup>, was considered an optional luxury. With component costs rising, new materials, allowing reduced tolerances, are employed to minimise construction costs [5, 6].

Unfortunately, the current structures most in need of SHM, are those already built, e.g. for the preservation of important cultural, historical & religious structures. When the state of a structure suggests the need for SHM, the utility has already been degraded [3], i.e. SHM would be a safety issue in this case. Even for more modern structures in this class, at the time of construction, the lower costs of maintenance, lower rate of use, and advancement of technology were such that tolerances provided for the intended life span made such an approach unnecessary.

Integrated sensors in the manufacturing process would allow *intelligent processing*, where the manufacturing process could be tailored by data-fed models to achieve the desired outcome [7, 8]. These sensors can then continue to monitor the component during testing and/or its service life, validating the part [2].

Operational costs can be reduced by practices such as *just-in-time*, JIT, maintenance [9, 10], facilitating optimised asset management such as minimal operational derating. Effective use of JIT maintenance is facilitated by the structure's sensor indicating the need for maintenance, rather than a degree of structural failure prompting emergency action. Alternatively, the required maintenance can be planned to occur at the next scheduled maintenance event.

In all these situation (re)insurance companies and their clients could benefit from more accurate information on the condition of the structure when deciding upon policies and premiums. The reinsurance industry suffered heavy losses from the 1992 hurricane Andrew total insurance bill of  $\sim$  \$15 bn [11]. After the 1989 hurricane Hugo, certain reinsurance investors consulted with climatologists beforehand, allowing them to minimise their exposure in areas at risk from hurricanes [11]. SHM could provide a similar competitive advantage to both the insured<sup>4</sup> and insurer<sup>5</sup>, albeit on a far smaller scale.

Sensors play a role in the standardisation and proving of components, either in their production or qualification. This work deals with fibre sensors, their demodulation and the mitigation of transmission effects on the signal quality, and, hence, resolution.

---

<sup>3</sup>Structural health monitoring is further discussed in §2.3.3.4 (page V.I - 75).

<sup>4</sup>Which may be beneficial in selling on the structure, as it would show that the insurance company did not have concerns regarding the structure's condition.

<sup>5</sup>Reduced premiums at much lower risk.

### 1.1.1 Fibre Sensors

The utility that customers can gain from the sensing technology determines its success. Fibre sensing technology is no different. Fibre sensing technologies must compete against established and new sensing technologies and approaches. This is done by emphasising strengths [12]:

- Electrical and chemical passivity<sup>6</sup>,
- Immunity to externally sourced electromagnetic interference,
- Small size and biocompatibility suitable for biomedical sensors,
- Ability to withstand high temperatures (until glass transition temperature),
- Small and lightweight (in comparison to electrical conductors),
- Transmission distances of kilometres without amplification,
- Sensitivity, dynamic range and resolution can be adjusted by employing different demodulation techniques,
- Capablity of being multiplexed via different techniques,
- Can be configured as distributed or quasi-distributed (multiple point sensors).

while admitting weaknesses:

- Cross-sensitivity, where different environmental parameters affect the quantity measured, e.g. strain-based extension and thermal expansion,
- Cost of sensing systems, including demodulation sub-system, currently greater than competitors.

Approaches to mitigate these disadvantages are addressed in this work. For most FBG-based sensor systems the demodulation system is the most expensive component. The more FBGs which can be demodulated with a single demodulation system, the lower the per sensor cost of the whole system. The desire to maximise the number of sensors while providing high individual sensor resolution was the motivation for the SpectroBragg spectrometer.

---

<sup>6</sup>I.e. fibre sensors may be used in environments where the risk of explosion or fire may preclude other sensors.

## 1.2 Thesis Overview

Chapter 2 is a literature review of the theory used for the subsequent experimental chapters. The literature review begins with an overview of electromagnetism, phase and polarisation representations.

The propagation of electromagnetic radiation in a single-mode optical fibre, and the effects of the material in its environment of the fibre upon the propagating electromagnetic radiation are then discussed, in particular strain and temperature. This leads to optical fibre sensing, and the fibre Bragg grating, FBG, types of which are employed in three of the experimental chapters.

An overview of structural health monitoring, SHM, which is a significant niche for FBG sensing, is provided.

The literature review concludes with an overview of signal demodulation schemes which are not developed, more appropriately, in the context of the experimental chapters.

The first experimental chapter, 3, discusses the development of a compact custom built diffraction grating based spectrometer, the SpectroBragg. For many optical fibre sensing systems the cost of signal recovery forms the largest contribution to the overall cost of the system. The two-step process of converting an optical to analog electrical signal and then to a digital electrical signal represents an extra step over electrical systems. However, traditional electrical systems can have disadvantages that can limit this advantage, e.g. electrical strain gauges require two leads and resistance balancing equipment per sensor, and the pickup of electrical noise. For several sensors, the wiring, configuration and maintenance of the accumulated equipment can become expensive.

For most FBG-based sensor systems the demodulation system is the most expensive component. The more FBGs which can be demodulated with a single demodulation system, the lower the per sensor cost of the whole system. The desire to maximise the number of sensors, while providing high individual sensor resolution, was the motivation for designing the SpectroBragg spectrometer.

The SpectroBragg was constructed using commercially available components, to ensure costs were as low as possible. The SpectroBragg operated natively in the telecomms spectral bands by using an InGaAs 512 pixels array. The SpectroBragg provided high-bandwidth, high-speed and high-resolution measurements of sensors, such as multiplexed FBG sensors in arrays. The SpectroBragg operated over a spectral bandwidth of  $\sim 70$  nm bandwidth centred at  $\sim 1550$  nm, with the 512 pixels providing a native resolution of  $\sim 0.13$  nm per pixel. A super-resolution, beyond the averaged native resolution of  $\sim 0.13$  nm, of  $< 0.5$  pm was obtained, using the centroid algorithm. In practice, vibrations reduced the instantaneous

operational resolution to, on average,  $\sim 0.9$  pm. By natively operating at telecomms wavelengths, the existing suite of telecomms components can be deployed for use with the SpectroBragg.

Chapter 4 reports the strain characterisation of a novel anisotropic FBG, inscribed by a two-photon femtosecond UV(264 nm) process into standard single-mode fibre. FBGs can be multiplexed, allowing multiple point sensors along a single fibre. The motivation for this work was to determine the suitability of these novel anisotropic FBGs for use as strain sensors comparable to standard telecomms FBGs. Quasi-steady-state strain characterisation of these novel FBGs over  $0 - 700 \mu\epsilon$ , using an optical spectrum analyser, returned a strain sensitivity of  $0.81 \times 10^{-6} \mu\epsilon^{-1}$ . Dynamic strain characterisation in steps of  $10.6 \mu\epsilon$  over the range  $0 - 265 \mu\epsilon$ , using the SpectroBragg spectrometer, returned a strain sensitivity of  $0.75 \times 10^{-6} \mu\epsilon^{-1}$ . The strain response for isotropic FBGs in the literature is  $0.78 \times 10^{-6} \mu\epsilon^{-1}$  [13] but a value of  $0.73 \times 10^{-6} \mu\epsilon^{-1}$  a value of was obtained from the dynamic strain characterisation experiment, for the co-located isotropic FBG.

FBGs are simultaneously sensitive to strain (pressures) and temperature. This cross-sensitivity is common to many strain sensors, and means of discriminating between temperature and strain induced changes is ongoing. Preliminary investigations of a potential method of simultaneous strain/temperature discrimination using these anisotropic FBGs are discussed.

Over the range tested, applied strain does not significantly alter the relative separation of the anisotropic FBGs orthogonal component peaks. A brief and truncated initial investigation indicated that temperature changes tested may have a much greater effect on the relative separation and so alter the spectral profile. The preservation of spectral profile under applied strain suggests that the anisotropic FBGs might allow strain-temperature discrimination. By measuring the bandwidth, such as the full-width at half-maximum, it would appear there is a possibility the temperature may be inferred, separately from the peak movement, which is sensitive to both strain and temperature.

Chapter 5 presents an initial examination of two alternatives to established means of mitigating the polarisation-sensitivity of demodulation systems, such as the SpectroBragg. When the polarisation-sensitive detectors are paired with state of polarisation, SOP, modifying fibre, spectral changes arising from changes in the state of polarisation may arise randomly, adding to the noise experienced by the demodulation system. No current passive optical device will coherently add the orthogonal SOP components when rotated into the same plane without converting the phase shift describing the ellipticity into a non-zero optical path difference, OPD [14].

The two most common depolarisation schemes, the polarisation scrambler and

Lyot depolariser, operate by decohering the signal to populate all possible polarisation angles equally in the temporal and spectral domains, respectively. The polarisation scrambler becomes expensive when high-speed depolarisation is required. The Lyot depolariser, and in particular fibre Lyot depolariser, becomes cumbersome when high-coherence signals need to be depolarised.

However, a subsequent polarisation-sensitive element, such as a diffraction grating in a spectrometer, can repolarise the signal. The motivation for the work reported in this chapter was to examine the possibility of effective depolarisation for mixed low- and high-coherence signals onto a device such as the SpectroBragg. The approaches investigated output a single linear SOP, making the signal effectively scalar. By combining the decoherence approach of Takada *et al.* with the polarisation fixing approach of Tateda *et al.*, the best polarisation mitigation, as measured, of the approaches tested was achieved for the anisotropic and isotropic FBGs at 22% and 76%, respectively.

By recombining the previously orthogonal but now parallel components, random SOP changes are converted to random phase changes. The greatest limitation to these techniques, as investigated, was the unwanted introduction of phase noise. Unbalancing the stationary Mach-Zehnder interferometer reduces the interferometric phase noise, but required *a priori* knowledge of the coherence length of the source to adhere most closely to stationarity requirements.

The final experimental chapter, 6, reports on the use of the Hilbert transform technique to analyse two-output  $\pi$ -shifted interferograms, which provide common-mode noise rejection to reduce accumulated noise from Rayleigh scattering, to demodulate FBG signals. The Hilbert transform technique provides higher resolution wavelength determination than Fourier transform spectroscopy, FTS, using short interferometer scans. Scan time limits the temporal resolution, and can introduce design complexity in equipment manufacture for applications such as in aircraft, where the size of a demodulation system is a limiting factor.

In this work, the FBG signals traversed a 19.5 km length of fibre. Rayleigh scattering, and the amplification required to obtain a signal, introduced significant noise onto the captured signal. Two-step recalibration provided a signal that retained the relative FBG to reference laser intensity ratios, as measured by an OSA over  $\sim 10$  m patch lead. This approach permits the recovery of low signal-to-noise ratio signals where single-output interferometry is otherwise obscured in noise, potentially increasing distances along the fibre over which sensors can be placed.

To separate the performance of the HTT from the  $\pi$ -shift common-mode noise rejection, the FTS (using the centroid algorithm) and HTT methods of determining the mean wavelength of the FBG were examined. The recovered temperature response of the sensor FBG was examined for variable, and different, fixed

interferogram lengths. The variable interferogram length temperature response was  $5.42 \times 10^{-6} \text{ }^\circ\text{C}^{-1}$ , with an uncertainty of 32 pm; the fixed interferogram length case was  $5.31 \times 10^{-6} \text{ }^\circ\text{C}^{-1}$ , with an uncertainty of 70 pm for the HTT. These values are lower than the literature value of  $6.67 \times 10^{-6} \text{ }^\circ\text{C}^{-1}$  [13], and may be due to different actual temperatures being experienced by the FBG and the oven's thermistor sensor, or incorrect thermistor values reported by the oven controller.

However, a dependence of the temperature response value on the length of the interferogram chosen was observed. This led to the optimum interferogram length,  $n_i$ , being ambiguous and the temperature response value changing between a minimum of  $5.29 \times 10^{-6} \text{ }^\circ\text{C}^{-1}$  and a maximum of  $5.34 \times 10^{-6} \text{ }^\circ\text{C}^{-1}$ .

### 1.2.1 Appendices

Material that was considered supplemental or ancillary has been collected into the appendices, in volume 2. The appendices contain additional theory and development of experimental results at a level which, while consistent with the level of the chapters, is sufficiently lengthy to obscure the results to be discussed.

## 1.3 Notation

In this work, computer program functions, e.g. *Matlab's* `interp1q`, will be written in constant width font as in the example. On the initial mention of a commercial product or term, it will be presented in italics, as with the product *Matlab*, The Mathworks, Inc.

### 1.3.1 Tensor representation of quantities

Given the scope of material covered in understanding sensor physics, the symbols used, e.g. alphabet letters, are frequently reused in specific subject domains. To distinguish between various uses, subscripts are employed which may be non-standard within the specific subject domains.

Tensors<sup>7</sup> of rank greater than one (e.g. vectors, dyadics, triadics, etc.) are bold faced, with the rank of the tensor indicated by the number of associated underlines<sup>8</sup>, e.g. vector: **X**, dyadic: **Y** and triadic: **Z**. Scalar quantities (tensor quantities of rank zero) have no underlines and are not in bold face, e.g. scalar: *A*.

---

<sup>7</sup>Quantities that have a magnitude and zero to many directional components along which the magnitude need be measured. The tensor itself is independent of the reference frame, but the magnitude of the constituent components will be reference frame dependent.

<sup>8</sup>Maxum [15] uses overbars instead of underlines. However, this use is in conflict with the common use of one overbar for mean quantities in the literature, so the underlines are used instead.

### 1.3.2 Measurement terminology

The emission, transmission and absorption/detection of light is fundamentally a statistical process [16]. Sources, media and detectors will all have random thermal motion, all imparting uncertainty onto a measurement. Components will have manufacturing quality tolerances and so will vary below those tolerances, increasing uncertainty. Measurement equipment will be variously subject to some electrical power variations, temperature variations and vibrations, all which need to be considered as statistical sources of noise, or measurement uncertainty.

The standardised treatment of statistical measurands is defined in the *Guide to the expression of uncertainty in measurement* or *GUM* [17,18]. This work follows the guidelines, as outlined in [19], in so far as available time and equipment permitted.

The following normative terminology, defined in [20], is used in this work:

- **Accuracy** is defined as the “closeness of the agreement between independent results of measurement and the true value<sup>9</sup> and
- **Precision** is defined as the “closeness of the mutual agreement between independent results of measurement<sup>10</sup>”.

## 1.4 References

- [1] S. Flynn. Minn. bridge collapse reveals brittle America: expert Op-Ed, October 2009.
- [2] W. B. Spillman Jr. *Fiber optics and smart structures*, volume 4 of *Optoelectronics Library*, chapter 16. Artech House, Inc., Boston, 1997. ISBN: 0890069409.
- [3] B. Glišić and D. Inaudi. *Fibre optic methods for structural health monitoring*. John Wiley & Sons, Ltd., Chichester, 2007. ISBN: 0470061421.
- [4] D. Inaudi and M. Bolster and R. Deblois and C. French and A. Phipps and J. Sebasky and K. Western. Structural health monitoring system for the new I-35W St Anthony Falls Bridge. In *4th Int. Conf. Struct. Health Monitor. Intell. Infrastruct. (SHMII-4)*, page 10, 2009.

---

<sup>9</sup>Presuming that there exists a true value, of which the statistical spread of data approximates [17].

<sup>10</sup>This definition of precision is similar to the concept of measurement repeatability. Note 3 of §2.15 of [20] states that “*Measurement precision is used to define **measurement repeatability***” as “*measurement precision under a set of repeatability conditions of measurement*” (§2.21). The understanding of precision as the number of decimal places is, instead, defined as the **resolution of a displaying device**(§4.15), i.e. the “*smallest difference between displayed indications that can be meaningfully distinguished*”. Thus, this understanding is a subset of the measurement precision definition, §2.15.

- 
- [5] R. A. Collacott. *Structural Integrity Monitoring*. Chapman & Hall Ltd., London, 1985. ISBN: 0412219204.
- [6] T. Bosselmann. Market potential for optical fiber sensors in the energy sector. In A. Cutolo, B. Culshaw, and J. M. López-Higuera, editors, *Third European Workshop on Optical Fibre Sensors*, volume 6619, page 661903. SPIE, 2007.
- [7] J. M. Menendez. Market opportunities on fiber optic sensors for aeronautics and aerospace applications. In A. Cutolo, B. Culshaw, and J. M. López-Higuera, editors, *Proc. SPIE*, volume 6619, page 661908. SPIE, 2007.
- [8] H. N. G. Wadley and R. Vancheeswaran. The intelligent processing of materials: An overview and case study. *JOM-J. Min. Met. Mat. S.*, 50:19–30, January 1998.
- [9] P. Dijkstra. Just in time maintenance, culture lessons from the past. [http://www.reliabilityweb.com/excerpts/excerpts/jit\\_maintenance.pdf](http://www.reliabilityweb.com/excerpts/excerpts/jit_maintenance.pdf).
- [10] P. Ferdinand, S. Magne, V. Dewynter-Marty, C. Martinez, S. Rougeault, and M. Bugaud. Applications of Bragg grating sensors in Europe. *Proceedings of the Optical fiber sensor conference (OFS12)*, pages 14–19, 1997.
- [11] J. Leggett. Who will underwrite the Hurricane?, August 1993.
- [12] J. M. Lopez-Higuera. *Introduction to fibre optic sensing technology*, chapter 1, pages 1–22. Handbook of Optical Fibre Sensing Technology. John Wiley & Sons, Ltd., Chichester, 2002. ISBN: 0471820539.
- [13] A. D. Kersey, M. A. Davis, H. J. Patrick, M. LeBlanc, K. P. Koo, C. G. Askins, M. A. Putnam, and E. J. Friebele. Fiber grating sensors. *J. Lightwave Technol.*, 15(8):1442–1463, August 1997.
- [14] M. Tateda and T. Omatsu. Polarization state fixer composed of passive optical devices. *J. Opt. Soc. Am. A*, 20(2):342–346, February 2003.
- [15] B. Maxum. *Field Mathematics for Electromagnetics, Photonics, and Materials Science*, volume TT64, chapter 1, pages 1.1–1.24. SPIE, Bellingham, 2005. ISBN: 0819455237.
- [16] J. W. Goodman. *Statistical Optics*, chapter 1, pages 1–6. Wiley Classics Library. John Wiley & Sons, Inc., New York, 2000. ISBN: 0471399167.
- [17] ISO. *Guide to the Expression of Uncertainty in Measurement*, chapter 2, pages 2–4. International Organisation for Standardisation, Geneva, Switzerland, 1995.
-

- [18] R. Kacker, K.-D. Sommer, and R. Kessel. Evolution of modern approaches to express uncertainty in measurement. *Metrologia*, 44(6):L57–L61, December 2007.
- [19] BIPM JCGM 104:2009. Evaluation of measurement data - An introduction to the “Guide to the expression of uncertainty in measurement” and related documents, 2009.
- [20] BIPM JCGM 200:2008. International vocabulary of metrology - Basic and general concepts and associated terms (VIM), 2008.

# Chapter 2

## Literature Review

---

### 2.1 Introduction

When a particle of matter interacts with another particle it does so subject to the theory of relativity, where the interaction is not instantaneous, but occurs after an interval of time. “*The field itself acquires physical reality*” [1]. The first particle interacts with the field, and the modified field then interacts with the second particle after the time interval. Additional implications of the theory of relativity are not required.

Quantum field theory provides the most complete theory of photons and their interactions with matter [2]. The quantum nature dominates in the absorption and emission processes, however, the wave aspect dominates in the propagation of light [3]. In this work no situations are encountered where the quantum nature of electromagnetic radiation is dominant, such as small numbers of photons (i.e. very low intensity signals) or squeezed states [4–6], and the classical stochastic approach to optics is adequate to describe the work given the relative dimensions of typical inter-atomic distances being  $\gtrsim 10^{-4}$  that of the radiation wavelength at 1550 nm and the macroscopic fluctuations density fluctuations occurring at 10 – 100 nm in glasses [7].

#### 2.1.1 Electromagnetic radiation

The electromagnetic field is defined as the *state of excitation* established in the presence of electric charges [8]. The charges are examples of the particles referred to previously. The interaction between charges, after an interval, is the propagation of the excitation from one charge to another. At macroscopic scales, where large

numbers of charges are encountered, the total number of degrees of freedom required to describe all the charges and their assorted mutual interactions becomes very large and thus intractable to direct calculation<sup>1</sup>.

Statistical optical approaches allow the electromagnetic field produced by large numbers of charges to be treated efficiently. Describing the set of the degrees of freedom of the collection of charges and the associated probabilities, allows a macroscopic average behaviour with associated error or confidence interval to be assigned. This reduces the computational effort required to describe electromagnetic phenomena that would otherwise deviate unacceptably from a full quantum field treatment.

A brief overview of the development of Maxwell's equations is provided in appendix A (page V.II A-1). The appendix also covers the incorporation of anisotropy into the theory, the transfer of energy (the Poynting vector) and the important plane wave solution to the propagating electromagnetic wave equation. The set of plane waves provides a basis set with which other more complicated signals may be described.

In practice no signal is purely monochromatic, and so the analytic signal is introduced in appendix C (page V.II C-1), which describes polychromatic signals. The analytic signal theory is directly employed in the signal processing used in chapter 6, along with second order coherence theory, which is described in appendix B (page V.II B-1). For completeness, appendix B also discusses the power spectrum, the concepts of coherence time and lengths, and the use of the terms high- and low-coherence.

### 2.1.1.1 Quantum limits on resolution

A fundamental limit to the spectral resolution obtainable by interference was obtained by Kafri using the uncertainty principle [9]. The following argument is based upon Kafri's paper. A Michelson interferometer does not record the entire interferogram in one instantaneous measurement, so the single measurement uncertainty principle may be overcome using the statistics of many measurements to improve the accuracy<sup>2</sup>.

The resolution possible by an interferometer, in terms of the fraction of a fringe that can be resolved,  $q$ , is

$$q \geq \frac{1}{4\pi\sqrt{m}} \quad (2.1)$$

where  $m = \delta\omega\delta t$  is the number of longitudinal modes in the interferometer,  $\delta\omega$  is the bandwidth of the beam being examined, and  $\delta t$  is the sampling time of a

---

<sup>1</sup>This statement must be considered in terms of neglecting the uncertainty inherent in the quantum nature of the charges.

<sup>2</sup>As the interferometer is scanned different instrument modes are generated, and therefore the limit of photons, in the same quantum state, providing no extra information is overcome.

measurement.

Assuming a symmetrical profile for the spectrum, the coherence time,  $\tau_c$  is  $\frac{1}{\delta\omega}$ , and so  $m = \frac{\delta t}{\tau_c}$ .

In principle, it is possible to obtain a desired resolution by increasing the measurement time or decreasing the coherence length. A real experimental apparatus will be subject to environmental vibrations and temperature fluctuations therefore short measurement times are desirable to mitigate the impact of these noise sources. Long coherence times facilitate alignment, but, in general, the coherence time of the signal being examined may not be known *a priori*.

The number of longitudinal modes is restricted, due to detuning, by the coherence length to

$$m \leq \frac{c\lambda q}{2l_c\nu_{\text{sys}}} \quad (2.2)$$

where  $\nu_{\text{sys}}$  is the scan speed of the interferometer and  $l_c$  is the coherence length of the signal.

Equation (2.1) and equation (2.2) give the best resolution of the interferogram, in terms of  $q$ , as

$$q = \left( \frac{1}{8\pi^2} \frac{l_c\nu_{\text{sys}}}{c\lambda} \right)^{\frac{1}{3}} \quad (2.3)$$

Under ideal conditions, a two-beam interferometer will provide the best resolution (discussed in appendix D (page V.II D-1)), so equation (2.3) presents a fundamental limit to the accuracy attainable.

### 2.1.1.2 Phase noise limitation

Noise is the practical limit to the resolution of a measurement of an optical quantity. Noise is the spontaneous fluctuation of the quantity being measured [10], and is inherent from quantum mechanics [4, 11]. The measurements are treated as statistical quantities with a mean value and associated standard deviation. An electromagnetic signal<sup>3</sup> passing through a medium will experience phase noise from the random fluctuations in the material density. Rayleigh scattering is the fundamental contribution to phase noise<sup>4</sup>, and is the dominant source of phase noise in telecomms fibres at 1550 nm. Rayleigh scattering is discussed further in §2.2.2.2 (page V.I - 28).

Rayleigh scattering appears as phase-noise on the signal that generated it. For a high-coherence source, the signal's phase will have interfering contributions from scattering within the coherence length as it traverses the fibre. This is a disadvantage

---

<sup>3</sup>The electromagnetic signal will already be a statistical quantity from the photon generation process.

<sup>4</sup>The spectrum will exhibit a broadened, lower-coherence profile due to the phase-noise components synthesising frequency components.

as high-coherence sources are desirable for long distance communications due to the power levels achievable and the density of information they enable.

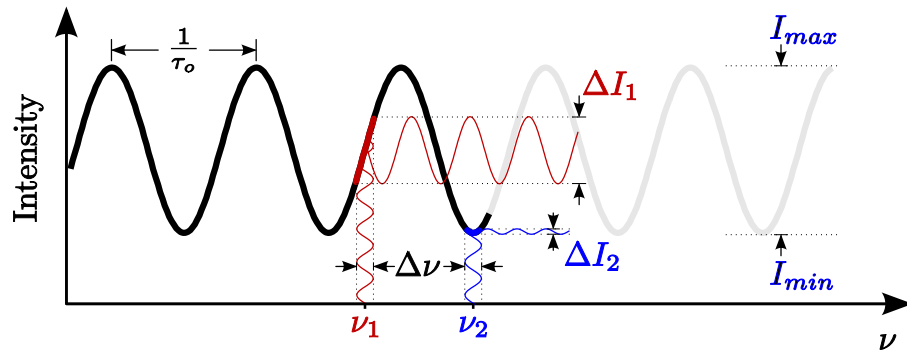


**Figure 2.1:** Effect of phase noise,  $\Delta\nu$ , on intensity from an interferometer with relative delay  $\tau_0$ . Phase noise converts frequency fluctuations into intensity fluctuations. This figure is after Derickson [12].

Figure 2.1 shows the effect of a periodic frequency variation on the intensity recorded by a detector. A fluctuation of magnitude  $\Delta\nu$  occurs at both  $\nu_1$  and  $\nu_2$ . The signal is in quadrature at  $\nu_1$  and so the intensity fluctuation is largest here. At  $\nu_2$ , the fluctuation is of minimum amplitude, but the period of the intensity fluctuations is halved.

Interferometric demodulation techniques, based upon Michelson or Mach-Zehnder interferometry, have the *Fellgett* or *multiplex advantage* [13]. The Fellgett advantage is where the time needed to obtain a given signal-to-noise ratio, SNR, across the whole spectrum window is reduced compared to other methods, by simultaneously recording the whole spectral window [14]. These demodulation techniques also suffer the multiplex disadvantage, where noise signal fluctuations are recorded just as effectively as the signal [15].

The phase-noise from a high-coherence source should not modulate the low-coherence signal, as the noise effect should be similar to non-white noise, which is spectrally associated with the generating signal [15]. However, the transmission distances may be considered the optical far-field for the scattering events, and may generate spatial coherence between the scattered beam from one signal and another signal [16]. This makes the phase noise ‘whiter’ than it would otherwise have been.

The impact of phase-noise is most significant in a two-beam interferometer demodulation scheme, as discussed in appendix §D (page V.II D-1). Thus the theoretical limit for interferometric accuracy is seldom achievable.

The signal information in an interferogram will be reduced by the presence of noise, limiting the resolution with which the measurand can be determined. For

low intensity signals, the intensity noise can reduce the recoverable signal to near or below background noise levels.

### 2.1.2 Wolf's polarisation representation

The polarisation of electromagnetic radiation has led to the development of different approaches to deal with the vectorial nature of electromagnetic radiation. The Stokes parameters, Mueller and Jones calculi are discussed in appendix sections E.1 (page V.II E-4), E.4 (page V.II E-10) & E.5 (page V.II E-12), respectively. The Stokes parameters allow the state of polarisation to be described in terms of observable quantities, e.g. the intensity, and the Mueller calculus models the Stokes vector passage through optical components. The Mueller calculus does not cater for the effects on phase of the optical components, as the intensity-based Stokes vector has already evaluated the phase. The Jones calculus deals with the electromagnetic signal amplitude, and so models the effects of phase changes, but with the restriction of fully polarised light only.

In addition to the Jones and Stokes calculi a third formalism to represent polarisation was introduced by Wolf in the *coherency matrix*<sup>5</sup> [17, 18] or *polarisation matrix* [19] as  $\underline{\underline{\mathbf{C}}}$ ,

$$\begin{aligned} \underline{\underline{\mathbf{C}}} &= \langle \underline{\mathbf{E}}(t) \otimes \underline{\mathbf{E}}(t + \tau) \rangle \\ &= \left\langle \begin{pmatrix} E_x^*(t) \\ E_y^*(t) \end{pmatrix} \otimes (E_x(t + \tau), E_y(t + \tau)) \right\rangle \\ &= \begin{pmatrix} \langle E_x^*(t) E_x(t) \rangle & \langle E_x^*(t) E_y(t) \rangle \\ \langle E_y^*(t) E_x(t) \rangle & \langle E_y^*(t) E_y(t) \rangle \end{pmatrix} \end{aligned} \quad (2.4)$$

where  $\underline{\mathbf{E}}(t)$  is the electric field and  $\otimes$  denotes the *Kronecker* or *direct product*<sup>6</sup>.

The polarisation matrix approach describes the optical state in terms of its coherency and polarisation and adds mathematical concepts to the Mueller and Jones calculus [20].

The Stokes parameters,  $S_j$ , are related to  $\underline{\underline{\mathbf{C}}}$  via [20]

$$S_j = \text{Tr} \left( \underline{\underline{\mathbf{C}}} \underline{\underline{\boldsymbol{\sigma}}}_{P_j} \right) \quad (2.5)$$

where ‘Tr’ is the trace of the matrix, and  $\underline{\underline{\boldsymbol{\sigma}}}_{P_j}$  are the *Pauli spin matrices* [21].

<sup>5</sup>Explicitly,  $\underline{\underline{\mathbf{C}}} = \underline{\underline{\mathbf{C}}}(\mathbf{r}, t)$ , but the  $\mathbf{r}$  dependence is typically omitted for clarity of presentation.

<sup>6</sup>Defined as [20]: for  $m \times n$  matrix  $\mathbf{A}$  and  $p \times q$  matrix  $\mathbf{B}$ , the Kronecker product is the  $mp \times nq$  partitioned matrix  $\mathbf{A} \otimes \mathbf{B} = \begin{pmatrix} a_{11}\mathbf{B} & a_{12}\mathbf{B} & \dots & a_{1n}\mathbf{B} \\ a_{21}\mathbf{B} & a_{22}\mathbf{B} & \dots & a_{2n}\mathbf{B} \\ \vdots & \vdots & \ddots & \vdots \\ a_{m1}\mathbf{B} & a_{m2}\mathbf{B} & \dots & a_{mn}\mathbf{B} \end{pmatrix}$ .

Completely polarised light is described by

$$\det \underline{\underline{\mathbf{C}}} \equiv C_{xx}C_{yy} - C_{xy}C_{yx} = 0 \quad (2.6)$$

and unpolarised light by

$$C_{xy} = 0 \quad (2.7)$$

i.e. there is no correlation between the components in the  $x$  and  $y$  directions.

Partial polarisation can be determined by separating  $\underline{\underline{\mathbf{C}}}$  into

$$\underline{\underline{\mathbf{C}}} = \underline{\underline{\mathbf{C}}}_{\text{pol}} + \underline{\underline{\mathbf{C}}}_{\text{unpol}} \quad (2.8)$$

where

$$\underline{\underline{\mathbf{C}}}_{\text{unpol}} = \begin{pmatrix} 1 & 0 \\ 0 & 1 \end{pmatrix}, \quad \underline{\underline{\mathbf{C}}}_{\text{pol}} = \begin{pmatrix} B & D \\ D^* & C \end{pmatrix}, \quad (2.9)$$

and solving for  $B$ ,  $C$  and  $D$  [19]. The trace of  $\underline{\underline{\mathbf{C}}}_{\text{pol}}$  and  $\underline{\underline{\mathbf{C}}}_{\text{unpol}}$  are proportional to the intensities of the polarised and unpolarised components, respectively. The degree of polarisation, equation (E.12) (page V.II E-5), can be written as

$$\mathcal{P} \equiv \frac{I_{\text{pol}}}{I_{\text{tot}}} = \sqrt{1 - \frac{4 \det \underline{\underline{\mathbf{C}}}}{(\text{Tr} \underline{\underline{\mathbf{C}}})^2}} \quad (2.10)$$

The Jones calculus describes completely polarised light using the amplitude and phases from Maxwells equations. The Mueller–Stokes calculus describe experimentally observable parameters which must be incoherently added. The relationship between the Jones calculus and Mueller calculus must therefore deal with the loss of information (i.e. the phase,  $\phi$ , is wrapped to the range  $0 \leq \phi < 2\pi$ ) that arises on moving from amplitudes to intensities [22].

The Kronecker product of the Jones vector (E.5) (page V.II E-12) and its complex conjugate forms

$$\underline{\underline{\mathbf{I}}}_{in} = \langle \underline{\underline{\mathbf{E}}} \otimes \underline{\underline{\mathbf{E}}}^* \rangle = \begin{pmatrix} \langle E_x E_x^* \rangle \\ \langle E_x E_y^* \rangle \\ \langle E_y E_x^* \rangle \\ \langle E_y E_y^* \rangle \end{pmatrix} = \begin{pmatrix} C_{xx} \\ C_{xy} \\ C_{yx} \\ C_{yy} \end{pmatrix} = \begin{pmatrix} \frac{1}{2}(S_0 + S_1) \\ \frac{1}{2}(S_0 - S_1) \\ \frac{1}{2}(S_2 + iS_3) \\ \frac{1}{2}(S_2 - iS_3) \end{pmatrix} \quad (2.11)$$

where  $C_{ij}$  are the elements of (2.4) rearranged as a column matrix.

The Stokes vector can be obtained from

$$\underline{\underline{\mathbf{S}}}_{in} = \underline{\underline{\mathbf{T}}} \bullet \underline{\underline{\mathbf{I}}}_{in} \quad (2.12)$$

where

$$\underline{\underline{\mathbf{T}}} = \begin{pmatrix} 1 & 0 & 0 & 1 \\ 1 & 0 & 0 & -1 \\ 0 & 1 & 1 & 0 \\ 0 & -i & -i & 0 \end{pmatrix} \quad (2.13)$$

Letting equation (2.11) describe the input amplitudes, and the Jones matrix,  $\underline{\underline{\mathbf{J}}}_{\text{sys}}$ , describe the system,

$$\underline{\underline{\mathbf{I}}}_{\text{out}} = \langle \underline{\underline{\mathbf{E}}}_{\text{out}} \otimes \underline{\underline{\mathbf{E}}}_{\text{out}}^* \rangle = \langle \underline{\underline{\mathbf{J}}}_{\text{sys}} \underline{\underline{\mathbf{E}}}_{\text{out}} \otimes \underline{\underline{\mathbf{J}}}_{\text{sys}}^* \underline{\underline{\mathbf{E}}}_{\text{out}}^* \rangle = \left( \underline{\underline{\mathbf{J}}}_{\text{sys}} \otimes \underline{\underline{\mathbf{J}}}_{\text{sys}}^* \right) \underline{\underline{\mathbf{I}}}_{\text{in}} \quad (2.14)$$

Using equation (2.12) and (2.14), the Stokes vector of the output beam is,

$$\begin{aligned} \underline{\underline{\mathbf{S}}}_{\text{out}} &= \underline{\underline{\mathbf{T}}} \cdot \underline{\underline{\mathbf{I}}}_{\text{out}} \\ &= \underline{\underline{\mathbf{T}}} \left( \underline{\underline{\mathbf{J}}}_{\text{sys}} \otimes \underline{\underline{\mathbf{J}}}_{\text{sys}}^* \right) \left( \underline{\underline{\mathbf{T}}}^{-1} \underline{\underline{\mathbf{T}}} \right) \underline{\underline{\mathbf{I}}}_{\text{in}} \\ &= \left[ \underline{\underline{\mathbf{T}}} \left( \underline{\underline{\mathbf{J}}}_{\text{sys}} \otimes \underline{\underline{\mathbf{J}}}_{\text{sys}}^* \right) \underline{\underline{\mathbf{T}}}^{-1} \right] \underline{\underline{\mathbf{S}}}_{\text{in}} \end{aligned} \quad (2.15)$$

which is of the form of equation (E.20) (page V.II E-10), i.e,

$$\underline{\underline{\mathbf{M}}}_{\text{J}} = \underline{\underline{\mathbf{T}}} \left( \underline{\underline{\mathbf{J}}}_{\text{sys}} \otimes \underline{\underline{\mathbf{J}}}_{\text{sys}}^* \right) \underline{\underline{\mathbf{T}}}^{-1} \quad (2.16)$$

which relates the Jones matrix to the corresponding Mueller matrix [20]. As the corresponding Mueller matrices are a subset of all the possible Mueller matrices,  $\underline{\underline{\mathbf{M}}}_{\text{J}}$  is also termed the *Mueller–Jones matrix*.

### 2.1.2.1 Unified theory of coherence and polarisation

The treatment of electromagnetic radiation has followed the pedagogical separation of coherence and polarisation. Coherence arises from the correlations between electromagnetic fluctuations at two or more points, and polarisation is the correlation between the fluctuating electromagnetic components at a single point [23].

A more comprehensive unification of the description of coherence and polarisation explains the interaction of the two phenomena [23–26]. The *cross-spectral*

density function, equation (B.14a) (page V.II B-5), is a function of two points<sup>7</sup>

$$\begin{aligned} \underline{\underline{\mathbf{W}}}(\underline{\mathbf{r}}_1, \underline{\mathbf{r}}_2, \omega) &= \begin{pmatrix} W_{xx}(\underline{\mathbf{r}}_1, \underline{\mathbf{r}}_2, \omega) & W_{xy}(\underline{\mathbf{r}}_1, \underline{\mathbf{r}}_2, \omega) \\ W_{yx}(\underline{\mathbf{r}}_1, \underline{\mathbf{r}}_2, \omega) & W_{yy}(\underline{\mathbf{r}}_1, \underline{\mathbf{r}}_2, \omega) \end{pmatrix} \\ &= \begin{pmatrix} \langle E_x^*(\underline{\mathbf{r}}_1, \omega) E_x(\underline{\mathbf{r}}_2, \omega) \rangle & \langle E_x^*(\underline{\mathbf{r}}_1, \omega) E_y(\underline{\mathbf{r}}_2, \omega) \rangle \\ \langle E_y^*(\underline{\mathbf{r}}_1, \omega) E_x(\underline{\mathbf{r}}_2, \omega) \rangle & \langle E_y^*(\underline{\mathbf{r}}_1, \omega) E_y(\underline{\mathbf{r}}_2, \omega) \rangle \end{pmatrix} \end{aligned} \quad (2.17)$$

whereas both  $\underline{\underline{\mathbf{C}}}$  and  $\underline{\underline{\mathbf{J}}}$  are functions of one point. Using the Young's slits experiment, figure B.1 (page V.II B-2), but describing the fields in terms of statistical ensembles,  $\underline{\mathbf{E}}(\underline{\mathbf{r}}, \omega)$ , instead of analytic signals,  $\underline{\mathbf{E}}(\underline{\mathbf{r}}, \tau)$ , the interfering field at  $Q(\underline{\mathbf{r}}_Q)$  is [23]

$$\underline{\mathbf{E}}_Q(\underline{\mathbf{r}}_Q, \omega) = \underline{\mathbf{K}}_1 \bullet \underline{\mathbf{E}}(\underline{\mathbf{r}}_1, \omega) + \underline{\mathbf{K}}_2 \bullet \underline{\mathbf{E}}(\underline{\mathbf{r}}_2, \omega) \quad (2.18)$$

where  $\underline{\mathbf{K}}_i$  and  $\underline{\mathbf{r}}_i$  are as defined for apertures  $P_i$ ,  $i = 1, 2$  in appendix §B.1 (page V.II B-1).

Thus, the spectral density is<sup>8</sup>

$$\begin{aligned} S_{W_Q}(\underline{\mathbf{r}}_Q, \omega) &= \langle \underline{\mathbf{E}}^*(\underline{\mathbf{r}}_Q, \omega) \bullet \underline{\mathbf{E}}(\underline{\mathbf{r}}_Q, \omega) \rangle \\ &= S_{W_1}(\underline{\mathbf{r}}_1, \omega) + S_{W_2}(\underline{\mathbf{r}}_2, \omega) \\ &\quad + 2\sqrt{S_{W_1}(\underline{\mathbf{r}}_1, \omega)}\sqrt{S_{W_2}(\underline{\mathbf{r}}_2, \omega)}\Re [\eta_W(\underline{\mathbf{r}}_1, \underline{\mathbf{r}}_2, \omega)e^{ik(R_2-R_1)}] \end{aligned} \quad (2.19)$$

where

$$S_{W_1} = |K_1|^2 \text{Tr } \underline{\underline{\mathbf{W}}}(\underline{\mathbf{r}}_1, \underline{\mathbf{r}}_1, \omega) = |K_1|^2 S_W(\underline{\mathbf{r}}_1, \omega) \quad (2.20)$$

is the spectral density in the absence of point  $P_2$ , and similarly for  $S_{W_2}$  in the absence of point  $P_1$ ; and the spectral degree of coherence is

$$\eta_W(\underline{\mathbf{r}}_1, \underline{\mathbf{r}}_2, \omega) = \frac{\text{Tr } \underline{\underline{\mathbf{W}}}(\underline{\mathbf{r}}_1, \underline{\mathbf{r}}_2, \omega)}{\sqrt{S_W(\underline{\mathbf{r}}_1, \omega)}\sqrt{S_W(\underline{\mathbf{r}}_2, \omega)}} \quad (2.21)$$

Equation (2.19) is the frequency domain equivalent of equation (B.4) (page V.II B-3), and is termed the *spectral interference law for the superposition of stochastic electromagnetic beam* [23].

<sup>7</sup>If the direction of propagation is not along the  $z$ -axis, then equation (2.17) would be

$$\underline{\underline{\mathbf{W}}}(\underline{\mathbf{r}}_1, \underline{\mathbf{r}}_2, \omega) = \begin{pmatrix} W_{xx}(\underline{\mathbf{r}}_1, \underline{\mathbf{r}}_2, \omega) & W_{xy}(\underline{\mathbf{r}}_1, \underline{\mathbf{r}}_2, \omega) & W_{xz}(\underline{\mathbf{r}}_1, \underline{\mathbf{r}}_2, \omega) \\ W_{yx}(\underline{\mathbf{r}}_1, \underline{\mathbf{r}}_2, \omega) & W_{yy}(\underline{\mathbf{r}}_1, \underline{\mathbf{r}}_2, \omega) & W_{yz}(\underline{\mathbf{r}}_1, \underline{\mathbf{r}}_2, \omega) \\ W_{zx}(\underline{\mathbf{r}}_1, \underline{\mathbf{r}}_2, \omega) & W_{zy}(\underline{\mathbf{r}}_1, \underline{\mathbf{r}}_2, \omega) & W_{zz}(\underline{\mathbf{r}}_1, \underline{\mathbf{r}}_2, \omega) \end{pmatrix}$$

<sup>8</sup>Common terminology for the *spectral density* is  $S_i$  for point  $i$  [23]. This conflicts with the standard terminology of the Stokes parameters, also using  $S_i$  but for parameter  $i$  [21, 27–29]. The label  $D$  is used for the spectral density in [29]. However, in this work  $D$  refers to the *electric displacement*, equation (A.2) (page V.II A-2). Thus, the subscripted  $S_W$  is used to refer to the spectral density.

The spectral visibility can be defined as

$$\mathcal{V}_{W_Q}(\underline{\mathbf{r}}_Q, \omega) = |\eta_W(\underline{\mathbf{r}}_1, \underline{\mathbf{r}}_2, \omega)| \quad (2.22)$$

and fluctuates between 0 and 1.

The spectral degree of coherence depends upon the diagonal elements via the trace operation. This intuitively follows as orthogonal components should not, by definition, interfere. The orthogonal components may still be correlated.

The *spectral degree of polarisation* replaces  $\underline{\mathbf{C}}(\underline{\mathbf{r}})$  in equation (2.10) (page V.I - 17) with  $\underline{\mathbf{W}}(\underline{\mathbf{r}}_1, \underline{\mathbf{r}}_2, \omega)$ , but restricted to  $\underline{\mathbf{r}}_1 = \underline{\mathbf{r}}_2 \equiv \underline{\mathbf{r}}_Q$  giving [23]

$$\mathcal{P}_{W_Q}(\underline{\mathbf{r}}_Q, \omega) = \sqrt{1 - \frac{4 \det \underline{\mathbf{W}}(\underline{\mathbf{r}}_Q, \underline{\mathbf{r}}_Q, \omega)}{[\text{Tr} \underline{\mathbf{W}}(\underline{\mathbf{r}}_Q, \underline{\mathbf{r}}_Q, \omega)]^2}} \quad (2.23)$$

The spectral degree of polarisation depends not only on the trace,  $S_W(\underline{\mathbf{r}}_Q, \omega) = \text{Tr} \underline{\mathbf{W}}(\underline{\mathbf{r}}_Q, \underline{\mathbf{r}}_Q, \omega)$ , but also on the off-diagonal elements through the determinant.

Wolf has used these results to show that, for a Gaussian Schell-model beam<sup>9</sup>, the degree of polarisation at the apertures  $P_1$  and  $P_2$ ,  $\mathcal{P}_{W_Q}(\underline{\mathbf{r}}_Q, \omega)$ , depends not only upon the degree of polarisation at the apertures  $P_1$  and  $P_2$ ,

$$\mathcal{P}_{W_0} \equiv \mathcal{P}_{W_i}(\underline{\mathbf{r}}_i, \omega) \quad (2.24)$$

but also on  $\eta_{W_0}(\underline{\mathbf{r}}_1, \underline{\mathbf{r}}_2, \omega)$  and the correlation of the off-diagonal elements of the fields at the apertures,  $\delta_{ij} = \delta_{ji} = \arg [W_{ij}] = k(R_i - R_j)$  [23]:

$$\mathcal{P}_{W_Q}(\underline{\mathbf{r}}_Q, \omega) = \frac{1 + \cos(k(R_2 - R_1)) e^{-\frac{2\underline{\mathbf{r}}_1^2}{\delta_{xy}^2}}}{1 + \cos(k(R_2 - R_1)) \eta_{W_0}(\underline{\mathbf{r}}_1, -\underline{\mathbf{r}}_1, \omega)} \mathcal{P}_{W_0} \quad (2.25)$$

The *generalised Stokes parameters* replace the terms  $C_{ij}$  with  $W_{ij}$  to give [23, 30]

$$\underline{\mathbf{S}}_{\text{gen}}(\underline{\mathbf{r}}_1, \underline{\mathbf{r}}_2, \omega) = \begin{pmatrix} S_{\text{gen}_0}(\underline{\mathbf{r}}_1, \underline{\mathbf{r}}_2, \omega) \\ S_{\text{gen}_1}(\underline{\mathbf{r}}_1, \underline{\mathbf{r}}_2, \omega) \\ S_{\text{gen}_2}(\underline{\mathbf{r}}_1, \underline{\mathbf{r}}_2, \omega) \\ S_{\text{gen}_3}(\underline{\mathbf{r}}_1, \underline{\mathbf{r}}_2, \omega) \end{pmatrix} = \begin{pmatrix} W_{xx}(\underline{\mathbf{r}}_1, \underline{\mathbf{r}}_2, \omega) + W_{yy}(\underline{\mathbf{r}}_1, \underline{\mathbf{r}}_2, \omega), \\ W_{xx}(\underline{\mathbf{r}}_1, \underline{\mathbf{r}}_2, \omega) - W_{yy}(\underline{\mathbf{r}}_1, \underline{\mathbf{r}}_2, \omega), \\ W_{xy}(\underline{\mathbf{r}}_1, \underline{\mathbf{r}}_2, \omega) + W_{yx}(\underline{\mathbf{r}}_1, \underline{\mathbf{r}}_2, \omega), \\ i(W_{yx}(\underline{\mathbf{r}}_1, \underline{\mathbf{r}}_2, \omega) - W_{xy}(\underline{\mathbf{r}}_1, \underline{\mathbf{r}}_2, \omega)) \end{pmatrix} \quad (2.26)$$

The generalised Stokes parameters are two-point polarisation quantities, and in general, are complex quantities [31]. When  $\underline{\mathbf{r}}_1 = \underline{\mathbf{r}}_2$  they reduce to the spectral Stokes parameters. An interpretation of the generalised Stokes parameters has been given [32]. The generalised Stokes parameters are no longer intensities but corre-

<sup>9</sup>A Gaussian Schell-model beam has a Gaussian profile in both the time and frequency domains.

lations. Comparing equations (E.11) (page V.II E-5) and (2.26),  $S_{\text{gen}_0}(\mathbf{r}_1, \mathbf{r}_2, \omega)$  is the sum of the linear horizontal polarisation,  $LHP$ , and linear vertical polarisation,  $LVP$ , components of the electric field at points  $\mathbf{r}_1$  and  $\mathbf{r}_2$ . The parameters  $S_{\text{gen}_1}(\mathbf{r}_1, \mathbf{r}_2, \omega)$ ,  $S_{\text{gen}_2}(\mathbf{r}_1, \mathbf{r}_2, \omega)$  and  $S_{\text{gen}_3}(\mathbf{r}_1, \mathbf{r}_2, \omega)$  describe the differences in correlations between the orthogonal components of  $\mathbf{r}_1$  and  $\mathbf{r}_2$  along the  $LHP$  and  $LVP$ ;  $L + 45P$  and  $L - 45P$ ; and  $RCP$  and  $LCP$  SOPs.

$S_0$  in equation (E.11) (page V.II E-5) is invariant under a rotation of the Poincaré sphere (see appendix §E.2 (page V.II E-5)), however, the roles of  $S_1$ ,  $S_2$  and  $S_3$  are interchangeable under unitary transformations. The corresponding values in equation (2.26) behave differently, as  $S_{\text{gen}_0}(\mathbf{r}_1, \mathbf{r}_2, \omega)$  is interchangeable with  $S_{\text{gen}_1}(\mathbf{r}_1, \mathbf{r}_2, \omega)$ ,  $S_{\text{gen}_2}(\mathbf{r}_1, \mathbf{r}_2, \omega)$  and  $S_{\text{gen}_3}(\mathbf{r}_1, \mathbf{r}_2, \omega)$ .

Applying a unitary transformation at  $\mathbf{r}_1$  or  $\mathbf{r}_2$ , any two of the generalised Stokes parameters may be freely interchanged. An unpolarised field can therefore have a zero  $S_{\text{gen}_0}(\mathbf{r}_1, \mathbf{r}_2, \omega)$  but a non-zero (modulated)  $S_{\text{gen}_1}(\mathbf{r}_1, \mathbf{r}_2, \omega)$ ,  $S_{\text{gen}_2}(\mathbf{r}_1, \mathbf{r}_2, \omega)$  or  $S_{\text{gen}_3}(\mathbf{r}_1, \mathbf{r}_2, \omega)$ , depending upon the unitary transform. The norm of both equations (E.11) (page V.II E-5) and (2.26) cannot change under these transformations.

Generalised Jones and Mueller calculi have been developed to use the unified theory of coherence and polarisation [33, 34]. In particular, the generalised Mueller calculus, operating upon the generalised Stokes vector, allows the coherence and polarisation aspects to be followed, combining the advantages of the Jones and Mueller calculi<sup>10</sup>.

The generalised Mueller calculus has the form [33]

$$\underline{\mathbf{S}}_{\text{gen}_{\text{out}}}(\mathbf{r}_1, \mathbf{r}_2, \omega) = \underline{\underline{\mathbf{M}}}_{\text{gen}}(\mathbf{r}_1, \mathbf{r}_2, \omega) \underline{\mathbf{S}}_{\text{gen}_{\text{in}}}(\mathbf{r}_1, \mathbf{r}_2, \omega) \quad (2.27)$$

where  $\underline{\underline{\mathbf{M}}}_{\text{gen}}$  is a  $4 \times 4$  matrix<sup>11</sup> expressing the same relationship between  $\underline{\mathbf{S}}_{\text{gen}_{\text{in}}}$  and  $\underline{\mathbf{S}}_{\text{gen}_{\text{out}}}$  as  $\underline{\underline{\mathbf{M}}}_{\text{sys}}$  does between  $\underline{\mathbf{S}}_{\text{in}}$  and  $\underline{\mathbf{S}}_{\text{out}}$  in equation (E.20) (page V.II E-10).  $\underline{\underline{\mathbf{M}}}_{\text{gen}}$  is a function of two points, allowing the coherence properties to be determined in addition to the polarisation properties provided by  $\underline{\underline{\mathbf{M}}}_{\text{sys}}$ .

The elements of  $\underline{\underline{\mathbf{M}}}_{\text{gen}}$  can be found following a similar argument to that used in §2.1.2 (page V.I - 16) [33].

---

<sup>10</sup>The Stokes parameters may be considered as consisting of modulated and unmodulated components. The unmodulated component is equal to the sum of the Stokes parameters from  $\mathbf{r}_1$  and  $\mathbf{r}_2$ . The modulated component is proportional to the generalised Stokes parameters evaluated at  $\mathbf{r}_1$  and  $\mathbf{r}_2$  [32].

<sup>11</sup>Again, in general with complex elements.

## 2.2 Optical fibres

Optical fibres are, in general<sup>12</sup>, cylindrical waveguides made of dielectric materials, typically silica with dopants to modify the dielectric properties, as illustrated in figure 2.2(a). A waveguide confines a propagating electromagnetic field by repeated reflections from the walls of the waveguide [36, 37], as represented in figure 2.2(b). The method of reflection in optical fibres is commonly total internal reflection, TIR, at the optical interface [38]. Certain photonic crystal fibres are based upon photonic bandgaps, which forbid the propagating electromagnetic field from exiting the waveguide.

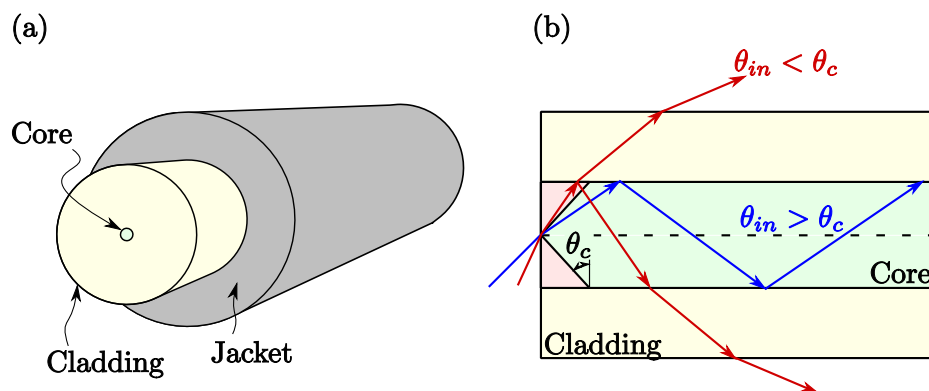


**Figure 2.2:** Illustration of optical fibre. (a) Guiding core surrounded by a lower index cladding. A protective jacket provides mechanical protection, ease of handling and some isolation from environmental contaminants. (b) Cross-section of fibre with a propagating guided ray, coloured blue,  $\theta_{in} > \theta_c$ ; and, a partially reflected, non-propagating lost ray, coloured red,  $\theta_{in} < \theta_c$ . The boundary wave,  $\theta_{in} = \theta_c$  is not shown.

The propagating electromagnetic field inside the device must obey Maxwell's equations (discussed in appendix A (page V.II A-1)) subject to the waveguide boundary conditions.

### 2.2.1 Historical overview

Optical fibres were suggested by Kao and Hockham as effective communications devices in 1966 [39]. Previously, the attenuation of glass waveguides was so large that only a few meters reduced the intensity of available light sources below the noise level of detectors. The attenuation was considered to be due to the presence of imperfections and not intrinsic to the silica material used.

<sup>12</sup>Types of structured and non-cylindrical fibres (e.g. chapters 6, 8 and 16 of [35]) are increasing, but are in a minority in terms of the quantity of deployed optical fibre.

During the 1970s improvements and refinements to the technology reduced the attenuation and improved the reliability of the fibres, thus extending the range over which they could be used for telecommunications.

Initially multimode fibres were produced due to easier manufacturing constraints, but the modal pulse dispersion and mixing of modes reduced the effectiveness of the technology. Gradient index fibres were developed to control the modal pulse dispersion [40]. By the 1980s monomode or single-mode fibres were capable of outperforming multimode fibres in terms of environmental insensitivity. As the demand for improved performance spurred new technologies in both the optical fibre technology and encoding and decoding technologies, impediments were overcome and previously lesser problems rose to the fore, motivating new technologies to mitigate them.

As these issues were encountered and dealt with, it was also appreciated that the very sensitivity that was detrimental to communications might also be used as a sensor. The effectiveness of an external influence to modulate the light would make the fibre a small and efficient sensor, drawing upon the benefits of the communications business.

As the technologies have developed, a range of fibre technologies, with associated environmental sensitivities, are now available [41]. Sixteen different fibre technologies are listed in *Specialty Optical Fibers Handbook* [35].

Total internal reflection provides the fundamental process by which guided electromagnetic radiation is confined within a fibre. TIR is briefly reviewed in appendix section F.1 (page V.II F-1), where subtleties such as the Goos–Hänchen and Imbert–Fedorov shifts are discussed. Although TIR provides the fundamental confinement, the guiding fibre further imposes a guiding mode structure upon the electromagnetic radiation launched into the fibre. The theory for the weakly guided approximation is briefly reviewed in appendix section F.2 (page V.II F-3).

### 2.2.1.1 Group and phase velocities, the cut-off frequency

The modes in an optical fibre are the eigenvalues of equation (F.13) (page V.II F-5) [42] and depend upon the polarisation of the incident electromagnetic wave [42, 43]. Letting the field components in the core and cladding be,

$$\begin{Bmatrix} E_r \\ H_r \end{Bmatrix} = \begin{Bmatrix} E_{co} \\ H_{co} \end{Bmatrix} J_l(\mathbf{U} \mathbf{r}) \quad 0 \leq \mathbf{r} \leq \mathbf{r}_{co} \quad (2.28a)$$

$$\begin{Bmatrix} E_r \\ H_r \end{Bmatrix} = \begin{Bmatrix} E_{cl} \\ H_{cl} \end{Bmatrix} K_l(\mathbf{W} \mathbf{r}) \quad \mathbf{r} > \mathbf{r}_{co} \quad (2.28b)$$

where  $J_l$  is a Bessel function of the first kind and  $K_l$  a modified Bessel function<sup>13</sup> of the second kind;  $\underline{\mathbf{U}} = \underline{\mathbf{q}} \mathbf{r}_{co}$  in the core and  $\underline{\mathbf{W}} = \underline{\mathbf{p}} \mathbf{r}_{co}$  cladding.  $\underline{\mathbf{U}}$  and  $l$  are the eigenvalues in the core, and  $\underline{\mathbf{W}}$  and  $l$  are the eigenvalues in the cladding which define the propagating mode [45].

The *normalised frequency* is defined as [45]

$$\underline{\mathbf{V}}^2 = \underline{\mathbf{U}}^2 + \underline{\mathbf{W}}^2 \quad (2.29)$$

For optical fibres, certain boundary conditions must be met. The component fields must be zero or continuous at  $r = r_{co}$ , the core boundary. Optical fibres have a  $\Delta n$  value  $\sim 1$ , which simplifies the determination of the modes, termed *the weak-guidance* approximation. The values  $E_{co}$ ,  $H_{co}$ ,  $E_{cl}$  and  $H_{cl}$  can be determined using the characteristic equation [45]

$$\frac{J'_l(\underline{\mathbf{U}})}{\underline{\mathbf{U}}J_l(\underline{\mathbf{U}})} + \frac{K'_l(\underline{\mathbf{W}})}{\underline{\mathbf{W}}K_l(\underline{\mathbf{W}})} + \left[ \frac{\underline{\mathbf{k}}_{co}^2 J'_l(\underline{\mathbf{U}})}{\underline{\mathbf{U}}J_l(\underline{\mathbf{U}})} + \frac{\underline{\mathbf{k}}_{cl}^2 K'_l(\underline{\mathbf{W}})}{\underline{\mathbf{W}}K_l(\underline{\mathbf{W}})} \right] = \underline{\beta}^2 l^2 \left[ \frac{1}{\underline{\mathbf{U}}^2} + \frac{1}{\underline{\mathbf{W}}^2} \right]^2 \quad (2.30)$$

where  $J'_l(\underline{\mathbf{U}}) = -J_{l+1}(\underline{\mathbf{U}})$  and  $K'_l(\underline{\mathbf{W}}) = K_{l+1}(\underline{\mathbf{W}})$ . When  $l = 0$  the modes are termed *transverse electric*,  $\text{TE}_{lm}$ ,<sup>14</sup> for  $E_z = 0$ , and *transverse magnetic*,  $\text{TM}_{lm}$ ,<sup>15</sup> for  $H_z = 0$ .  $m \in \mathbb{Z}$  is another integer eigenvalue, but the only permitted values are for  $\underline{\mathbf{V}}$ , termed *the cut-off frequency*, which are greater than the  $m^{\text{th}}$  root of  $J_0(\underline{\mathbf{V}}) = 0$  [43, 45, 47–49], or

$$\underline{\mathbf{V}}_{\text{cutoff}} = \underline{\mathbf{k}} \mathbf{r}_{co} \sqrt{n_{co}^2 - n_{cl}^2} = \underline{\mathbf{k}} \mathbf{r}_{co} NA \quad (2.31)$$

There is also the possibility of  $E_z$  and  $H_z$  not being zero, termed *hybrid modes*,  $\text{HE}_{lm}$  or  $\text{EH}_{lm}$ , [45, 50]. These correspond to the geometric skew (non-meridional) rays [49, 51]. The solutions are given by the product of  $l^{\text{th}}$  order Bessel functions and  $\cos(l\theta + \phi)$  or  $\sin(l\theta + \phi)$ , with  $E_z$  and  $H_\theta$  again continuous at the core/cladding boundary. The  $\text{HE}_{11}$  mode is the only mode that does not exhibit a  $\underline{\mathbf{V}}_{\text{cutoff}}$ , and can propagate independently of its value [45]. It is termed *the fundamental mode* and exists in isolation when [43]

$$0 < \underline{\mathbf{V}} < 2.405 \quad (2.32)$$

which yields the single mode in single-mode fibre. Using the desired wavelength and given refractive index values the core diameter for single-mode operation can be determined from equation (2.31).

TE, TM and EH/HE modes are one grouping of the fibre's modes. Another, more

<sup>13</sup>Also known as a *Hankel function* [44].

<sup>14</sup>Also termed *s waves*, from the German for polarisation, 'senkrecht' [46].

<sup>15</sup>Also termed *p waves*, from the German for polarisation, 'parallel' [46].

useful, grouping is in terms of *linearly polarised*, LP [42, 43, 45, 50–53], or *circularly polarised*, CP, modes [42]. In terms of LP modes,  $\text{HE}_{11}$  becomes  $\text{LP}_{01}$ , and the  $\text{TE}_{01}$ ,  $\text{TM}_{01}$  and  $\text{EH}_{21}$  modes group to become the leaky<sup>16</sup>  $\text{LP}_{11}$  [55], as modes that have the same azimuthal,  $l$ , and radial,  $\underline{U}$ , numbers. Thus, they share the same eigenvalue under the weakly guided approximation, and are indistinguishable from each other [45, 50, 51, 56]. The fundamental LP mode,  $\text{LP}_{01}$ , is therefore the single-mode condition [49].

The component plane waves propagate at  $\underline{v}_p = \frac{c}{\underline{n}_{\text{eff}}}$ , where  $\underline{n}_{\text{eff}} = \frac{\underline{\beta}}{\underline{k}}$  is the effective refractive index, which is a weighted average value between  $\underline{n}_{co}$  and  $\underline{n}_{cl}$ .  $\underline{n}_{\text{eff}}$  is the average refractive index experienced by the mode, and the weighting depends upon the degree to which the mode enters the cladding in addition to the core. Only certain discrete values of  $\underline{n}_{\text{eff}}$  allow modes to propagate and meet the boundary conditions [57]. The modal group velocity of the waves is [57, 58]

$$\underline{v}_g = \frac{d\omega}{d\underline{\beta}} = -\frac{2\pi c}{\lambda^2} \frac{d\lambda}{d\underline{\beta}} = \frac{c}{\underline{n}_g} \quad (2.33)$$

where  $\underline{n}_g$  is the group index and is given by

$$\underline{n}_g = |\underline{n}_{\text{eff}}| - \lambda \frac{d\underline{n}_{\text{eff}}}{d\lambda} \quad (2.34)$$

Thus, the waveguide adds another dispersion effect, as the modes propagate at different velocities. When the orthogonal components of a mode have different modal group velocities, the dispersion is termed *polarisation mode dispersion*.

Single-mode fibre has, potentially, thousands of cladding modes, but the use of the jacket material removes these cladding modes, preventing their propagation beyond a short distance [57].

## 2.2.2 Materials effects

Thus far the optical fibre has been an idealised device. In practice the materials used to manufacture the optical fibre introduce characteristics which depend upon the materials and upon the interactions of those materials.

### 2.2.2.1 Silica based Glass

*Glass* is a solid formed by quenching a molten liquid through the *glass transition temperature*<sup>17</sup>,  $T_g$  [60]. This process is termed *vitriification* [61]. The term *amorphous*

<sup>16</sup>A leaky or tunnelling modes has a complex propagation vector [54], e.g.  $\underline{\beta} = \underline{\gamma} + i\underline{\zeta}$ , where  $\underline{\gamma}$  and  $\underline{\zeta}$  are real. By contrast, a surface wave propagation vector will be real.

<sup>17</sup>The glass transition takes place over a temperature range (the glass is a super-cooled liquid), as opposed to exactly at  $T_g$  [59]. It is used as an indication to separate the liquid and solid phases.

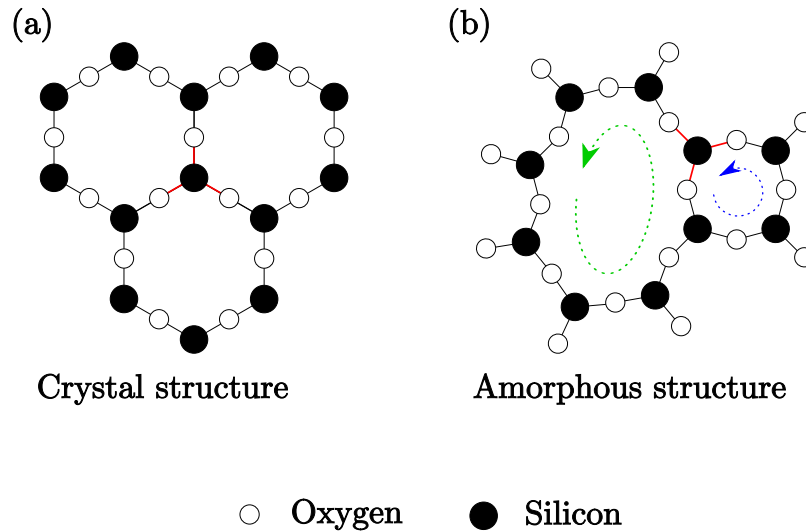


**Figure 2.3:** Two dimensional projection of Si—O—Si tetrahedra as triangles, in red. Bonds in (a) thermodynamic equilibrium crystal arrangement (quartz); (b) glass amorphous arrangement (fused silica). Two continuous random networks, CRNs, are indicated by green and blue loops. Direction arrows indicate loop as opposed to meaningful direction. After figure 5.3 of [63].

is used to describe a material lacking any long range atomic order<sup>18</sup> [60, 63]. Figure 2.3(b) illustrates Si—O—Si atoms in an amorphous glass structure.

Crystals are regular arrangements of atoms with long range order so that the pattern repeats throughout the crystal [64]. Crystalline materials can be quenched from a molten liquid phase, but upon crystallisation, the volume change with temperature is not continuous. Figure 2.3(a) illustrates Si—O—Si atoms in a hexagonal crystal structure. Glasses have a continuous transition from liquid to solid [65], i.e. a continuous volume change due to the viscosity of the material which extends the crystallisation time constants to the order of years, frustrating the process of crystallisation [60]. Crystallisation occurs at a well defined thermodynamic transition temperature, the crystallisation temperature [65]. In order to crystallise a glass forming material, termed *devitrification*, the crystallisation time constants<sup>19</sup> need to be reduced, which is achieved by keeping the material above  $T_g$ . Glasses are thus amorphous solids which exhibit a glass transition [63].

Glasses are described by three temperature based parameters: the *strain point*,

<sup>18</sup>The short range order is of the order of 3 – 10 times the interatomic distance (typically  $\sim 0.1 - 0.2$  nm). Crystals would exhibit order over a range of  $> 100$  times the interatomic distance. The interatomic distance is the equilibrium distance between bonded atoms [62].

<sup>19</sup>The time take for the structure to reach equilibrium [59].

the *annealing point* and the *softening point*. The strain point is the temperature at which the glass will begin to flow, rather than fracture. The annealing point is the temperature at which residual stresses and strains in the glass will relieve or relax on the order of minutes. The softening point is the temperature at which the glass can be worked or molded [60]. Amorphous silica glass exhibits no long range periodicity, and the material can be considered isotropic [66]. However, as  $T_g$  depends upon the rate of glass cooling, nonuniform cooling will cause variations in  $T_g$  which produce anisotropic density variations and, hence, anisotropic refractive index variations [60], producing Rayleigh scattering, discussed in section §2.2.2.2 (page V.I - 28). The manufacture of optical glasses attempts to minimise these cooling anisotropies or rates of crystallisation [65].

The glass used in the SMF-28 optical fibres is silica,  $\text{SiO}_2$ , based. The Si and O atoms form into tetrahedra, which share corner O atoms. The lines of Si—O—Si atoms can be an open 3D arrangement (glass) or a regular crystal arrangement (quartz). The silica forms large network structures as it forms a glass [63]. This open arrangement is known as the glass *continuous random network*, CRN, and is dependent upon the past thermal history. Rings of Si—O—Si atoms form, with the size dependent on the cooling rate, as illustrated in figure 2.3(b). The CRNs provide short range order of 3 – 10 times the interatomic distance, and so the wavelength of an electromagnetic radiation (both visible and IR) averages over many CRNs, reducing these density variations to a statistically continuous random quantity<sup>20</sup>.

To achieve a refractive index change<sup>21</sup> in the core of  $|\Delta n| = 0.36\%$ <sup>22</sup>, Group IVA Germanium is used as a dopant<sup>23</sup> to raise the core refractive index, substituting for silicon in the chemical arrangement [63, 67], e.g. at the silicon nodes in figure 2.3. The small percentage of  $\text{GeO}_2$  in the overall silica content in both the core and cladding allows the fibre to be considered as pure silica to within  $\pm 0.4\%$ <sup>24</sup> for bulk material properties.

Depressed cladding fibres also achieve a suitable  $\Delta n$ , where the cladding is doped, e.g. Fluorine. In this case the greater area of the cladding cross-section would require the dopant to be included in bulk material properties.

As the long range structure of glass has no discernible pattern, homogeneous glasses may be considered as spherically symmetric at macroscopic scales, in the absence of large scale cooling differences. This allows the waveguide geometry to

---

<sup>20</sup>X-ray diffraction and neutron diffusion techniques are used to investigate the short range structure of glass [63].

<sup>21</sup>The refractive index, here, is assumed to be anisotropic, for generality.

<sup>22</sup>From *Corning SMF-28e optical fiber product information*, Corning Inc. (<http://www.corning.com/assets/0/433/573/583/09573389-147D-4CBC-B55F-18C817D5F800.pdf>).

<sup>23</sup>Germania-doped silica fibres will be termed Ge:SiO<sub>2</sub> for brevity.

<sup>24</sup>Taking the core and cladding diameter as 8.2  $\mu\text{m}$  and 125  $\mu\text{m}$ , respectively<sup>25</sup>.

dictate the symmetry group. In cases where the glass is not homogeneous or deliberately stressed, as discussed in section §2.2.8.4 (page V.I - 55), the highest system symmetry will be the lowest symmetry from the waveguide point group and the symmetry Curie group of the material [55, 66].

When two symmetry groups are combined the restrictions on eigenvalues are preserved, known as *Neumann's principle* [68]. So, when isotropic spherically symmetric glass<sup>26</sup> is used with a cylindrical waveguide, cylindrical symmetry is the highest symmetry restriction [69]<sup>27</sup>.

In a silica fibre, either with a doped core or cladding, such crystal anisotropies are absent when considered at non-atomic scales. Any local anisotropy is quickly averaged with the subsequent sections to produce a very weak material anisotropy<sup>28</sup>, or effectively isotropic medium. However, isotropic materials can have an anisotropy introduced by boundary effects, as the interface between two media imposes boundary conditions not present in the rest of the media.

### 2.2.2.2 Rayleigh scattering

A material dissipating heat externally will experience internal density fluctuations, described by the *fluctuation-dissipation* theorem [74, 75], which relates a systematic extensive effect to a randomised intensive effect. The internal fluctuations can be characterised by a correlation function of relevant fluctuating physical properties or by the fluctuation spectra [74].

In optical fibres, scattering arises from molecular scale structural variations (e.g. CRNs), compositional variations in the material (e.g. variations in dopant density with CRNs) and structural inhomogeneities in the waveguide geometry (e.g. core ellipticity) [76]. The terminology for scattering processes has not always been used consistently [77]. Inelastic scattering processes, which shift the scattered wavelength by negative (Stokes shift) and positive (anti-Stokes shift) offsets, involve a Doppler-shifting propagating wave. For Raman scattering, phonons at optical frequencies provide this propagating wave, and for Brillouin scattering phonons at acoustic frequencies provide the propagating wave.

Molten glass contains local inhomogeneities due to material transport arising from convection. These local inhomogeneities contain temperature and density<sup>29</sup>,  $(\Delta T, \Delta \rho)$ , fluctuations which attempt to homogenise with a relaxation time which

<sup>26</sup>Randomly oriented molecules statistically have a spherical symmetry.

<sup>27</sup>The symmetry for a cylindrical waveguide, i.e. with degenerate propagation modes is, in Schoenflies and (Hermann-Mauguin) notations,  $C_{\infty v}$ ,  $(\frac{\infty}{m}m\uparrow)$ . With birefringence, the modes are no longer degenerate, and the symmetry reduces to  $C_{2v}$ ,  $(mm2)$  [69-72]. C, Cyclic, denotes a proper rotation axis, ( $m$  denotes a mirror plane).

<sup>28</sup>Materials showing a high binding energy show small thermal expansion [73].

<sup>29</sup>Any independent thermodynamic variables may be substituted as appropriate, e.g. temperature and pressure, or temperature and volume [78].

is a function of the temperature<sup>30</sup>. The concept of a fictive temperature,  $T_f$ , is introduced to model the glass melt system's structural relaxation time [61, 79].  $T_f$  is the temperature<sup>31</sup> at which the relaxation time for the fluctuations becomes very large, and decreasing the temperature below  $T_f$  has no appreciable effect on changing the rate of structural relaxation. The fluctuations are *frozen into* the glass.  $T_f$  and  $T_g$  are not necessarily the same value [61].

These fluctuations ( $\Delta T, \Delta\rho$ ) result in *frozen in* fluctuations in the *electric susceptibility* [78, 80]

$$\Delta\underline{\chi}_e(\underline{\mathbf{r}}, t) = \left( \frac{\partial\underline{\chi}_e}{\partial\rho} \right)_{T_0} [\Delta\rho(\underline{\mathbf{r}}, t)] + \left( \frac{\partial\underline{\chi}_e}{\partial T} \right)_{\rho_0} [\Delta T(\underline{\mathbf{r}}, t)] \quad (2.35)$$

where  $\Delta\rho(\underline{\mathbf{r}}, t)$  are local changes in density at constant temperature, and  $\Delta T(\underline{\mathbf{r}}, t)$  are local changes in temperature at constant density.

Optical fibres are manufactured to high tolerances to keep the waveguide geometry as close to uniform as possible, typically exceeding limits specified in ITU–T Recommendation G.652. However, small material density fluctuations and impurities occur [81], in addition to minor geometry fluctuations. These fluctuations arise from density fluctuations (inhomogeneities) that were in thermal equilibrium at the glass transition temperature, and were frozen into the fibre as it cooled [82, 83].

Over long distances, the integrated effect of all the minor fluctuations can become non-negligible. The scattering ‘particles’ may be actual particles, such as molecules, or scattering may occur due to fluctuations, such as density or waveguide geometry changes which will be dimensionally larger than molecules, such as network structures.

Scattering particles that are dimensionally small in comparison to the wavelength of light,  $kd \ll 1$ , are termed *Rayleigh scatterers*, i.e. the incident light at wavenumber  $k = 2\pi/\lambda$ , does not match any resonance or fluorescence conditions [84] of the scattering particles, of size  $d$ , such as the molecules in the core [85].

Rayleigh scattering is the fundamental limiting process for fibre transmission of signals, as it is inherent in the molecular nature of the constituent glass, which is shown in figure 2.4. The improvements in manufacture of fibres have reduced the losses in the 1550 nm region to near the Rayleigh scattering limit [85].

As  $kd \ll 1$ , the particle's shape is not considered important. Scatterer particles for which  $(kd \times \Delta n) \ll 1$ , where  $\Delta n$  is the refractive index difference between

---

<sup>30</sup>The Rayleigh scattering in a fibre therefore depends upon the fibre's thermal history. By extension, subsections of a fibre with different thermal histories will have different magnitudes of scattering.

<sup>31</sup>The glass has a distribution of relaxation times for the system as a whole, so a single  $T_f$  is an approximation [79]. Also, unlike the temperature,  $T_f$  relates to an extensive variable [61].

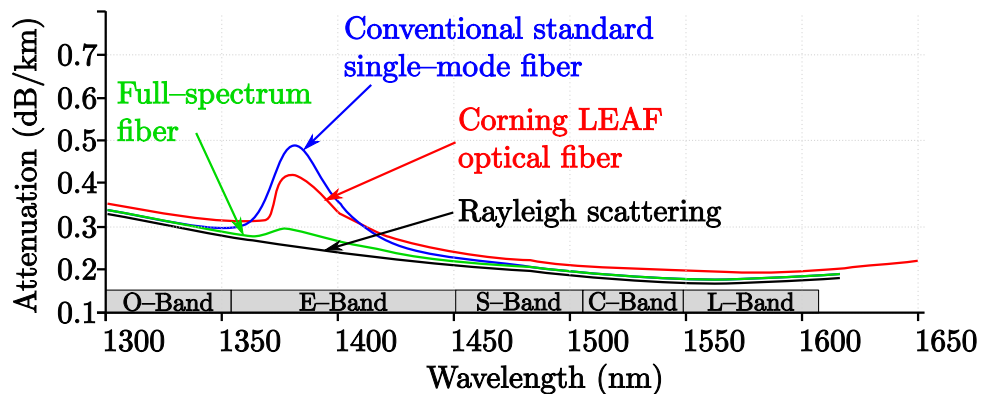


**Figure 2.4:** Attenuation spectrum for Corning SMF-28e and LEAF fibres<sup>32</sup>. The peaks about  $\sim 1380$  nm are OH absorption peaks.

the scatterer and fibre core, are termed *Rayleigh-Gans*<sup>33</sup> scatterers. This product allows for larger ‘tenuous particles’ [86] of negligible refractive index change to cause Rayleigh scattering. Small refractive index fluctuations, or small-scale extended geometry variations along a length of fibre, appear as a distribution of equivalent ‘tenuous particles’.

Both Rayleigh scattering and Rayleigh-Gans scattering are elastic scattering processes (i.e. there is no change in optical frequency) involving independent scatterers. No systematic structural arrangement of the scatterers is presumed. The scattering can therefore have a randomising effect on the scattered light’s polarisation and phase. Multiple scattering is discounted theoretically here<sup>34</sup>. Additionally, the scatterers are presumed to be wide-sense stationary, as discussed in appendix B.1 (page V.II B-1). Each scattering occurrence that propagates in the fibre will add random phase noise to the original signal [87].

The phase noise is an extensive parameter. As a signal traverses the fibre, the refractive index deviations can be considered as perturbations,  $\Delta n_{co}$ , in the averaged refractive index

$$n_s(\mathbf{r}) = \langle n_{co} \rangle + \Delta n_{co}(\mathbf{r}) \quad (2.36)$$

with the scattering fluctuations distribution given by the correlation relationship [87]

$$\langle \Delta n_{co}(\mathbf{r}_1) \Delta n_{co}(\mathbf{r}_2) \rangle = \langle \Delta n_{co}^2(\mathbf{r}) \rangle e^{-\frac{|\mathbf{r}_1 - \mathbf{r}_2|}{L_{coh}}} \quad (2.37)$$

<sup>32</sup>After *Corning SMF-28e+ optical fiber with NexCor Technology product information*, Corning Inc. (<http://www.corning.com/WorkArea/showcontent.aspx?id=27659>) and *Corning LEAF Optical fiber product information*, Corning Inc. (<http://www.corning.com/docs/opticalfiber/pi1107.pdf>).

<sup>33</sup>Or *Rayleigh-Gans-Born* scatterers [86]

<sup>34</sup>This may be justified by the quantity of light being multiply scattered being much lower than for single scattering, and that the randomising effect on the phase angle will be wrapped back into  $(-\pi, \pi]$ .

where  $\Delta \underline{n}_{\text{co}}(\mathbf{r}) = \underline{n}_{\text{co}}(\mathbf{r}) - \langle \underline{n}_{\text{co}} \rangle$ , and  $L_{\text{coh}}$  is the coherence length of the refractive index fluctuations [88]. As the value of  $\langle \Delta \underline{n}^2(\mathbf{r}) \rangle \ll 1$  the correlation can be rewritten as delta function correlated [89]

$$\langle \Delta \underline{n}(\mathbf{r}_1) \Delta \underline{n}(\mathbf{r}_2) \rangle = \underline{D}_{fl} \delta(\mathbf{r}_1 - \mathbf{r}_2) \quad (2.38)$$

where  $\underline{D}_{fl}$  is a constant characterising the magnitude of  $\Delta \underline{n}_{\text{co}}(\mathbf{r})$ .

As the scattered radiation arises from a perturbation of  $\underline{n}_{\text{co}}$ , the wave guiding solutions apply<sup>35</sup>. The scattered radiation will therefore couple to core and cladding modes depending upon the phase matching condition the radiation meets. The scattered radiation in the cladding modes is lost<sup>36</sup>, i.e. attenuated as  $e^{-\alpha_{sc}L}$ , where  $\alpha_{sc}$  is the loss coefficient.

In the absence of any other type of attenuation, Rayleigh scattering provides a minimum attenuation during signal transmission [82, 85]. As an extensive effect the captured signal intensity needs to be greater than the total Rayleigh scattering losses and co-propagating scattered light.

The impact of Rayleigh scattering on remote and distributed sensing is in limiting distances without increasing the incident intensity (and potentially introducing non-linear effects) or signal amplification at regular intervals along the transmission length (which will also amplify the Rayleigh scattered noise).

The total phase shift accumulated by radiation traversing a length  $L$  of the fibre is [89]

$$\begin{aligned} \underline{\Phi}_{\text{tot}}(L) &= \underline{\Phi}(L) + \Delta \underline{\Phi}(L) \\ \Rightarrow \frac{2\pi}{\lambda} \int_0^L \underline{n}_s(\mathbf{r}) d\mathbf{r} &= \frac{2\pi}{\lambda} \langle \underline{n}_{\text{co}} \rangle L + \frac{2\pi}{\lambda} \int_0^L \Delta \underline{n}_{\text{co}}(\mathbf{r}) d\mathbf{r} \end{aligned} \quad (2.39)$$

The perturbation of the phase is a random walk with mean square

$$\begin{aligned} \langle \Delta \underline{n}_{\text{co}}(\mathbf{r})^2 \rangle &= \left(\frac{2\pi}{\lambda}\right)^2 \iint_0^L \langle \Delta \underline{n}_{\text{co}}(\mathbf{r}_1) \Delta \underline{n}_{\text{co}}(\mathbf{r}_2) \rangle d\mathbf{r}_1 d\mathbf{r}_2 \\ &= \underline{D}_{fl} \left(\frac{2\pi}{\lambda}\right)^2 L \equiv \frac{2L}{L_{\text{coh}}} \end{aligned} \quad (2.40)$$

where  $L_{\text{coh}}$  is the coherence length<sup>37</sup> for the accumulated random phases equal to  $2\pi^2$  [89], as illustrated in figure 2.5.

The refractive index fluctuation consists of many independent random fluctuations, and so will be Gaussian distributed [89]. Using the Gaussian probability

---

<sup>35</sup>The perturbation method is used to model the FBG using a periodic modulation (appendix §G.2.2 (page V.II G-5)). The perturbation here is randomly distributed and individually of much smaller magnitude.

<sup>36</sup>Neglecting that small fraction of the cladding modes coupled back into a core mode, which just adds to the core mode phase noise.

<sup>37</sup>The coherence length is, by definition, a scalar quantity. However, the coherence length need not be the same under anisotropy along the orthogonal axes. Thus, it is conveniently represented as a vectorial quantity with the understanding that it be taken as the scalar length for the EM beam component along the corresponding axis.

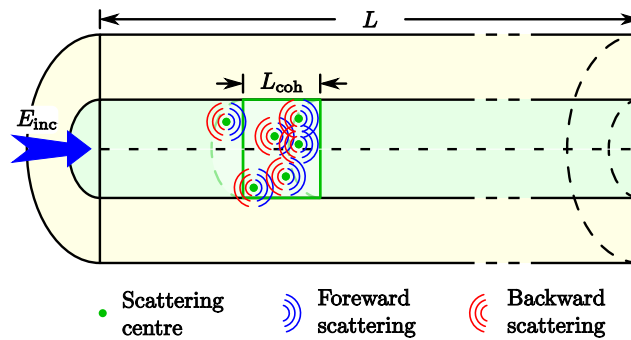


**Figure 2.5:** Incident light,  $E_{inc}(\mathbf{r})$ , forward (blue) and backward (red) scattered by refractive index fluctuation scatterers. The length  $L_{coh}$  is characteristic of the fibre, and is the length over which the phase undergoes a random walk of  $2\pi^2$  radians.

function the phase noise fluctuation can be written as [89]

$$\langle e^{i\Delta\Phi} \rangle = e^{-\frac{L}{L_{coh}}} \quad (2.41)$$

There exists the possibility of *Double Rayleigh backscattering* [90], where the scattered light experiences further scattering, reversing the direction again. Double scattering will be a weak contribution to phase noise. This does not violate the single-scattering condition, as the second scattering is assumed to be in the far-field, i.e independent, rather than multiply scattered in the near-field. The removal of Rayleigh scattering originating phase-noise can allow previously undetectable signals to be effectively demodulated, as discussed in chapter 6.

### 2.2.3 Physical (optical) properties

The internal geometry of materials determines the physical properties of the material [91]. The linear responses are first order responses, which are encountered in this work. The linear reversible relationship between physical properties<sup>38</sup> is illustrated in figure 2.6 using an extended Heckmann diagram [7, 66, 92, 93]<sup>39</sup>. The variables in figure 2.6 are defined in table 2.1 (page V.I - 35). The outer pyramid contains intensive parameters and the inner pyramid the extensive parameters.

For clarity, not all connections are shown, and a similar diagram may be constructed for transport phenomena such as electric field, temperature gradient and concentration gradient [66]. The omitted connections are shown in figure 2.7 (page

<sup>38</sup>A physical property is defined as a relationship between two measured quantities [68].

<sup>39</sup>The Heckmann diagram relates the intensive parameters  $T$ ,  $\mathbf{E}$  and  $\underline{\sigma}$  to their respective extensive parameters and to the other extensive and intensive parameters. The product of an intensive parameter and its associated extensive parameter is homogeneous to an energy [94]. The Heckmann diagram is extended by adding magnetic phenomena [66].

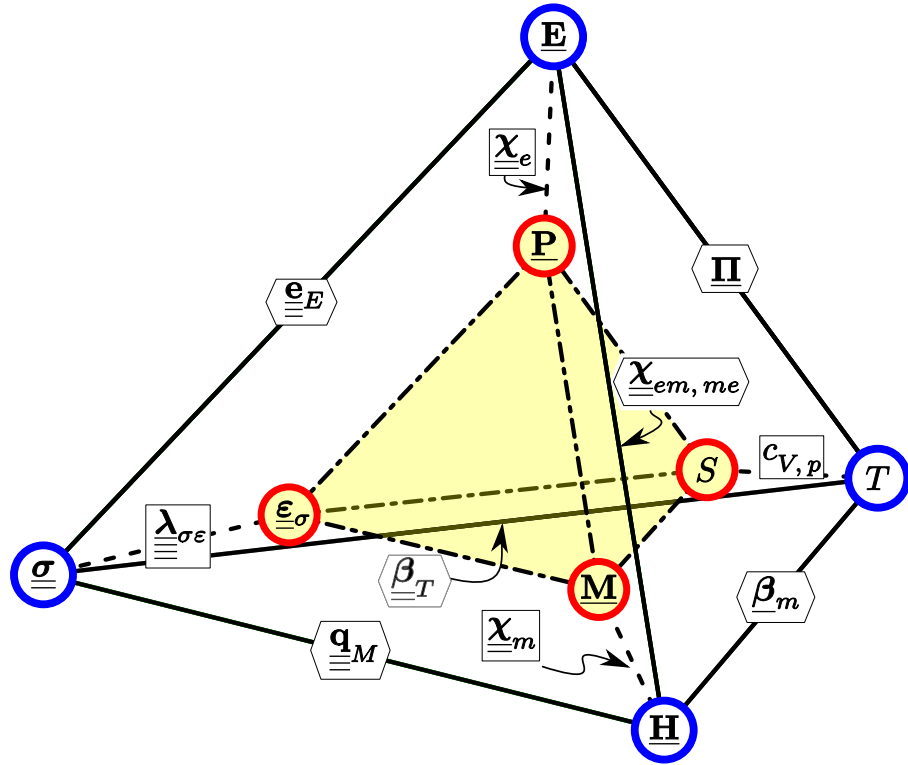


**Figure 2.6:** Linear inter-relationships of Electric field,  $\underline{\mathbf{E}}$ , Magnetic field,  $\underline{\mathbf{H}}$ , Stress,  $\underline{\boldsymbol{\sigma}}$ , and Temperature,  $T$ , on an extended Heckmann diagram, after figures 1.1 and 1.2 of [66]. Table 2.1 (page V.I - 35) contains the legend for clarity.

V.I - 34), with the names and tensor rank included. The linear relationships between intensive and extensive parameters may be summarised by the following matrix [94]

$$\begin{pmatrix} \underline{\boldsymbol{\varepsilon}}_{\sigma} \\ \underline{\mathbf{P}} \\ \underline{\mathbf{M}} \\ \delta S \end{pmatrix} = \begin{pmatrix} \underline{\lambda}_{\sigma\varepsilon} & \underline{C}_{\underline{\boldsymbol{\varepsilon}}_{\sigma}}^{\underline{\mathbf{E}}} & \underline{C}_{\underline{\boldsymbol{\varepsilon}}_{\sigma}}^{\underline{\mathbf{H}}} & \underline{\alpha}_{T\varepsilon_{\sigma}} \\ \underline{C}_{\underline{\mathbf{P}}}^{\underline{\boldsymbol{\sigma}}} & \underline{\chi}_e & \underline{C}_{\underline{\mathbf{P}}}^{\underline{\mathbf{H}}} & \underline{C}_{\underline{\mathbf{P}}}^T \\ \underline{C}_{\underline{\mathbf{M}}}^{\underline{\boldsymbol{\sigma}}} & \underline{C}_{\underline{\mathbf{M}}}^{\underline{\mathbf{E}}} & \underline{\chi}_m & \underline{C}_{\underline{\mathbf{M}}}^T \\ \underline{C}_{\underline{S}}^{\underline{\boldsymbol{\sigma}}} & \underline{C}_{\underline{S}}^{\underline{\mathbf{E}}} & \underline{C}_{\underline{S}}^{\underline{\mathbf{H}}} & c_{V,p} \end{pmatrix} \begin{pmatrix} \underline{\boldsymbol{\sigma}} \\ \underline{\mathbf{E}} \\ \underline{\mathbf{H}} \\ T \end{pmatrix} \quad (2.42)$$

where each element of the matrix and vectors is the sub-matrix of the appropriate tensor.

The physical properties may be represented as tensors<sup>40</sup>, which in turn may be

<sup>40</sup>Tensors do not depend upon the reference frame (co-ordinate system) used [7,95], whereas the scalar components do. The distinction between a matrix and tensor is that the tensor components may be rearranged into another matrix which is no longer a tensor, such as in contracted [96] or

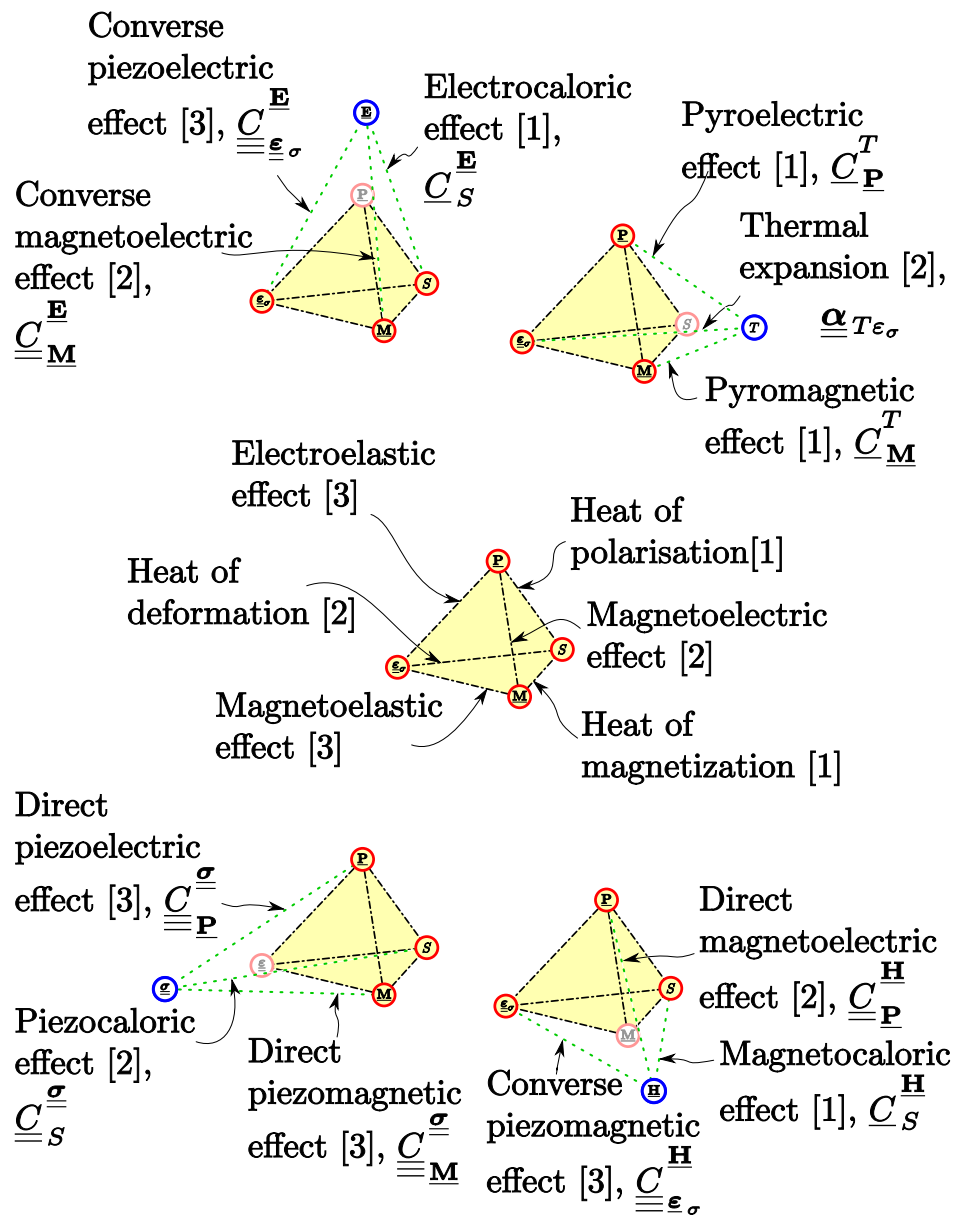


**Figure 2.7:** Linear cross-coupled relationships of Electric field,  $\underline{E}$ , Magnetic field,  $\underline{H}$ , Stress,  $\underline{\sigma}$ , and Temperature,  $T$ , from the extended Heckmann diagram of figure 2.6.

Variable	Name	Rank
$\underline{\underline{\lambda}}_{\sigma\varepsilon} \left( \underline{\underline{c}}_{\sigma\varepsilon}, \underline{\underline{s}}_{\varepsilon\sigma} \right)$	Elasticity (stiffness, compliance)	{4}
$\underline{\underline{E}}$	Electric Field	{1}
$\underline{\underline{\chi}}_e$	Electric Susceptibility	{2}
$S$	Entropy	{0}
$\underline{\underline{M}}$	Magnetisation	{1}
$\underline{\underline{\chi}}_{em,me}$	Magnetolectricity ( $\underline{\underline{\chi}}_{em}$ is not necessarily equal to $\underline{\underline{\chi}}_{me}$ )	{2}
$\underline{\underline{H}}$	Magnetic Field	{1}
$\underline{\underline{\chi}}_m$	Magnetic Susceptibility	{2}
$\underline{\underline{e}}_E$	Piezoelectricity	{3}
$\underline{\underline{q}}_M$	Piezomagnetism	{3}
$\underline{\underline{P}}$	Polarisation	{1}
$\underline{\underline{\Pi}}$	Electrothermal effects	{1}
$\underline{\underline{\beta}}_m$	Magneto thermal effects	{1}
$c_{V,p}$	Specific heat (fixed volume, $V$ , or fixed pressure, $p$ )	{0}
$\underline{\underline{\varepsilon}}_\sigma$	Strain	{2}
$\underline{\underline{\sigma}}$	Stress	{2}
$T$	Temperature	{0}
$-\underline{\underline{f}}_T$	Thermal pressure	{2}
$\underline{\underline{f}}_T$	Heat of deformation	{2}
$\underline{\underline{\alpha}}_T$	Thermal expansion	{2}

**Table 2.1:** Legend for variables in figure 2.6 (page V.I - 33).

represented as matrices. Temperature,  $T$ , is a rank zero tensor, or scalar quantity. The already introduced electric field,  $\underline{\underline{E}}$ , is a rank one tensor or vector quantity. The stress,  $\underline{\underline{\sigma}}$ , is a rank two matrix, or dyadic quantity.

The relationships in the plane defined by the variables  $T$ ,  $\underline{\underline{E}}$  and  $\underline{\underline{\sigma}}$  are polar quantities, while the magnetic  $\underline{\underline{H}}$  and  $\underline{\underline{M}}$  are axial quantities [66].

In general, the rank of the tensor connection between two nodes will be the sum of the ranks of those nodes<sup>41</sup>. For example, when the second rank dielectric constant,  $\underline{\underline{\varepsilon}} = \varepsilon_0 \left( \underline{\underline{I}} + \underline{\underline{\chi}}_e \right)$  from equation (A.5a) (page V.II A-2), interacts with an applied electric field,  $\underline{\underline{E}}$ , the relationship is termed the *reciprocal dielectric constant* or *impermeability* [7]

$$\underline{\underline{B}}_\varepsilon = \underline{\underline{\varepsilon}}^{-1} = \underline{\underline{r}} \underline{\underline{E}} \quad (2.43)$$

or

---

Voigt notation [7].

<sup>41</sup>The rank denotes the number of directions (axes) along which measurements of the property need to be made. The axes may not align, and so are counted separately [68].

$$\underline{\underline{\mathbf{B}}}_\varepsilon = \underline{\underline{\boldsymbol{\varepsilon}}}^{-1} = \underline{\underline{\mathbf{f}}} \underline{\underline{\mathbf{P}}} \quad (2.44)$$

where  $\underline{\underline{\mathbf{r}}}$  and  $\underline{\underline{\mathbf{f}}}$  are the *linear electro-optic*, *photoelastic* or the *Pockels* tensors in terms of  $\underline{\underline{\mathbf{E}}}$  or  $\underline{\underline{\mathbf{P}}}$ , respectively. Similarly, the polarisation,  $\underline{\underline{\mathbf{P}}}$  is related to stress,  $\underline{\underline{\boldsymbol{\sigma}}}$  by the third rank *piezoelectric stress* tensor or the *direct piezoelectric effect* [7].

Examples of a fourth rank tensor are: the *elastic stiffness* tensor<sup>42</sup>,  $\underline{\underline{\boldsymbol{\lambda}}}_{\sigma\varepsilon}$ , relating  $\underline{\underline{\boldsymbol{\sigma}}}$  to  $\underline{\underline{\boldsymbol{\varepsilon}}}_\sigma$ ; and the *photoelastic*, *elasto-optic* or *strain-optic* tensor,  $\underline{\underline{\mathbf{p}}}_{B\varepsilon\sigma}$ , relating  $\underline{\underline{\mathbf{B}}}_\varepsilon$  to  $\underline{\underline{\boldsymbol{\varepsilon}}}_\sigma$  [7].

The number of components of the various physical properties and their relations will scale as  $d^n$ , where  $d$  is the number of dimensions and  $n$  is the rank of the matrix describing that physical property.  $\underline{\underline{\mathbf{p}}}_{B\varepsilon\sigma}$  will therefore have 81 elements. At macroscopic scales, the properties may be grouped as point groups [7, 70]. Using Neumann's principle<sup>43</sup>, the symmetry of the system, such as the crystal planes of a crystal or cylindrical symmetry of a fibre, will reduce the number of independent components, i.e. degrees of freedom. Additionally, physical restrictions of the property can further reduce independent components by increasing symmetry, such as for *thermal expansion*,  $\underline{\underline{\boldsymbol{\alpha}}}_{T\varepsilon\sigma}$ , which is a symmetric tensor, i.e.  $\alpha_{T\varepsilon\sigma ij} = \alpha_{T\varepsilon\sigma ji}$  [7]. This results in six independent components rather than nine. The higher the symmetry of the system, the less independent non-zero components that remain. Point group transformations leave tensor components unchanged, preserving the reduced number of independent components.

The nodes of the intensive and extensive pyramids of figure 2.6 (page V.I - 33) are termed the *thermodynamic co-ordinates* describing the material [7]. For non-magnetic materials, there are twenty thermodynamic co-ordinates. The tensor connections between extensive nodes and their associated intensive nodes are calculated via the first law of thermodynamics<sup>44</sup> [7, 97]

$$dU = dQ + dW = TdS + \underline{\underline{\mathbf{E}}} \bullet d\underline{\underline{\mathbf{D}}} + \underline{\underline{\boldsymbol{\sigma}}} \bullet d\underline{\underline{\boldsymbol{\varepsilon}}}_\sigma \quad (2.45)$$

where  $dU$  is the change in internal energy per unit volume,  $dQ$  is the heat received by a unit volume, i.e.  $TdS$ , and  $dW$  is the work done by that unit volume, i.e.  $\underline{\underline{\mathbf{E}}} \bullet d\underline{\underline{\mathbf{D}}} + \underline{\underline{\boldsymbol{\sigma}}} \bullet d\underline{\underline{\boldsymbol{\varepsilon}}}_\sigma$ .

When cross-coupling occurs between  $T$ ,  $\underline{\underline{\mathbf{E}}}$  and  $\underline{\underline{\boldsymbol{\sigma}}}$ , the Gibbs free energy equation

---

<sup>42</sup>Also denoted as  $\underline{\underline{\mathbf{c}}}_{\sigma\varepsilon}$  [7].

<sup>43</sup>Which implies that no physical property can ever be of lower symmetry than that of the material [7].

<sup>44</sup>The product of an extensive parameter and its associated intensive parameter has the dimensions of energy [94]. This is not the case for the relationships illustrated in figure 2.7 (page V.I - 34).

[7, 98, 99],

$$G_b(T, \underline{\mathbf{E}}, \underline{\underline{\boldsymbol{\sigma}}}) = U - TS - \underline{\mathbf{E}} \bullet d\underline{\mathbf{D}} - \underline{\underline{\boldsymbol{\sigma}}} \bullet d\underline{\underline{\boldsymbol{\varepsilon}}}_\sigma \quad (2.46)$$

is used to define the relationships.

Differentiating (2.46) and substituting equation (2.45) gives

$$dG_b = -SdT - \underline{\underline{\boldsymbol{\varepsilon}}}_\sigma d\underline{\underline{\boldsymbol{\sigma}}} - \underline{\mathbf{D}}d\underline{\mathbf{E}} \quad (2.47)$$

from which, and by fixing the other two variables, we get [92, 99]

$$S = - \left( \frac{\partial G_b}{\partial T} \right)_{\underline{\underline{\boldsymbol{\sigma}}}, \underline{\mathbf{E}}} \quad (2.48a)$$

$$\underline{\mathbf{D}} = - \left( \frac{\partial G_b}{\partial \underline{\mathbf{E}}} \right)_{\underline{\underline{\boldsymbol{\sigma}}}, T} \quad (2.48b)$$

$$\underline{\underline{\boldsymbol{\varepsilon}}}_\sigma = - \left( \frac{\partial G_b}{\partial \underline{\underline{\boldsymbol{\sigma}}}} \right)_{T, \underline{\mathbf{E}}} \quad (2.48c)$$

The physical constants represented in figures 2.6 (page V.I - 33) and 2.7 (page V.I - 34) are defined by taking the appropriate second order derivative of equations (2.48), e.g.

$$\underline{\underline{\boldsymbol{\alpha}}}|_{\underline{\mathbf{E}}} = - \left( \frac{\partial^2 G_b}{\partial T \partial \underline{\underline{\boldsymbol{\varepsilon}}}_\sigma} \right)_{\underline{\mathbf{E}}} \quad \text{Thermal expansion effect} \quad (2.49a)$$

$$\underline{\underline{\mathbf{p}}}|_{B\varepsilon_\sigma} \Big|_T = - \left( \frac{\partial^2 G_b}{\partial \underline{\underline{\boldsymbol{\varepsilon}}}_\sigma \partial \underline{\underline{\boldsymbol{\varepsilon}}}_\sigma} \right)_T \quad \text{Elasto-optic effect} \quad (2.49b)$$

The direct and converse relationships can be obtained by reversing the order of differentiation [99]. When the order of differentiation doesn't matter the variables required to characterise the system are reduced by this increase in symmetry [7].

Measurements at optical frequencies are effectively clamped (constant strain) and adiabatic (constant entropy) as the thermal and elastic relaxation times are much longer than the optical period  $\sim 10^{-14}$  s [7].

### 2.2.4 Stress{2} and Strain{2}<sup>45</sup>

*Stress*,  $\underline{\underline{\boldsymbol{\sigma}}}$ , is a distributed force acting on an internal or external surface of an object [100], and is an intensive property. Pressure is an example of compressive stress. *Strain*,  $\underline{\underline{\boldsymbol{\varepsilon}}}_\sigma$ , is a material dependent response to the stress, and is an extensive property.

In the material's linear regime, the dependence is provided by the *modulus of*

<sup>45</sup>The section titles are using the rank notation from table 2.1 (page V.I - 35).

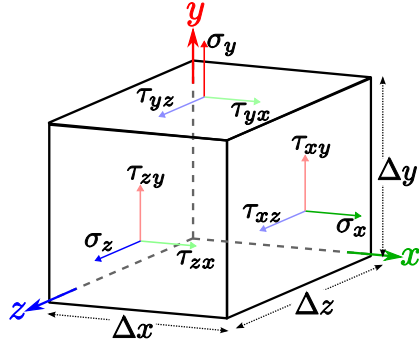


**Figure 2.8:** Stresses acting on three orthogonal surfaces (after figure 2.4 of [100], and figure 5.1 of [101]).

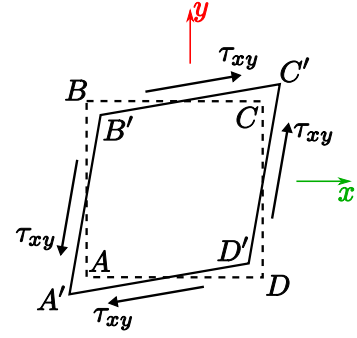


**Figure 2.9:** Shear deformation of one surface (after figure 2.7 of [100]).

*elasticity* or *Young's modulus*, and by *Poisson's ratio*, as in figure 2.6 (page V.I - 33).

The stress tensor for an object, as in figure 2.8, is (in an arbitrary Cartesian co-ordinate system)

$$\underline{\underline{\sigma}} = \begin{pmatrix} \sigma_{xx} & \tau_{xy} & \tau_{xz} \\ \tau_{yx} & \sigma_{yy} & \tau_{yz} \\ \tau_{zx} & \tau_{zy} & \sigma_{zz} \end{pmatrix} \quad (2.50)$$

where  $\sigma_{ii}$  is the *normal stress* acting along the surface normal  $i$ , or

$$\sigma_{ii} = \frac{dF_{ii}}{dA_i} \quad i = x, y, z \quad (2.51)$$

and  $\tau_{xy}$  is the *tangential* or *shear stress* from a force about  $x$  upon co-ordinate  $y$ ,

$$\tau_{ij} = \frac{dF_{ij}}{dA_i} \quad i, j = x, y, z; i \neq j \quad (2.52)$$

$dF_{ii}$  and  $dF_{ij}$  are, respectively, the normal force perpendicular to and tangential to infinitesimal area  $dA_i$ . For clarity of presentation the repeated index of on-diagonal elements is reduced to  $\sigma_i$ .

For most materials  $\tau_{ij} = \tau_{ji}$  and, by symmetry, six independent variables remain,

$$\underline{\underline{\sigma}} = \begin{pmatrix} \sigma_x & \tau_{xy} & \tau_{xz} \\ \tau_{xy} & \sigma_y & \tau_{yz} \\ \tau_{xz} & \tau_{yz} & \sigma_z \end{pmatrix} \quad (2.53)$$

Following from equations (2.51) and (2.52), each  $\underline{\underline{\sigma}}$  component has an associated strain,  $\varepsilon_{\sigma_i}$  for *normal strains*, and  $\gamma_{\sigma_{ij}}$  for *shear strains*. A normal strain involves extension along the normal's axis, and a contraction along the remaining axes.

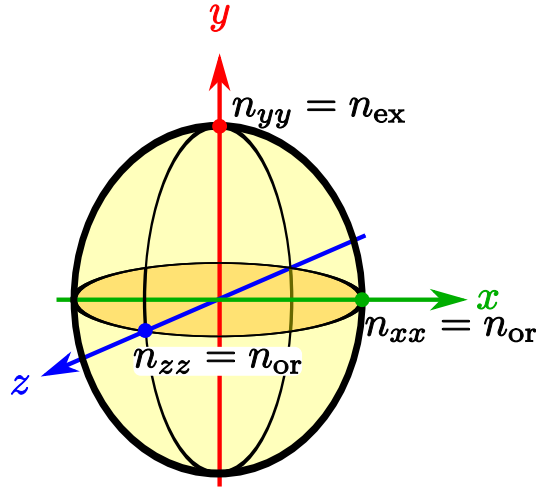


**Figure 2.10:** Ellipsoid of the indices, indicatrix, for a uniaxial material (after [102,103]).  $n_{or}$  and  $n_{ex}$  are the ordinary and extraordinary refractive indices, respectively.

Hooke's law is assumed for basic derivations and so the normal strains are given by

$$\varepsilon_{\sigma x} = \frac{1}{E_{\sigma}} (\sigma_x - \nu_{\sigma}(\sigma_y + \sigma_z)) \quad (2.54)$$

where  $E_{\sigma}$  is the *modulus of elasticity* and  $\nu_{\sigma}$  is *Poisson's ratio*. If all the normal strains,  $\varepsilon_{\sigma}$ , are known, then the normal stresses can be determined by solving simultaneously.

Shear strains involve a change in angles of the shape. The angle  $\angle BAC$  in figure 2.9 is changed to  $\angle B'A'C'$  under shear stress. The shear strains are linearly related to the shear stress by

$$\gamma_{\sigma xy} = \frac{\tau_{xy}}{G_{\sigma}} \quad (2.55)$$

where  $G_{\sigma}$  is the *shear modulus*, and similarly for  $\gamma_{\sigma xy}$  and  $\gamma_{\sigma xz}$ .

A linear strain is simply the change in length,  $\delta l_z$ , divided by the unstrained length,  $l_z$ ,

$$\varepsilon_{\sigma z} = \frac{\delta l_z}{l_z} \quad (2.56)$$

#### 2.2.4.1 Indicatrix{2}

Isotropic materials have no directional variation in their electromagnetic properties, e.g.  $\underline{n} = n$ , and scalar constitutive parameters link the induction fields  $\underline{\mathbf{D}}$  and  $\underline{\mathbf{B}}$  to the primitive fields  $\underline{\mathbf{E}}$  and  $\underline{\mathbf{H}}$  [104].

Crystals have a material based anisotropy, as the bonds occur in regular direc-

tions with consistent strengths. The directional dependence of the electromagnetic properties is expressed in the speed of propagation of the wave as in equation (A.12) (page V.II A-4), e.g.

$$n_x = \frac{c}{v_x} = \sqrt{\epsilon_{r_x} \mu_{r_x}} \approx \sqrt{\epsilon_{r_x}}$$

For anisotropic materials  $n_x \neq n_y$ , i.e. the material is birefringent.

The arrangement can be represented as an ellipsoid, the indicatrix, as in figure 2.10.

This arises from a generalisation of the polarisation ellipse, figure E.1 (page V.II E-2), to three-dimensions [105]. This is to account for any of the material axes not coinciding with the propagation vector of  $\underline{\mathbf{E}}$ . The material response induces a polarisation in the material, as represented in figure 2.6 (page V.I - 33). The response of the material, the refractive index, is therefore also described by an ellipsoid. A symmetric tensor, describing the ellipsoid, may be recast so that it is diagonal, by the suitable choice of co-ordinates [105]. When  $\underline{\mathbf{E}}$  is parallel to one of the axes of the diagonalised tensor two non-zero terms are left. Thus, these terms can be represented as a vector, i.e.  $\underline{\underline{n}} \rightarrow \underline{n}$ , which is the form used in this work.

The equation of the ellipsoid<sup>46</sup> is

$$\frac{x^2}{n_{xx}^2} + \frac{y^2}{n_{yy}^2} + \frac{z^2}{n_{zz}^2} + \frac{2xy^2}{n_{xy}^2} + \frac{2yz^2}{n_{yz}^2} + \frac{2xz^2}{n_{xz}^2} = 1 \quad (2.57)$$

and in the eigen-reference system of the medium OXYZ, this reduces to

$$\frac{X^2}{n_{XX}^2} + \frac{Y^2}{n_{YY}^2} + \frac{Z^2}{n_{ZZ}^2} = 1 \quad (2.58)$$

where  $n_{XX}$ ,  $n_{YY}$  and  $n_{ZZ}$  are the principal refractive indices, in the directions shown in figure 2.8 (page V.I - 38).

A polarisation retarder (waveplate) introduces a relative phase shift between the orthogonal components of the electromagnetic radiation, as illustrated in figure 2.11. The retarder is a birefringent optical element with the relative phase shift given by [108]

$$\Delta\Phi_B = \frac{2\pi}{\lambda} (n_{\text{ex}} - n_{\text{or}}) d \quad (2.59)$$

and is inversely proportional to wavelength, and  $\underline{n}_{\text{or}}$  and  $\underline{n}_{\text{ex}}$ , are the *ordinary* and *extraordinary* refractive indices, respectively. If the term  $(n_{\text{ex}} - n_{\text{or}})$  was directly proportional to wavelength then the two terms could be designed to cancel the

---

<sup>46</sup>The fractions in equation (2.57) (page V.I - 40) are the components of the tensor  $\underline{\underline{\mathbf{B}}}_\epsilon = \left(\underline{\underline{\epsilon}}_r\right)^{-1}$ , from the relation  $\underline{\mathbf{E}} = \epsilon_0^{-1} \left(\underline{\underline{\epsilon}}_r\right)^{-1} \underline{\mathbf{D}}$ , equation (2.43) (page V.I - 35), using the inverse of equation (A.5a) (page V.II A-2) [103, 106, 107].

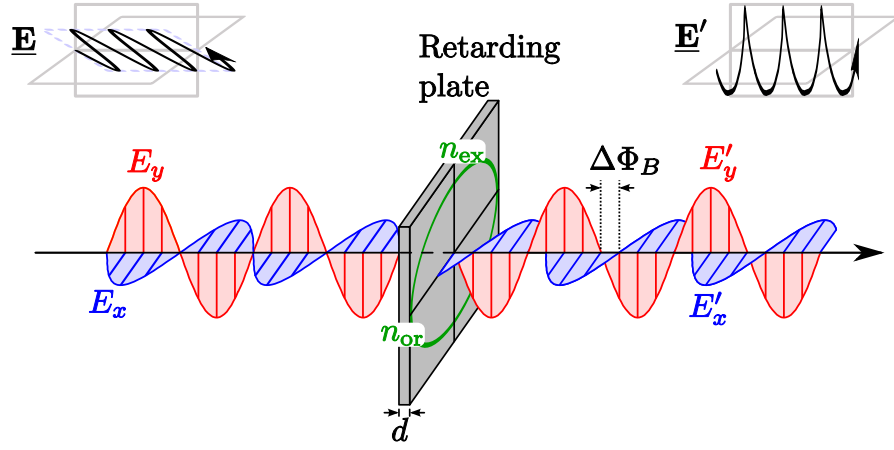


**Figure 2.11:** Retardation plate delaying  $E'_y$  with respect to  $E'_x$  by  $\Delta\Phi_B$ .

wavelength dependence, producing an achromatic retarder. This does not occur in practice and approximately achromatic retarders are possible by combining different materials [108]. Typically, an elliptically polarised beam is converted to an elliptically polarised beam of different ellipticity<sup>47</sup>.

Two readily commercially available retarders are the quarter- and half-waveplates, with  $\Delta\Phi_B = \frac{\pi}{2}$  and  $\pi$ , respectively. Linearly polarised light at  $\frac{\pi}{4}$  to the birefringent axes of a quarter-waveplate will result in circularly polarised light. Linearly polarised light at  $\frac{\pi}{4}$  to the birefringent axes of a half-waveplate will result in linearly polarised light in the orthogonal direction.

#### 2.2.4.2 Photoelasticity{4}

The effect of the stress field on certain optical media is termed the *photoelastic* or *strain-optic* effect,  $\underline{\underline{\mathbf{p}}}_{B\varepsilon\sigma}$  [7,109]. This is the introduction or alteration of the optical polarisation properties, which are wavelength dependent [110]. In the presence of the strain field,  $\underline{\underline{\varepsilon}}_\sigma$ , an isotropic medium may become anisotropic, and so the orthogonal components of propagating electromagnetic radiation separate by the different refractive indices,  $n_{or}$  and  $n_{ex}$ .

Elastic stress induces linear anisotropy, whereas torque elastic stress induces circular anisotropy. Taking the case of linear anisotropy in an initially isotropic medium, the optical axes will coincide with the applied stress.

Using the coefficients  $1/n_{ij}^2$  of the ellipsoid equation (2.57) gives

$$\frac{1}{n_{ij}^2} = \frac{1}{n_{ij}^2} \Big|_{[\sigma]=0} + \Delta \left[ \frac{1}{n_{ij}^2} \right] \quad (2.60)$$

<sup>47</sup>Due to elliptically polarised beams having a greater probability of occurring.

where  $\Delta \left[ \frac{1}{n_{ij}^2} \right]$  is a function of the applied stress field,  $\underline{\underline{\sigma}}$ . A first order expansion as a function of the stress tensor is usually sufficient [111]. Using Einstein's summation convention on repeated indices gives

$$\Delta \left[ \frac{1}{n_{ij}^2} \right] = q_{ijkl} \sigma_{kl} \quad (2.61)$$

where  $\underline{\underline{\mathbf{q}}}_{B\varepsilon\sigma}$  is the fourth rank *piezo-optical* tensor, which modifies the refractive indices  $n_{ij}$  [7, 109]. From Hooke's law  $\underline{\underline{\sigma}}$  induces  $\underline{\underline{\varepsilon}}_{\sigma}$ , and equation (2.61) can be rewritten as:

$$\Delta \left[ \frac{1}{n_{ij}^2} \right] = p_{B\varepsilon\sigma ijmn} \varepsilon_{\sigma mn} \quad (2.62)$$

where  $\underline{\underline{\mathbf{p}}}_{B\varepsilon\sigma}$  is the photoelastic tensor related to the piezo-optical tensor  $\underline{\underline{\mathbf{q}}}_{B\varepsilon\sigma}$  and to the elastic stiffness tensor  $\underline{\underline{\lambda}}_{\sigma\varepsilon}$  by

$$\underline{\underline{\mathbf{p}}}_{B\varepsilon\sigma} = \underline{\underline{\mathbf{q}}}_{B\varepsilon\sigma} \underline{\underline{\lambda}}_{\sigma\varepsilon} \quad (2.63)$$

Symmetry can reduce the independent components that need to be determined. The strain-optical effects of a given stress or strain can be calculated if the material properties are known. However, a complicating factor is that a given stress field may not produce the same strain instantaneously in different materials, or along different axes of anisotropic materials. This has been called *creep* [112], although the categorisation of creep varies, it can variously be a superset of or subset of strain relaxation depending upon the definition [113, 114]. The eventual magnitude of creep can exceed the elastic limit of materials [115].

Different types of elastic creep are recognised. *Primary creep* is a reversible change, and is a retarded elastic effect [7]. *Steady-state creep* is a highly temperature dependent creep, where the viscosity of the creeping material,  $\eta_{\text{creep}}$  exhibits a power law relation to stress [7, 116]

$$\frac{d\eta_{\text{creep}}}{dt} = A \underline{\underline{\sigma}}^m \sim e^{-\frac{E_c}{k_B T}} \quad (2.64)$$

where  $A$  and  $m$  are material constants,  $E_c$  is an activation energy and  $k_B$  is Boltzmann's constant.

The effect of creep is to change the strain after the original impulse has reached steady-state. This might present itself as a hysteresis effect or a limitation on the interval in which the sensor can accurately measure the impulse. Typically a transducer would be chosen so that its material properties would have a good response time with respect to the detection time of a single datum. Changes in temperature may alter the rate of strain relaxation/creep.

### 2.2.4.3 Stress/strain transfer to the fibre from surrounding material

A fibre embedded into a material matrix or surface mounted onto the material will retain some form of a protective coating over the cladding to maintain as much of the mechanical strength and environmental protection as possible. A measurand in the material must therefore transfer through the material to the sensor, through any bonding material, through the fibre's protective coating and through the cladding to the core, where the signal is eventually modulated by the measurand.

A measurand transfer tensor for each material encountered is therefore required between the sensor and measurand, e.g. the modulation of  $\Delta \underline{\mathbf{D}}$  by  $\underline{\underline{\boldsymbol{\sigma}}}$  would be

$$\Delta \underline{\mathbf{D}} = \underline{\underline{\mathbf{e}}}_{\boldsymbol{\sigma} \rightarrow \mathbf{d}} \left( \prod_{i=1}^m \underline{\underline{\mathbf{X}}}_i \right) \underline{\underline{\boldsymbol{\sigma}}} \quad (2.65)$$

where  $\underline{\underline{\mathbf{e}}}_{\boldsymbol{\sigma} \rightarrow \mathbf{d}}$  is the direct piezoelectric effect, and  $\underline{\underline{\mathbf{X}}}_i$  are the stress transfer matrices between the various materials.

### 2.2.4.4 Stress/strain effect on signal phase

A fibre under an applied stress will have three orthogonal contributions given in equation (2.53) (page V.I - 38). The stress field induced in the fibre, equation (2.65), can be decomposed into orthogonal transverse and longitudinal changes in the fibre [117]. The refractive index changes can be described by the indicatrix, and physical dimensional changes by compression or extension.

From [118], the phase shifts obtained by the orthogonal components traversing a path  $L$  of fibre under axial stress is given by

$$\underline{\Phi} = \int_L \underline{\beta} \underline{\mathbf{r}} dz \quad (2.66)$$

where  $\underline{\mathbf{r}} = (r, \phi, z)$  is the geometry vector describing the fibre core along path  $L(z)$ , and  $\underline{\beta}$  is the propagation vector. The change in the phase shift for an applied strain, under constant temperature, is

$$\Delta \underline{\Phi}_{\varepsilon\sigma} = \int_L \Delta \underline{\underline{\boldsymbol{\varepsilon}}}_{\sigma} \underline{\kappa}_{\varepsilon\sigma} dz \quad (2.67)$$

where, to a first order approximation,

$$\underline{\kappa}_{\varepsilon\sigma} = \left[ \underline{\mathbf{r}} \frac{\partial \underline{\beta}}{\partial \underline{\underline{\boldsymbol{\varepsilon}}}_{\sigma}} + \underline{\beta} \frac{\partial \underline{\mathbf{r}}}{\partial \underline{\underline{\boldsymbol{\varepsilon}}}_{\sigma}} \right]_{\Delta T=0} \quad (2.68)$$

is the strain sensitivity.

The first term incorporates the photoelasticity, and the second term the extension. The case for axial strain has been given by [119], where  $|\underline{\mathbf{r}}|$  is the length  $L$ . The more general case of a curved path and/or non-axial strain, i.e. where the off-diagonal terms from equation (2.53) (page V.I - 38) contribute to the strain induced birefringence, has been given by [117]. In this case,  $z$  would be defined as the positional vector in the global space of the system.

### 2.2.5 Temperature{0}

Temperature is a thermodynamic property of a system or part of a system. Heat, the flux of thermal energy, flows from hotter to colder regions or objects until both are in thermal equilibrium, i.e. at the same temperature [120].

Temperature is a scalar property, and so may be represented by a scalar field. Heat flux,  $\underline{\mathbf{q}}$ , is given by Fourier's law describing the macroscopic theory of conduction as [121]

$$\underline{\mathbf{q}} = -\underline{\mathbf{k}}_T \underline{\nabla} T \quad (2.69)$$

where  $\underline{\mathbf{k}}_T$  is the *thermal conductivity*<sup>48</sup>, and  $T$  is the system's temperature. Temperature change,  $\underline{\nabla} T$ , is a vector quantity due to the presence of the gradient operator.

Heat transfer occurs by two methods, conduction and radiation. Convection is material transfer, or fluid motion, as opposed to energy transfer. It is better to use the term 'heat transfer with convection' [122], as, even within a fluid, the mechanisms of heat transfer are still only conduction and radiation<sup>49</sup>.

Radiative transfer follows a process which may be described as electromagnetic energy transfer. The flux, or emissive power, for an ideal radiator describing the thermal emission is [121]

$$e_b = \sigma_{SB} T^4 \quad (2.70)$$

where  $\sigma_{SB}$  is the Stefan-Boltzmann constant, and not a stress term.

The temperature of an object is a combination of heat transfer in and out of the object by both processes. In many cases one process may be dominant, and the behaviour can be adequately described using that process alone. The shape and material affect the flux of heat within and into and out of an object.

---

<sup>48</sup>The thermal conductivity is a function of the temperature and transport materials of the fibre, and so may not be, in general, a scalar [60]. In isotropic amorphous materials the tensor can be replaced by a scalar at the scale of wavelengths used here.

<sup>49</sup>At the temperatures encountered in this work, and over the timescales of typical experiments, convection within the fibre should be effectively zero. Convection in the air about the fibre may be an issue and attempts were made to restrict turbulent convection during the experiment setup.

### 2.2.5.1 Thermal expansion{2}

When the temperature of a system does not change faster than heat changes can propagate through to a sensor, the sensor will accurately experience the system temperature.

Temperature changes can cause physical and chemical changes in a material or structure, as follows from figures 2.6 (page V.I - 33) and 2.7 (page V.I - 34). The changes can occur over both short and long timescales. Heating is frequently used to test the ageing of a material, so long term exposure can lead to premature ageing. For certain materials, e.g. glasses, temperature can accelerate re-crystallisation.

Optical changes due to temperature effects in materials manifest in two main effects. The first effect, linking  $T$  and  $\underline{\underline{\epsilon}}_\sigma$  on figure 2.7 (page V.I - 34), is *thermal expansivity*<sup>50</sup>, the expansion or contraction that occurs with changes in temperature [123]<sup>51</sup>,

$$\beta_T = \frac{1}{V} \left( \frac{\partial V}{\partial T} \right) \quad (2.71a)$$

$$\alpha_{T_i} = \frac{1}{L_i} \left( \frac{\partial L_i}{\partial T} \right) \quad (2.71b)$$

where  $\beta_T$  is the *volume thermal expansivity* and  $V$  is the volume of the object or material; in linear one dimensional equations,  $\alpha_{T_i}$  is the *linear expansion coefficient* along axis  $i$ , ( $\beta_T \sim 3\alpha_{T_i} = \alpha_{T_1} + \alpha_{T_2} + \alpha_{T_3}$  [60, 124])<sup>52</sup> and  $L_i$  is the length of the object or material along direction  $i$ .

The expansive change in volume may only significantly affect one dimension, hence the applicability of the linear  $\alpha_{T_i}$ .

### 2.2.5.2 Thermo-optic effect{2}

Just as stress/strain influences the refractive index, so too does temperature. This is termed the *thermo-optic effect*, linking  $T$  and the optical indicatrix,  $\underline{\underline{\mathbf{B}}}_\epsilon$ , as on figure 2.7 (page V.I - 34), and is defined as the variation of the refractive index with the temperature at a constant pressure [125]. By its definition, the thermo-optic effect has the same symmetry as the dielectric constant.

It may be denoted as

$$\frac{d\underline{\underline{\epsilon}}}{dT} = 2\underline{\underline{\mathbf{n}}} \frac{d\underline{\underline{\mathbf{n}}}}{dT} \quad (\text{as } \underline{\underline{\epsilon}} = \underline{\underline{\mathbf{n}}}^2) \quad (2.72)$$

In silica, the thermo-optic effect is of the order of  $10^{-5}$  [126].

<sup>50</sup>Assuming no phase change occurs over the temperature range in question.

<sup>51</sup>The distinctions between adiabatic and isobaric circumstances will be ignored. [123]

<sup>52</sup>Both  $\underline{\underline{\alpha}}_T$  and  $\beta_T$  will be scalars for isotropic amorphous materials.

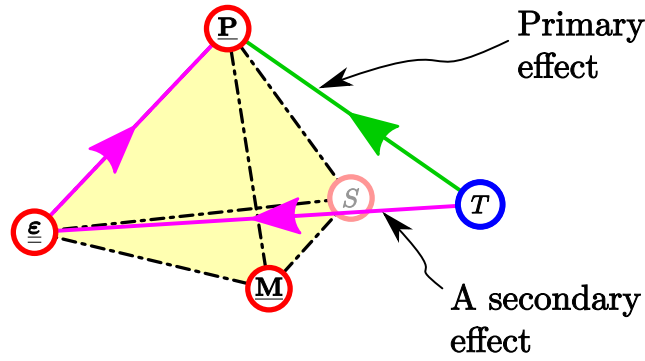


**Figure 2.12:** Primary effect (green) and a secondary effect (purple), or paths, on  $\underline{P}$ , from a stimulus at  $T$ .

A material with positive  $\underline{\alpha}_T$  will have a negative thermo-optic coefficient. This is a result of the expanded material being less dense, and of lower refractive index. A positive change in polarisability,  $\underline{P}$ , results in a positive thermo-optic coefficient [127].

### 2.2.5.3 Temperature effect on signal phase

The phase shift experienced by a path,  $L$ , of fibre experiencing a change in temperature,  $\underline{\Delta T}(\mathbf{r}, t)$ , is given by equation (2.66) (page V.I - 43). Under constant strain,

$$\Delta \underline{\Phi}_T = \int_L \underline{\kappa}_T \underline{\Delta T} dz \quad (2.73)$$

where, to a first order approximation,

$$\underline{\kappa}_T = \left[ \underline{\mathbf{r}} \frac{\partial \underline{\beta}}{\partial T} + \underline{\beta} \frac{\partial \underline{\mathbf{r}}}{\partial T} \right]_{\Delta \underline{\epsilon}_\sigma = 0} \quad (2.74)$$

is the temperature sensitivity of the length of fibre. The first term incorporates the thermo-optic effect, and the second term the thermal expansion.

## 2.2.6 Strain & temperature cross-sensitivity

The linear relationships between the intensive and extensive variables illustrated in figures 2.6 (page V.I - 33) and 2.7 (page V.I - 34) apparently simplify the effects of

a stimulus on any given parameter, i.e. the phase shift [118]

$$\Delta\Phi = \int_L \left[ \underline{\kappa}_T \underline{\Delta T} + \underline{\kappa}_{\varepsilon\sigma} \underline{\Delta\varepsilon}_\sigma \right] dz \quad (2.75)$$

For real systems, a stimulus has primary, secondary and tertiary effects via neighbouring nodes, collectively termed *cross-sensitivity*.

The primary, linear, effect has been discussed thus far, and is the largest contribution to the effect for small values of  $\Delta T$  and  $\underline{\Delta\varepsilon}_\sigma$  [118]. However, with a large enough stimulus or sufficient time, additional paths may contribute to the resultant change at the other nodes, as illustrated in figure 2.12. A change in  $T$  has a direct, primary effect upon  $\underline{\mathbf{P}}$  via the pyroelectric effect. However, the change in  $T$  results in a thermal expansion,  $\alpha_T$ , which produces an electroelastic,  $\underline{\mathbf{f}}$ , effect on  $\underline{\mathbf{P}}$ . There is a similar effect from the other nodes, i.e

$$\begin{aligned} \frac{d\underline{\mathbf{P}}}{dT} &= \left( \frac{d\underline{\mathbf{P}}}{dT} \right)_{\text{primary}} + \left( \frac{d\underline{\mathbf{P}}}{dT} \right)_{\text{secondary}} + \dots \\ &= \underline{\mathbf{\Pi}} T + \underline{\mathbf{f}} \underline{\alpha} + \dots \end{aligned} \quad (2.76)$$

where only one of the secondary effects is included.

Similarly, a change in  $\underline{\sigma}$  will have an effect on  $\underline{\mathbf{P}}$  via thermal secondary effects. When the material cannot respond quickly to a sudden impulse along the primary route, then the secondary routes become relatively more important.

Consequently, the phase shift over path  $L$  will, instead of equation (2.75), be [118]

$$\Delta\Phi_T = \int_L \left[ \left( \underline{\kappa}_T \underline{\Delta T} + \underline{\Delta\varepsilon}_\sigma \underline{\kappa}_{\varepsilon\sigma} \right) + \underline{\kappa}_{T\varepsilon\sigma} \left( \underline{\Delta\varepsilon}_\sigma \underline{\Delta T} \right) + \dots \right] dz \quad (2.77)$$

where, assuming  $\underline{\Delta\varepsilon}_\sigma \underline{\Delta T} = \underline{\Delta T} \underline{\Delta\varepsilon}_\sigma$ , i.e. there is no strain-temperature hysteresis,

$$\underline{\kappa}_{T\varepsilon\sigma} = \underline{\kappa}_{\varepsilon\sigma T} = \left[ \frac{\partial}{\partial \underline{\varepsilon}_\sigma} (\underline{\kappa}_T) \right]_{\underline{\varepsilon}_\sigma = \underline{\varepsilon}_{\sigma_0}, T = T_0} \quad (2.78)$$

### 2.2.6.1 Ideal and realistic sensing systems

An ideal sensor would measure one measurand only, in a linear fashion. Real sensors, however, incorporate materials with the previously discussed physical properties and, hence, their limitations. Every object will have a temperature,  $T$ , and so the material properties will change with  $\underline{\Delta T}$ . For strain gauges, the thermal response will add an unwanted component to the primary ‘real’ strain measurand. This situation is two unknowns,  $\underline{\varepsilon}_\sigma$  and  $T$ , in one equation.

The two approaches to overcoming this are to fix one variable, or find another

relationship to give two equations with two unknowns, allowing them to be solved simultaneously [118, 128, 129]. An additional sensor can provide the second relationship (equation).

The ideal response of a two sensor system would be as in figure 2.13(a), where the measurand responses are linear and orthogonal, thus minimising the coupled uncertainty,  $\Delta\varepsilon\Delta T$ , and maximising the possible resolution.

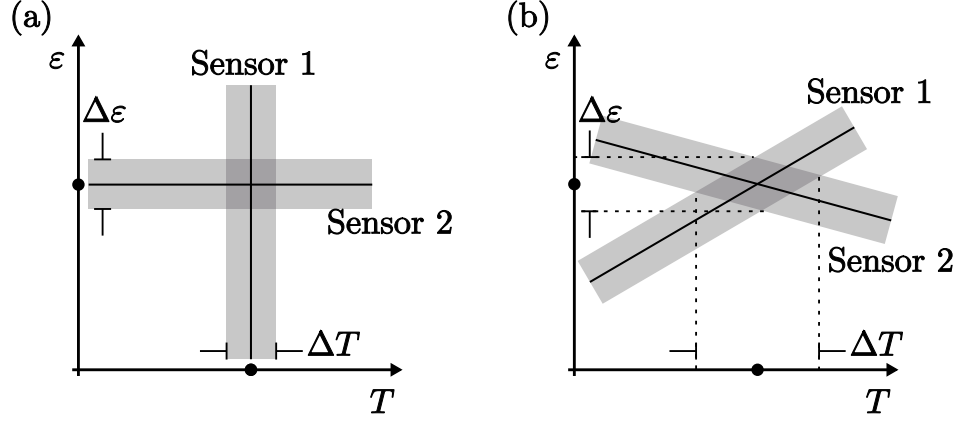


**Figure 2.13:** Strain–temperature plots for two sensors: (a) the ideal response and (b) a more realistic response. After [128, 129].

Figure 2.13(b) shows the more realistic linear situation. The two sensors respond differently,  $X_1$  and  $X_2$ , due to their different material properties, but not orthogonally, resulting in a larger uncertainty,  $\Delta\varepsilon\Delta T$ , and hence less than ideal resolution. The greater the difference in material properties responses,  $\kappa$ , the better the resolution.

$$\begin{pmatrix} X_1 \\ X_2 \end{pmatrix} = \begin{pmatrix} \kappa_{1T} & \kappa_{1\varepsilon} \\ \kappa_{2T} & \kappa_{2\varepsilon} \end{pmatrix} \begin{pmatrix} T \\ \varepsilon \end{pmatrix} \quad (2.79)$$

so that

$$\begin{pmatrix} T \\ \varepsilon \end{pmatrix} = \frac{1}{\kappa_{1T}\kappa_{2\varepsilon} - \kappa_{2T}\kappa_{1\varepsilon}} \begin{pmatrix} \kappa_{2\varepsilon} & -\kappa_{1\varepsilon} \\ \kappa_{2T} & \kappa_{1T} \end{pmatrix} \begin{pmatrix} X_1 \\ X_2 \end{pmatrix} \quad (2.80)$$

where  $\kappa_{1T}$  and  $\kappa_{2T}$  are the thermal sensitivities for sensors 1 and 2,  $\kappa_{1\varepsilon}$  and  $\kappa_{2\varepsilon}$  their respective strain sensitivities [128].

### 2.2.7 Magneto–optics: Faraday effect{2} and Faraday rotation

When electromagnetic radiation encounters a material in the presence of a stationary magnetic field,  $\underline{\mathbf{H}}_{\text{stat}}$ , the symmetry of the tensor  $\underline{\underline{\epsilon}}$  reduces [130, 131]. The loss of symmetry is through a supplementary  $\underline{\mathbf{P}}$  term introduced by  $\underline{\mathbf{H}}_{\text{stat}}$  [111].

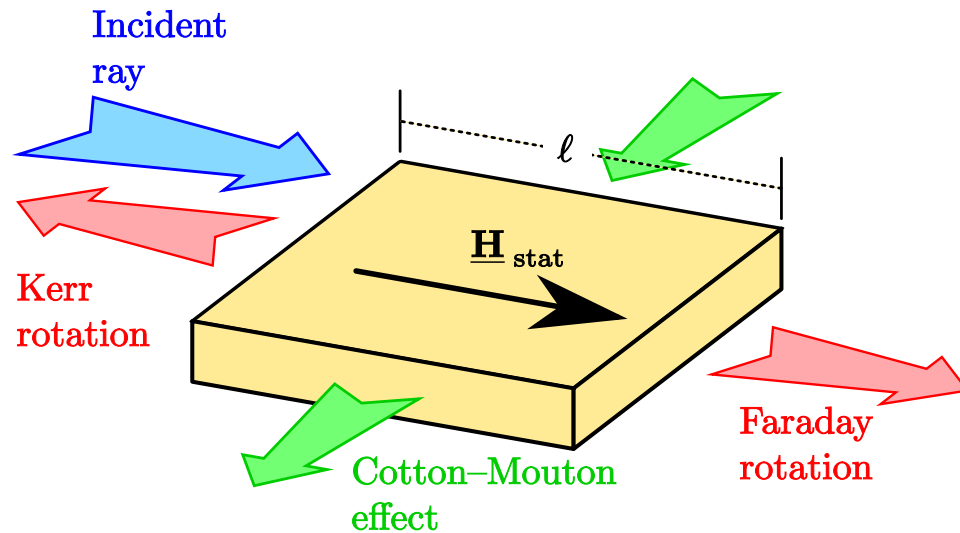


**Figure 2.14:** Optical effects from material in magnetic field. The Faraday effect rotates the incident (blue) about the axis of propagation, parallel to  $\underline{\mathbf{H}}_{\text{stat}}$ , upon transmission. The Kerr rotation effect occurs on reflection. The quadratic Cotton–Mouton effect dominates in the transverse direction to  $\underline{\mathbf{H}}_{\text{stat}}$  (green), where the Faraday effect disappears.

Figure 2.14 schematically shows the three magneto–optical effects. The linear effects<sup>53</sup> are, in transmission, the *Faraday effect*, and in reflection, the *magneto–optic Kerr effect*, when the incident electromagnetic radiation is parallel to  $\underline{\mathbf{H}}_{\text{stat}}$ . The quadratic *Cotton–Mouton effect* occurs when the incident electromagnetic radiation is perpendicular to  $\underline{\mathbf{H}}_{\text{stat}}$ , when the linear terms go to zero [130, 132].

In the presence of a magnetic field, Faraday rotation is observed in materials [132]. The material is said to be *gyrotropic* [130]. In nonmagnetic materials the effect is typically weaker than optical activity and natural birefringence.

The Faraday rotation is an extensive, temporal–dispersion based phenomenon, arising from the electromagnetic wave’s interaction with moving electrical charges. As  $\underline{\mathbf{H}}$  is an axial vector, its effects on the Heckmann diagram, figures 2.6 (page V.I - 33) and 2.7 (page V.I - 34), will be to introduce a rotation to the transmitted electromagnetic wave given by [132]

$$\theta_{FR}(\omega) = \underline{\underline{\mathbf{V}}}_{FR}(\omega) \ell \underline{\mathbf{N}} \bullet \int_{\ell} \underline{\mathbf{H}}_{\text{stat}}(z) dz \quad (2.81)$$

<sup>53</sup>Those effects can be described as linear due to their comparatively large linear terms, relative to their quadratic terms [130].

where  $\theta_{FR}$  is the angle of rotation,  $\underline{\mathbf{V}}_{FR}$  is the Faraday tensor<sup>54</sup>,  $\ell$  is the length of the material through which the radiation traverses, and  $\underline{\mathbf{N}}$  is the direction cosine for the electromagnetic wave normal,  $\underline{\mathbf{k}}$ , with respect to  $\underline{\mathbf{H}}_{\text{stat}}$ . When  $V_{FR11} = V_{FR22} = V_{FR33}$ ,  $\underline{\mathbf{V}}_{FR}$  is termed *Verdet's constant* [132].

The direction of rotation is reversed upon reflection (direction of propagation), and so is non-reciprocal, i.e. a double rotation is possible for a given length [130, 132, 134]. This effect is used to fabricate bulk and all-fibre isolators and circulators, in addition to Faraday mirrors.

In the Faraday mirror, a rotation of  $\frac{\pi}{4}$  is applied to a design wavelength,  $\omega$ , on both the incident and reflected paths, rotating an incoming electromagnetic wave into its orthogonal SOP. The rotation angles for the Faraday mirrors used in this work deviated linearly from  $\frac{\pi}{2}$  at 1550 nm by  $\sim 0.12^\circ$  per nm.

### 2.2.8 Structural/wave guiding and material anisotropy

For the perfect cylindrical geometry of section §F.2 (page V.II F-3), the LP<sub>01</sub> mode has two degenerate solutions. These are the orthogonal linear polarisations, LP<sub>01x</sub> and LP<sub>01y</sub> [55, 135], respectively.

In practice, an optical fibre is never perfectly cylindrical, and variations occur. The Heckmann diagram provides a visual method of understanding the generation of birefringence, and hence polarisation effects that may occur in optical fibres.

The quantities  $\underline{\mathbf{E}}$ ,  $\underline{\mathbf{H}}$ , and  $\underline{\underline{\sigma}}$  being tensors, can introduce, modify or remove anisotropy. Changes in these quantities can be the alteration of any individual component, and this can result in the increase, decrease or removal of the anisotropy. The orthogonal electromagnetic waves are cross-coupled by the off-diagonal elements of the permittivity tensor,  $\underline{\underline{\epsilon}}_r$ , resulting in a continuous variation in the SOP with propagation [136].

A change in  $T$  will not directly produce anisotropy as it is a scalar quantity, but it may alter the quantities  $\underline{\mathbf{E}}$ ,  $\underline{\mathbf{H}}$ , and  $\underline{\underline{\sigma}}$  to produce anisotropy. Thus, indirect changes in  $T$  can produce anisotropy through second order effects.

Coupled-mode theory can be used to describe the effect of twists and other deviations from the idealised cylindrical geometry [135, 137, 138]. A brief discussion of coupled-mode theory is provided in section §G.2.2 (page V.II G-5), where the FBG is described.

In modern single-mode fibres, the small variations  $\Delta\underline{\underline{n}}$  that arise are typically due to molecular inhomogeneity and stresses frozen into the fibre at the glass transition. The effect of random inhomogeneities on a signal has been discussed in §2.2.2.2 (page V.I - 28).

---

<sup>54</sup>Derived in [131] and [133].

The effect of waveguiding inhomogeneities on  $\Delta \underline{n}$  can be incorporated using a perturbation expansion<sup>55</sup> of the index [42, 139], e.g.,

$$\begin{Bmatrix} \underline{\mathbf{E}}_t \\ \underline{\mathbf{H}}_t \end{Bmatrix} = \begin{Bmatrix} \underline{\mathbf{E}}_{t_0} \\ \underline{\mathbf{H}}_{t_0} \end{Bmatrix} + \sum_{j=1}^{\infty} \Delta n^j \begin{Bmatrix} \underline{\mathbf{E}}_{t_j} \\ \underline{\mathbf{H}}_{t_j} \end{Bmatrix} \approx \begin{Bmatrix} \underline{\mathbf{E}}_{t_0} \\ \underline{\mathbf{H}}_{t_0} \end{Bmatrix} + \begin{Bmatrix} \underline{\Delta \mathbf{E}}_{t_1} \\ \underline{\Delta \mathbf{H}}_{t_1} \end{Bmatrix} \quad (2.82a)$$

$$\underline{\mathbf{U}} = \underline{\mathbf{U}}_0 + \sum_{j=1}^{\infty} \Delta n^j \underline{\mathbf{U}}_j \approx \underline{\mathbf{U}}_0 + \Delta \underline{\mathbf{U}}_1 \quad (2.82b)$$

which is approximately equivalent to

$$\underline{\underline{\epsilon}}_r = \underline{\underline{\epsilon}}_{r_0} + \Delta \underline{\underline{\epsilon}}_r \quad (2.83)$$

The perturbation removes the degeneracy of the LP<sub>01</sub> modes and introduces an apparent birefringence [45].

Electrical birefringence is thus associated with different propagation constants,  $\beta_x$  and  $\beta_y$  for LP<sub>01</sub><sup>x</sup> and LP<sub>01</sub><sup>y</sup>, respectively [45]. The macroscopic parameter describing the birefringence of a fibre is termed *the beat length* [45, 140],

$$L_B = \frac{\lambda}{n_y - n_x} = \frac{2\pi}{\beta_y - \beta_x} = \frac{\lambda_1 \lambda_2}{\lambda_2 - \lambda_1} \quad (2.84)$$

$L_B$  describes the distance at which the SOP rotates to the same value. The final fraction in equation (2.84) gives the beat length in terms of two wavelengths,  $\lambda_1$  and  $\lambda_2$ . As the beat length gives the same SOP, the mutual interference of  $\lambda_1$  and  $\lambda_2$  will change periodically with  $L_B$ .

The waveguide *birefringence*<sup>56</sup>,  $B_{f-s}$ , is defined as [76, 140]

$$B_{f-s} = \beta_f - \beta_s = \frac{\omega}{c}(n_f - n_s) \quad (2.85)$$

where  $f$  and  $s$  refer to the different orthogonal axes which are termed *fast* and *slow* depending upon the relative modal group velocities,  $\underline{v}_{g_x} \neq \underline{v}_{g_y}$ . Sources of induced birefringence,  $B_{\text{ind}}$ , can include lateral pressure, bending, twisting, external electric and magnetic fields and nonlinear optical fields [142].

Three cases are observed [135],

1.  $|B_{\text{ind}}| \ll |B_{f-s}|$
2.  $|B_{\text{ind}}| \approx |B_{f-s}|$
3.  $|B_{\text{ind}}| \gg |B_{f-s}|$

<sup>55</sup>As discussed in appendix §G.2.1 (page V.II G-3).

<sup>56</sup>The birefringence induced dispersion ranges from 0.1 to 1 ps/km<sup>1/2</sup> [141].

In the first case the waveguide birefringence dominates and the birefringence can be described effectively using the linear  $B_{f-s}$ . In the second case the induced and waveguide birefringence are of similar magnitude and  $B_{\text{ind}}$  is added to the linear birefringence  $B_{f-s}$ . In the last case the waveguide birefringence is neglected and the induced birefringence dominates. Two potentially useful, but frequently unavoidable sources of induced birefringence are now discussed.

### 2.2.8.1 Twisting–induced (torsion) birefringence

The rotation  $\theta_{\mathbf{t}}$  caused by a twist  $\mathbf{t}$  along  $z$ , illustrated in figure 2.15(b), is given as [135],

$$\theta_{\mathbf{t}} = \mathbf{t}z \quad (2.86)$$

This induces an elastic deformation which induces the dielectric perturbation [45]

$$\Delta \underline{\underline{\epsilon}}_r = \begin{pmatrix} 0 & p_{44}n_{0y}^4 \mathbf{t}y & 0 \\ -p_{44}n_{0y}^4 \mathbf{t}y & 0 & p_{44}n_{0x}^4 \mathbf{t}x \\ 0 & -p_{44}n_{0x}^4 \mathbf{t}x & 0 \end{pmatrix} \quad (2.87)$$

where  $p_{44}$  is an element of the reduced notation matrix version of  $\underline{\underline{\mathbf{p}}}_{B\varepsilon\sigma}$ .

The weakly guided mode coupling integrals are zero except for the  $m \neq q$  terms which couple  $\underline{\mathbf{E}}_{z_m}(z) \rightarrow \underline{\mathbf{E}}_{\mathbf{t}_q}(\mathbf{r})$  and  $\underline{\mathbf{E}}_{\mathbf{t}_m}(\mathbf{r}) \rightarrow \underline{\mathbf{E}}_{z_q}(z)$ <sup>57</sup>. The coupling coefficients are complex [143] and so a length,  $L$ , of twisted fibre acts as a rotator or fractional waveplate of angle

$$\theta_{\mathbf{t}} = p_{44} \Delta n_0^4 \mathbf{t}L \quad (2.88)$$

The change in SOP introduced by twisting a fibre is used in chapter 5 where an FC/APC connector is rotated, thus twisting the fibre, and producing different SOPs for use in the experiment.

Any birefringent optical element that maintains the orthogonal components as a beam may be considered as a retarder of some degree. If the orthogonal components are not maintained as a beam the optical element is a polariser.

### 2.2.8.2 Bending–induced birefringence

Induced birefringence is described by a perturbation of the refractive index of the ideal fibre [45]. The effect of the perturbation is incorporated by using coupled–mode theory. The birefringence introduced by a bend, as illustrated in figure 2.15(c), is

<sup>57</sup>If the guided wave was strictly transverse, i.e.  $\underline{\mathbf{E}}_{\mathbf{t}}(\mathbf{r})$  only, there would be no coupling, and hence no induced birefringence [45].

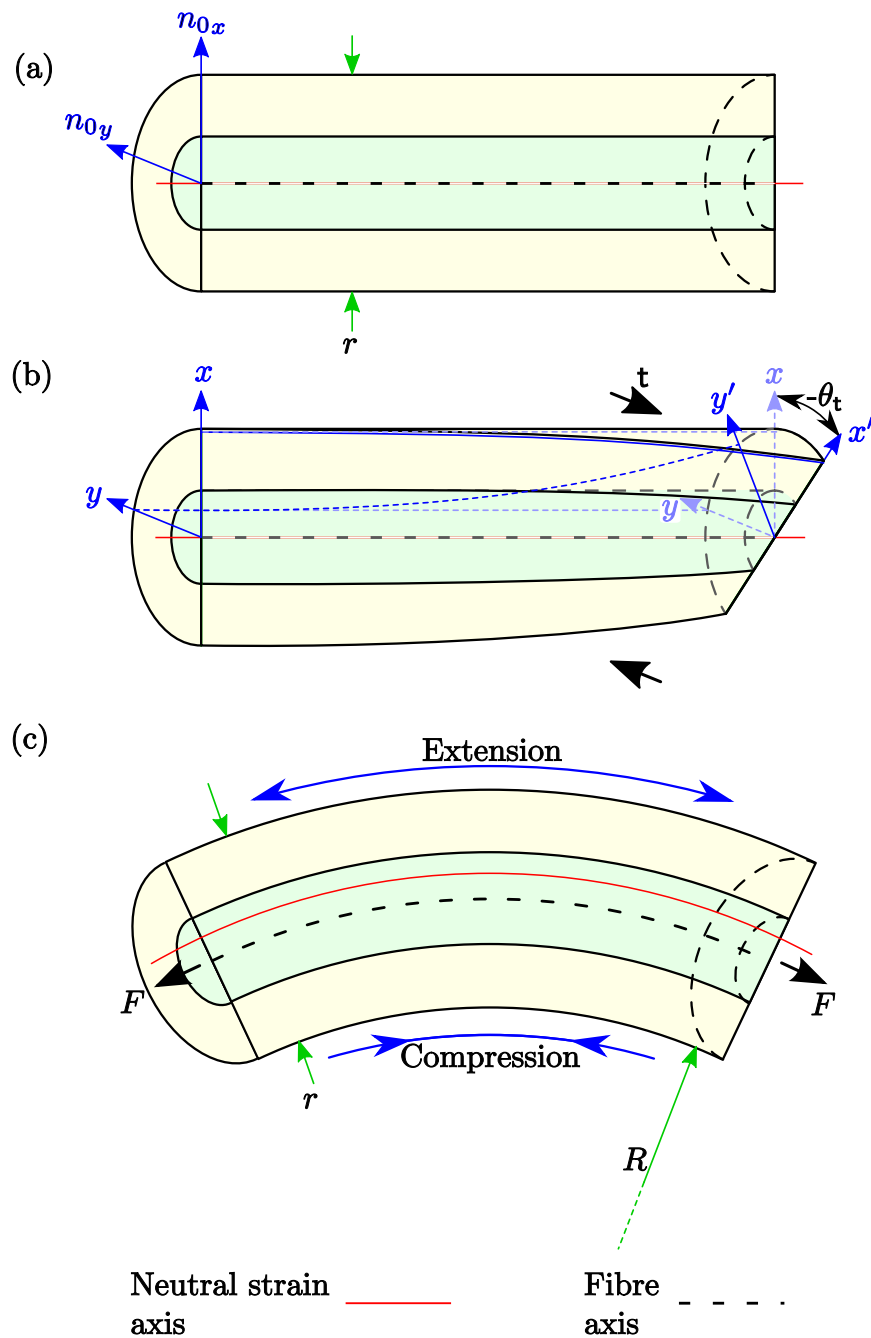


**Figure 2.15:** Induced strain by bending a fibre: (a) The straight fibre, as used in §F.2 (page V.II F-3), with the fibre (dashed) and neutral (red) strain axis co-linear, and with orthogonal refractive indices:  $n_{0x}$  and  $n_{0y}$ ; (b) the fibre twisted through an angle  $\theta$  about the fibre axis, rotates orthogonal axes  $x$  and  $y$  to  $x'$  and  $y'$ ; (c) the curved fibre (of radius  $R$ ) with the neutral strain axis shifted radially outwards in the azimuthal direction defined by the plane containing both axes. (a) and (c) after figure VI.21 of [45], (b) after figure 1(a) [135].

given by [45]:

$$B_{f-s} = n_y - n_x = C \left[ \frac{1}{2} \frac{r^2}{R^2} + 2\varepsilon_\sigma \frac{r}{R} \right] \quad (2.89)$$

and

$$C = \frac{1}{2} n_0^3 (p_{11} - p_{12}) (1 + \nu_\sigma) \quad (2.90)$$

where  $n_0$  is the mean refractive index of the fibre,  $p_{11}$  and  $p_{12}$  are the components of the photoelastic matrix,  $\nu_\sigma$  is Poisson's coefficient,  $r$  is the diameter of the fibre and  $R$  is the radius of curvature of the fibre.

The first term in equation (2.89) relates to the bending, and the second relates to bending under an applied stress,  $F$ .

The induced birefringence in fibre loops was employed by Lefèvre to produce a SOP controller [144]. The total birefringence is an extensive effect, so a suitable length of fibre with enough loops can rotate the SOP by introducing the appropriate phase shift between orthogonal components.

Fibre birefringence can thus arise from the material or the geometry, separately or in combination.

### 2.2.8.3 Induced birefringence application

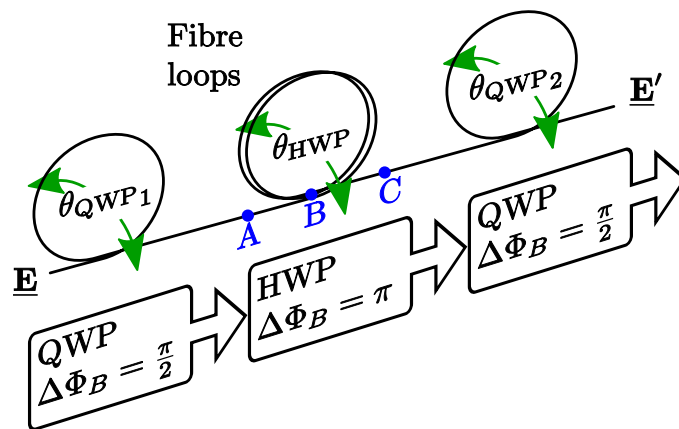


**Figure 2.16:** Three fibre loop Lefèvre polarisation controller. The QWP, HWP and QWP loops are placed at angles  $\theta_{\text{QWP}_1}$ ,  $\theta_{\text{HWP}}$  and  $\theta_{\text{QWP}_2}$ . to achieve the desired change in SOP from  $\underline{\mathbf{E}}$  to  $\underline{\mathbf{E}'}$ . After figure 9.71 [145], and figure 3(b) [144].

The twist- and bend-induced birefringence in curved fibre has been exploited by Lefèvre to produce an all-fibre polarisation controller [144, 146]. The fibre loop arrangement is shown figuratively in figure 2.16. The HWP and QWP<sup>58</sup> are con-

<sup>58</sup>The half-waveplate and quarter-waveplate introduce a phase shift of  $\frac{\pi}{2}$  and  $\frac{\pi}{4}$ , respectively, in one of the orthogonal SOP components, with respect to the other component.

structed by  $M$  windings of fibre in loops of radius  $R$  (from figure 2.15) to give a phase delay of  $\frac{\lambda}{2}$  or  $\frac{\lambda}{4}$ , respectively, using [144]

$$|B_{f-s}|2\pi MR(m, M) = \frac{\lambda}{m} \quad (2.91)$$

where

$$B_{f-s} = -a \left( \frac{r}{R} \right)^2 \quad (2.92)$$

and

$$R(m, M) = \frac{2\pi ar^2}{\lambda} Mm \quad (2.93)$$

where  $m = 2$  and  $4$  for the HWP and QWP, respectively.

Taking as an example the HWP, when the HWP waveplate loop is rotated at an angle  $\theta_{\text{HWP}}$ , the fibre sections AB and BC are twisted in opposite directions giving a behaviour analogous to a classical fractional waveplate [144]. For the loop between B and B, an incident SOP is rotated by

$$\theta_{\text{HWP}} = 2(1 - \alpha_t)\theta_{t_{\text{HWP}}} \quad (2.94)$$

where  $\theta_{\text{HWP}}$  is the rotation experienced by the SOP,  $\theta_{t_{\text{HWP}}}$  is the angle through which the coil is rotated, and  $\alpha_t$  is the coefficient of twist effect for any doped silica single-mode fibre [144]. A rotation through  $\theta_{t_{\text{HWP}}} = \pm 48.6^\circ$  will produce a rotation of  $\theta_{\text{HWP}} = \pm \frac{\pi}{2}$  [144]. The same rotations occur for QWPs 1 and 2. The three waveplate combination covers the full Poincaré sphere [145].

#### 2.2.8.4 Polarisation Maintaining Fibre

*Polarisation maintaining fibres*, PMF, or *high birefringence*, HiBi, fibres are specifically designed to have a large value of  $B_{f-s}$ ,  $B_{\text{PMF}}$ , so as to increase  $L_B$ . The aim of PMF is to “*faithfully preserve and transmit*” any SOP launched into the fibre, even under environmental perturbations [147]. PMF fibre satisfies the first case listed in §2.2.8 (page V.I - 50),  $|B_{\text{ind}}| \ll |B_{f-s}|$ . Under bending or twisting the polarisation axes simply follow the bend or twist, without introducing significant  $B_{\text{ind}}$ .

Conventional single-mode fibre’s degenerate  $\text{LP}_{01}$  modes facilitate transmission of power, or cross-coupling, between the orthogonal modes. This cross-coupling may occur at any perturbation in the fibre, and thus the SOP of a signal may be altered by transmission.

By introducing anisotropy through azimuthally varying cores or controlled uniaxial stress, the degenerate  $\text{LP}_{01}$  modes can be isolated from each other, preventing cross-coupling [147].

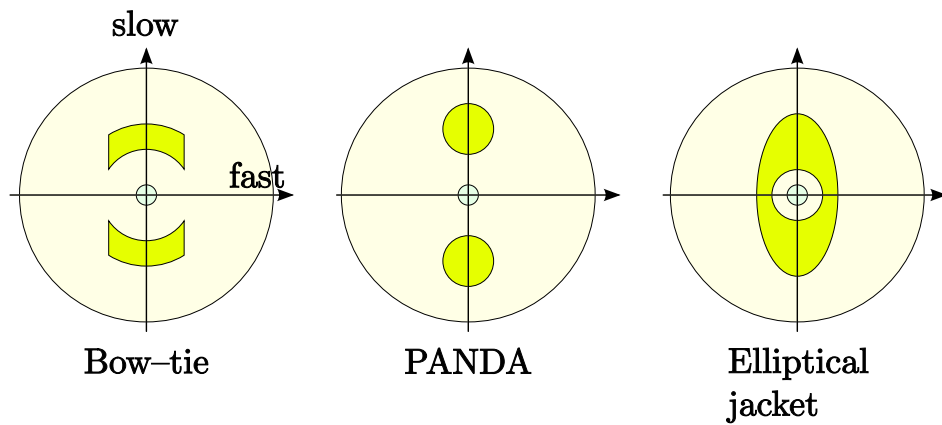


**Figure 2.17:** PMF types: Bow-tie, PANDA and elliptical jacket. After figure 8.7 [147].

The PMF may be characterised by a Jones matrix [45]

$$\underline{\underline{\mathbf{J}}}_{\text{PMF}} = \frac{i\eta_B}{2} \begin{pmatrix} 1 & 0 \\ 0 & -1 \end{pmatrix} \quad (2.95)$$

where  $\eta_B$  is the birefringence per unit length.

PM fibres are used in Lyot depolarisers, by concatenating two lengths of PMF oriented at  $\pi/4$  to each other. The fibre Lyot is discussed further in §5.2.1.1 (page V.I - 219).

### 2.2.8.5 Polarisation Dependent Loss

A limiting factor for signal transmission in fibres is the attenuation experienced by a signal over the transmission length of the fibre. The attenuation experienced by a guided mode is polarisation dependent, as the different modes experience different rates of attenuation. This phenomenon is termed *polarisation dependent loss*, PDL [148]. A closely related phenomenon in gain media is *polarisation dependent gain*, PDG.

PDL is defined as [148]

$$\text{PDL} = 10 \log_{10} \left( \frac{I_{max}}{I_{min}} \right) \text{ dB} \quad (2.96)$$

where  $I_{max}$  is the maximum signal transmitted, and  $I_{min}$  is the minimum signal transmitted, for all possible SOPs. Apart from the loss in signal strength, PDL can repolarise a signal by attenuating one mode significantly. The PDL of the fibre acts

as a partial polariser and waveplate, and can be represented as [148]

$$\underline{\underline{\mathbf{J}}}_{\text{PDL}} = \begin{pmatrix} p_x e^{-i\phi_x} & 0 \\ 0 & p_y e^{-i\phi_y} \end{pmatrix} \quad 0 \leq p_x, p_y \leq 1 \quad (2.97)$$

where  $p_x$  and  $p_y$  are polarisation dependent absorption parameters, and  $\phi_x$  and  $\phi_y$  are the phase retardances, in  $x$  and  $y$ , respectively.

### 2.2.9 Optical fibre sensing

Phase is the parameter most readily modulated by the environment. Under birefringent conditions phase changes will produce SOP changes [149].

The environmental sensitivity of optical fibres has suggested sensing application since the 1960s [150]. This may be through the modulation of the fibre's transmission characteristics: the fibre modes (i.e. phase and frequency), transmitted intensity or SOP. Temperature changes, bending and compression produced significant changes to the propagating signal, which spurred technological improvements to mitigate these effects for communications applications. The result is a range of fibres with different relative sensitivities to various measurands [151].

The advantages of optical fibre sensing include [41]:

- The dielectric materials of the fibre are generally chemically inert, making the sensor chemically and electrically passive. This makes them suitable for chemically corrosive, explosive [152] and electromagnetically noisy environments. Similarly, they can be used in biological/medical applications.
- High temperature operation as a result of silica's high melting point; dopants can alter the melting point.
- Small, lightweight sensors can be manufactured from the fibres.
- Kilometre scale transmission distances facilitate remote and distributed sensing.
- Amenable to interferometric interrogation, allowing high resolution.
- Easy multiplexing of sensors along the fibre.

There are two main disadvantages [41]:

- Cross-sensitivity to multiple measurands, such as temperature and strains/pressures.
- Cost of total sensor system (sources, fibre and demodulation equipment) can exceed one or more alternative technologies.

An optical fibre sensor uses the whole, or part of, the fibre as sensor, which transduces information from the environmental measurand into an optical signal, as opposed to a transmission fibre, which merely transmits the information from the source, or to the sensor [153].

Fibre sensors may be classified according to theory [153] as

- Measurand (e.g. strain, temperature).
- Method(s) of transduction (e.g. strain–optic effect, physical extension, thermo–optic effect, etc.).
- Spatial extent (e.g. distributed sensing, multi–point or point sensing).
- Interface level (the level at which the information is available to the user).

Examples of measurands, and how they may be measured, are listed in **section 7.1** and **Annex A** of [153], respectively. Sensor configurations exploiting the long distance capability can be grouped into spatially based categories:

- Distributed sensing: The whole, or part, of the length of fibre acts as the sensor. In the case where part of the fibre acts as the sensor, the remainder is not subject to environmental changes, or these changes can be selectively ignored. Integration of the measurand over a length of the sensing fibre is a feature of distributed sensing [154–156].

Time and frequency domain reflectivity approaches allow for a degree of localisation of the measurand. Changes to the fibre are observed, e.g. using Rayleigh, Brillouin or Raman scattering of the light, along the fibre. As the fibre changes under the measurand, the scattered light will be modified.

The relative ease of distributed sensing is a strength of fibre sensing [157]. Examples of sensing applications are the monitoring of oil wells, bridges, pipelines, dams and dykes where temperature changes will dissipate and are unlikely to stay highly localised [158–162].

- Point/Quasi–distributed sensing: Localised or point sensors are placed in the fibre at desired locations [154, 163]. The fibre is ideally insensitive between the point sensors. FBGs and Fabry–Perót sensors having unique free–spectral ranges allow for continuous sensing, and finer localisation than distributed sensing, but will not indicate any changes outside of their area of influence.

An example is the monitoring of a pipeline, where connections between pipe sections are of interest.

- Remote sensing: The sensor fibre is located remotely and uses the transmission properties of optical fibre to relay the sensor signals. The sensor network may not extend very far, but the demodulation system would be located at a greater distance [164], e.g. sensor system at the scale of a bridge with the monitoring of the bridge several kilometres away. Remote sensing, as defined here, is grouped under distributed sensing in [41], but the distinction is made as the experimental work in chapter 6 uses a remote sensing configuration. The challenges of remote sensing are similar to long-haul telecommunications challenges, where Rayleigh scattering, dispersion and polarisation mixing can reduce the temporal coherence and spectral resolution, thus reducing accuracy. The two measurands of most interest across different applications are temperature and strain.

The first efficient point transducer for fibre systems was the Fabry–Perót cavity [165, 166]. The Fabry–Perót is a resonant cavity which reflects light many times, and is discussed in §2.4.1.3 (page V.I - 81). The output is an interferogram that is very sensitive to changes. The initial Fabry–Perót cavities were the end faces of two fibres spaced closely together. This is also termed an extrinsic transducer, as the gauge is external to the fibre. Intrinsic Fabry–Perót versions followed, e.g. using splices to define the cavity. An external Fabry–Perót cavity has been used to measure the explosive blast shock wave [167]. The Fabry–Perót cavity does have a draw-back in that the free spectral range<sup>59</sup> can be limited due to its measurand sensitivity. The Fabry–Perót cavity also has a large temperature cross-sensitivity when measuring quantities other than temperature.

The field of composite materials<sup>60</sup> has benefited from the ease of embedding optical fibres. The small diameter and lack of an established sensing technology has encouraged much research on temperature and strain sensing in composite materials. The extrinsic Fabry–Perót has been used for monitoring composite structures [168].

Other interferometers have successfully been used as sensors. The Sagnac interferometer has been successfully deployed as an all-fibre gyroscope, when arranged as loops in three orthogonal directions [169, 170]. The Sagnac loop experiences different phase shifts depending upon the component of rotations in the plane of the loop. The angle of rotation is encoded into the phase of the recirculating signal.

Mach–Zehnder and Michelson arrangements have been successfully deployed as hydrophones [157, 171, 172]. One arm is wrapped around an acoustic sensitive mandril which modulates the phase, encoding the local sound. The gyroscope [173],

---

<sup>59</sup>The free spectral range is the range over which an input gives a unique output and is small for the Fabry–Perót, and cyclical over  $2\pi$ .

<sup>60</sup>The field of composite materials research is new compared to that of metallurgy.

distributed temperature sensing and the hydrophone are amongst the most successful and long established fibre sensor technologies.

Mach–Zehnder interferometers have also been used as strain sensors, measuring cantilever deflection [119], and measuring pressure and temperature [174]. Low-coherence sources have also been used to avail of low-coherence interferometry [175]. The Michelson/Mach–Zehnder interferometer can be variously used for point or distributed sensing by the arrangement of the sensing arm, e.g. the length over which the phase is modulated [176].

Fibre sensors based upon modulation of the state of polarisation have also been used [177]. The polarisation-sensitivity of the optical leads to and from the sensor complicate the demodulation process. PMF fibre is ideally suited in these circumstances, as the large beat length prevents polarisation states mixing. The separated SOPs provide two measurements if interrogated individually or a differential measurement when interrogated together.

Fibre optic current sensors have been successfully developed [173, 178–181]. The control of unwanted ambient influences has seen continued research, as strains, e.g of acoustic origin, and temperature changes also modulate the signal. Different fibres, providing different responses, have been evaluated for their suitability [182].

Fibres have been used for medical examination since the clad fibre was developed, e.g. the endoscope [183]. An optical coherence tomography ‘endoscopic’ fibre sensor has been reported [184]. The fibre also allows targeted delivery of treatments, e.g laser scalpel in keyhole surgery. Fibres are similarly being used for biological sensing applications [185].

Fibre use in the field of non-invasive health-care has also been investigated. A fibre instrumented mat, such as for the detection of falls by the elderly, has been developed [186].

The chemically inert silica from which fibres are manufactured has made them attractive for chemical sensing applications. Unfortunately, for direct spectroscopy, most absorption spectra reside outside the principal telecomms range, but there are overtones which can be detected [157]. The fibre can be sensitised with chemically appropriate coatings, e.g. palladium for hydrogen [187], Neutral Red nano-film U-bend coated fibre for pH sensing [188]. The fibre can also be used for conveniently coupling sources and detectors to fibre coupled sensors, e.g. ozone measurements via UV resistant fibres coupled to a PTFE<sup>61</sup> cell [189], or determination of salt-induced corrosion of roads and bridges [190].

The OPD introduced into a Mach–Zehnder can be spread along a distributed sample, as opposed to being wound at a point for point sensing [176]. Installation and perimeter security are a suitable fibre sensor application domain. The perimeter

---

<sup>61</sup>Poly(tetrafluoroethylene)

sensor should be durable, reliable and as cheap as possible. Fibre sensors using Rayleigh scattering based OTDR for perimeter security sensing have been reported [191]. OTDR in single-mode fibres allows changes in the SOP to provide spatial information on localised changes in the propagation properties of the fibre, termed POTDR [173, 192]. Similarly Raman and Brillouin scattering have been used in fibre sensing [155, 156].

## 2.3 Fibre Bragg gratings

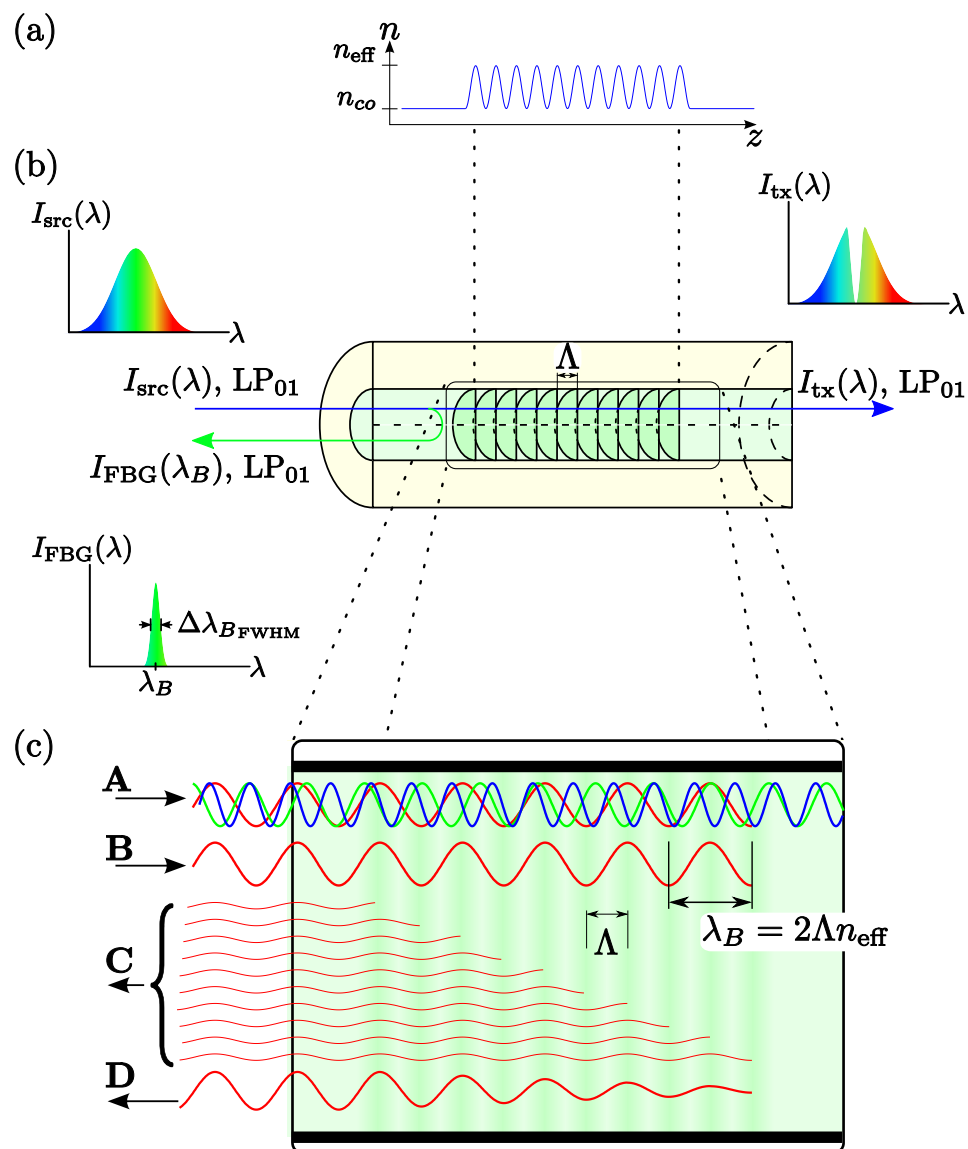


**Figure 2.18:** Schematic FBG operation:(a) Sinusoidal refractive index variation, with period  $\Lambda$ , (b) Longitudinal section of fibre with planes of  $n_{\text{eff}}$ , (c) Phase matching condition matches **B**, with distributed partial reflection from each plane **C** to give reflected signal **D**.

A *fibre Bragg grating*, FBG, is a periodic modulation of the refractive index of the core of an optical fibre, shown figuratively in figure 2.18(a). The modulation coherently scatters electromagnetic radiation via diffraction into directions satisfying the Bragg condition [138,193–199], i.e. a wavelength,  $\lambda_B$ , selective mirror. The FBG achieves *grating-assisted resonant coupling* when the interference pattern of the two modes matches the grating pattern in period and orientation (i.e. the modulation's

wave vectors have the same phase vectors) [198]

$$\frac{2\pi}{k_1 - k_2} = \Lambda \quad (2.98)$$

where  $k_1$  and  $k_2$  are the wavevectors for the incident and coherently scattered propagating modes, and  $\Lambda$  is the grating pitch, as in figure 2.18(b).

When the incident and coherently scattered modes are anti-parallel, equation (2.98) reduces to

$$\lambda_B = 2n_{\text{eff}}\Lambda \quad (2.99)$$

which is the Bragg condition for reflected scattering. Each plane of the FBG couples more of the radiation at  $\lambda_B$  in the forward propagating mode into the counter-propagating mode via partial scattering [198]. This adds to give the total reflectivity of the grating, as illustrated in 2.18(c).

A uniform FBG refractive index profile, as illustrated in figure 2.18(a), will have a spectral response analogous to a truncated high-coherence interferogram, i.e. a rectangular (boxcar) window applied to a near monochromatic signal. Symmetrical side lobe structure will be evident, just as for the interferogram, due to the presence of high frequency components in the boxcar window.

Apodisation [200] to remove side lobes ‘decreases’ the effective grating length and broadens bandwidth, as in windowing a signal [201]. Just as the interferogram can be convolved with an appropriate window to reduce the side structure at the expense of broadening the central peak, apodisation of the FBG refractive index profile suppresses side-peaks while broadening the central peak. Thus equation (2.98) will, in reality, refer to a bandwidth of phase matching conditions, termed the *detuning* as opposed to a single value.

The length of FBGs can be of the order of 10s of mm [193] or  $\sim 0.5$  mm [202].

### 2.3.1 Historical overview

*Photosensitivity* was discovered by K. O. Hill<sup>62</sup> and co-workers in 1977 at the Communications Research Centre, CRC, Ottawa, Canada [205]. An Ar laser at 514.5 nm was launched into the core of a Germanium doped fibre. The transmitted intensity progressively dropped and, when checked, was found to be reflected. The reflectivity rose steadily until all the incident radiation was reflected. It was recognised as a holographically inscribed grating produced by the resonant cavity created by the Fresnel reflections of the cleaved end-faces, via a two-photon process. These self-inscribed gratings are termed *Hill gratings*.

---

<sup>62</sup>A brief personal recollection is provided by K. O. Hill in [203]. The patent licensing is now bundled into a joint licensing operated by The United Technologies Research Center, East Hartford, Connecticut, USA, except in Canada, where CRC is the licensing authority [204].

The process by which the gratings are inscribed is termed *photosensitivity*. Photosensitivity refers to a permanent refractive index change induced by exposure to electromagnetic radiation, by a modification of its physical or chemical properties [206], where the internal field (at thermodynamic equilibrium) has no influence [207].

The effect was initially confined to grating structures at the writing wavelength of the guided inscribing wavelength. In 1989 Meltz and co-workers used 244nm single-photon absorption introduced from the side of the fibre to produce refractive index changes with arbitrary grating period [208]. This allowed the UV-inscribed pattern to operate away from the UV wavelength. Two methods of FBG generation via

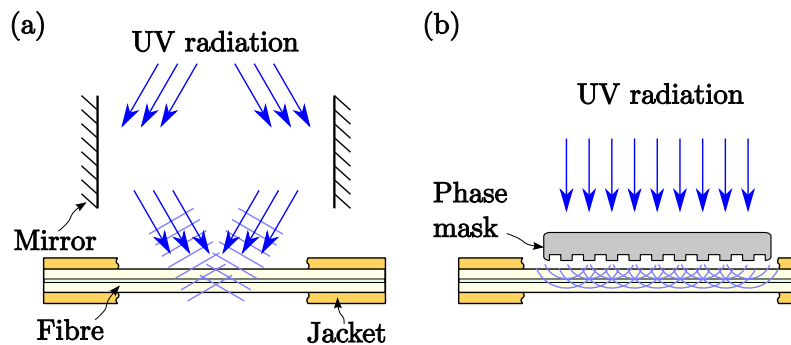


**Figure 2.19:** FBG inscription techniques; (a) Interferometric UV inscription using glancing reflection from mirrors to generate interference pattern, (b) Diffraction grating inscription using a phase mask to produce  $\pm 1$  orders which interfere.

lateral inscription are commonly used: interferometric and phase mask [193–196, 198, 209, 210], as illustrated in figure 2.19. Figure 2.20 shows the UV-absorption sensitivity of Ge-doped fused silica.

A grazing incidence interferometer<sup>63</sup> creates an interference pattern at the desired period,  $\Lambda$ . The fibre, and interferometer, must be held steady as shifted FBGs, or FBGs of different  $\lambda_B$ , may be inscribed, respectively. A modification of the interferometric approach is achieved by modification of the UV source spectrum, changing the interference pattern in a static interferometer [193].

The use of phase mask allows lower coherence UV sources like excimer lasers to be used, and facilitates the alignment of fibre and grating [195]. The fixed phase restricts the FBG periods that can be written, although some adjustment is possible by straining the fibre during inscription. The phase mask is the more common method of inscribing FBGs.

<sup>63</sup>Grazing incidence is used due to the absence of affordable, strong reflectivity mirrors at UV wavelengths.

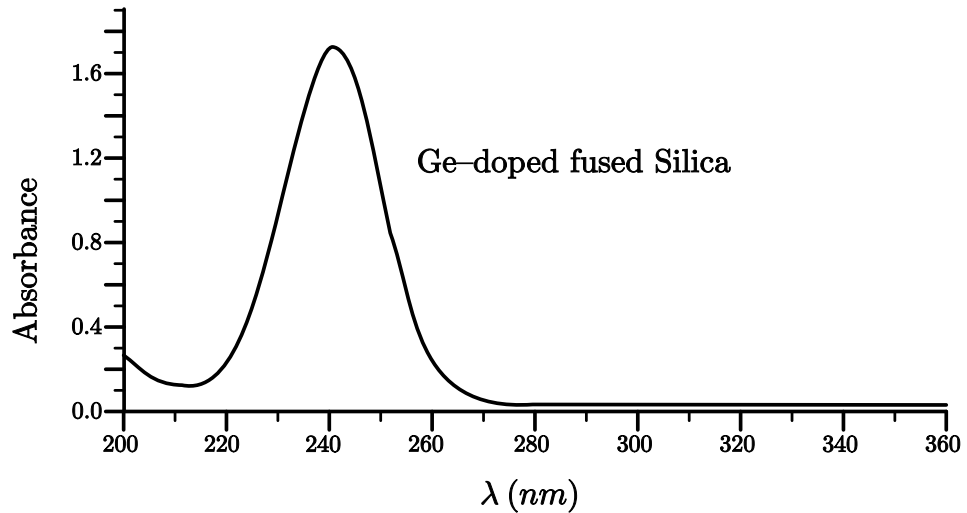


**Figure 2.20:** Graph showing the strong absorption peak of Ge-doped fused silica (after Adrian Dragomir *et al.* [213]).

The phase mask also facilitates greater control of the apodisation of side lobes, of the order of 30 – 40 dB [195]. A uniform grating or interference pattern will have large side lobes, so the interference pattern can be tailored to minimise the side lobes via apodisation. In the interferometric approach, the coherence properties of the UV source would need to be adjusted to achieve the same apodisation effect.

A disadvantage of FBG inscription had been the need to strip the protective buffer from the section where the FBG has to be inscribed. While this is still commonly done, mechanical stripping typically weakens the fibre below its pristine strength. Chemical stripping preserves the pristine strength more effectively [211]. It is possible to inscribe FBGs while the fibre is on the drawing tower, prior to the buffer being applied [212]. Chapter 4 discusses an FBG inscription technology which can also be deployed on a draw tower.

### 2.3.2 Photorefractive sensitivity mechanism

The refractive index change in fibres is achieved by densification, i.e. becoming relatively more crystalline than the neighbouring vitreous silica [207]. The change in refractive index changes with volume, analogous to the changes produced by the thermo-optic effect,

$$\frac{\Delta n_{co}}{n_{co}} \approx \frac{\Delta V}{V} \approx \frac{3n}{2}l \quad (2.100)$$

where  $l$  is the fractional change in the linear dimension of the glass. Using the linear approximation is justified by the transverse changes having negligible effect relative

to the longitudinal change.

Using perturbation methods to model the refractive index modulation of the FBG in terms of powers of the applied electric field  $\underline{\mathbf{E}}_{\text{app}}$  in equation (A.4a) (page V.II A-2)<sup>64</sup>, gives

$$\Delta n_{co} = \frac{1}{2n_{co}} \left[ \underline{\chi}_e^{(2)} \underline{\mathbf{E}}_{\text{app}} + \underline{\chi}_e^{(3)} \underline{\mathbf{E}}_{\text{app}}^* \underline{\mathbf{E}}_{\text{app}} + \dots \right] \quad (2.101)$$

The second order  $\underline{\chi}_e^{(2)}$  describes *photorefractivity*<sup>65</sup>, which is typically zero in amorphous materials<sup>66</sup>. The third order  $\underline{\chi}_e^{(3)}$  terms are found in all Curie groups [214].  $\underline{\chi}_e^{(3)}$  is not large,  $\sim 10^{-7}$ , and so does not produce the larger refractive index changes observed in FBGs,  $\sim 10^{-3}$ . The refractive index changes observed in FBGs, therefore, cannot simply be due to nonlinearities in the material.

To achieve the desired refractive index changes, the photosensitivity of the fibre material must be enhanced. The photosensitivity of standard fibres has been significantly improved by loading with hydrogen [217]. The fibre is soaked in hydrogen at high pressure (800 bar) and/or high temperature ( $< 150^\circ\text{C}$ ) [207]. After the hydrogen that has in-diffused into the fibre has reached equilibrium the grating can be inscribed. The formation of GeH upon irradiation can lead to enhanced refractive index changes [207].

After the inscription hydrogen will begin to out-gas from the fibre unless stored at  $\sim -70^\circ\text{C}$ . Unless the FBG is annealed, a wavelength shift associated with the loss of hydrogen is observed [218].

The resultant refractive index change thus depends upon several factors, including the inscribing radiation, the glassy material composition, and pre- and post-inscription processing (e.g. thermal history) [196]. Lasers illuminate the fibre for several minutes and produce  $\Delta n$  between  $10^{-5}$  and  $10^{-3}$ .

A brief review of the FBG inscription mechanism is provided in appendix G (page V.II G-1) and the basic FBG classification is discussed in appendix §G.1 (page V.II G-2). Although the inscription mechanism is not fully understood, and will most likely require a full understanding of glass formation, the current understanding is adequate for the manufacture of FBG-based sensors. The FBG classification scheme describes the different FBG generation processes and their characteristics for use as sensors.

<sup>64</sup>The derivation is given as an example in appendix §G.2.1 (page V.II G-3), following [207].

<sup>65</sup>Usually denoted by  $\underline{\mathbf{d}}$  in second harmonic experiments [214], but kept as  $\underline{\chi}_e^{(2)}$  for consistency of presentation, after [207].

<sup>66</sup>The  $\underline{\chi}_e^{(2)}$  term can arise in poling of glasses [215, 216] due to its inversion symmetry [207].

### 2.3.3 FBGs as sensors

The reflected wavelength,  $\lambda_B$ , allows an FBG to be used in reflection or transmission mode, and the grating's sensitivity to environmental conditions, with the other advantages of fibres, provides another method of transduction.

FBGs are long range<sup>67</sup> structures inscribed into the core. The longitudinal profile may be considered as the recorded visibility of the inscribing UV radiation. The captured reflected sensor signal will therefore depend upon the illuminating sources coherence and polarisation profile at the FBG, the coherence and polarisation coupling of the inscribed FBG and the modification of that coupled signal en-route to the demodulation system. The FBG therefore appears as a, strictly, non-deterministic source whose coherence and polarisation is modified on transmission to the detector.

An FBG is an intrinsic sensor, modulating the absolute parameter, reflected wavelength,  $\lambda_B$  [41, 194, 195]. FBG sensors can be multiplexed by concatenating sensors and arranging the sensors in different configurations [219, 220], and the multiplexed sensor transmission bandwidth requirements are typically not an issue for fibres [221].

In FBG sensing applications, the control over environmental conditions will be less than in other FBG applications. The reflected signal will be described by an analytic signal with a degree of coherence and polarisation as given by equations (2.21) (page V.I - 19) and (2.23) (page V.I - 20), respectively. FBGs are sensitive to changes in the variables  $n_{\text{eff}}$  and  $\Lambda$  as described by equation (2.99) [222, 223]. Neglecting exposed core FBGs, the change in the Bragg wavelength is [224]

$$d\lambda_B = \left[ 2\lambda_{B_0} \left( \frac{\partial n_{\text{eff}}}{\partial \underline{\underline{\epsilon}}_\sigma} \right) + 2n_{\text{eff}0} \left( \frac{\partial \lambda_B}{\partial \underline{\underline{\epsilon}}_\sigma} \right) \right]_{T=T_0} d\underline{\underline{\epsilon}}_\sigma + \left[ 2\lambda_{B_0} \left( \frac{\partial n_{\text{eff}}}{\partial T} \right) + 2n_{\text{eff}0} \left( \frac{\partial \lambda_B}{\partial T} \right) \right]_{\underline{\underline{\epsilon}}_\sigma = \underline{\underline{\epsilon}}_{\sigma_0}} dT \quad (2.102)$$

$$\Rightarrow \Delta\lambda_B = \left( \Delta\underline{\underline{\epsilon}}_\sigma \kappa_{\underline{\underline{\epsilon}}_\sigma} + \kappa_T \Delta T \right) + \kappa_{T\underline{\underline{\epsilon}}_\sigma} \left( \Delta\underline{\underline{\epsilon}}_\sigma \Delta T \right) + \dots \quad (2.103)$$

where, after equations (2.68) (page V.I - 43), (2.74) (page V.I - 46) and (2.78) (page V.I - 47), respectively:

$$\kappa_{\underline{\underline{\epsilon}}_\sigma} = 2 \left[ \lambda_{B_0} \left( \frac{\partial n_{\text{eff}}}{\partial \underline{\underline{\epsilon}}_\sigma} \right) + n_{\text{eff}0} \left( \frac{\partial \lambda_B}{\partial \underline{\underline{\epsilon}}_\sigma} \right) \right]_{T=T_0} \quad (2.104)$$

$$\kappa_T = 2 \left[ \lambda_{B_0} \left( \frac{\partial n_{\text{eff}}}{\partial T} \right) + n_{\text{eff}0} \left( \frac{\partial \lambda_B}{\partial T} \right) \right]_{\underline{\underline{\epsilon}}_\sigma = \underline{\underline{\epsilon}}_{\sigma_0}} \quad (2.105)$$

<sup>67</sup>Long range with respect to glass network structures.

$$\underline{\kappa}_{\underline{\epsilon}_\sigma T} = \underline{\kappa}_{T\underline{\epsilon}_\sigma} = 2 \left[ \frac{\partial}{\partial \underline{\epsilon}_\sigma} (\underline{\kappa}_T) \right]_{\underline{\epsilon}_\sigma = \underline{\epsilon}_{\sigma_0}, T=T_0} \quad (2.106)$$

and where the 0 subscript refers to the at rest values.

For a fibre with full cladding, the principal quantities that modify  $\lambda_B$  are  $\underline{\epsilon}_\sigma$  and  $T$ . When the cladding is partially removed to expose the core, then  $\underline{n}_{\text{eff}}$  may be directly modified [225, 226]. These are collectively termed *direct measurands*.

When another measurand is transduced into  $\underline{\epsilon}_\sigma$ ,  $T$  or  $\underline{n}_{\text{eff}}$ , it can be indirectly measured via the transduction mechanism. These are collectively termed *indirect measurands*.

### 2.3.3.1 Temperature sensitivity

Temperature sensitivity is primarily due to the thermo-optic effect ( $\sim 95\%$ ). At constant strain, the normalised wavelength response is given by [194, 195, 227]<sup>68</sup>,

$$\begin{aligned} \left( \frac{\Delta \lambda_B}{\lambda_B} \right)_{\underline{\epsilon}_\sigma = \underline{\epsilon}_{\sigma_0}} &= \underline{\alpha}_T + \frac{1}{\underline{n}} \frac{d\underline{n}}{dT} \\ &\approx 6.678 \times 10^{-6} \text{ }^\circ\text{C}^{-1} \end{aligned} \quad (2.107)$$

#### 2.3.3.1.1 Nonlinearities and second order effects

Silica fibres do not have a purely linear thermal response, and, consequently, FBGs do not have a purely linear response. Nonlinearity of FBG thermal response, principally the thermo-optic effect, should be incorporated<sup>69</sup> into systems aiming to achieve accuracy of  $\leq 35$  pm over temperature ranges of  $-70$  °C to  $80$  °C [228].

This temperature range has been presumed to be the most stable regime for Type I FBGs, which have been erased at  $\sim 200$  °C. However, down-well fibre sensing applications require temperature stability of hundreds of degrees. Type II FBGs have been considered as the most appropriate candidate for these applications as they have been observed to be stable at  $800$  °C, and to be in the process of being erased at  $\sim 1000$  °C [201]. Recently regenerated Type I FBGs have been reported [229], with reflectivities  $\sim 35\%$  that of the seed grating in  $\text{H}_2$  loaded SMF-28 [230]. The FBG is heated (annealed) at  $800-900$  °C, after which the erased Type I FBG begins to be regenerated. The regenerated FBG has a length dependence, so, in principle, a long seed grating will produce a long (higher reflectivity) regenerated grating.

A nonlinear thermal dependence of the coupling coefficients has been reported [231]. The UV inscription process introduces a weak absorption term into the mode

<sup>68</sup>The components of  $\underline{\alpha}_T$  are the linear thermal expansion coefficients along the length of the FBG in the orthogonal directions specified by  $\underline{n}$ .

<sup>69</sup>The non-linear response will differ by  $\sim 20$  pm ( $\sim 2$  °C) from the linear response over the range  $-30$  to  $80$  °C [228].

coupling equation, which produces localised heating. For a high strength FBG a wavelength shift of  $\sim 0.5$  pm/mW at 1550 nm. The impact of this heating effect should be negligible for the work in this thesis, where power levels at FBG wavelengths are lower.

FBG strain sensors also have a temperature dependent strain response, i.e. temperature induced stress, as suggested by the Heckmann diagram, figure 2.6 (page V.I - 33). An increase in temperature stiffens the fibre thus reducing the strain-optic coefficient. A value of 1.22% per 100 K for  $\frac{d\lambda_B}{d\sigma}$  has been reported [232].

### 2.3.3.2 Strain sensitivity

The normalised Bragg wavelength shift  $\delta\lambda_B$  produced by a strain  $\underline{\underline{\epsilon}}_\sigma$ , at constant temperature, is given by [195]

$$\left(\frac{\Delta\lambda_B}{\lambda_B}\right)_{T=T_0} = \varepsilon_{\sigma_z} - \left(\frac{n^2}{2}\right) [p_{11}\underline{\underline{\epsilon}}_{\sigma_t} + p_{12}(\varepsilon_{\sigma_z} + \underline{\underline{\epsilon}}_{\sigma_t})] \quad (2.108)$$

where  $\underline{\underline{\epsilon}}_{\sigma_t}$  is strain transverse to the fibre axis,  $\varepsilon_{\sigma_z}$  is strain along the fibre axis, and  $p_{11}$  and  $p_{12}$  are the components of the photoelastic tensor,  $\underline{\underline{\mathbf{p}}}_{B\varepsilon_\sigma}$ .

When strain is homogeneous and isotropic, and at constant temperature, the above becomes [194, 227]

$$\begin{aligned} \left(\frac{\Delta\lambda_B}{\lambda_B}\right)_{T=T_0} &= [1 - p_e] \varepsilon_\sigma \\ &= 0.78 \times 10^{-6} \mu\varepsilon^{-1} \end{aligned} \quad (2.109)$$

where the photoelastic contribution has been incorporated into  $p_e$  as [194]

$$p_e = \left(\frac{n^2}{2}\right) [p_{12} - \nu_\sigma(p_{11} + p_{12})] \approx 0.22 \quad (2.110)$$

with Poisson ratio  $\nu_\sigma$ <sup>70</sup>. Strain response is linear, with no hysteresis exhibited, up to  $\sim 370$  °C [195]. A change in temperature of 1 K can therefore appear as a *temperature-correlated strain* of  $\sim 1$  m $\varepsilon$  [234].

For a strain gauge transducer, non-isotropic strain configurations are important: longitudinal strains, acting along the axis of greatest sensitivity; axial or radial strains, acting transversely to the axis of greatest sensitivity; and unidirectional transverse strains which are a special case of axial strains.

The transducer will experience the stress field locally and respond by deforming itself to adopt a minimum energy configuration, which will differ from the envi-

---

<sup>70</sup>For embedded FBGs the shear strains,  $\gamma_{\sigma_{ij}}$ ;  $i \neq j$ , cannot be neglected as strains in the host material may not align with the fibre axis, nor any possible birefringent axes that existed prior to the applied strain [233].

ronmental stress by the differences in *modulus of elasticity*:  $E_{\sigma \text{ sensor}}$ ,  $E_{\sigma \text{ environs}}$  and *Poisson's ratios*:  $\nu_{\sigma \text{ sensor}}$ ,  $\nu_{\sigma \text{ environs}}$ .

Further complicating the result is that not all materials will have an isotropic or homogeneous structure, such as crystalline or fibre-reinforced materials. These circumstances typically require the use of tensor forms for  $E_{\sigma}$ ,  $\nu_{\sigma}$  and  $G_{\sigma}$ , denoted by  $\underline{\underline{\lambda}}_{\sigma\varepsilon} \left( \underline{\underline{c}}_{\sigma\varepsilon}, \underline{\underline{s}}_{\varepsilon\sigma} \right)$  on the Heckmann diagram, figure 2.6 (page V.I - 33) and table 2.1 (page V.I - 35). Consequently the stress and strains experienced by the environment, the desired measurand, may not be uniformly transmitted to the transducer, the recorded measurand.

Similar to electrical strain gauges, FBGs are inherently more sensitive in one direction, the fibre axis, than in orthogonal directions. The conventional solution is to arrange a 'rosette' arrangement, where the sensors measure the same local strain along different angles [211, 235]. The sensor multiplex advantage presents itself here, as electrical strain gauges require two leads to each component sensor of the rosette [235].

### 2.3.3.2.1 Contracted notation

Contracted notation<sup>71</sup> [96, 236] for tensors and vectors is employed. The symmetry reduced components, six independent strains (three normal and three shear in Cartesian co-ordinates) are re-written as [96]

$$\underline{\underline{e}}_{\sigma} = \begin{pmatrix} \varepsilon_{\sigma 1} \\ \varepsilon_{\sigma 2} \\ \varepsilon_{\sigma 3} \\ \varepsilon_{\sigma 4} \\ \varepsilon_{\sigma 5} \\ \varepsilon_{\sigma 6} \end{pmatrix} = \begin{pmatrix} \varepsilon_{\sigma x} \\ \varepsilon_{\sigma y} \\ \varepsilon_{\sigma z} \\ \gamma_{\sigma yz} \\ \gamma_{\sigma xz} \\ \gamma_{\sigma xy} \end{pmatrix} \quad (2.111)$$

Note that equation (2.111) is not a tensor, just a matrix. Similarly, any matrices operating on (2.111) will not be tensors. Strains in different co-ordinate systems are then determined by matrix transformations such as those shown in equation (2.65) (page V.I - 43).

The transducer can only detect changes that it experiences. These will be modified by the transducer's effective mechanical coupling to the environment and the differences in material properties.

An embedded transducer also modifies its local environment, in comparison to its absence<sup>72</sup>. This occurs as the transducer appears as an inclusion, or an external

<sup>71</sup>Also called as *Voigt short notation* [111].

<sup>72</sup>This is an area of current intense research [237].

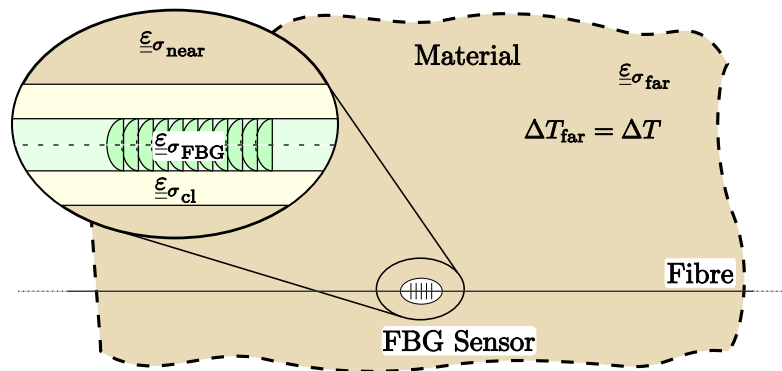


**Figure 2.21:** Diagram of different strains in material due to presence of sensors. The value  $\underline{\underline{\epsilon}}_{\sigma_{far}}$ , is the intended measurand. The presence of the sensor causes a redistribution of stress (and hence strain), and in the vicinity of the fibre  $\underline{\underline{\epsilon}}_{\sigma_{near}}$  is experienced. The cladding experiences  $\underline{\underline{\epsilon}}_{\sigma_{cl}}$  which produces  $\underline{\underline{\epsilon}}_{\sigma_{FBG}}$ , which is measured (after Van Steenkiste and Springer [96]).

surface to the material, rather than as part of the interior of the material [96, 117, 238]. The surface effects may modify the measurands further from the desired actual bulk (internal) values.

A final complication is that the temporal response of the material properties may not be on similar time scales. When the relaxation times are different, the recorded measurand can temporally average the desired measurand if an intervening material has a longer relaxation time than the sensor or target material. Consequently, the distinction is made between far-field strain, the desired measurand; near-field strain, which is in the vicinity of the transducer; and the transducer strain which is what the sensor transduces and is captured, which are illustrated in figure 2.21.

The translations between the far-field strain and sensor strain can be incorporated by multiple translations of co-ordinates and the use of stiffness matrices<sup>73</sup>,  $c_{ij}$ , for each co-ordinate system:

$$\sigma_i = c_{ij'} (\epsilon_{\sigma_{j'}}) \quad (2.112)$$

where  $i$  is the index for  $(x_1, x_2, x_3)$  and  $j'$  is the index for  $(x'_1, x'_2, x'_3)$ .

The linear thermal expansion coefficient can be conveniently described in con-

<sup>73</sup>Note these are the contracted notation values and not the fourth rank tensor.

tracted notation as [239]:

$$\alpha_{T_j} = \begin{pmatrix} \alpha_{T_{xx}} \\ \alpha_{T_{yy}} \\ \alpha_{T_{zz}} \\ \alpha_{T_{yz}} \\ \alpha_{T_{xz}} \\ \alpha_{T_{xy}} \end{pmatrix} \quad (2.113)$$

and incorporated into equation (2.112) as

$$\sigma_i = c_{ij'} \left( \varepsilon_{\sigma_{j'}} - \alpha_{T_{j'}} \Delta T \right) \quad (2.114)$$

### 2.3.3.3 Isotropic and Anisotropic FBGs

A purely isotropic grating structure would exhibit no intrinsic polarisation–sensitivity (ignoring any present in the geometry or form of the fibre, e.g. PMF).

In reality slight anisotropies do occur. The fibre core itself will not be perfectly uniform. The ITU–T Recommendation G.652<sup>74</sup> specifies the geometric tolerances a single–mode optical fibre needs to meet. The mode field diameter is to be within  $\pm 0.7 \mu\text{m}$ . These deviations from the idealised core–cladding structure are one origin of Rayleigh scattering by fluctuations [240–242]. Their influence on an FBG can be neglected as total Rayleigh scattering only becomes significant over long distances ( $\sim\text{km}$ ) compared to FBG gauge lengths ( $\sim\text{cm}$ ).

Other sources of weak anisotropy arise in the geometry of the side writing approach, which is the dominant technique for FBG fabrication. The irradiating UV flux across the fibre diameter will differ due to absorption [208, 210, 243–245], or the polarisation plane of inscribing UV radiation may not lie in the plane of the fibre core [246]. The focusing of the writing beams (typically UV) through a phase–mask or by the overlap of interfering beams, i.e. visibility of the UV interference pattern, may not coincide with the centre of the fibre core, as illustrated in figure 2.22.

The grating structure should be more developed, or overdeveloped, i.e. have a larger ‘DC’ term, on the incident side, as illustrated in figure 2.23. The UV absorption by the core is so low ( $\sim 1 \text{ dB}$  [207] across the core diameter) that the difference in flux for Type I FBGs is small across the core. For Type II FBGs the bi–lateral approach can reduce the birefringence [244].

When an FBG is inscribed inside a PMF<sup>75</sup> core, it possesses two orthogonal–polarisation eigenmodes [247]. The anisotropies discussed above are still present,

<sup>74</sup>From *Corning SMF-28e+ optical fiber with NexCor Technology product information*, Corning Inc. (<http://www.corning.com/WorkArea/showcontent.aspx?id=27659>).

<sup>75</sup>Section §2.2.8.4 (page V.I - 55).

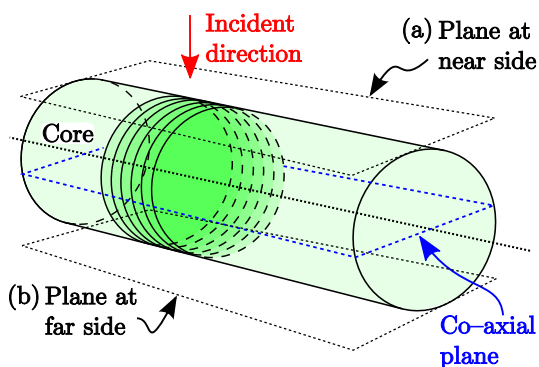


**Figure 2.22:** Writing plane asymmetry arising due to the fibre axis not coinciding with the focal plane (zero-OPD) of the inscribing UV radiation.

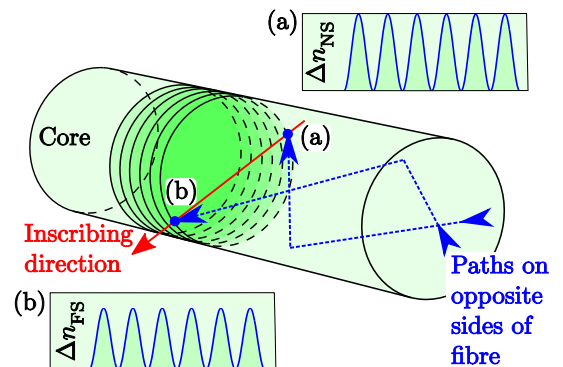


**Figure 2.23:** Uni-lateral writing asymmetry arising due to the absorption of the inscribing UV radiation as the UV flux traverses the fibre.

but are dwarfed by the intrinsic birefringence of the PM fibre,  $B_{\text{PMF}} \gg B_{\text{UV}}$ .

In highly birefringent fibres, the birefringent FBG periods,  $\Lambda$ , of the two orthogonal FBGs are the same. However, the orthogonal  $\underline{n}$  differ by  $B_{\text{PMF}}$ , and so the orthogonal components of  $\underline{\lambda}_B$  are shifted with respect to each other by  $2B_{\text{PMF}}\Lambda$ . However, the observed spectrum is typically<sup>76</sup> the combined reflection spectrum is the sum of both orthogonal-polarisation eigenmodes, i.e. the sum of two Gaussian spectra corresponding to the two polarisation eigenmodes, displaced slightly in wavelength, illustrated in simulated<sup>77</sup> spectra in figure 2.24.

Two equal intensity FBGs of Gaussian profile are inscribed into PM fibre with birefringence  $B_{\text{PMF}}$ . The resulting spectrum is shown as the red line in figure 2.24. The Gaussian profile is replaced by a super-Gaussian, or flat-top profile, which is further discussed in §3.2.3.2 (page V.I - 133). If the positioning of the shifted spectra is done properly, the top becomes almost flat. However, the double peak shown illustrates that if the shift exceeds this ideal condition, then the spectra may begin to separate. This can result in the occurrence of a double peaked profile, and eventually two separate peaks being established [248].

With the large difference in refractive indices of the two orthogonal-polarisation eigenmodes, the overlapping FBGs might be expected to respond at different rates to temperature or strain changes:

$$\frac{\partial \lambda_{B_i}}{\partial X} \neq \frac{\partial \lambda_{B_j}}{\partial X} \quad X = \underline{\underline{\epsilon}}_{\sigma}, T \quad (2.115)$$

where  $(\underline{i}, \underline{j})$  are the two orthogonal-polarisation eigenstates perpendicular to the core

<sup>76</sup>Assuming no significant PDL.

<sup>77</sup>Simulated in Matlab.

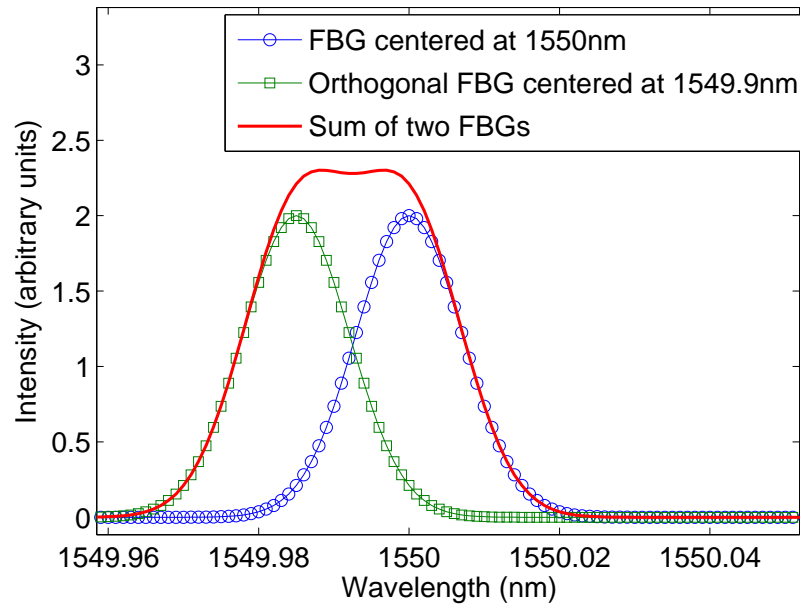


**Figure 2.24:** Simulated inscription in PM fibre: two equal strength Gaussian FBG spectra are shifted relative to each other by  $B_{\text{PMF}}$ , with one FBG at 1550 nm, and the other at 1549.9 nm. The resultant sum spectrum is shown in red, a flat-top profile.

axis. After annealing PMF FBGs, a permanent relative shift is introduced, which, not being equal in both polarisation eigenstates, typically produces a permanent flat-topped reflection spectrum. When used as a sensor, these PM-FBGs exhibit strong spectral profile changes, relative to FBGs in SMF, as the orthogonal peaks shift relative to each other.

The orthogonal Bragg wavelength changes,  $\Delta\lambda_B$ , for PMF FBGs are large enough that they may be used for the two sensors,  $X_1$  and  $X_2$ , in equation (2.80) (page V.I - 48). In practice the at-rest birefringence needs to be large to resolve the individual wavelengths, and PMF leads should be used to prevent subsequent mixing or signal fading.

Throughout this thesis FBGs are used as sources in the experiments. The SpectroBragg spectrometer, chapter 3, was designed for use in FBG sensor demodulation. The novel anisotropic FBGs strain characterised in chapter 4 are intended to be suitable alternatives to standard telecomms range FBGs. A brief review of a significant use of FBGs, structural health monitoring, is now presented to indicate the potential scope of the work in this thesis.

### 2.3.3.4 Structural Health Monitoring

Structural health monitoring, SHM, is one niche application area in which FBGs have been historically forecasted [150, 238, 249, 250] and are anticipated to have an impact [158, 251]. SHM refers to the application of sensor networks to a structure, which monitor the environmental effects upon that structure, providing accurate and timely information on the ‘health’ of the structure towards its intended function. The paradigm draws upon the biological sensory system, where the nervous system provides notification of problems before the problems jeopardise the organism’s viability.

The environmental effects can include the curing of materials, the settling of a newly constructed structure, the chemical properties of the structure, the habitat of the structure for occupants, the effects of weather on the structure, the deterioration of the structure or its components through use and age, and the survivability of that structure after accident or extreme event. Two measurands of general interest are temperature and strain, apart from application-specific measurands.

In comparison to copper conductors, optical fibres benefit from the distances over which they can be used ( $\sim 10\text{km}$ ), without signal amplification (fibre loss at 1550nm is  $\sim 0.2\text{ dB km}^{-1}$ <sup>78</sup>, copper is  $\sim 10\text{ dB km}^{-1}$  at 50 MHz [51].). Wireless-radio based sensors may compete on range in certain cases (i.e. where there is no obstruction to the signal between transmitter and receiver) but requires power sources for the wireless transmitter and any repeaters<sup>79</sup>.

In addition to decades of research on optical fibre and FBG-based sensing, commercially available fibre and FBG-based sensor systems have been available for over a decade. Although the adoption of fibre and FBG sensors has not been as rapid and universal as initially forecast, fibre sensing for SHM applications is now commonly available from commercial sensing vendors<sup>80</sup>, as described in [251].

FBGs have predicted lifespans of 25 years [196, 201, 252]. This compares favourably with electrical strain gauges which are considered suitable for shorter lifespans [253]. While electrical strain gauges and FBGs can be retrofitted to structures, the need to do so with greater frequency for electrical strain gauges is both an additional cost and an inconsistency in the lifetime data.

A bare fibre with the cladding exposed is fragile, while providing the best coupling of measurands to the sensor. The FBG sensor needs to be packaged in a manner that protects the sensor during installation but does not desensitise the sen-

---

<sup>78</sup>From *Corning SMF-28e optical fiber product information*, Corning Inc. (<http://www.corning.com/assets/0/433/573/583/09573389-147D-4CBC-B55F-18C817D5F800.pdf>).

<sup>79</sup>Wireless systems must be immune to interference from local electromagnetic interference sources, or risk being unavailable when needed.

<sup>80</sup>A list of vendors is available from [www.opticalfibersensors.org](http://www.opticalfibersensors.org).

sor. The appropriate packaging depends upon the application [254]. An externally fitted extension based strain gauge requires two points to attach to the structure, and the remaining components can be hermetically sealed. An embedded sensor must have as small a shape as possible, with high reliability<sup>81</sup> and consistency over its lifetime.

In the following, the categories are not mutually exclusive and the distinctions can be arbitrary. A partial list of structural sensing problems where FBGs have been used is:

- Bridges [255–263],
- Tunnels [256, 264–267],
- Dams [255, 256],
- Ships [250, 268–274],
- Aircraft [211, 264, 275–278],
- Spacecraft [279–282],
- Oil rigs [283–292],
- Culturally significant structures [161, 293–296],
- Railways [263, 297],
- Seismic sensors [293–295, 295, 298–303],
- Power lines/grids [304–311],
- Pipelines [312],
- Nuclear facilities [264, 313–320],
- Composite Curing [223, 249, 264, 321–328],
- Concrete curing [257, 329–332],
- Prestressed concrete [333].

FBGs have also been used for monitoring within structures:

- Humidity and temperature of indoor structures [334, 335],
- Chemical sensing [336–342],

---

<sup>81</sup>Reliability here includes surviving the structure's casting process.

- Liquid level/flow monitoring [343, 344],
- Health & safety applications [345, 346],
- Medical applications [347, 348].

A restriction of FBG sensors, and sensors in general, is separation from the structure during the anticipated lifetime. For example, with vibrating structures, adhered sensors can debond, and embedded sensors can delaminate. Ideally, the sensor system should indicate such events prior to the structure reaching design limitations [349].

For most FBG-based sensor systems the demodulation system is the most expensive component. The more FBGs which can be demodulated with a single demodulation system, the lower the per sensor cost of the whole system. The desire to maximise the number of sensors while providing high individual sensor resolution was the motivation for the SpectroBragg spectrometer.

## 2.4 Demodulation systems

An FBG modulates an intrinsic parameter, the wavelength of electromagnetic radiation. The wavelength is not directly obtainable via electro-optic conversion, which converts intensity to current or voltage. There is a square-law proportional relationship between the optical energy and electrical energy [350]. For wavelength determination, the main effect of the square-law behaviour is the loss of phase information. The phase can only be recovered by conversion to amplitude changes, e.g. by coherent superposition, discussed in appendix B (page V.II B-1).

Demodulation is the term used for recovery of the transduced measurand modulation, the measurement, into a usable format, e.g. converting the measured wavelength  $\lambda_B$  into an electrical signal in this case. For FBGs, spectroscopic techniques are used to demodulate the measurand-induced wavelength changes in this work. Demodulation requires the faithful conversion of the intensity to a usable electronic signal, with which appropriate analysis can recover the wavelength to a given resolution. Interferometry is capable of providing the highest resolution of wavelength changes at  $\sim \lambda \times 10^{-3}$ , under ideal conditions [9].

The demodulation system should maximise the advantages of the fibre sensor system, by being capable of: [193]

- High resolution, sufficient to determine measurand
- cost effectiveness
- dealing with multiplexed sensors.

For many optical fibre sensing systems the cost of signal recovery forms the largest contribution to the overall cost of the system. The two step process of converting an optical to analog electrical signal and then to a digital electrical signal represents an extra step over electrical systems. However, traditional electrical systems can have disadvantages that can limit this advantage, e.g. electrical strain gauges require two leads and resistance balancing equipment per sensor, and the pickup of electrical noise. For several sensors, the wiring, configuration and maintenance of the accumulated equipment can become expensive.

### 2.4.1 Optical subsystem

There are many different methods of demodulating the FBG signal. Early approaches to demodulation are illustrated in figure 2.25 [193, 351]. The edge filter is a wavelength dependent attenuator, where the transmitted intensity increases with increasing wavelength, as illustrated in figure 2.25(a). To remove incident intensity variations, the signal is split before the edge filter and the ratio of the filtered

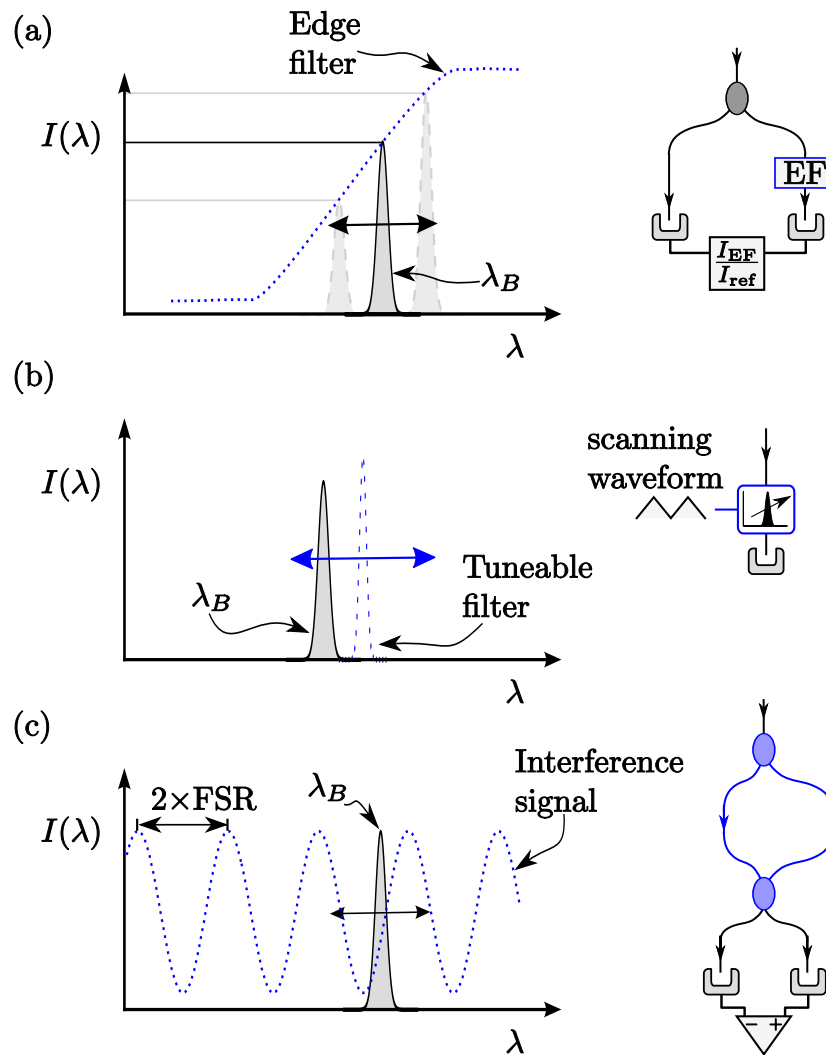


**Figure 2.25:** Intensity based FBG demodulation via (a) Edge filter, (b) scanning tuneable cavity filter, and (c) resonant cavity filter. After figure 8 of [193].

to unfiltered intensities returns the wavelength. The disadvantages are nonuniform SNR across the spectral range of the edge filter. The edge filter also has a limited spectral range. The slope of the edge filter determines the number of multiplexed FBGs that can be demodulated or the resolution obtained.

The scanning tuneable filter, figure 2.25(b), is a narrow band-pass filter, e.g. a Fabry-Perot cavity, acousto-optical tuneable cavity or thin-film based resonant cavity. The filter is deterministically tuned across its spectral range and the location of intensity maximum returns the FBG peak. The disadvantage of the scanning tuneable filter is that the scan time limits the temporal resolution, as in all scanning systems.

The bandwidth of the tuneable filter should be less than the FBG bandwidth

across the full scan length. If the time that the peak region is admitted changes, the resolution achievable will correspondingly decrease. An issue that may arise with mixed high- and low-coherence sources is an interference pattern within the bandwidth of the tuneable filter when the filter peak matches the high-coherence source wavelength. The least problematic arrangement is to combine the tuneable filter and illumination source into a tuneable laser to scan the spectral range.

A stationary unbalanced two beam interferometer can demodulate the FBG signal by acting as a phase sensitive filter, figure 2.25(c). The fixed OPD produces a standing wave, and as the FBG changes  $\lambda_B$ , the received intensity is sinusoidally modulated, within the free spectral range. This approach provides the greatest resolution of the three approaches in figure 2.25. The disadvantage of this technique is that the vibration/thermal stability of the unbalanced interferometer produces large non-FBG intensity changes.

A limitation of these intensity based approaches is that multiplexed FBGs produce a single intensity. Multiplexed FBGs require a method of demultiplexing the multiplexed FBG spectral responses prior to using these approaches.

#### **2.4.1.1 Diffraction gratings**

Diffraction gratings are interferometric devices which disperse incident electromagnetic radiation into discrete angular orders based on the wavelength of that electromagnetic radiation [352]. The diffraction grating thus provides demultiplexing, within the free spectral range of the grating.

As a result of the spatial presentation, diffraction grating spectrometers cannot achieve the same resolution as two-beam interferometers of the same size. A fuller discussion of diffraction grating spectrometers is deferred to chapter 3, which describes the construction of a diffraction grating spectrometer, the SpectroBragg, used in this work.

#### **2.4.1.2 Interferometry**

From the definitions of interference, outlined in appendix section B.5.1 (page V.II B-10), interferometry is the use of the intentional interference of light to obtain information about that light. Two-beam interferometry is used in chapter 6, with the Hilbert transform technique. Multiple beam interferometry is also used in this thesis, as the diffraction grating used in the SpectroBragg can be considered a multiple beam interferometer. A review of multiple beam and two-beam interferometry is now provided. The basic ideas of interferometry are introduced in appendices B (page V.II B-1)– D (page V.II D-1).

## 2.4.1.3 Fabry–Perót interferometer

The Fabry–Perót interferometer is a multiple beam or multiple reflection interferometer. An incident beam undergoes multiple, diminishing reflections within a cavity consisting of two partially reflecting surfaces [353–355], as illustrated in figure 2.26. The etalon has transmitted,  $t$ , and reflected,  $r$ , components which add to give the incident intensity, for a lossless cavity. In the Fabry–Perót interferometer/spectrometer configuration, the emerging collimated beams are focused, and an Airy pattern is observed. The spacing  $d$  can be modified or the refractive index changed for a scanning interferometer [354]. The phase shift introduced by traversing the space  $d$  is<sup>82</sup>

$$\delta\Phi = \frac{4\pi}{\lambda_0} nd \cos \theta_2 \quad (2.116)$$

The superposition of the  $p$  beams will add coherently once  $pn_2d \leq l_{\text{coh}}$ . The

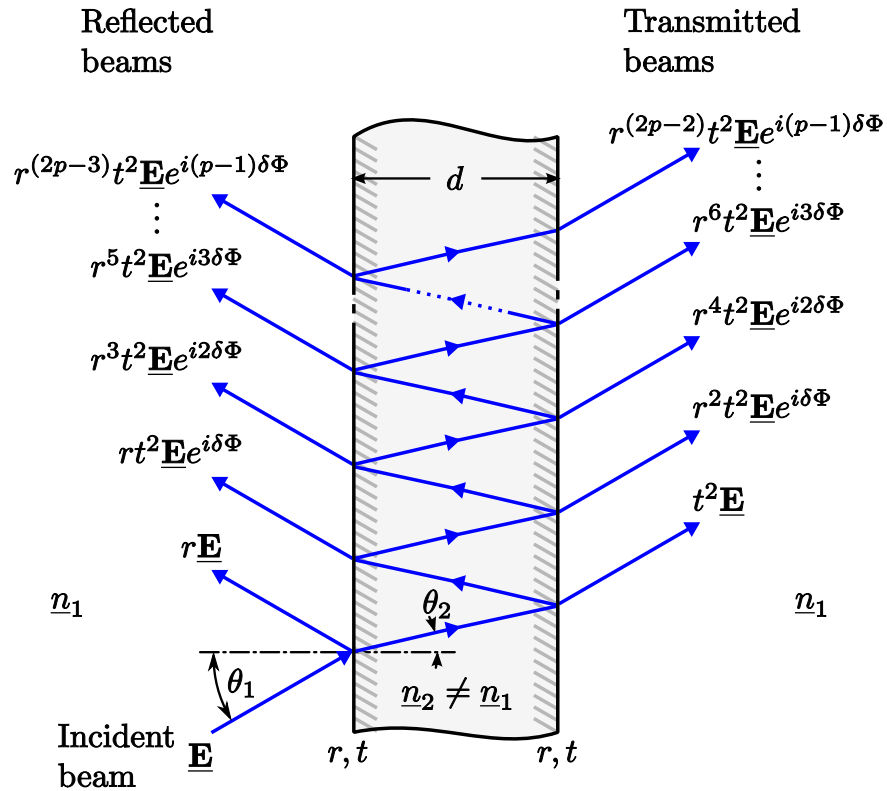


**Figure 2.26:** Fabry–Perót etalon where the incident beam is multiply reflected within the cavity, coherently superposing upon itself within its coherence length.

Fabry–Perót interference occurs in both directions. The reflected intensity is given

<sup>82</sup>As the orthogonal components of  $\underline{n}$  may differ,  $\delta\Phi$  and  $l_{\text{coh}}$  may also have different orthogonal components. In which case the treatment from equation (2.116) on would need to incorporate two differing orthogonal values.

by [354, 355]

$$\frac{I_{FP_r}}{I_{in}} = \frac{4R \sin^2 \frac{\delta\Phi}{2}}{(1-R)^2 + 4R \sin^2 \frac{\delta\Phi}{2}} = \frac{F \sin^2 \frac{\delta\Phi}{2}}{1 + F \sin^2 \frac{\delta\Phi}{2}} \quad (2.117)$$

where  $R = r^2$ , and  $F$  is the finesse,

$$F = \frac{4R}{(1-R)^2} \quad (2.118)$$

The transmitted intensity is given by [354, 355]

$$\frac{I_{FP_t}}{I_{in}} = \frac{T^2}{(1+R)^2 + 4R \sin^2 \frac{\delta\Phi}{2}} = \frac{1}{1 + F \sin^2 \frac{\delta\Phi}{2}} \quad (2.119)$$

where  $T = t^2$ .

The FWHM bandwidth of the Fabry–Perót is given by [353, 355]

$$\delta\lambda_{FP} = \frac{1-R}{\sqrt{R}} = \frac{4}{\sqrt{F}} \quad (2.120)$$

Within a fibre, splices and physical connectors, such as FC/PC connections, introduce low finesse parasitic Fabry–Perót cavities [356]. Angled connectors, FC/APC, are used to prevent establishing these cavities. However, they will still occur at splice points. The Fabry–Perót acts as a filter, similarly to the FBG, and has also been used as a sensor [357–359] and demodulator [193, 351].

When an unintentional Fabry–Perót is established it is termed a ‘parasitic Fabry–Perót’, as it introduces unintended signal modulation at the matching cavity frequencies. Due to the environmental sensitivity of the fibre, the ‘parasitic Fabry–Perót’ follows the measurands and the unwanted modulation cannot be considered static.

When an FBGs signal’s spectral bandwidth overlaps a Fabry–Perót cavity’s spectral bandwidth, the FBG signal will be modulated. If the resulting spectrum is passed through a demodulating interferometer, a channelled spectrum is produced.

A bulk optic Michelson interferometer exhibits a parasitic Fabry–Perót between the beam–splitter and mirrors. To remove these the mirrors are placed at a slight angle. In an all–fibre Michelson interferometer, the splices cannot be easily angled and a low finesse cavity exists.

#### 2.4.1.4 Two–beam interferometry

Two beam interferometry is the recovery of phase information from a known phase shift of the signal against a reference signal [360]. The phase shift can be a function of position, as in the Young’s slits experiment, or time, the Michelson experiment. Low–coherence interferometry using Michelson and Mach–Zehnders is an established

technique for FBG demodulation [321, 361, 362].

The most significant difference between the bulk and all-fibre equivalents of interferometric and spectroscopic devices is that the intervening space between the components of the instruments are described by E and D, respectively. The effects of the (possibly different) materials used must now be dealt with in determining system resolution and performance. The physical layout of all-fibre components can introduce topological phase shifts, and birefringence, that are easier to neglect in the bulk equivalent [363].

The advantages of the all-fibre versions are

- generally reduced size of apparatus/instrument,
- ease of assembly (particularly for connectorised components),
- relative immunity to vibration.

The bulk and all-fibre Michelson interferometers are shown schematically in figure 2.27(a) and 2.27(b), respectively. The all-fibre<sup>83</sup> and bulk versions are conceptually the same, but differ in the details. The all-fibre version will be discussed here.

If the interferometer arms require splices, parasitic Fabry-Perót cavities can be formed. The presence of bends and twists of fibres<sup>84</sup> within the arms of the interferometer will introduce phase and polarisation changes, as discussed in appendix section E.3 (page V.II E-7) and sections 2.2.8.2 (page V.I - 52) and 2.2.8 (page V.I - 50). Geometric phase shifts are achromatic, but bends and twists will not necessarily be achromatic. The change in OPD is introduced by a piezoelectric stretcher in the scanning arm, which introduces varying birefringence in the scanning arm. The SOP of the signals in both arms are therefore unlikely to maintain their initial SOP or OPD-only phase difference.

Optical frequencies of  $\sim 10^{14}$  Hz cannot be directly observed with current electronics. When the signal and reference arms have the same incident wave, the beating of the interferometer cavity and the incident waveform produce a lower frequency signal which can be detected [364]

$$f_d = V_{\text{OPD}} \frac{1}{\lambda} \quad \text{Hz} \quad (2.121)$$

where  $V_{\text{OPD}}$  is the velocity of the component which produces the OPD. For a Michelson interferometer the velocity is doubled due to the traversal of the path upon reflection.

Ideally,  $V_{\text{OPD}}$  is linear over the operational range and  $f_d = f_d(t, \lambda)$ . In practice  $V_{\text{OPD}}$  is nonlinear, due to acceleration/deceleration of components and vibrational

<sup>83</sup>An all-fibre Michelson interferometer is used in chapter 6.

<sup>84</sup>The fibre is not in a straight line for tidiness and safety.

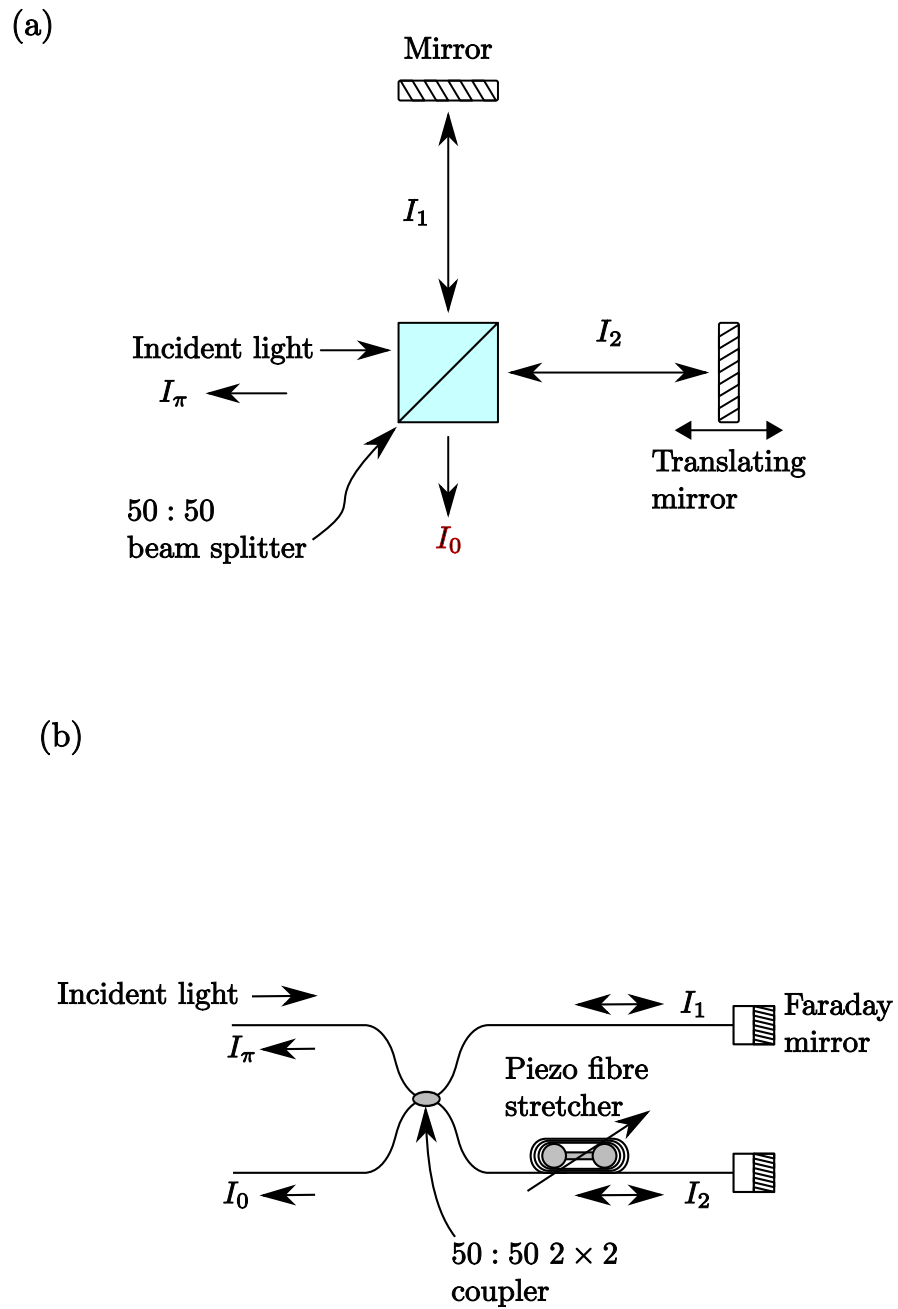


**Figure 2.27:** Michelson interferometer providing two  $\pi$ -shifted outputs. (a) The bulk optic Michelson and (b) the all-fibre equivalent.

noise. Two approaches are used to overcome these nonlinearities, which add on higher powers of the intensity as noise [365]. The first is to register the minimum or the zero-crossings of the intensity axis by a high-coherence reference signal co-propagating or propagating in parallel [366–368]. The zero-crossings will then be at equal OPD intervals, and will produce a linear  $V_{\text{OPD}}$  with arbitrary linear timescale.

This approach removes the nonlinearity of  $V_{\text{OPD}}$ , but introduces the difficulty of ensuring that the captured signal coincides with the high-coherence reference signal. If any delay is not consistent a new variation of  $V_{\text{OPD}}$  is introduced. The positional errors depend upon the derivative of the interferogram [365].

The second approach is to capture the reference and signal intensities at equal, or near equal, time intervals and to reconstruct the reference signal. The reconstruction of the reference will correct the signal interferogram as if there were no nonlinearities present in  $V_{\text{OPD}}$ . This is the approach used in chapter 6.

Both these approaches rely upon a best-effort reduction in vibration and nonlinearities during the capture of the interferogram. If the nonlinearities were such as to instantaneously change<sup>85</sup> by several wavelengths, the high-coherence reference interferogram would be relatively unchanged at the next zero-crossing, compared to the lower-coherence signal interferogram. Consequently, the zero-crossing captured or reconstructed interferogram would not produce the correct spectrum.

### 2.4.2 Fourier transform spectroscopy

A. A. Michelson demonstrated that the intensity of light,  $I(\phi)$ , at an exit of a two-beam interferometer with a variable phase difference,  $\phi$ , is the Fourier cosine spectrum of the incident light,  $I_0$ .  $I_0$  could, therefore, be obtained by using the inverse Fourier transform<sup>86</sup> [369]. For very narrow sources, measuring the visibility allowed the highest resolution measurements of the time. Determination of complex and long interferograms was too laborious until the availability of digital computers. The interferogram is recorded and the FT performed after the recording is complete.

In Fourier transform spectroscopy, the interference pattern is measured, which gives  $\mathcal{V}_Q(\tau)$ . A window is applied by multiplication, to apodise the interferogram. Taking the FFT of the interferogram gives the spectrum of that interferogram.

The resolution obtained from an interferogram depends upon the OPD. A FT is evaluated from  $-\infty$  to  $+\infty$ . A realisable interferogram will be finite, and hence limited to the range  $t$  to  $t + \tau$ . This is equivalent to multiplying (convolving) a rectangular or boxcar function with the infinite interval interferogram (FT). The spectral features of the boxcar function are thus repeated on signal spectral features.

---

<sup>85</sup>Instantaneously with respect to the detector's sampling rate.

<sup>86</sup>The Fourier transform and its properties are briefly described in appendix H (page V.II H-1).

Apodisation or windowing of the interferogram can reduce the spectral effects of the abrupt rectangular profile, as discussed in §P.2 (page V.II P-3).

The longer the OPD,  $v\tau$ , the higher the resolution<sup>87</sup> obtainable will be. When the signal is digitised, the OPD is not the only limit to accuracy. The sampling rate at which the signal is digitised also limits resolution. The fringes need to be sampled adequately. This highest frequency component accurately measured is half that determined from the period of the sampling interval, and is termed the *Nyquist frequency* [370,371]. Frequency components higher than the Nyquist frequency are ‘folded’ or aliased into the sampled spectral range. At each folding the profile is reversed.

Source noise is a cause of multiplex disadvantage compared to dispersed detection systems [365]. In the case of source noise, the noise scales with the intensity. For multiple spectral features, e.g. an array of FBGs, the intensity noise from the illuminating SLED will be reflected from each FBG, and so the length of time increases to get the same SNR as the dispersed detection system. Mitigation of source noise effects can be achieved through rapid scanning, at the expense of fringe resolution [365].

#### 2.4.2.1 Phase noise in interferometer

As the interferometer uses structured phase modulation, phase noise becomes a significant limitation towards ideal operation. Phase noise is a measure of the spectral purity of a source or fidelity to the initial signal after transmission [38].

The demodulation instrument response is convolved with the input signal. If the input signal has phase noise, the instrument process and the spectrum obtained will be broader and noisier.

Phase noise occurs within the arms of the all-fibre interferometer. Using a perturbation  $\Delta\underline{n}$ , and for unity input, the intensity is given as [89],

$$I = \frac{1}{2} \left[ 1 + \cos \left( \frac{2\pi \langle \underline{n}_{\text{eff}} \rangle L_{\text{OPD}}}{\lambda} \right) e^{-\left( 2 \frac{L+L_{\text{OPD}}}{L_{\text{coh}}} \right)} \right] \quad (2.122)$$

where  $L_{\text{OPD}}$  is the OPD between the two arms, and  $L$  is the length of fibre arm 1,  $L + L_{\text{OPD}}$  is the length of arm 2.  $L_{\text{coh}}$  is the length of  $L$  for which  $\langle \Delta\Phi^2 \rangle = 2\pi$ . Designating the phase shifts that arise in arms 1 and 2 as  $\Phi_1$  and  $\Phi_2$ , respectively, the intensity is a minimum or zero when  $\Phi_1 - \Phi_2 = 2\pi m$ , where  $m$  is a half integer. The phase shifts consist of the optical path lengths and the respective phase noises,

---

<sup>87</sup>This statement relies upon the signal being stationary over the full OPD. The longer the OPD the more difficulty there will be in meeting this requirement.

$\Delta\Phi_1$  and  $\Delta\Phi_2$ . The zero-crossing condition is then [89]

$$\frac{2\pi\langle n_{\text{eff}} \rangle L_{\text{OPD}}}{\lambda} - \frac{2\pi\langle n_g \rangle L_{\text{OPD}} \Delta\lambda}{\lambda^2} + \Delta\Phi_1 - \Delta\Phi_2 = 2\pi m \quad (2.123)$$

where  $n_g$  is the average group refractive index.

In the absence of phase noise fluctuations  $\Delta\phi_1 = \Delta\phi_2 = \Delta\lambda = 0$  and  $L_{\text{OPD}} = m \left( \frac{\lambda}{\langle n_{\text{eff}} \rangle} \right)$ . The first and last terms of equation (2.123) are equal and cancel, giving [89]

$$\Delta\phi_1 - \Delta\phi_2 = \frac{2\pi\langle n_g \rangle L_{\text{OPD}} \Delta\lambda}{\lambda^2} = \frac{2\pi n_g m \Delta\lambda}{\langle n_{\text{eff}} \rangle \lambda} \approx \frac{2\pi m \Delta\lambda}{\lambda} \quad (2.124)$$

The difference of group and effective refractive indices,  $n_g - \langle n_{\text{eff}} \rangle \sim 1\%$  and so can be neglected. Phase changes  $\Delta\phi_1$  and  $\Delta\phi_2$  are uncorrelated, and, if  $L_{\text{OPD}}$  can be neglected compared to  $L$ , the mean squares of the phase changes are [89]

$$\frac{L}{L_{\text{coh}}} = \frac{\pi^2 m^2 \langle \Delta\lambda^2 \rangle}{\lambda^2} \quad (2.125)$$

### 2.4.2.2 Polarisation-sensitivity

As discussed in appendix B (page V.II B-1), the theoretical ideal for interferometry is that the interfering beams be scalar equivalents. If the SOPs of the beams are mutually orthogonal, then the visibility will be zero and the detector measures a DC signal<sup>88</sup>.

A mixing of SOP types will also produce non-interferometric intensity modulation. One example is the mixing of linear and circularly-polarised beams from the two arms, as might arise from one arm acting as a retarder. At the same  $\lambda$ , as the beams propagate the same conditions are met every  $2\pi$  of phase difference. The circularly polarised beam will, therefore, be in the same plane every integer multiple of  $\pi$  of phase difference, and orthogonal  $\frac{\pi}{2}$  of phase difference later. An interferogram is produced, but with poor visibility as the orthogonal fields add incoherently [372]. If there are variations in the SOPs of the wavelengths to be demodulated, there is the possibility of the visibility depending upon the wavelength [373].

As has been discussed, fibre loops act as retarders, changing the SOP. Changes arising in the DOP can alter the DOC and hence the spectral DOC. With the reduced visibility the calculation of the spectrum from the inverse FT will differ from the actual spectrum.

<sup>88</sup>Neglecting non-interferometer based modulation of the signal, such as source fluctuations.

### 2.4.2.3 Thermal drift

The interferometer can become a thermometer, as any change in temperature between the two arms will produce a thermal expansion based OPD. This can move the zero-OPD point for interferograms so that the mechanically induced scan does not achieve the same OPD across measurements performed at different temperatures. For a short scan interferometer arrangement, a change in temperature will have a more significant effect than for longer scan arrangements, e.g. a shift of the zero position in figure B.2(a) (page V.II B-7) will have less of an effect than for figure B.2(b) (page V.II B-7). The thermal shift can prevent a full two sided interferogram being obtained.

Within components which are fixed and not free to move, e.g. FC/APC connectors, the thermal expansion will introduce a strain, and hence a birefringence. Within the interferometer arms this should be compensated by the Faraday mirrors. However, the components leading to and from the interferometer will not be compensated, and the localised polarisation splitting amongst many connections can increase the PDL and phase noise.

### 2.4.2.4 Zero-OPD point

In an ideal two-beam interferometer, the zero-OPD point, where the OPD in both arms is exactly equal, will be the only location at which every wavefront will be in phase. For a symmetric interferogram the same information is present on both sides of the zero-OPD point. Thus, apart from redundancy, a single-sided interferogram should suffice.

In practice the sampled interferogram recorded by continuous- or stepping-translation is unlikely to have a balance point coincide with a sampling position of the data capturing device. It is, thus, more typical to obtain double-sided interferograms<sup>89</sup>, preferably symmetric interferograms [364].

In a dispersive medium, the zero-OPD position can become wavelength dependent [374]. The all-fibre Mach-Zehnder or Michelson will also have waveguide induced modal dispersion in the coupler overlap area<sup>90</sup>.

The OPD does not need to be introduced by scanning. Non-scanning interferometry can be achieved by using a Tyman-Green type arrangement, with the OPD introduced across a spatial extent by angling the mirror, and detected upon an array [376]. This arrangement retains the Fellgett advantage as each diode is illuminated by all wavelengths simultaneously. Pixel noise, vibrations, array pixel

---

<sup>89</sup>Single-sided interferometers typically record asymmetric two-sided interferograms to ensure the zero-OPD position has been covered [364].

<sup>90</sup>The coupler's wavelength efficiency will introduce a wavelength dependent change to the visibility at that wavelength. The magnitude of this change will be smaller than noise in effect [375].

density and read-out times will provide device limitations, although the use of a reference signal should reduce their impairments. The beam expander will have a dispersive effect and geometric aberrations may be introduced which the referencing may not fully correct.

Michelson and Mach–Zehnder interferometers are widely used due to their simplicity. The development of new methods of obtaining two beam interferometers continues. An interferometer employing two-core fibre with OPD scanning via cantilever has been reported [377].

### 2.4.3 Receiver unit

The receiver will have a detector and associated amplifier/filter electronics. The detector signal,  $i_d$ , has a spectral response function,  $R_d(\lambda)$ , which scales the optical intensity,  $I_d$ , as a function of wavelength [76],

$$i_d = R_d(\omega)I_d \quad (2.126)$$

where

$$R_d(\omega) = \eta_{d0}(\omega) \frac{q_e}{\hbar\omega_0} \quad (2.127)$$

is the responsivity [378],  $\eta_{d0}$  is the material's quantum efficiency,  $q_e$  is the electron's charge and  $\hbar\omega_0$  is the photon's energy. Assuming no saturation, the flatter the spectral response, the more uniform the resulting signal captured.

Depending upon the integration time of the detector and the spectroscopic instrument's coherence function, the DOP and DOC of a given signal will produce different spectra. Using the two-point Stokes parameters, the correlations describe the field at an interval  $\tau$  for a Michelson or Mach–Zehnder interferometer. If  $\tau$  differs, then the DOP and DOC, and hence recovered spectrum, change.

#### 2.4.3.1 Detector noise

Demodulation systems must ultimately provide the measured values in a useful format. Typically this is in the form of digitised electrical signals. Detector noise imposes a performance limitation on experimental systems. InGaAs photodiodes are the detectors used in this work and are noise limited devices. The major sources of noise in photodiodes can be grouped into [38]:

- *Thermal noise*: Also called *Johnson noise* [379], is a white noise from the associated load resistor, the mean-square thermal noise current is given as

$$\langle i_{T_n}^2 \rangle = \frac{4k_B T B_D}{R_L} \quad (2.128)$$

where  $B_D$  is the electrical bandwidth,  $R_L$  is the load resistance,  $k_B$  is Boltzmann's constant and  $T$  is the absolute temperature. Thermal noise arises from fluctuations in voltage across circuit components induced by internal current fluctuations [379] and so is often dominant with weak optical signals.

- *Shot noise*: A Poisson distributed noise arising from the quantum statistics of detection [11]. The mean-square thermal noise current is given by the *Schottky formula* [379]:

$$\langle i_{\text{sh}}^2 \rangle = 2q_e I_s B_D \quad (2.129)$$

where  $q_e$  is the electron charge and  $I_s$  is the signal photocurrent. From equation (2.126), it follows that shot noise tends to be the dominant noise with strong optical signals.

- *Dark current noise*: the reverse saturation current, which exists when no photocurrent, i.e. light, is present. The mean-square thermal noise current is given as

$$\langle i_{\text{dk}}^2 \rangle = 2q_e I_D B_D \quad (2.130)$$

where  $I_D$  is the average dark current.

Adding  $\langle i_{\text{amp}}^2 \rangle$ , the mean-square noise current for any electrical amplifiers, the *signal to noise ratio*, SNR, for the receiver is [38]:

$$\text{SNR} = \frac{\langle i_s^2 \rangle}{\langle i_{T_n}^2 \rangle + \langle i_{\text{sh}}^2 \rangle + \langle i_{\text{dk}}^2 \rangle + \langle i_{\text{amp}}^2 \rangle} \quad (2.131)$$

The larger the value of SNR the better. In chapter 5 approaches to mitigating polarisation induced noise to improve the SNR are discussed. In chapter 6 a method of improving the SNR, using common-mode rejection of phase noise, is discussed.

In addition to detector noise there will also be *readout noise* (also termed *the noise floor* [380]), which occurs at the readout/amplification of the signal by the on-chip amplifier is a function of circuit configuration and layout design [381], where noise in the readout clock, amplifier and the diodes combine [382]. The readout noise is a fixed quantity for the fixed integration time of amplifier [350].

#### 2.4.3.1.1 Benefit of two differenced outputs: CMRR

The result of phase noise in an interferometer is to broaden and distort strong spectral features by adding spurious spectral components, and to obscure the presence of weaker spectral features by reducing the visibility of fringes. Phase noise, as a statistical quantity, is equally split into both arms by the beam-splitter of an interferometer. *Common-mode rejection ratio*, CMRR, approaches can be used to

eliminate most of the noise, in a Michelson or Mach–Zehnder by using the complementary outputs of the interferometer [14, 383].

The phase noise arising within the interferometer are not common–mode, but the accumulated phase noise from the fibre up to the  $2 \times 2$  50:50 coupler is common to both arms. The inputs of an differential amplifier, attached to photodiodes, is termed a balanced receiver. When a balanced receiver measures the complementary outputs, all common–mode signal components appear as a DC signal. If the intensities at both detectors are not equal, then the compensation is not a maximum, and the improvement in the signal is a ratio of the intensities.

### 2.4.3.2 Digitising noise

The dynamic range of the digitising system, the analog–to–digital converter or ADC, is [365]

$$D_R = \frac{\text{full scale}}{\text{least bit}} = 2^n \quad (2.132)$$

for  $n$  bits, excluding the sign bit.

When the optical and receiver system are adjusted so that the interferogram peak is close to, but not clipped by, the full scale of the ADC, the digitising noise is [365]

$$\Delta I(\tau) = \frac{\text{full scale}}{2\sqrt{3}D_R} \Delta I(\omega) = \frac{\pi}{\sqrt{3}D_R\sqrt{N}} \quad (2.133a)$$

where  $N$  is the number of digitised data points in the signal.

### 2.4.3.3 RIN

*Relative intensity noise*, RIN, is used to measure the ratio of optical noise power to total optical power of a source [38],

$$\text{RIN} = \frac{S_n(\lambda)}{I_{\text{tot}}^2} \quad (2.134)$$

where  $S_n(\lambda)$  is the intensity noise power spectral density [38], or mean square intensity noise spectral density [384], and  $I_{\text{tot}}$  is the total optical power. RIN is used as a measure of the quality of a source, and as a measure of the signal after propagation. The lower the RIN value the higher the signal quality.

In a fibre device Rayleigh–scattering induced phase–noise will be unavoidable. The mean magnitude of the noise will scale with distance, as Rayleigh scattering is an extensive effect. Attenuation scales with distance, so, in general, the RIN will increase with distance.

For a two-beam interferometer, such as a Michelson interferometer, the relative intensity noise from Rayleigh scattering for a high-coherence source is given as [384]

$$\text{RIN}_{\Delta\phi_{coh}} \cong \frac{2R_p}{(1 + R_p^2)} 8\pi\tau_0^2 \Delta\nu_{lw} \text{sinc}^2(\tau_0 f) \quad [\text{Hz}^{-1}] \quad (2.135)$$

where  $R_p$  is the ratio of the interfering intensities from the two interferometer arms. The line profile is assumed to be Lorentzian, the *sinc* term, with linewidth  $\Delta\nu_{lw}$ .  $\tau_0$  is the differential time delay between the interferometer arms and  $f$  is the *Fourier frequency* [364].

The random nature of Rayleigh scattering results in a spread of the laser's spectrum with low intensity, thickening the tails of the profile. The RIN of an incoherent signal is given by [12]

$$\text{RIN}_{\Delta\phi_{incoh}} = \frac{2R_p}{(1 + R_p^2)} \frac{2}{\pi\Delta\nu_{lw}} \frac{1}{1 + (f/\Delta\nu_{lw})^2} \quad [\text{Hz}^{-1}] \quad (2.136)$$

where the line shape is again assumed to be Lorentzian. For a strong laser signal accompanied by lower intensity low-coherence signals, the  $\text{RIN}_{\Delta\phi_{incoh}}$  will apply for the laser noise experienced by the FBGs.

Low-coherence signals will also experience Rayleigh scattering, but by containing more frequencies reduce the magnitude of the intensity fluctuations shown in figure 2.1 (page V.I - 15). The RIN will be between extremes of  $\text{RIN}_{\Delta\phi_{coh}}$  and  $\text{RIN}_{\Delta\phi_{incoh}}$  from equations (2.135) and (2.136), respectively.

## 2.5 Summary of theoretical background in the context of experimental work

This chapter, and its associated appendices, provides the common theoretical background and literature review for the subsequent chapters. FBGs are promising candidates for applications such as SHM. Their small size, long life, ease of multiplexing, immunity to electromagnetic interference and direct measurand encoding in the reflected wavelength, make them competitive sensors for a range of applications.

FBGs in standard telecomms fibres, e.g. SMF-28, are considered to be isotropic structures [222]. However, even 'isotropic' FBGs are very weakly anisotropic. In chapter 4, a novel anisotropic FBG is strain characterised. The strain and temperature responses differ subtly, suggesting that strain-temperature discrimination may be achievable. These novel FBGs are inscribed in standard SMF-28 by a two-photon process at 264 nm, producing an anisotropy. These FBGs have the material response of SMF-28, but with anisotropy closer to FBGs in PMF.

Typically, the most expensive component for FBG sensor systems is the demodulation (sub)system. This work reports on the construction of a custom Čzerny–Turner, diffraction–grating–based spectrometer, the SpectroBragg, in chapter 3. An all–fibre Michelson interferometer was used in chapter 6. The component parts of both devices cost more than the single FBG sensors interrogated. Consequently, to be commercially viable, both systems were designed to be used with multiplexed FBG sensors, to reduce the per sensor cost of demodulation.

However, the optical fibre can further modify the reflected signal, either through polarisation or coherence changes. These changes can be introduced by the material itself, through bends and twists, applied temperature or strain changes or simply by the topological arrangement of the fibres. The unified theory of coherence and polarisation [24], provides a convenient framework to follow both coherence and polarisation effects as FBG signals traverse the system.

For demodulation systems which use the phase of the signal to return the peak wavelength value<sup>91</sup>, these modifications can alter the recovered measurement. The basics of polarisation and coherence, optical fibre propagation and optical fibre environmental sensitivity has been covered in this chapter.

Two approaches to the mitigation of *state of polarisation* induced measurement changes are discussed in chapter 5. These approaches differ from conventional depolarisation schemes as they are adaptable to the demodulation scheme being used, but cheaper to assemble.

The distances over which fibres can faithfully transmit signals enables remote sensing to be achieved. In chapter 6, the mitigation of accumulated phase noise, through the extensive Rayleigh scattering process, is used with short–scan interferometry and the HTT. The phase noise from Rayleigh scattering will, typically, have a deleterious effect on interferometrically demodulated signal, as the signal’s coherence is lowered.

For a two–beam interferometer, the multiplex disadvantage will maximise the impact<sup>92</sup> of the accumulated phase noise [15]. By using the common–mode rejection provided by the complementary outputs of the all–fibre Michelson, and the high resolution the HTT enables with short–scan interferometry, robust, high–speed, high resolution remote sensing with FBGs is demonstrated in chapter 6, with commercially available off–the–shelf components.

---

<sup>91</sup>These systems are typically the highest resolution systems.

<sup>92</sup>As described in appendix D (page V.II D-1).

---

## 2.6 References

- [1] L. D. Landau and E. M. Lifshitz. *The Classical Theory of Fields*, volume 2 of *Course of Theoretical Physics*, chapter 3, pages 46–69. Butterworth-Heinemann, Oxford, 4th edition, 1975. ISBN: 0750627689.
- [2] B. J. Smith and M. G. Raymer. Photon wave functions, wave-packet quantization of light, and coherence theory. *New J. Phys.*, 9:414, November 2007.
- [3] W. Lauterborn, T. Kurz, and M. Wiesenfeldt. *Coherent Optics: Fundamentals and Applications*, chapter 3, pages 15–29. Springer-Verlag, Berlin, 1995. ISBN: 3540583726.
- [4] L. Mandel and E. Wolf. *Optical Coherence and Quantum Optics*, chapter 10, pages 465–521. Cambridge University Press, New York, sep 1995. ISBN: 0521417112.
- [5] M. Fox. *Quantum Optics*, chapter 7, pages 126–150. Oxford University Press, Oxford, 2006. ISBN: 0198566735.
- [6] W. H. Carter. *Coherence Theory*, volume 1 of *Handbook of Optics*, chapter 5. McGraw-Hill Companies, Inc., New York, 3 edition, 2010. ISBN: 0071498893.
- [7] M. E. Lines. *Physical properties of materials: theoretical overview*, volume 30 of *Handbook of infrared Optical Materials*, chapter 1, pages 1–70. Marcel Dekker, Inc., New York, 1991. ISBN: 0824784685.
- [8] M. Born and E. Wolf. *Principles of Optics: Electromagnetic Theory of Propagation, Interference and Diffraction of Light*, chapter 1, pages 1–74. Cambridge University Press, Cambridge, 7th edition, 1999. ISBN: 0521642221.
- [9] O. Kafri. Fundamental limit on accuracy in interferometry. *Opt. Lett.*, 14(13):657, 1989.
- [10] A. van der Ziel. *Noise*, chapter 1, pages 1–7. Prentice-Hall, Inc., Englewood Cliffs, N. J., 1954.
- [11] M. Fox. *Quantum Optics*, chapter 5, pages 75–104. Oxford University Press, Oxford, 2006. ISBN: 0198566735.
- [12] W. V. Sorin. *Fiber Optic Test and Measurement*, chapter Appendix A, pages 597–613. Prentice Hall, Inc., New Jersey, 1998. ISBN: 0135343305.
- [13] H. A. Gebbie. Fourier transform versus grating spectroscopy. *Appl. Opt.*, 8(3):501, 1969.
- [14] S. Davis, M. C. Abrams, and J. W. Brault. *Fourier Transform Spectrometry*, chapter 3, pages 29–39. Academic Press, San Diego, 2001. ISBN: 9780120425105.
- [15] E. Voigtman and J. D. Winefordner. The multiplex disadvantage and excess low-frequency noise. *Appl. Spectrosc.*, 41(7):1182–1184, September 1987.

- 
- [16] E. Wolf. *Introduction to the Theory of Coherence and Polarization of Light*, chapter 5, pages 79–110. Cambridge University Press, Cambridge, 2007. ISBN: 9780521822114.
- [17] E. Wolf. Optics in terms of observable quantities. In L. Mandel and E. Wolf, editors, *Selected Papers on Coherence and Fluctuations of Light*, volume 1, pages 194–198. Dover Publications, Inc., New York, 1970. ISBN: 0486625702.
- [18] E. Wolf. Coherence properties of partially polarized electromagnetic radiation. In L. Mandel and E. Wolf, editors, *Selected Papers on Coherence and Fluctuations of Light*, volume 1, pages 364–380. Dover Publications, Inc., New York, 1970. ISBN: 0486625702.
- [19] E. Wolf. *Introduction to the Theory of Coherence and Polarization of Light*, chapter 8, pages 154–173. Cambridge University Press, Cambridge, 2007. ISBN: 9780521822114.
- [20] E. Collett. *Polarized Light in Fiber Optics*, chapter 14, pages 379–432. SPIE Press/Polawave Group, New Jersey, nov 2004. ISBN: 0819457612.
- [21] D. Goldstein. *Polarized Light*, volume 83 of *Optical Engineering*, chapter 4, pages 31–64. Marcel Dekker, Inc., New York, 2 edition, 2003. ISBN: 082474053X.
- [22] C. Brosseau. *Fundamentals of Polarized Light: A Statistical Optics Approach*, chapter 4.1, pages 181–243. John Wiley & Sons, Inc., New York, 1998. ISBN: 0471143022.
- [23] E. Wolf. *Introduction to the Theory of Coherence and Polarization of Light*, chapter 9, pages 174–201. Cambridge University Press, Cambridge, 2007. ISBN: 9780521822114.
- [24] E. Wolf. Unified theory of coherence and polarization of random electromagnetic beams. *Phys. Lett. A*, 312(5-6):263–267, 2003.
- [25] C. Brosseau. *Polarization and coherence optics: Historical perspective, status, and future directions*, volume 54 of *Progress in Optics*, chapter 3. Elsevier, Amsterdam, 2009. ISBN: 9780444535283.
- [26] E. Wolf. *The influence of Young’s interference experiment on the development of statistical optics*, volume 50 of *Progress in Optics*, chapter 7. North-Holland Publishing Co., Amsterdam, 2007. ISBN: 9780444530233.
- [27] S. Huard. *Polarization of Light*, chapter 3, pages 86–131. John Wiley & Sons, Ltd., London, feb 1997. ISBN: 0471965367.
- [28] E. Collett. *Polarized Light in Fiber Optics*, chapter 6, pages 77–114. SPIE Press/Polawave Group, New Jersey, nov 2004. ISBN: 0819457612.
- [29] C. Brosseau. *Fundamentals of Polarized Light: A Statistical Optics Approach*, chapter 3.1, pages 69–122. John Wiley & Sons, Inc., New York, 1998. ISBN: 0471143022.
-

- 
- [30] O. Korotkova and E. Wolf. Generalized Stokes parameters of random electromagnetic beams. *Opt. Lett.*, 30(2):198–200, January 2005.
- [31] J. Ellis and A. Dogariu. Complex degree of mutual polarization. *Opt. Lett.*, 29(6):536–538, March 2004.
- [32] J. Tervo, T. Setälä, A. Roueff, P. Réfrégier, and A. T. Friberg. Two-point Stokes parameters: interpretation and properties. *Opt. Lett.*, 34(20):3074–3076, October 2009.
- [33] O. Korotkova and E. Wolf. Effects of linear non-image-forming devices on spectra and on coherence and polarization properties of stochastic electromagnetic beams: part I: general theory. *J. Mod. Optic.*, 52(18):2659–2671, 2005.
- [34] O. Korotkova and E. Wolf. Effects of linear non-image-forming devices on spectra and on coherence and polarization properties of stochastic electromagnetic beams: part II: examples. *J. Mod. Optic.*, 52(18):2673–2685, 2005.
- [35] A. Mendez and T. F. Morse, editors. *Specialty Optical Fibers Handbook*. Academic Press, Amsterdam, 2007. ISBN: 012369406X.
- [36] T. L. Koch, F. J. Leonberger, and P. G. Suchoski. *Integrated optics*, volume 1 of *Handbook of Optics*, chapter 21. McGraw-Hill Companies, Inc., New York, 3 edition, 2010. ISBN: 0071498893.
- [37] S. N. Ghosh. *Electromagnetic Theory and Wave Propagation*, chapter 6, pages 56–78. Alpha Science International, Ltd., Pangbourne, 2nd edition, 2002. ISBN: 1842650971.
- [38] R. Hui and M. O’Sullivan. *Fiber Optic Measurement Techniques*, chapter 1, pages 1–128. Academic Press, New York, 2009. ISBN: 0123738652.
- [39] K. C. Kao and G. A. Hockham. Dielectric-fibre surface waveguides for optical frequencies. In D. B. Keck, editor, *Proceedings of the IEE*, volume Selected Papers on Opt. Fiber Technol., MS 38 of *Milestone Series*, pages 35–42. SPIE Press, Bellingham, 1966. ISBN: 9780819407375.
- [40] P. J. B. Clarricoats. *Optical fibre waveguides - A review*, volume 14 of *Progress in Optics*, chapter 7, pages 327–402. North-Holland Publishing Co., Amsterdam, 1977.
- [41] J. M. Lopez-Higuera. *Introduction to fibre optic sensing technology*, chapter 1, pages 1–22. Handbook of Optical Fibre Sensing Technology. John Wiley & Sons, Ltd., Chichester, 2002. ISBN: 0471820539.
- [42] R. J. Black and L. Gagnon. *Optical Waveguide Modes: Polarization, Coupling and Symmetry*, chapter 2, pages 19–34. McGraw-Hill Companies, Inc., New York, 2010. ISBN: 0071622969.
- [43] A. Rogers. *Polarization in Optical Fibers*, chapter 2, pages 41–74. Artech House, Inc., Boston, 2008. ISBN: 1580535348.
-

- 
- [44] F. W. J. Oliver, D. W. Lozier, R. F. Boisvert, and C. W. Clark. *NIST Handbook of Mathematical Functions*, chapter 10, pages 215–286. Cambridge University Press, Cambridge, 1st edition, may 2010. ISBN: 0521140633.
- [45] S. Huard. *Polarization of Light*, chapter 6, pages 243–296. John Wiley & Sons, Ltd., London, feb 1997. ISBN: 0471965367.
- [46] C.-L. Chen. *Foundations for Guided-Wave Optics*, chapter 1, pages 1–23. John Wiley & Sons, Inc., Hoboken, New Jersey, 2007. ISBN-10: 0471756873.
- [47] A. W. Snyder and J. D. Love. *Optical Waveguide Theory*, chapter 14, pages 301–335. Chapman & Hall, Ltd., London, 1983. ISBN: 0412242508.
- [48] S. G. Lipson, H. Lipson, and D. S. Tannhauser. *Optical Physics*, chapter 10, pages 263–289. Cambridge University Press, Cambridge, 3rd edition, 1995. ISBN: 0521436311.
- [49] R. Drougard and R. J. Potter. *Fiber Optics*, chapter 11. Advanced Optical Techniques. North-Holland Publishing Co., Amsterdam, 1967.
- [50] K. Okamoto. *Fundamentals of Optical Waveguides*, chapter 3, pages 57–158. Academic Press, Amsterdam, 2nd edition, 2006. ISBN: 0125250967.
- [51] K. Iizuka. *Elements of Photonics*, volume 2, chapter 11, pages 692–796. John Wiley & Sons, Inc., New York, 2002. ISBN: 0471408158.
- [52] A. W. Snyder and J. D. Love. *Optical Waveguide Theory*, chapter 13, pages 280–300. Chapman & Hall, Ltd., London, 1983. ISBN: 0412242508.
- [53] D. Gloge. Weakly guiding fibers. *Appl. Opt.*, 10(10):2252–2258, October 1971.
- [54] T. Tamir and H. L. Bertoni. Lateral displacement of optical beams at multi-layered and periodic structures. *J. Opt. Soc. Am.*, 61(10):1397–1413, October 1971.
- [55] R. J. Black and L. Gagnon. *Optical Waveguide Modes: Polarization, Coupling and Symmetry*, chapter 3, pages 35–66. McGraw-Hill Companies, Inc., New York, 2010. ISBN: 0071622969.
- [56] C.-L. Chen. *Foundations for Guided-Wave Optics*, chapter 11, pages 275–308. John Wiley & Sons, Inc., Hoboken, New Jersey, 2007. ISBN-10: 0471756873.
- [57] R. J. Black and L. Gagnon. *Optical Waveguide Modes: Polarization, Coupling and Symmetry*, chapter 1, pages 1–18. McGraw-Hill Companies, Inc., New York, 2010. ISBN: 0071622969.
- [58] A. Rogers. *Polarization in Optical Fibers*, chapter 1, pages 1–40. Artech House, Inc., Boston, 2008. ISBN: 1580535348.
- [59] J. E. Shelby. *Introduction to Glass Science and technology*, chapter 1, pages 1–6. The Royal Society of Chemistry, Cambridge, 2nd edition, 2005. ISBN-10: 0854046399.
-

- 
- [60] J. S. Browder, S. S. Ballard, and P. Klocek. *Physical properties of infrared optical materials*, volume 30 of *Handbook of infrared Optical Materials*, chapter 4, pages 141–153. Marcel Dekker, Inc., New York, 1991. ISBN: 0824784685.
- [61] E. Donth. *The Glass Transition: Relaxation Dynamics in Liquids and Disordered Materials*, chapter 2, pages 11–225. Springer series in Materials Science. Springer-Verlag, 2001. ISBN: 3540418016.
- [62] E. Le Bourhis. *Glass: Mechanics and Technology*, chapter 2, pages 5–23. Wiley-VCH Verlag GmbH & Co. KGaA, Weinheim, 2008. ISBN: 3527315497.
- [63] E. Le Bourhis. *Glass: Mechanics and Technology*, chapter 5, pages 53–81. Wiley-VCH Verlag GmbH & Co. KGaA, Weinheim, 2008. ISBN: 3527315497.
- [64] D. R. Lovett. *Tensor Properties of Crystals*, chapter 1, pages 1–18. IOP Publishing, Ltd., Bristol, 2nd edition, 1999. ISBN: 0750306262.
- [65] E. Donth. *The Glass Transition: Relaxation Dynamics in Liquids and Disordered Materials*, chapter 1, pages 1–10. Springer series in Materials Science. Springer-Verlag, 2001. ISBN: 3540418016.
- [66] R. E. Newnham. *Properties of Materials: Anisotropy, Symmetry, Structure*, chapter 1, pages 1–8. Oxford University Press, jan 2005. ISBN: 019852076X.
- [67] R. Kashyap. *Fiber Bragg Gratings*, chapter 1, pages 1–12. Academic Press, San Diego, 1999. ISBN: 0124005608.
- [68] R. E. Newnham. *Properties of Materials: Anisotropy, Symmetry, Structure*, chapter 5, pages 30–36. Oxford University Press, jan 2005. ISBN: 019852076X.
- [69] P. R. McIsaac. Symmetry-induced modal characteristics of uniform waveguides. I, II. *IEEE T. Microw. Theory*, 23:421–433, May 1975.
- [70] R. E. Newnham. *Properties of Materials: Anisotropy, Symmetry, Structure*, chapter 3, pages 14–22. Oxford University Press, jan 2005. ISBN: 019852076X.
- [71] R. J. Black and L. Gagnon. *Optical Waveguide Modes: Polarization, Coupling and Symmetry*, chapter 4, pages 67–82. McGraw-Hill Companies, Inc., New York, 2010. ISBN: 0071622969.
- [72] J. F. Nye. *Physical Properties of Crystals: Their Representations by Tensors and Matrices*, chapter Appendix D, pages 293–294. Oxford University Press, Oxford, 1985. ISBN: 0198511655.
- [73] E. Le Bourhis. *Glass: Mechanics and Technology*, chapter Appendix 3, pages 271–274. Wiley-VCH Verlag GmbH & Co. KGaA, Weinheim, 2008. ISBN: 3527315497.
- [74] R. Kubo. The fluctuation-dissipation theorem. *Rep. Prog. Phys.*, 29(1):255, 1966.
- [75] P. D. C. Hobbs. *Building Electro-Optical Systems*, chapter 13, pages 448–508. John Wiley & Sons, Inc., Hoboken, New Jersey, 2nd edition, 2009. ISBN: 9780470402290.
-

- 
- [76] F. Chiaraluca. *Single-mode optical fibers and devices*, chapter 2. Single-Mode Optical Fiber Measurement: Characterization and Sensing. Artech House, Inc., Boston, 1993. ISBN: 0890066027.
- [77] A. T. Young. Rayleigh scattering. *Phys. Today*, 35(1):42–48, 1982.
- [78] B. Chu. *Laser Light Scattering: Basic Principles and Practice*, chapter 2, pages 13–61. Dover Publications, Inc., New York, 2nd edition, 2007. ISBN: 0486459782.
- [79] J. Schroeder. *Light Scattering of Glass*, volume 12 of *Treatise on Materials Science and Technology.*, chapter 5, pages 158–222. Academic Press, Inc., New York, 1977. ISBN: 0123418127.
- [80] L. D. Landau, E. M. Lifshitz, and L. P. Pitaevskii. *Electrodynamics of Continuous Media*, volume 8 of *Course of Theoretical Physics*, chapter 15, pages 413–438. Butterworth-Heinemann, Oxford, 2nd edition, 1984. ISBN: 0750626348.
- [81] A. Rogers. Distributed optical-fibre sensing. *Meas. Sci. Technol.*, 10(8):R75–R99, 1999.
- [82] M. E. Lines. *Interaction of light with matter: theoretical overview*, volume 30 of *Handbook of infrared Optical Materials*, chapter 2, pages 71–132. Marcel Dekker, Inc., New York, 1991. ISBN: 0824784685.
- [83] S. A. Dembovsky. Symmetry of a liquid and symmetry breaking at the glass transition. *Phys. Lett. A*, 238(4-5):315–321, 1998.
- [84] F. A. Jenkins and H. E. White. *Fundamentals of Optics*, chapter 22, pages 457–473. Physics Series. McGraw-Hill, 4 edition, 2001. ISBN: 0072561912.
- [85] T. G. Brown. *Optical fibers and fiber-optic communications*, volume 4 of *Handbook of Optics: Fiber Optics & Nonlinear Optics*, chapter 1. McGraw-Hill, New York, 2nd edition, 2001. ISBN: 0071364560.
- [86] V. Twersky. Rayleigh scattering. *Appl. Opt.*, 3(10):1150–1150, 1964.
- [87] S. Wu, A. Yariv, H. Blauvelt, and N. Kwong. Theoretical and experimental investigation of conversion of phase noise to intensity noise by Rayleigh scattering in optical fibers. *Appl. Phys. Lett.*, 59(10):1156–1158, 1991.
- [88] A. Yariv, H. Blauvelt, and S. W. Wu. A reduction of interferometric phase-to-intensity conversion noise in fiber links by large index phase modulation of the optical beam. *J. Lightwave Technol.*, 10(7):978–981, 1992.
- [89] R. Adar, C. H. Henry, M. A. Milbrodt, and R. C. Kistler. Phase coherence of optical waveguides. *J. Lightwave Technol.*, 12(4):603–606, April 1994.
- [90] G. A. Cranch, A. Dandridge, and C. K. Kirkendall. Suppression of double Rayleigh scattering-induced excess noise in remotely interrogated fiber-optic interferometric sensors. *IEEE Photonic. Tech. L.*, 15:1582–1584, November 2003.

- 
- [91] A. A. Kokhanovsky. *Polarization Optics of Random Media*, chapter 1, pages 1–12. Springer-Verlag Berlin, Berlin, 2003. ISBN: 3540426353.
- [92] J. F. Nye. *Physical Properties of Crystals: Their Representations by Tensors and Matrices*, chapter 10, pages 170–191. Oxford University Press, Oxford, 1985. ISBN: 0198511655.
- [93] A. D. Boardman, D. E. O’Connor, and P. A. Young. *Symmetry and its Applications in Science*, chapter 5, pages 91–104. McGraw-Hill Book Company Ltd., 1973. ISBN: 047008412x.
- [94] T. Hahn, A. Authier, and International Union of Crystallography. *International Tables for Crystallography: Physical properties of crystals*, chapter 1, pages 3–264. International Tables for Crystallography. Kluwer Academic Publishers, 2003.
- [95] B. Maxum. *Field Mathematics for Electromagnetics, Photonics, and Materials Science*, volume TT64, chapter 1, pages 1.1–1.24. SPIE, Bellingham, 2005. ISBN: 0819455237.
- [96] R. J. Van Steenkiste and G. S. Springer. *Strain and Temperature Measurement with Fiber Optic Sensors*, chapter 3, pages 16–21. Technomic Publishing Company, Inc., Lancaster, 1997. ISBN: 1566764807.
- [97] C. B. P. Finn. *Thermal Physics*, chapter 3, pages 34–50. Chapman & Hall, London, 2nd edition, 1993. ISBN: 0412495406.
- [98] C. B. P. Finn. *Thermal Physics*, chapter 6, pages 96–123. Chapman & Hall, London, 2nd edition, 1993. ISBN: 0412495406.
- [99] R. E. Newnham. *Properties of Materials: Anisotropy, Symmetry, Structure*, chapter 6, pages 37–42. Oxford University Press, jan 2005. ISBN: 019852076X.
- [100] W. C. Young and R. G. Budynas. *Roark’s Formulas for Stress and Strain*, chapter 2, pages 9–34. McGraw-Hill Publishing Co., New York, 7th edition, 2001. ISBN-10: 0071210598.
- [101] J. F. Nye. *Physical Properties of Crystals: Their Representations by Tensors and Matrices*, chapter 5, pages 82–92. Oxford University Press, Oxford, 1985. ISBN: 0198511655.
- [102] S. Huard. *Polarization of Light*, chapter 2, pages 36–85. John Wiley & Sons, Ltd., London, feb 1997. ISBN: 0471965367.
- [103] R. E. Newnham. *Properties of Materials: Anisotropy, Symmetry, Structure*, chapter 25, pages 274–285. Oxford University Press, jan 2005. ISBN: 019852076X.
- [104] T. G. Mackay and A. Lakhtakia. *Electromagnetic fields in linear bianisotropic mediums*, volume 51 of *Progress in Optics*, chapter 3. Elsevier, Amsterdam, 2008. ISBN: 9780444532114.
-

- 
- [105] R. P. Feynman, R. B. Leighton, and M. Sands. *The Feynman Lectures on Physics*, volume 2, chapter 31, pages 31.1–31.14. Addison-Wesley, Massachusetts, 1964. ISBN: 020102117x.
- [106] C.-L. Chen. *Foundations for Guided-Wave Optics*, chapter Appendix D, pages 421–436. John Wiley & Sons, Inc., Hoboken, New Jersey, 2007. ISBN-10: 0471756873.
- [107] J. F. Nye. *Physical Properties of Crystals: Their Representations by Tensors and Matrices*, chapter 13, pages 235–259. Oxford University Press, Oxford, 1985. ISBN: 0198511655.
- [108] D. Goldstein. *Polarized Light*, volume 83 of *Optical Engineering*, chapter 26, pages 511–532. Marcel Dekker, Inc., New York, 2 edition, 2003. ISBN: 082474053X.
- [109] R. E. Newnham. *Properties of Materials: Anisotropy, Symmetry, Structure*, chapter 27, pages 294–301. Oxford University Press, jan 2005. ISBN: 019852076X.
- [110] M. Bass, editor. *Handbook of Optics CD-ROM*, volume 2, chapter 33, pages 33.1–33.101. McGraw-Hill, 2nd edition, 2001. ISBN: 007852993x.
- [111] S. Huard. *Polarization of Light*, chapter 4, pages 132–178. John Wiley & Sons, Ltd., London, feb 1997. ISBN: 0471965367.
- [112] E. Le Bourhis. *Glass: Mechanics and Technology*, chapter 6, pages 83–134. Wiley-VCH Verlag GmbH & Co. KGaA, Weinheim, 2008. ISBN: 3527315497.
- [113] S. H. Crandall, N. C. Dahl, and T. J. Lardner. *An Introduction to Mechanics of Solids (with SI Units)*, chapter 5, pages 265–363. The McGraw-Hill Companies, Inc., Boston, 2nd edition, 1999. ISBN: 00072380411.
- [114] W. C. Young and R. G. Budynas. *Roark's Formulas for Stress and Strain*, chapter Appendix B, pages 813–826. McGraw-Hill Publishing Co., New York, 7th edition, 2001. ISBN-10: 0071210598.
- [115] B. Glivsić and D. Inaudi. *Fibre optic methods for structural health monitoring*, chapter 3, pages 41–81. John Wiley & Sons, Ltd., Chichester, 2007. ISBN: 0470061421.
- [116] R. F. Bartholomew and H. M. Garfinkel. *Chemical strengthening of glass*, volume 5 of *Glass Science and Technology*, chapter 6, pages 218–270. Academic Press, Inc., New York, 1980. ISBN: 0127067051.
- [117] J. S. Sirkis. Unified approach to phase-strain-temperature models for smart structure interferometric optical fiber sensors.1. Development. *Opt. Eng.*, 32(4):752–761, 1993.
- [118] F. Farahi, D. J. Webb, J. D. C. Jones, and D. A. Jackson. Simultaneous measurement of temperature and strain: cross-sensitivity considerations. *J. Lightwave Technol.*, 8(2):138–142, February 1990.
-

- 
- [119] C. D. Butter and G. B. Hocker. Fiber optics strain gauge. *Appl. Opt.*, 17(18):2867–2869, 1978.
- [120] C. B. P. Finn. *Thermal Physics*, chapter 1, pages 1–15. Chapman & Hall, London, 2nd edition, 1993. ISBN: 0412495406.
- [121] W. M. Deen. *Analysis of Transport Phenomena*, chapter 1, pages 1–29. Oxford University Press, Inc., New York, 1998. ISBN: 0195084942.
- [122] D. R. Poirier and G. H. Geiger. *Transport Phenomena in Materials Processing*, chapter Part 2, pages 185–186. The Minerals, Metals & Mining Society (TMS), Warrendale, 1994. ISBN: 0873392728.
- [123] C. B. P. Finn. *Thermal Physics*, chapter 2, pages 16–33. Chapman & Hall, London, 2nd edition, 1993. ISBN: 0412495406.
- [124] R. E. Newnham. *Properties of Materials: Anisotropy, Symmetry, Structure*, chapter 11, pages 79–86. Oxford University Press, jan 2005. ISBN: 019852076X.
- [125] G. Ghosh. *Handbook of Thermo-Optic Coefficients of Optical Materials with Applications*, chapter 3, pages 115–261. Academic Press, San Diego, 1998. ISBN: 0122818555.
- [126] R. E. Newnham. *Properties of Materials: Anisotropy, Symmetry, Structure*, chapter 26, pages 286–293. Oxford University Press, jan 2005. ISBN: 019852076X.
- [127] W. J. Tropf, M. E. Thomas, and T. J. Harris. Properties of crystals and glasses. In M. Bass, J. M. Enoch, E. W. Van Stryland, and W. L. Wolfe, editors, *Handbook of Optics: Devices, Measurements & Properties*, Handbook of Optics: Devices, Measurements & Properties, chapter 33, pages 33.1–33.101. McGraw-Hill, New York, 2nd edition.
- [128] J. D. C. Jones. Review of fibre sensor techniques for temperature-strain discrimination. In *Optical Fiber Sensors*, volume 16 of *OSA Technical Digest Series*, page OTuC1. Optical Society of America, 1997.
- [129] J. D. C. Jones and W. N. MacPherson. *Discrimination techniques for optical sensors*, chapter 19, pages 403–420. Handbook of Optical Fibre Sensing Technology. John Wiley & Sons, Ltd., Chichester, 2002. ISBN: 0471820539.
- [130] L. D. Landau, E. M. Lifshitz, and L. P. Pitaevskii. *Electrodynamics of Continuous Media*, volume 8 of *Course of Theoretical Physics*, chapter 11, pages 331–357. Butterworth-Heinemann, Oxford, 2nd edition, 1984. ISBN: 0750626348.
- [131] C. G. Darwin. Notes on magneto-optics. *P. Roy. Soc. Lond. A Mat.*, 151(874):512–539, October 1935.
- [132] R. E. Newnham. *Properties of Materials: Anisotropy, Symmetry, Structure*, chapter 31, pages 342–353. Oxford University Press, jan 2005. ISBN: 019852076X.
-

- 
- [133] P. R. Berman. Optical Faraday rotation. *Am. J. Phys.*, 78(3):270–276, 2010.
- [134] E. Collett. *Polarized Light in Fiber Optics*, chapter 10, pages 227–280. SPIE Press/Polawave Group, New Jersey, nov 2004. ISBN: 0819457612.
- [135] R. Ulrich and A. Simon. Polarization optics of twisted single-mode fibers. *Appl. Opt.*, 18(13):2241–2251, July 1979.
- [136] R. Ulrich. Representation of codirectional coupled waves. *Opt. Lett.*, 1(3):109–111, September 1977.
- [137] S. C. Rashleigh and R. Ulrich. Polarization mode dispersion in single-mode fibers. *Opt. Lett.*, 3(2):60–62, August 1978.
- [138] R. Kashyap. *Fiber Bragg Gratings*, chapter 4, pages 119–193. Academic Press, San Diego, 1999. ISBN: 0124005608.
- [139] A. H. Nayfeh. *Perturbation Methods*, chapter 1, pages 1–22. Wiley-VCH Verlag GmbH & Co. KGaA, Weinheim, 2004. ISBN: 0471399175.
- [140] E. Collett. *Polarized Light in Fiber Optics*, chapter 2, pages 3–26. SPIE Press/Polawave Group, New Jersey, nov 2004. ISBN: 0819457612.
- [141] I. Jacobs. *Optical fiber communication technology and system overview*, volume 5 of *Handbook of Optics*, chapter 9. McGraw-Hill Companies, Inc., New York, 3 edition, 2010. ISBN: 0071633138.
- [142] V. A. Henderek. *Foundations of optical fiber technology*, chapter 2, pages 45–84. Optical Fiber Sensor Technology: Fundamentals. Kluwer Academic Publishers, Dordrecht, 2000. ISBN: 0792378520.
- [143] C.-L. Chen. *Foundations for Guided-Wave Optics*, chapter Appendix E, pages 437–442. John Wiley & Sons, Inc., Hoboken, New Jersey, 2007. ISBN-10: 0471756873.
- [144] H. C. Lefevre. Single-mode fibre fractional wave devices and polarisation controllers. *Electron. Lett.*, 16(20):778–780, September 1980.
- [145] E. Collett. *Polarized Light in Fiber Optics*, chapter 9, pages 183–226. SPIE Press/Polawave Group, New Jersey, nov 2004. ISBN: 0819457612.
- [146] J.-P. Goure and I. Verrier. *Optical Fibre Devices*, chapter 4, pages 129–164. Optics and Optoelectronics. IOP Publishing Ltd., Bristol, 2002. ISBN: 0750308117.
- [147] C. Emslie. *Polarization maintaining fibers*, chapter 8. Specialty Optical Fibers Handbook. Academic Press, Inc., Amsterdam, 2007. ISBN: 012369406X.
- [148] E. Collett. *Polarized Light in Fiber Optics*, chapter 15, pages 433–482. SPIE Press/Polawave Group, New Jersey, nov 2004. ISBN: 0819457612.
- [149] J.-P. Goure and I. Verrier. *Optical Fibre Devices*, chapter 1, pages 1–30. Optics and Optoelectronics. IOP Publishing Ltd., Bristol, 2002. ISBN: 0750308117.
-

- 
- [150] B. Culshaw and J. Dakin. *Basic concepts of optical fiber sensors*, volume 1 of *Optical Fiber Sensors: Systems and Applications*, chapter 1. Artech House, Inc., Boston, 1988. ISBN: 0890063176.
- [151] BIPM JCGM 200:2008. International vocabulary of metrology - Basic and general concepts and associated terms (VIM), 2008.
- [152] Micron Optics, Inc. Micron Optics Sensing System Approved for Use in Explosive Environments.
- [153] Committee 86C - Fibre optic systems and active devices. Fibre optic sensors - Part 1: Generic specification, November 1998.
- [154] A. Rogers. *Distributed optical-fiber sensing*, chapter 14, pages 271–311. Handbook of Optical Fibre Sensing Technology. John Wiley & Sons, Ltd., Chichester, 2002. ISBN: 0471820539.
- [155] K. T. V. Grattan and T. Sun. *Fiber optic sensor technology: Introduction and overview*, chapter 1, pages 1–44. Optical Fiber Sensor Technology: Fundamentals. Kluwer Academic Publishers, Dordrecht, 2000. ISBN: 0792378520.
- [156] J. Dakin. *Distributed optical fiber sensor systems*, volume 2 of *Optical Fiber Sensors: Systems and Applications*, chapter 15. Artech House, Inc., Boston, 1989. ISBN: 0890063761.
- [157] B. Culshaw. Fiber optics in sensing and measurement. *IEEE J. Sel. Top. Quant.*, 6(6):1014–1021, 2000.
- [158] M. Majumder, T. K. Gangopadhyay, A. K. Chakraborty, K. Dasgupta, and D. K. Bhattacharya. Fibre Bragg gratings in structural health monitoring—Present status and applications. *Sensor. Actuat. A-Phys.*, 147(1):150–164, 2008.
- [159] E. Udd. *Overview of fiber optic sensors*, chapter 1. Fiber Optic Sensors. Marcel Dekker, Inc., New York, 2002. ISBN: 082470732x.
- [160] S. Yin. *Distributed fiber optic sensors*, chapter 5. Fiber Optic Sensors. Marcel Dekker, Inc., New York, 2002. ISBN: 082470732x.
- [161] B. Glivsić and D. Inaudi. *Fibre optic methods for structural health monitoring*, chapter 5, pages 133–249. John Wiley & Sons, Ltd., Chichester, 2007. ISBN: 0470061421.
- [162] E. Udd. *Fiber Optic Sensors: An Introduction for Engineers and Scientists*. Wiley Series in Pure and Appl. Opt. John Wiley & Sons, Inc., Hoboken, New Jersey, 2006. ISBN: 0470068108.
- [163] B. T. Meggitt. *Fiber optic white light interferometric sensors*, chapter 6. Optical Fiber Sensor Technology: Fundamentals. Kluwer Academic Publishers, Dordrecht, 2000. ISBN: 0792378520.
- [164] T. Saitoh, K. Nakamura, Y. Takahashi, H. Iida, Y. Iki, and K. Miyagi. Ultra-long-distance fiber Bragg grating sensor system. *IEEE Photonic. Tech. L.*, 19(20):1616–1618, October 2007.
-

- 
- [165] G. L. Mitchell. *Intensity-based and Fabry-Pérot interferometer sensors*, chapter 6, pages 139–156. Wiley Series in Pure and Appl. Opt. John Wiley & Sons, Inc., Hoboken, New Jersey, 2006. ISBN: 0470068108.
- [166] D. A. Jackson and J. D. C. Jones. *Interferometers*, volume 2 of *Optical Fiber Sensors: Systems and Applications*, chapter 10. Artech House, Inc., Boston, 1989. ISBN: 0890063761.
- [167] S. Watson, W. N. MacPherson, J. S. Barton, J. D. C. Jones, A. Tyas, A. V. Pichugin, A. Hindle, W. Parkes, C. Dunare, and T. Stevenson. Investigation of shock waves in explosive blasts using fibre optic pressure sensors. *Meas. Sci. Technol.*, 17(6):1337, 2006.
- [168] H.-J. Bang, H.-K. Kang, C.-S. Hong, and C.-G. Kim. Optical fiber sensor systems for simultaneous monitoring of strain and fractures in composites. *Smart. Mater. Struct.*, 14(5):N52, 2005.
- [169] E. Udd. *Fiber optic sensors based on the Sagnac interferometer and passive ring resonator*, chapter 9, pages 233–270. Wiley Series in Pure and Appl. Opt. John Wiley & Sons, Inc., Hoboken, New Jersey, 2006. ISBN: 0470068108.
- [170] H. C. Lefèvre. *Fiber-optic gyroscopes*, volume 2 of *Optical Fiber Sensors: Systems and Applications*, chapter 11. Artech House, Inc., Boston, 1989. ISBN: 0890063761.
- [171] V. A. Henderik. *Single mode optical fiber sensors*, chapter 3, pages 85–114. *Optical Fiber Sensor Technology: Fundamentals*. Kluwer Academic Publishers, Dordrecht, 2000. ISBN: 0792378520.
- [172] A. Dandridge. *Fiber optic sensors based on the Mach-Zehnder and Michelson interferometers*, chapter 10, pages 271–324. Wiley Series in Pure and Appl. Opt. John Wiley & Sons, Inc., Hoboken, New Jersey, 2006. ISBN: 0470068108.
- [173] A. Rogers. *Polarization in Optical Fibers*, chapter 6, pages 193–223. Artech House, Inc., Boston, 2008. ISBN: 1580535348.
- [174] G. B. Hocker. Fiber-optic sensing of pressure and temperature. *Appl. Opt.*, 18(9):1445–1448, May 1979.
- [175] Y. J. Rao and D. A. Jackson. Recent progress in fibre optic low-coherence interferometry. *Meas. Sci. Technol.*, 7(7):981, 1996.
- [176] E. Udd. *Overview of fiber optic sensors*, chapter 1. *Fiber Optic Sensors*. Marcel Dekker, Inc., New York, 2002. ISBN: 082470732x.
- [177] C. Michie. *Polarimetric optical fiber sensors*, chapter 3. *Fiber Optic Sensors*. Marcel Dekker, Inc., New York, 2002. ISBN: 082470732x.
- [178] A. H. Rose and G. W. Day. *Optical fibre current and voltage sensors for the electric power industry*, chapter 27, pages 569–618. *Handbook of Optical Fibre Sensing Technology*. John Wiley & Sons, Ltd., Chichester, 2002. ISBN: 0471820539.
-

- 
- [179] K. Bohnert, P. Gabus, J. Nehring, and H. Brandle. Temperature and vibration insensitive fiber-optic current sensor. *J. Lightwave Technol.*, 20(2):267, February 2002.
- [180] K. Bohnert, P. Gabus, J. Kostovic, and H. Brändle. Optical fiber sensors for the electric power industry. *Opt. Laser Eng.*, 43(3-5):511–526, 2005. Optics in Switzerland.
- [181] K. Kurosawa, K. Shirakawa, and T. Kikuchi. Development of optical fiber current sensors and their applications. In *Transmission and Distribution Conference and Exhibition: Asia and Pacific*, pages 1–6, 2005. ISBN: 0780391144.
- [182] K. Hotate, B. T. Thai, and T. Saida. Comparison between flint glass fiber and twisted/bent single-mode fiber as a Faraday element in an interferometric fiber optic current sensor. In B. Culshaw and J. D. C. Jones, editors, *European Workshop on Optical Fibre Sensors*, volume 3483, pages 233–237. SPIE, 1998. doi:10.1117/12.309681.
- [183] M. Ben-David and I. Gannot. *Optical fibers for biomedical applications*, chapter 23. Specialty Optical Fibers Handbook. Academic Press, Inc., Amsterdam, 2007. ISBN: 012369406X.
- [184] R. A. McLaughlin, J. P. Williamson, A. Curatolo, V. A. Baker, D. R. Hillman, P. R. Eastwood, and D. D. Sampson. In vivo 4D imaging of the human lower airway using anatomical optical coherence tomography. In Julian D. C. Jones, editor, *20th International Conference on Optical Fibre Sensors*, volume 7503, page 75034X. SPIE, 2009.
- [185] P. Rolfe, F. Scopesi, and G. Serra. Advances in fibre-optic sensing in medicine and biology. *Meas. Sci. Technol.*, 18(6):1683, 2007.
- [186] K. B. Ozanyan, N. Nurgiyatna, E. P. A. Constantino, J. Vaughan, and P. Scully. Photonic Guided-Path Tomography sensor for deformation in a non-planar surface. *J. Phys. Conf. Ser.*, 178(1):012025, 2009.
- [187] K. Gleeson and E. Lewis. Response changes of thin film palladium based optical fibre hydrogen sensors over time. *J. Phys. Conf. Ser.*, 76(1):012004, 2007.
- [188] F. Surre, W. B. Lyons, T. Sun, K. T. V. Grattan, S. O’Keeffe, E. Lewis, C. Elosua, M. Hernaez, and C. Barian. U-bend fibre optic pH sensors using layer-by-layer electrostatic self-assembly technique. *J. Phys. Conf. Ser.*, 178(1):012046, 2009.
- [189] S. O’Keeffe, G. Dooly, C. Fitzpatrick, and E. Lewis. Optical fibre sensor for the measurement of ozone. *J. Phys. Conf. Ser.*, 15(1):213, 2005.
- [190] P. L. Fuhr and D. R. Huston. Corrosion detection in reinforced concrete roadways and bridges via embedded fiber optic sensors. *Smart. Mater. Struct.*, 7(2):217, 1998.
- [191] J. C. Juarez and H. F. Taylor. Field test of a distributed fiber-optic intrusion sensor system for long perimeters. *Appl. Opt.*, 46(11):1968–1971, April 2007.
-

- 
- [192] A. J. Rogers. Polarization-optical time domain reflectometry: a technique for the measurement of field distributions. *Appl. Opt.*, 20(6):1060–1074, March 1981.
- [193] Y. J. Rao. In-fibre Bragg grating sensors. *Meas. Sci. Technol.*, 8(4):355–375, April 1997.
- [194] A. D. Kersey, M. A. Davis, H. J. Patrick, M. LeBlanc, K. P. Koo, C. G. Askins, M. A. Putnam, and E. J. Friebele. Fiber grating sensors. *J. Lightwave Technol.*, 15(8):1442–1463, August 1997.
- [195] K. O. Hill and G. Meltz. Fiber Bragg grating technology fundamentals and overview. *J. Lightwave Technol.*, 15(8):1263–1276, August 1997.
- [196] K. O. Hill. *Fiber Bragg gratings*, volume 5 of *Handbook of Optics*, chapter 17. McGraw-Hill Companies, Inc., New York, 3 edition, 2010. ISBN: 0071633138.
- [197] R. Kashyap and J. M. Lopez-Higuera. *Fibre grating technology: theory, photosensitivity, fabrication and characterization*, chapter 17, pages 349–377. Handbook of Optical Fibre Sensing Technology. John Wiley & Sons, Ltd., Chichester, 2002. ISBN: 0471820539.
- [198] P. St. J. Russell and J. L. Archambault. *Fiber Gratings*, volume 3 of *Optoelectronics Library*, chapter 2. Artech House, Inc., Boston, 1997. ISBN: 0890069328.
- [199] A. Othonos and K. Kalli. *Fiber Bragg Gratings : Fundamentals and Applications in Telecommunications and Sensing*, chapter 1, pages 1–7. Optoelectronics Library. Artech House, Inc., Boston, 1999. ISBN: 0890063443.
- [200] P. Jacquinot and B. Roizen-Dossier. *Apodisation*, volume 3 of *Progress in Optics*, chapter 2. North-Holland Publishing Co., Amsterdam, 1964.
- [201] A. Othonos and K. Kalli. *Fiber Bragg Gratings : Fundamentals and Applications in Telecommunications and Sensing*, chapter 3, pages 95–147. Optoelectronics Library. Artech House, Inc., Boston, 1999. ISBN: 0890063443.
- [202] P. G. van 't Hof, L. K. Cheng, J. H. G. Scholtes, and W. C. Prinse. Dynamic pressure measurement of shock waves in explosives by means of a fiber Bragg grating sensor. In Xun Hou, Wei Zhao, and Baoli Yao, editors, *Proc. SPIE*, volume 6279, page 62791Y. SPIE, 2007.
- [203] F. Ouellette. Fiber Bragg gratings. *SPIE OE magazine*, 1(1):38–41, January 2001.
- [204] Communications Research Centre Canada. Licensing fiber Bragg gratings, July 2010.
- [205] K. O. Hill, Y. Fujii, D. C. Johnson, and B. S. Kawasaki. Photosensitivity in optical fiber waveguides: Application to reflection filter fabrication. *Appl. Phys. Lett.*, 32(10):647 – 649, 1978.
-

- 
- [206] A. Croteau and A. C. Jacob Poulin. *Photosensitive Fibers*, chapter 9. Specialty Optical Fibers Handbook. Academic Press, Inc., Amsterdam, 2007. ISBN: 012369406X.
- [207] R. Kashyap. *Fiber Bragg Gratings*, chapter 2, pages 13–54. Academic Press, San Diego, 1999. ISBN: 0124005608.
- [208] G. Meltz, W. W. Morey, and W. H. Glenn. Formation of Bragg gratings in optical fibers by a transverse holographic method. *Opt. Lett.*, 14(15):823–825, 1989.
- [209] A. Othonos and K. Kalli. *Fiber Bragg Gratings : Fundamentals and Applications in Telecommunications and Sensing*, chapter 4, pages 149–187. Optoelectronics Library. Artech House, Inc., Boston, 1999. ISBN: 0890063443.
- [210] R. Kashyap. *Fiber Bragg Gratings*, chapter 3, pages 55–118. Academic Press, San Diego, 1999. ISBN: 0124005608.
- [211] P. Foote, M. Breidne, K. Levin, P. Papadopolous, I. Read, M. Signorazzi, L. K. Nilsson, R. Stubbe, and A. Claesson. *Operational load monitoring using optical fibre sensors*, chapter 3, pages 75–124. John Wiley & Sons, Ltd., Chichester, 2004. ISBN: 0470843403.
- [212] C. G. Askins, M. A. Putnam, G. M. Williams, and E. J. Friebele. Stepped-wavelength optical-fiber Bragg grating arrays fabricated in line on a draw tower. *Opt. Lett.*, 19(2):147–149, January 1994.
- [213] A. Dragomir, D. N. Nikogosyan, K. A. Zagorul’ko, and P. G. Kryukov. Inscription of long-period fiber gratings by femtosecond UV radiation. *Proc. SPIE, Opto-Ireland 2002: Optics and Photonics Technologies and Applications*, 4876:313–320, March 2003.
- [214] R. E. Newnham. *Properties of Materials: Anisotropy, Symmetry, Structure*, chapter 29, pages 313–324. Oxford University Press, jan 2005. ISBN: 019852076X.
- [215] R. A. Myers, N. Mukherjee, and S. R. J. Brueck. Large second-order nonlinearity in poled fused silica. *Opt. Lett.*, 16(22):1732–1734, November 1991.
- [216] U. Österberg and W. Margulis. Dye laser pumped by Nd:YAG laser pulses frequency doubled in a glass optical fiber. *Opt. Lett.*, 11(8):516–518, August 1986.
- [217] A. V. Lanin, O. V. Butov, and K. M. Golant. Response of in-fiber Bragg gratings to hydrogen loading and subsequent heat treatment in H<sub>2</sub> ambience. *Appl. Opt.*, 45(23):5800–5807, August 2006.
- [218] Y. Masuda, M. Nakamura, C. Komatsu, K. Fujita, M. Yamauchi, M. Kimura, Y. Mizutani, S. Kimura, Y. Suzuki, T. Yokouchi, K. Nakagawa, and S. Ejima. Wavelength evolution of fiber Bragg gratings fabricated from hydrogen-loaded optical fiber during annealing. *J. Lightwave Technol.*, 22(3):934, March 2004.
-

- 
- [219] S. LaRochelle, P.-Y. Cortes, H. Fathallah, L. A. Rusch, and H. B. Jaafar. Writing and applications of fiber Bragg grating arrays. volume 4087, pages 140–149. SPIE, 2000.
- [220] B. A. L. Gwandu, L. Zhang, K. Chisholm, Y. Liu, X. Shu, and I. Bennion. Compact FBG array structure for high spatial resolution distributed strain sensing. *Meas. Sci. Technol.*, 12(7):918–921, 2001.
- [221] A. D. Kersey. *Distributed and multiplexed fiber optic sensors*, chapter 11, pages 325–368. Wiley Series in Pure and Appl. Opt. John Wiley & Sons, Inc., Hoboken, New Jersey, 2006. ISBN: 0470068108.
- [222] Technical Division Process Measurement Technology and Structural Health Monitoring. *Experimental stress analysis - Optical strain sensor based on fibre Bragg grating - Fundamentals, characteristics and sensor testing*, chapter 4, pages 8–16. VDI/VDE-Society Measurement and Automation Committee, Dusseldorf, jul 2010.
- [223] Y. J. Rao. Recent progress in applications of in-fibre Bragg grating sensors. *Opt. Laser Eng.*, 31(4):297–324, 1999.
- [224] R. Gafsi and M. A. El-Sherif. Analysis of induced-birefringence effects on fiber Bragg gratings. *Opt. Fiber Technol.*, 6(3):299–323, 2000.
- [225] K. Schroeder, W. Ecke, R. Mueller, R. Willsch, and A. Andreev. A fibre Bragg grating refractometer. *Meas. Sci. Technol.*, 12(7):757–764, 2001.
- [226] B. Yun, N. Chen, and Y. Cui. Highly sensitive liquid-level sensor based on etched fiber Bragg grating. *IEEE Photonic. Tech. L.*, 19(21):1747–1749, November 2007.
- [227] L. Zhang, W. Zhang, and I. Bennion. *In-fiber grating optic sensors*, chapter 4. Fiber Optic Sensors. Marcel Dekker, Inc., New York, 2002. ISBN: 082470732x.
- [228] G. M. H. Flockhart, R. R. J. Maier, J. S. Barton, W. N. MacPherson, J. D. C. Jones, K. E. Chisholm, L. Zhang, I. Bennion, I. Read, and P. D. Foote. Quadratic behavior of fiber Bragg grating temperature coefficients. *Appl. Opt.*, 43(13):2744–2751, 2004.
- [229] J. Canning, S. Bandyopadhyay, M. Stevenson, P. Biswas, J. Fenton, and M. Aslund. Regenerated gratings. *J. Europ. Opt. Soc. Rap. Public.*, 4, December 2009.
- [230] S. Bandyopadhyay, J. Canning, P. Biswas, M. Stevenson, and K. Dasgupta. A study of regenerated gratings produced in germanosilicate fibers by high temperature annealing. *Opt. Express*, 19(2):1198–1206, January 2011.
- [231] I. C. M. Littler, T. Grujic, and B. J. Eggleton. Photothermal effects in fiber Bragg gratings. *Appl. Opt.*, 45(19):4679–4685, 2006.
- [232] R. R. J. Maier, W. N. MacPherson, J. S. Barton, J. D. C. Jones, S. McCulloch, and G. Burnell. Temperature dependence of the stress response of fibre Bragg gratings. *Meas. Sci. Technol.*, 15(8):1601–1606, 2004.
-

- 
- [233] M. S. Müller, T. C. Buck, H. J. El-Khozondar, and A. W. Koch. Shear strain influence on fiber Bragg grating measurement systems. *J. Lightwave Technol.*, 27(23):5223–5229, December 2009.
- [234] Technical Division Process Measurement Technology and Structural Health Monitoring. *Experimental stress analysis - Optical strain sensor based on fibre Bragg grating - Fundamentals, characteristics and sensor testing*, chapter 5, pages 16–28. VDI/VDE-Society Measurement and Automation Committee, Dusseldorf, jul 2010.
- [235] R. A. Collacott. *Structural Integrity Monitoring*, chapter 8, pages 286–311. Chapman & Hall Ltd., London, 1985. ISBN: 0412219204.
- [236] R. E. Newnham. *Properties of Materials: Anisotropy, Symmetry, Structure*, chapter 10, pages 72–78. Oxford University Press, jan 2005. ISBN: 019852076X.
- [237] P. J. Withers. Residual stress and its role in failure. *Rep. Prog. Phys.*, 70(12):2211, 2007.
- [238] W. B. Spillman Jr. *Fiber optics and smart structures*, volume 4 of *Optoelectronics Library*, chapter 16. Artech House, Inc., Boston, 1997. ISBN: 0890069409.
- [239] R. J. Van Steenkiste and G. S. Springer. *Strain and Temperature Measurement with Fiber Optic Sensors*. Technomic Publishing Company, Inc., Lancaster, 1997. ISBN: 1566764807.
- [240] M. Born and E. Wolf. *Principles of Optics: Electromagnetic Theory of Propagation, Interference and Diffraction of Light*, chapter 14, pages 735–789. Cambridge University Press, Cambridge, 7th edition, 1999. ISBN: 0521642221.
- [241] B. J. Berne and R. Pecora. *Dynamic Light Scattering: With Applications to Chemistry, Biology, and Physics*, chapter Appendix 10.C, pages 263–272. Dover Publications, Inc., New York, 2000. ISBN: 0486411559.
- [242] C. F. Bohren and D. R. Huffman. *Absorption and Scattering of Light by Small Particles*, chapter 1, pages 3–11. Wiley-VCH Verlag GmbH & Co. KGaA, Weinheim, 1st edition, 2004.
- [243] A. Othonos and K. Kalli. *Fiber Bragg Gratings : Fundamentals and Applications in Telecommunications and Sensing*, chapter 2, pages 9–94. Optoelectronics Library. Artech House, Inc., Boston, 1999. ISBN: 0890063443.
- [244] A. M. Vengsarkar, Q. Zhong, D. Inniss, W. A. Reed, P. J. Lemaire, and S. G. Kosinski. Birefringence reduction in side-written photoinduced fiber devices by a dual-exposure method. *Opt. Lett.*, 19(16):1260–1262, 1994.
- [245] H. Renner. Effective-index increase, form birefringence and transition losses in UV-side-illuminated photosensitive fibers. *Opt. Express*, 9(11):546–560, 2001.
-

- 
- [246] T. Erdogan and V. Mizrahi. Characterization of UV-induced birefringence in photosensitive Ge-doped silica optical fibers. *J. Opt. Soc. Am. B*, 11(10):2100–2105, 1994.
- [247] S. Pereira, J. E. Sipe, R. E. Slusher, and S Spälter. Enhanced and suppressed birefringence in fiber Bragg gratings. *J. Opt. Soc. Am. B*, 19(7):1509–1515, 2002.
- [248] R. B. Wagreich and J. S. Sirkis. Distinguishing fiber Bragg grating strain effects. In *Optical Fiber Sensors*, page OTuB2. Optical Society of America, 1997.
- [249] R. M. Measures, S. Melle, and K. Liu. Wavelength demodulated Bragg grating fiber optic sensing systems for addressing smart structure critical issues. *Smart. Mater. Struct.*, 1:36–44, March 1992.
- [250] S. T. Vohra. *Optical fibre gratings applications*, chapter 23, pages 475–504. Handbook of Optical Fibre Sensing Technology. John Wiley & Sons, Ltd., Chichester, 2002. ISBN: 0471820539.
- [251] B. Glivsić and D. Inaudi. *Fibre optic methods for structural health monitoring*, chapter 2, pages 19–40. John Wiley & Sons, Ltd., Chichester, 2007. ISBN: 0470061421.
- [252] S. Kannan and P. Lemaire. *Optical reliability of fibre gratings*, chapter 20, pages 421–431. Handbook of Optical Fibre Sensing Technology. John Wiley & Sons, Ltd., Chichester, 2002. ISBN: 0471820539.
- [253] S. E. Watkins, A. Nanni, and J. W. Fonda. Assessment of an instrumented reinforced-concrete bridge with fiber-reinforced-polymer strengthening. *Opt. Eng.*, 46(5):051010–051010–10, 2007.
- [254] S. Fischer, B. Verwilghen, M. Voet, M. Jobmann, F. Gloetzel, M. Bugaud, and P. Ferdinand. Fibre Bragg grating sensors and sensing systems for civil engineering and mine applications. In Byoung Yoon Kim and K. Hotate, editors, *13<sup>th</sup> International Conference on Optical Fiber Sensors*, volume 3746, pages 16–20, Bellingham, September 1999. SPIE.
- [255] H.-N. Li, D.-S. Li, and G.-B. Song. Recent applications of fiber optic sensors to health monitoring in civil engineering. *Eng. Struct.*, 26(11):1647–1657, 2004.
- [256] D. Inaudi. *Photonic sensing technology in civil engineering applications*, chapter 25, pages 517–542. Handbook of Optical Fibre Sensing Technology. John Wiley & Sons, Ltd., Chichester, 2002. ISBN: 0471820539.
- [257] A. Quintela, C. Jauregui, J. Echevarria, and J. M. Lopez-Higuera. Embedded temperature-strain fibre Bragg grating sensor system validation for concrete structures. *J. Opt. A-Pure Appl. Op.*, 4(6):S387–S390, 2002.
- [258] Y. B. Lin, C. L. Pan, Y. H. Kuo, K. C. Chang, and J. C. Chern. Online monitoring of highway bridge construction using fiber Bragg grating sensors. *Smart. Mater. Struct.*, 14(5):1075, 2005.
-

- 
- [259] Y. M. Gebremichael, W. Li, W. J. O. Boyle, B. T. Meggitt, K. T. V. Grattan, B. McKinley, G. F. Fernando, G. Kister, D. Winter, L. Canning, and S. Luke. Integration and assessment of fibre Bragg grating sensors in an all-fibre reinforced polymer composite road bridge. *Sensor. Actuat. A-Phys.*, 118(1):78–85, 2005.
- [260] T. H. T. Chan, L. Yu, H. Y. Tam, Y. Q. Ni, S. Y. Liu, W. H. Chung, and L. K. Cheng. Fiber Bragg grating sensors for structural health monitoring of Tsing Ma bridge: Background and experimental observation. *Eng. Struct.*, 28(5):648–659, 2006.
- [261] A. Cheng, D. Wu, V. ChangChien, P. Tsai, and I-Wen Wu. An industrial perspective on the applications of optical sensing technology in selected Fields.
- [262] Y.-B. Lin, J.-C. Chen, K.-C. Chang, J.-C. Chern, and J.-S. Lai. Real-time monitoring of local scour by using fiber Bragg grating sensors. *Smart. Mater. Struct.*, 14(4):664, 2005.
- [263] A. Kerrouche, J. Leighton, W. J. O. Boyle, Y. M. Gebremichael, T. Sun, K. T. V. Grattan, and B. Täljisten. Strain measurement on a rail bridge loaded to failure using a fiber Bragg grating-based distributed sensor system. *IEEE Sens. J.*, 8(12):2059–2065, December 2008.
- [264] P. Ferdinand, S. Magne, V. Dewynter-Marty, C. Martinez, S. Rougeault, and M. Bugaud. Applications of Bragg grating sensors in Europe. *Proceedings of the Optical fiber sensor conference (OFS12)*, pages 14–19, 1997.
- [265] P. Miao, S. N. Kukureka, N. Metje, D. N. Chapman, C. D. F. Rogers, and P. Henderson. Mechanical reliability of optical fibre sensors and SmartRods for tunnel displacement monitoring. *Smart. Mater. Struct.*, 16(2):382, 2007.
- [266] W. N. MacPherson, M. Silva-Lopez, J. S. Barton, A. J. Moore, J. D. C. Jones, D. Zhao, L. Zhang, I. Bennion, N. Metje, D. N. Chapman, and C. D. F. Rogers. Tunnel monitoring using multicore fibre displacement sensor. *Meas. Sci. Technol.*, 17(5):1180, 2006.
- [267] R. Duncan. Sensing shape: Fiber-Bragg-grating sensor arrays monitor shape at a high resolution. *SPIE OE magazine*, pages 18–21, September 2005.
- [268] A. E. Jensen, G. B. Havsgard, K. Pran, G. Wang, S. T. Vohra, M. A. Davis, and A. Dandridge. Wet deck slamming experiments with a FRP sandwich panel using a network of 16 fibre optic Bragg grating strain sensors. *Compos. Part B-Eng.*, 31(3):187–198, 2000.
- [269] B. Lee. Review of the present status of optical fiber sensors. *Opt. Fiber Technol.*, 9(2):57–79, 2003.
- [270] H. C. H. Li, I. Herszberg, C. E. Davis, A. P. Mouritz, and S. C. Galea. Health monitoring of marine composite structural joints using fibre optic sensors. *Compos. Struct.*, 75(1-4):321–327, 2006. Thirteenth International Conference on Compos. Struct. - ICCS/13.
-

- 
- [271] G. Wang, G. B. Havsgård, E. Urnes, K. Pran, S. Knudsen, A. D. Kersey, M. A. Davis, T. A. Berkoff, A. Dandridge, R. T. Jones, T. Tsai, and G. Cogdell. Digital demodulation and signal processing applied to fiber Bragg grating strain sensor arrays in monitoring transient loading effects on ship hulls. *OFA5-1*, pages 612–614, 1997.
- [272] G. Wang, K. Pran, G. Sagvolden, G. B. Havsgard, A. E. Jensen, G. A. Johnson, and S. T. Vohra. Ship hull structure monitoring using fibre optic sensors. *Smart. Mater. Struct.*, 10(3):472–478, 2001.
- [273] I. Herszberg, H. C. H. Li, F. Dharmawan, A. P. Mouritz, M. Nguyen, and J. Bayandor. Damage assessment and monitoring of composite ship joints. *Compos. Struct.*, 67(2):205–216, 2005. US Air Force Workshop Damage Assessment of Compos. Struct.
- [274] K. Pran, G. B. Havsgard, G. Sagvolden, O. Farsund, and G. Wang. Wavelength multiplexed fibre Bragg grating system for high-strain health monitoring applications. *Meas. Sci. Technol.*, 13(4):471–476, 2002.
- [275] A. Ezbiri, S. E. Kanellopoulos, and V. A. Handerek. High resolution instrumentation system for fibre-Bragg grating aerospace sensors. *Opt. Commun.*, 150(1-6):43–48, 1998.
- [276] S. Takeda, Y. Aoki, T. Ishikawa, N. Takeda, and H. Kikukawa. Structural health monitoring of composite wing structure during durability test. *Compos. Struct.*, 79(1):133–139, 2007.
- [277] W. Baker, I. McKenzie, and R. Jones. Development of life extension strategies for Australian military aircraft, using structural health monitoring of composite repairs and joints. *Compos. Struct.*, 66(1-4):133–143, 2004. Twelfth International Conference on Compos. Struct.
- [278] J. M. Menendez. Market opportunities on fiber optic sensors for aeronautics and aerospace applications. In A. Cutolo, B. Culshaw, and J. M. López-Higuera, editors, *Proc. SPIE*, volume 6619, page 661908. SPIE, 2007.
- [279] E. J. Friebele, C. G. Askins, A. B. Bosse, A. D. Kersey, H. J. Patrick, W. R. Pogue, M. A. Putnam, W. R. Simon, F. A. Tasker, W. S. Vincent, and S. T. Vohra. Optical fiber sensors for spacecraft applications. *Smart. Mater. Struct.*, 8(6):813–838, 1999.
- [280] W. Ecke, I. Latka, R. Willsch, A. Reutlinger, and R. Graue. Fibre optic sensor network for spacecraft health monitoring. *Meas. Sci. Technol.*, 12(7):974–980, 2001.
- [281] S. Rapp and H. Baier. Integrated fiber optic sensors for hot spot detection and temperature field reconstruction in satellites. *Smart. Mater. Struct.*, 19(7):075007, 2010.
- [282] X. Chang, X. He, J. Hu, and J. Li. Experimental research on embedded fiber Bragg grating sensors network for solid rocket motors health monitor. *International workshop on intelligent networks and intelligent systems*, 0:170–173, 2008. ISBN: 978-0-7695-3391-9.
-

- 
- [283] L. Ren, H.-N. Li, J. Zhou, D.-S. Li, and L. Sun. Health monitoring system for offshore platform with fiber Bragg grating sensors. *Opt. Eng.*, 45(8):084401, 2006.
- [284] C. Staveley. Applications of optical fibre sensors to structural health monitoring, optimisation and life-cycle cost control for oil and gas infrastructures. Technical report, Touch Oil and Gas, 2004.
- [285] L. Sun, H.-N. Li, L. Ren, and Q. Jin. Dynamic response measurement of offshore platform model by FBG sensors. *Sensor. Actuat. A-Phys.*, 136(2):572–579, 2007. Micromechanics Section of Sensors and Actuators, Based on Contributions revised from the Technical Digest of the 2006 Solid-State Sensor, Actuator and Microsystems Workshop.
- [286] R. J. Schroeder, R. T. Ramos, T. Yamate, and E. Udd. *Fibre optic sensors for oilfield services*, chapter 31, pages 671–686. Handbook of Optical Fibre Sensing Technology. John Wiley & Sons, Ltd., Chichester, 2002. ISBN: 0471820539.
- [287] A. D. Kersey. Optical fiber sensors for permanent downwell monitoring applications in the oil and gas industry. *IEICE T. Electron.*, E83-C(3):400–404, 2000.
- [288] O. V. Butov, K. M. Golant, V. I. Grifer, Y. V. Gusev, A. V. Kholodkov, A. V. Lanin, R. A. Maksutov, and G. I. Orlov. Versatile in-fiber Bragg grating pressure sensor for oil and gas industry. In *Optical Fiber Sensors*, page TuB6. Optical Society of America, 2006.
- [289] R. J. Schroeder, T. Yamate, and E. Udd. High pressure and temperature sensing for the oil industry using fiber Bragg gratings written onto side hole single mode fiber. In B. Y. Kim & K. Hotate, editor, *SPIE Conference Series*, volume 3746 of *SPIE Conference Series*, pages 42–+, 1999.
- [290] Y. Zhang, S. Li, Z. Yin, B. Chen, H.-L. Cui, and J. Ning. Fiber-Bragg-grating-based seismic geophone for oil/gas prospecting. *Opt. Eng.*, 45(8):084404, 2006.
- [291] Ph. M. Nellen, P. Mauron, A. Frank, U. Sennhauser, K. Bohnert, P. Pequignot, P. Bodor, and H. Brändle. Reliability of fiber Bragg grating based sensors for downhole applications. *Sensor. Actuat. A-Phys.*, 103(3):364–376, March 2003.
- [292] J. Lim, Q. P. Yang, B. E. Jones, and P. R. Jackson. DP flow sensor using optical fibre Bragg grating. *Sensor. Actuat. A-Phys.*, 92(1-3):102–108, 2001.
- [293] H. Iwaki, K. Shiba, and N. Takeda. Structural health monitoring system using FBG-based sensors for a damage-tolerant building. In S.-C. Liu, editor, *SPIE Conference Series*, volume 5057 of *SPIE Conference Series*, pages 392–399, August 2003.
- [294] H. F. Lima, R. da Silva Vicente, R. N. Nogueira, I. Abe, P. S. de Brito Andre, C. Fernandes, H. Rodrigues, H. Varum, H. J. Kalinowski, A. Costa, and J. de Lemos Pinto. Structural health monitoring of the Church of Santa Casa da Misericórdia of Aveiro using FBG sensors. *IEEE Sens. J.*, 8(7):1236–1242, July 2008.
-

- 
- [295] H. Gnewuch, E. Smeu, D. A. Jackson, and A. G. Podoleanu. Long range extensometer for civil structure monitoring using fibre Bragg gratings. *Meas. Sci. Technol.*, 16(10):2005, 2005.
- [296] R. Falciai, C. Trono, G. Lanterna, and C. Castelli. Continuous monitoring of wooden works of art using fiber Bragg grating sensors. *J. Cult. Herit.*, 4(4):285–290, 2003.
- [297] W. Zhang, J. Dai, B. Sun, and Y. Du. FBG sensor network in Qinghai-Tibet railway. In Jianli Wang, Gee-Kung Chang, Yoshio Itaya, and Herwig Zech, editors, *Proc. SPIE*, volume 6784, page 678439. SPIE, 2007.
- [298] A. Laudati, F. Mennella, M. Giordano, G. D’Altrui, C. C. Tassini, and A. Cusano. A fiber-optic Bragg grating seismic sensor. *IEEE Photonic. Tech. L.*, 19(24):1991–1993, December 2007.
- [299] P. Ferraro and G. De Natale. On the possible use of optical fiber Bragg gratings as strain sensors for geodynamical monitoring. *Opt. Laser Eng.*, 37(2-3):115–130, 2002.
- [300] G. Gagliardi, M. Salza, P. Ferraro, P. De Natale, A. Di Maio, S. Carlino, G. De Natale, and E. Boschi. Design and test of a laser-based optical-fiber Bragg-grating accelerometer for seismic applications. *Meas. Sci. Technol.*, 19(8):085306, 2008.
- [301] EE Times. The day the lights went out in Japan, March 2011.
- [302] Y.-T. Ho, A.-B. Huang, and J.-T. Lee. Development of a fibre Bragg grating sensed ground movement monitoring system. *Meas. Sci. Technol.*, 17(7):1733, 2006.
- [303] S. Kato and H. Kohashi. Research on the monitoring system of road slope failures with optical fiber sensors. In *Proceedings of 16<sup>th</sup> International Conference on Optical Fibre Sensors, Nara, Japan*, pages 488–491. IEICE, 2003.
- [304] T. Bosselmann. Market potential for optical fiber sensors in the energy sector. In A. Cutolo, B. Culshaw, and J. M. López-Higuera, editors, *Third European Workshop on Optical Fibre Sensors*, volume 6619, page 661903. SPIE, 2007.
- [305] X. Tian and Y. Cheng. The Investigation of FBG sensor system for the transmission line icing measurement. In *Proceedings of International Conference on High Voltage Engineering and Application, ICHVE*, pages 154–157. IEEE, November 2008. ISBN: 9781424438235.
- [306] A. B. Lobo Ribeiro, N. Eira, J. M. Sousa, P. T. Guerreiro, and J. A. R. Salcedo. Multi-point fibre optic hot-spot network integrated into a high power transformer. In A. Cutolo, B. Culshaw, and J. M. López-Higuera, editors, *Third European Workshop on Optical Fibre Sensors*, volume 6619, page 66193V. SPIE, 2007.
- [307] N. E. Fisher, P. J. Henderson, and D. A. Jackson. The interrogation of a conventional current transformer using an in-fibre Bragg grating. *Meas. Sci. Technol.*, 8(10):1080, 1997.
-

- 
- [308] T. E. Hammon and A. D. Stokes. Optical fibre Bragg grating temperature sensor measurements in an electrical power transformer using a temperature compensated optical fibre Bragg grating as a reference. In *Optical Fiber Sensors*, page Th337. Optical Society of America, 1996.
- [309] M. Benedetti, V. Fontanari, and D. Zonta. Structural health monitoring of wind towers: remote damage detection using strain sensors. *Smart. Mater. Struct.*, 20(5):055009, 2011.
- [310] X. Huang, Y. Liu, D. Luo, G. Wang, N. Ding, J. Xu, and X. Huang. Wavelet analysis on vibration modal frequency measurement at a low level of strain of the turbine blade using FBG sensors. *Meas. Sci. Technol.*, 21(1):015305, 2010.
- [311] J. M. Lee and Y. Hwang. A novel online rotor condition monitoring system using fiber Bragg grating (FBG) sensors and a rotary optical coupler. *Meas. Sci. Technol.*, 19(6):065303, 2008.
- [312] T. Guo, Q. Zhao, H. Zhang, C. Zhang, G. Huang, L. Xue, and X. Dong. Temperature-insensitive fiber Bragg grating dynamic pressure sensing system. *Opt. Lett.*, 31(15):2269–2271, August 2006.
- [313] P. Ferdinand and S. Magne. *Applications of optical fibre sensors for the nuclear power industry*, chapter 26, pages 543–568. Handbook of Optical Fibre Sensing Technology. John Wiley & Sons, Ltd., Chichester, 2002. ISBN: 0471820539.
- [314] A. F. Fernandez, A. Gusarov, B. Brichard, M. Décréton, F. Berghmans, P. Mégret, and A. Delchambre. Long-term radiation effects on fibre Bragg grating temperature sensors in a low flux nuclear reactor. *Meas. Sci. Technol.*, 15(8):1506–1511, August 2004.
- [315] A. F. Fernandez, A. I. Gusarov, B. Brichard, S. Bodart, K. Lammens, F. Berghmans, M. Décréton, P. Mégret, M. Blondel, and A. Delchambre. Temperature monitoring of nuclear reactor cores with multiplexed fiber Bragg grating sensors. *Opt. Eng.*, 41(6):1246–1254, June 2002.
- [316] A. F. Fernandez, F. Berghmans, B. Brichard, P. Borgermans, A. I. Gusarov, M. Van Uffelen, P. Megret, M. Decreton, M. Blondel, and A. Delchambre. Radiation-resistant WDM optical link for thermonuclear fusion reactor instrumentation. *IEEE T. Nucl. Sci.*, 48(5):1708–1712, October 2001.
- [317] K. Krebber, H. Henschel, and U. Weinand. Fibre Bragg gratings as high dose radiation sensors? *Meas. Sci. Technol.*, 17(5):1095, 2006.
- [318] A. I. Gusarov, F. Berghmans, O. Deparis, A. F. Fernandez, Y. Defosse, P. Megret, M. Decreton, and M. Blondel. High total dose radiation effects on temperature sensing fiber Bragg gratings. *IEEE Photonic. Tech. L.*, 11(9):1159–1161, September 1999.
- [319] M. Aleixandre, P. Corredera, M. L. Hernanz, and J. Gutierrez-Monreal. Development of fiber optic hydrogen sensors for testing nuclear waste repositories. *Sensor. Actuat. B-Chem.*, 107(1):113–120, 2005. Proceedings of the 7th European Conference on Optical Chemical Sensors and Biosensors - EUROPT(R)ODE VII.
-

- 
- [320] Y. B. Lin, T. K. Lin, C.-C. Chen, J. C. Chiu, and K. C. Chang. Online health monitoring and safety evaluation of the relocation of a research reactor using fiber Bragg grating sensors. *Smart. Mater. Struct.*, 15(5):1421, 2006.
- [321] D. A. Flavin, R. McBride, and J. D. C. Jones. Short optical path scan interferometric interrogation of a fibre Bragg grating embedded in a composite. *Electron. Lett.*, 33(4):319–321, 1997.
- [322] Y. Fan and M. Kahrizi. Characterization of a FBG strain gage array embedded in composite structure. *Sensor. Actuat. A-Phys.*, 121(2):297–305, 2005.
- [323] V. M. Murukeshan, P. Y. Chan, L. S. Ong, and L. K. Seah. Cure monitoring of smart composites using fiber Bragg grating based embedded sensors. *Sensor. Actuat. A-Phys.*, 79(2):153–161, 2000.
- [324] F. Colpo, L. Humbert, P. Giaccari, and J. Botsis. Characterization of residual strains in an epoxy block using an embedded FBG sensor and the OLCR technique. *Compos. Part A-Appl. S.*, 37(4):652–661, 2006. Internal Stresses in Polymer Composites.
- [325] Y. J. Rao, D. A. Jackson, L. Zhang, and I. Bennion. Dynamic range enhancement of in-fibre Bragg grating sensors with two cascaded scanning interferometers. *OThC27-1*, pages 512–515, 1997.
- [326] W. Ecke, J. Schauer, K. Usbeck, R. Willsch, and J. P. Dakin. Improvement of the stability of fiber grating interrogation systems and using active and passive polarization scrambling devices. *Proceedings of the Optical fiber sensor conference (OFS12)*, pages 484–487, 1997.
- [327] J. Botsis, L. Humbert, F. Colpo, and P. Giaccari. Embedded fiber Bragg grating sensor for internal strain measurements in polymeric materials. *Opt. Laser Eng.*, 43(3-5):491–510, 2005. Optics in Switzerland.
- [328] S. Kojima, S. Komatsuzaki, Y. Kurosawa, and A. Hongo. Embedding type strain sensors using small-diameter fiber Bragg grating to composite laminate structures. *Hitachi Cable Review*, 23(1):11–15, August 2004. [www.hitachicable.co.jp/en/review/23/pdf/h-03.pdf](http://www.hitachicable.co.jp/en/review/23/pdf/h-03.pdf).
- [329] P. Childs, A. C. L. Wong, W. Terry, and G. D. Peng. Measurement of crack formation in concrete using embedded optical fibre sensors and differential strain analysis. *Meas. Sci. Technol.*, 19(6):065301, 2008.
- [330] H.N. Li, D.S. Li, and G.B. Song. Recent applications of fiber optic sensors to health monitoring in civil engineering. *Eng. Struct.*, 26(11):1647 – 1657, September 2004.
- [331] B. Culshaw, C. Michie, P. Gardiner, and A. McGown. Smart structures and applications in civil engineering. *P. IEEE*, 84(1):78–86, 1996.
- [332] S. C. Tjin, Y. Wang, X. Sun, P. Moyo, and J. M. W. Brownjohn. Application of quasi-distributed fibre bragg grating sensors in reinforced concrete structures. *Meas. Sci. Technol.*, 13(4):583–589, 2002.
-

- 
- [333] Y. B. Lin, K. C. Chang, J. C. Chern, and L. A. Wang. The health monitoring of a prestressed concrete beam by using fiber Bragg grating sensors. *Smart. Mater. Struct.*, 13(4):712, 2004.
- [334] T. L. Yeo, T. Sun, and K. T. V. Grattan. Fibre-optic sensor technologies for humidity and moisture measurement. *Sensor. Actuat. A-Phys.*, 144(2):280–295, 2008.
- [335] P. Kronenberg, P. K. Rastogi, P. Giaccari, and H. G. Limberger. Relative humidity sensor with optical fiber Bragg gratings. *Opt. Lett.*, 27(16):1385–1387, 2002.
- [336] A. Cusano, A. Iadicicco, S. Campopiano, M. Giordano, and A. Cutolo. Thinned and micro-structured fibre Bragg gratings: towards new all-fibre high-sensitivity chemical sensors. *J. Opt. A-Pure Appl. Op.*, 7(12):734, 2005.
- [337] P. Lu, L. Men, and Q. Chen. Polymer-coated fiber Bragg grating sensors for simultaneous monitoring of soluble analytes and temperature. *IEEE Sens. J.*, 9(4):340–345, April 2009.
- [338] A. Trouillet, E. Marin, and C. Veillas. Fibre gratings for hydrogen sensing. *Meas. Sci. Technol.*, 17(5):1124, 2006.
- [339] R. R. J. Maier, B. J. S. Jones, J. S. Barton, S. McCulloch, T. Allsop, J. D. C. Jones, and I. Bennion. Fibre optics in palladium-based hydrogen sensing. *J. Opt. A-Pure Appl. Op.*, 9(6):S45, 2007.
- [340] R. R. J. Maier, J. S. Barton, J. D. C. Jones, S. McCulloch, B. J. S. Jones, and G. Burnell. Palladium-based hydrogen sensing for monitoring of ageing materials. *Meas. Sci. Technol.*, 17(5):1118, 2006.
- [341] C. Caucheteur, M. Debliquy, D. Lahem, and P. Megret. Catalytic fiber Bragg grating sensor for hydrogen leak detection in air. *IEEE Photonic. Tech. L.*, 20(2):96–98, January 2008.
- [342] W. Z. Zhao, T. Suna, K. T. V. Grattana, Y. H. Shen, C. L. Wei, and A. I. Al-Shammaa. Temperature monitoring of vehicle engine exhaust gases under vibration condition using optical fibre temperature sensor systems. *J. Phys. Conf. Ser.*, 45(1):215, 2006.
- [343] D. Song, J. Zou, Z. Wei, Z. Chen, and H. Cui. Liquid-level sensor using a fiber Bragg grating and carbon fiber composite diaphragm. *Opt. Eng.*, 50(1):014401, 2011.
- [344] S. Takashima, H. Asanuma, and H. Niitsuma. A water flowmeter using dual fiber Bragg grating sensors and cross-correlation technique. *Sensor. Actuat. A-Phys.*, 116(1):66–74, 2004.
- [345] M. O’Farrell, C. Sheridan, E. Lewis, W. Z. Zhao, T. Sun, K. T. V. Grattan, J. Kerry, and N. Jackman. Detection of premature browning in ground beef with an integrated optical-fibre based sensor using reflection spectroscopy and fibre Bragg grating technology. *J. Phys. Conf. Ser.*, 76(1):012026, 2007.
-

- 
- [346] C. Elosua, I. R. Matias, C. Barriain, and F. J. Arregui. Volatile organic compound optical fiber sensors: A review. *Sensors*, 6(11):1440–1465, 2006.
- [347] V. Mishra, N. Singh, U. Tiwari, and P. Kapur. Fiber grating sensors in medicine: Current and emerging applications. *Sensor. Actuat. A-Phys.*, 167(2):279–290, 2011. Solid-State Sensors, Actuators and Microsystems Workshop.
- [348] C. R. Dennison, P. M. Wild, D. R. Wilson, and P. A. Cripton. A minimally invasive in-fiber Bragg grating sensor for intervertebral disc pressure measurements. *Meas. Sci. Technol.*, 19(8):085201, 2008.
- [349] Z. Wu, X. P. Qing, K. Ghosh, V. Karbhar, and F.-K. Chang. Health monitoring of bonded composite repair in bridge rehabilitation. *Smart. Mater. Struct.*, 17(4):045014, 2008.
- [350] P. D. C. Hobbs. *Building Electro-Optical Systems*, chapter 1, pages 1–51. John Wiley & Sons, Inc., Hoboken, New Jersey, 2nd edition, 2009. ISBN: 9780470402290.
- [351] A. D. Kersey. *Multiplexing techniques for fiber-optic sensor*, volume 4 of *Optoelectronics Library*, chapter 15. Artech House, Inc., Boston, 1997. ISBN: 0890069409.
- [352] P. Jacquinot. Interferometry and grating spectroscopy: an introductory survey. *Appl. Opt.*, 8(3):497–499, March 1969.
- [353] S. Tolansky. *Multiple-Beam Interferometry of Surfaces & Films*, chapter 2, pages 8–24. Dover Publications, Inc., New York, 1970. ISBN: 0486622150.
- [354] G. Hernandez. *Fabry-Perot Interferometers*, chapter 2, pages 9–54. Cambridge Studies in Modern Optics, 3. Cambridge University Press, Cambridge, 1986. ISBN: 052136812X.
- [355] M. Born and E. Wolf. *Principles of Optics: Electromagnetic Theory of Propagation, Interference and Diffraction of Light*, chapter 7, pages 286–411. Cambridge University Press, Cambridge, 7th edition, 1999. ISBN: 0521642221.
- [356] G. Hernandez. *Fabry-Perot Interferometers*, chapter 4, pages 91–117. Cambridge Studies in Modern Optics, 3. Cambridge University Press, Cambridge, 1986. ISBN: 052136812X.
- [357] R. J. Van Steenkiste and G. S. Springer. *Strain and Temperature Measurement with Fiber Optic Sensors*, chapter 19, pages 134–139. Technomic Publishing Company, Inc., Lancaster, 1997. ISBN: 1566764807.
- [358] Y. J. Rao, M. R. Cooper, D. A. Jackson, C. N. Pannell, and L. Reekie. Absolute strain measurement using an in-fibre-Bragg-grating-based Fabry-Perot sensor. *Electron. Lett.*, 36(8):708–709, 2000.
- [359] M. N. Inci, S. R. Kidd, J. S. Barton, and J. D. C. Jones. High-temperature miniature fiber optic interferometric thermal sensors. *Meas. Sci. Technol.*, 4(3):382–387, 1993.
-

- 
- [360] P. Kurzynowski, W. A. Woźniak, and M. Szarycz. Geometric phase: two triangles on the Poincaré sphere. *J. Opt. Soc. Am. A*, 28(3):475–482, March 2011.
- [361] D. A. Flavin, R. McBride, and J. D. C. Jones. Short-scan interferometric interrogation and multiplexing of fibre Bragg grating sensors. *Opt. Commun.*, 170(4-6):347 – 353, November 1999.
- [362] S. Dyer, K. Rochford, and A. Rose. Fast and accurate low-coherence interferometric measurements of fiber Bragg grating dispersion and reflectance. *Opt. Express*, 5(11):262–266, November 1999.
- [363] S. G. Lipson, H. Lipson, and D. S. Tannhauser. *Optical Physics*, chapter 9, pages 220–262. Cambridge University Press, Cambridge, 3rd edition, 1995. ISBN: 0521436311.
- [364] P. R. Griffiths and J. A. de Haseth. *Fourier Transform Infrared Spectrometry*, chapter 2, pages 19–55. Chemical Analysis. John Wiley & Sons, Inc., New York, 2nd edition, 2007. ISBN: 9780471194040.
- [365] S. Davis, M. C. Abrams, and J. W. Brault. *Fourier Transform Spectrometry*, chapter 8, pages 119–141. Academic Press, San Diego, 2001. ISBN: 9780120425105.
- [366] S. Davis, M. C. Abrams, and J. W. Brault. *Fourier Transform Spectrometry*, chapter 11, pages 179–212. Academic Press, San Diego, 2001. ISBN: 9780120425105.
- [367] P. R. Griffiths and J. A. de Haseth. *Fourier Transform Infrared Spectrometry*, chapter 5, pages 97–142. Chemical Analysis. John Wiley & Sons, Inc., New York, 2nd edition, 2007. ISBN: 9780471194040.
- [368] S. D. Dyer, P. A. Williams, R. J. Espejo, J. D. Kofler, and S. M. Etzel. Fundamental limits in fiber Bragg grating peak wavelength measurements. In *Proceedings of the 17th International Conference on Optical Fibre Sensors*, volume 5855, pages 88–93. SPIE, May 2005.
- [369] J. Connes and Naval ordnance test station, China Lake, CA. Spectroscopic studies using Fourier transformations (Recherches sur la spectroscopie par transformation de Fourier). page 180, January 1963. Translation of Revue d’Optique (France) v40 p45-78, 116-140, 171-190, 231-265, 1961, by Czerna A. Flanagan.
- [370] R. W. Hamming. *Digital Filters*, chapter 3, pages 36–70. Dover Publications, Inc., New York, 3rd edition, 1998. ISBN: 048665088X.
- [371] P. R. Griffiths and J. A. de Haseth. *Fourier Transform Infrared Spectrometry*, chapter 3, pages 57–74. Chemical Analysis. John Wiley & Sons, Inc., New York, 2nd edition, 2007. ISBN: 9780471194040.
- [372] S. Huard. *Polarization of Light*, chapter 5, pages 179–242. John Wiley & Sons, Ltd., London, feb 1997. ISBN: 0471965367.
-

- [373] A. D. Kersey, A. Dandridge, and A. B. Tveten. Dependence of visibility on input polarization in interferometric fiber-optic sensors. *Opt. Lett.*, 13(4):288–290, April 1988.
- [374] M. Dobosz, H. Matsumoto, and S. Iwasaki. Beamsplitter path equalization for white-light interferometry. *Opt. Eng.*, 34(2):493–498, 1995.
- [375] K. Morishita and K. Yamazaki. Wavelength and polarization dependences of fused fiber couplers. *J. Lightwave Technol.*, 29(3):330–334, February 2011.
- [376] D. F. Murphy, D. A. Flavin, R. McBride, and J. D. C. Jones. Interferometric interrogation of in-fiber Bragg grating sensors without mechanical path length scanning. *J. Lightwave Technol.*, 19(7):1004–1009, 2001.
- [377] L. Yuan, J. Yang, Z. Liu, and J. Sun. Sensing characteristics of an in-fiber integrated Michelson interferometer. In *Optical Fiber Sensors*, page ThE35. Optical Society of America, 2006.
- [378] M. Johnson. *Photodetection and Measurement: Maximizing Performance in Optical Systems*, chapter 1, pages 1–18. McGraw-Hill Companies, Inc., New York, 2003. ISBN: 0071409440.
- [379] M. Johnson. *Photodetection and Measurement: Maximizing Performance in Optical Systems*, chapter 3, pages 45–77. McGraw-Hill Companies, Inc., New York, 2003. ISBN: 0071409440.
- [380] G. C. Holst. *Solid-State Cameras*, volume 1 of *Handbook of Optics*, chapter 26, pages 26.1–26.21. McGraw-Hill Companies, Inc., New York, 3 edition, 2010. ISBN: 0071498893.
- [381] J. L. Vampola. Readout electronics for infrared sensors. In W. D. Rogatto, editor, *The Infrared & Electro-Optical Systems Handbook: Electro-Optical components*, volume 3, pages 285–342. SPIE Press, Bellingham, 1993.
- [382] B. D. *Metrology of Optical Components and Systems*. Handbook of Optical Systems.
- [383] S.-C. Lin and T. G. Giallorenzi. Sensitivity analysis of the Sagnac-effect optical-fiber ring interferometer. *Appl. Opt.*, 18(6):915–931, 1979.
- [384] C. A. Miller. *Intensity modulation and noise characterization of optical signals*, chapter 7, pages 246–283. Fiber Optic Test and Measurement. Prentice Hall, Inc., New Jersey, 1998. ISBN: 0135343305.

# Chapter 3

## SpectroBragg characterisation

---

### 3.1 Introduction

This chapter reports on the development of a robust high-bandwidth ( $\sim 50$  nm), high-resolution ( $\sim 1$  pm) and high-speed ( $\sim 0.1$  ms) simultaneous demodulation scheme, the SpectroBragg, for the individual sensing locations of FBG sensor arrays forming sensor networks. There is a need for high-speed FBG demodulation for applications such as in-flight monitoring of structures in the aviation/aerospace sector, where the use of novel materials are meeting the limits of traditional sensor technologies [1]. Distributed/multiplexed sensing arrangements also benefit by simultaneous interrogation of the sensor array or arrays, e.g for the detection of high-frequency vibrations [2].

Scanning systems are limited by the need to rapidly change direction while maintaining a repeatable, consistent speed over the scanning window. The higher the scanning speed the more limited the resolution achievable with that system compared to when it is run at a lower speed. Acousto-optically modulated tuneable filters enable fast and repeatable scanning.

An effective and simple alternative non-scanning high-speed demodulation approach uses edge filters, outlined in §2.4.1 (page V.I - 78), with high-speed detectors. The disadvantage of edge filter approaches is the inverse resolution/bandwidth relationship. Splitting the signal to use multiple edge filters/ detectors reduces the SNR.

A diffraction grating/linear array based measurement system circumvents these limitations enabling simultaneous high-resolution, high-speed measurement of measurands (typically strain, temperature, pressure) of an FBG array. The FBG spectra

are spatially dispersed by the diffraction grating, as discussed in appendix D (page V.II D-1), reducing the computation required to demodulate an array of sensors.

The aim of the SpectroBragg project was to develop a compact, custom spectrometer providing high-speed wide-bandwidth demodulation natively in the telecomms bands, using a linear InGaAs array, enabling the lower cost telecomms fibre components to be used<sup>1</sup>. The spectral bandwidth could then be extended to cover the S,C, L & U telecomms bands ( $\sim 1460\text{--}1675\text{ nm}$ ) by sequentially addressing  $\sim 50\text{ nm}$  bands across the  $\sim 1460\text{--}1675\text{ nm}$  range, ideally at  $\sim 2\text{ s}$ .

This chapter discusses the background theory to the SpectroBragg, details the assembly of and characterises the completed spectrometer. The SpectroBragg is employed in the subsequent two chapters.

## 3.2 Theory

### 3.2.1 Diffraction gratings

A diffraction grating is a regular series of diffracting obstacles<sup>2</sup> that, when the resultant wavefronts are added together for all the diffracting obstacles, produces a set of unique angles where the wavefronts are in phase [3]. The angle depends upon the wavelength of the incident radiation and obstacle spacing. For a fixed obstacle spacing, and varying wavelengths, the wavelength spectrum can be obtained.

The phasor representation<sup>3</sup> of the scalar plane wave solution to the general wave equation is

$$\underline{\mathbf{E}}(\underline{\mathbf{r}}, t) = E_0(\underline{\mathbf{r}}, t)e^{i[\omega t - \mathbf{k} \cdot \underline{\mathbf{x}}]} = E_0(\underline{\mathbf{r}}, t)e^{i[\omega t]}e^{-i[\mathbf{k} \cdot \underline{\mathbf{x}}]} \quad (\text{A.26})$$

A linear diffraction grating, consisting of a series of  $N$  equally spaced slits, as in figure 3.1, is placed into the uniformly illuminating radiation, as described by [4]. Each slit contributes a component amplitude,  $a$ , having a relative phase difference of  $\varphi$  from the neighbouring slit to the resultant amplitude, where [4]

$$\begin{aligned} Ae^{i\phi} &= a(1 + e^{i\varphi} + e^{i2\varphi} + e^{i3\varphi} + \dots + e^{i(N-1)\varphi}) \\ &= a\frac{1 - e^{iN\varphi}}{1 - e^{i\varphi}} \end{aligned} \quad (3.1)$$

---

<sup>1</sup>At the time of the project proposal, linear InGaAs arrays had not been used in diffraction grating based spectrometer systems, due to the technology for their commercial production being then new.

<sup>2</sup>In transmission the obstacles are slits and in reflection the obstacles are grooves.

<sup>3</sup>The temporal part of the complex amplitude can be separated out for plane waves as all plane waves have the same temporal origin [4].

The diffracted intensity is the square of the resultant amplitudes

$$I = (Ae^{i\phi})^2 = a^2 \frac{1 - e^{iN\varphi}}{1 - e^{i\varphi}} \frac{1 - e^{-iN\varphi}}{1 - e^{-i\varphi}} = a^2 \frac{2 - 2 \cos N\varphi}{2 - 2 \cos \varphi} \quad (3.2)$$

the phase term of which may be rewritten using the trigonometric identity

$$\sin^2 \theta = \frac{1 - \cos 2\theta}{2}$$

as

$$I = a^2 \frac{\sin^2 N\gamma}{\sin^2 \gamma} \quad (3.3)$$

where

$$\gamma = \frac{\varphi}{2} = \frac{\pi d \sin \theta}{\lambda} \quad (3.4)$$

The intensity contribution from each individual slit,  $a^2$ , may be rewritten as

$$a^2 = \frac{\sin^2 \beta_\phi}{\beta_\phi^2} \quad (3.5)$$

to give

$$I = \frac{\sin^2 \beta_\phi}{\beta_\phi^2} \frac{\sin^2 N\gamma}{\sin^2 \gamma} \quad (3.6)$$

where  $\beta_\phi$  is the phase difference between the centre and edge of the beam. When  $N$  is an integer multiple of  $\pi$ , then  $\gamma = p\pi/N = 0$ , except for  $p = mN$  where  $m$  is an integer multiple. Then the function is indeterminate. To cater for this case, it may be shown that [4]

$$\lim_{\gamma \rightarrow m\pi} \left( \frac{\sin N\gamma}{\sin \gamma} \right) = \lim_{\gamma \rightarrow m\pi} \frac{N \cos N\gamma}{\cos \gamma} = \pm N \quad (3.7)$$

so the intensity at  $\gamma = m\pi$ , when the phase term has a maximum, is  $N^2$  times the intensity diffracted by a single slit. The locations where  $\gamma = m\pi$  are called *principal maxima*. Between principal maxima are a series of *subsidiary maxima* at  $\gamma = (p\pi/N) + (\pi/2)$

### 3.2.1.1 Grating equation

The condition that a diffracted order exists is that the relative optical path difference between individual slits or grooves should all be in phase, or out of phase, by integer numbers of  $2\pi$  radians, or a whole number of wavelengths,  $\lambda$ , i.e.

$$\sin(\theta_i) + \sin(\theta_d) = \frac{m\lambda}{d} \quad (3.8)$$

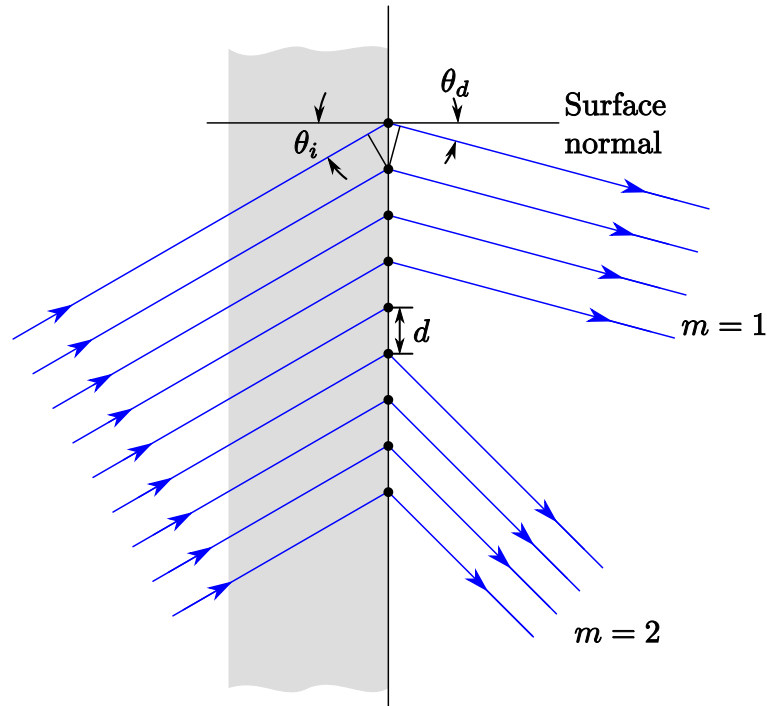


**Figure 3.1:** Diffraction grating orders, after figure 2.8(a) of [4]

where  $\theta_i$  is the incident angle,  $\theta_d$  is the diffracted angle,  $d$  is the obstacle/groove separation and  $m$  is the diffracted order, as illustrated in figure 3.1. This is the *general grating equation*.  $m = 0$  refers to the undeviated beam, or specular reflection beam, for reflective gratings. The sign convention used here is that angles have the same sign when they are on the same side of the grating normal, and change sign when they cross the surface normal.

The first minimum on either side of a principal maximum occur at  $\gamma = \pm\pi/N$ , so the angular half-width  $\theta'$  of the principal maximum is

$$\gamma = \frac{\pi}{N} = \frac{\pi d \sin \theta'}{\lambda} \quad \text{or} \quad \sin \theta' = \frac{\lambda}{dN} = \frac{\lambda}{W_g} \quad (3.9)$$

where  $W_g = dN$  is the illuminated width of the grating. The principal maximum profile may be modulated by additional terms when relative phase shifts are present in the incident beam, as discussed in section §3.2.4.3 (page V.I - 140).

### 3.2.1.2 Grating Dispersion

To determine how the diffracted angle varies with wavelength, the grating equation is differentiated with respect to  $\theta_d$

$$\begin{aligned} \frac{\partial}{\partial \theta_d} [d(\sin \theta_i + \sin \theta_d) &= m\lambda] \\ \Rightarrow d \cos \theta_i \frac{\partial \theta_i}{\partial \theta_d} + d \cos \theta_d &= m \frac{\partial \lambda}{\partial \theta_d} \end{aligned} \quad (3.10)$$

In a spectrograph arrangement, the angle of incidence is fixed, so  $\partial \theta_i / \partial \theta_d = 0$  and the *angular dispersion* of the grating is given by

$$\frac{\partial \theta_d}{\partial \lambda} = \frac{m}{d \cos \theta_d} \quad (3.11)$$

The *linear dispersion*, the change in distance,  $x$ , in the plane of the focused spectrum with change in wavelength, is the product of the angular dispersion and the effective focal length,  $f$ , of the focusing element

$$\frac{\partial x}{\partial \lambda} = f \frac{\partial \theta_d}{\partial \lambda} \quad (3.12)$$

The *grating resolution* of a diffraction grating is a measure of its ability to separate neighbouring spectral features. In grating terms, resolution and *resolving power* are used interchangeably and distinctly in different sources. Resolution is preferred in [3] as the term power has the mechanical meaning of the rate of doing work, whereas [4] prefers resolving power as the whole spectrometer system can be said to have a resolution, somewhat independent of the diffraction grating<sup>4</sup>. Here the term grating resolution is used as the manufactured resolution of the grating is not discussed in detail, and the term (system) resolution is reserved for the SpectroBragg as a device.

The Rayleigh criterion for resolution,  $R_{Rayleigh}$ , states that two features are resolvable if the maximum of the second feature occurs at the first minimum of the first feature [3,4],

$$\frac{\lambda}{\Delta \lambda} = \frac{W_g m}{d} = mN \quad (3.13)$$

The larger the width,  $W_g$ , of the grating, the greater the spectral line resolution will be. When considered as a Fourier transform, the greater the number of diffracting obstacles, the greater the definition of spatial frequency achieved and the presence of side-lobes can be reduced. For improved resolution, improved side-lobe suppression and improved energy localisation, the widest ruled-area grating that can be illuminated should be used.

---

<sup>4</sup>For example, where the detector is the limiting factor, or aberrations dominate.

### 3.2.1.3 Grating Free spectral range

The diffraction grating has a principal maximum when  $\gamma = m\pi$ . The integer  $m$  allows for multiple orders to be diffracted, and so for  $\lambda_2 = 2\lambda_1$ , the first order ( $m = 1$ ) diffracted principal maximum of  $\lambda_2$  will be at the same angle as the second order ( $m = 2$ ) diffracted principal maximum of  $\lambda_1$ . The *free spectral range* is the largest wavelength range between a given order,  $m$ , which does not overlap an adjacent order,  $m \pm 1$  [4]

$$\lambda_2 m = \lambda_1(m + 1), \quad \lambda_1 m = \lambda_2(m - 1) \quad (3.14)$$

so, to avoid overlapping orders,

$$\lambda_2 - \lambda_1 \geq \lambda_1/m. \quad (3.15)$$

### 3.2.1.4 Conical diffraction grating mounting

The diffraction grating surface normal, as used in this work, is in the plane of the surface normals of the focusing elements. When the diffraction grating is not in this plane the diffracted shape of an incident line is a curve following a conical curve and the general diffraction equation has an additional term  $\cos \theta_c$ ,

$$(\sin(\theta_i) + \sin(\theta_d)) \cos \theta_c = \frac{m\lambda}{d} \quad (3.16)$$

where  $\theta_c$  is the out-of-plane angle between the grating normal and the incident beam [5]. This is termed the *conical diffraction mounting* [3]. The Littrow diffraction grating mounting [3–5] aligns the angle of the diffracted beam,  $\theta_d$ , with the angle of the incident beam,  $\theta_i$ , for a design wavelength. In order to access the diffracted beam, the diffraction grating is set at an angle,  $\theta_c$ , to have the diffracted beam above or below the entrance aperture. In this arrangement the diffracted beam obtains the conical curvature. The conical curvature of the diffracted beams makes use of out-of-plane diffraction angles less appealing.

### 3.2.1.5 Ghosts and grating accuracy

Diffraction gratings are manufactured by either the ruled or interferometric/holographic methods [6, 7]. The ruled method involves mechanically inscribing the grating onto a surface [8]. The interferometric/holographic method involves projecting an interferogram onto photoresist material, then developing it [9]. This process is strictly not a hologram, as phase information is not retained. However, the term is often used.

The holographic method produces sinusoidal gratings, where the stability of the interferogram determines the accuracy of the diffraction grating produced. Any in-

stabilities in the recorded pattern will appear as phase-shifted gratings, and produce ‘ghosts’ when used as a spectrometer [10]. These are unwanted spectral artefacts or modulation of the desired spectral profiles. The recommended tolerances for the diffraction grating are that the grating be flat to  $\lambda/20$  and the regularity of the groove spacing be of the order of  $\lambda/100$  [3]. The sensitivity of the grating to manufacturing defects is, thus, wavelength dependent.

The grating used in this work for the SpectroBragg spectrometer was a copy generated from a master produced by the *interferography method*.

### 3.2.1.6 Evanescent orders

The grating equation provides the diffracted angle with respect to the grating surface normal,  $\theta_d$ , for a given combination of incident angle,  $\theta_i$ , wavelength,  $\lambda$ , and diffracted order,  $m$ . When  $|\sin \theta_d| \geq 1$ , the diffracted beam is said to be an evanescent order [3]. When  $|\sin \theta_d| < 1$  the diffracted beam is a propagating order.

The radiation is coupled into surface plasmon modes in the grating surface. The field normal to the grating surface is evanescent, i.e. it decays exponentially normal to the surface and can usually only be detected on the order of wavelengths from the surface [3].

### 3.2.1.7 Grating efficiency

Diffraction grating efficiency is defined as the fraction of incident monochromatic radiation diffracted into a specific order [3]. The efficiency is not constant but varies as a function of wavelength. The materials used in the grating can affect the efficiency, either in terms of transmission or reflection coefficients.

With ruled gratings the profile can be changed to couple more radiation into a specific order. Such a grating is termed a ‘blazed’ grating. For interferometric/holographic gratings, the modulation is symmetric and consists of a spatial sine or cosine frequency component.

Normal illumination will, by mirror symmetry, generate symmetrical diffraction orders with the positive and negative orders having equivalent power [9]. In most cases the grating is not normally illuminated, and mirror symmetry is not preserved. When one order is evanescent, the power coupled into the propagating order can approach that of a blazed ruled grating.

For a sinusoidal grating modulation, the *diffraction efficiency*,  $\eta_m$  of the  $m^{\text{th}}$  order is [11]

$$\eta_m = J_m^2(A_g) \quad (3.17)$$

where  $J_m$  is an  $m^{\text{th}}$  order Bessel function, and  $A_g$  is the amplitude of the grating modulation or modulation depth. As the depth increases more radiation is coupled

into higher orders [11] but the Fraunhofer approximation becomes increasingly less valid, as there is an increased probability of the radiation interacting with more than one surface. It is not possible to optimise a depth to produce only one diffraction order [11].

### 3.2.2 Diffraction grating spectrometers

Diffraction gratings have been used in various types of spectrometer devices and configurations to obtain spectral information [5, 8, 12–15]. The type of device used in this work is a spectrograph. A spectrograph displays the whole spectrum at the output, as opposed to a monochromator, which displays a small band at the system resolution, i.e. a monochromatic signal<sup>5</sup>. The Ando OSA [16] referred to in this thesis is a double-pass scanning monochromator.

Historically, the monochromator was favoured over the spectrograph as the spectrograph suffered from stray light, and was limited to film as the detector. The advent of the CCD array increased the popularity of the spectrograph design, as the spectrum could be read out quickly and used in a computer without the need to mechanically scan as in the monochromator [14, 17, 18].

Ecke provides an example of a typical modern use of Čzerny–Turner spectrometers [19]. A silicon CCD array is used as the sensing element. The CCD based Čzerny–Turner linear spectrometer design has been successfully commercialised as *the BlueBox FBG sensor system*<sup>6</sup>. However, silicon CCD arrays are not sensitive to IR radiation around 1550 nm, and so do not benefit from the lower costs and ubiquity of components available to the telecomms bands.

The highest resolution<sup>7</sup> for a given illumination is provided by the Michelson. While typically operated as scanning devices, stationary Michelson devices are achieved by replacing temporal scanning with spatial scanning across an array [20]. The spatial scanning systems still require the type of post-processing as the temporal scanning system. This is discussed further in appendix D (page V.II D-1).

The Fabry–Perót provides the next best resolution. The Fabry–Perót has a small free spectral range and does not allow the tailoring of energy, e.g. blazing. Diffraction grating spectrometers follow the Fabry–Perót in terms of resolution for a given illumination. However, the access to that spectral information reverses the performance order. The diffraction grating provides easier access to the spectral

---

<sup>5</sup>There is no formal classification scheme. A useful classification scheme is presented in §12.2 of [14].

<sup>6</sup>From *JENAer Messtechnik GmbH, Structure Health Monitoring System - BlueBox* (<http://www.jenaer-mt.com/web/index.php/lang-en/fiber-bragg-sensorsystem/59-structure-health-monitoring-system-bluebox?format=pdf>).

<sup>7</sup>For the devices considered.

information than the Fabry–Perót or the Michelson interferometers.

There are different designs of non-scanning diffraction grating spectrometer, generally grouped into plane- and concave-grating arrangements [5, 14]. The concave diffraction grating mountings use a concave diffraction grating with a fixed radius of curvature to disperse and focus the signal in one component. The geometric aberrations are part of the diffraction grating performance, and make the component more expensive.

The spectrometer design used for the SpectroBragg is a Čzerny–Turner design [5, 14]. The Čzerny–Turner design consists of an input aperture at the focal length of a collimating spherical mirror, which reflects the collimated radiation onto the diffraction grating. The diffracted order is focused by a second spherical mirror onto the detector, as illustrated in figure 3.2.

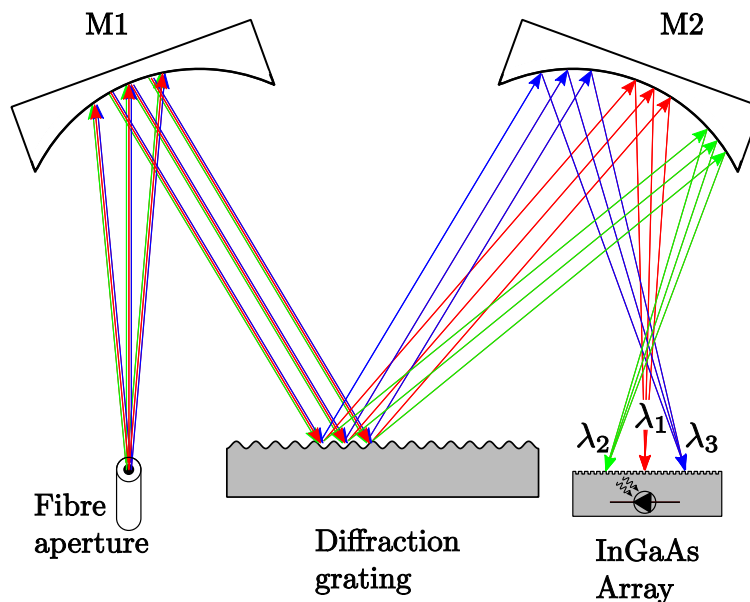


**Figure 3.2:** Schematic of Čzerny–Turner for SpectroBragg. The reflected signal from the FBGs is collimated by the first mirror, diffracted onto the focusing mirror which concentrates the radiation onto the InGaAs array.

The Čzerny–Turner is similar to the Ebert–Fastie design which replaces the two mirrors with a single mirror arranged in auto-collimation. The Ebert–Fastie and the Čzerny–Turner are the two principle plane diffraction grating mounts<sup>8</sup> [14]. The Čzerny–Turner design has the advantage of allowing different focal lengths for the two mirrors.

The component cost of manufacturing a Čzerny–Turner spectrometer is comparatively cheap<sup>9</sup>, requiring two spherical focusing elements, a plane diffraction grating,

<sup>8</sup>The Monk–Gillison [14] mount is a simpler mount to construct but retains sufficient aberrations so as not to be considered.

<sup>9</sup>Compared to a scanning diffraction grating spectrometer or a concave grating spectrometer.

and their mounts [14]. As discussed in section §K.2 (page V.II K-5), the Čzerny–Turner can also eliminate coma aberration, but retains spherical aberration and astigmatism [14].

Plane diffraction gratings are typically cheaper than concave diffraction gratings. They also have advantages over concave gratings in terms of imaging quality: the image will be stigmatic, if anamorphic. The usable wavelength range of plane diffraction gratings is typically larger than for concave gratings [14].

The entrance aperture, or field, of spectrometers has traditionally been a slit, either linear or a long arc of a circle [13]. The slit was typically a few microns wide, and provided an identifiable feature for detection. The length of the slit also allowed more radiation from the source to be passed through the spectrometer. The SpectroBragg is fibre coupled, so that the source is confined to the guided mode of the fibre. As such, the end face of the fibre can be used as the entrance slit. The diameter of the fibre core is  $\sim 10\ \mu\text{m}$ , which is of the order of traditional slit widths. The detector array used in the SpectroBragg is linear, i.e.  $1 \times 512$  pixels. The use of linear or curved entrance slits would result in perfectly focused radiation falling outside, above or below, the area of the pixel. By using a point entrance source, the energy concentration at the detector should be higher.

Geometric aberrations impose a significant limitation upon the performance of Čzerny–Turner-type spectrometers, as the paraxial condition cannot be maintained without beam obstruction. The illumination of the diffraction grating by non-collimated light is not ideal as the performance of a diffraction grating is typically specified in terms of collimated illumination. A discussion of the Seidel geometric aberrations is provided in appendix §K.1 (page V.II K-1).

The most significant of the Seidel aberrations of concern are the astigmatism and coma which alter the spectral profile, although the field curvature is enhanced in such a compact arrangement compared to traditional sizes. Fortunately, the Čzerny–Turner can be arranged to minimise astigmatism and coma, as is discussed in the next section.

### 3.2.2.1 Čzerny–Turner mount

The Čzerny–Turner mount has the advantage of minimising coma [14] aberrations inherent to spherical mirrors. To remove astigmatism a curved entrance slit was historically used so that the astigmatism of the system produced a straight image. Curving the film of the spectrograph or using a rotating platform for the spectrometer reduced spherical aberrations.

In the absence of the diffraction grating, the two mirrors in the Čzerny–Turner could compensate for aberrations by symmetry. The presence of the diffraction grating breaks the symmetry, and the aberrations cannot be fully eliminated.

The SpectroBragg design uses a linear InGaAs array with no moving parts. Field curvature's effects could be minimised in an analog spectrometer and spectrographs by moving the detector along the mean surface in a spectrometer or curving the film to conform to the mean surface in a spectrograph. The linear array prevents these techniques being applied and the aberrations are a limiting factor to the spectrometer operation [5, 18].

Rosendahl derived an optimised configuration which describe the optimum angles for the elimination of coma in spectrometers with radii  $R_1 = R_2$  [21]. This was improved by Shafer *et al.* [22] taking  $R_1 \neq R_2$  to give

$$\frac{\sin \beta}{\sin \alpha} = \frac{R_1^2 \cos^3 \beta \cos^3 \theta_i}{R_2^2 \cos^3 \alpha \cos^3 \theta_d} \quad (3.18)$$

where the angles and lengths are as illustrated in figure 3.3. Equation (3.18), known as the *Rosendahl cos-cubed equation*, describes the arrangement of angles that produce the best approximation to the ideal symmetrical compensation of aberrations.

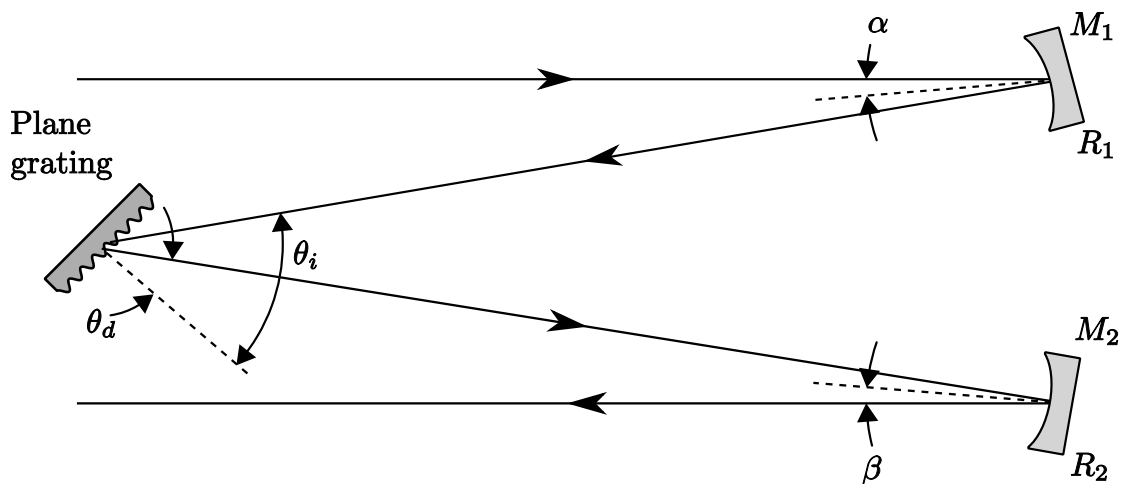


**Figure 3.3:** Selecting angles to minimise aberrations in a Čzerny–Turner spectrometer.  $R_1$  and  $R_2$  are the radii of mirrors  $M_1$  and  $M_2$ , respectively.

Plane reflection diffraction gratings have the advantage that they do not exhibit the chromatic focal shift present in transmission diffraction gratings [23]. If collimated radiation is not used the plane diffraction grating may produce coma. By design  $M_2$  compensates for aberrations introduced by  $M_1$ , and so the diffraction grating is illuminated with non-collimated radiation.

### 3.2.3 Super-resolution by signal analysis for SpectroBragg

The SpectroBragg's detector was a linear array of 512 elements. The 512 elements spanned a bandwidth of  $\sim 70$  nm. Each detector would therefore observe a spectral window width of  $\sim 0.13$  nm on average. An FBG signal, with the remaining aberrations, typically illuminated several pixels. Native sub-nanometre resolution of the peak wavelength was not possible. Achieving picometre or sub-picometre super-resolution required signal analysis.

To achieve super-resolution, three signal processing approaches were considered:

1. Centroid calculation,
2. Curve fitting,
3. Cubic spline interpolation.

The computational complexity increases with each approach; however, the theoretical accuracy increases too.

#### 3.2.3.1 Centroid approach

The centroid calculation is a weighted average sum:

$$\lambda_c = \frac{\sum_{i=1}^N I_i \lambda_i}{\sum_{i=1}^N I_i} \quad (3.19)$$

where  $I_i$  is the intensity recorded at the array element centred on  $\lambda_i$  for  $N$  array elements.

The calculated centroid wavelength does not necessarily indicate the peak location of the profile. For any asymmetric profile the calculated centroid location will not be located at the maximum intensity. This makes the centroid value sensitive to any changes in the profile in addition to movements of the profile in the wavelength direction.

Where the profile remains unchanged the centroid calculation is a fast and effective measure of the profile movement. Profile changes, which limit the reliability, include the presence of noise on the signal.

The centroid calculation is used to calculate the super-resolution for the SpectroBragg signal processing, with the rationale for this decision provided in §3.4.2.1.

#### 3.2.3.2 Non-linear regression curve fitting

Curve fitting is the non-linear least-squares regression fit of a suitable function to the captured data. A suitable function is chosen to match the general profile shape.

The suitable function, of more than one parameter,<sup>10</sup> describing the theoretical profile is provided. The combination of parameters which provides the minimum residual between the data and fit is taken to describe the data profile. The profile can then have the centroid calculation performed upon it, or, if a unique profile peak exists, the profile function is differentiated and the evaluated turning point used as the peak value.

This process has the potential to be the most accurate, as known information, the profile, is used to determine the location. Additionally, the effects of signal noise are constrained by the profile being fit to the data, and removed once a solution is obtained. The profile is then used for peak location, rather than the data.

For standard telecomms FBGs the spectral profile is usually Gaussian [24],

$$G(x; \underline{\underline{a}}) = G(x, \sigma, \mu, \gamma) = Ae^{[-(\frac{|x-\mu|}{2\sigma})^\gamma]} \quad (3.20)$$

For flat-top FBGs, such as the novel anisotropic FBGs characterised in Chapter 4, the spectral profile is better described by a super-Gaussian profile [24],

$$SG(x; \underline{\underline{a}}) = SG(x, w_{SG}, \mu, \gamma) = Ae^{[-(\frac{|x-\mu|}{w_{SG}})^\gamma]} \quad (3.21)$$

which are plotted in figure 4.3 (page V.I - 179).

The general approach to determining the optimal fit is termed Levenberg–Marquardt minimisation [25]. Given the set of unknown parameters to be optimised,  $\underline{\mathbf{x}}$ , the first step is to supply an initial guess for the parameters to be fit,  $p$ , e.g. the at-rest values of  $G$  or  $SG$ . The Jacobian, the first order partial derivatives of the function to be fitted,  $\underline{\mathbf{a}}$ , with respect to the components of  $\underline{\mathbf{x}}$ , are taken

$$\underline{\underline{J}}_{\underline{\mathbf{a}}}(x) = \frac{\partial \underline{\mathbf{a}}}{\partial \underline{\mathbf{x}}} = \begin{pmatrix} \frac{\partial a_1}{\partial x_1} & \frac{\partial a_1}{\partial x_2} & \dots & \frac{\partial a_1}{\partial x_N} \\ \frac{\partial a_2}{\partial x_1} & \frac{\partial a_2}{\partial x_2} & \dots & \frac{\partial a_2}{\partial x_N} \\ \vdots & \vdots & \ddots & \vdots \\ \frac{\partial a_M}{\partial x_1} & \frac{\partial a_M}{\partial x_2} & \dots & \frac{\partial a_M}{\partial x_N} \end{pmatrix} \quad (3.22)$$

Solving the linear equations [26] gives

$$(J_k^T J_k + \lambda_{fit} I) p_k = -J_k^T r_k \quad (3.23)$$

where  $p$  is the approximate solution to be improved,  $J$  is the Jacobian matrix;  $I$  is the identity matrix, and  $\lambda_{fit}$  is the Levenberg–Marquardt parameter; and  $r_k = y(x) - p_{k-1}(x)$ , the residual vector between the approximate solution and the data to be fitted.  $\lambda_{fit}$  is used to get an improved approximate solution, as it alternates

---

<sup>10</sup>A function of one parameter is simply linear regression.

between *steepest descent* and *inverse-Hessian* methods [25]. An initial solution,  $p_0$ , needs to be provided, but this may be no more than an approximation of the at-rest profile as it converges towards the data rapidly, at first.

A conservative value of  $\lambda_{fit} = 0.001$  is taken, which controls the alternation between the two convergence approaches incorporated into the Levenberg–Marquardt method.

There is also the general numerical problem of obtaining the desired global minimum versus a local minimum. The convergence profile will not be known ahead of the calculation, and the convergence criterion may never be achieved, or may time out, if trapped in a local minimum. This can potentially lead to sudden jumps in the determined peak location due to the different convergence conditions from one set of data to another. As the Levenberg–Marquardt method is an iterative process, the most significant limitation is the unknown time taken to converge on a solution of set quality, or the quality of a solution obtained in a fixed time. Also unknown is the relative quality of that solution when compared with solutions obtained from preceding and subsequent data. The profile may not match the supplied function which will also affect the convergence time.

However, the presence of noise can affect the convergence time significantly. The effect of noise can be reduced by sampling the spectrum at greater resolution, limiting the effect of individual pixels, but this requires an array with more pixels or reduced wavelength bandwidth.

### 3.2.3.3 Cubic Spline interpolation

The cubic spline approach fits a cubic spline to the data. The cubic spline interpolation scheme calculates values between the captured data points using the interpolation formula that is smooth in its first derivative and continuous in its second derivative, both within the interval and at the captured data points [27].

Given data point indices  $x_1 < x_2 < \dots < x_n$ ;  $n \geq 3$ , with their corresponding data values  $y_k$ ;  $k = 1, \dots, n$ , the cubic polynomial

$$S_k(x) = A_k + B_k(x - x_k) + C_k(x - x_k)^2 + D_k(x - x_k)^3 \quad (3.24)$$

is defined, so that  $S$  is twice continuously differentiable. The cubic spline calculation is typically faster than the curve fitting approach. The cubic spline equation can be differentiated to obtain the turning point, and, using the parameters obtained from the fitting of the cubic spline to the data, the location of turning points will coincide with the peak(s) in the data.

This approach suffers from the *roughening* effect of differentiation. Any noise in the system is thus exacerbated. Additionally, the spline fitting will try to follow

the noise so that the combined effect of the spline fit and the differentiation can be considerable enhancement of the presence of noise, and thus on the uncertainty of the measurement value returned.

#### 3.2.3.4 Thresholding and noise

The disadvantage of using the above approaches is that they are sensitive to noise. The spline, and to a greater extent the non-linear regression curve fitting, have subtle non-linear responses to noise. In general, these approaches benefit from pre-processing to reduce the impact of noise. Pre-processing can be as simple as averaging data. Such pre-processing does have the penalty of delaying the overall system response time.

The process of thresholding [28] is the partitioning of data dependent upon whether data values are greater than a threshold level. Data values above the threshold are retained and those below the threshold set to zero. The thresholded data may be used to eliminate the contribution from noise below a certain SNR level,  $t_{\text{level}}$ . The threshold function is given by

$$T_{\text{level}}(x) = \begin{cases} f(x), & f(x) \geq t_{\text{level}} \\ 0, & \text{otherwise} \end{cases} \quad (3.25)$$

Directly thresholding data with noise is more difficult. The approaches of data smoothing or edge-detection discussed in [28] would limit the resolution that is to be achieved.

Ares and Arines have reported [29] that the use of thresholding modifies the Gaussian statistics for data [30]. This can introduce an offset in the determined centroid, depending upon the ordinates vertical distance from the thresholding value. As the signal intensity for the various FBGs and lasers was variable, and hence the signal to noise ratio was not approximately constant, the impact of this effect upon changing signals varied.

#### 3.2.3.5 Alternative data selection method

To limit any possible effects of thresholding upon the centroid calculation, while eliminating as much unwanted noise as possible, a rectangular window of data was taken about the maximum value,  $x_{\text{max}}$ , in a range containing one signal. The window was specified as the data in the range  $x_{\text{max}} - n : x_{\text{max}} + n$ . This differed from the thresholded data in that the optimum window was found to be approximately the width of the signal at the background level, and so retained points just above background noise. The window approach produced results with less noise and jumps in value, than the thresholding approach for the same dataset.

### 3.2.4 Depolarising signal

Diffraction gratings are in general polarisation-sensitive. Designing polarisation insensitive diffraction gratings is an ongoing area of research [31]. The polarisation-sensitivity for the grating used in the SpectroBragg is shown in figure 3.7 (page V.I - 143).

If the state of polarisation, SOP, of incident radiation is variable and unknown then the spectrum at the array is a function of both the spectral distribution and the SOP of the radiation. The diffraction grating can be considered as a polarisation analyser in addition to a spectral disperser. Non-uniform SOP changes will appear as spectral changes across the bandwidth of the array for an otherwise stationary system.

There are two variables and one equation, with the simplest approach being to fix one variable and solve for the other. As the wavelength spectrum is of interest the SOP must be fixed.

The historical approach has been to depolarise the signal immediately before the entrance slit, effectively removing the polarisation as a variable. The spectrometer as a whole is presumed to introduce no changes in the SOP apart from the diffraction grating itself. By effectively depolarising the signal before it enters the spectrometer, all SOPs are equally populated and so the diffraction grating has only a wavelength dependence. The polarisation-sensitive efficiency is reduced to a general wavelength dependent efficiency.

An alternative approach is to lock the SOP to a single fixed value for either all wavelengths or for a fixed SOP per wavelength. Again, the polarisation dependence is made constant (or constant for each wavelength), and the temporal spectral changes are dependent upon wavelength only.

Approaches to reducing the polarisation-sensitivity are the subject of chapter 5. To summarise, the two principle depolarisation schemes are the Lyot depolariser [32] and the polarisation scrambler [32] or Billing depolariser [33].

#### 3.2.4.1 Lyot depolariser

The Lyot depolariser<sup>11</sup> operates by pseudo-depolarising a spectral window  $d\lambda$ . The greater the retardation of a section, the narrower the window  $d\lambda$  will be. A wavelength dependent retardation is introduced so that in the window  $d\lambda$  all polarisation orientations are populated equally. The Lyot has the advantage of being a passive device. The spectral window that the Lyot depolarises must, necessarily, be smaller than the minimum spectral range resolved by the spectrometer, lest the polarisation be partially recovered. Consequently, the lengths required to depolarise

<sup>11</sup>The theory is discussed in §5.2.1.1 (page V.I - 219).

high-coherence sources may be prohibitive in cost or in transmission losses.

### 3.2.4.2 Polarisation scrambler

The polarisation scrambler is based upon the Billings depolariser [33]. The Billings depolariser can depolarise monochromatic radiation, i.e.  $d\lambda \rightarrow 0$ . The Billings depolariser consists of two rotating retarders with different rotation frequencies in a 1 : 2 ratio. Instead of depolarising over a spectral window the Billings depolarises over a temporal window. The faster the retarders can be made to spin, maintaining the 1 : 2 ratio, the shorter the temporal window required.

Polarisation scramblers generalise the Billings temporal approach with varying schemes to temporally change the retardation, so as to keep the monochromatic depolarisation advantage. Fibre based temporal scramblers have been reported, e.g. [34]. As the polarisation scramblers are active devices and require that the moving components maintain their relative frequencies, polarisation scramblers are typically more expensive than Lyot-based schemes. Being active devices they must be powered and may generate noise, potentially restricting environments where it can be used.

### 3.2.4.3 Talbot Bands and Channelled Spectra

The objective of depolarising the signal entering a spectrometer is to ultimately reduce intensity variations in the captured spectrum due to either different wavelength having different SOPs or temporal evolution of those SOPs. Ideally, polarisation changes would be eliminated and the spectrum would be dependent upon wavelength.

The fibre Lyot depolariser consists of two lengths of PM fibre in series, with their axes arranged at  $\pi/4$  to each other. The PM fibre has a fast and a slow axis, which is achieved by anisotropic geometry of the fibre, achieving a difference in effective group refractive index,  $n_{gf} - n_{gs} = \Delta n_g$ .  $\Delta n_g$  is sufficiently large that the temporal delay over the beat length (equation (2.84) (page V.I - 51)) decorrelates any random SOP change. In effect the orthogonal SOPs of radiation ( $\lambda$ ) not uniformly launched into either axis experiences two paths over a length  $l$  of fibre, with an optical path difference of

$$\Delta n_g l \geq \lambda \quad (3.26)$$

If the path lengths in the Lyot are not long enough to depolarise a signal, i.e.  $2\pi$  rotation over the spectral element  $\Delta\lambda$ , when observed by a spectrometer with resolution  $> \Delta\lambda$ , then the phase shifts introduced by the OPD between the fast and slow axis will appear as phase shifts within  $\Delta\lambda$ . Figure 3.4 illustrates the effect, for two wavelengths of a spectrum. The blue light is in phase and experiences

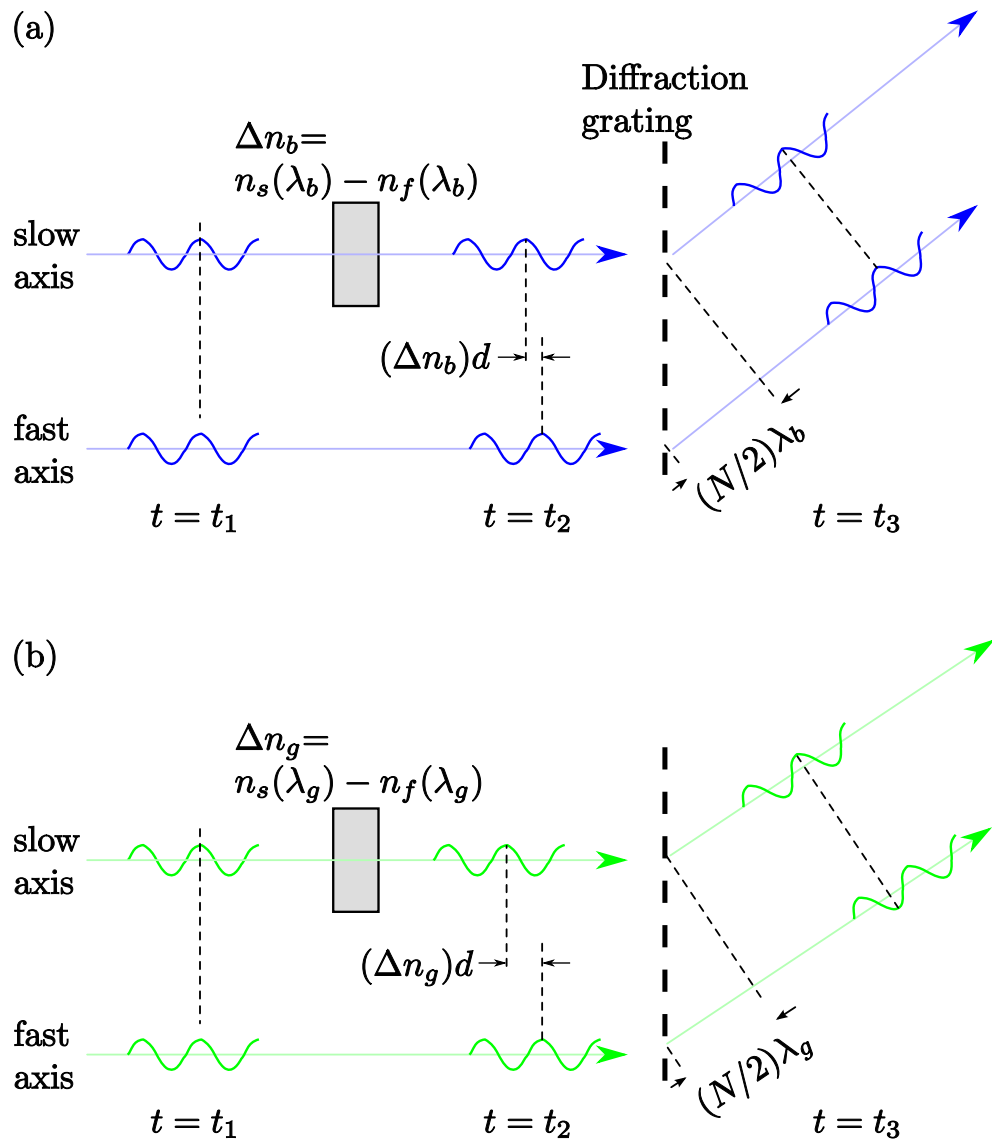


**Figure 3.4:** Talbot band effect: A phase delay is inserted into part of a beam illuminating a diffraction grating, e.g. by a glass slide, of thickness  $d$ . The phase delay introduced between the two paths combines with the phase delay introduced by the diffraction grating to shift the relative phase difference by, (a) integer,  $m$ , multiples of  $\pm\pi$ , i.e. constructive interference; and (b)  $\pm m\pi + \frac{\pi}{2}$ , i.e. destructive interference. (After Jahns *et al.* [35].)

constructive interference. The green light is  $\pi$  out of phase and so experiences destructive interference. Within the spectrum appears a periodic channelling that does not represent the true spectrum.

As the Lyot design is two lengths at  $\pi/4$ , a signal at any polarisation orientation will experience a phase shift, with the majority of orientations experiencing two phase-shifts. The Lyot behaves as two sequential Mach-Zehnder interferometers, with the complementary outputs co-propagating<sup>12</sup>. The phase shifts manifest themselves as spectral sub-structure within the envelope of the depolarised signal profile. When the sub-structure is only evident either in the negative or positive diffracted orders it is termed *Talbot bands* [35,36]. The more general condition is termed *channelled spectra* [37–39] or *fringes of equal chromatic order* [40].

The diffraction grating separates the various wavelengths into angles, thus recovering the phase differences. Depending upon how fast the phase changes with wavelength, the modulation of the envelope can be rapid or slow, manifesting itself at different resolutions.

The effect is to modulate the phase of the signal's constituent wavelengths, so that at the detector the phase changes modulate the signal intensity, altering the spectrum. Inadequate depolarisation using a Lyot may make the intensity changes captured by the detector greater by modulating the phase. If the signal does not have widely varying SOPs, then the phase changes dominate, and may, by destructive interference, reduce the signal intensity to the minimum defined by the ratio of signal power in the fast and slow axis. Alternatively, if the signal has orthogonal components, then interference is minimised and the grating's polarisation efficiency dominates. For random SOPs, the dominant effect may change randomly between the two processes.

For the effective use of the Lyot depolariser the minimum spectral window to be observed determines  $\Delta\lambda$ . If  $\Delta\lambda$  is greater than the minimum spectral window to be observed, the use of the Lyot depolariser may introduce worse system performance than without.

### 3.3 Experimental apparatus/setup

The aim of the SpectroBragg work was to build a spectrograph with an InGaAs array. The advantage of the InGaAs array is the sensitivity to telecomms band wavelengths. Devices designed for telecomms applications, such as WDM, have the advantage of defined channel spacings that conforming equipment must meet<sup>13</sup>. In

<sup>12</sup>Minus coupling losses from the discontinuity in waveguide geometry at the splice point.

<sup>13</sup>Coarse WDM, ITU-T G.694.2 [41], has channel spacings of 20 nm, and dense WDM, ITU-T G.694.1 [42], has channel spacings of  $\sim 0.1$  nm.

a sensing configuration, the nominal wavelength of sensors, and their operational range, may not match the channel spacings. The spectrometer would need not to present a per channel interface, as several sensors may reside in the channel, or a sensor may occupy two channels.

The motivation for this work was to develop a device similar to the Čzerny–Turner–based device reported in [19], but using an InGaAs array in place of the CCD array. The InGaAs array technology is not as advanced as the more mature CCD technology, and similar pixel densities were not available.

The intended resolution and spectral range of the SpectroBragg was  $\sim 1$  pm and 50 nm, respectively. It was originally intended to use a *Sensors Unlimited*<sup>14</sup> 1024 element array. This would give a native resolution of  $\sim 49$  pm, with super–resolution to the desired 1 pm in software based post–processing. It was not possible, however, to procure the 1024 element array. A 512 element *Hamamatsu* InGaAs array was the alternative chosen. The G9214-512S InGaAs array was supplied by *Tec5 Ag*, Oberursel, Germany as the array was not available for retail sale directly from Hamamatsu.

In contrast to the Ando OSA used in chapter 4, the objective of the SpectroBragg was not to accurately obtain high resolution spectral data. The type of sensors envisioned to be used with the SpectroBragg would be standard (e.g. telecomms) FBGs. The SpectroBragg would return a high resolution measurand value via a single high resolution wavelength value obtained by spectral averaging and super–resolution post processing.

The SpectroBragg design thus did not provide a highly resolved spectral profile. The design did provide a wide spectral range and high resolution value for the centroid value of the sensor reflected spectrum.

### 3.3.1 Tec5 Array

The SpectroBragg included an InGaAs array manufactured by Hamamatsu Photonics, model G9214-512S. The array had 512 pixels in two 256 interleaved arrays, with a pitch of 25  $\mu\text{m}$ . The pixel size was 25  $\times$  500  $\mu\text{m}$ . The array was cooled via an integrated Peltier thermo–electric cooler, TEC, packaged with the array in the array housing, shown in figure 3.5. The array and TEC were packaged and combined with interfacing electronics and cooling by Tec5 Ag, Oberursel, Germany to provide one 512 output via USB. The InGaAs sensor housing is shown in figure 3.5 with the control unit and data cable.

The array was connected by a USB2 cable to a data–capture PC. The array was

---

<sup>14</sup>Sensors Unlimited, Inc. are now named Goodrich ISR systems. Goodrich Corporation acquired Sensors unlimited in November 2005. From *Sensors Unlimited, Inc., part of Goodrich Corporation., About Us: The History of SWIR Imaging* (<http://www.sensorsinc.com/background.html>).

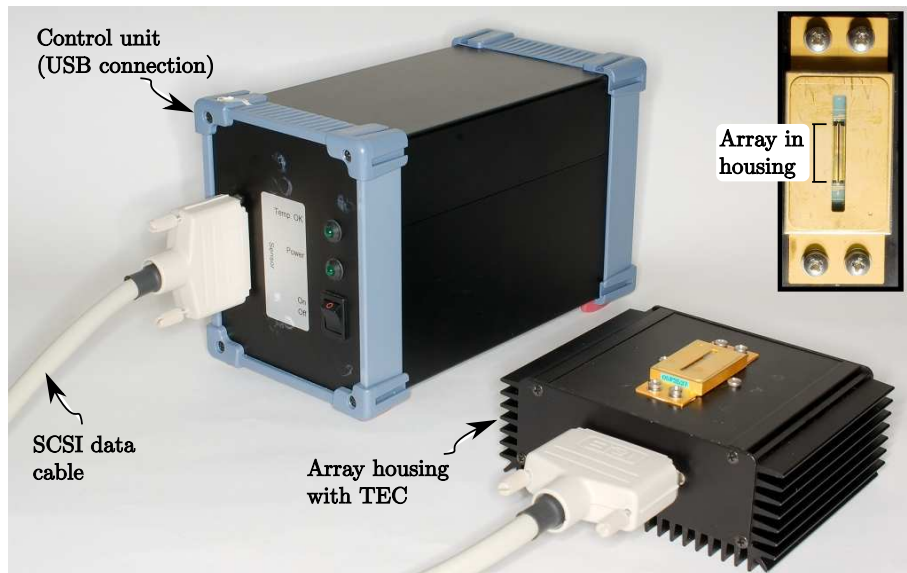


**Figure 3.5:** InGaAs array mounting with USB controller unit. Inset shows array in housing.

controlled by a customised LabVIEW program, based upon a supplied LabVIEW program from Tec5 Ag. The system had a maximum read-out time of 30 ms, but was performance limited by the hard-disk databus write speed on the controlling PC to  $\sim 80 - 100$  ms.

### 3.3.2 Newport plane diffraction grating

The diffraction grating governs the maximum spectral resolution of the Spectro-Bragg. The mirror  $M_2$  allowed the tuning of the linear resolution provided by the diffraction grating, by adjusting the parameter  $R$  in figure K.11 (page V.II K-16) and equation (K.30) (page V.II K-17). The mirrors are discussed in the next section, §3.3.3. The design requirement of a small area footprint also restricts the diffraction grating choice.

The larger the number of grooves/mm the larger the dispersion achieved. As the number of grooves/mm approaches the design wavelength, the angles at which diffracted radiation remain real decrease for non-normal incidence, as shown in figure 3.6. These considerations for the SpectroBragg are discussed in §3.4.1.3 (page V.I - 152).

For the calculation of figure 3.6, equation (K.27) (page V.II K-15) was rearranged in terms of  $r$ . An  $M_2$  width of 50 mm was assumed for  $w_{\text{total}}$ , as the largest, cheapest mirrors available were of 50 mm diameter. The mirrors are discussed in the next section, §3.3.3. The full mirror width was taken, so the angles shown are the maximum possible from equation (K.27) (page V.II K-15).

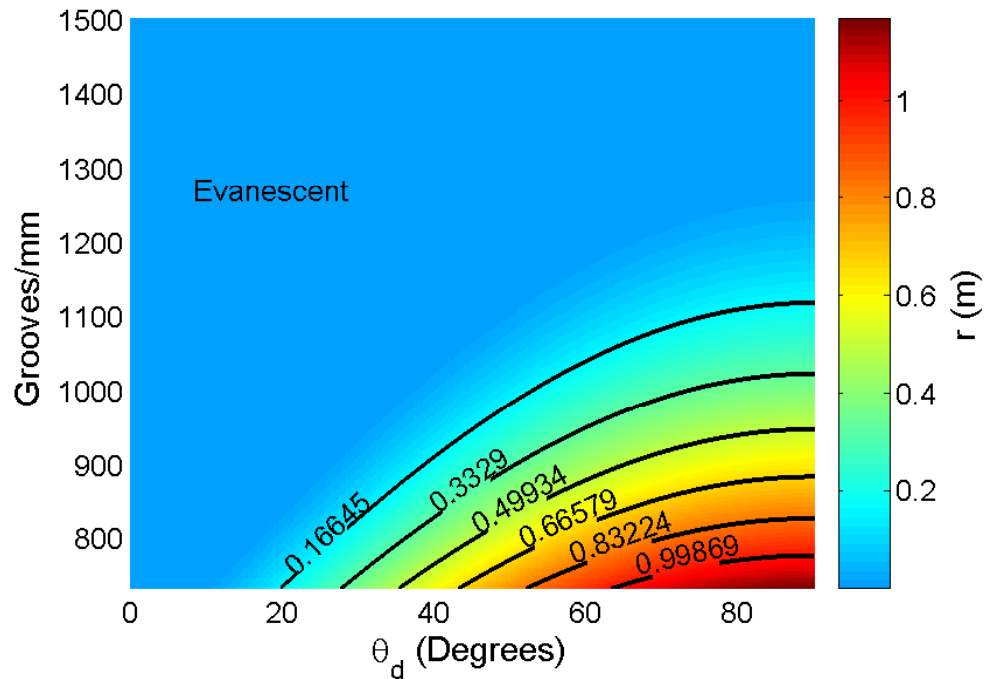


**Figure 3.6:** The distance between the diffraction grating and  $M_2$ ,  $r$ , shown when plotted against diffraction grating grooves/mm and diffracted angle,  $\theta_d$ . The value of  $r$  is obtained by rearranging equation (K.27) (page V.II K-15) in terms of  $r$ . The constant blue area denotes complex (evanescent) diffracted angles. To obtain a smaller  $\theta_d$  a smaller number of grooves/mm is desirable.

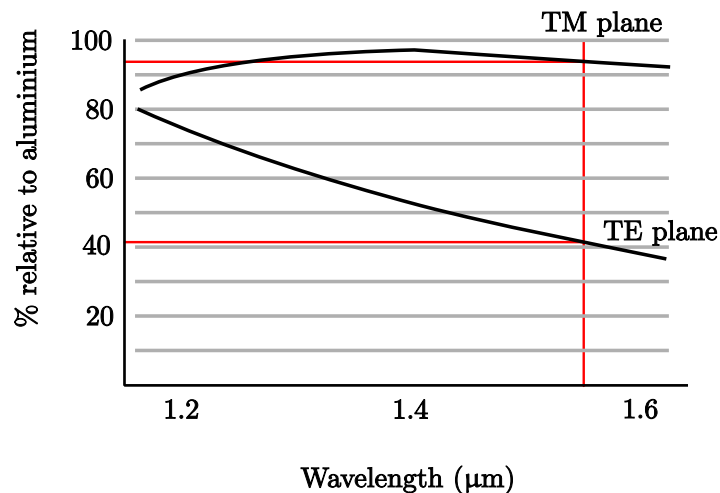


**Figure 3.7:** Diffraction Grating polarisation efficiency curves for telecomms region, after Newport efficiency curves for 53-\* -175H grating. ([http://gratings.newport.com/products/efficiency/effFrame.asp?sku=020\\$|53-\\* -175H](http://gratings.newport.com/products/efficiency/effFrame.asp?sku=020$|53-* -175H))

The diffraction grating chosen needed to have at least the same dimensions as the mirrors, so a minimum size of 50 mm was required. Again, the cheapest high-quality holographic diffraction gratings available at the required size were sought. Newport holographic diffraction gratings met the requirements. Gratings available and recommended for use in the telecomms bands were 750, 900, 1050, 1200, 1312 and 1350 grooves/mm. In order to keep the incident and diffracted angles as small as possible, and the aberrations at a minimum, the 750 grooves/mm grating was selected.

The diffraction grating used is described in table 3.1. The TE and TM diffraction efficiencies are shown in figure 3.7.

catalogue number	53067BK01-175H
serial number	5218-1-2-1-1-2-2-5
grooves/mm	750
blank material	BK
coating	Aluminium
Recommended Spectral Region	850 nm – 2.3 $\mu$ m
Wavelength of Maximum	1.2 $\mu$ m
Efficiency (unpolarised)	
Ruled area <sup>15</sup>	46 $\times$ 46 mm
Blank size <sup>16</sup>	50 $\times$ 50 $\times$ 10 mm

**Table 3.1:** Newport specifications for SpectroBragg diffraction grating.

### 3.3.3 Concave mirrors

The optimum angles that  $M_1$  and  $M_2$  are oriented at with respect to the diffracted design wavelength are determined by equation (3.18) (page V.I - 132). The positioning of  $M_2$  may also be restricted by the requirement that the diffracted or reflected beams not be obstructed by other components, nor obstruct the directed radiation of other components.

As shown in figure K.8 (page V.II K-14), the placement of  $M_2$  can reduce the resolution of the spectrometer when placed too near the diffraction grating, or spread a spectral feature across several array diodes. This may facilitate post-processing based super-resolution when placed further from the diffraction grating, but achieving a lower SNR.

Conversely, the spectral bandwidth observed by the array is increased when  $M_2$  is closer to the diffraction grating and reduced when  $M_2$  is further from the diffraction grating.

<sup>15</sup>Groove length  $\times$  ruled width.

<sup>16</sup>Diameter or length  $\times$  width  $\times$  thickness.

The largest, cheapest mirrors available were of 50 mm diameter. The mirrors were available from Thorlabs and available in four focal lengths: 50, 100, 150, and 200 mm. A 150 and 200 mm lens were acquired.

The 150 mm mirror was used for  $M_1$  and the 200 mm mirror used for  $M_2$ , as the 150 mm mirror would obstruct other components.

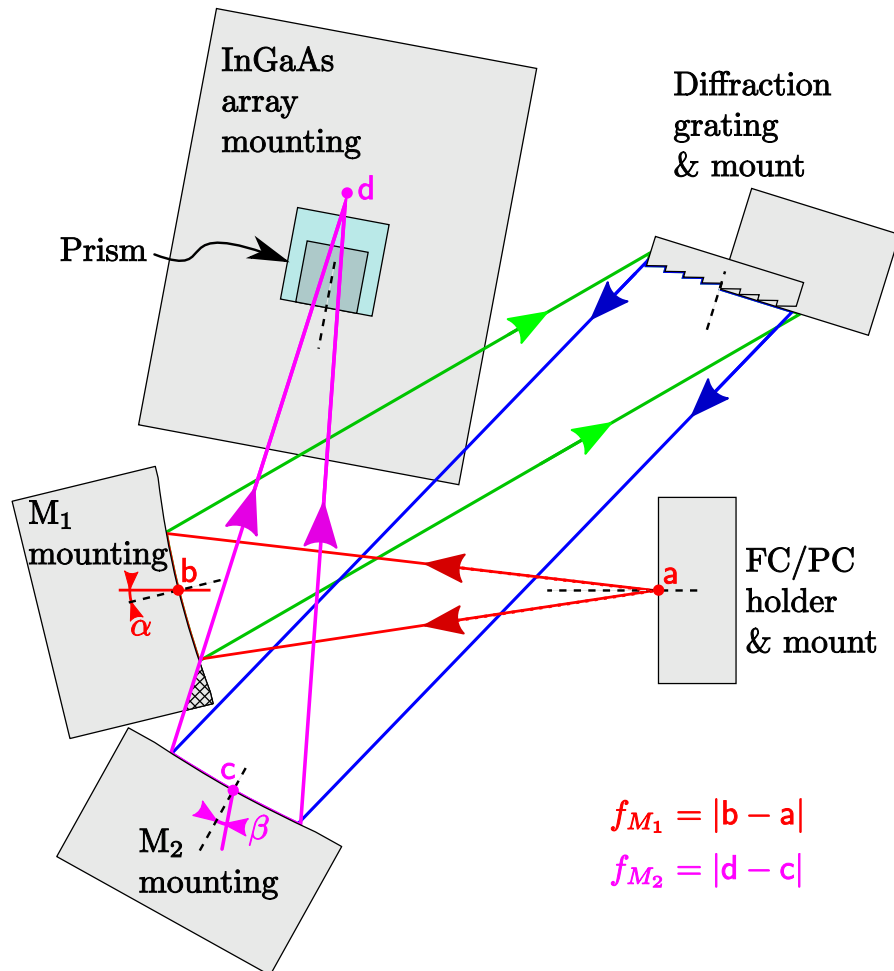


**Figure 3.8:** Block diagram of the SpectroBragg plan layout. The *FC/PC holder & mount* and *mirror  $M_1$*  are fixed relative to each other by the focal length,  $f_{M_1}$ , and angle  $\alpha$  (defined in figure 3.3, page V.I - 132). The *mirror  $M_2$*  and *InGaAs array* are fixed relative to each other by the focal length,  $f_{M_2}$ , and the angle  $\beta$  (figure 3.3). The diffraction grating has freedom to intercept the reflection from  $M_1$  along its path.  $M_2$  is restricted in the distance from the diffraction grating. The one area of overlap is highlighted by cross-hatching.

Figure 3.8 shows a block schematic of the SpectroBragg layout. The blocks encompass the plan area occupied by the component and its mounting. The mirror  $M_1$  is fixed with respect to the FC/PC holder and its mount by the angle  $\alpha$ , figure

3.3 (page V.I - 132), and  $f_{M_1}$ . The mirror  $M_2$  is fixed with respect to the InGaAs array by the angle  $\beta$  and  $f_{M_2}$ , and with respect to the diffraction grating by the length  $r$  and the requirement that  $\alpha$  be collinear with  $\theta_d(\lambda_{\text{design}})$  at the centre points of  $M_2$  and the diffraction grating.

The placement of the diffraction grating with respect to  $M_1$  is the largest degree of freedom. However, taking aberrations into account, the distance should not be very large. For the SpectroBragg two considerations restricted the length between  $M_1$  and the diffraction grating. The first was the requirement for the SpectroBragg to have as small a footprint as possible. The second was the need to keep the components as close to the edge of the optical bench as possible<sup>17</sup>.

The one area of overlap has been coloured yellow. This was minimised in terms of its impact by the fact that the cross-section of the beam was approximately Gaussian, and so less energy was contained in the obstructed part of the beam. Additionally, the  $M_2$  mount did not occupy the full footprint shown, at the 75 mm optical plane. No other position provided less obstruction.

The two concave mirrors were supplied by Thorlabs. One mirror had a focal length of 150 mm and the other of 200 mm. This allowed for flexibility in the resolution at the array plane. The mirrors were based on a N-BK7 blank, then ground to shape. The ground surface was coated with aluminium and a thin layer of  $\text{SiO}_2$  placed onto the metal to protect the metal finish.

The common mirror specifications are given in table 3.2:

Clear aperture	> 90% of diameter
Front surface flatness	< $\lambda/4$ at 633 nm
Front surface quality	40–20 scratch-dig
Diameter tolerance <sup>18</sup>	+0.0 / – 0.2 mm

**Table 3.2:** Thorlabs specifications for SpectroBragg Mirrors.

### 3.3.4 Prism

The prism was employed to direct the signal perpendicular to the spectrometer optical plane, as the InGaAs array mount was more stable parallel to the optical bench. The prism also reduced the accumulation of dust onto the cover-slide over the array. The prism used was of unknown origin. It is likely to be made of BK7, but this cannot be confirmed. It was the only right-angle prism available for this work.

<sup>17</sup>This requirement is discussed further in §3.3.5.

<sup>18</sup> $R_{\text{avg}} > 90\%$  from 400 nm to 10.0  $\mu\text{m}$ .

The prism also had the indirect advantage of preventing stray light in the optical plane from impinging upon the array, unless the light entered the prism. In this regard it behaved as an aperture or stop.

Prisms are frequently used to provide negative dispersion to the diffraction grating, to tailor the diffraction based dispersion. As this prism was of unknown material, the dispersion aspect of the prism is unknown, and cannot be considered as part of the design.

A potential approach to extending the bandwidth of the SpectroBragg was to use the vertical triangular facets of the prism as mirrors to extend the span that could be demodulated. The triangular facets could be silvered if necessary, to achieve the reflection of the diffracted beam. The SpectroBragg would then switch between the original and reflected bandwidths, possibly by using a fibre switch. The prism available had ground glass (frosted) triangular faces to facilitate handling of the prism. A product search for clear or mirrored triangular facets failed to locate any prism suitable for the project.

### 3.3.5 SpectroBragg Apparatus construction

The construction of the SpectroBragg was complicated (compared to constructing interferometers) by the need to align several components in relation to the preceding components using large angles with converging and diverging beams. Each component could be configured with relative ease with respect to one neighbouring component in isolation, where available space was not an issue. However, the subsequent component became substantially more difficult to align with equal accuracy, as space was now restricted. Additionally, the expanded beam had low intensity, which required a darkened environment; the effect of this was that positioning and alignment occurred in the near-dark making locating equipment and accurately fixing it with clamps difficult. To compound the difficulties, the SpectroBragg spectrometer design was to be as compact as possible, occupying a small area footprint, limiting the space available for alignment.

The apparatus was constructed at the corner of an optical bench to minimise the influence of acoustic noise vibrations on the spectrometer. The optical bench used did not meet the manufacturer's vibration claims, and was likely to have been faulty. As such, certain acoustic modes were not effectively damped. By placing the apparatus at the corner, the amplitude of any vibrations would be minimised.

The assembly steps taken to complete the SpectroBragg are detailed in appendix §L.3 (page V.II L-4). The use of the optical components employed in the assembly is not typical of spectrograph design. The unwanted degrees of freedom retained by the commercial off-the-shelf components added significantly to the time needed

for assembly. The most detailed advice for assembly and alignment that was found in the literature was given in [43]. The advice is, to have the people creating the spectrograph optical table, drill holes into the optical table to facilitate alignment.

The Čzerny–Turner design was not a crossed Čzerny–Turner, despite the appearance.  $\theta_d$  was smaller than  $\theta_i$  so that the spectrometer layout appears crossed, as shown in figure 3.9. The assembled SpectroBragg is shown in figure 3.10.

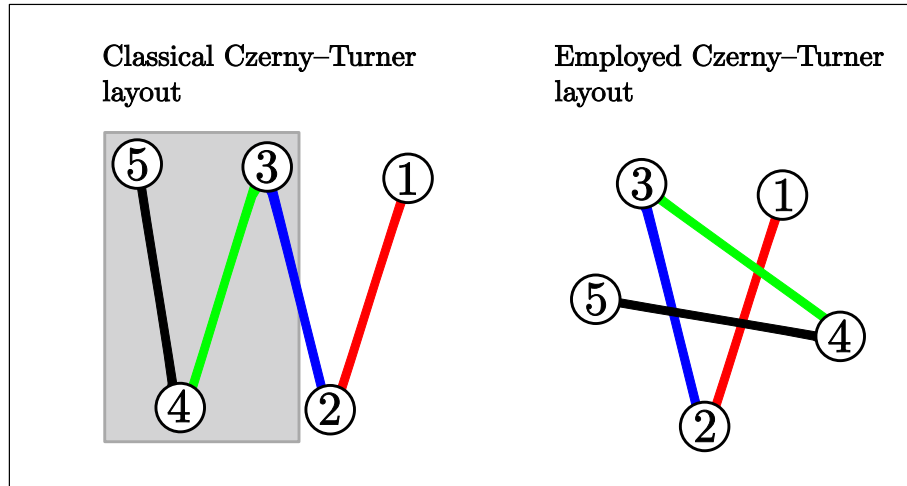


**Figure 3.9:** Schematic layout of the Čzerny–Turner spectrometer arrangement, due to diffracted angle of 1550 nm radiation. The numbers are as in figure 3.10.

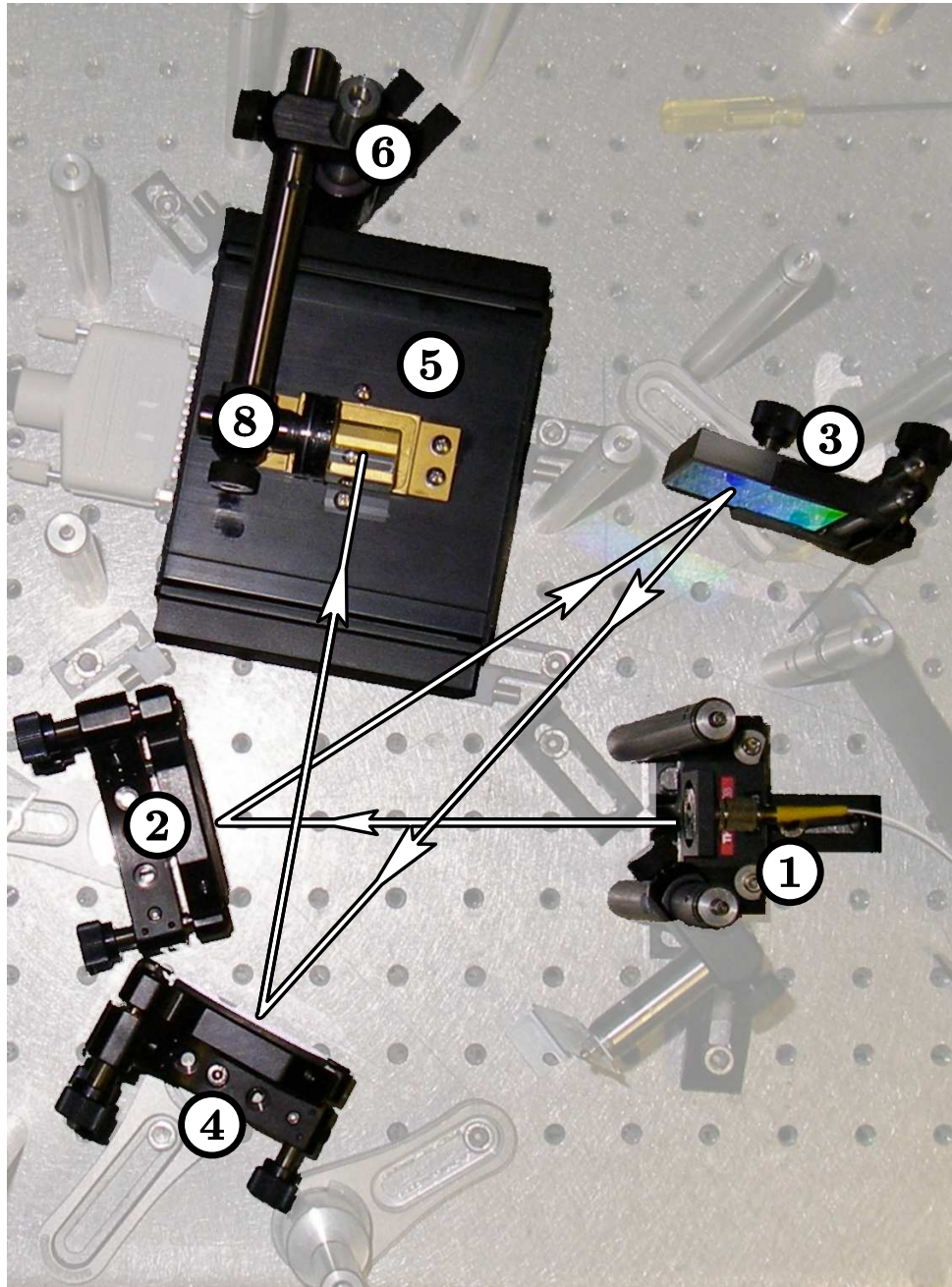


**Figure 3.10:** The assembled SpectroBragg apparatus, emphasised against the associated apparatus.

- 1: AMA025/m platform with HFB003 FC/PC fibre holder,
- 2: Collimating mirror KS2D,
- 3: Diffraction grating mount,
- 4: Focusing mirror KS2D,
- 5: Photodiode array mount,
- 6: KL02 kinematic positioner,
- 7: Prism mount,
- 8: Prism.

## 3.4 Results/Discussion

### 3.4.1 SpectroBragg Construction

The aim of the SpectroBragg work was to produce a small footprint spectrograph, that operated natively in the telecomms IR bands and would allow the use of components developed for the telecomms industry to be employed. The use of the telecomms IR bands would allow distributed and remote sensing arrangements to be demodulated. The design chosen can be described as compact [14], i.e.  $< 1/4$  m, as the largest focal length is  $1/5$  m.

The SpectroBragg design was to obtain sub-picometre resolution through post-processing, while providing a wide operational spectral bandwidth. These are not complementary objectives, with gains in one limiting the other.

The SpectroBragg should minimise aberrations as far as was possible. The presence of aberrations could limit the free-spectral range of sensors demodulated by the device. Additionally, severe aberrations could introduce profile changes that would adversely affect the post-processing to achieve super-resolution.

The SpectroBragg components were aligned using both 635 nm and 1550 nm radiation, up to the diffraction grating. Thereafter, only 1550 nm radiation was suitable. An IR card was used for the visualisation of the 1550 nm radiation. The assembly of the SpectroBragg, with all alignment steps is detailed in appendix §L.3 (page V.II L-4).

#### 3.4.1.1 SpectroBragg assembly angles

The Rosendahl equation (3.18) (page V.I - 132) was used to determine the optimum angles  $\alpha$ ,  $\beta$  and  $\theta_i$  for a design wavelength of 1550 nm. The three independent variables do not allow a unique solution to be obtained. The layout shown in figure 3.10 shows that the angle  $\alpha$  was constrained by the entrance aperture obstructing  $\theta_d$ . The minimum value of  $\alpha$  that could be used was therefore set by the equipment. Figure 3.11 shows the parameter  $\beta$  numerically evaluated<sup>19</sup> for the four values of  $\alpha = \frac{\pi}{100}, \frac{\pi}{50}, \frac{\pi}{10}, \frac{\pi}{6}$ . Using both the physical constraints and equation (3.18) (page V.I - 132) the angles used were  $\alpha \sim 15^\circ$ ,  $\theta_i \sim 47^\circ$  and  $\beta \sim 18^\circ$ . The angles were achieved to within the measurement accuracy of the equipment available.

---

<sup>19</sup>The other quantities from equation (3.18) (page V.I - 132) were  $R_1 = 15$  cm,  $R_2 = 20$  cm, and  $\theta_d$  obtained from equation (3.8) (page V.I - 124), with  $m = 1$  and  $d = 750$  grooves/mm.

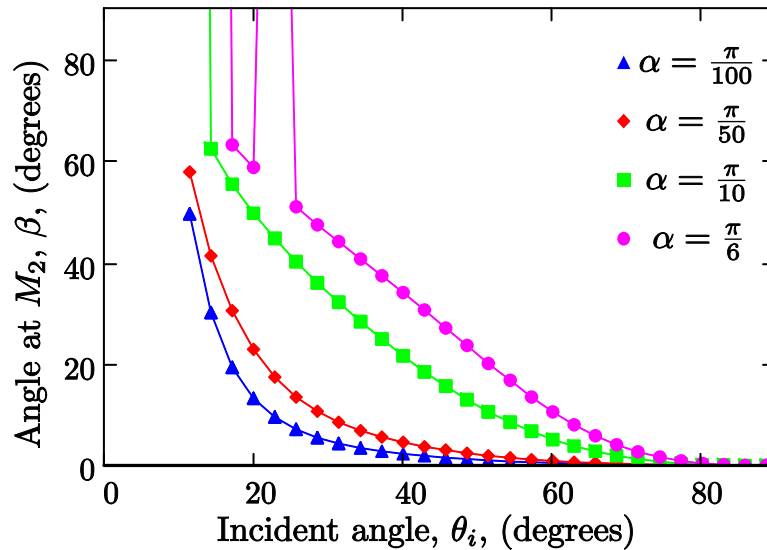


**Figure 3.11:**  $\beta$  evaluated using the Rosendahl  $\cos^3$  equation, (3.18) (page V.I - 132), for four values of  $\alpha = \frac{\pi}{100}, \frac{\pi}{50}, \frac{\pi}{10}, \frac{\pi}{6}$ .

### 3.4.1.2 SpectroBragg wavelength angles

The use of the 0.15m mirror for  $M_1$ , with a fibre numerical aperture of 0.14<sup>20</sup> resulted in a spot diameter at the focal length of  $\sim 40$  mm, while the diameter of the mirror is 50.8 mm, which made the fibre aperture the field stop<sup>22</sup> prior to the diffraction grating<sup>23</sup>. The ruled surface of the diffraction grating was  $46 \times 46$  mm, but at the assembled angle of  $\sim 43^\circ$  presents a surface of  $\sim 33.6 \times 46$  mm

The use of commercially available off-the-shelf, COTS, parts enabled the SpectroBragg to be constructed with cheap components (apart from the array). The disadvantage of the use of general purpose components was the unwanted degrees of freedom present during assembly [44]. These degrees of freedom, and the ability to measure them, contributed to the aberrations present in the final design, but were unavoidable given the measurement and alignment capabilities during the assembly. For example, the protractor used to determine the angles was accurate to the degree mark, but the calculated angles could not be accurately marked upon the optical table.

The focusing mirror  $M_2$  will not reflect equal radiation for uniformly illuminated diffracted orders for all wavelengths. At a certain angle the mirror clipped the diffracted spot beam. Mirror  $M_2$  was at a distance of  $\sim 0.24$  m from the diffraction

<sup>20</sup>Strictly quoted for 1310 nm<sup>21</sup>, but should not differ significantly at 1550 nm, so as to alter the result.

<sup>22</sup>The field stop is the effective aperture experienced by the radiation.

<sup>23</sup>The ellipse presented by the angling of the mirror at  $\sim 15^\circ$  had a minor axis length of 49.1 mm; thus, it did not affect the conclusion.

grating. The diffracted angles for 1535 nm and 1567 nm differed from 1550 nm by approximately  $\sim -0.73^\circ$  and  $\sim 0.83^\circ$ , respectively. A representation of the geometrical clipping is shown in figure 3.12.

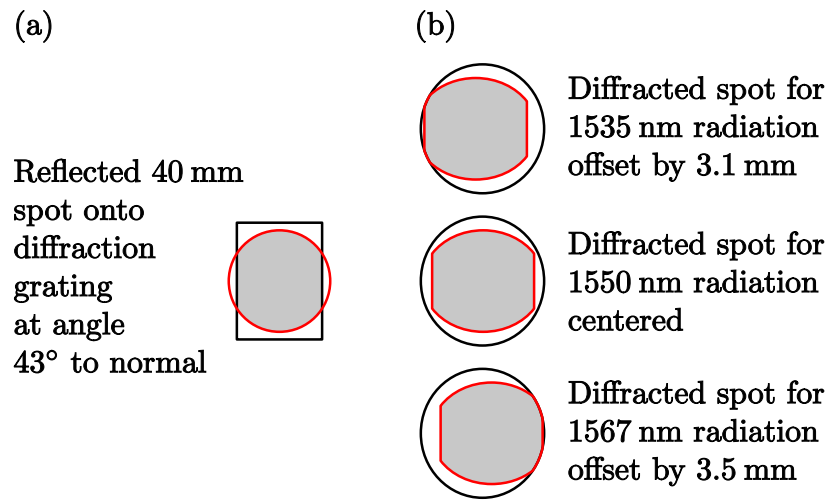


**Figure 3.12:** (a) Approximate graphical representation of the collimated spot overlap with the diffraction grating area. (b) Representation of overlap of the focusing mirror and the propagating diffracted first order,  $m = 1$  spots for wavelengths 1535 nm, 1550 nm and 1567 nm at the respective diffracted angles.

The location of the best focal distance is  $\left(1 - \frac{1}{\sqrt{3}}\right) R_2 = 0.42R_2 \sim 0.17$  m from [14], where  $R_2$  is the radius of curvature of  $M_2$ . This provides the best approximation to a planar focal surface. The positioning of the prism and array as independent objects made it difficult to measure distances from the mirror surfaces. The array was placed where the brightest spot was obtained. The two astigmatic focal points were determined and the array and prism placed roughly midway between these extremes, approximately 1 cm apart. Then the array and prism were moved until the circle of least confusion was found, providing the maximum energy density at the pixel.

### 3.4.1.3 Evanescent orders

The first grating considered for the SpectroBragg was a 1100 lines/mm grating of the same width and height. The dispersion of the 1100 lines/mm grating would allow for a shorter focal length for mirror  $M_2$ . The range of diffracted angles was

limited as the diffracted orders became evanescent, as shown in figure 3.13 for a design wavelength of  $\lambda = 1550$  nm. The propagating/evanescent cutoff is illustrated by the red line.

The limited diffracted angles, coupled with the need for the diffracted radiation not to be obstructed by subsequent components, caused the 1100 lines/mm grating to be unsuitable.

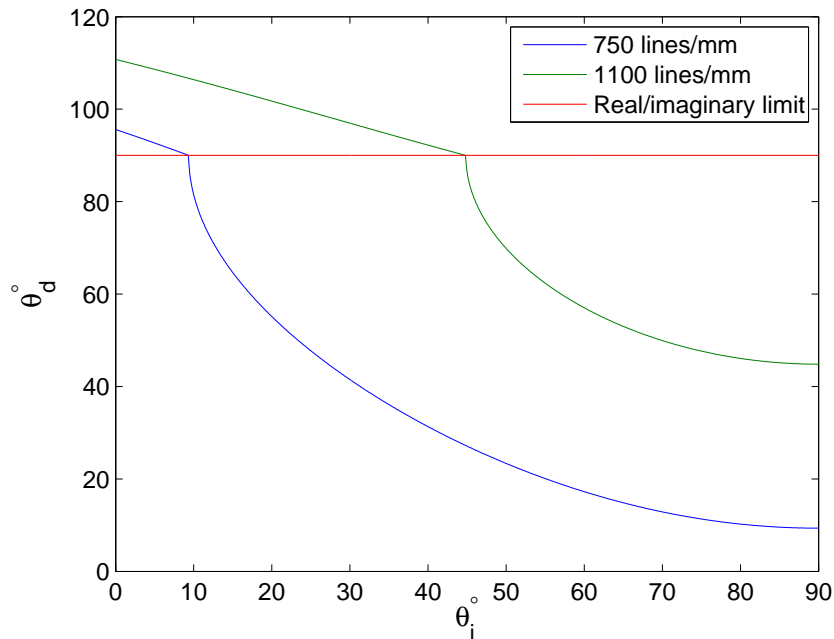


**Figure 3.13:** Plot of propagating and evanescent diffracted angle against incident angle, for first order,  $m = 1$ . Diffraction gratings with 750 lines/mm and 1100 lines/mm with  $\lambda = 1550$  nm.

It was calculated that the best diffraction grating would have  $\sim 650$  lines/mm and would need a focal length of 0.35 m to replace the intended resolution of the 1100 lines/mm grating. The closest available diffraction grating was at 750 lines/mm. Given the need to keep the size of the spectrometer as small as possible, the 0.35 m focal length was unsuitable in an uncrossed Čzerny–Turner.

It was decided to use the 0.2 m focal length mirror for  $M_2$  and the 0.15 m mirror for  $M_1$ . The linear dispersion curves for the (0.15 m, 1100 lines/mm) and (0.2 m, 750 lines/mm) arrangements are shown in figure 3.14.

The large angles needed for the 1100 lines/mm grating restricted the placement of components and resulted in severe changes in anamorphic diffracted image shape across the bandwidth of interest.

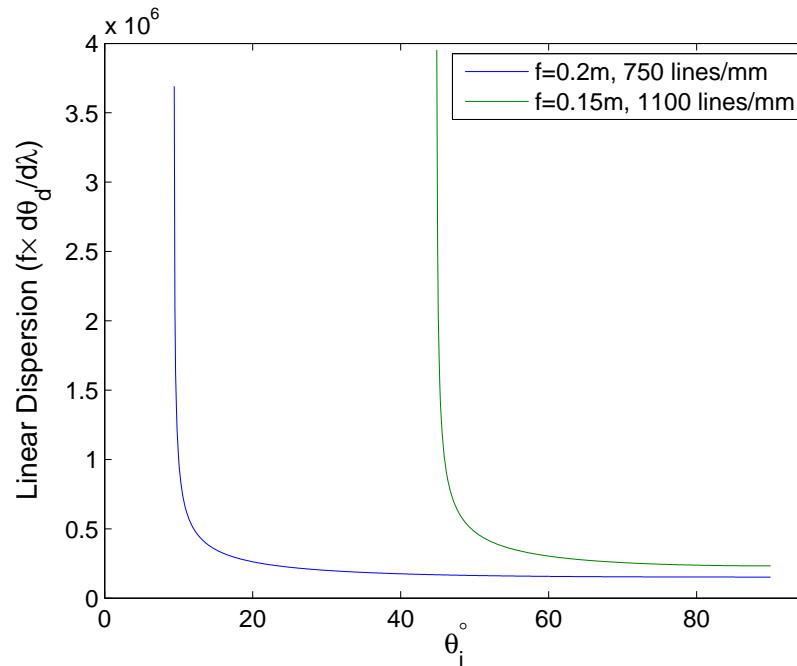


**Figure 3.14:** Plot of linear dispersion against incident angle, for first order,  $m = 1$ . Diffraction gratings with 750 lines/mm and 1100 lines/mm with  $\lambda = 1550$  nm.

### 3.4.2 SpectroBragg Signal processing

#### 3.4.2.1 Choice of algorithm

The centroid algorithm was chosen for both its speed and simplicity. Although susceptible to noise, the centroid algorithm did not suffer from the noise present in the SpectroBragg data more than the alternative algorithms. The computation time was also predictable, being a single iteration algorithm.

The non-linear regression curve fitting exhibited severe convergence issues. The magnitude of  $\lambda_{fit}$  can produce different convergence times with results of varying precision. It was not uncommon for a dataset fit with a small  $\lambda_{fit}$  to eventually fail to converge at one data profile. The larger the value of  $\lambda_{fit}$ , the faster the convergence but the greater the spread of the resulting data, as the convergence was prematurely stopped for some data profiles. The approximation of a function such as  $G$  or  $SG$ , using at most  $\sim 10$  data points, makes the convergence performance unpredictable.

The cubic spline interpolation approach was similarly sensitive on an individual data profile basis. The interpolation procedure's attempt to follow the data meant that noise could produce unpredictably large spikes that complicated wavelength determination using the first derivative of the spline. Restricting the current value to the region about the previous value did not aid in the elimination of spurious

peak values, as the noise about the base of the FBG or laser profiles produced large oscillations, as the spline attempted to fit to the rapid oscillations. The most effective approach to eliminating spurious peak values was to average many data runs to suppress individual noise fluctuations. This requirement made the cubic spline slower than the non-linear regression curve fitting at the data capture step, and did not provide much of an improvement over the centroid calculation.

### 3.4.2.2 SpectroBragg data capture

The SpectroBragg data were read over a USB2 connection by a custom LabVIEW program based upon a LabVIEW VI program supplied by Tec5. The program saved the data to disk in a binary format. Matlab was then used for signal processing.

The data capture PC limited the data capture speed. The data were written in binary format by the LabVIEW program to a single file for the duration of the experiment. The initial invocation of the program captured data close to the array speed of 30 ms; however it rapidly dropped to  $\sim 100$  ms after a few hundred iterations.

The transfer of data via USB2 to the data capture PC could be affected by interrupt requests within the PC. Consequently, it was not possible to be certain that the data would be uniformly sampled, as was the case with the National Instruments DAQ card used for the work in chapter 6, which had its own internal data buffer.

### 3.4.3 Preliminary SpectroBragg work

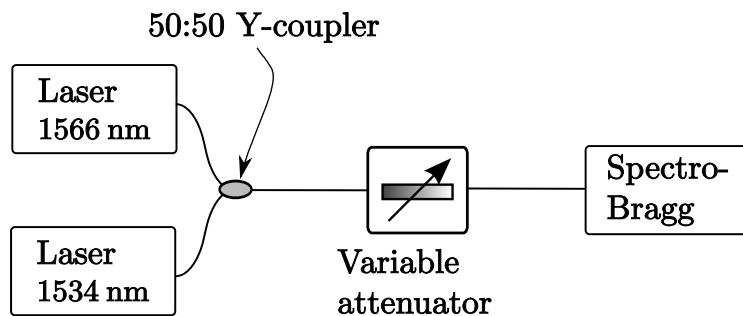
To determine that the SpectroBragg would provide a locally linear response, and determine the temporal stability of the system, three Thorlabs WDM telecomms lasers at 1535 nm, 1549 nm and 1566 nm were used. The telecomms lasers were tuneable over a  $\pm 1$  nm range. The performance of the SpectroBragg was characterised at the centre, 1549 nm, and near the edge<sup>24</sup>, 1566 nm, of the array. The experimental arrangement is illustrated schematically in figure 3.15.

Figure 3.16 shows the captured spectrum using the 1534 nm and 1566 nm lasers. The inset figure illustrates the offset voltage between the two 256 element interleaved arrays.

The time taken for the tuned laser to reach stability was several hours, as opposed to the quoted time of 15 min in the manufacturer's specifications. This was tested by observing a change in the tuned laser wavelength overnight, which approached a stable asymptote after  $\sim 8$  hours. The effect on the SpectroBragg could

---

<sup>24</sup>This was the furthest from the design wavelength of 1550 nm for which a stable source was available.



**Figure 3.15:** Schematic arrangement to test temporal stability of the Spectro-Bragg and characterise linearity of local response.

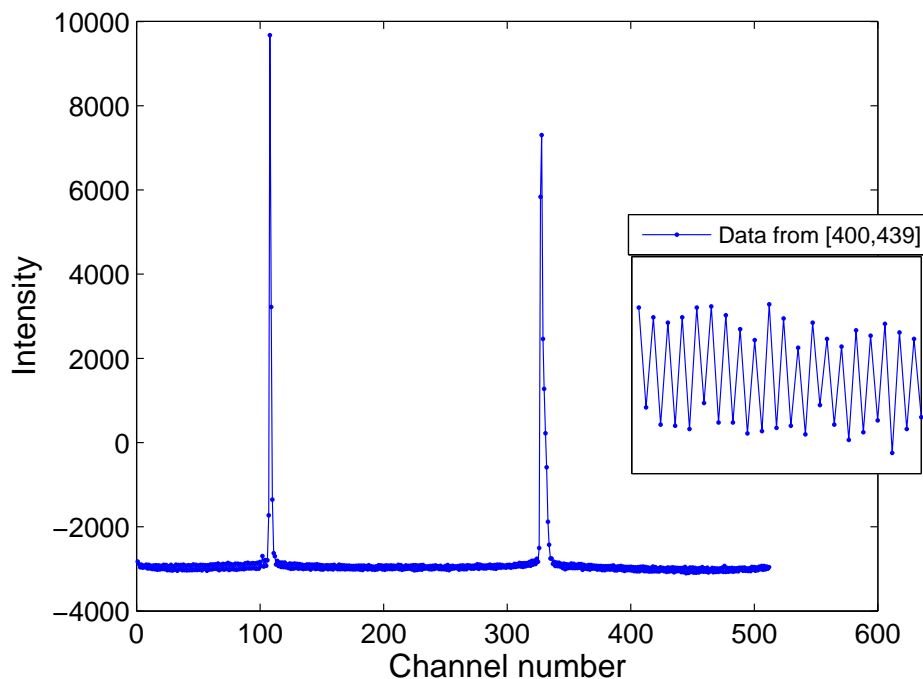


**Figure 3.16:** Two telecomms-band lasers were used for the SpectroBragg calibration, 1534 nm and 1566 nm. Inset shows the different background voltages from the interlaced 256 arrays, for channel numbers 400 – 439.

be minimised by waiting an hour for the laser to stabilise before taking data, as the rate of change was not significant over the experiment time scale of minutes.

It was also observed that the tuning dial on the telecomms laser control chassis had what appeared to be backlash, where the dial, when set to a value, was at a different position when arriving from a lower or higher value. It appeared, from testing, that the displayed resolution of 10 pm was less than that achieved by the tuning dial. This effect was minimised by only moving the dial slowly in one direction, until the display changed.

Both lasers were given what was considered to be sufficient time to reach internal equilibrium, after which 10002 frames were captured. The 1534 nm laser was kept constant, while the 1566 nm laser was increased by the minimum configurable step size of 10 pm in one direction. The stability of the 1534 nm laser would improve towards the asymptote over the datasets, while the 1566 nm laser only had an hour's stability.

The dataset was analysed using the centroid calculation on the central peak window. The profiles for the 1566 nm and 1534 nm lasers are shown in figures 3.17 and 3.18, respectively. The corresponding traces are indicated by the same colour.

It can be seen that the laser traces exhibit drifts over time and are not correctly located relative to each other. Two possibilities were considered; that the lasers were not yet at thermal stability and that the SpectroBragg had a (thermal) drift.

To determine whether the drift was introduced by the SpectroBragg itself, the 1566 nm laser was corrected by subtraction of the 1534 nm laser. Any systematic movements introduced by the SpectroBragg would then be removed. The recalibrated 1566 nm data is shown in figure 3.19. The temporal stability is improved for most of the traces, and their relative positions are correct. The systematic effects of the SpectroBragg dominated after the above steps were taken to minimise laser effects. Henceforth, a laser reference was used to provide correction for systematic drifts in the system<sup>25</sup>.

Two experiments were performed to determine the local linearity of the SpectroBragg response. The first was to analyse the above data by averaging the 10002 data points to return the mean centroid value in channel numbers. In order to scale the channel numbers to wavelength, the initial centroid positions of the 1566 nm

---

<sup>25</sup>The long wave systematic wavelength drifts were likely due to ambient temperature changes. The temperature of the laboratory could change faster than the laboratory air-conditioning would respond, e.g. when a door was left open. Additionally, the air-conditioning thermostat sensitivity would have allowed small changes to occur beneath its minimum sensitivity. The optical bench would have expanded or contracted during these small changes. The short wave oscillations are likely of acoustic origin. As stated, the bench displayed a strong acoustic resonance at the lower end of the human voice range. An opaque, cardboard box was placed over the SpectroBragg to protect it, prevent stray light entering and limit dust deposition on the components. It is possible that acoustic standing waves could have formed within the box, adding to vibrations.

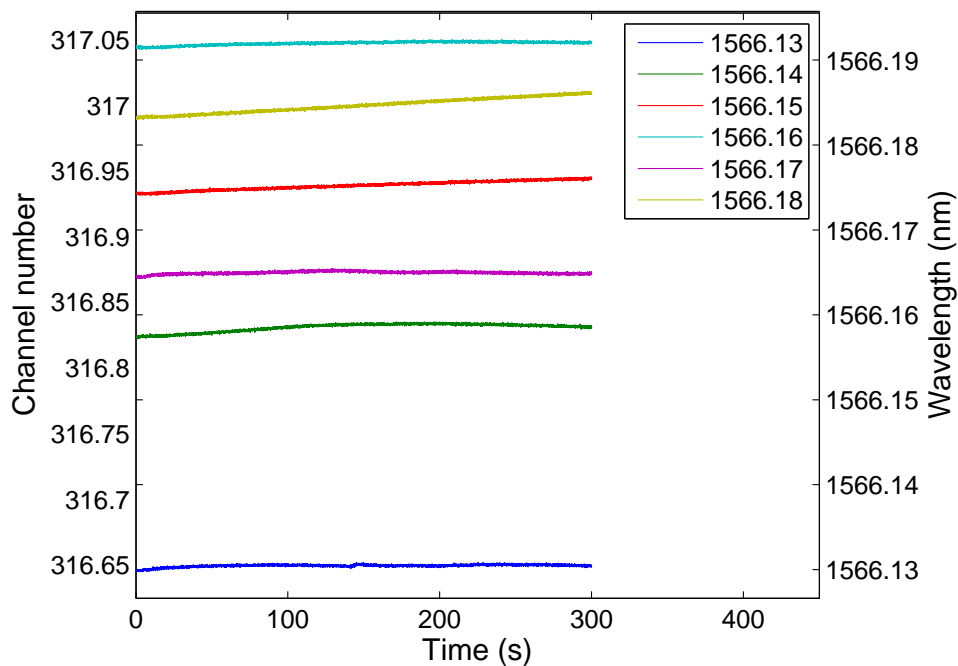


**Figure 3.17:** SpectroBragg stability test, laser tuned from 1566.13 nm to 1566.18 nm in 10 pm steps.

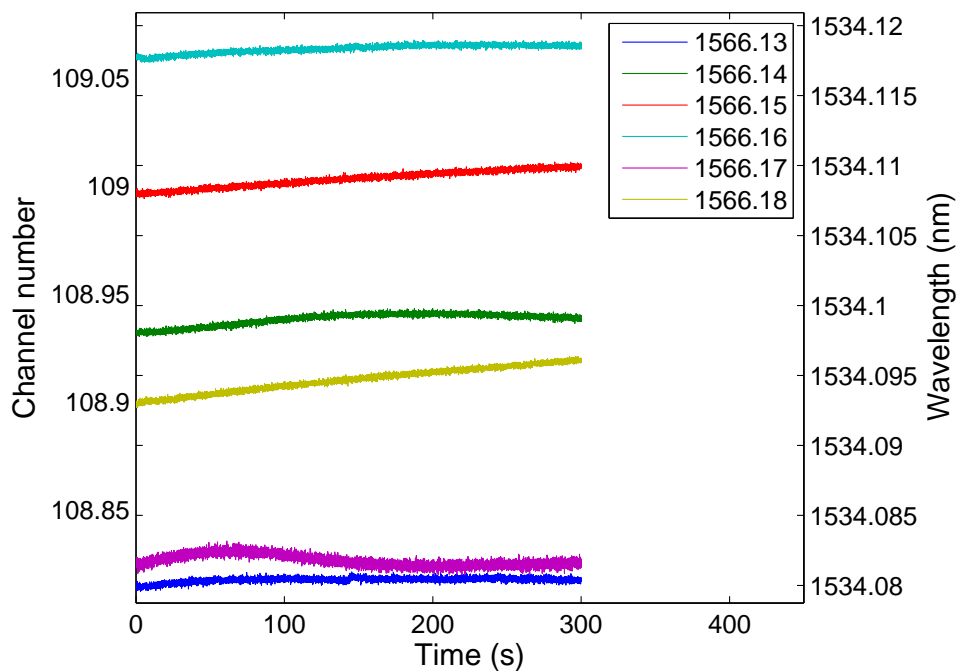


**Figure 3.18:** SpectroBragg stability test, the reference traces of the 1534.08 nm laser. The colours correspond to traces in figure 3.17.

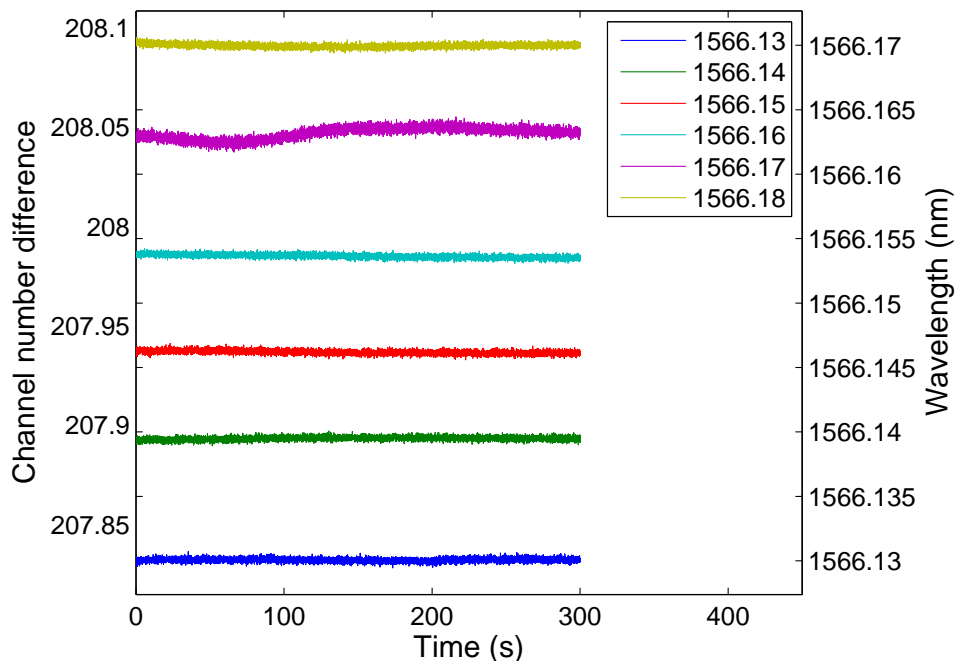


**Figure 3.19:** 1566.13 nm to 1566.18 nm recalibrated by subtraction of corresponding 1534.08 nm data.

Set Wavelength (nm) $\pm$ 0.01 nm [45]	Calculated Wavelength (nm)	Standard deviation (pm)	slope of fit (channel number/s)
1566.13	1566.130	0.15	0.001
1566.14	1566.139	0.15	0.04
1566.15	1566.146	0.16	-0.08
1566.16	1566.153	0.17	-0.11
1566.17	1566.163	0.47	0.35
1566.18	1566.169	0.16	-0.02

**Table 3.3:** Mean calculated centroid wavelength, standard deviation and slope of linear fit to channel number against time plots for set wavelength data shown in figure 3.20.

and 1534 nm lasers were taken to be equal to 1566.13 nm and 1534.08 nm, and that scale applied to the other data. Figure 3.20 shows the plot of the mean over the 10002 data for each calculated wavelength against the set wavelength from the tuneable laser. The values are tabulated in table 3.3. The wavelength accuracy of the tuneable laser is 10 pm [45], which is  $\sim 10^2$  larger than the associated standard deviations obtained from the 10002 data points. The slopes of the linear fits to the data in figure 3.19 are also tabulated.

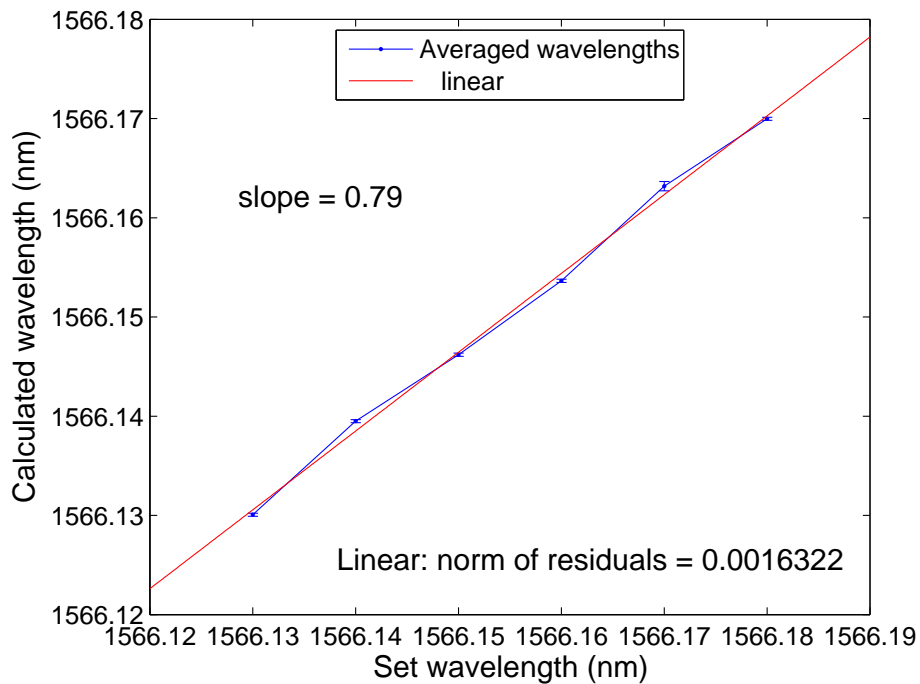


**Figure 3.20:** Recalibrated 1566.13 nm to 1566.18 nm data averaged, with corresponding standard deviations against set wavelength values. The oscillation about the linear fit is possibly as a result of backlash in the tuneable laser tuning dial.

To determine the performance at the centre of the SpectroBragg the 1566 nm laser in figure 3.16 (page V.I - 156) was replaced with a tuneable 1549 nm laser. Figure 3.21 shows the captured spectrum using the 1534 nm and 1549 nm lasers which is not dissimilar to figure 3.16, in terms of the spectral profile at 1549 nm.

Data were captured for a series of 10 pm steps. Using the 1534 nm data as a reference, the recalibrated 1549 nm data is shown in figure 3.22. The irregular step sizes shown may have been due to the backlash of the laser dial, despite efforts to minimise it.

The mean over the 10002 data for each wavelength against the set wavelength from the tuneable laser is tabulated in table 3.4 and shown in figure 3.23.

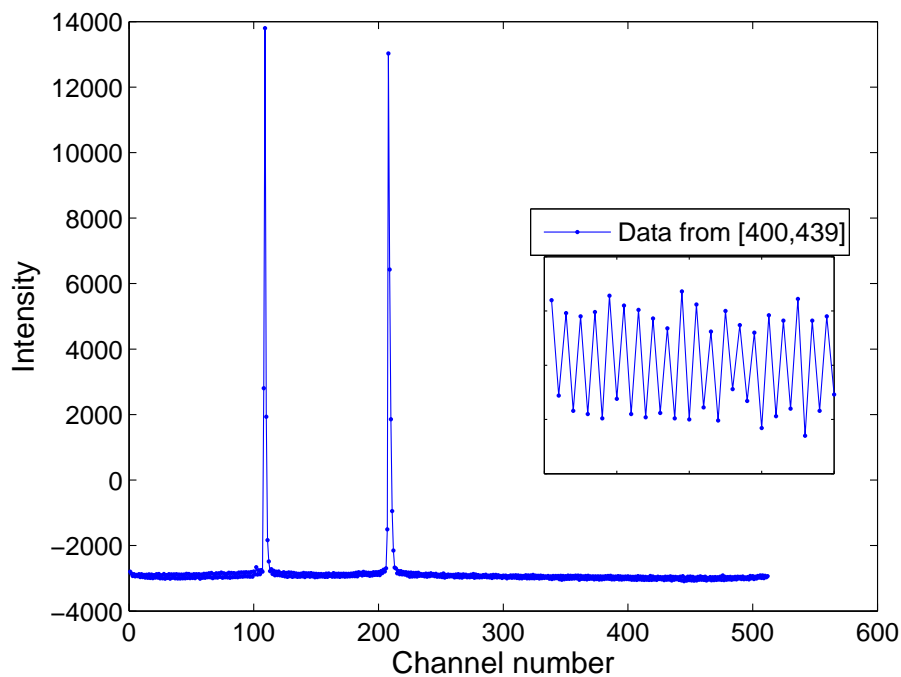


**Figure 3.21:** Two telecomms lasers for the SpectroBragg calibration, 1534 nm and 1549 nm. Inset shows the different background voltages from the interlaced 256 arrays, for channel numbers 400 – 439.

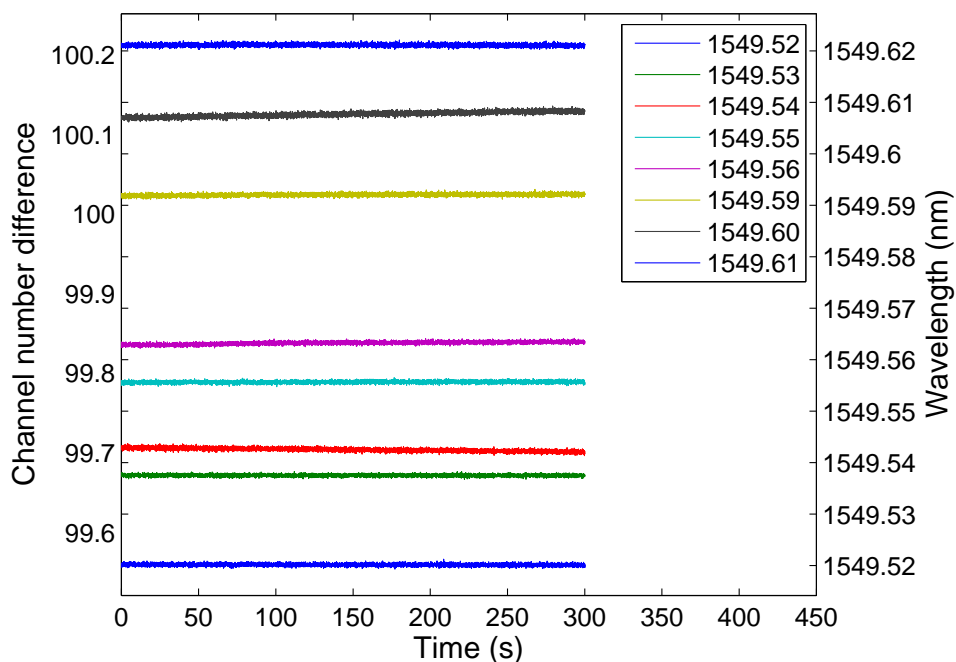


**Figure 3.22:** 1549.52 nm to 1549.61 nm recalibrated by subtraction of corresponding 1534.13 nm data.

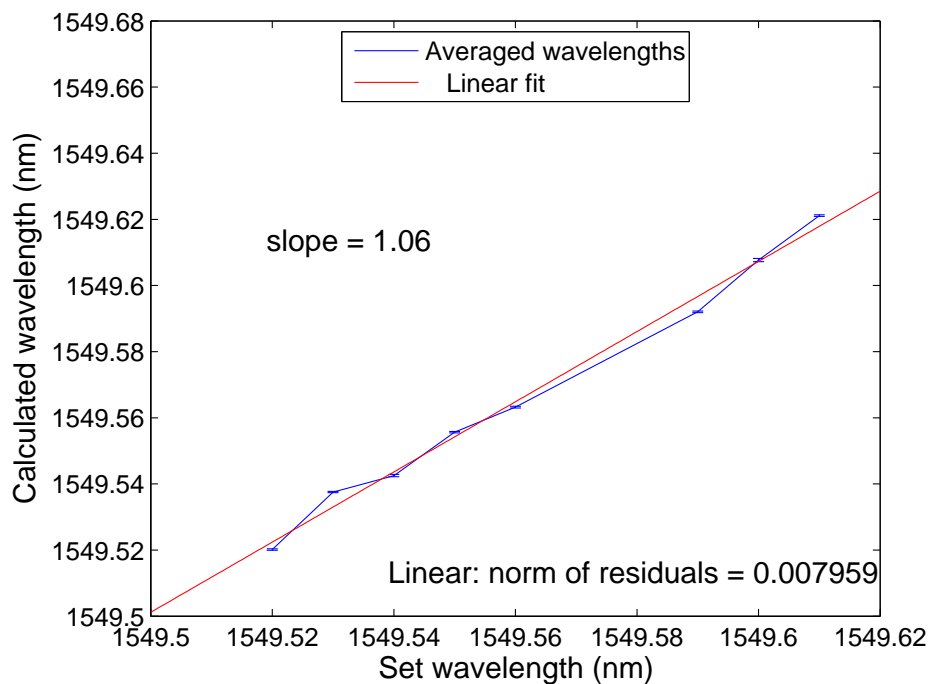


**Figure 3.23:** Recalibrated 1549.52 nm to 1549.61 nm data averaged, with corresponding standard deviations against set wavelength values.

Wavelength (nm)	Calculated Wavelength (nm)	Standard deviation (pm)	slope of fit
1549.52	1549.520	0.22	-0.04
1549.53	1549.537	0.19	-0.01
1549.54	1549.542	0.34	-0.29
1549.55	1549.555	0.22	0.05
1549.56	1549.563	0.28	0.20
1549.59	1549.592	0.25	0.09
1549.60	1549.607	0.48	0.45
1549.61	1549.621	0.25	-0.03

**Table 3.4:** Mean calculated centroid wavelength, standard deviation and slope to linear fit of set wavelength data shown in figure 3.23.

The standard deviation is effectively unchanged between the two lasers at 1549 nm and 1566 nm. The slopes of the linear fits to the traces over time are comparable; however, the slope of the wavelength response is different. The slope of the wavelength response of the SpectroBragg is nearly unity, 1.06, at the centre of the array. This is the design wavelength, and would be expected to have the best performance. At 1566 nm the slope of the wavelength response is 0.79.

The SpectroBragg spectrometer provided stable data once a stabilised reference system was used.

### 3.4.3.1 Sub-picometre system resolution

The next phase in characterising the SpectroBragg was to determine the maximum resolution that could be obtained via the signal processing. The ‘native resolution’<sup>26</sup> of the array was, on average,  $\sim 0.13$  nm. The intent of this work was to obtain sub-picometre system resolution, i.e. super-resolution, via signal processing.

The tuneable lasers, which had a configurable resolution<sup>27</sup> of 10 pm, were unsuitable for this part of the experiment. The laser could be used as a reference as the quoted stability of  $< 2$  pm over 24 hours would be sufficient for the duration of the data capture.

In order to provide wavelength changes smaller than that achievable with the tuneable laser, an FBG was strained with increasing strain increments that would provide sub-picometre wavelength changes<sup>28</sup>. The apparatus used is described in chapter 4, and shown in figure 4.10 (page V.I - 188). The apparatus is shown schematically in figure 3.24. A length of fibre  $\sim 1.3$  m long<sup>29</sup> containing the FBG to be strained was mounted onto a fixed platform at one end and a translatable platform at the other.

The translation stage was an Ealing MacroMech stage with a PMC encoder driver. The driver had a minimum movement resolution of  $0.02 \mu\text{m}$ . Using the linear strain equation (2.56) (page V.I - 39) provides a strain of  $0.7 \mu\epsilon$  for an extension,  $\Delta\ell = 1 \mu\text{m}$  over the fibre span length,  $\ell = 1.3$  m. Using the strain response of the anisotropic FBGs<sup>30</sup> discussed in chapter 4, of  $0.75 \times 10^{-6} \mu\epsilon^{-1}$ , gave a wavelength change of  $\sim 0.81$  pm.

A minimum visible step size of  $\Delta\ell = 0.5 \mu\text{m}$  produced a wavelength change of

---

<sup>26</sup>The ‘native resolution’ is the spectral range on the array divided by the number of pixels.

<sup>27</sup>As stated above, the lasers did seem to be tuneable below 10 pm, but without any indication on the display.

<sup>28</sup>The SpectroBragg was intended to operate with an FBG as instrument reference. Here, the advantage of the tuneable laser is the quoted specification of the wavelength stability. An FBG as instrument reference has the advantage of lower cost and being a passive device. The FBG’s broader profile would allow comparable determination of the reference and signal wavelengths.

<sup>29</sup>This was the longest continuous length of fibre available with an FBG.

<sup>30</sup>This preserved the spectral profile under the strain setting used in this work.

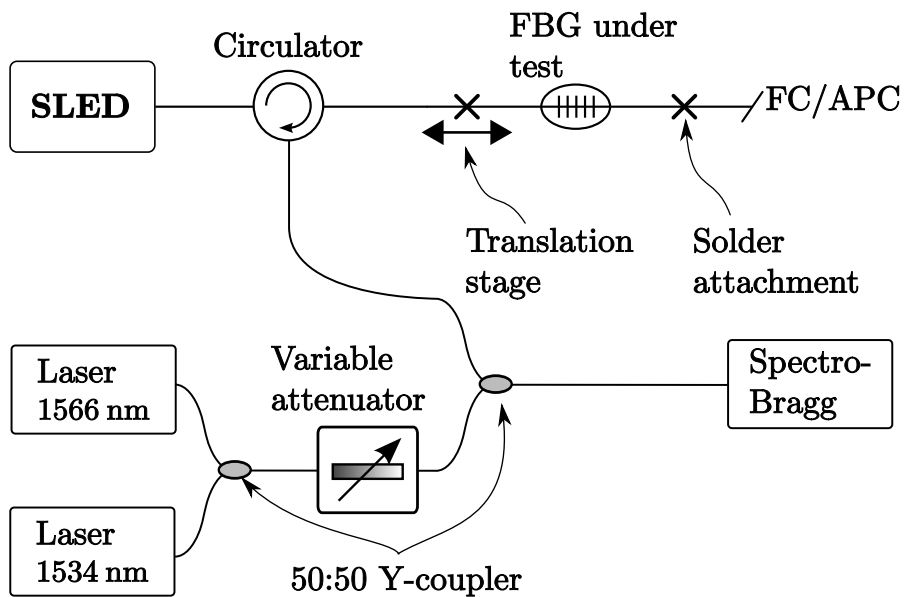


**Figure 3.24:** Schematic arrangement to determine the SpectroBragg sub-picometre resolution capability.

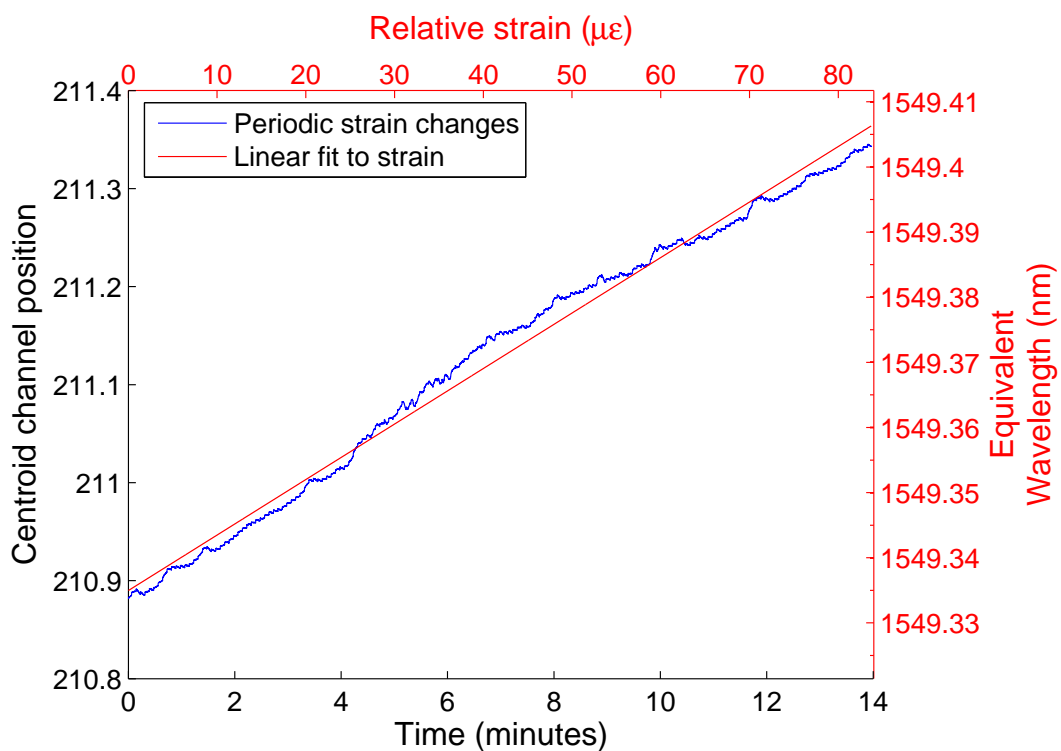


**Figure 3.25:** Strain steps of  $0.5 \mu\epsilon$  every 5 seconds.

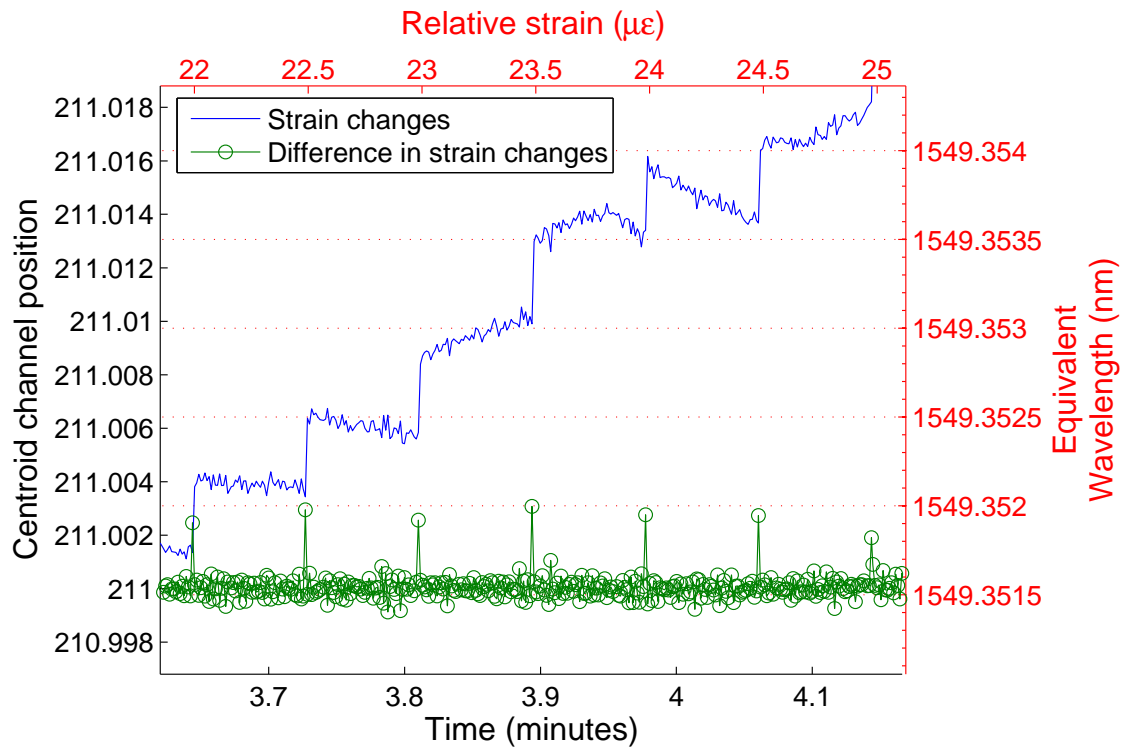


**Figure 3.26:** Magnified view of figure 3.25, with differences ( $i - (i - 1)$ ) for index  $i$ .

$\sim 0.4$  pm. Figure 3.25 shows the centroid calculated response for incremental steps of  $\sim 0.4$  pm every 5s over 14minutes. Figure 3.26 shows a magnified section with the centroid data differences. The differences are calculated by  $y_t - y_{t-1}$  for the centroid peak position,  $y$ , at time  $t$ . The changes in step are visible; hence, a resolution of  $\sim 0.4$  pm is possible. The stability requirements to employ this resolution for measurements of unknown measurands was not met by the laboratory conditions, and, hence, the minimum step size used in experiments was typically an order of magnitude greater.

A step size of  $\sim 0.2$  pm was attempted. The encoder driver was near the limits of its performance with this step size. The encoder would move by a regular number of counts when the step size was  $\sim 0.4$  pm, but failed to consistently register changes in counts at step sizes of  $\sim 0.2$  pm. The effect was for the stage to accumulate step increments and then move by the accumulated step size. The SpectroBragg may be able to observe wavelength changes lower than  $\sim 0.4$  pm, but it was not possible to test this with the equipment available.

The sub-picometre requirement of the SpectroBragg was achieved, and provides the instrumental resolution limit of  $\sim 0.4$  pm.

### 3.4.4 Comparison of the SpectroBragg to contemporary spectrometers

After the construction of the SpectroBragg was completed, and during the calibration work, a commercial diffraction grating based spectrometer, *SDH-IV*, using the Hamamatsu G9214-512S InGaAs array was announced by *Solar Laser Systems*, Minsk, Belarus<sup>31</sup>. Also, Yokogawa Electric Corporation, Japan had the *WDM200* WDM monitor spectrometer available from 2002 to August 2006<sup>32</sup>. The SpectroBragg performance is compared against these alternatives in table 3.5.

	SpectroBragg	Yokogawa wd200	Solar SDH-IV
Wavelength Range	70 nm	40 nm	190 nm
Readout Resolution	< 0.5 pm	1 pm	±6 pm
Readout Repeatability	< 0.2 pm	±5 pm	±3 pm
Number of FBGs readable(1)	~ 70	~ 40	~ 190
Sampling Interval	30 ms	10 ms – 360 ms	7.3 ms

**Table 3.5:** Comparison of the SpectroBragg spectrometer performance against Solar Laser Systems, Belarus, and Yokogawa, Japan. (1) Assuming 1 FBG per nm spacing.

The SpectroBragg device was mounted onto an optical bench and consisted of generic optical components, whereas the commercial spectrometers were custom engineered mounts with optimised components. The SpectroBragg provided a wider spectral window than the WD200 unit, but not as wide as the maximum offered by the SDH-IV. The SpectroBragg provided greater resolution than that quoted by the commercial units, but the environmental limitation of the laboratory prevented the testing of the operational limit. The speed of the SpectroBragg was limited by the supplied read-out electronics and cooling system. As the SDH-IV could sample at 7.3 ms, it should be possible to achieve this speed with the SpectroBragg. However, it may require the replacement of SpectroBragg controller electronic components between the array and computer.

## 3.5 Conclusion

The development of a custom Čzerny–Turner type spectrometer, the SpectroBragg, with native sensitivity in the telecomms bands is reported. The SpectroBragg

<sup>31</sup>From *SDH-IV High-Aperture Compact Spectrometers*, SOLAR Laser Systems, Minsk ([http://www.solarls.eu/pdf/data\\_sdh.pdf](http://www.solarls.eu/pdf/data_sdh.pdf)).

<sup>32</sup>From *WDM200 WDM Monitor*, Yokogawa Electric Corporation, Japan (<http://www.yokogawa.com/rd/pdf/TR/rd-tr-r00034-004.pdf>).

spectrometer consists of a Hamamatsu InGaAs array, with 512 pixels, observing a  $\sim 70$  nm bandwidth centred at  $\sim 1550$  nm.

Using a stable reference source, good wavelength repeatability was obtained<sup>33</sup>. The use of the centroid algorithm enabled super-resolution beyond the averaged native resolution of  $\sim 0.13$  nm to be obtained. The best system resolution that was obtained in tests using the equipment available was sub-picometre wavelength resolution,  $< 0.5$  pm. This was observed by the recovery of a periodic signal. However, the vibrational sensitivity of the system, either the SpectroBragg itself or the sensor under test, reduced the operational resolution.

The SpectroBragg was intended to provide sub-picometre resolution using a 1024 pixel InGaAs array over a bandwidth of 50 nm. The implemented SpectroBragg design achieved sub-picometre resolution with 512 pixels, over a bandwidth of  $\sim 70$  nm. The additional pixel density would have improved the SNR in the centroid calculations, but would double the data transmitted to the PC and increased processing time. The extended spectral bandwidth arose, primarily, from the restriction of the components due to availability and physical extent of components.

Commercially available diffraction grating spectrometers use machined mounting plates, upon which the optical components are attached. This reduces the difficulties in component placement. The components of the SpectroBragg are COTS optical components, obtained from catalogues. Despite the non-specialised component mounts, the SpectroBragg maintained a consistent performance over the years it operated, indicating that the components were not unsuitable for long term use.

The mounting components used had unused degrees of freedom, and future work could look at the use of cheaper mounting components, which provide reduced degrees of freedom. The assembly of the SpectroBragg on a movable optical bench or optical board would have been beneficial. However, the alignment process outlined in appendix §L.3 (page V.II L-4) does require a larger area than the finished device occupies.

The SpectroBragg was used in the characterisation of a novel FBG, as reported in chapter 4, and for the polarisation work reported in chapter 5.

## 3.6 References

- [1] P. Marks. Testing times for composite flight, May 2005.
- [2] S. P. Christmas and D. A. Jackson. A new method for interrogation of serial arrays of dynamic fbg strain sensors. *Meas. Sci. Technol.*, 12(7):897–900, 2001.

---

<sup>33</sup>Wavelength repeatability to one standard deviation at centre = 0.28pm, and at edge = 0.21 pm

- 
- [3] E. G. Loewen and E. Popov. *Diffraction Gratings and Applications*, volume 58 of *Optical Engineering*, chapter 2, pages 25–55. Marcel Dekker, Inc., New York, 1997. ISBN: 0824799232.
- [4] M. C. Hutley. *Diffraction Gratings*, chapter 2, pages 13–56. Techniques in Physics. Academic Press, Inc. Ltd., London, 1982. ISBN: 0123629802.
- [5] J. F. James. *Spectrograph Design Fundamentals*, chapter 8, pages 63–88. Cambridge University Press, Cambridge, 2007. ISBN: 0521864631.
- [6] M. C. Hutley. *Diffraction Gratings*, chapter 1, pages 1–12. Techniques in Physics. Academic Press, Inc. Ltd., London, 1982. ISBN: 0123629802.
- [7] E. G. Loewen and E. Popov. *Diffraction Gratings and Applications*, volume 58 of *Optical Engineering*, chapter 3, pages 57–69. Marcel Dekker, Inc., New York, 1997. ISBN: 0824799232.
- [8] G. W. Stroke. *Diffraction Gratings*, volume 29 of *Handbuch der Physik (Encyclopedia of Physics)*, chapter 8. Springer-Verlag, 1967.
- [9] M. C. Hutley. *Diffraction Gratings*, chapter 4, pages 71–128. Techniques in Physics. Academic Press, Inc. Ltd., London, 1982. ISBN: 0123629802.
- [10] E. G. Loewen and E. Popov. *Diffraction Gratings and Applications*, volume 58 of *Optical Engineering*, chapter 15, pages 531–554. Marcel Dekker, Inc., New York, 1997. ISBN: 0824799232.
- [11] H. Gross, W. Singer, and M. Totzeck. *Physical Image Formation*, volume 2 of *Handbook of Optical Systems*, chapter 18, pages 41–97. Wiley-VCH Verlag GmbH & Co. KGaA, Weinheim, 2005. ISBN: 3527403787.
- [12] M. C. Hutley. *Diffraction Gratings*, chapter 3, pages 57–70. Techniques in Physics. Academic Press, Inc. Ltd., London, 1982. ISBN: 0123629802.
- [13] J. F. James and R. S. Sternberg. *The Design of Optical Spectrometers*, chapter 5, pages 51–80. Chapman & Hall Ltd., London, 1969. ISBN: 0412093200.
- [14] E. G. Loewen and E. Popov. *Diffraction Gratings and Applications*, volume 58 of *Optical Engineering*, chapter 12, pages 437–480. Marcel Dekker, Inc., New York, 1997. ISBN: 0824799232.
- [15] R. J. Meltzer. *Spectrographs and Monochromators*, volume 5 of *Applied Optics and Optical Engineering*, chapter 3. Academic Press, Inc., New York, 1969.
- [16] Ando Electric Co., Ltd., Japan. *AQ6317B Optical Spectrum Analyzer instruction manual*, 1.1 edition, 2000.
- [17] J. F. James. *Spectrograph Design Fundamentals*, chapter 12, pages 120–127. Cambridge University Press, Cambridge, 2007. ISBN: 0521864631.
- [18] J. F. James. On the design of Czerny-Turner charge-coupled-cevice spectrographs. *J. Modern Opt.*, 41(10):2033–2042, October 1994.
-

- 
- [19] W. Ecke, I. Latka, R. Willsch, A. Reutlinger, and R. Graue. Fibre optic sensor network for spacecraft health monitoring. *Meas. Sci. Technol.*, 12(7):974–980, 2001.
- [20] D. F. Murphy, D. A. Flavin, R. McBride, and J. D. C. Jones. Interferometric interrogation of in-fiber Bragg grating sensors without mechanical path length scanning. *J. Lightwave Technol.*, 19(7):1004–1009, 2001.
- [21] G. R. Rosendahl. Contributions to the optics of mirror systems and gratings and oblique incidence. II A discussion of aberrations. *J. Opt. Soc. Am.*, 52(4):408–411, 1962.
- [22] A. B. Shafer, L. R. Megill, , and L. Droppleman. Optimization of the Czerny-Turner spectrometer. *J. Opt. Soc. Am.*, 54(7):879, 1964.
- [23] W. T. Welford. *Aberration theory of gratings and grating mountings*, volume 4 of *Progress in Optics*, chapter 6. North-Holland Publishing Co., Amsterdam, 1965.
- [24] M. Santarsiero and R. Borghi. Correspondence between super-Gaussian and flattened Gaussian beams. *J. Opt. Soc. Am. A*, 16(1):188–190, 1999.
- [25] W. H. Press, B. P. Flannery, S. A. Teukolsky, and W. T. Vetterling. *Numerical Recipes in C: The Art of Scientific Computing*, chapter 15, pages 656–706. Cambridge University Press, 2 edition, oct 1992. ISBN: 0521431085.
- [26] J. Nocedal and S. J. Wright. *Numerical Optimization*, chapter 10, pages 250–275. Springer series on Operations Research. Springer, 1999. ISBN: 0387987932.
- [27] W. H. Press, B. P. Flannery, S. A. Teukolsky, and W. T. Vetterling. *Numerical Recipes in C: The Art of Scientific Computing*, chapter 3, pages 105–128. Cambridge University Press, 2 edition, oct 1992. ISBN: 0521431085.
- [28] R. C. Gonzalez and R. E. Woods. *Digital Image Processing*, chapter 10, pages 689–794. Prentice Hall, 1992.
- [29] J. Ares and J. Arines. Influence of thresholding on centroid statistics: full analytical description. *Appl. Opt.*, 43(31):5796–5805, 2004.
- [30] J. Ares and J. Arines. Effective noise in thresholded intensity distribution: influence on centroid statistics. *Opt. Lett.*, 26(23):1831–1833, 2001.
- [31] N. Bonod, E. Popov, S. Enoch, and J. Neauport. Polarization insensitive blazed diffraction gratings. *J. Europ. Opt. Soc. Rap. Public.*, 1:06029, 2006.
- [32] E. Collett. *Polarized Light in Fiber Optics*, chapter 12, pages 319–354. SPIE Press/Polawave Group, New Jersey, nov 2004. ISBN: 0819457612.
- [33] B. H. Billings. Monochromatic depolarizer. *J. Opt. Soc. Am.*, 41(12):966–975, 1951.
- [34] A. D. Kersey and A. Dandridge. Monomode fibre polarisation scrambler. *Electron. Lett.*, 23(12):634–636, 1987.
-

- [35] J. Jahns, A. W. Lohmann, and M. Bohling. Talbot bands and temporal processing of optical signals. *J. Europ. Opt. Soc. Rap. Public.*, 1, 2006.
- [36] A. G. Podoleanu, S. R. Taplin, D. J. Webb, and D. A. Jackson. Theoretical study of Talbot-like bands observed using a laser diode below threshold. *J. Opt. A: Pure Appl. Opt.*, 7(3):517–536, 1998.
- [37] F. A. Jenkins and H. E. White. *Fundamentals of Optics*, chapter 14, pages 286–314. Physics Series. McGraw-Hill, 4 edition, 2001. ISBN: 0072561912.
- [38] M. Born and E. Wolf. *Principles of Optics: Electromagnetic Theory of Propagation, Interference and Diffraction of Light*, chapter 7, pages 286–411. Cambridge University Press, Cambridge, 7th edition, 1999. ISBN: 0521642221.
- [39] G. Chartier. *Introduction to Optics*, chapter Annex 5.C, pages 240–249. Advanced Texts in Physics. Springer Science+Business Media, Inc., New York, 2005. ISBN: 0387403469.
- [40] S. Tolansky. *Multiple-Beam Interferometry of Surfaces & Films*, chapter 8, pages 96–103. Dover Publications, Inc., New York, 1970. ISBN: 0486622150.
- [41] ITU-T. Spectral grids for WDM applications: CWDM wavelength grid, 2003.
- [42] ITU-T. Spectral grids for WDM applications: DWDM frequency grid, 2002.
- [43] J. F. James. *Spectrograph Design Fundamentals*, chapter 17, pages 172–174. Cambridge University Press, Cambridge, 2007. ISBN: 0521864631.
- [44] J. F. James. *Spectrograph Design Fundamentals*, chapter 15, pages 150–167. Cambridge University Press, Cambridge, 2007. ISBN: 0521864631.
- [45] Thorlabs GmbH. Operation Manual for Thorlabs Blueline Series PRO8000(-4)/PRO800 Optical Sources WDM8XXX, 2006.

# Chapter 4

## Strain characterisation of novel anisotropic fibre Bragg gratings

---

### 4.1 Introduction

This chapter discusses the strain characterisation of a novel anisotropic fibre Bragg grating, FBG, inscribed in Corning SMF-28 standard telecomms fibre. The technology to produce these novel anisotropic FBGs, using a two-photon process at 264nm, was developed by Professor David N. Nikogosyan [1,2]. The two-photon process at 264nm is more efficient at FBG inscription, allowing FBGs to be inscribed faster [3], e.g. on the fibre drawing tower. The inscription of the FBG was undertaken by S. A. Slattery and Prof. D. N. Nikogosyan of the Femtosecond Group at University College Cork.

At low intensity UV only a single photon interaction is likely. The two-step (photon) process requires the molecule to remain in the excited state from the first photon long enough for the second photon interaction. Long lifetimes ( $\sim 1$  ms) or high intensities ( $10^6 - 10^8 \text{ Wcm}^{-2}$ ) [2] achieve this result. The distinction between two-step and two-photon processes lies in the intermediate state. A two-step process has a real intermediate step and a two-photon process has a virtual intermediate step [2]. A two photon process therefore requires a higher intensity ( $10^9 - 10^{11} \text{ Wcm}^{-2}$ ) [2], than an equivalent two-step process. In approximately geometrically isotropic<sup>1</sup> SMF-28 fibres that have not been hydrogen loaded<sup>3</sup>, these

---

<sup>1</sup>Corning states that “SMF-28 meets or exceeds ITU-T Recommendation G.652”<sup>2</sup>, which specifies a core/cladding concentricity error of  $\leq 0.5 \mu\text{m}$  and a permitted mode field diameter tolerance of  $\pm 0.7 \mu\text{m}$ .

<sup>3</sup>Hydrogen loaded SMF-28 fibres experience a strain relaxation upon inscription [4].

FBGs become anisotropic during the inscription process. The conditions for two-photon excitation occur more frequently on the side of the fibre on which the UV is incident. The resulting transverse strain pattern is shown in figure 2(b) in [4]. A symmetrical pattern is established about the plane containing the core and fibre edge nearest the phase mask. The stress experienced in this plane is approximately 0...10MPa, whereas the stress orthogonal varies between  $\sim -10 \dots 0$ MPa for most of the cladding. The fibre therefore has a strong asymmetric stress distribution, producing an anisotropic FBG.

The FBGs are, thus, structurally anisotropic in isotropic fibre, i.e. the FBG has a reflectivity dependent on the state of polarisation, SOP. A more generally available anisotropic FBG is achieved by inscribing a structurally isotropic FBG in anisotropic fibre, *highly birefringent* or polarisation maintaining, PM, fibre [5], as discussed in §2.2.8.4 (page V.I - 55). These novel anisotropic FBGs can thus be compared and contrasted against isotropic FBGs in both isotropic and anisotropic fibres.

The main experimental objective of this chapter is to characterise the strain response of these novel anisotropic FBGs and to test their applicability as strain sensors. Standard telecomms FBGs have been demonstrated as strain sensors [6–14], and these novel FBGs would complement and compete with standard FBGs. An objective was thus to determine whether the anisotropy in these novel FBGs conferred any particular advantages in comparison with nominally axially-symmetric types (although it should be noted that *all* FBGs exhibit some degree of anisotropy, albeit generally to a much lesser extent). The investigation required apparatus suitable for applying axial strain but not inducing clamping, bending or other transverse stress-induced birefringence in the fibres containing the FBGs. Ideally the apparatus should

- be reusable and capable of quick turnaround between sample FBGs,
- allow control over the applied strain and provide quick and repeatable strain conditions,
- be experimentally extensible to facilitate new experiments.

This chapter discusses the development of a flexible apparatus designed and built to characterise the strain response of the novel anisotropic FBGs; the comparison of these novel FBGs with standard telecomms FBGs as strain sensors; and discovery of possible strain/temperature discrimination by using the distinctive response of these novel anisotropic FBGs to both strain and temperature. The results of the strain characterisation and FBG comparison work have been reported at *the third European Workshop on Optical Fibre Sensing* [15] and in *IEEE Sensors Journal* [16].

## 4.2 Theory

### 4.2.1 Isotropic and anisotropic FBGs

The basic theory of FBGs is covered in section §2.3 (page V.I - 62), and assumes that the resultant FBG consists of radially uniform refractive index changes (i.e. longitudinal structure only). Such a purely isotropic grating structure exhibits no intrinsic polarisation-sensitivity (ignoring any present in the geometry or form of the fibre).

In reality slight anisotropies do occur. The fibre core itself will not be perfectly uniform. The ITU-T Recommendation G.652<sup>4</sup> specifies the geometric tolerances a single-mode optical fibre needs to meet. The mode field diameter, is to be uniform within  $\pm 0.7 \mu\text{m}$ . These deviations from the idealised core-cladding structure are the origin of Rayleigh scattering by fluctuations [17–19].

Manufacturing techniques can reduce the magnitude of these effects. The alignment of the core and focusing region can be determined by trial and error on a single fibre, and then repeated by automated positioning devices. The polarisation of the inscribing UV beam can be made to lie in the plane of the fibre core. The UV absorption by the core is so low ( $\sim 1 \text{ dB}$  [20] across the core diameter) that the difference in flux for Type I FBGs is small across the core, and for Type II FBGs the two-side approach can reduce the birefringence [21], as discussed in section G.1 (page V.II G-2).

*High-birefringence* or *polarisation maintaining*, PM<sup>5</sup>, fibres are fibres designed with large linear birefringence values,  $B$ . Upon the fibre preform being drawn and cooled, large permanent birefringence is incorporated to effectively isolate orthogonal polarisation states from each other, as described in §2.2.8.4 (page V.I - 55).

The FBGs strain-characterised in this chapter are distinct from effectively isotropic FBGs<sup>6</sup>, including those in highly birefringent fibres, as the grating structure is strongly asymmetric, hence anisotropic. The two-photon inscription process is responsible for the strong anisotropy in the geometry of the FBG. By using the three birefringence cases listed in §2.2.8 (page V.I - 50) to compare the birefringence due to inscription,  $B_{\text{ins}}$ , with induced birefringence,  $B_{\text{ind}}$ ; the isotropic FBG's inscribed birefringence is then case 3,  $|B_{\text{ins}}| \gg |B_{\text{ind}}|$ ; the anisotropic FBG's inscribed birefringence is either case 2 or 1,  $|B_{\text{ins}}| \lesssim |B_{\text{ind}}|$ . An FBG inscribed into PMF would be case 1 except for larger  $B_{\text{ind}}$ , e.g. large strain values.

Apart from the refractive index modulation the material and waveguiding prop-

---

<sup>4</sup>From *Corning SMF-28e+ optical fiber with NexCor Technology product information*, Corning Inc. (<http://www.corning.com/WorkArea/showcontent.aspx?id=27659>).

<sup>5</sup>Introduced in §2.2.8.4 (page V.I - 55)

<sup>6</sup>As discussed in §2.3.3.3 (page V.I - 72), 'isotropic' FBGs are weakly anisotropic

erties of the anisotropic FBG in SMF-28 remain those of the initial SMF-28 fibre, after inscription. As such, the anisotropic FBG exhibits preservation of its flat-top spectral shape comparable to that of isotropic FBGs spectral shape preservation.

### 4.2.2 Inscribing anisotropic FBGs in isotropic fibre

The two-photon, 264nm femtosecond pulse technology was developed by Prof. Nikogosyan [2]. The inscription of the anisotropic FBGs was undertaken by S. A. Slattery and Prof. Nikogosyan. What follows is a summary of the writing process as provided by Prof. Nikogosyan for the strain characterisation paper [16].

Standard SMF-28 with 3 mol.% Ge-doped fibre was sensitised in a hydrogen atmosphere at 150 bar and 75 °C for 2 weeks to enhance the fibre's photosensitivity. 264 nm femtosecond pulses, Gaussian in both space and time, generated by Nd:glass laser (Twinkle, Light Conversion Ltd. Lithuania), were used to inscribe the FBGs. The pulse duration was  $220 \pm 10$  fs [22], and the beam width was  $1.51 \pm 0.05$  mm.

The UV pulses were focused onto the fibre by a fused silica cylindrical lens of focal length 21.8 cm, through an *Ibsen Photonics* phase-mask. The phase-mask had a pitch,  $\Lambda_{\text{PM}}$ , of  $1.07 \mu\text{m}$  and thickness of 1 mm to minimise losses due to two-photon absorption in the phase-mask substrate. Most of the energy in the incident UV pulses is distributed into the  $\pm 1$  diffraction orders.

The focused beam width was approximately equal to the width of the stripped fibre. The horizontal diameter was 3 mm, or the gauge length of the FBG. The relative accuracy of the fluence ( $\sim 0.68 \text{ kJ/cm}^2$ ) and intensity ( $\sim 70 \text{ GW/cm}^2$ ) were 1 and 4% respectively. The phase-mask<sup>7</sup> produces an FBG of pitch  $\Lambda_{\text{FBG}} = \Lambda_{\text{PM}}/2$ .

The induced refractive index modulation,  $\Delta \underline{n}_{\text{FBG}}$ , and mean index,  $\overline{\Delta n}$ , were calculated using the expressions given in [23]:

$$\begin{aligned} \Delta \underline{n}_{\text{FBG}} &= \frac{\underline{\lambda}_B}{\pi \underline{\eta} L_{\text{FBG}}} \tanh^{-1}(\sqrt{\mathcal{R}_{\text{FBG}}}) \\ &= \frac{\underline{\lambda}_B}{2\pi \underline{n} L_{\text{FBG}}} \ln \left( \frac{1 + \sqrt{\mathcal{R}_{\text{FBG}}}}{1 - \sqrt{\mathcal{R}_{\text{FBG}}}} \right) \end{aligned} \quad (4.1)$$

$$\overline{\Delta n} = \frac{n_{\text{eff}} \Delta \underline{\lambda}_{\text{res}}}{\underline{\eta} \underline{\lambda}_{\text{res}}} = \frac{\Delta \underline{\lambda}_{\text{res}}}{\underline{\eta} \Lambda_{\text{PM}}} = \frac{\Delta n_{\text{eff}}}{\underline{\eta}} \quad (4.2)$$

where  $\mathcal{R}_{\text{FBG}}$  is the reflectivity of a uniform grating;  $L_{\text{FBG}}$  is the gauge length of the FBG;  $\underline{\lambda}_B$  is the FBG operation wavelength;  $\Delta \underline{\lambda}_{\text{res}}$  is the shift in the peak wavelength from its initial position;  $\Delta n_{\text{eff}}$  is the effective index change; and  $\underline{\eta}$  is the mode overlap parameter (fraction of the fibre mode power contained in the core), which can be

<sup>7</sup>Introduced in §2.3 (page V.I - 62).

estimated from

$$\underline{\eta} = \frac{\pi^2 d^2 K_{\text{NA}}^2}{\underline{\lambda}_B^2 + \pi^2 d^2 K_{\text{NA}}^2} \quad (4.3)$$

where  $d$  is the fibre core diameter and  $K_{\text{NA}}$  is the numerical aperture of the fibre.

The anisotropy of these FBGs arises due to both the SOP of the inscribing femtosecond–UV pulses and the geometric asymmetry of the writing process, i.e. refractive index changes in the cladding and core [2,4]. Unlike typical FBGs (written using single–photon 244 nm UV), the multi–photon high–intensity pulses result in an asymmetric index change that produces higher polarisation dependent loss, PDL.

These FBGs are closer to PM fibre inscribed FBGs in their asymmetry, but closer to standard isotropic FBGs in their spectral response to changing measurands. The temperature response of the reflection wavelength of the FBGs was measured by Nikogosyan *et al* and was in the range  $(0.9 - 1.1) \times 10^{-2}$  nm/°C [3], which is comparable to standard isotropic FBGs [24].

### 4.2.3 Use of FBGs as sensors

Figures 4.1 and 4.2 show the spectral profiles of a sample anisotropic FBG and a sample standard isotropic FBG (supplied by Laser2000 Ltd., UK). The anisotropic FBG is deliberately of poor quality with a significant side–lobe on the shorter wavelength side, and noticeable ripple. These FBGs were chosen by Dónal Flavin for their rich sub–structure, and are not representative of typical FBGs produced by the Femtosecond Group. As a consequence, all the anisotropic FBGs supplied were extremely rich in side structure. Figure 17 of [3] shows a cleaner anisotropic FBG reflection profile from approximately two years before these were characterised.

The FBG equation, equation (2.99) (page V.I - 63), is modified to incorporate the anisotropy of the refractive index

$$\underline{\lambda}_{\text{FBG}} = 2n_{\text{eff}} \bullet \underline{\Lambda}_{\text{FBG}} \quad (4.4)$$

$\Lambda_{\text{FBG}x} = \Lambda_{\text{FBG}y}$  at inscription as they are produced by the phase–mask,  $\Lambda_{\text{PM}}$ . From equation (G.5) (page V.II G-5), however,  $n_{\text{eff}x}$  will be of different strength to  $n_{\text{eff}y}$ ,

$$\begin{pmatrix} n_{\text{eff}x} \\ n_{\text{eff}y} \end{pmatrix} = \begin{pmatrix} n_{co} \\ n_{co} \end{pmatrix} + \begin{pmatrix} \Delta n_x \\ \Delta n_y \end{pmatrix} \quad (4.5)$$

where  $n_{co}$  is the common initial refractive index and  $\Delta n_x \neq \Delta n_y$  are the inscribed refractive index modulations. At inscription the modulation terms have common Bragg wavenumbers of the FBG defined by the phase–mask.

In use, the polarisation states  $(x, y)$  will not remain totally isolated (discussed in §2.2.8 (page V.I - 50)), and, unless viewed with polarisation–sensitive detectors,

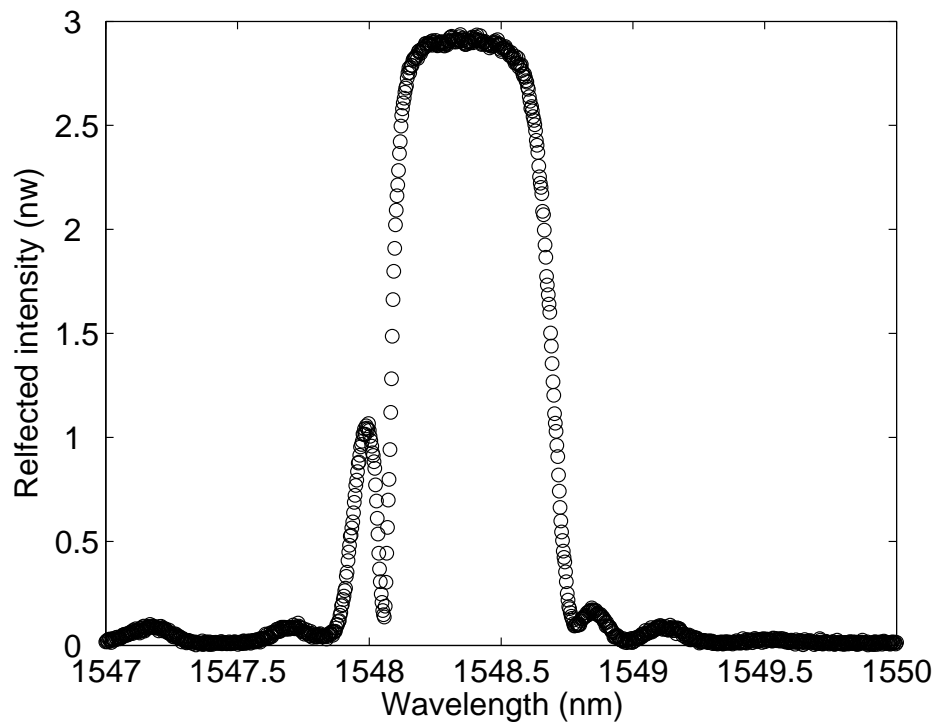


**Figure 4.1:** Example profile of anisotropic FBG profile. The side lobe is not representative of the process and was specifically requested. Note the flat-top profile.

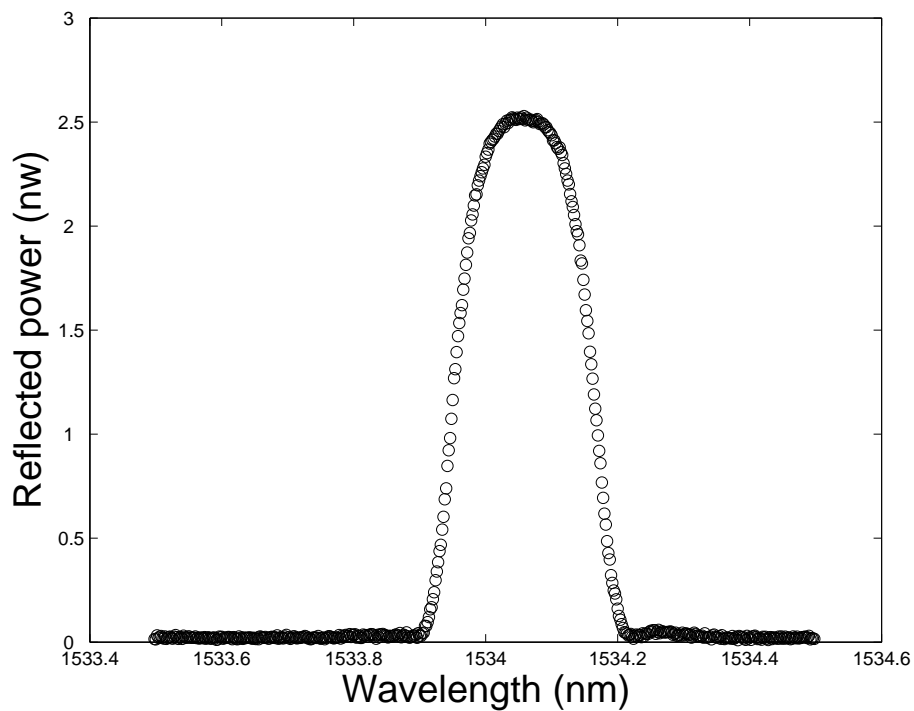


**Figure 4.2:** Typical profile of standard FBG. Note the Gaussian profile.

both  $(x, y)$  FBGs will be recorded together. Thus, it is convenient to define the average and differential wavelength

$$\lambda_{B_{\text{avg}}} = \frac{\lambda_{B_x} + \lambda_{B_y}}{2} \quad \lambda_{B_{\text{dif}}} = \frac{\lambda_{B_x} - \lambda_{B_y}}{2} \quad (4.6)$$

and similarly average and differential refractive indices

$$n_{\text{avg}} = \frac{n_{\text{eff}x} + n_{\text{eff}y}}{2} \quad n_{\text{dif}} = \frac{n_{\text{eff}x} - n_{\text{eff}y}}{2} \quad (4.7)$$

to give

$$\frac{\Delta\lambda_{B_{\text{avg}}}}{\lambda_{B_{\text{avg}}}|_0} = \varepsilon_{\sigma_z} + \frac{\Delta n_{\text{avg}}}{n_{\text{avg}}|_0} \quad (4.8)$$

and

$$\frac{\Delta\lambda_{B_{\text{dif}}}}{\lambda_{B_{\text{dif}}}|_0} = \frac{\Delta n_{\text{dif}}}{n_{\text{dif}}|_0} \quad (4.9)$$

The separation of the  $(x, y)$  FBG peaks is described by  $\Delta\lambda_{B_{\text{dif}}}$ , which is smaller for these anisotropic FBGs than for FBGs inscribed into PM fibre.

Equation (4.8) indicates that the averaged signal behaves just as a theoretical isotropic FBG would, and so we can treat  $\Delta\lambda_{B_{\text{avg}}} \equiv \Delta\lambda_{\text{isotropic}}$ , once  $\Delta\lambda_{B_{\text{dif}}}$  remains small, i.e. the profile remains unchanged at the resolution of the demodulation system.

#### 4.2.4 Signal processing considerations

The most common parameter used to determine  $\Delta\lambda_B$  is the location of the spectrum's maximum. For a spectral profile such as figure 4.2 the position of the maximum intensity may be a suitable approach if the noise is not significant. Otherwise, averaging of spectra can reduce the noise to recover a usable  $\Delta\lambda_B$  for sensing purposes; however, sufficient averaging depends upon the noise level at the peak. The use of averaging requires accepting slower temporal resolution or the use of faster equipment to maintain a given temporal resolution.

For FBGs with a flat-top profile, as in figure 4.1, noise becomes more limiting. The flat-top means that a peak determination using the position of the maximum may not be centred on the spectrum<sup>8</sup>, and the presence of noise has a greater effect, requiring more averaging.

Additionally, flat-top spectra have been encountered more frequently in PM fibres, where the two orthogonal FBG spectra produce large relative movements that can produce split double-peaks [25, 26]. These complications have dissuaded many

---

<sup>8</sup>This is not a problem for changes if the same part of the spectrum is always seen as the position of maximum intensity.

researchers from using flat-top super-Gaussian FBG spectra as sensors, preferring FBGs with Gaussian profiles.

With these novel anisotropic FBGs, the material birefringence dominates under strain, which for SMF-28 is low. Consequently these FBGs experience a similar strain response to isotropic FBGs,  $\Delta\lambda_{B_{\text{dif}}}^{(\text{aniso})} \approx \Delta\lambda_{B_{\text{dif}}}^{(\text{iso})}$ . Changes predominantly occur at the edges of the spectral profile, rather than across the full width.

More advanced signal processing approaches deal, with varying levels of sophistication, with the limitations of simple peak location. Three approaches are discussed in section §3.2.3 (page V.I - 133), of which the centroid algorithm, equation (3.19) (page V.I - 133), is used here to determine the peak value

$$\lambda_c = \frac{\sum_{i=1}^{n_w} I_i \lambda_i}{\sum_{i=1}^{n_w} I_i} \quad (3.19)$$

where  $I_i$  is the intensity at wavelength  $\lambda_i$  and  $n_w$  is the ‘window’ over which the centroid value is calculated. The centroid algorithm is a weighted sum, which synthesises resolution beyond that of the sampling of the data. It is thus very sensitive to relative changes in the weighting of index points. The ideal circumstances to use the centroid algorithm are where the spectrum shifts but does not change shape as the measurand changes.

As illustrated in figure 4.3 the super-Gaussian profile has more points above a threshold intensity than does the Gaussian profile. This enhances the weighting of more wavelength positions for use in the centroid calculation. For FBG spectra for which the average peak value is significantly greater than the noise level, the flat-top profile can improve detection of peak movements. This may reduce the number of spectra required to be averaged for a given resolution.

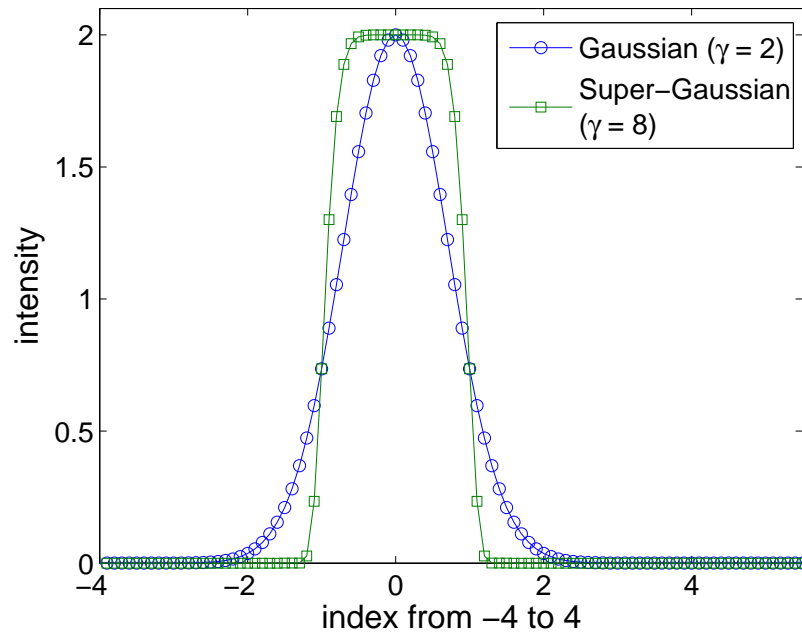


**Figure 4.3:** Plot of Gaussian ( $\gamma = 2$ ) and Super-Gaussian ( $\gamma = 8$ ) profiles generated in Matlab. The generating function is  $I(x, \sigma, \mu, \gamma) = Ae^{-\left(\frac{x-\mu}{2\sigma}\right)^\gamma}$ , where  $A$  is the maximum value of the function,  $\mu$  is the mean value,  $\sigma$  is the standard deviation and  $\gamma$  is the super-Gaussian power  $> 2$  [27].  $\gamma$  is related to the rapidity of the transition from maximum intensity to minimum intensity.

## 4.3 Experimental apparatus/setup

### 4.3.1 Strain characterisation approach

The experiment to strain-calibrate these novel anisotropic FBGs required the design of a reusable apparatus to allow repeatable strain settings to be applied adiabatically, i.e. no heat is gained or lost by the system, so non-ambient temperature changes can be removed as a perturbing factor. The apparatus should also be extensible to allow other experimental conditions such as isothermal experiments, where a heater would keep the section of fibre containing the FBG at a fixed temperature.

The fundamental effect is to apply a linear extension to the fibre. The literature suggested several approaches. A conceptually simple approach involves running the fibre under test over a pulley and adding weights to the fibre section hanging vertically [28–32]. The FBG can be either on the lateral or vertical length of fibre, with the weight applied producing the strain. Alternatively, the fibre can be fixed vertically and weights attached to provide strain [33]. Another possible approach involves attaching the fibre to a translation stage to produce strain by moving the fibre attachment on the translation stage [34–36]. More elaborate approaches involve

embedding or attaching the FBG to a coupon [37–40], or placing the fibre on a cantilever [41–43].

Of these, the first three approaches provide the simplest metrological configurations. Provided ambient temperature and pressure can be controlled, the linear response of the FBGs under test can be uniquely determined.

The pulley and weight approach has the disadvantage of relying upon the pulley to be frictionless, free from inertia and not introducing damage to the fibre [44]. Generally, the use of weights limits the resolution of the applied strain to the weights available and requires the calibration of the weights. The translation stage is limited to the precision of the stage driver and its maximum load.

### 4.3.2 Fibre attachment approaches

The next complication to be addressed is the attachment used to hold the fibre to the apparatus. As the fibre is to experience many strain cycles, with good repeatability of applied strain, a reliable attachment is required. Given the polarisation-sensitivity of the FBGs, the attachment should have minimal impact on the polarisation properties of the fibre under test. This can be most easily achieved by not introducing a transverse force, such as clamping the fibre [33].

A commonly used approach is to use epoxy resins or glues to adhere the fibre to the mount [45–48]. The resin or polymers used in these approaches do not have a similar strain response to silica [49, 50]. Under applied strain the response of the silica fibre and epoxy differ, which can lead to creep and strain relaxation<sup>9</sup> [33] effects occurring over longer time-scales. In practice this results in small scale dynamic changes during an experiment. After many readings the final applied strain can differ from the initial strain, integrating the small changes occurring in each reading and producing a larger standard deviation uncertainty for the data [51]. For high-precision measurements this change in strain will affect accuracy, as the final strain will depend upon the applied extension and the history of previously applied strain.

An alternative to epoxy/glue is to use glass solder [52]. Glass solder is a low melting point glass ( $\sim 400$  °C) with almost identical mechanical characteristics to silica fibres. The thermal response is substantially different, but for strain characterisation of an FBG, the fibre and solder need not experience any temperature in excess of  $\sim 20$  °C.

### 4.3.3 Strain approach and attachment

Given the available equipment and lab environment, a translation stage was used to apply strain. The pulley system was considered unsuitable, as the orientation of

---

<sup>9</sup>Discussed in section §2.2.4.2 (page V.I - 41)

the optical bench dictated that using the longer dimension would require the pulley extend out into the common walkway of the lab.

To decide upon the method by which the fibres would be attached to the strain apparatus, only two approaches appeared feasible: epoxy or glass solder. A wide variety of epoxies and glues are available, with various curing accelerating additives, which could prevent exact duplication of mount conditions.

Approaches to attaching the fibre were raised in private discussions with Prof. Julian D. C. Jones and Dr. Robert R. J. Maier<sup>10</sup>, who had recently evaluated several approaches to this problem for work reported in [52], in addition to past experience with alternative attachment approaches. Dr. Maier was able to recommend glass solder over epoxy. Glass solder also allowed for easy reuse of the apparatus.

In further discussions with Dr. Joe O'Mahony<sup>11</sup> it was indicated that the dissolving of most epoxies could be achieved with either isopropyl alcohol, IPA, or chloroform. Removing a mounted fibre would require a fume cupboard at the very least, and would no longer be easily reusable.

#### 4.3.4 Glass solder for attachment of fibre

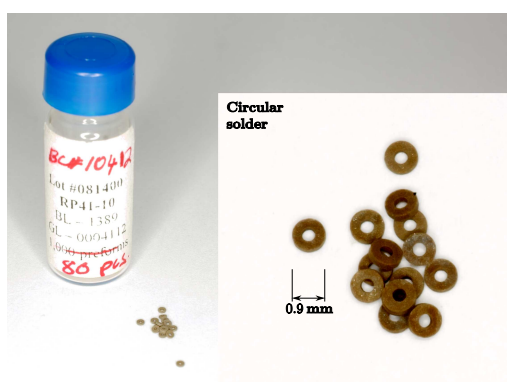


**Figure 4.4:** Oz Optics circular glass solder preforms.



**Figure 4.5:** Oz Optics oval ribbon glass solder preforms.

The glass solder used by Dr. Maier and acquired for the work reported here was supplied by *Oz Optics Ltd., Ottawa, Canada*. Two glass solder preform shapes were purchased: circular and ribbon, shown in figures 4.4 and 4.5, respectively. The quoted<sup>12</sup> glass transition is 215 °C; however it was found in practice that to achieve wetting to an amenable surface a higher temperature of  $\sim 350$  °C was needed.

<sup>10</sup>Both Prof. Jones and Dr. Maier are with the School of Engineering and Physical Sciences, Heriot-Watt University, Edinburgh EH14 4AS, UK.

<sup>11</sup>Head of the Nanotechnology Research Group, WIT.

<sup>12</sup>[http://www.ozoptics.com/ALLNEW\\_PDF/DTS0034.pdf](http://www.ozoptics.com/ALLNEW_PDF/DTS0034.pdf)

The quoted modulus of elasticity of 6.3 GPa is  $\sim 8.9 - 9.2\%$  that of silica fibre, 69 – 72 GPa [53,54].

Upon reheating, the glass solder became more ash-like in consistency. This made the quick application more difficult. The reheated solder glass colour is darker and the appearance is matt rather than gloss. By adding a small amount of solder preform, e.g. the smallest piece shown in figure 4.6 the ash-like solder would regain the performance of the solder preform, if not fully regain its colour.

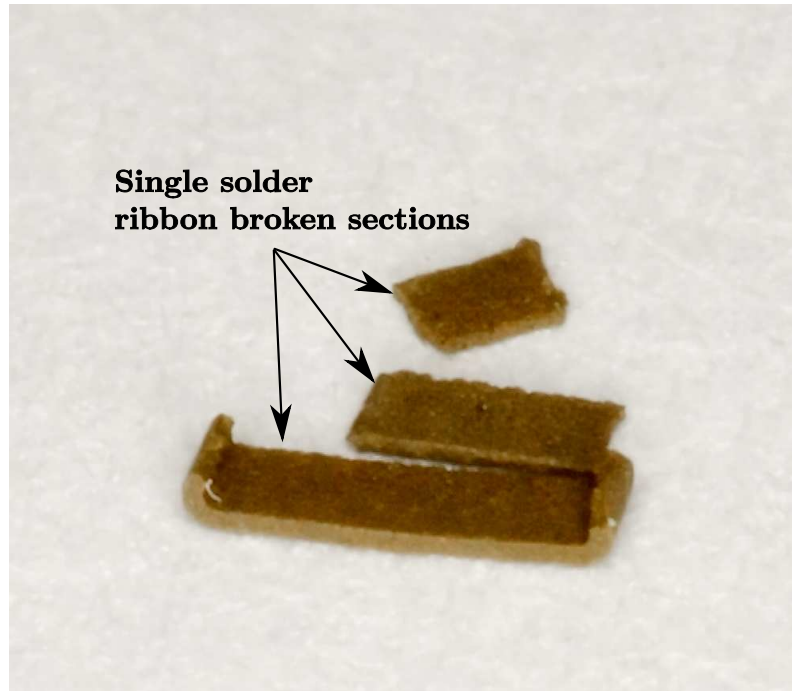


**Figure 4.6:** Broken sections of ribbon solder facilitated rapid attachment of the fibre.

#### 4.3.5 Construction of the fibre mount

The initial plan was to use a *Thorlabs HFV001* standard v-groove fibre holder to mount the fibre. The Oz Optics specification documentation for the glass solder indicated that the glass solder would adhere to nickel; however, the nickel-plated HFV001 proved unsuitable. After many attempts to adhere a sample fibre to the HFV001, only one attempt succeeded. This attempt did not survive strain, as slight movement of the fibre separated the fibre.

The most effective mount found was a glass microscope slide. The test fibre broke outside the solder point but the solder did not separate under strain. The mounting of the microscope slide then became an issue. Clamping pressure could fracture the microscope slide. Figure 4.7 shows the mount that was adopted. A *Thorlabs BA2* base was secured to the top of a *Thorlabs RS2P4/M* pillar post. On each

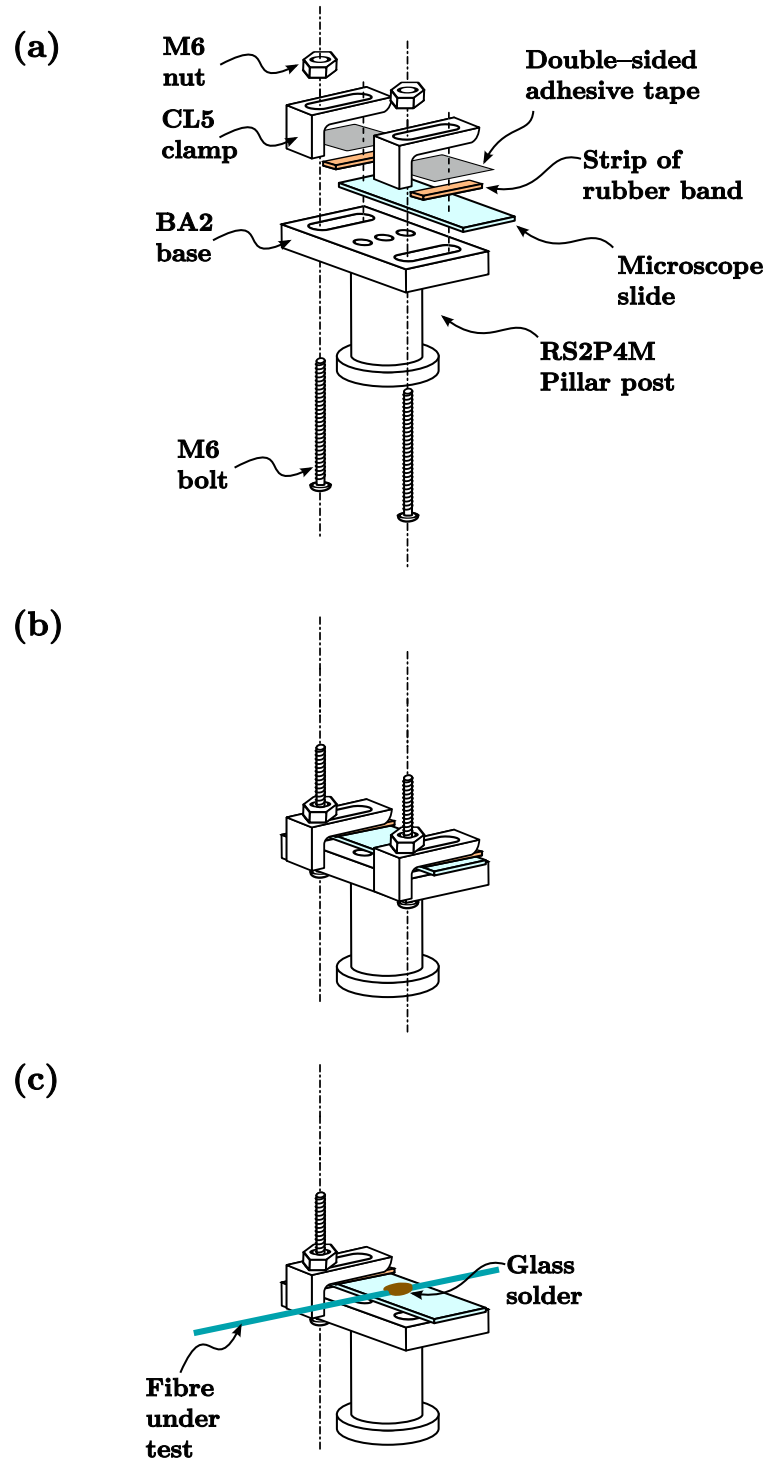


**Figure 4.7:** Mount for soldering fibres. (a) Exploded view of fibre mount (parts CL5 clamp and BA2 base are Thorlabs catalogue labels); (b) Assembled mount, slide held by M6 bolt and rubber clamp; (c) Front clamp removed to show soldered fibre.

side, two lengths of rubber band were adhered to a *Thorlabs CL5* clamp by double-sided adhesive tape. An M6 bolt secured the CL5 clamp over the microscope slide on the BA2 base. By keeping the microscope slide against the M6 bolt, and securely tightening the locking bolt, the microscope slide was securely held, without fracture. A finished mount is shown in figure 4.8.

The Thorlabs RS2P4M pillar post is 50 mm in length. To get the whole system as parallel to the bench as possible, a post of length 29.5 mm was needed for the mount on the translation stage, height 20.5 mm. The closest suitable component available was a *Thorlabs RS25/M* extension post of length 25 mm. The RS25/M was placed atop an *Ealing MacroMech* stage (incorporating a *PMC* encoder driver).

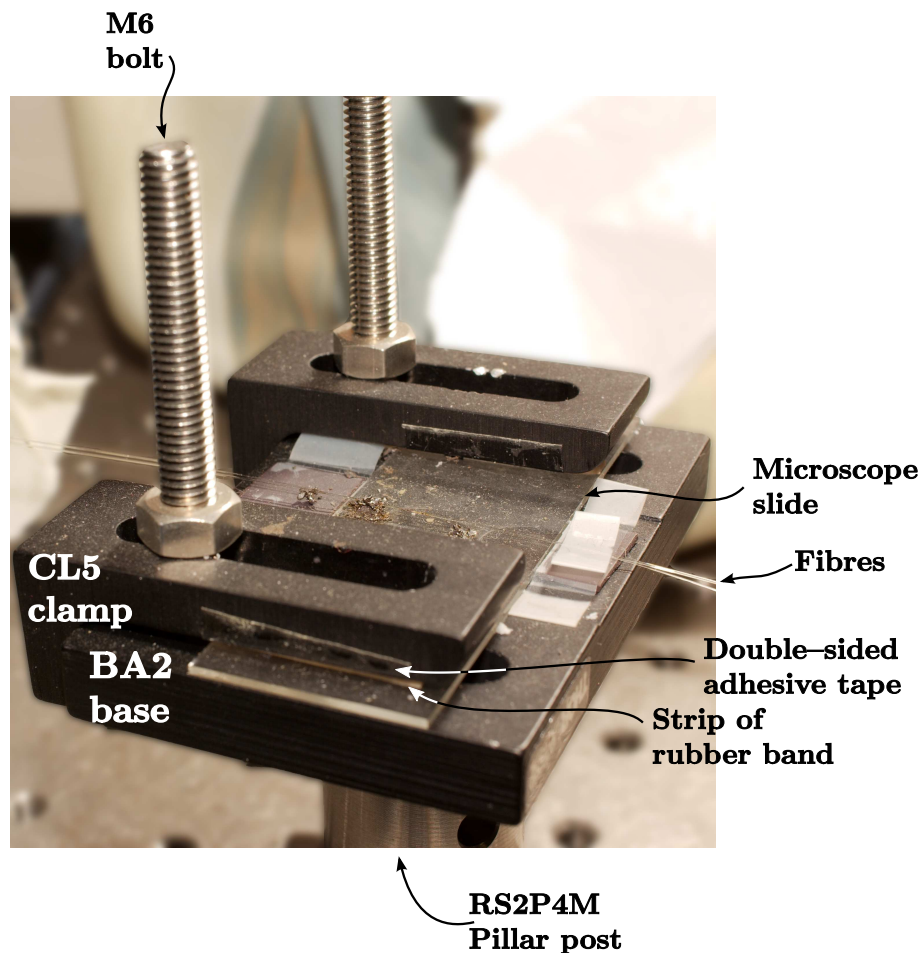


**Figure 4.8:** Image of completed fibre mount, with two fibres soldered.

#### 4.3.6 Attaching the fibre under test

The fibre under test first was measured to determine what the maximum unbroken length was. If the fibre span was longer than the length required for the desired

minimum strain (equation (2.56) (page V.I - 39)), then the region where the appropriate anchor point would occur was stripped using a Siemens single-mode fibre jacket stripper tool.

FC/APC-pigtails were spliced onto the fibre under test to facilitate quick rearrangement of the apparatus, couple multiple FBGs in series and to reduce end face 4% Fresnel reflections.

Initially the fibre was carefully passed through the perspex cylinder. After the first fibre under test broke it became evident that it would be more convenient to have the cylinder consist of two half-cylinders, requiring only the removal of the top half-cylinder to allow access to the fibres under test, shown figuratively in figure 4.9. This greatly reduced the time and effort needed to replace broken fibres.

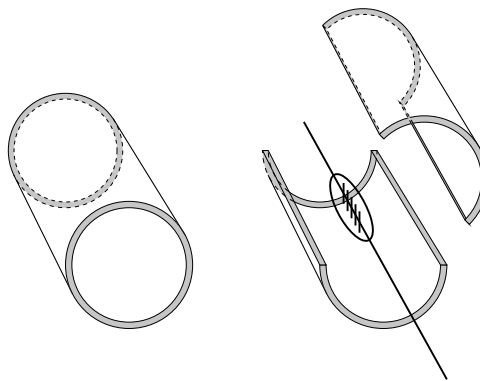


**Figure 4.9:** Replacing the perspex cylinder with two half-cylinders. The two half-cylinders enabled faster replacing of broken fibres and proved safer for fibre handling. Hinges were not used. The increase on weight on the hinged side when in the open position would require extra bracing on the lower half to hold the weight.

Once the fibre was laid across the rig, the solder attachments were made. The fibre was lightly held in position by scotch adhesive tape<sup>13</sup> and a tweezers with an integrated LED was used to carefully place sections of broken ribbon solder beside the fibre<sup>14</sup>. The soldering iron was then brought vertically down onto the glass solder pieces and pulled away from the rig along the fibre, creating an attachment area of 1 – 2 mm.

With the other end of the fibre under test lightly held by scotch tape, a measurement of the length from the first anchor point was made to determine where on the second mount the fibre under test should be soldered. The procedure was then repeated for this location.

<sup>13</sup>Scotch tape was used as it presented the least problems on removal.

<sup>14</sup>The circular solder pieces stuck to the soldering iron, rather than the glass. The extra time and effort to scrape the solder off the iron meant more flux was lost and the fibre exposed to more potential damage.

### 4.3.7 Laboratory environmental conditions

As the FBG in a fibre with full cladding is most sensitive to temperature and strain, the exclusive examination of the strain response requires the control of temperature. Effective temperature isolation can be attempted by insulating the device under test from the local environment, or by turning the local environment into a constant temperature heat bath.

A *Mitsubishi Electric* air conditioner system had a single input (with temperature monitor) near to the laboratory window, with one output over each of the four bays. Two cross-linked extractors removed air from the lab. If the extraction of air conflicted with the temperature to be achieved, the extractors were closed.

This system provided the laboratory with a constant<sup>15</sup> temperature, preventing the optical benches from following the daily solar heating cycle, which had complicated previous interferometric work in this laboratory.

The output vent did introduce moving air and low-frequency noise from above the bench. This could be countered by either turning off the air conditioner during an experiment, or by shielding the equipment from the moving air by enclosing the fibre.

The experimental work was performed under non-optimal conditions, as air movements could not be guaranteed to be absent in the vicinity of the FBGs. While any effect on the FBG signal value should have been very small, every effort was made to minimise sources of air movement around the optical bench.

The spans of fibre that were provided by the Femtosecond group, UCC, were not of equal length. Consequently, at least one of the mount points for the strain apparatus needed to be free to be repositioned. This constrained the type of enclosure that could be used with the fibres.

Given the available resources, space constraints on the optical bench and the range of fibre span lengths, the following approach was used:

- the air conditioner would be kept on to keep the laboratory temperature as constant as possible,
- the fibre span with the FBGs under test would be enclosed in a perspex tube,
- cardboard boxes would be placed at the ends of the perspex tube, with cutouts to allow the perspex tube fit inside, thus allowing repositioning of the mount for the different fibre lengths,

---

<sup>15</sup>Constant within the resolution of the air-conditioner thermostat. As temperature measurement of the laboratory, the available anisotropic FBG was left open in the lab, with a reference laser and data captured for 8 non-consecutive 17 minute intervals. Using the temperature response of  $10.7 \text{ pm}^\circ\text{C}^{-1}$  [2]. The largest individual dataset temperature difference was, at one standard deviation, from among the datasets was  $\sim 0.6^\circ\text{C}$  (16 pm), while the overall full-scale movement of the 8 datasets was just less than twice this.

- a reference standard isotropic FBG would be colocated on the strain rig with the anisotropic FBG under test,
- a second reference standard isotropic FBG would be placed in the perspex cylinder free of strain to monitor temperature.

The arrangement is shown in figure 4.10(a). The perspex cylinder was held in place by four RS2P4/M pillar posts, separated to allow the cylinder rest between two sets of two. An aluminium block was placed between the pillar posts to prevent the cylinder falling between the posts and potentially breaking the fibre under test when the pillar posts were being situated.

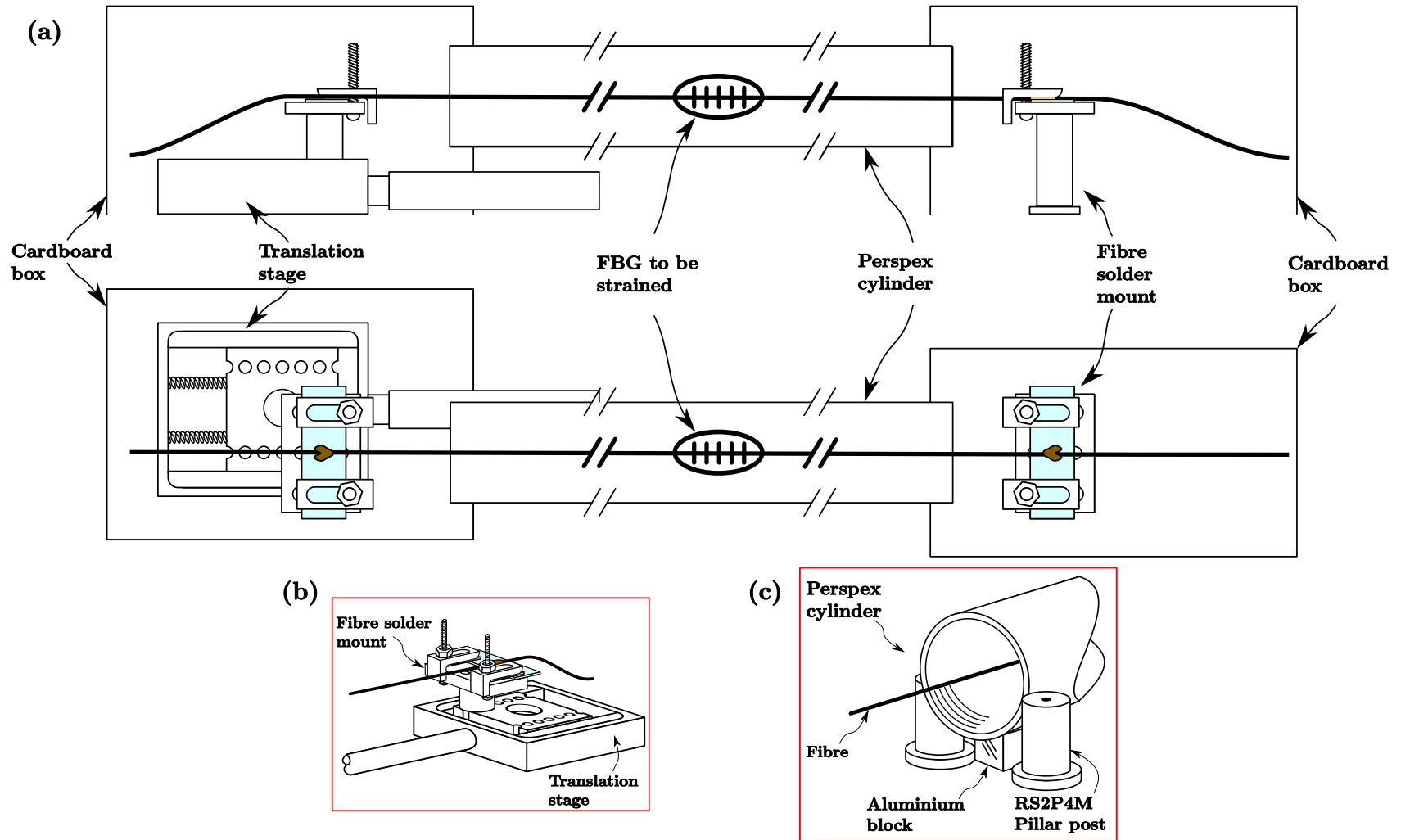


**Figure 4.10:** (a) Strain rig in elevation and plan view, (b) Isometric view of translation stage with mount, (c) Isometric view of perspex tube with RS2P4/M pillar posts, and aluminium block supports.

### 4.3.8 Cautions on soldering the attachment

The most significant risk of this procedure is fracturing the fibre during the solder process. Typically this was easily detected as a soft audible click and the two sections moving independently.

The next most pressing concern was the alignment of the fibre with the direction of movement of the translation stage. If the fibre attachment points were not located on the same line of movement then a transverse shear strain on the fibre would occur, removing one of the benefits of using glass solder over clamping. This arrangement was distinguished by fracture at or very near ( $\sim 1$  mm) the edge of the solder.

### 4.3.9 Recoated isotropic FBGs

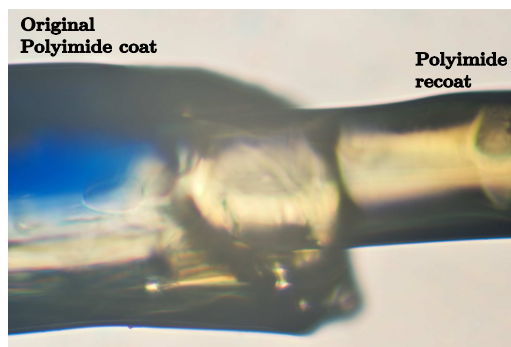


**Figure 4.11:** Laser2000 supplied isotropic FBG, showing detail of the original and recoated section of fibre.

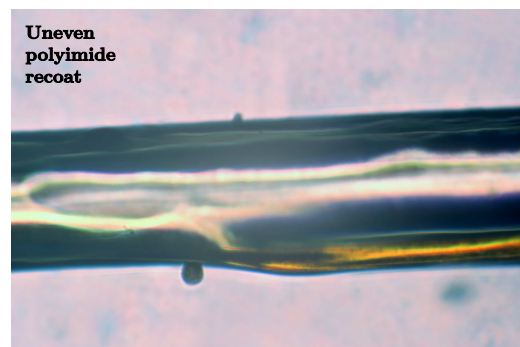


**Figure 4.12:** Laser2000 supplied isotropic FBG, showing the non-uniformity of the recoating.

The motivation for this chapter was to compare the novel anisotropic FBG's linear strain response with that of an isotropic FBG. To this end, two isotropic FBGs were used, one for the strain comparison, and another as a temperature reference. The temperature reference FBG provided a common-mode rejection of temperature, and the isotropic strain FBG gave a method of comparing the novel FBGs' response to those in the literature. The fibre's buffer coating was removed prior to grating inscription, with the option for either acrylate or polyimide<sup>16</sup> recoating afterwards.

The specifications<sup>17</sup> of the FBGs purchased from Laser2000 are shown in table 4.1. Figure 4.11 shows the original and recoated sections of one fibre. Figure 4.12 shows an example of the non-uniform application of the recoating to the fibre. The

<sup>16</sup>Polyimide was the coating chosen.

<sup>17</sup>From the Laser2000 quotation

---

FBG written in 2 m of SMF fibre	
	$\lambda_B = 1534.1 \pm 0.5 \text{ nm}$
Centre wavelengths of either:	$\lambda_B = 1549.6 \pm 0.5 \text{ nm}$
	$\lambda_B = 1566.2 \pm 0.5 \text{ nm}$
Bandwidth	$< 0.3 \text{ nm}$
Reflectance	$> 80\%$
PDL value	around 0.3 db
Grating length	10 . . . 14 mm
Proof test	$> 120 \text{ kPSI}$
Fibre coating	Polyimide fibre
Recoating	Polyimide

---

**Table 4.1:** Laser2000 FBG specifications.

recoating was very effective mechanically. None of the Laser2000 FBGs broke at the FBG during experimental use or during handling.

Polyimide jacket coatings was chosen in favour of acrylate jacket coatings due to their more consistent performance [38]<sup>18</sup>. As mentioned in §2.2.4.2 (page V.I - 41), the jacket will have a different strain response to the silica fibre. Time must therefore be allowed for the strain relaxation of the jacket after application of strain to the silica fibre.

#### 4.3.10 Quasi-static strain experimental apparatus

As the deadline for abstract submission to the third European Workshop on Optical Fibre Sensing, EWOF07, arrived before the isotropic FBGs were delivered, it was decided to use large strain step sizes to minimise the impact of non-strain effects upon the calculated strain values. The available anisotropic FBGs were approximately the same wavelength; thus a simultaneous independent temperature reference was not available. The large strain steps would provide a greater difference than likely temperature changes for the duration of the application of strain and relaxation time. Temperature changes would exhibit a more gradual change, with a significant likelihood of the temperature change trend being visible across the increase in strain step.

The data were recorded using an *Ando AQ6317B* optical spectrum analyser, OSA. By averaging the data capture over two days, small scale effects such as creep, strain-relaxation and thermal expansion of the bench should be minimised. Thus quasi-static strain characterisation could be performed in the absence of reference FBGs.

---

<sup>18</sup>The effectiveness of the bonding of polyimide to the silica can change [55], which, although it should not be an issue with the apparatus used here, might affect embedded results.

The fibre with the anisotropic FBG was attached to the mounts, protected by the perspex cylinder and boxes over each mount. The FBG was illuminated by an *Exalos ESL1505-2100 Super Luminescent diode*, SLED, passing through an Oz Optics circulator<sup>19</sup>. The reflected signal was passed by the circulator to the OSA. The arrangement is shown schematically in figure 4.13.

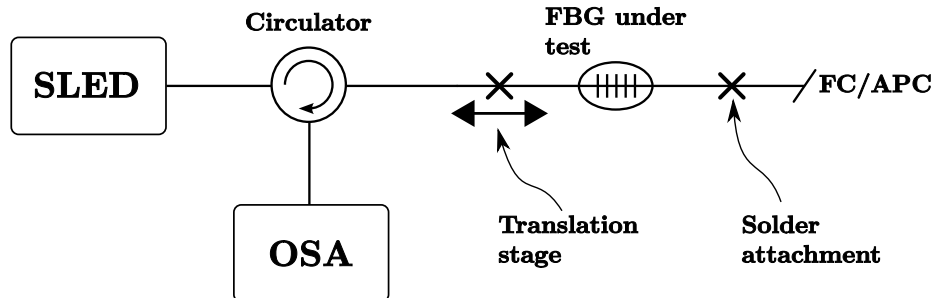


**Figure 4.13:** Schematic diagram of apparatus used for EWOFS work.

The Ando AQ6317B OSA has a native resolution of 10 pm. The Ealing translation stage’s linear actuator has a precision of  $0.02\ \mu\text{m}$  [56]<sup>20</sup>. The translation stage was controlled by a *National Instruments LabVIEW* program, where the intended movement could be input. Use of unidirectional step sizes of  $200\ \mu\text{m}$  ensured that the precision and accuracy limits of the translation stage were four orders of magnitude smaller than the step size.

The apparatus allowed the minimum step size of the translation stage to determine the minimum applied strain for a given length of fibre. Longer spans of fibre resulted in smaller applied strain.

A limitation to the manual use of the OSA for this work was the speed of saving data to disk. The time taken for this task reduced the scan time to that achievable by the operator. To improve the OSA’s performance a GBIP connection was acquired to allow the OSA to be controlled by LabVIEW. This was not available at the time of the EWOFS work, but was for the patent work reported in section §4.4.3.

### 4.3.11 Dynamic strain characterisation experimental apparatus

For the experiments described in this section, the isotropic FBGs were available, with one used as an unstrained temperature reference. The results detailed in section §4.4.1 (page V.I - 197) were obtained by use of an Ando AQ6317B OSA [57].

<sup>19</sup>An Oz Optics *FOC-12N-111-9/125-SSS-1550-55-3A3A3A-1-1* circulator.

<sup>20</sup>The specifications also quote a backlash of  $6\ \mu\text{m}$  and a directional repeatability of  $0.1\ \mu\text{m}$  [56].

The OSA used a scanning diffraction grating in a double pass arrangement to scan the spectral window specified. Averaging is done on a per pixel basis, i.e. the average of a single spectral resolution window is completed before data begin to be captured for the next spectral resolution window, a point-by-point approach. The alternative approach is to use an array of detectors for near-simultaneous recording of a spectrum, such as was adopted in the SpectroBragg spectrometer arrangement covered in Chapter 3.

The results obtained with the OSA were meaningful for characterisation if the experiment exhibited *statistical control* [58], i.e. the data captured was ergodic<sup>21</sup> in a *wide-sense-stationary* manner. This means that the FBG spectra should not have changed faster than the scan time of the OSA.

The OSA's fastest scan time, i.e. with no averaging, was 0.5 s [57]. To demonstrate that no spectral changes occurred on faster timescales, the SpectroBragg spectrometer was used to test the stability of the FBGs under test. The SpectroBragg has a maximum effective scan time of 30 ms, as determined by the hardware drivers run through LabVIEW.

The SpectroBragg had a 512 element InGaAs diode array covering a  $\sim 70$  nm window, to produce a native resolution of  $\sim 137$  pm. Using the postprocessing covered in section §3.2.3 (page V.I - 133), changes equivalent to 0.4 pm have been detected.

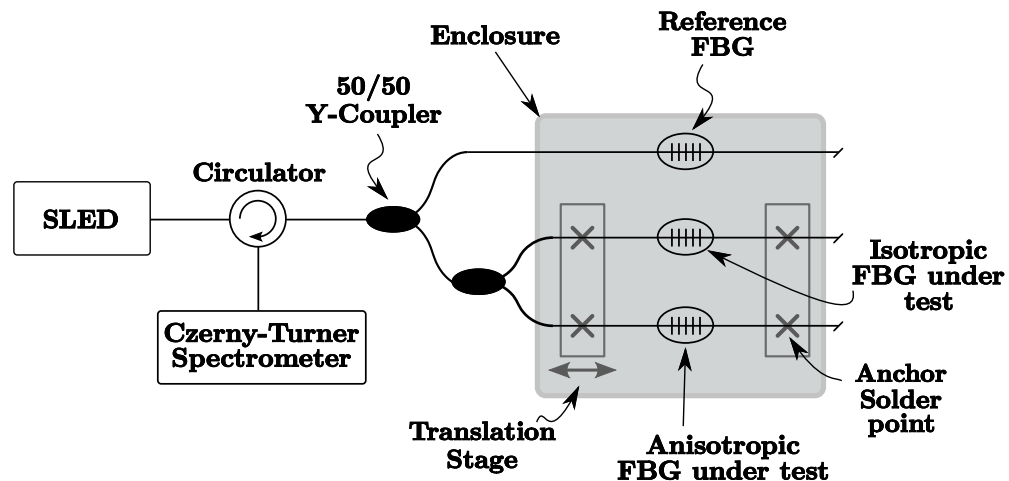


**Figure 4.14:** Schematic diagram of apparatus used for IEEE sensors paper work.

The experimental configuration is shown in figure 4.14. Two isotropic Laser2000 FBGs were used as references. One was colocated alongside the anisotropic FBG on the strain apparatus. The other FBG was placed unconstrained alongside the

<sup>21</sup>Ergodicity is defined in appendix B.1 (page V.II B-4)

FBGs under strain to determine any temperature changes.

To attach the two fibres, the procedure outlined in §4.3.6 (page V.I - 184) was followed for both fibres on the first mount. With the two fibres attached on one mount the next problem was to keep the two fibres under roughly equivalent tension so that one fibre did not have more slack in it than the other after soldering the second attachment.

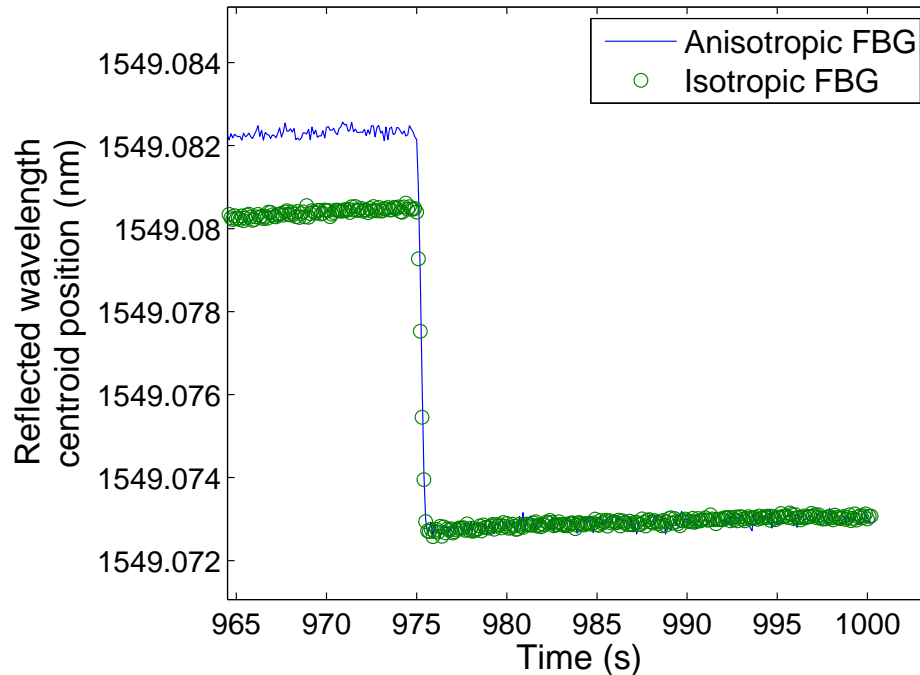


**Figure 4.15:** Temporal response of co-anchored FBGs. Applying low tension to the FBGs during soldering prevents significant differences in slack.

The two fibres were held under tension while solder was melted alongside. By soldering both fibres at the same time the differences in slack were minimised. Figure 4.15 shows the recorded response of the anisotropic FBG (blue line) and offset isotropic FBG (green circles) to the same applied strain, indicating that both fibres experienced changes in strain from rest in the same time interval of 0.1 s<sup>22</sup>.

Figures 4.16 and 4.17 illustrate the soldering of two fibres<sup>23</sup>.

<sup>22</sup>Cross-correlating the two datasets (isotropic and anisotropic fibres) yields zero time difference, at the full overlap, from the autocorrelation of either dataset.

<sup>23</sup>The appearance of the glass solder also changed on reheating. Figure 4.17 shows a fresh application of glass solder and figure 4.16 shows glass solder after several reheatings.

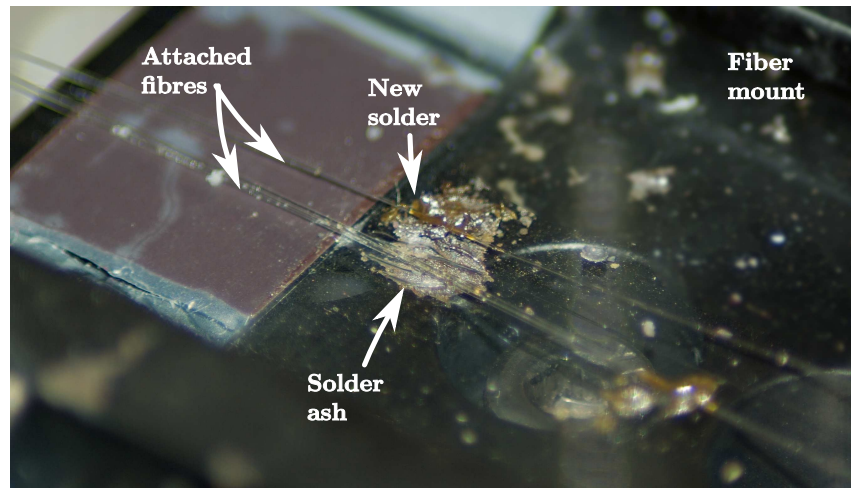


**Figure 4.16:** Image of the solder mount with two FBGs soldered.



**Figure 4.17:** Close up image of soldered fibres.

### 4.3.12 Adding a temperature reference FBG

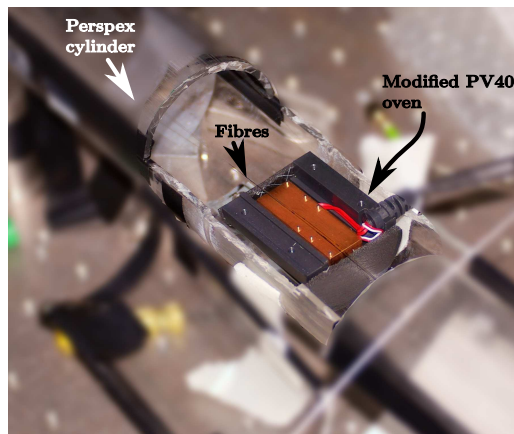


**Figure 4.18:** Modified Thorlabs PV40 oven placed within the perspex cylinder.

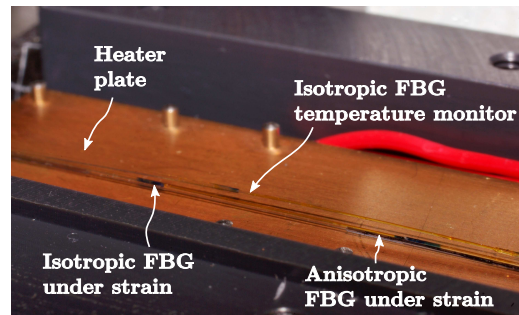


**Figure 4.19:** Two FBGs to undergo applied strain with temperature reference placed in close proximity.

To position the temperature reference FBG close to the FBGs under strain a platform to situate the FBG was needed. In anticipation of work for section §4.4.3 (page V.I - 208) an isolated temperature environment was required. Both these requirements could be met by using the flat plate of a heater as the platform to place the temperature reference.

A modified *Thorlabs PV40 PPLN*<sup>24</sup> oven<sup>25</sup> was placed upon a mount within the cylinder, shown in figure 4.18, with a closer view of the oven plate in figure 4.19. The modifications consisted of replacing the end-plates with Thermoflex insulating foam. The end-plates have a window to admit light to the heated cavity as the oven is designed for the purpose of controlling the temperature of a PPLN crystal. The solder-attached fibre would need to be broken to pass through the window, or the end-plate cut. It was easier to remove the plates and attach insulating material providing a smaller window in two semi-circular sections adhered to the top and lower cylindrical oven body parts, as illustrated in figure 4.20. A narrow gap in the Thermoflex semi-circles allows unimpeded passage for the fibre through the oven. This is to ensure that the fibre strain applied is experienced by the FBG located in the oven.

The cavity volume is far larger than that required to accommodate the fibres. Given the dimensions of the fibre, the thermal convection permitted in the cavity might introduce large temperature effects. Suitably sized Thermoflex insulating foam was fitted to the top half of the oven body, to occupy as much of the PPLN

<sup>24</sup>PPLN: Periodically-poled lithium niobate.

<sup>25</sup>The PV40 has since been discontinued (as of or before 15<sup>th</sup> November, 2009).

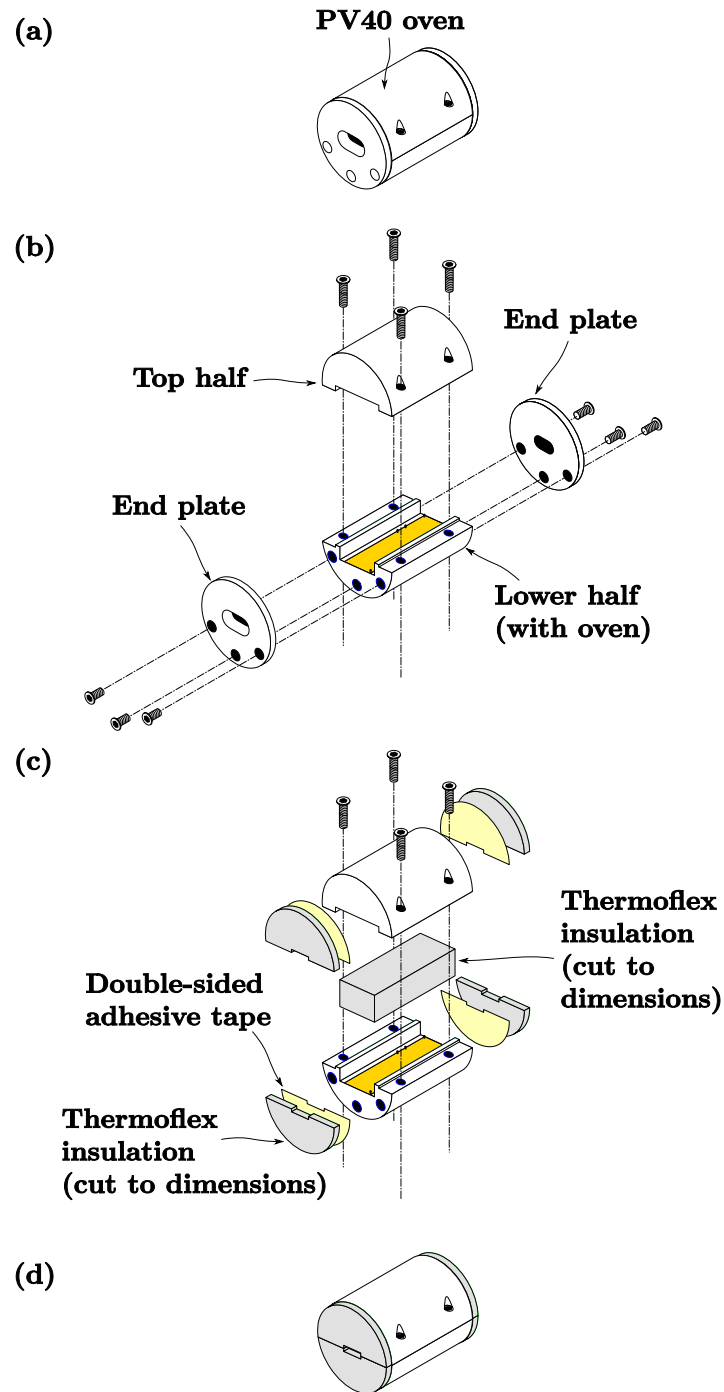


**Figure 4.20:** Modified *Thorlabs* PV40 oven. (a) Schematic of PV40 oven (power cord not shown); (b) Exploded view of PV40, indicating the disassembly required; (c) End-plates replaced with Thermoflex foam insulation, adhered to PV40 top and lower sections by double sided adhesive, and a parallelepiped of insulation foam to occupy the cavity above the fibres where the PPLN crystal would sit; (d) modified PV40 reassembled.

crystal cavity as possible without impinging on the fibres and influencing the strain measurements. A schematic representation of the modifications is shown in figure 4.20.

## 4.4 Results & Discussion

The results are presented for the quasi-static strain characterisation, dynamic strain characterisation and strain-temperature discrimination patent application work separately.

### 4.4.1 Quasi-static strain characterisation results & discussion

While the OSA can average data to produce smoother scans, it does so on a point-by-point basis. The scan time of the OSA is therefore increased by the number of averages performed. As the spectrum may be changing due to strain relaxation, temperature and/or vibration it is desirable to keep the scan time as short as possible. This allows as close as possible to an ‘instantaneous’ spectrum to be obtained.

This suggests taking single scans and averaging them. The disadvantage of this approach is the requirement to manually save each scan to a file on disk. To complete a single scan and save to file, with required menu navigation, took up to two minutes. It was found that despite the minute-scale time difference between scans the averaged spectral profiles at different strain settings agreed better than using the OSA’s averaging. It was, therefore, better to scan the spectrum quickly than aim for low noise by point-by-point averaging.

Ten scans per strain setting were averaged to smooth the noise present in an individual scan. The anisotropic FBG under test was in a fibre of length<sup>26</sup> 1.175 m. The translation stage steps<sup>27</sup> of 200  $\mu\text{m}$  resulted in applied strain steps of 0.17  $m\epsilon$ .

The change in wavelength for applied strain is shown in figure 4.21. The strain response is determined to be  $1.2601 \pm 0.00013 \text{ pm}/\mu\epsilon$  [15], with the residuals to the fit shown in figure 4.22. The normalised strain response, i.e. dividing by the nominal at rest wavelength value,  $\lambda_B$ , is  $0.8135 \times 10^{-6} \mu\epsilon^{-1}$ . While compensating errors might explain the 1 in  $10^4$  uncertainty, it is also observed that the spectral profile remains comparatively unchanged, as shown in figure 4.23. The apparent preservation of spectral profile would account for the low uncertainty, and suggests that the accuracy of the recording system is the limiting factor. The quasi-static

---

<sup>26</sup>The length thus greatly exceeded the recommended lengths to eliminate [59] possible shear lag of the sensor [60].

<sup>27</sup>The temperature equivalent would be steps of 20 °C, using the anisotropic FBG temperature response of 10.7 °C [2].

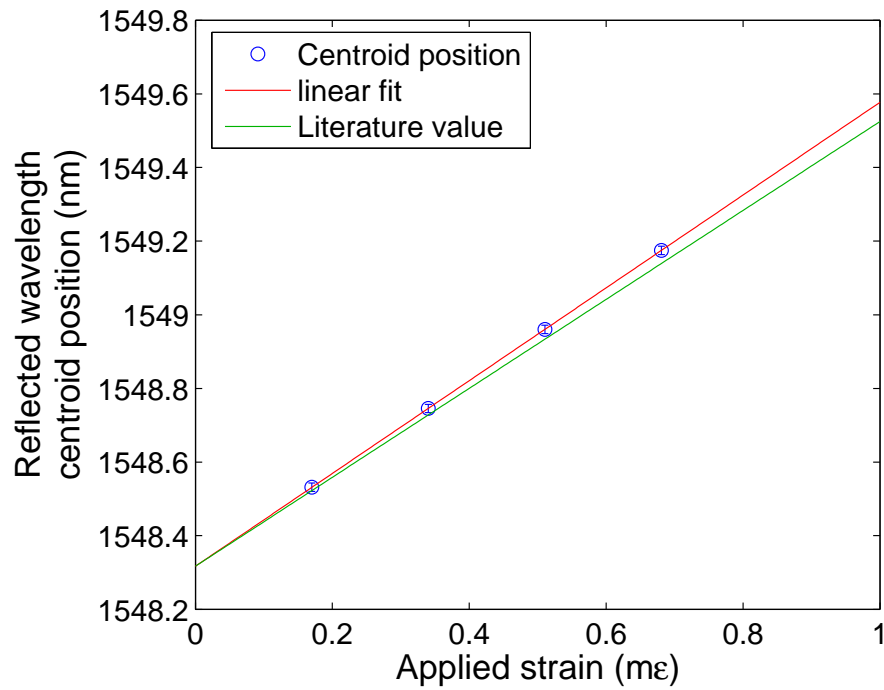


**Figure 4.21:** Strain response of anisotropic FBG. Slope of fit to data is  $1.2601 \pm 0.00013 \text{ pm}/\mu\epsilon$  ( $0.8135 \times 10^{-6} \mu\epsilon^{-1}$ ). Also shown is the literature value ( $0.78 \times 10^{-6} \mu\epsilon^{-1}$ ) slope [9].

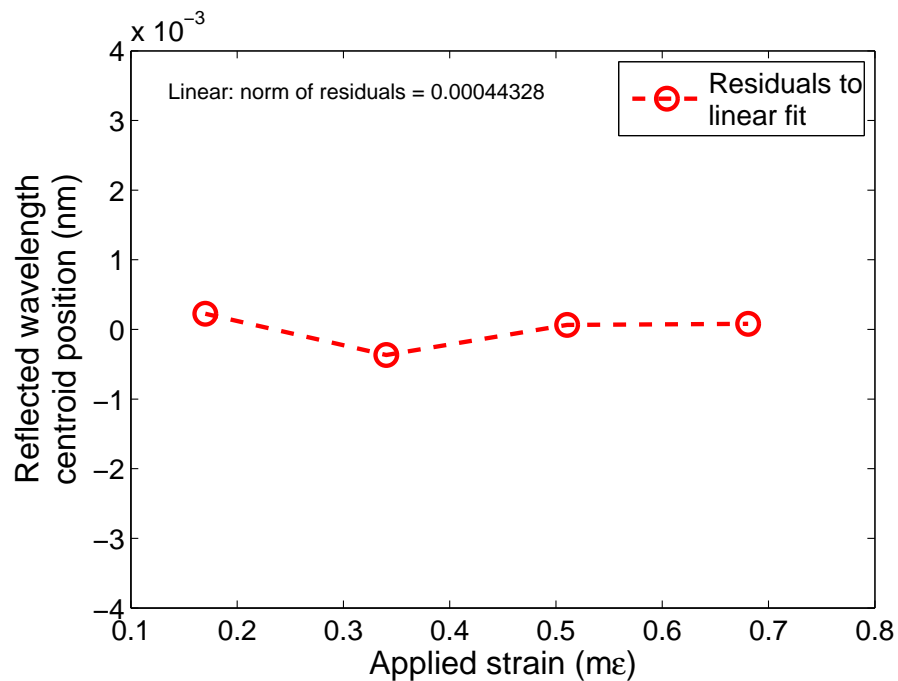


**Figure 4.22:** Residual of linear fit to data from 4.21.

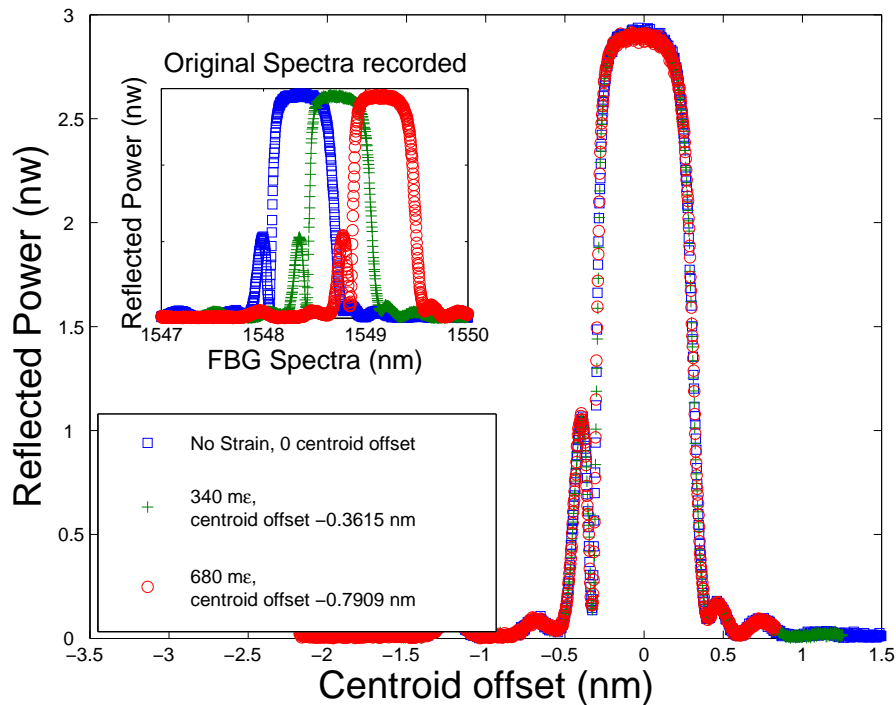


**Figure 4.23:** Apparent preservation of spectral profile, with original data inset. The inset shows the FBG reflection spectra for the anisotropic FBG at rest, with  $340 \mu\epsilon$  and with  $680 \mu\epsilon$ . The main figure shows the spectral profiles offset by their respective calculated centroids. The high degree of overlap suggests good spectral profile preservation.

strain characterisation was reported in the EWOFS submission [15]. The spectral profile preservation was not fully investigated and so was examined in the following section.

#### 4.4.2 Dynamic strain characterisation results & discussion

It was intended to characterise the strain response at a smaller scale in addition to the large strain steps reported in §4.4.1. With the Laser2000 isotropic FBGs it was possible to compare the Anisotropic FBGs with other FBGs and confirm that the response was strain related<sup>28</sup>.

Figure 4.24 shows an example of the spectrum recorded by the SpectroBragg

<sup>28</sup>The temperature response of the anisotropic FBGs is assumed the same as the isotropic FBGs. This assumption is made as the temperature response of hydrogen loaded 264 nm FBGs was found to be dependent upon the material properties of the fibre [2, 3, 61, 62]. The anisotropic FBGs discussed here were inscribed in hydrogen free SMF-28, which is not explicitly characterised in these references. The hydrogen loading leads to the absence of the anisotropic transverse stress distribution [4]. The index modulation arises from compaction in the hydrogen free case and colour-centres in the hydrogenated case. The FBG temperature response should be dominated by the fibre material properties response to temperature.

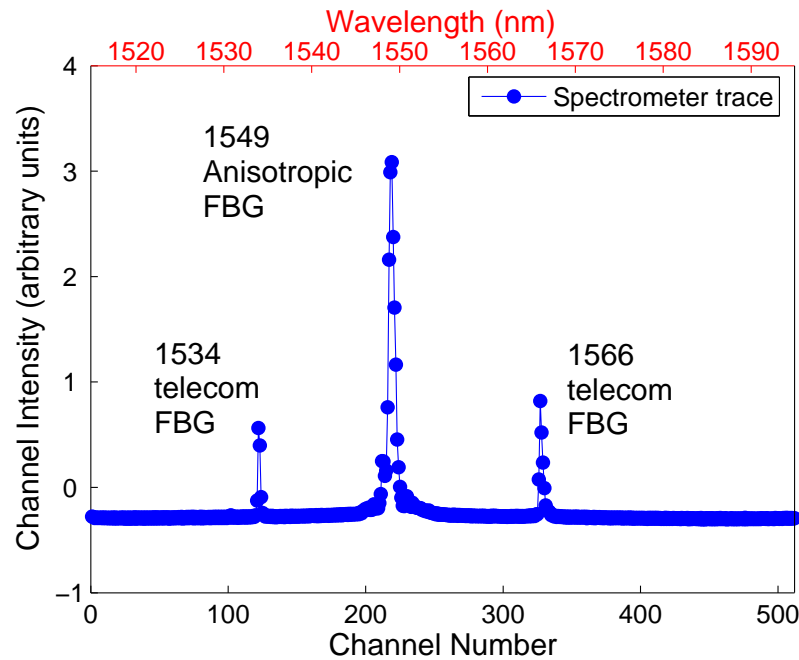


**Figure 4.24:** Example spectrum from the SpectroBragg spectrometer. The spectrometer’s InGaAs array has 512 elements, covering approximately a 70 nm window. Shown in the figure are Laser2000 telecoms FBGs at 1534 nm and 1566 nm; and an anisotropic FBG at 1549 nm.

spectrometer. The isotropic FBGs are of lower reflectance than the anisotropic FBG under test. Additionally, the anisotropic FBG has a greater bandwidth than the isotropic FBGs, as evident in figures 4.1 (page V.I - 176) and 4.2 (page V.I - 176).

The narrower spectral profile reduces the number of data points in a centroid calculation, decreasing the signal to noise ratio. Similarly, the lower spectral intensity reduced the signal to noise, as per pixel noise is relatively larger. This results in the anisotropic FBG having a higher SNR than the strain comparison isotropic FBG and temperature reference isotropic FBG. Decreasing steps of  $10.6 \mu\epsilon$  were applied every 30 s. For a total dataset of  $10^4$  scans, these strain steps are approximately 350 scans each.

The centroid algorithm, equation (3.19) (page V.I - 133), was used to determine the peak wavelength. As discussed in section §3.2.3 (page V.I - 133), instead of a threshold cut based upon intensity, a window of  $2n_w + 1$  was taken about the position of maximum intensity.  $n_w$  was typically in the range of  $n_w = 3 - 7$  about the maximum, depending upon the width of the FBG.

A different anisotropic FBG was used for this work as the previously characterised FBG was broken before the apparatus for the dynamic strain-characterisation was ready. The length of fibre used for this experiment was 0.945 m long, with

the FBG located approximately midway. Figure 4.19 (page V.I - 195) shows the FBGs in the apparatus used here. The black marks along the fibre delimit the few cm within which the FBGs are inscribed.

Taking the mean value of the central 300 data of each strain step, and plotting against strain returns the strain response of the FBGs. Figures 4.26 and 4.28 show the strain responses for the anisotropic and isotropic FBGs respectively. The normalised strain responses, equation (2.109) (page V.I - 69),  $\frac{1}{\lambda_{B0}} \frac{\Delta\lambda_B}{\Delta\varepsilon_\sigma}$ , are  $0.75 \times 10^{-6} \mu\varepsilon^{-1}$  and  $0.73 \times 10^{-6} \mu\varepsilon^{-1}$  respectively. Also shown is the reported literature value of  $0.78 \times 10^{-6} \mu\varepsilon^{-1}$  [9]. Figures 4.27 and 4.29 show the residual to the linear fits for the anisotropic and isotropic FBGs respectively. It should be noted that the double dipped, ‘w’ shape of the residual in figure 4.27 is visible when overlaying the isotropic and anisotropic data from figure 4.25, as the anisotropic FBG crosses over the isotropic FBG.

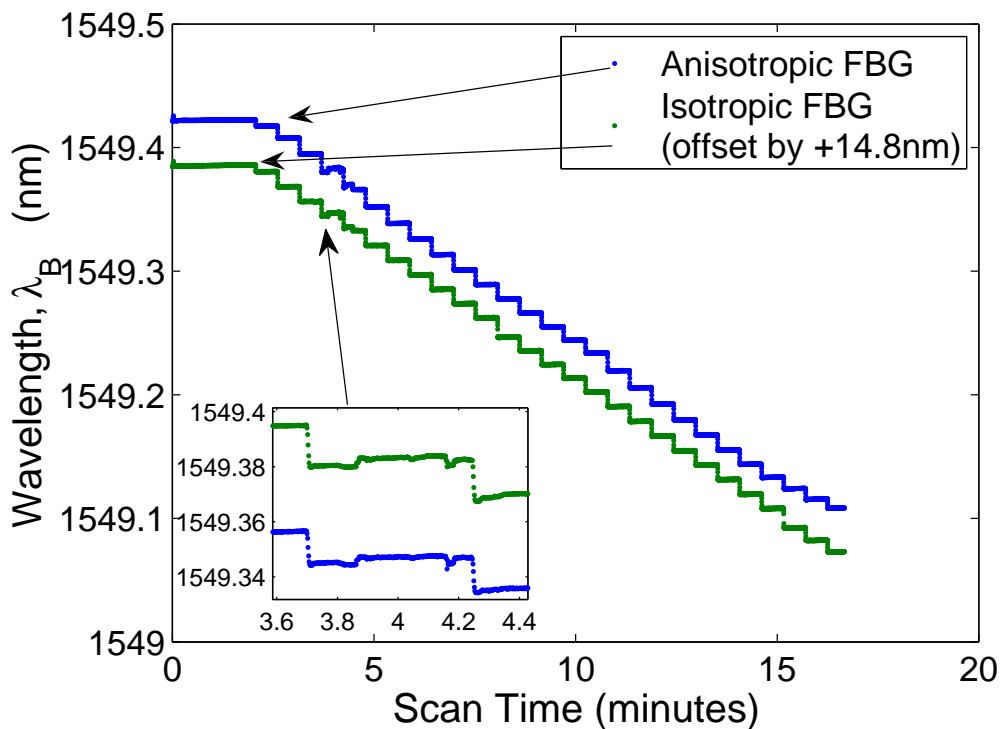


**Figure 4.25:** Calculated centroid for the anisotropic and isotropic FBGs under strain. The stability of the centroid value demonstrates the stability of the environmental enclosure. Inset is an example of low scale noise, replicated in time and profile by both FBGs.

The strain response values are lower than the literature value [9]. The change in the temperature reference is smaller than the difference between the literature value and those calculated for the strained anisotropic and isotropic FBGs. The strain

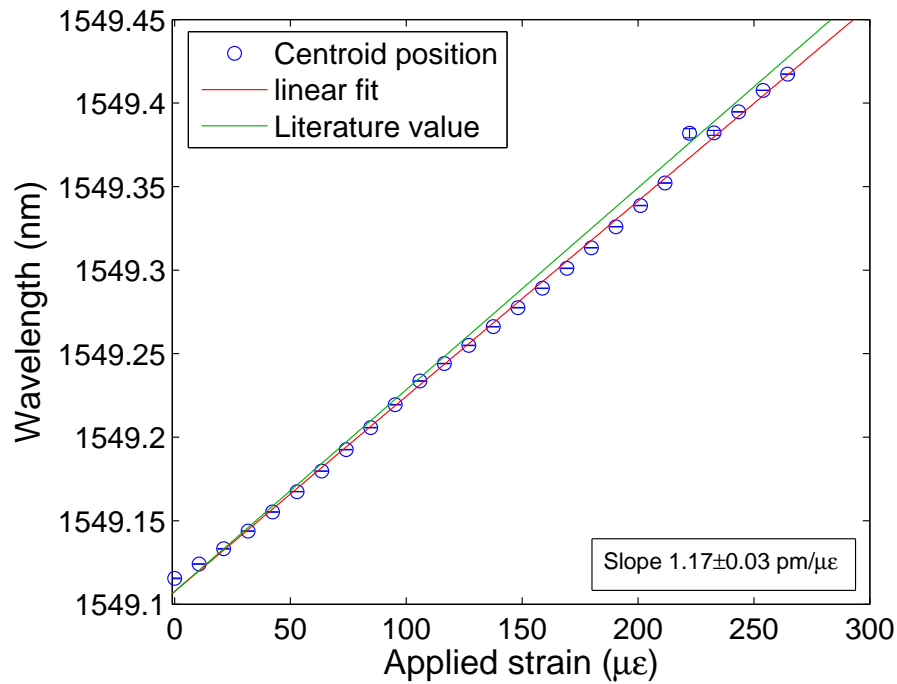


**Figure 4.26:** Plot of strain response for the anisotropic FBG over 0 – 265  $\mu\epsilon$ . Strain response is  $\sim 1.17 \pm 0.03 \text{ pm}/\mu\epsilon$  ( $0.75 \times 10^{-6} \mu\epsilon^{-1}$ ). The corresponding strain response of the isotropic FBG literature value ( $0.78 \times 10^{-6} \mu\epsilon^{-1}$ ) is also plotted [9].

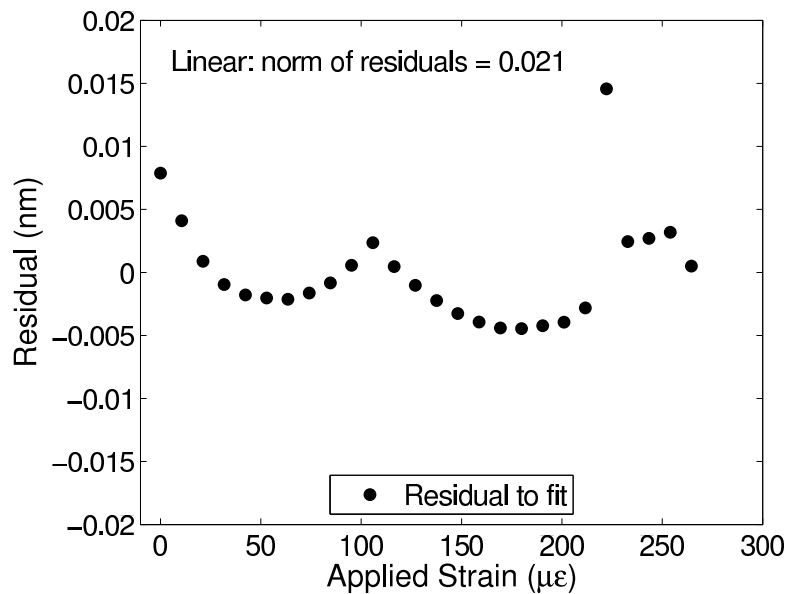


**Figure 4.27:** Plot of residual to linear fit for anisotropic FBG. Note the double dipped ‘w’ shape of the residual, which is absent from the residual to the fit for the isotropic FBG, figure 4.29.

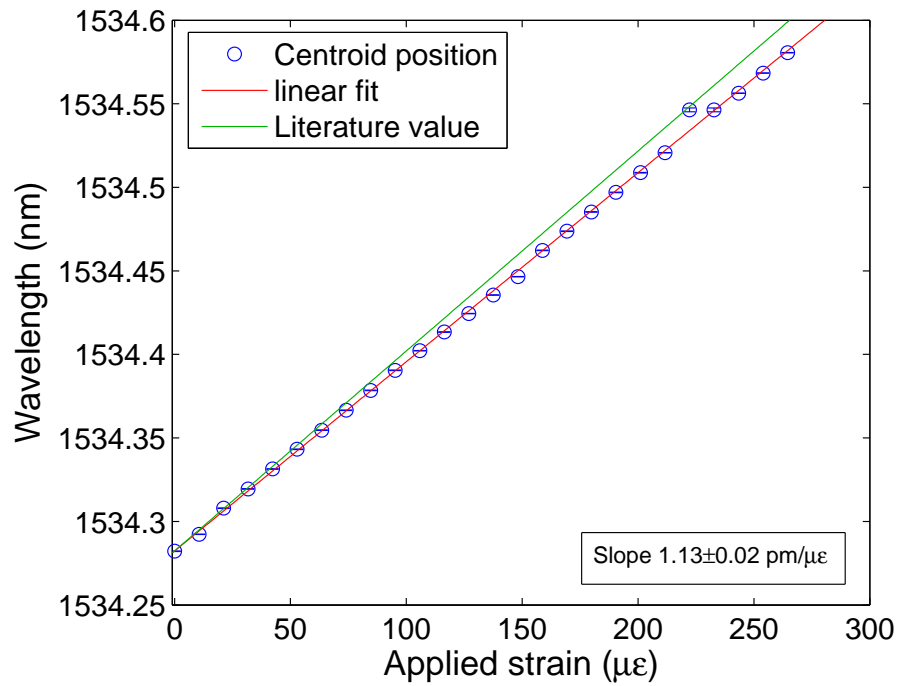


**Figure 4.28:** Plot of strain response for the isotropic FBG over 0 – 265  $\mu\epsilon$ . Strain response is  $\sim 1.13 \pm 0.02$  pm/ $\mu\epsilon$  ( $0.74 \times 10^{-6} \mu\epsilon^{-1}$ ). The corresponding strain response of the isotropic FBG literature value ( $0.78 \times 10^{-6} \mu\epsilon^{-1}$ ) is also plotted [9].

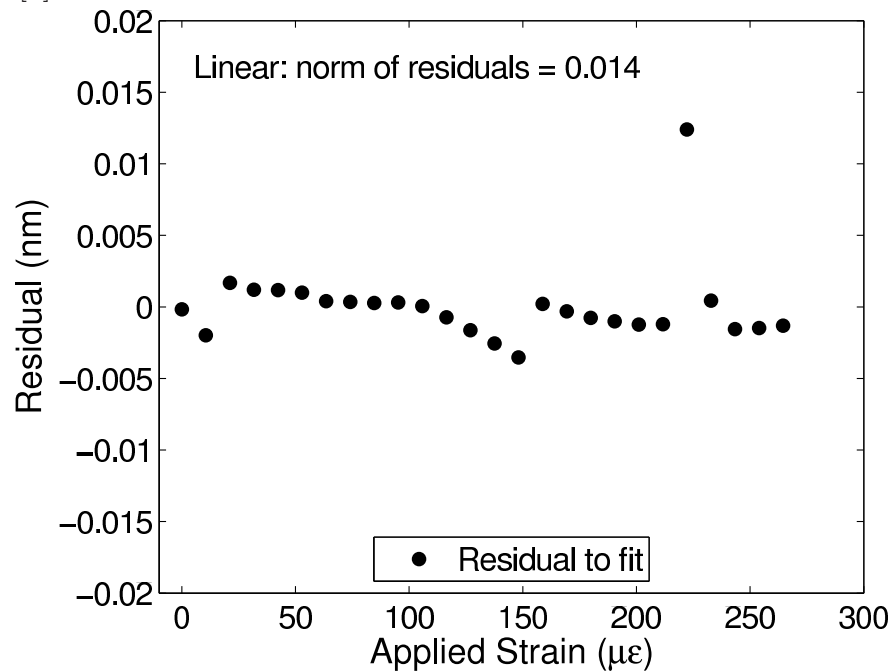


**Figure 4.29:** Plot of residual to linear fit for isotropic FBG.

response values for the quasi-static and dynamic experiments are gathered in table 4.2, along with the temperature reference FBG and literature value.

Experiment	FBG	$\frac{1}{\lambda_{B0}} \frac{\Delta\lambda_B}{\Delta\varepsilon_\sigma}$ ( $\times 10^{-6} \mu\varepsilon^{-1}$ )	Act. Step ( $\mu\varepsilon$ )	Ideal step ( $\mu\varepsilon$ )
Quasi-static	Aniso.	0.81	170	178
Dynamic	Aniso.	0.75	10.6	10
	Iso.	0.74	10.6	10
	Temp.	-0.0082	—	—
Lit. value	Iso.	0.78	—	—

**Table 4.2:** Strain response values for the quasi-static and dynamic anisotropic FBG strain response experiments, with actual and idealised (i.e. would return literature value) strain steps.

The quasi-static strain response value exceeds the literature value, unlike the dynamic strain response value. A possible explanation for these discrepancies may be that, for the quasi-static experiment, the strain step sizes induced a cantilever motion on the fibre solder mounts shown schematically in figure 4.10 (page V.I - 188). This would have understated the step size, as presented in the difference between the actual and ‘ideal’<sup>29</sup> step sizes in table 4.2.

For the dynamic strain experiment, the length step size may not have equalled the intended step size, as the motor had to accelerate and then decelerate over a short interval. This would have overstated the step size, again presented in the difference between the actual and ‘ideal’ step sizes in table 4.2. The possible effects of fibre tension on the step size was the motivation to use decreasing steps, as the motor acceleration would be in the same direction as the fibre tension, if it had an appreciable effect.

As discussed in section §4.3.11 (page V.I - 191), differences in the lengths of the fibre due to soldering are unlikely to be a significant issue<sup>30</sup>, and would not account for the ‘w’ profile of the residual. Figures 4.30 and 4.31 show the response of the isotropic FBG used as a temperature reference. The temperature reference isotropic FBG records the outlier in the fifth and fourth-last data in figures 4.26 – 4.29. However there is no ‘w’ shape, and demonstrates a mild cooling of the environment,  $\sim 0.026 \text{ }^\circ\text{C}$ , using the normalised thermal responsivity value of  $6.67 \times 10^{-6} \text{ }^\circ\text{C}^{-1}$  from [9].

The anisotropic FBG fibre was clad in acrylate and the isotropic FBG fibre clad in polyimide. The strain responses of these materials are not the same, which may

<sup>29</sup>The step sizes which would produce the literature value slope, given the captured wavelengths.

<sup>30</sup>If the fibre responses were equal the difference in length required to provide the reported slopes would be 0.11% or  $\sim 1 \text{ mm}$ . As the fibres were held under the same tension during the soldering process, it is unlikely a difference of 1 mm between fibres would arise.

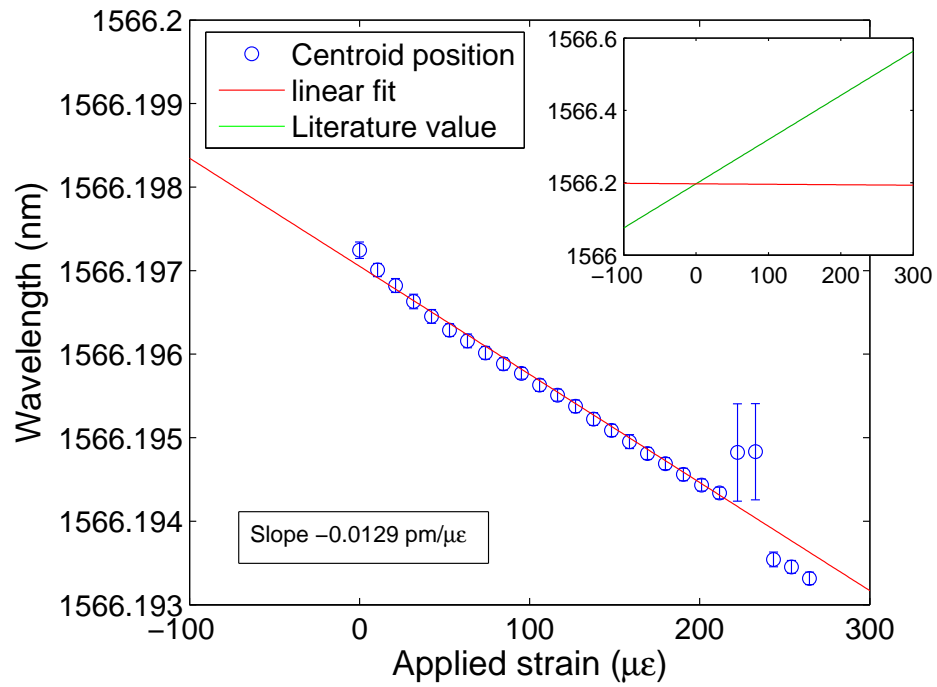


**Figure 4.30:** Plot of strain response for the temperature reference isotropic FBG. Strain response is  $\sim -0.013 \text{ pm}/\mu\epsilon$  ( $-0.0082 \times 10^{-6} \mu\epsilon^{-1}$ ), equivalent to a maximum temperature difference of  $0.37 \text{ }^\circ\text{C}$  using the temperature response value of  $10.7 \text{ pm}/^\circ\text{C}^{-1}$  [2]. Inset shows the isotropic FBG literature strain response value ( $0.78 \times 10^{-6} \mu\epsilon^{-1}$  [9]).

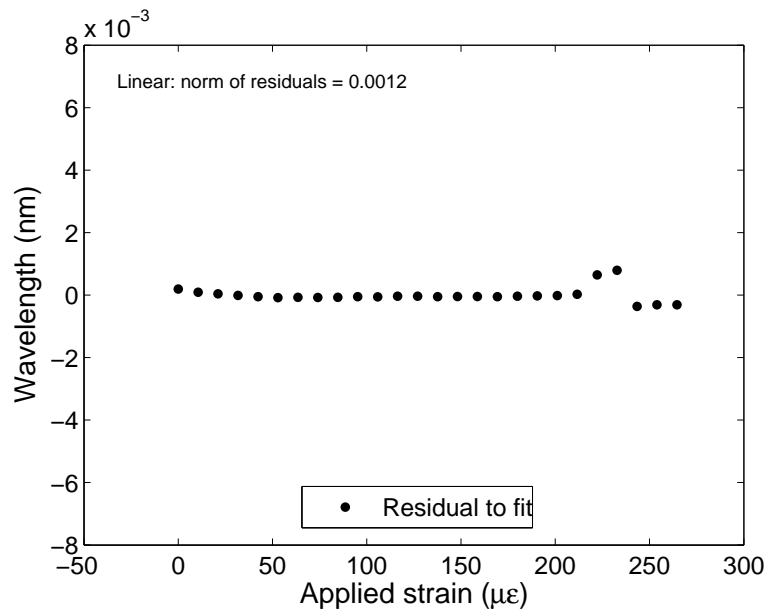


**Figure 4.31:** Plot of residual to linear fit for isotropic FBG.

have some small effect on the FBGs over the longer timescale shown (minutes). This could become an issue for the detection of small strains with large lengths of fibre.

In the current experiment, the FBG characterised in [15] was not the same as that in [16] perhaps explaining the difference between the values of  $\sim 1.26 \pm 0.03$  pm/ $\mu\epsilon$  [15] and  $\sim 1.17 \pm 0.03$  pm/ $\mu\epsilon$  [16]. The PDL values for the two anisotropic FBGs were different, with that for the FBG in [15] being larger than for the FBG in [16]. It may also be a temperature effect that occurred over the period of hours during which the data were taken, but to explain such a difference would require an increase of  $1.43 \pm 0.05^\circ\text{C}$  per step between data points, for the data captured over two days.

The discrepancy is unlikely to be a calibration issue. The OSA was calibrated using the tuneable telecomms lasers. Five steps in the range of 1567.13 nm... 1568.13 nm were measured by the OSA. The slope of the plot of the wavelength centroid value against configured wavelength deviated from unity by 0.667%.

Assuming the recorded values are correct, the imposed values of strain could be incorrect. Using the value of  $\sim 1.17 \pm 0.03$  pm/ $\mu\epsilon$  to determine the strain steps from the obtained wavelength values gives a step size of  $183.3 \pm 0.4$   $\mu\epsilon$  instead of  $170$   $\mu\epsilon$ . These correspond to linear extensions of  $215.4 \pm 0.5$   $\mu\text{m}$  instead of  $200$   $\mu\text{m}$ , or  $\sim 7.7\%$  greater than configured. As the same stage and control systems were used for both experiments, it is unlikely that the behaviour of the stage differed so significantly, considering the full range of strain in figure 4.26 (page V.I - 202) exceeds an individual step in figure 4.21 (page V.I - 198).

By using the speed of the SpectroBragg to observe dynamic behaviour beyond that visible to the OSA, the linearity observed with the SpectroBragg complemented the larger range strain calibration performed by the OSA. The spectral profile preservation observed during the quasi-static strain characterisation work was also characterised. The spectral profiles of the applied strain spectra are cross-correlated with the zero applied strain spectrum. Figure 4.32 shows the cross-correlations for the four strain settings  $170$   $\mu\epsilon$ ,  $340$   $\mu\epsilon$ ,  $510$   $\mu\epsilon$ ,  $680$   $\mu\epsilon$ . The spectral profiles were also interpolated and offset to find the minimum difference (i.e. where the profiles were of most similar shape). Figure 4.33 shows the applied strain spectra overlayed on the zero applied strain spectrum. The centroid calculated offsets, the offset interpolated minima and the cross-correlated maxima differed by two parts in  $10^3$ . This exceeds the native resolution of the OSA, and so it can be said that no discernable change could be detected in the spectral profiles under the applied strains reported here.

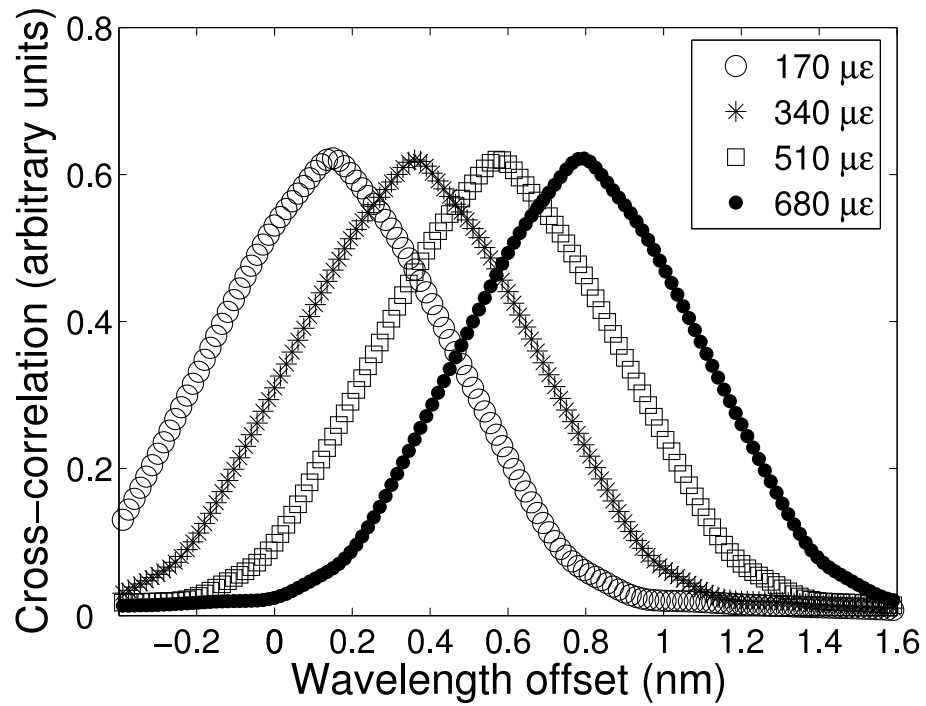


**Figure 4.32:** Plot showing every 50<sup>th</sup> point in the cross-correlations of strained spectra with the unstrained spectrum, obtained by the OSA. The maxima indicate the position of best correlation.

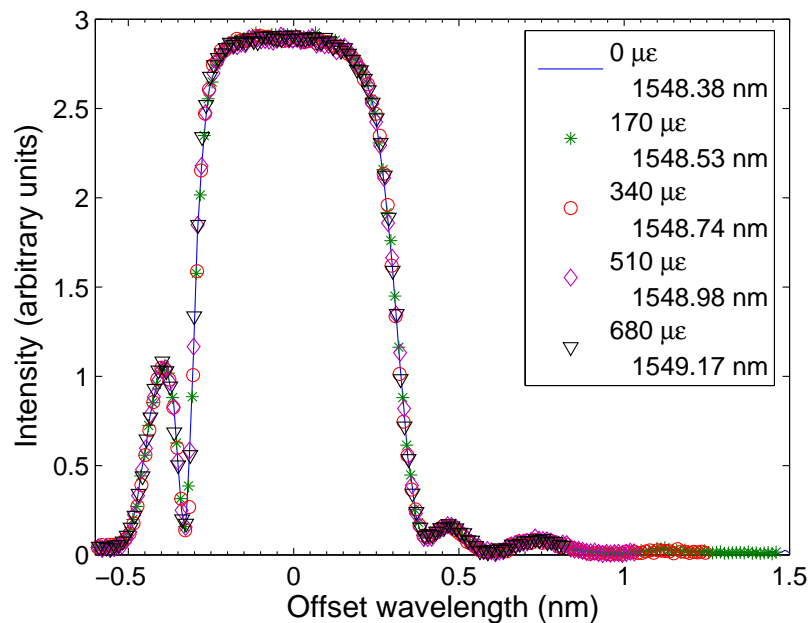


**Figure 4.33:** Plot showing every 4<sup>th</sup> point of strained FBG spectra, offset by centroids. The zero-strain spectra is a continuous blue line, with the strained spectra overlaid.

### 4.4.3 Results of work for strain–temperature discrimination

The preservation of spectral shape under strain prompts the question: does the spectral shape change under temperature? If so, and the shape change could be detected, it might be possible to simultaneously detect *and discriminate* temperature and strain changes.

The possibility of this temperature–strain discrimination was the motivation for the purchase of the PPLN oven. The same setup as shown in figure 4.14 (page V.I - 192) was employed, but with the OSA in place of the Čzerny–Turner SpectroBragg. The intention was to perform strain measurements at controlled temperature settings to produce a  $2 \times 2$  matrix of strain and temperature settings, as discussed in section §2.2.6.1 (page V.I - 47).

The experimental work programme was interrupted by the Optics Research Group moving laboratory, so a reduced programme was performed to attempt to demonstrate the possibility of temperature–strain discrimination. The OSA was controlled over GPIB<sup>31</sup> by LabVIEW. The GPIB control of the OSA was time consuming when scanning three FBGs, with much time spent on configuring the OSA for each scan.

Approximately forty scans were performed in a cyclical sequential fashion for each FBG: the first FBG was scanned, then the second and third, then back to the first FBG.

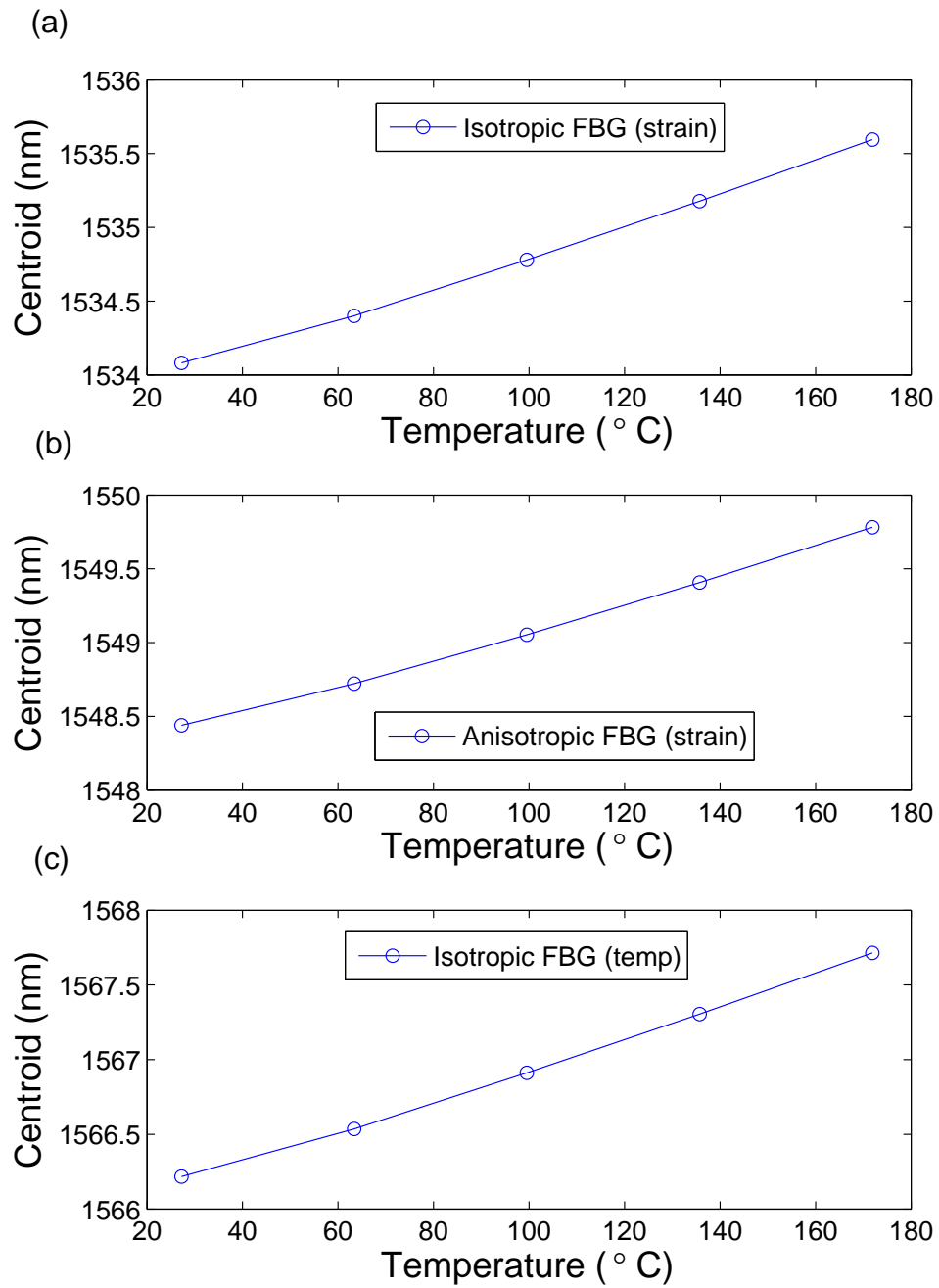
Figure 4.34 shows the centroid calculated on the profiles of the three FBGs (two attached to be strained, one free as in figure 4.19 (page V.I - 195)) over five temperature steps. The flat–top of the anisotropic FBG exhibited greater change in spectral bandwidth under temperature changes than the more Gaussian shaped isotropic FBGs. To determine the bandwidth, the height was calculated. The points nearest to half the height were subtracted to give the bandwidth. To check that the OSA’s maximum sampling was sufficient, test FBG profiles were interpolated by cubic–spline, but this yielded no improvement over the cruder method described.

Figure 4.35 shows the response of the bandwidth to temperature. The results are more apparent from comparing the changes as a percentage from the initial temperature of 27.2 °C. Figure 4.36 (page V.I - 211) shows the data of figure 4.35 rescaled as percentage changes against temperature changes. The third point is anomalous in both the anisotropic and isotropic applied strain datasets and may be discounted.

The anisotropic FBG appears to exhibit a dramatically different response to temperature than do both isotropic FBGs. Despite the anisotropic FBG being of originally greater bandwidth, the flat–top spectral profile enables a more pronounced

---

<sup>31</sup>IEEE-488 General Purpose Interface Bus.



**Figure 4.34:** Plot of the centroid response to temperature changes of the three FBGs: (a) Isotropic (strain); (b) Anisotropic (strain); and (c) Isotropic (temperature reference).

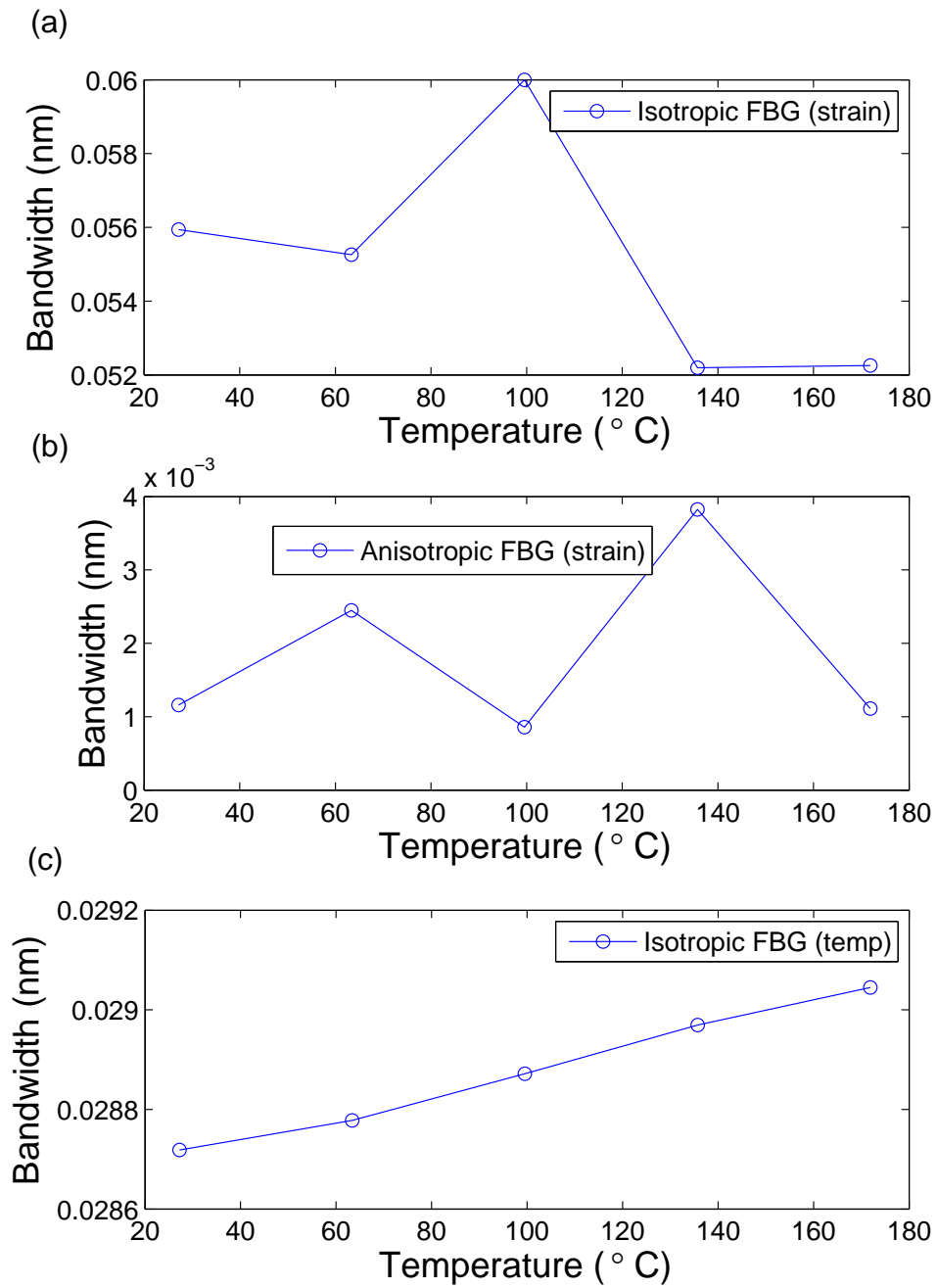


**Figure 4.35:** Plot of the spectral bandwidth response to temperature changes of three FBGs: (a) Isotropic (strain); (b) Anisotropic (strain); and (c) Isotropic (temperature reference).

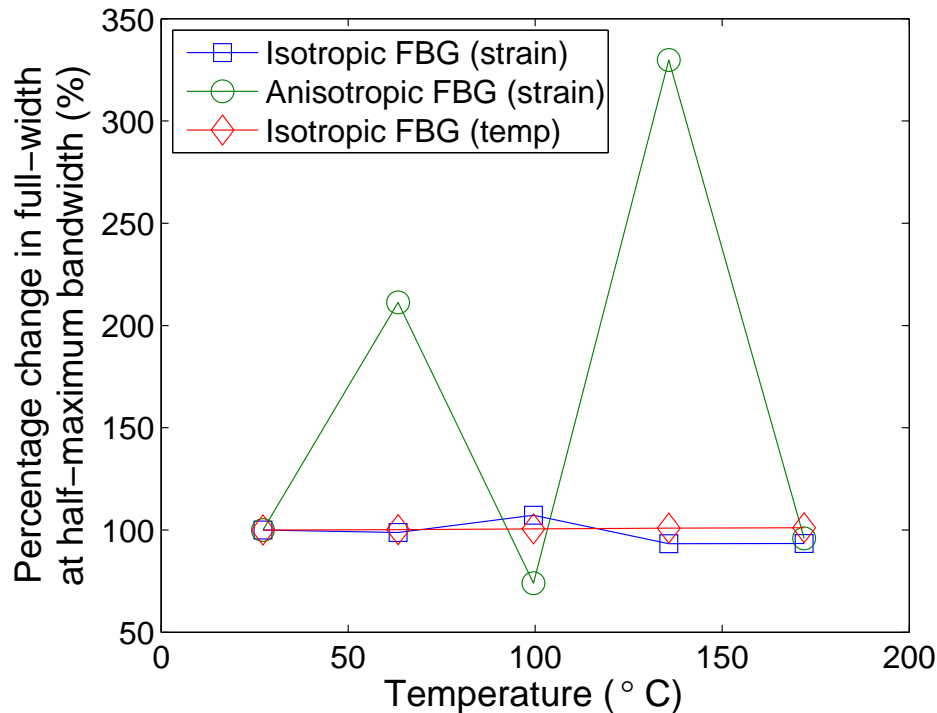


**Figure 4.36:** Plot of the percentage change in spectral bandwidth of three FBGs in response to temperature changes.

change to be detected than does the Gaussian profile, where the down sloping sides scale the broadening.

The final point does not conform to the trend shown in the figure 4.34. However, the time-constraints for the experiment meant that the data could not be processed before disassembly had to be begun, and so the patent application proceeded with these data. The behaviour of the third and fifth point could not, therefore, be further examined.

Consequently, a thorough examination of the strain-temperature would require further work: to understand or discount the anomalous fifth data point, and to determine any strain or temperature limitations to this technique. Strain relaxation will eventually occur, as the FBG's annealing temperature is eventually exceeded. The temperature response might also be used as a probe of glass temperature dynamics, as reduced anisotropy tends toward the isotropic FBG response.

## 4.5 Conclusion

The strain characterisation of a novel anisotropic FBG inscribed into SMF-28 fibre has been established. The suitability of these novel anisotropic FBGs for use as

strain sensors comparable to standard telecomms FBGs has been demonstrated.

An adaptable apparatus for strain characterisation was developed, which enabled quasi-steady-state strain characterisation of these novel FBGs over  $0 - 700 \mu\epsilon$  using an optical spectrum analyser, and dynamic strain characterisation in steps of  $10.6 \mu\epsilon$  over the range  $0 - 265 \mu\epsilon$ , using the SpectroBragg spectrometer. The strain response of these anisotropic FBGs ( $0.75 \times 10^{-6} \mu\epsilon^{-1}$ ) was similar to standard telecomms FBGs (from the literature [9]:  $0.78 \times 10^{-6} \mu\epsilon^{-1}$ ; from the experiment:  $0.73 \times 10^{-6} \mu\epsilon^{-1}$ ). These novel anisotropic FBGs can be used as drop-in replacements to standard telecomms FBGs, without requiring the alteration of sensing systems or demodulation systems parameters (such as free spectral range).

The preservation of spectral profile suggests that the anisotropic FBGs might allow strain-temperature discrimination. In the range tested, thorough measurements suggest that strain does not significantly alter the separation of the anisotropic FBGs component peaks. Conversely, a brief initial investigation (truncated by the exigencies of a laboratory-move) indicated that temperature changes tested might have a much greater effect and so alter the spectral profile. By measuring the bandwidth, such as the full-width at half-maximum, it would appear there is a possibility the temperature may be inferred. The width of a standard telecomms FBG requires greater resolution<sup>32</sup> to detect temperature-induced changes in spectral width. The initial experimental results are at least of sufficient interest and promise, to suggest that further work would be justified.

---

<sup>32</sup>Using the values which generated the curves in figure 4.3 (page V.I - 179), the increase in resolution required to detect changes in the FWHM of the Gaussian curve to the same resolution as the FWHM of the Super-Gaussian curve, is  $\sim 1.4\%$ . This would correspond to an extra  $\sim 7.3$  pixels on a 512 pixel array over the same spectral bandwidth as the 512 pixel array.

---

## 4.6 References

- [1] A. Dragomir, D. N. Nikogosyan, K. A. Zagorulko, P. G. Kryukov, and E. M. Dianov. Inscription of fiber Bragg gratings by ultraviolet femtosecond radiation. *Opt. Lett.*, 28(22):2171–2173, 2003.
- [2] D. N. Nikogosyan. Multi-photon high-excitation-energy approach to fibre grating inscription. *Meas. Sci. Technol.*, 18(1):R1–R29, January 2007.
- [3] S. A. Slattery, D. N. Nikogosyan, and G. Brambilla. Fiber Bragg grating inscription by high-intensity femtosecond UV laser light: comparison with other existing methods of fabrication. *J. Opt. Soc. Am. B*, 22(2):354–361, February 2005.
- [4] H. G. Limberger, C. Ban, R. P. Salathé, S. A. Slattery, and D. N. Nikogosyan. Absence of UV-induced stress in Bragg gratings recorded by high-intensity 264 nm laser pulses in a hydrogenated standard telecom fiber. *Opt. Express*, 15(9):5610–5615, 2007.
- [5] E. Chehura, C. C. Ye, S. E. Staines, S. W. James, and R. P. Tatam. Characterization of the response of fibre Bragg gratings fabricated in stress and geometrically induced high birefringence fibres to temperature and transverse load. *Smart. Mater. Struct.*, 13(4):888–895, 2004.
- [6] J. D. C. Jones. Review of fibre sensor techniques for temperature-strain discrimination. In *Optical Fiber Sensors*, volume 16 of *OSA Technical Digest Series*, page OTuC1. Optical Society of America, 1997.
- [7] B. Lee. Review of the present status of optical fiber sensors. *Opt. Fiber Technol.*, 9(2):57–79, 2003.
- [8] Y. J. Rao. In-fibre Bragg grating sensors. *Meas. Sci. Technol.*, 8(4):355–375, April 1997.
- [9] A. D. Kersey, M. A. Davis, H. J. Patrick, M. LeBlanc, K. P. Koo, C. G. Askins, M. A. Putnam, and E. J. Friebele. Fiber grating sensors. *J. Lightwave Technol.*, 15(8):1442–1463, August 1997.
- [10] A. Rogers. Distributed optical-fibre sensing. *Meas. Sci. Technol.*, 10(8):R75–R99, 1999.
- [11] B. Culshaw. Fiber optics in sensing and measurement. *IEEE J. Sel. Top. Quant.*, 6(6):1014–1021, 2000.
- [12] A. Othonos and K. Kalli. *Fiber Bragg Gratings : Fundamentals and Applications in Telecommunications and Sensing*, chapter 7, pages 301–396. Optoelectronics Library. Artech House, Inc., Boston, 1999. ISBN: 0890063443.
- [13] K. T. V. Grattan and B. T. Meggitt, editors. *Optical Fiber Sensor Technology: Fundamentals*, chapter 1, pages 1–44. Kluwer Academic Press, Dordrecht, 2000. ISBN: 0792378520.

- 
- [14] R. Kashyap and J. M. Lopez-Higuera. *Fibre grating technology: theory, photosensitivity, fabrication and characterization*, chapter 17, pages 349–377. Handbook of Optical Fibre Sensing Technology. John Wiley & Sons, Ltd., Chichester, 2002. ISBN: 0471820539.
- [15] R. P. O’Byrne, S. V. Sergeyev, D. A. Flavin, and D. N. Nikogosyan. Strain characterization of fiber Bragg gratings inscribed by high-intensity femtosecond UV pulses. In A. Cutolo, B. Culshaw, and J. M. Lopez-Higuera, editors, *Proceedings of the Third European Workshop on Optical Fibre Sensors*, volume 6619. SPIE, July 2007. ISBN: 9780819467614.
- [16] R. P. O’Byrne, S. V. Sergeyev, D. A. Flavin, S. A. Slattery, D. N. Nikogosyan, and J. D. C. Jones. Anisotropic fiber Bragg gratings inscribed by high-intensity femtosecond-UV pulses: manufacturing technology and strain characterization for sensing applications. *IEEE Sens. J.*, 8(7):1256–1263, July 2008.
- [17] M. Born and E. Wolf. *Principles of Optics: Electromagnetic Theory of Propagation, Interference and Diffraction of Light*, chapter 14, pages 735–789. Cambridge University Press, Cambridge, 7th edition, 1999. ISBN: 0521642221.
- [18] B. J. Berne and R. Pecora. *Dynamic Light Scattering: With Applications to Chemistry, Biology, and Physics*, chapter Appendix 10.C, pages 263–272. Dover Publications, Inc., New York, 2000. ISBN: 0486411559.
- [19] C. F. Bohren and D. R. Huffman. *Absorption and Scattering of Light by Small Particles*, chapter 1, pages 3–11. Wiley-VCH Verlag GmbH & Co. KGaA, Weinheim, 1st edition, 2004.
- [20] R. Kashyap. *Fiber Bragg Gratings*, chapter 2, pages 13–54. Academic Press, San Diego, 1999. ISBN: 0124005608.
- [21] A. M. Vengsarkar, Q. Zhong, D. Inness, W. A. Reed, P. J. Lemaire, and S. G. Kosinski. Birefringence reduction in side-written photoinduced fiber devices by a dual-exposure method. *Opt. Lett.*, 19(16):1260–1262, 1994.
- [22] A. Dragomir, J. G. McInerney, and D. N. Nikogosyan. Femtosecond measurements of two-photon absorption coefficients at  $\lambda = 264$  nm in glasses, crystals, and liquids. *Appl. Opt.*, 41(21):4365–4376, July 2002.
- [23] N. H. Ky, H. G. Limberger, R. P. Salathé, and F. Cochet. Effects of drawing tension on the photosensitivity of Sn-Ge- and B-Ge-codoped core fibers. *Opt. Lett.*, 23(17):1402–1404, September 1998.
- [24] R. Kashyap. *Fiber Bragg Gratings*, chapter 3, pages 55–118. Academic Press, San Diego, 1999. ISBN: 0124005608.
- [25] E. Udd, W. L. Schulz, J. M. Seim, E. D. Haugse, A. Trego, P. E. Johnson, T. E. Bennett, D. V. Nelson, and A. Makino. Multidimensional strain field measurements using fiber optic grating sensors. In R. O. Claus and W. B. Spillman Jr., editors, *SPIE’s 7<sup>th</sup> Annual International Symposium on Smart Structures and Materials*, volume 3986, pages 254–262. SPIE, 2000.
-

- 
- [26] R. J. Schroeder, R. T. Ramos, T. Yamate, and E. Udd. *Fibre optic sensors for oilfield services*, chapter 31, pages 671–686. Handbook of Optical Fibre Sensing Technology. John Wiley & Sons, Ltd., Chichester, 2002. ISBN: 0471820539.
- [27] M. Santarsiero and R. Borghi. Correspondence between super-Gaussian and flattened Gaussian beams. *J. Opt. Soc. Am. A*, 16(1):188–190, 1999.
- [28] J. Smith, A. Brown, M. DeMerchant, and X. Bao. Simultaneous distributed strain and temperature measurement. *Appl. Opt.*, 38(25):5372–5377, 1999.
- [29] S. J. Zhang, D. I. Forsyth, T. Sun, Z. Y. Zhang, and K. T. V. Grattan. Tm/Ho co-doped optical fibre sensor -: strain and temperature characteristics of a sensor probe. In A. G. Mignani and H. C. Lefevre, editors, *14<sup>th</sup> International Conference on Optical Fiber Sensors*, volume 4185, pages 154–157. SPIE, 2000.
- [30] S. Trpkovski, S. A. Wade, S. F. Collins, and G. W. Baxter. Comparison of two simultaneous temperature and strain sensors utilizing a combined fiber Bragg grating/fluorescence intensity ratio technique. In K. Hotate and H. Nagai, editors, *16<sup>th</sup> International Conference on Optical Fiber Sensors*, pages 108–111. The institute of Electronics, Information and Communication Engineers, Japan, 2003.
- [31] M. N. Alahbabi, Y. T. Cho, and T. P. Newson. Coherent detection of spontaneous Brillouin scattering combined with Raman amplification for long range distributed temperature and strain measurements. In M. Voet, R. Willsch, W. Ecke, J. Jones, and B. Culshaw, editors, *17<sup>th</sup> International Conference on Optical Fiber Sensors*, volume 5855, pages 84–87. SPIE, 2005.
- [32] G. S. Glaesemann and D. J. Walter. Method for obtaining long-length strength distributions for reliability prediction. *Opt. Eng.*, 30(6):746–748, 1991.
- [33] A. Bertholds and R. Dändliker. Deformation of single-mode optical fibers under static longitudinal stress. *J. Lightwave Technol.*, 5(7):895–900, July 1987.
- [34] R. W. Fallon, L. Zhang, L. A. Everall, J. A. R. Williams, and I. Bennion. All-fibre optical sensing system: Bragg grating sensor interrogated by a long-period grating. *Meas. Sci. Technol.*, 9(12):1969–1973, 1998.
- [35] B.-O. Guan, H.-Y. Tam, X.-M. Tao, and X.-Y. Dong. Simultaneous strain and temperature measurement using a superstructure fiber Bragg grating. *IEEE Photonic. Tech. L.*, 12:675–677, June 2000.
- [36] A. A. Chtcherbakov and P. L. Swart. Chirped fiber-optic Bragg grating interrogator in a multiplexed Bragg grating sensor configuration. *J. Lightwave Technol.*, 22(6):1543, 2004.
- [37] F. M. Haran, J. R. Rew, and P. D. Foote. A strain-isolated fibre Bragg grating sensor for temperature compensation of fibre Bragg grating strain sensors. *Meas. Sci. Technol.*, 9(8):1163–1166, 1998.
- [38] E. Rivera, D. J. Thomson, and A. A. Mufti. Comparison of recoated fiber Bragg grating sensors under tension on a steel coupon. *Proc. SPIE*, 5767:163–174, May 2005.
-

- 
- [39] Y. Fan and M. Kahrizi. Characterization of a FBG strain gage array embedded in composite structure. *Sensor. Actuat. A-Phys.*, 121(2):297–305, 2005.
- [40] F. T. S. Yu and Yin. Shizhuo, editors. *Fiber Optic Sensors*, volume 76 of *Optical Engineering*. Marcel Dekker, Inc., New York, 2002. ISBN: 082470732x.
- [41] C. D. Butter and G. B. Hocker. Fiber optics strain gauge. *Appl. Opt.*, 17(18):2867–2869, 1978.
- [42] T. Allsop, K. Chisholm, I. Bennion, A. Malvern, and R. Neal. A strain sensing system using a novel optical fibre Bragg grating sensor and a synthetic heterodyne interrogation technique. *Meas. Sci. Technol.*, 13(5):731–740, 2002.
- [43] K. Tian, Y. Liu, and Q. Wang. Temperature-independent fiber Bragg grating strain sensor using bimetal cantilever. *Opt. Fiber Technol.*, 11(4):370–377, 2005.
- [44] J. M. Jacobs. Suggested guidelines for the handling of optical fiber. Technical Report WP3627, Corning Inc., December 2001.
- [45] B. A. L. Gwandu, L. Zhang, K. Chisholm, Y. Liu, X. Shu, and I. Bennion. Compact FBG array structure for high spatial resolution distributed strain sensing. *Meas. Sci. Technol.*, 12(7):918–921, 2001.
- [46] D. C. Betz, G. Thursby, B. Culshaw, and W. J. Staszewski. Advanced layout of a fiber Bragg grating strain gauge rosette. *J. Lightwave Technol.*, 24(2):1019, 2006.
- [47] O. Frazão, M. Melo, P. V. S. Marques, and J. L. Santos. Chirped Bragg grating fabricated in fused fibre taper for strain temperature discrimination. *Meas. Sci. Technol.*, 16(4):984–988, April 2005.
- [48] R. M. Groves, E. Chehura, W. Li, S. E. Staines, S. W. James, and R. P. Tatam. Surface strain measurement: a comparison of speckle shearing interferometry and optical fibre Bragg gratings with resistance foil strain gauges. *Meas. Sci. Technol.*, 18(5):1175–1184, 2007.
- [49] N. Mohammad, W. Szyszkowski, W. J. Zhang, E. I. Haddad, J. Zou, W. Jamroz, and R. Kruzelecky. Analysis and development of a tunable fiber Bragg grating filter based on axial tension/compression. *J. Lightwave Technol.*, 22(8):2001, 2004.
- [50] F. Colpo, L. Humbert, P. Giaccari, and J. Botsis. Characterization of residual strains in an epoxy block using an embedded FBG sensor and the OLCR technique. *Compos. Part A-Appl. S.*, 37(4):652–661, 2006. Internal Stresses in Polymer Composites.
- [51] ISO. *Guide to the Expression of Uncertainty in Measurement*, chapter 5, pages 18–23. International Organisation for Standardisation, Geneva, Switzerland, 1995.
- [52] R. R. J. Maier, W. N. MacPherson, J. S. Barton, J. D. C. Jones, S. McCulloch, and G. Burnell. Temperature dependence of the stress response of fibre Bragg gratings. *Meas. Sci. Technol.*, 15(8):1601–1606, 2004.
-

- [53] E. Udd. *Fiber Optic Sensors: An Introduction for Engineers and Scientists*. Wiley Series in Pure and Appl. Opt. John Wiley & Sons, Inc., Hoboken, New Jersey, 2006. ISBN: 0470068108.
- [54] R. H. Doremus. *Glass Science*, chapter 9, pages 150–171. John Wiley & Sons, Inc., New York, 2nd edition, 1994. ISBN: 0471891746.
- [55] P. Foote, M. Breidne, K. Levin, P. Papadopolous, I. Read, M. Signorazzi, L. K. Nilsson, R. Stubbe, and A. Claesson. *Operational load monitoring using optical fibre sensors*, chapter 3, pages 75–124. John Wiley & Sons, Ltd., Chichester, 2004. ISBN: 0470843403.
- [56] Ealing Catalog, Inc. OPTO MECHANICS: Motorized Micropositioners, 2010.
- [57] Ando Electric Co., Ltd., Japan. *AQ6317B Optical Spectrum Analyzer instruction manual*, 1.1 edition, 2000.
- [58] R. Kacker, K.-D. Sommer, and R. Kessel. Evolution of modern approaches to express uncertainty in measurement. *Metrologia*, 44(6):L57–L61, December 2007.
- [59] Technical Division Process Measurement Technology and Structural Health Monitoring. *Experimental stress analysis - Optical strain sensor based on fibre Bragg grating - Fundamentals, characteristics and sensor testing*, chapter 4, pages 8–16. VDI/VDE-Society Measurement and Automation Committee, Dusseldorf, jul 2010.
- [60] W. C. Young and R. G. Budynas. *Roark's Formulas for Stress and Strain*, chapter Appendix B, pages 813–826. McGraw-Hill Publishing Co., New York, 7th edition, 2001. ISBN-10: 0071210598.
- [61] J.-F. Rysman and D. N. Nikogosyan. Thermal sensitivity studies of fibre Bragg gratings inscribed by high-intensity femtosecond UV laser pulses. *Opt. Commun.*, 282(6):1120–1122, 2009.
- [62] S. A. Slattery, D. N. Nikogosyan, and G. Brambilla. Fiber Bragg grating inscription by high-intensity femtosecond UV laser light: comparison with other existing methods of fabrication: erratum. *J. Opt. Soc. Am. B*, 22(5):1143, May 2005.

# Chapter 5

## Polarisation mitigation approaches

---

### 5.1 Introduction

Polarisation effects occur due to the vectorial nature of electromagnetic radiation. In optical fibre sensing, polarisation effects arise from multiple causes, such as an intrinsic or introduced birefringence of the medium. An isotropic waveguide may lose polarisation–degenerate propagation characteristics upon bending or applied stress (strain). Polarisation changes can also be introduced via topological means. As fibre sensors commonly sense temperature and/or stress (strain), changes to the state of polarisation, SOP, can be introduced at many timescales in a random manner.

Demodulation systems, that have polarisation–sensitivity, behave as polarisation analysers. A polarisation analyser interrogates the SOP, producing a modulation. The parameter modulated is often intensity, which can have a deleterious effect upon the accuracy and repeatability (i.e. precision) of the sensor system.

SOP is closely related to phase, and their relationship is still the subject of continued investigation [1]. High–accuracy phase sensitive wavelength interrogation schemes, such as interferometers or diffraction grating based systems, must manage the SOP of signals to be examined.

SOP changes in interferometry introduce non–phase shifting related intensity changes, which complicate signal analysis. For diffraction grating systems, the polarisation efficiency of the diffraction grating is, typically, the ultimate polarisation analysing effect. The analysing effect of the diffraction grating may introduce spurious intensity changes and hence movements of the peak wavelength captured by the diffraction grating based system.

In this chapter two schemes, a modified polarisation fixer system based upon

Takada *et al.* [2] and a PDL balancing system by Dong *et al.* [3], are examined in an attempt to depolarise anisotropic and isotropic FBG signals demodulated by the SpectroBragg spectrometer. A comparison is made with a more traditional depolarisation method, the Lyot depolariser. The Lyot depolariser used does not adequately depolarise the signals and introduces wavelength dependent phase shifts which result in channelled spectra on the SpectroBragg.

## 5.2 Theory

### 5.2.1 Depolarisation & polarisation mitigation approaches

Depolarisation is the process of converting a signal with a DOP  $> 0$  to a signal with a DOP  $\simeq 0$ . Polarisation mitigation is a reduction in the apparent sensitivity of a detection system, often through depolarisation. Different pseudo-depolarisation approaches are possible, which use a specific property of the signal. For a device measuring that specific property over which the SOP is effectively decorrelated, a DOP = 0 is achieved.

#### 5.2.1.1 Fibre Lyot depolariser

A depolariser is a device which produces depolarised or pseudo-depolarised light which is mathematically equivalent to unpolarised light for the detector/demodulation system in which it is being used. The Mueller matrix of an ideal depolariser has  $m_{00} = 1$  as the only non-zero element, i.e. maximum intensity throughput and a DOP = 0. A brief discussion of the Lyot depolariser is provided in appendix M (page V.II M-1).

The Fibre Lyot depolariser was first described by Boehm *et al.* [4,5] and consists of two lengths (1 : 2 ratio) of PMF spliced at  $\theta = \pi/4$ , where the lengths are determined by the design coherence length to be depolarised, as schematically illustrated in figure 5.1. The two lengths of fibre in figure 5.1 have different coloured cores for clarity of presentation only, and are typically the same type of fibre.

Lyot depolarisers are passive optical devices with the main limitation being the total length of fibre needed to depolarise narrow signals. Using<sup>1</sup>  $\Delta\phi_2 = 2\Delta\phi_1$ , equations (B.22) (page V.II B-6) and (M.7) (page V.II M-3) yield

$$|3(\Delta\phi)| = 3\ell(\Delta n) \gtrsim \frac{c}{\Delta\nu} \quad (5.1)$$

$$\Rightarrow 3\ell \gtrsim \frac{c}{\Delta\nu\Delta n} \quad (5.2)$$

---

<sup>1</sup> $\Delta\phi_i = \ell_i\Delta n$  is the optical path difference between the orthogonal eigenaxes of the length  $\ell_i$  of PMF, which are of refractive index  $\Delta n$ .

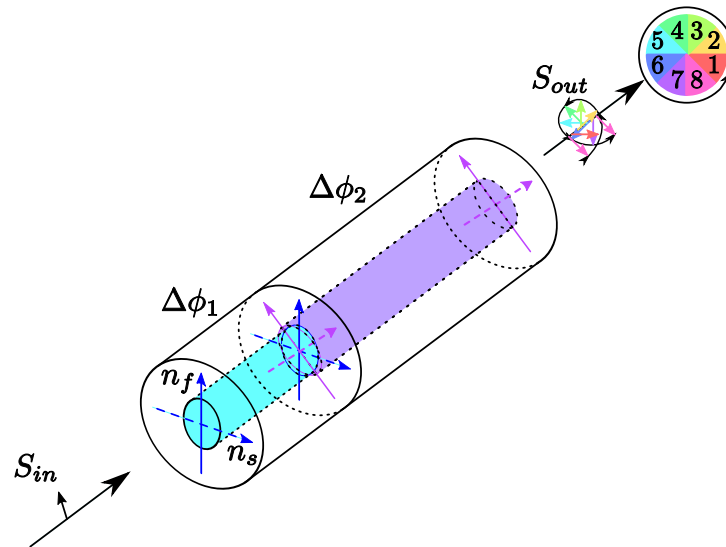


**Figure 5.1:** Fibre Lyot pseudo-depolariser. The input SOP,  $S_{in}$ , experiences a wavelength dependent rotation to produce  $S_{out}$ , which occupies all orthogonal directions to the direction of propagation.

Taking a value of  $3 \times 10^{-4}$  for  $\Delta n$  and a value<sup>2</sup> of  $\sim 100$  GHz ( $\sim 1$  nm) for the spectral bandwidths of an FBG, and a value of  $< 10$  MHz ( $< 0.1$  pm) for a high-coherence laser, the total length of a Lyot depolariser,  $3\ell$ , will need to be 10 m and  $10^5$  m, respectively. The length of fibre required for such a high-coherence laser would exhibit large losses. It is for this reason that polarisation scramblers, which operate along the temporal pseudo-depolarisation approach, are used with high-coherence sources.

### 5.2.2 Fixing linear SOP as alternative

The pseudo-depolariser makes all linear SOPs degenerate, so that there is no preferential SOP. Thus the system symmetry is increased to scalar symmetry. The degenerate removal of the vectorial aspect of a signal by a pseudo-depolariser is not the only manner to mitigate polarisation-sensitivity.

A device that fixed the output SOP,  $\underline{\mathbf{E}}_{out}$ , into one orientation regardless of the input SOP,  $\underline{\mathbf{E}}_{in}$ , would achieve the same result of removing the polarisation-sensitivity. This is in effect, similar to the pedagogical approach to phase effects, where one linear SOP is assumed. The orientation  $\underline{\mathbf{E}}_{out}$  and the detector/analyser would be at fixed angles and only subject to Malus' law [6], i.e. the intensity

<sup>2</sup>Evaluated at 1550 nm.

evaluated at the detector is then

$$S_{0_{\text{detector}}}(\theta) = S_{0_{\text{out}}} \cos^2 \theta \quad (5.3)$$

where  $S_{0_{\text{out}}}$  is the intensity at the output of the SOP fixing device, and  $\theta$  is the angle between  $\underline{\mathbf{E}}_{\text{out}}$  and polarising angle of the analyser.

A polarising stationary Mach–Zehnder interferometer is used to fix the output SOP. The input SOP,  $\underline{\mathbf{S}}_{in}$ , is split into two linear orthogonal SOPs,  $\underline{\mathbf{S}}_{\parallel}$  (oriented along  $\underline{\mathbf{E}}_{\parallel}$ ) and  $\underline{\mathbf{S}}_{\perp}$  (oriented along  $\underline{\mathbf{E}}_{\perp}$ ), by a polarising beam–splitter, as shown in figure 5.2. One arm contains a half–waveplate, HWP, i.e. a  $\pi$  rotator. The HWP rotates  $\underline{\mathbf{E}}_{\perp}$  SOP to its orthogonal SOP,  $\underline{\mathbf{E}}'_{\parallel}$ . The two arms are now re–combined, and, being in the same orientation, will superpose to give  $\underline{\mathbf{E}}_{\text{out}}$  in the same orientation.

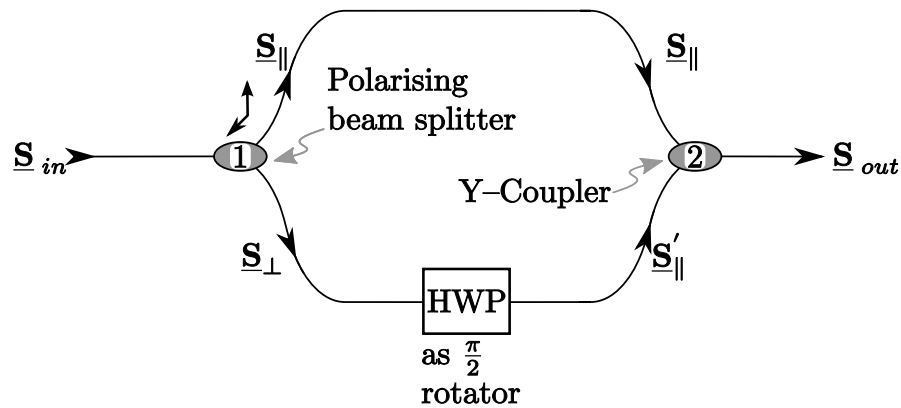


**Figure 5.2:** Fixed output SOP via polarising stationary Mach–Zehnder interferometer. Input  $\underline{\mathbf{S}}_{in}$  is split into orthogonal linear SOPs  $\underline{\mathbf{S}}_{\parallel}$  and  $\underline{\mathbf{S}}_{\perp}$ . The half–waveplate, HWP, acts as a rotator to rotate  $\underline{\mathbf{S}}_{\perp}$  into  $\underline{\mathbf{S}}'_{\parallel}$ , in the same orientation as  $\underline{\mathbf{S}}_{\parallel}$ .  $\underline{\mathbf{S}}_{\parallel}$  and  $\underline{\mathbf{S}}'_{\parallel}$  are superposed to produce  $\underline{\mathbf{S}}_{out}$ .

Ideal polarising beam–splitter 1 produces completely linearly polarised light. The Jones calculus<sup>3</sup> can thus be used to describe the evolution of light through the system.

Letting an arbitrary Jones vector represent the radiation incident on the SOP fixing device gives,

$$\underline{\mathbf{E}}_{in} = \begin{pmatrix} E_x \\ E_y \end{pmatrix} \quad (5.4)$$

The polarising beam–splitter produces two orthogonally linearly polarised beams. Without loss of generality, let LHP be parallel and LVP be perpendicular, and using

<sup>3</sup>Outlined briefly in appendix §E.5 (page V.II E-12).

the Jones matrices defined in equation (E.29) (page V.II E-13) gives

$$\underline{\mathbf{E}}_{\parallel} = \underline{\mathbf{J}}_{\text{LHP}} \underline{\mathbf{E}}_{in} = \frac{1}{\sqrt{2}} \begin{pmatrix} E_x \\ 0 \end{pmatrix} \quad (5.5a)$$

$$\underline{\mathbf{E}}_{\perp} = \underline{\mathbf{J}}_{\text{LVP}} \underline{\mathbf{E}}_{in} = \frac{1}{\sqrt{2}} \begin{pmatrix} 0 \\ E_y \end{pmatrix} \quad (5.5b)$$

$\underline{\mathbf{E}}_{\perp}$  is then rotated to its orthogonal orientation by the HWP oriented at  $\pi/4$  to the perpendicular direction,

$$\underline{\mathbf{E}}'_{\parallel} = \underline{\mathbf{J}}_{\text{rot}} \underline{\mathbf{E}}_{\perp} = \frac{1}{\sqrt{2}} \begin{pmatrix} 0 & 1 \\ -1 & 0 \end{pmatrix} \begin{pmatrix} 0 \\ E_y \end{pmatrix} = \begin{pmatrix} E_y \\ 0 \end{pmatrix} \quad (5.6)$$

Combining the two beams with Y-coupler 2, results in

$$\underline{\mathbf{E}}_{out} = \underline{\mathbf{J}}_{\text{Y-coupler}} (\underline{\mathbf{E}}_{\parallel} + \underline{\mathbf{E}}'_{\parallel}) = \frac{1}{\sqrt{2}} \underline{\mathbf{J}}_{\text{ID}} \begin{pmatrix} E_x + E_y \\ 0 \end{pmatrix} \quad (5.7)$$

where

$$\underline{\mathbf{J}}_{\text{Y-coupler}} = \frac{1}{\sqrt{2}} \underline{\mathbf{J}}_{\text{ID}} \quad (5.8)$$

and  $\underline{\mathbf{J}}_{\text{ID}}$  is the  $2 \times 2$  identity matrix. The system has converted an arbitrary SOP into a single SOP, parallel to LHP light. The Y-coupler halves the intensity, and so is represented by halving the intensity ( $-3$  dB) as  $\frac{1}{\sqrt{2}}$  times the identity matrix  $\underline{\mathbf{J}}_{\text{ID}}$ .

The SOP fixing system may be represented by the following Jones matrix

$$\begin{aligned} \underline{\mathbf{J}}_{\text{SOP-f}} &= \frac{1}{\sqrt{2}} \left[ \frac{1}{\sqrt{2}} \underline{\mathbf{J}}_{\text{LHP}} + \frac{1}{\sqrt{2}} \underline{\mathbf{J}}_{\text{rot}} \underline{\mathbf{J}}_{\text{LVP}} \right] \\ &= \frac{1}{2} \begin{pmatrix} 1 & 1 \\ 0 & 0 \end{pmatrix} \end{aligned} \quad (5.9)$$

Using equation (2.16) (page V.I - 18) to obtain the associated Mueller matrix from

the Jones matrix of (5.9) gives

$$\begin{aligned}
\underline{\underline{\mathbf{M}}}_{\text{SOP-f}} &= \underline{\underline{\mathbf{T}}} \left( \underline{\underline{\mathbf{J}}}_{\text{SOP-f}} \oplus \underline{\underline{\mathbf{J}}}_{\text{SOP-f}}^* \right) \underline{\underline{\mathbf{T}}}^{-1} \\
&= \frac{1}{4} \begin{pmatrix} 1 & 0 & 0 & 1 \\ 1 & 0 & 0 & -1 \\ 0 & 1 & 1 & 0 \\ 0 & -i & i & 0 \end{pmatrix} \begin{pmatrix} 1 \begin{pmatrix} 1 & 1 \\ 0 & 0 \end{pmatrix} & 1 \begin{pmatrix} 1 & 1 \\ 0 & 0 \end{pmatrix} \\ 0 \begin{pmatrix} 1 & 1 \\ 0 & 0 \end{pmatrix} & 0 \begin{pmatrix} 1 & 1 \\ 0 & 0 \end{pmatrix} \end{pmatrix} \begin{pmatrix} 1 & 1 & 0 & 0 \\ 0 & 0 & 1 & i \\ 0 & 0 & 1 & -i \\ 1 & -1 & 0 & 0 \end{pmatrix} \\
&= \frac{1}{4} \begin{pmatrix} 1 & 0 & 0 & 1 \\ 1 & 0 & 0 & -1 \\ 0 & 1 & 1 & 0 \\ 0 & -i & i & 0 \end{pmatrix} \begin{pmatrix} 1 & 1 & 1 & 1 \\ 0 & 0 & 0 & 0 \\ 0 & 0 & 0 & 0 \\ 0 & 0 & 0 & 0 \end{pmatrix} \begin{pmatrix} 1 & 1 & 0 & 0 \\ 0 & 0 & 1 & i \\ 0 & 0 & 1 & -i \\ 1 & -1 & 0 & 0 \end{pmatrix} \\
&= \frac{1}{2} \begin{pmatrix} 1 & 0 & 1 & 0 \\ 1 & 0 & 1 & 0 \\ 0 & 0 & 0 & 0 \\ 0 & 0 & 0 & 0 \end{pmatrix} \tag{5.10}
\end{aligned}$$

Hence, for an arbitrary input Stokes vector,  $\underline{\mathbf{S}}_{in}$  the output will be

$$\underline{\mathbf{S}}_{out} = \underline{\underline{\mathbf{M}}}_{\text{SOP-f}} \underline{\mathbf{S}}_{in} \tag{5.11}$$

$$= \frac{1}{2} (S_{in_0} + S_{in_2}) \begin{pmatrix} 1 \\ 1 \\ 0 \\ 0 \end{pmatrix} \tag{5.12}$$

By definition of the Stokes parameters, equation (E.11) (page V.II E-5),  $\underline{\mathbf{S}}_{out}$  is then

$$\underline{\mathbf{S}}_{out} = \frac{1}{2} \left( \langle E_x E_x^* + E_y E_y^* \rangle + \langle E_x E_y^* + E_y E_x^* \rangle \right) \begin{pmatrix} 1 \\ 1 \\ 0 \\ 0 \end{pmatrix} \tag{5.13}$$

If there is an optical path difference between the arms of the stationary Mach-Zehnder interferometer, then from equation (A.18) (page V.II A-5),  $E_{out}$  becomes

$$E_{out_x} = E_{0x} e^{-i\delta_x} \tag{5.14}$$

$$E_{out_y} = E_{0x} e^{-i\delta_y} = E_{0x} e^{-i\delta_x - \delta_{OPD}} \tag{5.15}$$

and  $E_{out_x}$  and  $E_{out_y}$  must be used in place of, respectively,  $E_x$  and  $E_y$  in equation

(5.13). Inserting (5.15) into equation (5.13) and evaluating gives

$$\begin{aligned}
\underline{\mathbf{S}}_{out} &= \frac{1}{2} \left( [E_{out_x}^2 + E_{out_y}^2] + [2E_{out_x}E_{out_y} \cos \delta_{OPD}] \right) \begin{pmatrix} 1 \\ 1 \\ 0 \\ 0 \end{pmatrix} \\
&= \frac{1}{2} \left( I_{out_x} + I_{out_y} + 2\sqrt{I_{out_x}I_{out_y}} \cos \delta_{OPD} \right) \begin{pmatrix} 1 \\ 1 \\ 0 \\ 0 \end{pmatrix} \\
&= \frac{1}{2} (I_{in} [1 + \gamma \cos \delta_{OPD}]) \begin{pmatrix} 1 \\ 1 \\ 0 \\ 0 \end{pmatrix} \\
&= \frac{I_{MZ(\delta_{OPD})}}{2} \begin{pmatrix} 1 \\ 1 \\ 0 \\ 0 \end{pmatrix} \tag{5.16}
\end{aligned}$$

where  $I_{MZ(\delta_{OPD})} = I_{in} [1 + \gamma \cos \delta_{OPD}]$  and  $\gamma$  is the fringe visibility, which is the standard two-beam interference expression, as in equation (6.7) (page V.I - 268). The fixed output SOP may thus be modulated by interference fringes if  $\delta_{OPD} \neq 2n\pi$  for  $n \in \mathbb{Z}$ .

As the DOP,  $\mathcal{P}$ , is a function of  $S_1$ ,  $S_2$  and  $S_3$ , equation (E.12) (page V.II E-5) can be rewritten using 5.16,

$$\mathcal{P} = \frac{I_{pol}}{I_{tot}} = \frac{\sqrt{S_{out_1}^2 + 0 + 0}}{S_{out_0}} = 1 \tag{5.17}$$

If  $\delta_{OPD}$  is a function of time, or any other parameter which changes during the experiment, the modulation of the interference fringes will oscillate between  $I_{out_{min}} \leq I_{out}(\delta_{OPD}) \leq I_{out_{max}}$ , where  $I_{out_{max}} = I_{in} [1 + \gamma]$  and  $I_{out_{min}} = I_{in} [1 - \gamma]$ .

$\delta_{OPD}$  places a limit upon the SOP fixing that can be achieved by passive optical components. As discussed by Tateda *et al.* [7], the relative phase retardance between orthogonal components for elliptically polarised light becomes a constant  $\delta_{OPD}$ . For randomly changing elliptical SOPs, i.e. any SOP not in the  $S_1$ - $S_2$  plane, the  $\delta_{OPD}$  term becomes random, and hence the intensity can be randomly modulated. Unbalancing the Mach-Zehnder interferometer arms so that the phase difference exceeds the signal's coherence length removes the interference term.

Takada *et al.* reported a depolarising arrangement<sup>4</sup> using a fibre-based delay in one arm of a bulk stationary Mach–Zehnder interferometer to depolarise light and reported a depolarisation value of  $-23$  dB [2]. In this approach the orthogonal orientation of the PBS separated beams was maintained, introducing the OPD phase shift to remove the correlation between the beams.

In this experiment, the modification is to rotate one of the orthogonal components so that both reside in the same plane. Hence, instead of depolarising the signal, the orientation of the output signal is fixed, reducing the polarisation based intensity changes to interference based intensity changes<sup>5</sup>. By operating the stationary Mach–Zehnder interferometer outside the coherence length of the input signal,  $\underline{\mathbf{E}}_{in}$ , i.e.  $OPD > L_c$ , the interference should be minimised and the incoherent sum of intensities can be used in equation (5.16), as  $\gamma \rightarrow 0$ .

For multiple component input signals, the  $OPD$  chosen must exceed the longest component coherence length or suffer a modulation for that component. For very long  $OPD$ , the stationarity requirement of the sources may not be preserved, and, hence, modulation will be reintroduced.

An unbalanced stationary Mach–Zehnder interferometer may also generate spurious coherence effects, from synthesised mutual coherence, termed the *Wolf effect* [8, 9]. The likelihood is small of such occurrences noticeably affecting the output SOP. The actual statistics, as opposed to presumed statistics, of the source will provide the greatest contribution to the generation of this effect.

The greatest advantage of the output SOP fixing approach is that the only losses should be due to splices and connectors and the 3dB loss from  $2 \times 1$  Y-coupler number 2<sup>6</sup>. Unlike the PDL compensation approach no additional losses are introduced<sup>7</sup>. The spectral effectiveness of the HWP rotation will depend upon the wavelength dependence of the approach used to achieve the rotation.

In this work a Lefèvre fibre polarisation controller and a Faraday mirror were used. The Faraday mirror could not be optimised for different wavelengths. The best performance was observed at 1550 nm, with a decrease in performance of  $\lesssim 7\%$  at 1535 nm.

The polarisation controller was tuneable, and when optimised at either 1550 nm or 1535 nm, produced  $\gtrsim 7\%$  increase in noise at the other wavelength.

---

<sup>4</sup>Equal intensity in both orientations, similar to a Lyot, as opposed to a polarisation orientation fixer.

<sup>5</sup>The problem of a passive device which would convert any arbitrary input SOP into a fixed linear output SOP was addressed by Tateda *et al.* [7], who showed that a passive device cannot, within the beat length, simultaneously correct for SOP rotation and retardation. The  $\delta_{OPD}$  term becomes to the phase retardation describing the SOP ellipticity and is, by definition, within the coherence length.

<sup>6</sup>As the Y-coupler is a truncated  $2 \times 2$  coupler.

<sup>7</sup>If  $\gamma > 0$ , the Y-coupler 3 dB loss may be reduced, although the interferometer  $OPD$  will need to be stable to within  $< 10^{-3}$  of a fringe [10].

### 5.2.3 Polarisation Dependent Loss

Passive optical components exhibit a degree of polarisation–sensitivity. For fibre based systems an important polarisation–sensitivity is *polarisation dependent loss*, PDL, which is defined by Collett [11] as “*The absolute value or the relative difference between an optical component’s maximum and minimum transmission loss, given all possible input states of polarisation*”, or as

$$\text{PDL} = 10 \log_{10} \left( \frac{I_{T_{max}}}{I_{T_{min}}} \right) \text{ dB} \quad (5.18)$$

where  $I_{T_{max}}$  and  $I_{T_{min}}$  are the maximum and minimum transmitted intensities, respectively [12].

The effect of PDL is to repolarise depolarised signals by preferentially attenuating one SOP more than its orthogonal counterpart. It can arise from material effects (e.g. dichroism), waveguiding effects (e.g. bends in the fibre) or from bulk optic effects (e.g. angled optical interfaces). PDL has an extensive nature, as the more fibre and fibre–based components encountered the greater the PDL observed at the system output. As the SOP is in general not preserved by passage through a fibre system, the magnitude of the cumulative effect of PDL will depend upon the stability of the system and input SOP. Consequently, the PDL value of standard telecomms fibre components is designed to be as low as attainable [11, 12].

Diffraction gratings’ polarisation dependent efficiency may be considered as a PDL. In the case of the diffraction grating used in the SpectroBragg the difference between orthogonal efficiencies is  $\sim 50\%$ , i.e. the PDL would be  $\sim 3$  dB.

#### 5.2.3.1 PDL balancing approach

An approach to mitigate the polarisation–sensitivity of the system proposed by Dong *et al.* is to separate the input SOP into orthogonal linear polarisation SOPs via a polarising beam–splitter, attenuate the arm with greatest intensity to equal the orthogonal intensity, and recombine using a second polarising beam–splitter [3], as shown schematically in figure 5.3.

The input SOP,  $\underline{\mathbf{S}}_{in}$ , is split into orthogonal SOPs by the first polarising beam–splitter. The PDL experienced by the orthogonal components,  $\underline{\mathbf{S}}_{\perp}$  and  $\underline{\mathbf{S}}_{\parallel}$ , will not, in general, be equivalent<sup>8</sup>. Letting  $S_{\perp_0} > S_{\parallel_0}$ , the attenuator is set to provide an

---

<sup>8</sup>The PDL will have a wavelength dependence, as all standard fibre and PMF components have some dispersion effects over a wide enough range. In this work, the signals are presumed to be  $\sim 1$  nm, e.g. FBG signals with a similar free spectral range. The wavelength dependence will be comparatively steady in this regim and so the efficiency with which the PDL balancing occurs for a given signal can be considered fixed.

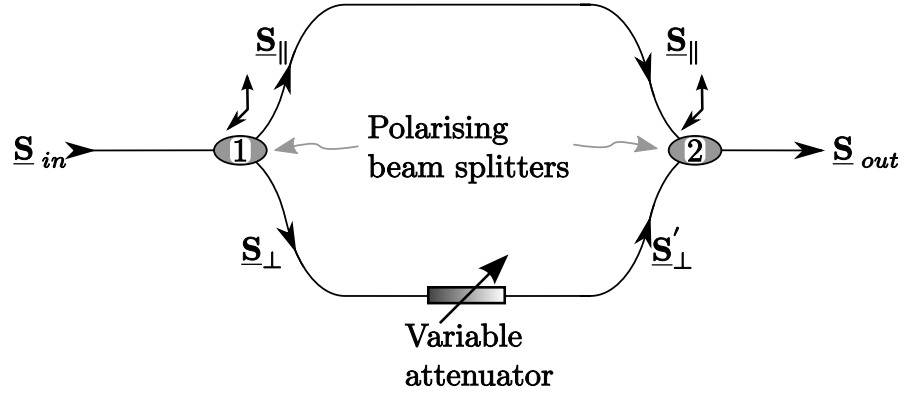


**Figure 5.3:** PDL compensation scheme using variable attenuator to balance losses in orthogonal SOPs.

attenuation =  $|S_{\perp 0} - S_{\parallel 0}|$ . The output,  $\underline{\mathbf{S}}_{out}$ , will therefore be

$$\underline{\mathbf{S}}_{out} = \underline{\mathbf{S}}_{\parallel} + \underline{\mathbf{S}}'_{\perp} \quad (5.19)$$

$$= \underline{\underline{\mathbf{M}}}_{\parallel} \underline{\mathbf{S}}_{in} + \underline{\underline{\mathbf{M}}}_{\perp} \underline{\underline{\mathbf{M}}}_{attenuator} \underline{\mathbf{E}}_{in} \quad (5.20)$$

where  $\underline{\underline{\mathbf{M}}}_{\perp}$  would be given by one of the equations (E.23) or (E.24) (page V.II E-11), and  $\underline{\underline{\mathbf{M}}}_{\parallel}$  by the other, and

$$\underline{\underline{\mathbf{M}}}_{attenuator} = \begin{pmatrix} |S_{\perp 0} - S_{\parallel 0}| & 0 & 0 & 0 \\ 0 & 1 & 0 & 0 \\ 0 & 0 & 1 & 0 \\ 0 & 0 & 0 & 1 \end{pmatrix} \quad (5.21)$$

This approach requires the PDL to be quasi-static, and the appropriate attenuation to be applied prior to data capture. The polarising beam-splitter may not have its axes aligned with the effective axes of the accumulated PDL. The quasi-static PDL requirement and the application of appropriate attenuation cater for this. The projection of the incident intensity onto axes of the PDL compensator will exhibit quasi-static losses that are matched by the PDL compensator. Incoherent superposition of intensities is possible due to the two polarising beam-splitters maintaining orthogonal SOPs at recombination, with equal intensities.

As the intensities in the orthogonal components are equal, the output SOP is restricted to the  $S_2S_3$  great circle, marked in red on figure 5.4. The position on the great circle, will depend upon the incident SOP's ellipticity as, for no other phase difference, the incident  $\phi_{pr}$  value would remain unchanged.

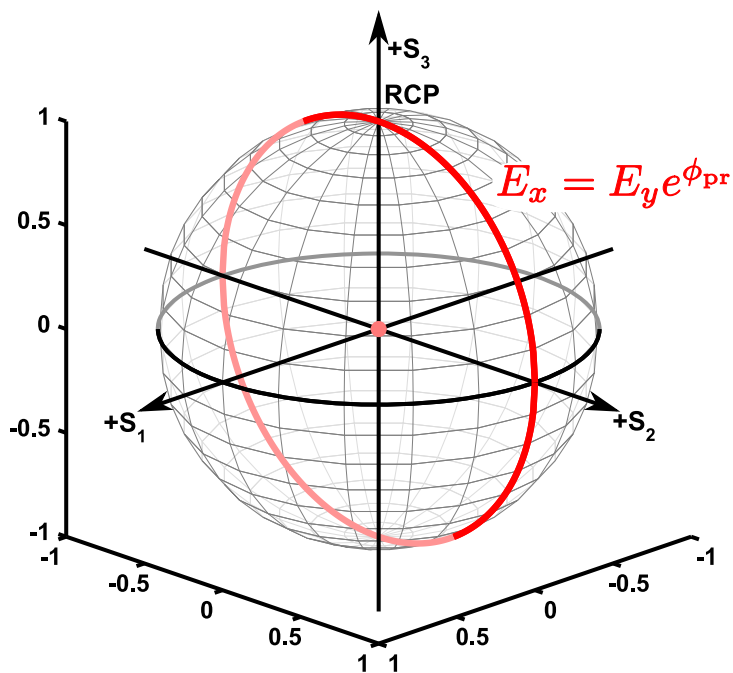


**Figure 5.4:** Balanced amplitudes in orthogonal components restricts SOPs to  $S_2S_3$  great circle (in red). The term  $\phi_{pr}$ , the phase retardation between the orthogonal components, is zero at  $\pm S_2$

## 5.3 Experimental apparatus/setup

### 5.3.1 Apparatus for generating polarisation changes

The experimental apparatus arrangement for generation of SOP changes, along with the general layout, is shown in figure 5.5. The *Exalos ESL1505–2100 Super Luminescent diode*, SLED, source illuminates an FBG, with an Oz Optics circulator<sup>9</sup> directing the reflected FBG signal to the *Thorlabs IPM5300* in-line polarimeter. The signal then passes through the system under test and onto the detector, which acts as the polarisation analyser.

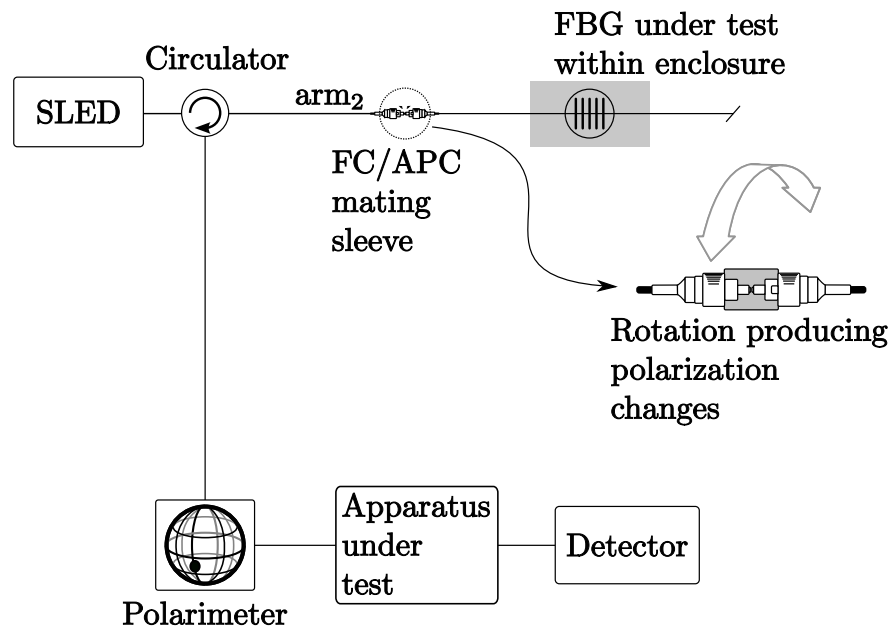


**Figure 5.5:** Method for generation of polarisation changes to apparatus, achieved by rotating the FC/APC connector.

The FBGs in this test were housed in the apparatus shown in figure 4.10 (page V.I - 188) in the arrangement shown as the *enclosure* (shaded area) of figure 4.14 (page V.I - 192). The fibres were not strained or heated. The strain test apparatus provided the best available environmental isolation. The soldering of the fibres limited movement of the FBGs, and restricted vibrations that might be transmitted along the fibre to the FBG.

Polarisation changes were introduced by rotating the FC/APC connector between the circulator's arm<sub>2</sub> and the length of fibre containing the FBG. As discussed in §§2.2.8.1, 2.2.8.2 and 2.2.8.3 (pages V.I - 52 & V.I - 54) fibre twists and bends introduce birefringence<sup>10</sup>. The presence of birefringent axes will alter all correlated

<sup>9</sup>Model FOC-12N-111-9/125-SSS-1550-55-3A3A3A-1-1.

<sup>10</sup>Geometric phase shifts (§E.3 (page V.II E-7)) may occur between coupled fibres experiencing

SOPs. To achieve as close to full coverage of the Poincaré sphere as possible, the FC/APC was alternately held along three orthogonal spatial directions and rotated. The reflected FBG signal provided a double pass through the birefringent section. Care was taken to avoid tight bends along the different axes, which would add bend–radius attenuation to the resultant signal.

### 5.3.2 Depolarisation schemes

#### 5.3.2.1 Apparatus for Lyot depolariser approach

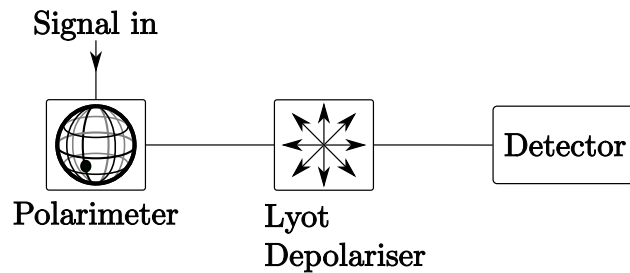


**Figure 5.6:** Apparatus using the Lyot depolariser.

The experimental apparatus arrangement for the Lyot depolariser is shown in figure 5.6. The reflected FBG signal from the circulator passed through the Thorlabs IPM5300 polarimeter. The signal then passed through the Lyot depolariser from Phoenix Photonics (Surrey, UK) and onto the detector. The Lyot depolariser required no configuration, being manufactured to produce a fixed performance.

#### 5.3.2.2 Stationary Mach–Zehnder interferometer depolarisation/polarisation fixer

The following three approaches discussed in this chapter involved a polarising stationary Mach–Zehnder interferometer. The incident signal was separated into two orthogonal SOPs. Modifications were made to the SOP in one arm, and then the signal was recombined. The effectiveness of the recombined signal in suppressing polarisation changes was then tested.

#### 5.3.2.3 Approach employing Lefèvre polarisation controller

The experimental apparatus for the Lefèvre polarisation controller based stationary Mach–Zehnder interferometer depolariser is shown in figure 5.7. The reflected FBG

---

different twists or bends in a sensing array. For the single fibre, the movement about the Poincaré sphere would need to subtend different solid angles for the orthogonal SOPs as defined by the twist and/or bend induced resultant birefringent axes for geometric effects to arise.

signal was split into orthogonal SOPs by the polarising beam-splitter. One arm passes through a Melles-Griot Lefèvre type polarisation controller which is configured as a half-waveplate. The other arm has an *OzOptics ODL650MC* optical delay line, ODL, to adjust the length of the arms. The two arms are recombined by the 50:50 Y-coupler.

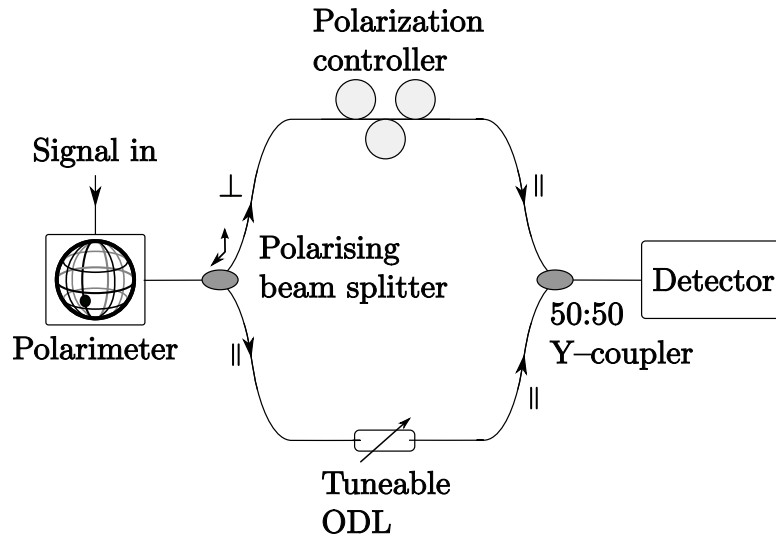


**Figure 5.7:** Apparatus using the Lefèvre polarisation controller to change SOP to the orthogonal SOP, matching the SOP in the other arm, which is then superposed at the output.

The Lefèvre polarisation controller and the ODL both require configuration. The Lefèvre polarisation controller provides full coverage of the Poincaré sphere, and so must be configured to operate as a half-waveplate. Configuring the Lefèvre polarisation controller as a HWP was achieved using the apparatus shown in figure 5.7. The first step was to position the fibre loop holders so as to produce the minimum output change for the isotropic and anisotropic FBG signals. Once configured the output was checked using the apparatus shown in figure 5.8 to observe that SOP changes were minimised.

The second step was to position the ODL. Two approaches were tested: at the balance point of the stationary Mach-Zehnder interferometer, and far from the balance point, after a modified version of Takada *et al.* [2]. To determine where the balance point was located the ODL was scanned through its tuneable range and the interferogram from one detector of the balanced receiver was used to determine where the balance point occurred.

The ODL was then set to the appropriate distance, which was checked for accuracy by determining if the calculated value produced the appropriate signal, an interferogram maximum at the balance point, or a DC value away from the balance

point.

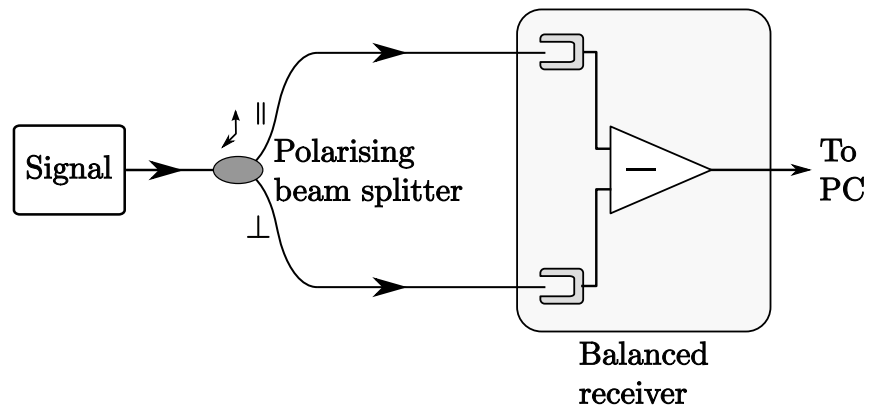


**Figure 5.8:** Apparatus consisting of polarising beam-splitter and balanced receiver, measures  $S_1$ .

#### 5.3.2.4 Apparatus for Circulator/Faraday mirror approach

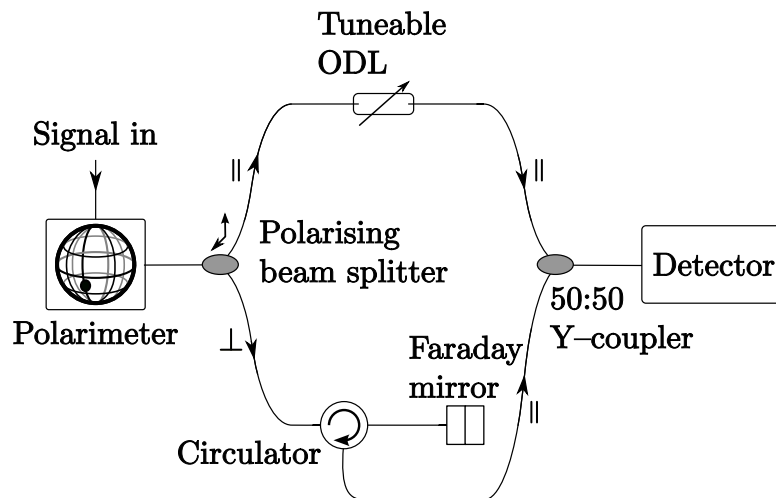


**Figure 5.9:** Apparatus using Faraday Mirror and circulator to change SOP to the orthogonal SOP, matching the SOP in the other arm, which is then superposed at the output.

The experimental apparatus arrangement for the circulator/Faraday mirror based stationary Mach-Zehnder interferometer depolariser is shown in figure 5.9. The reflected FBG signal is split into orthogonal SOPs by the polarising beam-splitter. One arm passes the signal through a circulator to a Faraday mirror, which behaves

as a HWP upon reflection. The other arm has an optical delay line, ODL, to adjust the length of the arms. The two arms are recombined by the 50:50 Y-coupler.

The Faraday mirror requires no configuration and, like the Lyot depolariser, has a fixed performance based upon design and manufacture.

### 5.3.2.5 Apparatus for PDL balancing approach

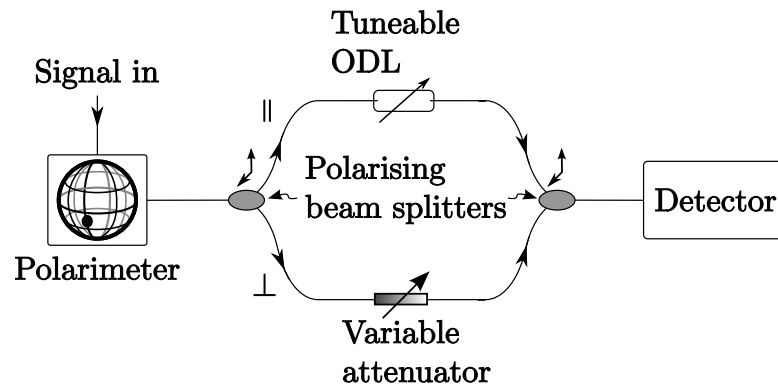


**Figure 5.10:** Matching PDL in both SOP using variable attenuator. The output has equal intensities from both SOP, reducing intensity fluctuations due to polarisation changes.

The experimental apparatus arrangement for the PDL balancing based stationary Mach-Zehnder interferometer depolariser is shown in figure 5.10, after Dong *et al.* [3]. The reflected FBG signal was split into orthogonal SOPs by the polarising beam-splitter. One arm contained a variable attenuator, which added to the attenuation experienced by the SOP in that arm. The two arms were recombined by the second polarising beam-splitter.

The polarising beam-splitter arms were matched so that there was no extinction introduced from axis misalignment when combining the two polarising beam-splitter's arms. The attenuator was placed in the arm with greater signal strength. By coupling the initial polarising beam-splitter to the balanced receiver, as in figure 5.8, the arm with the greatest signal strength was determined. To ensure that this arm retained the larger signal strength throughout, polarisation changes as described in §5.3.1 (page V.I - 229) were applied.

The attenuator was then configured to provide the appropriate attenuation. This was achieved by adjusting the attenuation while providing the different SOPs, until the output signal exhibited minimal, or no, changes.

The ODL was configured to unbalance the stationary Mach-Zehnder interferometer, following Dong *et al.* [3].

### 5.3.3 The SpectroBragg spectrometer as a polarisation–sensitive detector scheme

As only one polarimeter was available, alternative methods to determine the effectiveness of the depolarising schemes were used.

The polarisation–sensitivity of the SpectroBragg was principally determined by the polarisation efficiency of TE and TM radiation onto the diffraction grating, as shown in figure 3.7 (page V.I - 143). The SpectroBragg’s polarisation–sensitivity made the SpectroBragg a polarisation analyser, which could return information on the effectiveness of the system under test once the wavelength of the illuminating radiation remained unchanged.

Also, the SpectroBragg’s phase sensitivity indicated the effectiveness of the system under test at not introducing additional phase effects that would mitigate any benefit from the reduction in polarisation fluctuations.

## 5.4 Results/Discussion

### 5.4.1 Comment on detection systems

The ideal circumstances for determining the effectiveness of a depolarisation scheme would be to have a polarimeter placed before and after the depolarising apparatus. Then the input and output states could be known. However, with only one polarimeter available, the ideal experimental conditions could not be achieved.

The motivation for this chapter arose from a need to determine what effect the polarising anisotropic FBG had when the SpectroBragg demodulated the signal, where the SpectroBragg diffraction grating would act as a polarisation analyser.

In order to determine the SOP produced by the FBG, the available polarimeter measured the SOP input into the depolarising scheme. The SpectroBragg captured the effectiveness of the scheme when polarisation changes were the only variable. The experiments discussed here, therefore, did not compare the incident and resultant SOPs with equivalent measurement devices. The Stokes parameters of the input to the depolarising system are known, whereas the combined effect on the output in terms of phase and polarisation was captured by the SpectroBragg.

### 5.4.2 Representing polarisation

The Poincaré sphere has been the most commonly used approach to graphically present<sup>11</sup> the Stokes parameters,  $S_1$ ,  $S_2$  and  $S_3$ . For large datasets with movement

---

<sup>11</sup>The radius is typically 1, achieved by dividing by  $S_0$ . For partially polarised light, the coordinates represented by  $S_1$ ,  $S_2$  and  $S_3$  would reside within this unit sphere, but are typically

of the SOP about the surface of the sphere, the usefulness of a two dimensional projection of the Poincaré sphere decreases as there might not be unambiguous information on the evolution of the SOP. Points on the near side of the sphere may obstruct points on the far side of the sphere.

In an attempt to convey this temporal information, the approach used is to omit the absolute SOP representation, but represent the changes in terms of the angle between neighbouring SOP values, subtended at the centre of the sphere by the arc of the great circle<sup>12</sup> containing points at  $t_1$  and  $t_2$ , as illustrated in figure 5.11. Plotting the angles against time shows the change in polarisation, modulo  $\pi$  radians.

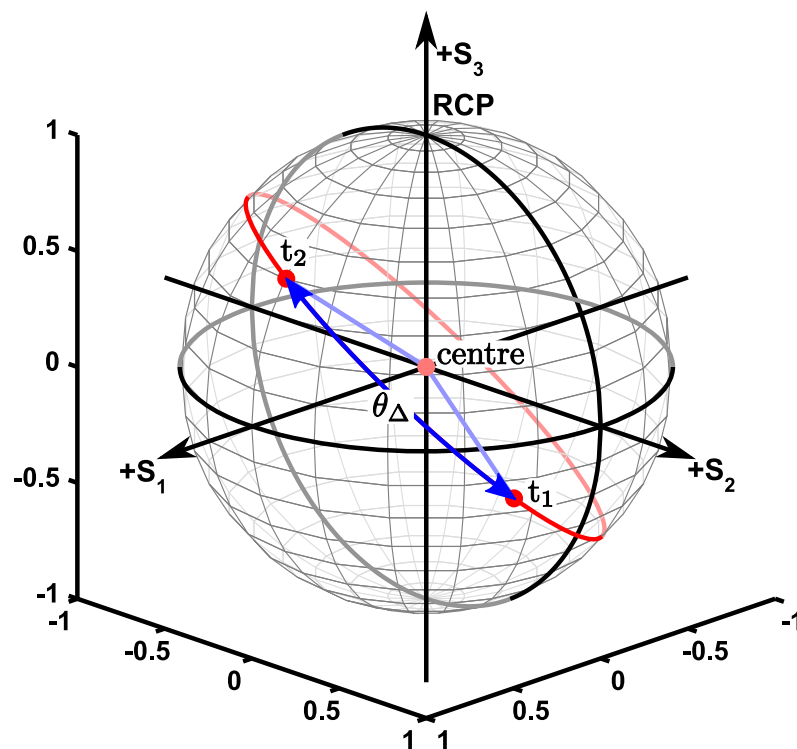


**Figure 5.11:** Poincaré sphere showing the angle, in blue, between data at  $t_1$  and  $t_2$ .

The Stokes parameters can be expressed in terms of the latitude and longitude angles  $\psi$  and  $\chi$ , as defined in figure E.2 (page V.II E-6), which can be calculated

represented as lying upon the unit sphere by projecting from the sphere's center through the  $S_1$ ,  $S_2$  and  $S_3$  co-ordinate onto the surface of the unit sphere.

<sup>12</sup>A great circle on a sphere is of the same radius as the sphere, e.g. the meridians or equator on a globe. The other circles defined by the lines of latitude are of smaller radius, and hence only referred to as small circles<sup>13</sup>.

as [13]

$$2\psi = \tan^{-1} \left( \frac{S_2}{S_1} \right) \quad (5.22)$$

$$2\chi = \sin^{-1} \left( \frac{S_3}{S_0} \right) \quad (5.23)$$

The angle,  $\theta_\Delta$ , between subsequent Stokes vectors  $S_{t_1}$  and  $S_{t_2}$ , was calculated using [14]

$$\theta_\Delta = \cos^{-1} [\sin 2\chi_{t_1} \sin 2\chi_{t_2} + \cos 2\chi_{t_1} \cos \chi_{t_2} \cos 2(\psi_{t_2} - \psi_{t_1})] \quad (5.24)$$

The quantity  $\cos^2(\frac{1}{2}\theta_\Delta)$  is a similarity factor [14] between states of polarisation, but does not add any information beyond  $\theta_\Delta$  for the purposes of this work.

### 5.4.3 Polarisation changes introduced by rotating FC/APC connector

The polarisation changes achieved by rotating the FC/APC connector between the circulator and the fibre containing the FBGs are shown in the following figures.

Figure 5.12 shows the Poincaré sphere representation of the SOP data from an anisotropic FBG, such as that characterised in chapter 4. Figure 5.13 shows the Poincaré sphere representation for the isotropic FBG. The anisotropic FBG covers more of the Poincaré sphere than the isotropic FBG. However, the anisotropic FBG does not cover all the Poincaré sphere, with one zone not populated and the opposite side weakly populated over a wider area<sup>14</sup>. The absolute position and orientation of the isotropic FBG Stokes' parameters on the Poincaré sphere do not remain unchanged across datasets, but maintain a restricted space beyond which data points are not populated, another example of which is shown in figure 5.14. As most of the apparatus was fixed to the bench and immobile, the most likely sources that might have produced the rotations between datasets were<sup>15</sup>

- the connections to the polarisation mitigation scheme under test,
- the connectors to the FBGs,
- the FC/APC connector used to generate changing SOPs.

---

<sup>14</sup>These features may be more easily seen in figures N.1(e) and (f) (page V.II N-8). The unpopulated region is in the  $+S_1, +S_2$  quadrant of figure N.1(e). The weakly populated opposite side is shown in figure N.1(f).

<sup>15</sup>Temperature effects are unlikely to be a contribution as there are no changes within a dataset on the same magnitude as between datasets. The time intervals between subsequent datasets were on occasion shorter than the time interval over which the dataset was captured.

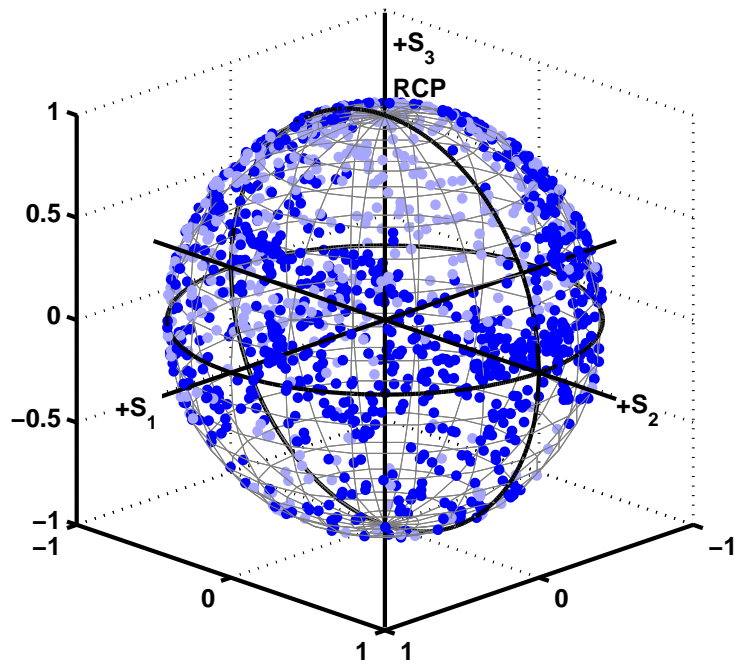


**Figure 5.12:** Poincaré sphere of the SOPs produced by fibre rotation of anisotropic FBG signal.

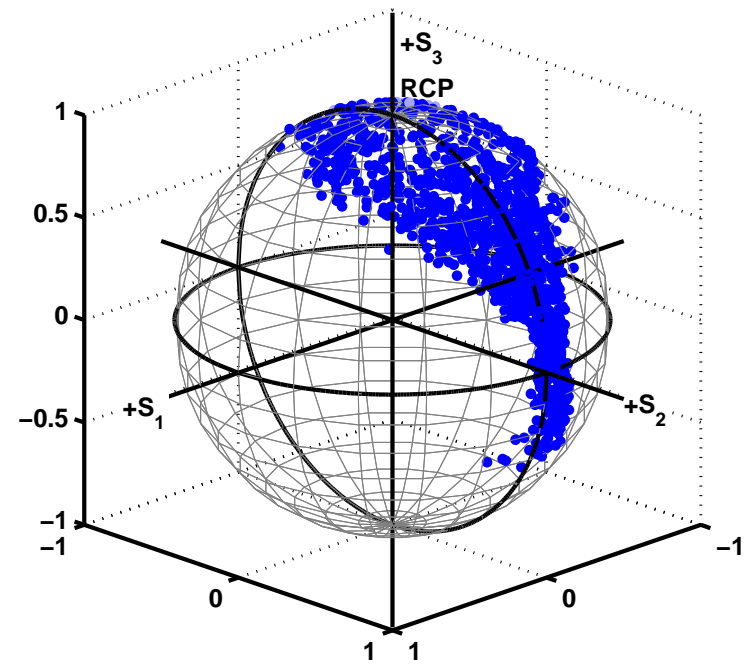


**Figure 5.13:** Poincaré sphere of the SOPs produced by fibre rotation of isotropic FBG signal.

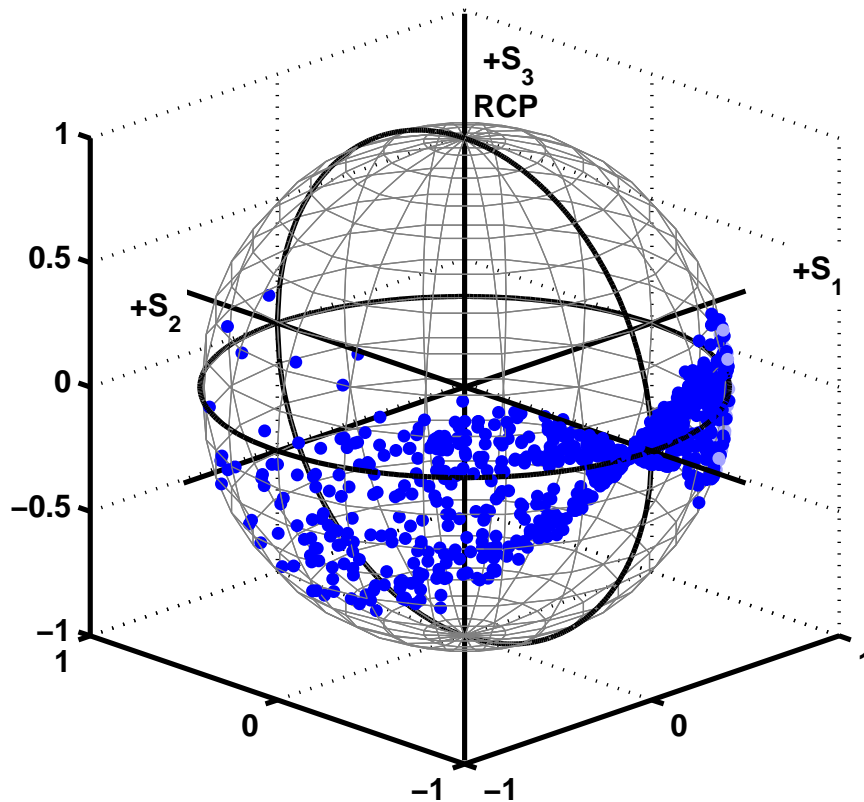


**Figure 5.14:** Poincaré sphere of the SOPs produced by fibre rotation of isotropic FBG signal, with profile rotated with respect to figure 5.13.

Figure 5.15 shows the angle between neighbouring SOPs as a function of time for the anisotropic FBG (a), and the isotropic FBG (b). The angle is representative of the change in the SOP to a maximum value of  $2\pi$  radians.

The changes in the SOP produced by the anisotropic and isotropic FBGs are different as can be seen from figures 5.12 and 5.13. The SOP evolution as seen in the changes in angles shown in figure 5.15, which shows that the changes in SOP introduced by rotating the FC/APC connector varied quickly for both anisotropic and isotropic FBGs.

The connectors to the fibre containing the FBGs were approximately a metre from the nearest anchor point holding the fibre in the strain apparatus. It is most unlikely that the FBGs experienced any strain or movement from the FC/APC

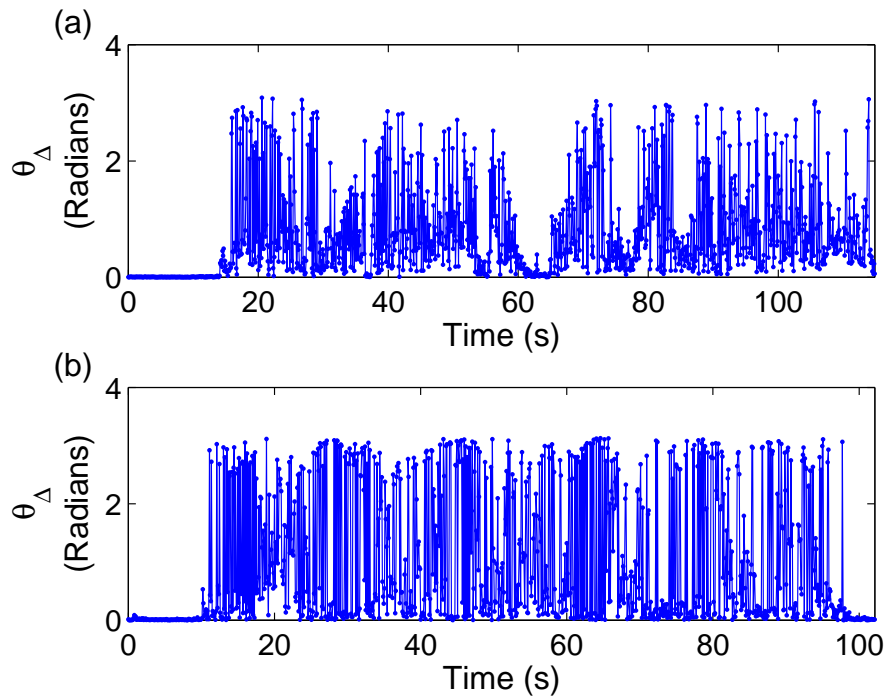


**Figure 5.15:** Plot of the angle  $\theta_{\Delta}$  between SOPs produced by fibre rotation of (a) the anisotropic FBG signal (figure 5.13) and (b) the isotropic FBG signal (figure 5.12).

connector rotation. Additionally, although connected by patch leads, the FC/APC connector was located on a separate bench, which should have isolated the strain apparatus from any remaining vibrations associated with rotating the FC/APC connector.

#### 5.4.4 Effect of SOP changes upon the SpectroBragg

In order to illustrate the effects of the changes in SOP on the SpectroBragg, the SOP changes produced by the anisotropic and isotropic FBGs were captured without any depolarisation scheme, as a control experiment. The figures 5.12 and 5.13 were obtained without any depolarising scheme.

From figure 3.7 (page V.I - 143) it can be seen that at 1550 nm the efficiency of TE polarisation is approximately half that of the TM polarisation, as defined by the grating surface normal. The diffraction grating thus behaves as a poor TM linear polariser, with a diffraction efficiency approximately at 50% for the TE light, i.e.

$$\underline{\mathbf{S}}_{\text{SB}} = \underline{\mathbf{M}}_{TE} \underline{\mathbf{S}}_{\text{SB}_{\text{in}}} + \underline{\mathbf{M}}_{TM} \underline{\mathbf{S}}_{\text{SB}_{\text{in}}} \quad (5.25)$$

where  $\underline{\mathbf{M}}_{TE}$  and  $\underline{\mathbf{M}}_{TM}$  are the Mueller matrices for orthogonal linear polarisers.

The relative magnitude of the components are

$$\left| \underline{\underline{\mathbf{M}}}_{TE} \right| = \frac{1}{2} \left| \underline{\underline{\mathbf{M}}}_{TM} \right| \quad (5.26)$$

The alignment of the TE and TM axes with respect to the data captured by the polarimeter was unknown, and was unlikely to be aligned. The angle of the rotation and phase changes with the movement of any of the fibre leads and connectors.

To attempt to cater for these effects, the Stokes vector from the polarimeter was modelled as though it underwent an arbitrary phase retardation and rotation, and then projected onto the idealised diffraction grating of the SpectroBragg. The calculated Stokes vector was then cross-correlated<sup>16</sup> with the captured SpectroBragg data.

For a Stokes vector,  $\underline{\mathbf{S}}_{\text{pol}}$ , at the polarimeter, the calculated oscillation at the detector of the SpectroBragg would be in  $\underline{\mathbf{S}}_{\text{SB}_0}$  on top of the uncorrelated component in the signal.

The Stokes vector  $\underline{\mathbf{S}}_{\text{SB}}$  is given by

$$\underline{\mathbf{S}}_{\text{SBin}} = \underline{\underline{\mathbf{M}}}_{\text{rot}} \underline{\underline{\mathbf{M}}}_{\text{pr}} \underline{\mathbf{S}}_{\text{pol}} \quad (5.29)$$

where the phase retardation was provided by [17, 18]

$$\underline{\underline{\mathbf{M}}}_{\text{pr}}(\phi_{\text{pr}}) = \begin{pmatrix} 1 & 0 & 0 & 0 \\ 0 & 1 & 0 & 0 \\ 0 & 0 & \cos \phi_{\text{pr}} & \sin \phi_{\text{pr}} \\ 0 & 0 & -\sin \phi_{\text{pr}} & \cos \phi_{\text{pr}} \end{pmatrix}; \quad \phi_{\text{pr}} = -\frac{\pi}{2} \dots \frac{\pi}{2} \quad (5.30)$$

The rotation was provided by

$$\underline{\underline{\mathbf{M}}}_{\text{rot}}(\theta_{\text{rot}}) = \begin{pmatrix} 1 & 0 & 0 & 0 \\ 0 & \cos 2\theta_{\text{rot}} & \sin 2\theta_{\text{rot}} & 0 \\ 0 & -\sin 2\theta_{\text{rot}} & \cos 2\theta_{\text{rot}} & 0 \\ 0 & 0 & 0 & 1 \end{pmatrix}; \quad \theta_{\text{rot}} = 0 \dots \pi \quad (5.31)$$

<sup>16</sup>The cross-correlation,  $\mathcal{R}_{xy}$ , is defined as [15, 16]

$$\mathcal{R}_{xy}(\tau) = \mathbb{E} [x_k(t)y_k^*(t + \tau)] \quad (5.27)$$

$$= \lim_{T \rightarrow \infty} \frac{1}{2T} \int_{-T}^T x(t + \tau)y^*(t)dt \quad (5.28)$$

where  $\mathbb{E}$  is the expected value,  $x(t)$  and  $y^*(t)$  are the functions being correlated.

<sup>17</sup>I.e. from  $-S_3$ (LCP) to  $+S_3$ (RCP).

<sup>18</sup>The factor of 2 in sines and cosines covers the full  $2\pi$  of rotation [19].

The phase retardation was applied prior to the rotation<sup>19</sup> as the rotation of the diffraction grating with respect to the SOP occurred after fibre introduced phase-shifts to the SOP would have concluded.

The temporal cross-correlation between the SpectroBragg FBG peak intensity changes and the polarimeter derived  $\underline{\mathbf{S}}_{\text{SB}}$  was evaluated for each integer value of  $\theta_{\text{rot}}$  and  $\phi_{\text{pr}}$ .

The maximum absolute value is reported as this would indicate the alignment with least decorrelation, i.e. worst polarisation mitigation performance. The greater the correlation of a given TE–TM arrangement to the SpectroBragg data, the closer the alignment of those TE–TM axes to the SpectroBragg axes.

The figures shown here used Matlab’s `xcorr` function, shown here as  $\mathcal{R}_{\text{Int.}}$ , and the tabulated values were obtained using Matlab’s `corrcoef` function, shown as  $\rho_{\text{Int.}}$ <sup>20</sup>.

The data obtained from the SpectroBragg and polarimeter were not of equivalent length, as the sampling rate of the SpectroBragg and the polarimeter differed slightly. The larger dataset was linearly interpolated to reduce it to the length of the smaller dataset using Matlab’s `interp1` function.

#### 5.4.4.1 Phase noise and the SpectroBragg

The captured intensity levels used should not have exhibited any intensity related non-linear behaviour, as the SLED provided a maximum power of 2.35 mW over a 59.4 nm bandwidth. The intensity of the noise should therefore have a linear dependence on the intensity throughout the fibre in the system under test.

The stationary Mach–Zehnder interferometer based approaches<sup>21</sup> to separating the orthogonal SOPs, and subsequently recombining them, relied upon the stability of the interferometer. It was hoped that any instabilities would be slow compared to the polarisation changes and would appear as low-frequency intensity changes.

The Oz Optics ODLs available proved to be very susceptible to ambient acoustic vibrations. The ODL used in these experiments was an ODL650MC, which suffered the least from vibration, being an enclosed unit. Figure 5.16 illustrates the susceptibility of the polarisation mitigation systems to interference noise. The arrows indicate where the applied polarisation changes were stopped, i.e. the FC/APC connector was not rotated, and the corresponding SpectroBragg output becomes a smoother, lower-frequency oscillation. The high frequency oscillations correspond to the applied polarisation changes, where the larger-amplitude lower-frequency

<sup>19</sup>As mentioned in §E.3 (page V.II E-7), matrix product operations in the three-dimensional space of the Poincaré sphere do not, in general, commute.

<sup>20</sup>The correlation coefficient is discussed in §5.4.4.2 (page V.I - 246).

<sup>21</sup>The two approaches described in §5.3.2.3 (page V.I - 230) and §5.3.2.4 (page V.I - 232).

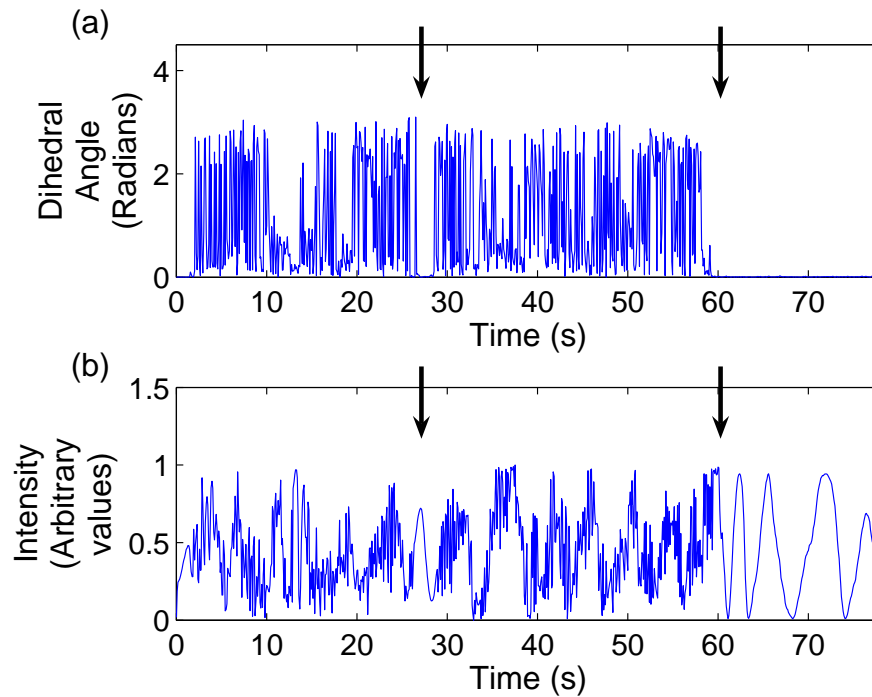


**Figure 5.16:** Demonstrating the sensitivity of the stationary Mach–Zehnder interferometer based systems to interference noise produced by vibrations at the ODL. Arrows indicate sections of no added polarisation noise. (a) shows the dihedral angle between subsequent SOPs and (b) shows the corresponding output of the SpectroBragg.

oscillations are due to acoustic vibrations coupling-in phase noise.

In an attempt to eliminate the unwanted low frequency oscillations, on the assumption that the frequency bands of the phase and polarisation noise are well separated, Fourier transform frequency filtering was applied to the SpectroBragg data. The Fourier transform of the SpectroBragg data from figure 5.12 (page V.I - 237) is illustrated in figure 5.17.

By incrementally zeroing additional low-frequency elements and calculating the standard deviation of their inverse Fourier transforms, the plot of these standard deviations indicates that a change from the low frequency band to a higher frequency band can be observed by the change in slope. Figure 5.18 shows the standard deviations for the FFT filtered data shown in figure 5.17. The change in slope at about 0.5 Hz indicates a change in the spectral composition of the data. Zeroing all non-DC components beneath this value should return data with reduced interference and be more representative of the polarisation noise. The result is illustrated in figure 5.19.

This approach is far from ideal, as the point at which filtering occurs is not consistent across all datasets, nor is the separation of low frequency components always as obvious, as is illustrated by the data shown in figure 5.20, obtained from

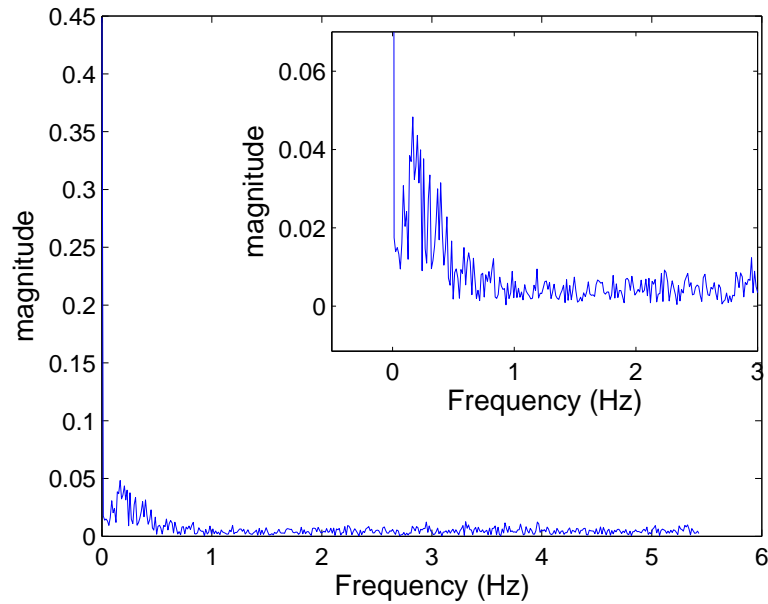


**Figure 5.17:** The FFT of the SpectroBragg data with polarisation and interference noise.

a different set of data.

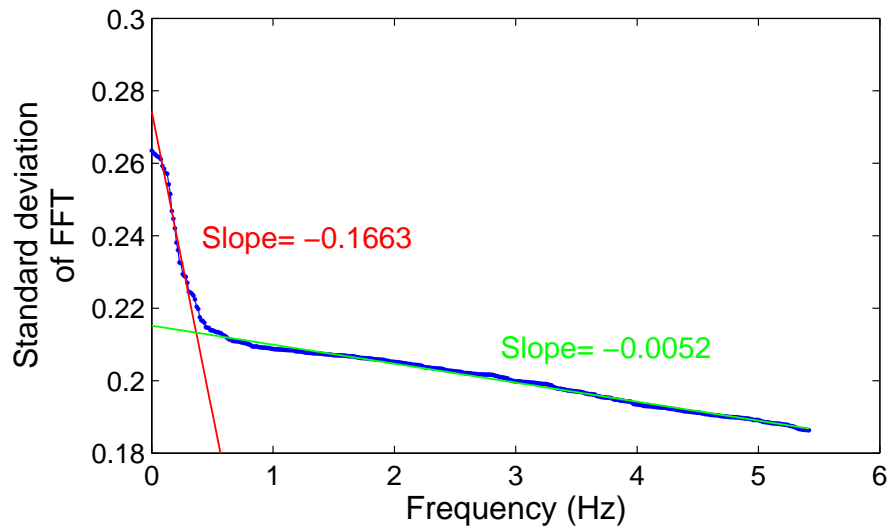
Shown in figure 5.21, as an example, are the effects of the FFT filtering upon the cross-correlation plots for the anisotropic and isotropic FBGs in the absence of any mitigation scheme. The datasets were normalised prior to correlation. The detailed discussion of the results<sup>22</sup> appears in appendix N (page V.II N-1).

Figure 5.21(a) shows the normalised temporal correlation,  $\mathcal{R}_{\text{Int.}}(\tau)$ , between the unfiltered intensity captured by the SpectroBragg and the simulated intensity from the polarimeter, for the anisotropic and isotropic FBGs. Figures 5.21(b) shows the corresponding  $\mathcal{R}_{\text{Int.}}(\tau)$  for the filtered data captured by the SpectroBragg and the simulated data from the polarimeter.

The differences in the anisotropic FBG data are more pronounced than for the isotropic FBG data. As there was no polarisation mitigation scheme used in this control experiment, the FFT filtering removed frequency components that were not introduced as a result of interferometric phase noise to intensity noise conversion. The sources of this low-frequency noise may be vibrations within the SpectroBragg itself or longer period intensity changes occurring within the experimental system.

---

<sup>22</sup>The quantity of material is quite large, and obscured the more cohesive argument that is presented by summarising the results in this chapter.



**Figure 5.18:** Plot of the standard deviation of the SpectroBragg data after FFT filtering of low frequency components.

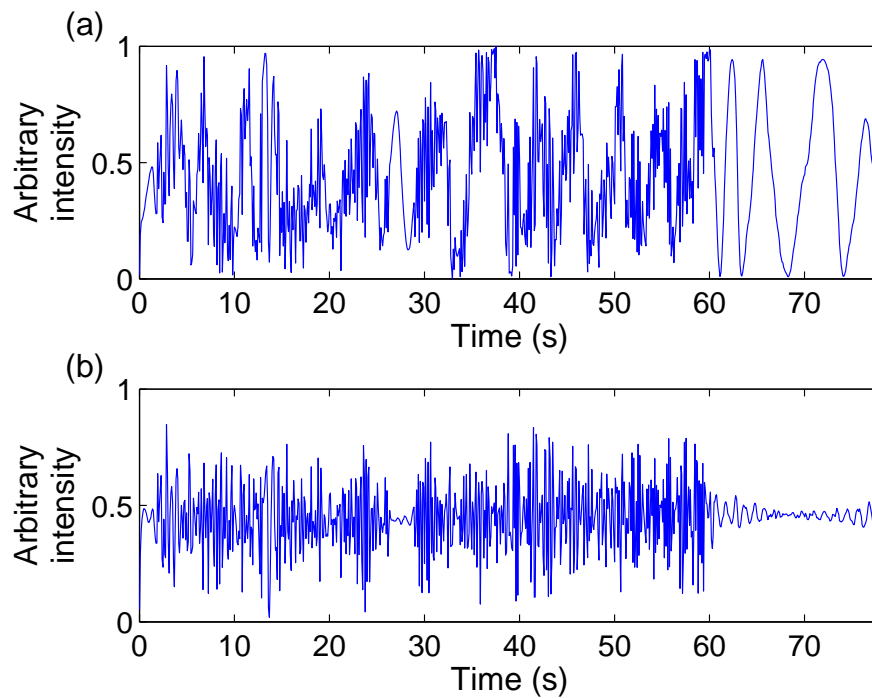


**Figure 5.19:** (a) shows the original SpectroBragg data (from figure 5.16) and (b) shows the filtered SpectroBragg data.

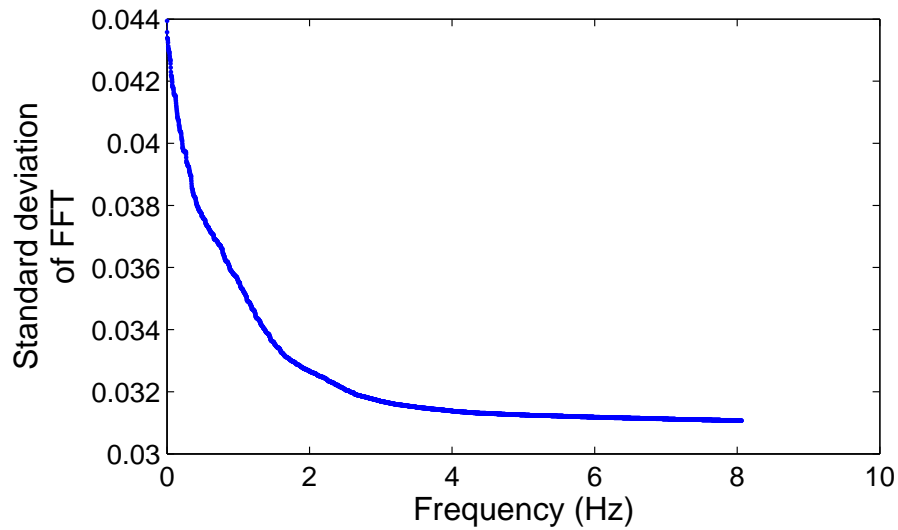


**Figure 5.20:** Plot of ambiguous separation of low and high frequency components using the approach used to produce figure 5.18.

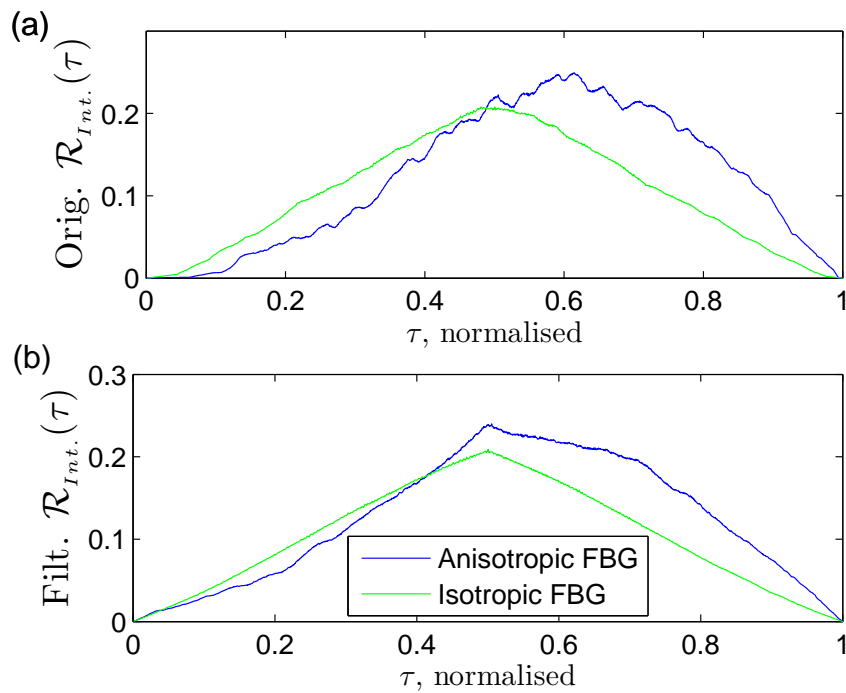


**Figure 5.21:** Plots of (a) The normalised cross-correlation,  $\mathcal{R}_{Int.}(\tau)$ , between the unfiltered SpectroBragg output and the unfiltered optimum alignment of the diffraction grating axes with the rotated SOP,  $\underline{\mathbf{S}}_{SB}(\theta)$ , for the anisotropic and isotropic FBGs; (b) The normalised cross-correlation,  $\mathcal{R}_{Int.}(\tau)$ , between the respective filtered data, for the anisotropic and isotropic FBGs;

#### 5.4.4.2 Quantifying the effect of the polarisation mitigation schemes

In order to quantify the effect of the polarisation changes upon the signal captured by the SpectroBragg in the presence of filtered interference noise and possible changing alignment of the polarimeter and the SpectroBragg linear polarisation axes, four (two sets of two) quantities are presented. The first value is the correlation coefficient (normalised cross-covariance function [20]),  $\rho_{xy}(\tau)$ , defined as

$$\rho_{xy}(\tau) = \frac{C_{xy}(\tau)}{\sigma_x \sigma_y} \quad (5.32)$$

where  $\sigma_i$ ; ( $i = x, y$ ) are the ensemble standard deviations, and  $C_{xy}$  is the covariance function defined as

$$C_{xy}(\tau) = \mathcal{R}_{xy}(\tau) - \mu_x \mu_y \quad (5.33)$$

and  $\mu_i$ ; ( $i = x, y$ ) are the ensemble mean values [16]. The correlation coefficient provides an indication of the preservation of a pattern, e.g. the captured data at the SpectroBragg and the modeled data of the ideal polarisation mitigation scheme, using the data captured by the polarimeter.

Two correlation coefficients are presented. The first is the correlation coefficient of the temporal intensity patterns of the SpectroBragg,  $y$ , and polarimeter<sup>23</sup>,  $x$ .  $\rho_{xy}(\tau)$  would then be a measure of how consistently the changes in the SOP induced intensity pattern were preserved through the different polarisation mitigation approaches. An improvement in polarisation mitigation would reduce the correlation coefficient. For brevity, this correlation coefficient will be termed  $\rho_{\text{Int}}$ .

The second correlation coefficient is a measure of the temporal pattern in centroid calculated SpectroBragg peak wavelength  $\lambda_B$ ,  $x$ , and the SpectroBragg intensity value,  $y$ . The centroid calculation depends upon the weighting of the contributing pixels, i.e. the intensity profile of the signal. If the changing SOPs do not alter the intensity at each pixel equally, there will be some correlation of changes in both quantities. Again, for brevity this correlation coefficient will be termed  $\rho_{\lambda_B}$ .

The correlation coefficient may be negative, indicating that the alignment is negative, i.e.  $x \rightarrow -x'$  for axis  $x$  at the polarimeter and  $x'$  at the SpectroBragg. As the positive or negative alignment of the axes is only a matter of sign, the absolute value is presented in the table.

The second measure used for comparison is the mean normalised standard deviation of the polarisation changes observed by the Polarimeter and the SpectroBragg after the signal has been normalised to the average power level. This provides a

---

<sup>23</sup>Changes in polarimeter measured SOP refer to the polarised component only. The unpolarised component will appear as a DC offset. The purpose of the polarisation mitigation approaches is to mitigate the effects of changes in the polarised component.

means of comparing the standard deviation of the magnitude of the oscillation after the polarisation mitigation approach. This is presented as the polarisation mitigation approach may exhibit a reduced correlation, but may also introduce a worse signal to noise ratio<sup>24</sup>. To compare datasets from different dates, and with different depolarisation or polarisation fixing systems in place, the standard deviation of any background oscillations are also presented. In the case of a completely depolarised or polarisation fixed signal, the SpectroBragg signal should be close to the background signal level.

The approach adopted was to take the standard deviation and mean value of the background data, i.e. before polarisation changes were applied,  $\mu_{\text{bg}}$  and  $\sigma_{\text{bg}}$ , and during the application of the polarisation changes,  $\mu_{\Delta\text{SOP}}$  and  $\sigma_{\Delta\text{SOP}}$ . The dihedral angles between subsequent SOPs, as in figure 5.15 (page V.I - 239), from the polarimeter data were used to determine where the boundary between these regimes occurred.

The normalised standard deviations

$$\sigma_{\text{Int.}\Delta\text{SOP}} = \frac{\sigma_{\Delta\text{SOP}}}{\mu_{\Delta\text{SOP}}} \quad \text{and} \quad \frac{\sigma_{\text{bg}}}{\mu_{\text{bg}}} \quad (5.34)$$

are used to compare the effects of the polarisation noise across the different systems under test. These values were calculated for both the SpectroBragg data and the polarimeter data, to provide a *before-and-after* comparison of the changes in polarisation observed by both systems. If the output is effectively depolarised or SOP insensitive, there should be little difference between the two values for SOP induced intensity changes only.

The second standard deviation measure is of the peak wavelength,  $\sigma_{\lambda_B}$ , as calculated by the centroid algorithm using the SpectroBragg data. As the FBG is nominally stable, the peak wavelength should, ideally, not change. Changes observed may be attributed to changes in the coherence and/or polarisation of the illuminating or reflected radiation by different means. Additionally, as the intensity is filtered to reduce the effect of low-coherence oscillations, which are unlikely to originate from changes in SOP,  $\sigma_{\lambda_B}$  is presented for the filtered SpectroBragg data and the original SpectroBragg data, for comparison.

---

<sup>24</sup>In the ideal case of two polarimeters, one before and after the polarisation mitigation approach, this would appear as a decorrelation

Quantity	FBG		Control	Lyot	Lefèvre cont.	Circ. / FM	PDL comp.	
(a) $ \rho_{\text{Int.}} $	Aniso.		0.22 (0.28)	0.36 (0.62)	0.14 (0.09)	0.22 (0.34)	0.10 (0.06)	
	Iso.		0.20 (0.18)	0.23 (0.47)	0.21 (0.35)	0.03 (0.08)	0.26 (0.51)	
(b) $\sigma_{\text{Int.}}$ (pm)	Aniso.	SB.	w. $\Delta$ SOP	0.25 (0.56)	0.32 (0.42)	0.06 (0.09)	0.15 (0.25)	0.26 (0.79)
			background	0.07 (0.03)	0.02 (0.0005)	0.01 (0.01)	0.02 (0.02)	0.03 (0.02)
		Pol.	w. $\Delta$ SOP	0.38 (0.56)	0.46 (0.61)	0.40 (0.60)	0.62 (1.02)	0.39 (0.76)
			background	0.04 (0.03)	0.02 (0.01)	0.03 (0.02)	0.12 (0.03)	0.36 (0.58)
	Iso.	SB.	w. $\Delta$ SOP	0.13 (0.18)	0.25 (0.35)	0.06 (0.09)	0.38 (2.07)	0.12 (0.33)
			background	0.03 (0.001)	0.05 (0.002)	0.01 (0.01)	0.13 (0.05)	0.02 (0.0004)
		Pol.	w. $\Delta$ SOP	0.50 (0.55)	0.25 (0.26)	0.30 (0.36)	0.22 (0.25)	0.27 (0.48)
			background	0.07 (0.18)	0.08 (0.11)	0.01 (0.03)	0.05 (0.004)	0.03 (0.002)
(c) $\sigma_{\lambda_B}$ (pm)	Aniso.	{	w. $\Delta$ SOP	5.80 (7.41)	47.55 (59.11)	1.84 (2.41)	3.30 (4.05)	4.78 (7.18)
			background	0.25 (0.07)	3.48 (0.06)	1.46 (2.94)	0.81 (0.42)	0.77 (0.70)
	Iso.	{	w. $\Delta$ SOP	0.88 (1.05)	2.86 (3.42)	0.91 (1.40)	3.54 (5.11)	1.55 (2.89)
			background	0.88 (0.28)	0.23 (0.21)	0.43 (0.60)	1.28 (0.73)	0.40 (0.16)
(d) $ \rho_{\lambda_B} $	Aniso.		0.24 (0.40)	0.69 (0.75)	0.11 (0.08)	0.37 (0.38)	0.001 (0.05)	
	Iso.		0.46 (0.46)	0.12 (0.16)	0.69 (0.80)	0.74 (0.79)	0.63 (0.81)	

**Table 5.1:** Combined summary of (a) correlation coefficient,  $\rho_{\text{Int.}}$ , values for correlation between captured SpectroBragg intensity and calculated  $\underline{\mathbf{S}}_{\text{SB}}$ , in subsequent tables, the rotation and phase retardation angles which produced the value are listed under the  $\rho_{\text{Int.}}$  value; (b) the FFT filtered and unfiltered (in parentheses) normalised standard deviations,  $\sigma_{\text{Int.}}$ , for both SpectroBragg and polarimeter data; (c) the FFT filtered and unfiltered (in parentheses) standard deviation  $\sigma$  of centroid calculated wavelength,  $\sigma_{\lambda_B}$ , for the anisotropic and isotropic FBGs. The values are for the data with applied SOP changes and without applied SOP changes (i.e. background); (d) the SpectroBragg intensity–centroid  $\lambda_B$  correlation coefficient,  $\rho_{\lambda_B}$ , as a measure of intensity’s influence on  $\lambda_B$ .

### 5.4.5 Summary of results

The results of the different polarisation mitigation schemes are discussed in more detail in appendix N (page V.II N-1). Here a summary of the results is presented. Table 5.1 contains **(a)** the correlation coefficient of the SpectroBragg and polarimeter data,  $\rho_{\text{Int.}}$ , which is a measure of how consistently the SOP changes are repeated on both devices; **(b)** the normalised standard deviations of the applied SOP and background oscillations,  $\sigma_{\text{Int.}}$ , as measured by the SpectroBragg and polarimeter; **(c)** the standard deviation of the applied SOP oscillations in the centroid calculated wavelength,  $\sigma_{\lambda_B}$ , for the SpectroBragg data; **(d)** the correlation coefficient of the centroid calculated wavelength oscillations and the SpectroBragg data intensity oscillations,  $\rho_{\lambda_B}$ .

As measured by the polarimeter, both the anisotropic and isotropic FBGs had similar degrees of polarisation, being  $\sim 98\% \pm 4\%$ . This indicates that the fibre leads and the large SOP changes applied by the rotation of the FC/APC connector were sufficient to reduce any effectively depolarised component<sup>25</sup> of the radiation relative to the polarised component. The anisotropic FBG may be considered as a polarised reflector, whereas the isotropic FBG's signal is polarised en-route to the polarimeter<sup>26</sup>. As shown in figures 5.12 and 5.13 (page V.I - 237), this did not result in equivalent coverage of the Poincaré sphere.

The anisotropic FBG would reflect a polarised signal, which would then experience phase retardation/rotations en-route to the SpectroBragg. The isotropic FBG would, in contrast, reflect more evenly in both orthogonal orientations, with the fibre en-route to the SpectroBragg polarising the signal.

The partial coverage of the Poincaré sphere by the isotropic FBG for all rotations of the FC/APC connector meant that if the SOP changes were poorly mitigated in one orientation of the FC/APC connector, the other orientations would not produce substantial improvement as the SOPs would be similar. The converse was also true. If the SOP changes were effectively mitigated, then the different orientations of the FC/APC connector similarly benefited.

In contrast the anisotropic FBG had, in general, much broader coverage of the Poincaré sphere<sup>27</sup>. Apart from poorly populated areas, most of the surface was eventually sampled. This allowed the polarisation mitigation approach to be more comprehensively investigated, and was consequently a more thorough test. If one orientation of the FC/APC connector poorly mitigated SOP changes, another would provide a sufficiently different effect. This could lead to one FBG type having an

<sup>25</sup>The aim of depolarisation as achieved by a Lyot depolariser, Takada depolariser *et al.* [2] or polarisation scrambler is to have equal intensity in any arbitrarily chosen orthogonal axes system.

<sup>26</sup>Assuming that the at-rest isotropic FBG does not polarise upon reflection.

<sup>27</sup>Except for the Lyot & Circulator / Faraday Mirror dataset, shown in figures N.12 (page V.II N-19) & N.32 (page V.II N-41).

inconsistent result relative to the other type of FBG.

As the reported values in table 5.1 are evaluated on all the SOP changes, this can lead to an averaging of relatively good and bad polarisation mitigation performance into a single value<sup>28</sup>. As such, the value reported may not match the apparent improvement in the figures in appendix N (page V.II N-1). Conversely, the unimproved parts will have a smaller value in this case. The single value is presented as the polarisation mitigation approach should operate independent of input SOP.

The values in table 5.1 require some elaboration. As a graphical aid to the following discussion, figures 5.22 to 5.25 are presented. These are graphical representations of table 5.1(b), showing the anisotropic FBG SpectroBragg  $\sigma_{\text{Int.}}$  values (figure 5.22), the anisotropic FBG Polarimeter  $\sigma_{\text{Int.}}$  values (figure 5.23), the isotropic FBG SpectroBragg  $\sigma_{\text{Int.}}$  values (figure 5.24) and the isotropic FBG Polarimeter  $\sigma_{\text{Int.}}$  values (figure 5.25)<sup>29</sup>. The discussion will also refer to the Poincaré sphere figures in appendix N (page V.II N-1).

Of the various polarisation mitigation approaches investigated, the Lyot depolariser that was tested provided the worst performance. This was expected as the device was designed to depolarise a broad band signal and both the FBG bandwidth and the minimum SpectroBragg spectral range natively resolved were smaller than this minimum requirement.

The Lyot, as a consequence, converted SOP changes into phase noise (see §3.2.4.3 (page V.I - 140)), providing worse performance than the control experiment<sup>30</sup>. The only values smaller than the equivalent control experiment values, are the isotropic  $\lambda_B$ -intensity correlation coefficient,  $\rho_{\lambda_B}$ , and the isotropic background  $\sigma_{\lambda_B}$  values<sup>31</sup>. As such, the performance is as expected and it does not require further comment.

#### 5.4.5.1 Lefèvre controller approach

The first polarisation mitigation approach attempted was to do SOP fixing using the Lefèvre polarisation controller. The design was arrived at due to the available apparatus, and was later found to be a modification of the approach reported by Takada *et al.* during the literature review for the work.

The Lefèvre polarisation controller approach decorrelated the SpectroBragg and polarimeter intensities by  $\sim 34\%$  for the anisotropic FBG. The correlation is  $\sim 6\%$

---

<sup>28</sup>It was not always possible to determine where one set of SOP changes concluded and the next commenced, e.g. figures N.35 (page V.II N-44) and N.37 (page V.II N-45).

<sup>29</sup>A ratio of the SpectroBragg values to Polarimeter values could be considered as a measure of the effectiveness in reducing of the changing SOP oscillations. However, a large Polarimeter value in the denominator would be indistinguishable from a small SpectroBragg value in the numerator, and so this approach is not used for this discussion.

<sup>30</sup>The Lyot and control experiment can be compared using the unfiltered values, as neither had the facility to couple in the acoustic noise, as do the other approaches.

<sup>31</sup>The low correlation coefficient refers to the applied SOP  $\sigma_{\lambda_B}$  value only.

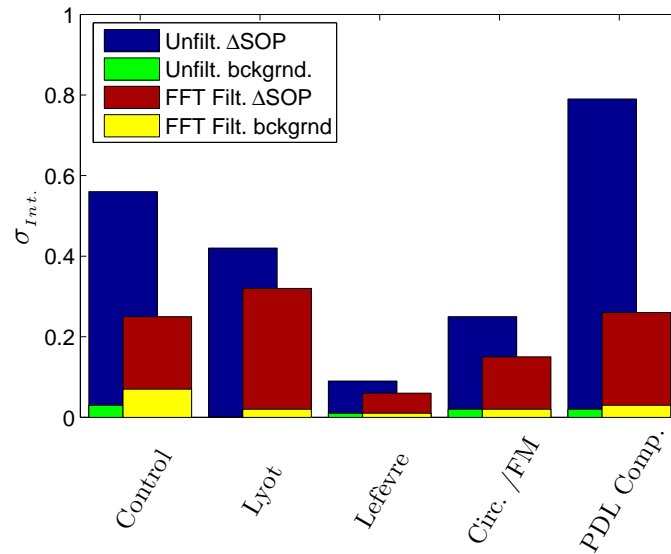


**Figure 5.22:** Anisotropic FBG values for unfiltered and FFT filtered SpectroBragg data showing the intensity standard deviations for the applied SOP changes and background, from table 5.1(b) (page V.I - 248).

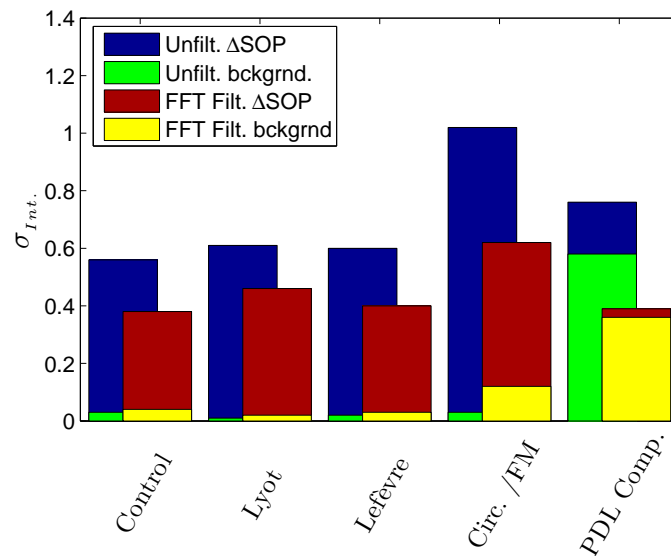


**Figure 5.23:** Anisotropic FBG values for unfiltered and FFT filtered Polarimeter data showing the intensity standard deviations for the applied SOP changes and background, from table 5.1(b) (page V.I - 248).

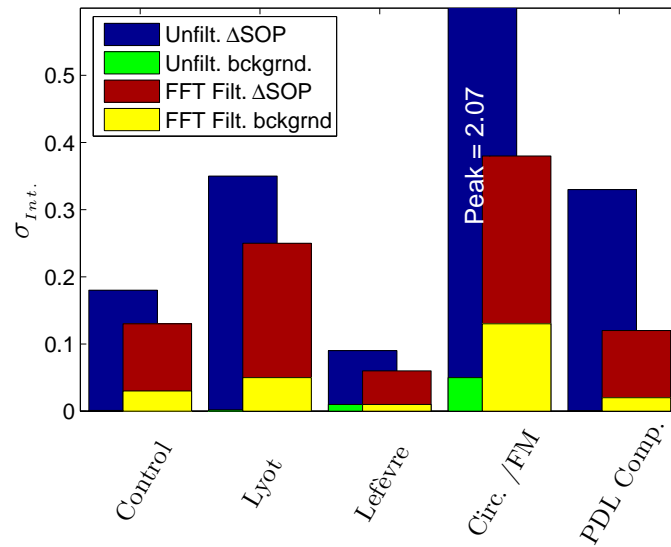


**Figure 5.24:** Isotropic FBG values for unfiltered and FFT filtered SpectroBragg data showing the intensity standard deviations for the applied SOP changes and background, from table 5.1(b) (page V.I - 248). Unfiltered Circ. /FM value, 2.07, is off figure scale and listed.

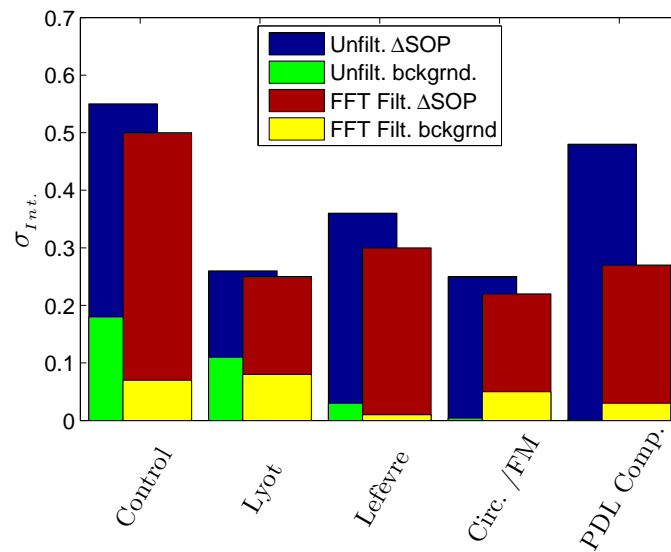


**Figure 5.25:** Isotropic FBG values for unfiltered and FFT filtered Polarimeter data showing the intensity standard deviations for the applied SOP changes and background, from table 5.1(b) (page V.I - 248).

larger for the isotropic FBG. This apparently contradictory result may be explained by the distribution of SOP changes upon the Poincaré sphere. The changes in SOP for the anisotropic FBG (figure N.22 (page V.II N-31) covered the Poincaré sphere more completely than did the isotropic FBG (figure N.23 (page V.II N-32)). For any rate of efficiency in polarisation fixing, the anisotropic FBG would exhibit a greater decorrelation than the isotropic FBG.

From figure 5.23 (page V.I - 251), the anisotropic FBG Polarimeter  $\sigma_{\text{Int.}}$  values for the control, Lyot and Lefèvre controller approach are roughly equivalent despite not having the same Poincaré sphere coverage. The corresponding SpectroBragg values in figure 5.22 (page V.I - 251), show a drop of  $\sim 76\%$  in the FFT filtered value from the control level.

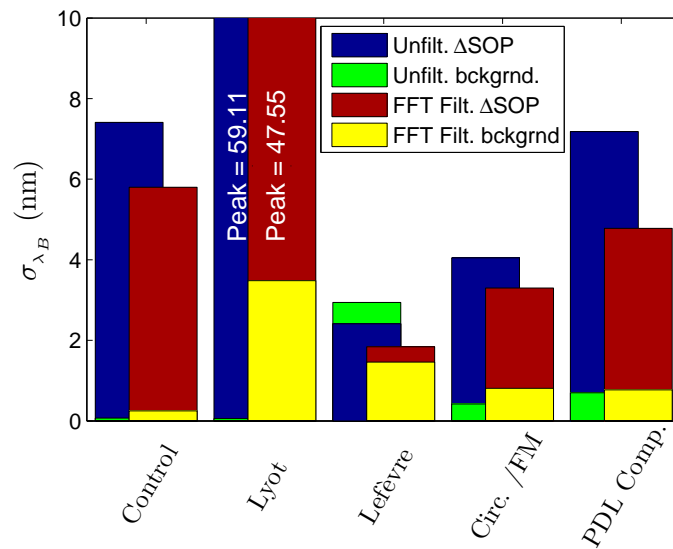
In contrast to the anisotropic FBG, the isotropic FBG Polarimeter  $\sigma_{\text{Int.}}$  values in figure 5.25 (page V.I - 252) do not show the same consistency. This again may be an issue of the Poincaré sphere coverage, as is evident in figure N.23 (page V.II N-32), or with the less clearly separated high frequency SOP changes and lower frequency acoustic noise during FFT filtering.

Taking the latter case first, inadequate low-frequency FFT filtering would increase the  $\rho_{\text{Int.}}$  value, and as the low-frequency oscillations were typically larger than the higher-frequency SOP induced oscillations, would also increase the  $\sigma_{\text{Int.}}$  value. In the former case, the restricted SOPs occupied by the isotropic FBG would yield similar performance in comparison to the anisotropic FBGs.

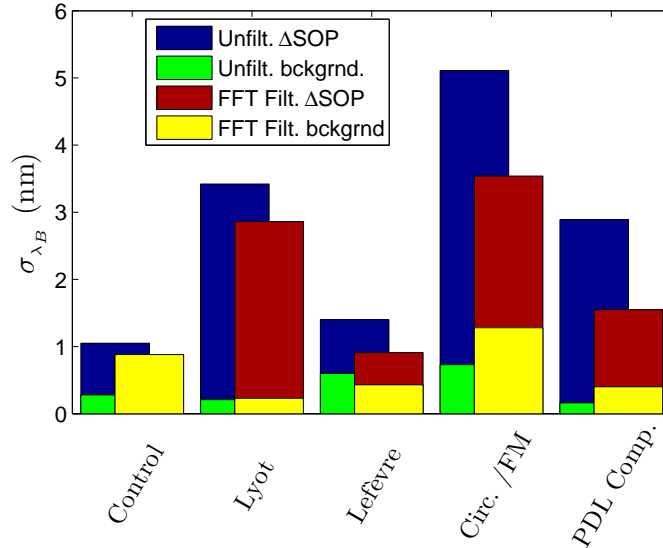
As the different polarisation mitigation approaches were tested, the fibre leads to the FBG would have been moved as the different apparatus were connected and disconnected. Despite the attempt to minimise differences in movements, these relative movements would equate to a fixed translation/rotation about the Poincaré sphere. By covering less of the Poincaré sphere, the isotropic FBG SOPs would be more variant under fixed rotations/ phase retardations which may account for the less consistent distribution of  $\sigma_{\text{Int.}}$ .

Figure 5.24 (page V.I - 252) shows an improvement for the Lefèvre controller approach, agreeing with the anisotropic FBG values. The drop in the FFT filtered  $\sigma_{\text{Int.}}$  value is  $\sim 54\%$ , less than for the anisotropic FBG.

The centroid calculated  $\lambda_B$  values in tables 5.1(c) (page V.I - 248) & 5.1(d) follow the same pattern as the intensity values. Figures 5.26 & 5.27 show the  $\sigma_{\lambda_B}$  values for the anisotropic and isotropic FBGs, respectively. For the anisotropic FBG, the relative performance in figure 5.26 is qualitatively similar to that in figure 5.22 (page V.I - 251) under applied SOP changes. The main difference is that the background level is much larger than for the control experiment background  $\sigma_{\lambda_B}$  value, by 584%. Consequently, the difference is reduced between the background and applied changing SOP  $\sigma_{\lambda_B}$  values,  $\sim 126\%$ , compared to the control experiment difference of



**Figure 5.26:** Anisotropic FBG values for unfiltered and FFT filtered SpectroBragg data showing the centroid standard deviations for the applied SOP changes and background, from table 5.1(c) (page V.I - 248). Anisotropic FBG unfiltered & FFT filtered Lyot values, 59.11 nm & 47.55 nm, are off figure scale and listed.



**Figure 5.27:** Isotropic FBG values for unfiltered and FFT filtered SpectroBragg data showing the centroid standard deviations for the applied SOP changes and background, from table 5.1(c) (page V.I - 248).

2320%. This is the largest background  $\sigma_{\lambda_B}$  value of any of the approaches tested. Although the FFT filtering does introduce some Gibbs effect oscillations, the unfiltered background  $\sigma_{\lambda_B}$  value exceeds the corresponding value for the applied SOP changes.

For the isotropic FBG, there is almost no change between the control experiment and the Lefèvre controller approach. The control experiment applied SOP changes and background  $\sigma_{\lambda_B}$  values are the same, but the Lefèvre controller background  $\sigma_{\lambda_B}$  value is less than half the applied SOP change value. This is the lowest isotropic FBG value of the polarisation mitigation approaches tested.

Despite the non-linear relationship between the SOP changes, the  $\rho_{\lambda_B}$  for the centroid calculated anisotropic FBG values are smaller than the control experiment but larger for the isotropic FBG. This difference between the anisotropic and isotropic FBG values may, again, be to do with the relative coverage of the Poincaré sphere by the two FBG types, or the effectiveness of the FFT filtering.

#### 5.4.5.2 Circulator/Faraday Mirror approach

The Lefèvre polarisation controller was easy to approximately configure. However, as the oscillations were progressively suppressed, the determination of further improvements became more difficult. The fibre loop holders could not be locked into position, and, when nearly parallel with the optics bench, would on occasion fall under their own weight onto the optical table unless supported.

The Circulator/Faraday Mirror approach promised a much simpler assembly, as the Faraday Mirror's fixed half-waveplate effect required no configuration, and was only limited in terms of the wavelength sensitivity of the Faraday rotator. This version should have exhibited polarisation fixing as good as or better than the Lefèvre controller approach.

As shown in figures 5.22 (page V.I - 251) and 5.24 (page V.I - 252), the Circulator/Faraday mirror does not perform as well as the Lefèvre controller. The correlation coefficient  $\rho_{\text{Int.}}$  is unchanged from the control experiment for the anisotropic FBG. The value is similar to the isotropic FBG values for the other polarisation mitigation approaches. The SpectroBragg  $\sigma_{\text{Int.}}$  value is smaller than the control experiment value ( $\sim 60\%$ ) but larger than the Lefèvre controller value ( $\sim 250\%$ ). In contrast, the isotropic FBG  $\rho_{\text{Int.}}$  value is the lowest of any of the  $\rho_{\text{Int.}}$  values on the table, and the same for the unfiltered  $\rho_{\text{Int.}}$  value.

The anisotropic FBG  $\sigma_{\text{Int.}}$  value is  $\sim 60\%$  of the control experiment value, figure 5.22 (page V.I - 251). The corresponding Polarimeter  $\sigma_{\text{Int.}}$  value is  $\sim 160\%$  of the control and Lefèvre controller values, figure 5.23 (page V.I - 251), despite having reduced coverage of the Poincaré sphere.

The isotropic FBG  $\sigma_{\text{Int.}}$  value provides the largest value in the table at  $\sim 292\%$

that of the control experiment value, figure 5.24 (page V.I - 252), despite having a lower Polarimeter  $\sigma_{\text{Int.}}$  of  $\sim 44\%$ . The low correlation coefficient  $\rho_{\text{Int.}}$  is of little benefit given the control experiment's improved performance.

The centroid calculated  $\sigma_{\lambda_B}$  values follow the qualitative pattern of the intensity values. The anisotropic FBG values are similarly smaller than the control experiment value ( $\sim 57\%$ ) but larger than the Lefèvre controller value ( $\sim 179\%$ ). The isotropic FBG  $\sigma_{\lambda_B}$  value follows the SpectroBragg  $\sigma_{\text{Int.}}$  pattern, being  $\sim 402\%$  of the control experiment value.

As for  $\rho_{\text{Int.}}$ , the anisotropic FBG  $\rho_{\lambda_B}$  value is larger than both the control and Lefèvre controller values,  $\sim 154\%$  and  $\sim 226\%$ , respectively. The isotropic FBG  $\rho_{\lambda_B}$  value is the largest of all  $\rho_{\lambda_B}$  values on the table, diverging from the  $\rho_{\text{Int.}}$  value being the lowest. The anisotropic FBG performance is the second best, despite the largest Polarimeter  $\sigma_{\text{Int.}}$  value, as can be seen in figures 5.23 (page V.I - 251) and 5.26 (page V.I - 254). The different distribution of SOPs on the Poincaré sphere may have been responsible for the increased  $\sigma_{\text{Int.}}$  value, however the correlation value indicates that the SOP oscillations were not effectively removed.

The isotropic values are the largest in both figures 5.24 (page V.I - 252) and 5.27 (page V.I - 254). The distribution pattern of isotropic FBG SOPs on the Poincaré sphere, figure N.35 (page V.II N-44), differed from those of the Lefèvre controller, figure N.25 (page V.II N-34), but was closer to the distribution patterns for the other polarisation mitigation approaches<sup>32</sup>.

The most likely cause of the decreased performance, relative to that achieved by the Lefèvre controller approach, was that the fixed half-waveplate rotation may have been modified by residual twists or turns in the fibre of the circulator or Y-coupler arms used to combine the SOPs. Consequently, the SOPs may not have been parallel or at the same intended OPD. The unfiltered SpectroBragg intensity for the anisotropic FBG shown in figure N.32(a) (page V.II N-41) does not exhibit much obvious low-frequency oscillation, but the isotropic FBG shown in figure N.33(a) (page V.II N-42) does. A circulator using PMF was not available, and so the possible performance was unlikely to have been achieved.

In contrast, the Lefèvre controller was configured by observing the output on the SpectroBragg and on a polarising beam-splitter connected to a balanced detector. Any modification of the SOPs from the Lefèvre controller to the Y-coupler could have been minimised during this configuration, improving the performance over the fixed Faraday mirror.

Although it was not tested, the use of a Lefèvre polarisation controller after the circulator may have improved performance, but this arrangement would combine

---

<sup>32</sup>The anisotropic FBG coverage of the Poincaré sphere was the closest to the isotropic FBG shape of all the anisotropic FBG experiments. The cause of this difference in coverage is unknown.

the expense and difficulty of configuration of both approaches.

### 5.4.5.3 PDL balancing approach

The PDL balancing approach, figure 5.10 (page V.I - 233), matched the losses in both orthogonal SOPs so that the effective signal captured by the SpectroBragg had  $|E_{\parallel}| = |E_{\perp}|$ . This approach departs from the previous approaches in that the losses are matched, thus decreasing the intensity throughput to achieve a polarisation mitigation benefit.

The approach also requires quasi-static PDL through the whole apparatus. This condition was unlikely to have been kept, as the rotation of the FC/APC connector would have locally altered the PDL at the FC/APC connector. Additionally, although the SMF based attenuator and ODL were unwound and fixed to the bench between the PMF polarising beam-splitters, any residual twists or turns may have resulted in both axes of the second PMF section being illuminated, and hence a mixing of SOPs at recombination.

The  $\rho_{\text{int.}}$  is the lowest across all the approaches for the anisotropic FBG, with the nearest being the Lefèvre controller value. In contrast the isotropic FBG  $\rho_{\text{int.}}$  value is the largest.

However, as shown in figures 5.22 (page V.I - 251) and 5.24 (page V.I - 252), the PDL balancing approach does not differ much from the control experiment. The SpectroBragg anisotropic and isotropic FBG  $\sigma_{\text{int.}}$  values are almost identical to the control experiment values ( $\sim 104\%$  &  $\sim 92\%$ , respectively). The corresponding Polarimeter anisotropic FBG  $\sigma_{\text{int.}}$  value is  $\sim 103\%$  of the control experiment value, while the isotropic FBG  $\sigma_{\text{int.}}$  value is  $\sim 54\%$  of the control experiment value. As observed by the SpectroBragg, the PDL balancing approach has only attenuated the intensity oscillations in line with the overall intensity.

Figure 5.26 (page V.I - 254) shows that the centroid calculated anisotropic FBG  $\sigma_{\lambda_B}$  PDL balancing value is only a slight improvement over the control experiment value (by  $\sim 83\%$ ), while figure 5.27 (page V.I - 254) shows the isotropic FBG  $\sigma_{\lambda_B}$  value is almost double the control experiment value ( $\sim 176\%$ ).

The anisotropic FBG  $\rho_{\lambda_B}$  value is almost totally decorrelated, despite the control experiment and PDL balancing  $\sigma_{\lambda_B}$  values being similar. Again, as for the small isotropic FBG Circulator/Faraday mirror  $\rho_{\text{int.}}$  value, the correlation is of little benefit here. The isotropic FBG  $\rho_{\lambda_B}$  value is larger compared to the control experiment value ( $\sim 137\%$ ). As the two correlation coefficients are low, but the magnitude of the oscillations remains unchanged, the failure to meet the quasi-static PDL requirement and the phase and polarisation-sensitivity of the diffraction grating are likely to be the reason the quoted depolarisation performance was not achieved. Overall, for the phase and polarisation-sensitivity of the SpectroBragg the PDL

balancing approach did not improve the SpectroBragg performance over the control experiment in terms of intensity or centroid calculated  $\lambda_B$ .

## 5.5 Conclusion

The ideal polarisation fixer would take all arbitrarily polarised input SOPs and output a single SOP, coherently added, but with zero OPD. As reported by Tateda *et al.*, no current passive optical device will coherently add rotated SOP components without converting the phase shift describing the ellipticity into a non-zero OPD [7].

By combining the decoherence approach of Takada *et al.* with the polarisation fixing approach of Tateda *et al.*, the best polarisation mitigation, as measured, of the approaches tested was achieved for the anisotropic FBG. Any reduction in the coverage of the Poincaré sphere achieved by an approach would exhibit a larger difference for the anisotropic FBG which covered more of the Poincaré sphere to begin with.

Comparing figures 5.22 (page V.I - 251), 5.24 (page V.I - 252), 5.26 (page V.I - 254) and 5.27 (page V.I - 254) shows that the Lefèvre polarisation controller approach produced an improvement, or at least approximately equivalent performance, to the control experiment; the isotropic FBG  $\sigma_{\lambda_B}$  value is  $< 4\%$  larger than the control experiment value.

However, the conceptually similar Circulator/Faraday mirror approach does not exhibit similar performance. The anisotropic FBG values are improved over the control experiment values, but the isotropic FBG values are larger than the control experiment values. The lack of all PMF circulator and combining Y-coupler are possible sources for the drop in performance.

The different experimental apparatus had limitations that compromised the performance that may have been possible. At the time of data capture, these limitations were not as evident as the results in table 5.1 (page V.I - 248) make clear. Indeed, when comparing the SpectroBragg and Polarimeter  $\sigma_{\text{Int.}}$  values, as in figure 5.28 showing the respective ratios, the circulator/ Faraday mirror approach is not too far behind the Lefèvre polarisation controller approach for the anisotropic FBG.

The spectral bandwidth differences between the isotropic and anisotropic FBGs with the unbalanced Mach-Zehnder based polarisation mitigation schemes may have benefited from being repeated at different OPD values, such that any acoustic vibrations being interferometrically coupled into the signal were minimised. As the experiments were performed, the unbalanced Mach-Zehnder were already limiting the phase noise, but further improvements may have been attainable.

The greatest limitation to these techniques, as investigated, was the unwanted introduction of phase noise, which dominated the signal over the polarisation noise.

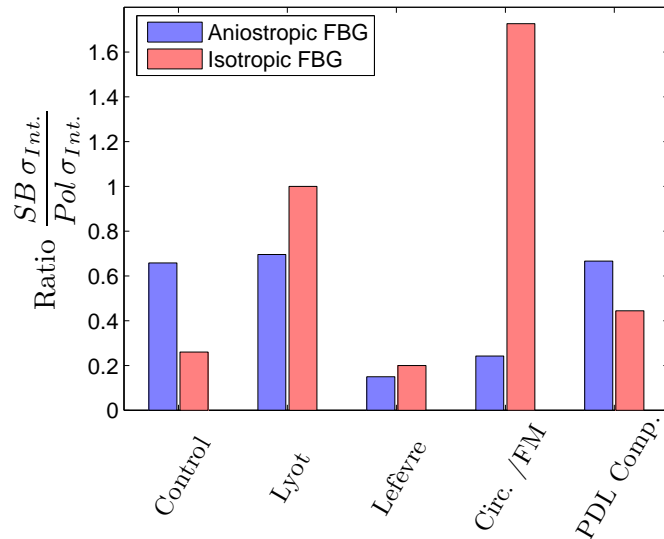


**Figure 5.28:** Ratios of the FFT filtered SpectroBragg  $\sigma_{\text{Int.}}$  values (figures 5.22 (page V.I - 251) & 5.24 (page V.I - 252)) to the FFT filtered Polarimeter  $\sigma_{\text{Int.}}$  values (figures 5.23 (page V.I - 251) & 5.25 (page V.I - 252)) for the anisotropic and isotropic FBGs.

Unbalancing the stationary Mach–Zehnder interferometer reduces the interferometric phase noise, but requires *a priori* knowledge of the coherence length of the source to adhere most closely to stationarity requirements.

The disadvantage of the unbalanced stationary Mach–Zehnder interferometer is that the SOPs that are combined are not from the same input signal (i.e. the OPD results in a relative time difference  $\tau > 0$ ). The mismatch is greatest for higher-coherence signals, where the side-lobes of signals from different times may interfere to produce significant phase noise artefacts.

An additional source of variation was in the distribution or coverage of the SOPs on the Poincaré sphere for the different FBGs. Appendix N (page V.II N-1) contains the Poincaré sphere plots for the anisotropic and isotropic FBGs as captured by the Polarimeter. As the Poincaré sphere is a three-dimensional structure, different 2D projections are supplied.

Comparing the *azimuthal equidistant projection*<sup>33</sup> figures shows that neither the individual anisotropic or isotropic FBG distributions were the same. While the

<sup>33</sup>The azimuthal equidistant projection takes a point on the sphere<sup>34</sup>( $-S_2$ ) and plots the distance of each point along the great circle containing  $-S_2$ , the point and  $+S_2$  at the angle that point resides with respect to  $+S_1$ . As such the outer diameter of the plots represents  $+S_2$ , i.e. a distance of  $\pi$  along the great circle. Relative areas are not preserved, but this projection does allow for comparison.

<sup>34</sup>This was chosen for convenience in demonstrating the ring like distribution of the Lefèvre controller isotropic FBG set, in figure N.57 (page V.II N-62).

anisotropic FBGs sampled most of the Poincaré sphere, the isotropic FBGs sampled only a small area, which was not consistent across the figures.

An interesting question which could not be addressed in the time available for the experimental work was whether the performance of the approaches relied upon the specific area of the Poincaré sphere covered, and in particular the improvement obtained by the Lefèvre controller approach?

The work presented here was limited by the time available for the experimental work and apparatus to test the various questions the experiments prompted. The PDL balancing approach's requirement for quasi-static system PDL was limited by the method of changing SOPs, which a deterministic polarisation controller may not have necessarily introduced. However, even under laboratory conditions with most fibre taped to a bench, the necessity of connecting to or reconnecting equipment that does not share the same plane as the bench will limit the quasi-static PDL achievable.

Further investigation of the various issues mentioned in determining the performance limits of the different approaches is needed before a proper conclusion can be arrived at. This work may be considered as an initial investigation of these approaches for use with devices such as the SpectroBragg.

## 5.6 References

- [1] E. Wolf. *Introduction to the Theory of Coherence and Polarization of Light*, chapter 9, pages 174–201. Cambridge University Press, Cambridge, 2007. ISBN: 9780521822114.
- [2] K. Takada, K. Okamoto, and J. Noda. New fiber-optic depolarizer. *J. Lightwave Technol.*, 4(2):213–219, February 1986.
- [3] H. Dong, J. Q. Zhou, M. Yan, P. Shum, L. Ma, Y. D. Gong, and C. Q. Wu. Quasi-monochromatic fiber depolarizer and its application to polarization-dependent loss measurement. *Opt. Lett.*, 31(7):876–878, 2006.
- [4] K. Boehm, K. Petermann, and E. Weidel. Performance of Lyot depolarizers with birefringent single-mode fibers. *J. Lightwave Technol.*, 1:71–74, March 1983.
- [5] E. Collett. *Polarized Light in Fiber Optics*, chapter 12, pages 319–354. SPIE Press/Polawave Group, New Jersey, nov 2004. ISBN: 0819457612.
- [6] D. Goldstein. *Polarized Light*, volume 83 of *Optical Engineering*, chapter 26, pages 511–532. Marcel Dekker, Inc., New York, 2 edition, 2003. ISBN: 082474053X.
- [7] M. Tateda and T. Omatsu. Polarization state fixer composed of passive optical devices. *J. Opt. Soc. Am. A*, 20(2):342–346, February 2003.

- [8] V. I. Tatarskii. An intuitive introduction to the Wolf effect. *J. Opt. A-Pure Appl. Op.*, 7(5):953, 1998.
- [9] W. H. Knox, M. Alonso, and E. Wolf. Spatial coherence from ducks. *Phys. Today*, 63(3):11–11, 2010.
- [10] O. Kafri. Fundamental limit on accuracy in interferometry. *Opt. Lett.*, 14(13):657, 1989.
- [11] E. Collett. *Polarized Light in Fiber Optics*, chapter 15, pages 433–482. SPIE Press/Polawave Group, New Jersey, nov 2004. ISBN: 0819457612.
- [12] A. Rogers. *Polarization in Optical Fibers*, chapter 5, pages 153–192. Artech House, Inc., Boston, 2008. ISBN: 1580535348.
- [13] M. Born and E. Wolf. *Principles of Optics: Electromagnetic Theory of Propagation, Interference and Diffraction of Light*, chapter 1, pages 1–74. Cambridge University Press, Cambridge, 7th edition, 1999. ISBN: 0521642221.
- [14] S. Pancharatnam. Generalized theory of interference, and its applications, Part I. Coherent pencils. *P. Indian Acad. Sci. A*, 44:247–262, 1956. 10.1007/BF03046050.
- [15] W. B. Davenport Jr. and W. L. Root. *Random Signals and Noise (Lincoln Library Productions)*, chapter 4, pages 45–75. McGraw-Hill Book Company Inc. (The Maple Press Company), New York, 1958.
- [16] J. S. Bendat and A. G. Piersol. *Random Data Analysis and Measurement Procedures*, chapter 5, pages 118–188. John Wiley & Sons, Inc., New York, 3rd edition, 2000. ISBN: 0471317330.
- [17] D. Goldstein. *Polarized Light*, volume 83 of *Optical Engineering*, chapter 5, pages 65–86. Marcel Dekker, Inc., New York, 2 edition, 2003. ISBN: 082474053X.
- [18] E. Collett. *Polarized Light in Fiber Optics*, chapter 9, pages 183–226. SPIE Press/Polawave Group, New Jersey, nov 2004. ISBN: 0819457612.
- [19] E. Collett. *Polarized Light in Fiber Optics*, chapter 6, pages 77–114. SPIE Press/Polawave Group, New Jersey, nov 2004. ISBN: 0819457612.
- [20] J. S. Bendat and A. G. Piersol. *Random Data Analysis and Measurement Procedures*, chapter 3, pages 48–85. John Wiley & Sons, Inc., New York, 3rd edition, 2000. ISBN: 0471317330.

# Chapter 6

## $\pi$ -shift Interferometry with HTT

---

### 6.1 Introduction

Distributed and remote sensing configurations, as in figure 6.1 (a) & (b), respectively, use the passive long distance transmission capabilities of fibres. The distances are limited by the attenuation or extinction [1] of the signal as it passes through the fibre. The attenuation experienced is the sum of the absorption of the light and scattering of the light out of the guided modes of the fibre.

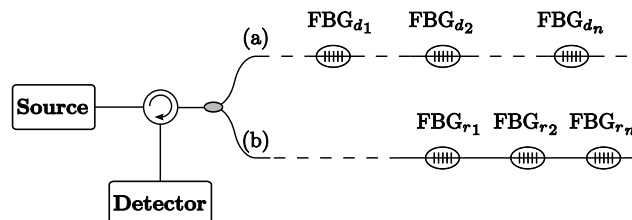


**Figure 6.1:** (a) Distributed sensing: the sensors are located distances from each other; (b) Remote sensing: The sensors are located closer together, but at a distance from the source and detector.

Rayleigh scattering provides the fundamental minimum to signal attenuation, as molecular based scattering cannot be totally eliminated [2–4]. For SMF-28 the attenuation is quoted at  $\gtrsim 0.2$  dB/km<sup>1</sup> at 1550 nm<sup>2</sup>. For distributed fibre sensing the light must travel from the light source along the fibre, and then be reflected back

<sup>1</sup>The ITU G652 recommended value of  $< 0.28$  dB/km.

<sup>2</sup>From *Corning SMF-28e+ optical fiber with NexCor Technology product information*, Corning Inc. (<http://www.corning.com/WorkArea/showcontent.aspx?id=27659>).

along the length from the sensor to the detector or transmitted along the remainder of the fibre to the detector. The light will experience attenuation in both directions, and for longer distances requires amplification or the use of higher power sources (which may introduce non-linear effects into the system).

The scattered and guided radiation can be considered as consisting of two components, incoherent and coherent radiation. The scattered radiation outside the coherence length adds incoherently. The scattered radiation within the coherence length of a source adds coherently, modifying the guided mode. The observed intensity is the result of the beating of the original signal and the coherently scattered light and a background of incoherently scattered light.

For a phase sensitive demodulation system, such as an interferometer, the coherently scattered radiation is recovered as phase noise. The narrower the source spectrum (i.e. higher the coherence), the greater the relative effect of phase noise will be. For low-coherence and incoherent sources, the scattered radiation reduces the visibility of fringes. Rayleigh scattering is an extensive effect, and so impairs the resolution with which remote sensors can be demodulated.

Optical noise arising in the system prior to entering the interferometer will be split between the paths of the interferometer equivalently to the desired signal. Common-mode rejection of this optical noise using the two  $\pi$ -shifted complementary interferograms output by a two-beam interferometer is reported here. The common-mode noise is removed as a DC component during the signal processing. This is used to extend the range over which a transmitted signal can be consistently demodulated [5].

In this chapter the Hilbert transform technique, HTT [6], is used to analyse two-output,  $\pi$ -shifted interferograms to demodulate fibre Bragg grating, FBG, signals. The Hilbert transform technique has been demonstrated to provide higher resolution wavelength determination than Fourier transform spectroscopy using shorter interferometer scans [6-9]. The  $\pi$ -shifted interferograms should allow for the recovery of interferograms not detectable with single-output interferograms. The centroid and Hilbert transform techniques are used to determine the mean or peak wavelength position, for comparison purposes.

The Hilbert transform technique using  $\pi$ -shifted interferograms is examined with varying noise levels provided by a laser co-propagating with the reflected FBG signals. The amplitude of the noise at the detector can be tuned by varying the attenuation of the laser. The phase noise introduced by the laser will also degrade the spectrum returned and reduce resolution.

Instead of placing the reference laser at the interferometer, the reference beam traversed the same distance as the FBG signal. This provided the greatest scattering based noise on the reference signal. The recalibration process could then have intro-

duced the reference noise onto the FBG signal, decreasing the SNR below that from the FBGs alone. The common-mode noise rejection provided by the two-output,  $\pi$ -shift interferograms is measured by the noise reduction of the high-coherence telecomms laser, rather than the lower-coherence FBGs.

The experiment is undertaken at the limit of the two-output  $\pi$ -shift technique's sensitivity, where the recovered signal is just above the background noise level, and unrecoverable using single-output interferometry. The experimental conditions are thus at the limit of the technique's effectiveness. This is to demonstrate the advantage of the two-output,  $\pi$ -shift technique in extending the range over which FBGs can be effectively demodulated.

## 6.2 Theory

This chapter reports the use of the Hilbert transform technique [6, 7] together with two-output,  $\pi$ -shifted phase-shifting interferometry [5], appendix 12.B of [10]. This would primarily be of benefit in quasi-distributed and remote sensing applications where Rayleigh scattering noise can accumulate. For quasi-distributed sensing the distant sensors would return lower signal levels than the nearer sensors due to greater attenuation, unless the reflectivity were tailored to be lower for closer sensors. Such customisation would increase costs, and is therefore less likely to occur than the situation where different strength sensor signals are encountered at the detector.

Transmission of light over optical fibres is limited by two processes, absorption and scattering<sup>3</sup>, which equal the total attenuation experienced by the signal [1]. Absorption in fibres in the telecomms bands<sup>4</sup> largely occurs where contaminants or defects occur within the guiding mode field. The absorbers can be introduced during manufacturing, by diffusion from the environment and by unclean splices. Absorption can also occur due to the presence of Hydrogen atoms which form OH<sup>-</sup> molecules [14] at defect sites<sup>5</sup>, see §2.2.2.1 (page V.I - 25).

The manufacturing process has been refined to reduce the presence of absorbers in fibre beyond ITU-T standards [15], due to the commercial competitive advantage held by lower absorption fibre. Absorption losses have been minimised by the manufacturing process but are never totally eliminated in practice.

Attenuation losses also occur due to scattering processes. Light may be scattered in directions outside the range for waveguiding and be quickly lost from

---

<sup>3</sup>Ignoring radiation losses due to bend curvature [11].

<sup>4</sup>The telecomms bands are defined, but not specified, by the ITU-T [12, 13]. The bands are indicated in figure 2.4 (page V.I - 30) above the wavelength axis.

<sup>5</sup>To a lesser extent H<sub>2</sub>O [15]. OH<sup>-</sup> molecules have absorption peaks at  $\sim 700$ nm,  $\sim 900$ nm and  $\sim 1380$ nm [11] in the fibre [16]. Hydrogen may diffuse through the fibre after manufacture and its impact can be controlled by the use of Deuterium after drawing [17], which shifts the resonance peak to longer wavelengths [18].

the fibre. The quoted scattering-dominated attenuation losses are  $\leq 0.22$  dB/km and  $\sim 0.2$  dB/km at 1550 nm for Corning LEAF and SMF-28e fibre. There are three forms of scattering typically encountered in currently produced optical fibres<sup>6</sup>: Rayleigh, Brillouin and Raman. Raman scattering and Brillouin scattering are inelastic scattering processes<sup>7</sup>, i.e. they involve the redistribution of part of the optical energy into frequencies,  $\omega_s$ , differing from the original signal,  $\omega_i$ , by the sum and difference of phonons,  $\omega_p$ , occurring at optical and acoustic frequencies, respectively [20]. For the present work, Rayleigh scattering<sup>8</sup> is the elastic scattering process of the incident Poynting vector by randomly distributed scatterers, dimensionally smaller than the incident wavelength. The incident and scattered frequencies are the same, as there are no Doppler shifts present, but the polarisation and phase are altered and randomised [22]. The randomly distributed scatterers arise from non-propagating diffusive fluctuations [23], and is discussed in §2.2.2.2 (page V.I - 28). Rayleigh scattering provides a fundamental limit to minimisation of attenuation.

### 6.2.1 Phase noise

Rayleigh scattering attenuation of a transmitted signal limits the distance over which the signal can be transmitted. For lengths shorter than this limit, the scattered light guided by the fibre has the same frequency as the original signal, but random phase differences<sup>9</sup>, as discussed in section §2.2.2.2 (page V.I - 28).

Interferometric demodulation techniques based upon Michelson or Mach-Zehnder interferometry have the Fellgett or Multiplex advantage [24], where the time needed to obtain a given signal-to-noise ratio, SNR, across the whole spectrum window is reduced compared to other methods, by simultaneously recording the whole spectral window [25]. These demodulation techniques also suffer the multiplex disadvantage, where signal carried fluctuations are recorded simultaneously for all wavelengths [26].

Rayleigh scattering appears as phase-noise on the unmodified, generating signal. For a source, the signal's phase will have interfering contributions from scattering within the coherence length as it traverses the fibre. The longer the coherence length, as for high-coherence sources, the greater the accumulation of phase noise. This is a disadvantage as high-coherence sources are desirable for long distance

---

<sup>6</sup>Currently manufactured fibres are made with highly refined manufacturing processes. Prior to this, fibres could contain scattering centres large in comparison to the guided wavelength, resulting in Mie scattering.

<sup>7</sup>Raman and Brillouin scattering are typically 30 – 20 db weaker than Rayleigh scattering [19].

<sup>8</sup>Under which all elastic scattering processes may be (and frequently are) grouped. It is usually understood that the Rayleigh scattering name is used for scattered intensity that has a  $\lambda^{-4}$  dependence. The extent of Rayleigh's work on scattering and the varying naming conventions, variously including -Gans, -Debye and -Mie for example, are grouped under Rayleigh scattering [21]. Here, Rayleigh scattering is the  $\lambda^{-4}$  dependence.

<sup>9</sup>The spectrum will exhibit a broadened, lower-coherence profile due to the phase-noise components synthesising frequency components.

communications due to the power levels achievable and the spectral density for information transfer they facilitate.

The phase-noise from a high-coherence source should not modulate the low-coherence signal, as the noise effect should be similar to non-white noise, which is spectrally associated with the generating signal [26]. However, the transmission distances may be considered the optical far-field for the scattering events, and may generate spatial coherence between the scattered beam from one signal and another signal [27]. This makes the phase noise ‘whiter’ than it would otherwise have been.

There exists the possibility of *Double Rayleigh backscattering* [28, 29], where the scattered light experiences further scattering, reversing the direction again. Double scattering will be a weak contribution to phase noise. This does not violate the single-scattering condition, as the second scattering is assumed to be in the far-field, rather than multiply scattered in the near-field.

The field at the input to an interferometer, after traversing a length  $L$  of fibre, is the sum of the direct radiation and the scattered radiations [30],

$$\underline{\mathbf{E}}_{\text{total}}(L, t) = \underline{\mathbf{E}}_{\text{signal}}(L, t) + \underline{\mathbf{E}}_{\text{noise}}(L, t) \quad (6.1)$$

where  $\underline{\mathbf{E}}_{\text{signal}}$  is the direct amplitude

$$\underline{\mathbf{E}}_{\text{signal}}(L, t) = \underline{\mathbf{E}}_0 e^{i(\omega t - \Phi(L))} e^{-\alpha_{\text{sc}} L} \quad (6.2)$$

and

$$\underline{\mathbf{E}}_{\text{noise}}(L, t) = \underline{\mathbf{E}}_{\text{source}}(L, t) + \underline{\mathbf{E}}_{\text{fs}}(L, t) + \underline{\mathbf{E}}_{\text{ds}}(L, t) + \dots \quad (6.3)$$

where  $\underline{\mathbf{E}}_{\text{source}}$  is the source amplitude,  $\underline{\mathbf{E}}_{\text{fs}}$  is the forward scattered amplitude and  $\underline{\mathbf{E}}_{\text{ds}}$  is the double backward scattered amplitude. The magnitudes of the scattered amplitudes will be smaller than the magnitude of the direct radiation, with the amplitude decreasing with more scattering events.

A two-beam interferometer autocorrelates  $\underline{\mathbf{E}}_{\text{total}}$  by modulating  $\underline{\mathbf{E}}_{\text{total}}$  in one arm. The detector measures the intensity, and so the self- and cross-products of the different scattered radiation terms become very small and may be neglected. The cross-products of the scattering terms with the direct signal, although small compared to the direct signal, cannot be neglected. For equal intensities in the two arms, the interferometer output intensity is given by equation (B.25) (page V.II B-10)

$$\begin{aligned}
I_{\text{Interferometer}}(L, t) &= \langle \underline{\mathbf{E}}_{\text{total}}(L, t) \underline{\mathbf{E}}_{\text{total}}^*(L, t + \tau) \rangle \\
&= 2 \underline{\mathbf{E}}_{\text{signal}}(L, t) \underline{\mathbf{E}}_{\text{signal}}^*(L, t + \tau) \\
&\quad + 2 \underline{\mathbf{E}}_{\text{noise}}(L, t) \underline{\mathbf{E}}_{\text{noise}}^*(L, t + \tau) \\
&\quad + 2 \underline{\mathbf{E}}_{\text{signal}}(L, t) \underline{\mathbf{E}}_{\text{noise}}^*(L, t)
\end{aligned} \tag{6.4}$$

The result is that the scattering observed at detection can be enhanced over the single pass scattering, and may fall into a different temporal databin to the generating signal, but still have intensity fluctuations due to its (reduced) mutual coherence. Double Rayleigh scattering is more of an issue in amplifier systems, where the noise is amplified and the impact on the final recorded signal can be due to the accumulated amplified noise in addition to the randomised phase. These considerations can be ignored within this work as the intensities are likely to be very low and the only amplifiers are in receivers, after the optical signal has been converted to an electrical signal.

The information in the interferogram will be degraded by the presence of noise, limiting the resolution with which the measurand can be determined. The intensity noise can reduce the recoverable signal by reducing the SNR. The removal of Rayleigh scattering originating phase-noise can allow previously undetectable signals to be effectively demodulated.

### 6.2.2 Phase-shift interferometry

Interferometry uses information obtained from the interference of light to determine properties of the light, as has been outlined in section §B.1 (page V.II B-4). For sensing purposes with FBGs, the property most frequently sought is the mean wavelength.

A monochromatic electromagnetic plane wave propagating in the  $z$ -direction is described by

$$\underline{\mathbf{E}}(t, z) = \underline{\mathbf{E}}_{\text{inc}}(t) e^{i\phi(t)} e^{-ikz} \tag{6.5}$$

where  $\underline{\mathbf{E}}_{\text{inc}}(t)$  is the incident amplitude,  $\phi(t)$  is the temporal phase fluctuation, and  $k = \frac{\omega}{c}$  is the wavenumber;  $\omega$  is the angular frequency and  $c$  is the speed of light. For wide-sense stationary conditions, we can take  $\underline{\mathbf{E}}_{\text{inc}}(t) e^{i\phi(t)} = \text{constant} = \underline{\mathbf{E}}_{\text{inc}}$ , i.e. no source amplitude variations. Scanning two-beam interferometers, e.g. Michelson and Mach-Zehnder, rely upon wide-sense stationary conditions to scan through  $z$  to obtain the interferogram of the source. Otherwise the interferometer scan samples different source conditions at different times, and the resulting interferogram does not return the signal spectrum.

For sensors, the wide-sense stationary condition may not be met. The measurand

may change faster than the system can scan, so

$$\int_t^{t+t_{scan}} \underline{\mathbf{E}}_{inc}(t) e^{i\phi(t)} dt = g(t) \neq \text{const.} \quad (6.6)$$

For wide-sense stationary ergodic processes [31, 32], the single detector observing at a range of times can be replaced by a range of detectors looking at an instant of time [33]. Minimising the number of detectors to achieve unambiguous phase determination is the subject of *phase-shift interferometry*.

To demonstrate the benefits of phase shifting interferometry, the basic case of two beams interfering is considered. As illustrated in figure 2.27(a) (page V.I - 84), and summarising the results of appendix §B.1 (page V.II B-1), at the point where the two beams from arms 1 and 2 interfere, the observed intensity is [34]

$$\begin{aligned} I &= [\underline{\mathbf{E}}_1^* e^{i\phi(t)} + \underline{\mathbf{E}}_2^* e^{i\phi(t)+\phi_{exp}}] [\underline{\mathbf{E}}_1 e^{i\phi(t)} + \underline{\mathbf{E}}_2 e^{i\phi(t)+\phi_{exp}}] \\ &= I_1 + I_2 + \sqrt{I_1 I_2} \cos(\phi_{exp}) \end{aligned} \quad (6.7)$$

or<sup>10</sup>

$$I = I_{inc} [1 + \gamma \cos(\phi_{exp})]; \quad \gamma = \frac{\sqrt{I_1 I_2}}{I_{inc}} \quad (6.8)$$

where  $\underline{\mathbf{E}}_1$  and  $\underline{\mathbf{E}}_2$  are the amplitudes in arms 1 and 2,  $I_{inc}$  is the incident DC intensity,  $I_1$  and  $I_2$  are the intensities in arms 1 and 2 (and  $I_1 + I_2 = I_{inc}$ ),  $\gamma$  is the fringe visibility,  $\phi_{exp}$  is a relative known phase shift between the test and reference beams. Figure 2.27(b) shows a fibre equivalent of 2.27(a).

There are three unknowns in (6.8):  $\phi_{exp}$ ,  $\gamma$  and  $I_{inc}$ , requiring three equations to solve simultaneously. Therefore the minimum number of detectors for unambiguous determination is three, with different known phase shifts of  $\phi_{exp}$ .

The phase can be uniquely determined from the three instantaneous intensities [34]

$$\begin{aligned} I_a &= I_{inc} [1 + \gamma \cos(\phi(t) - \phi_{exp})] \\ I_b &= I_{inc} [1 + \gamma \cos(\phi(t))] \\ I_c &= I_{inc} [1 + \gamma \cos(\phi(t) + \phi_{exp})] \end{aligned} \quad (6.9)$$

by rearranging the terms to give

$$\phi(t) = \tan^{-1} \left[ \left( \frac{1 - \cos(\phi_{exp})}{\sin(\phi_{exp})} \right) \frac{I_a - I_c}{2I_b - I_a - I_c} \right] \quad (6.10)$$

Equation (6.8) requires three equations for unambiguous determination of  $\phi(t)$ . Three evenly spaced phase-shifted interferograms, i.e. phase steps of  $2\pi/3$ , in an all-fibre arrangement, can be achieved using a  $3 \times 3$  coupler [35, 36], as shown

<sup>10</sup>As discussed in Appendix §B.1 (page V.II B-1).

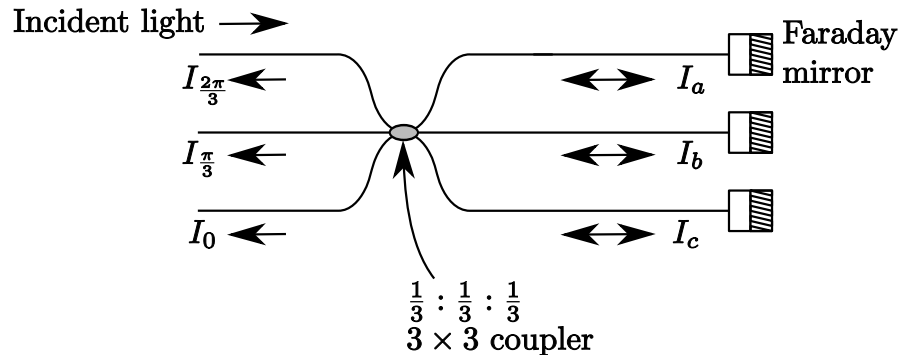


**Figure 6.2:** All-fibre three-output phase-shift interferometer arrangement. A  $3 \times 3$  coupler splits the incident light into three arms, each with 33% of the incident light. Upon reflection, the light exits the  $3 \times 3$  coupler and the  $\pi/3$  phase shifts are obtained.

schematically in figure 6.2. This arrangement requires the three arms to be balanced, in a non-scanning mode. The balancing of these arms is a complication that can make the design difficult to achieve. The phase modulation occurs in a  $3 \times 3$  coupler, with the outputs  $2\pi/3$  out of phase with respect to each other. A  $3 \times 3$  coupler is marginally more expensive than a  $2 \times 2$  coupler, but the three-output phase shift technique is sensitive to noise and requires three receivers, which may significantly increase the cost of the setup. A circulator can be used to obtain the signal reflected along the input arm.

The three-output phase-shift interferometry technique is sensitive to noise. To remove the necessity of phase-shift calibration Carré proposed a four output technique [34, 37]. Thus, to provide unambiguous phase retrieval double the number of detectors and channels of data as used in this work are required. Consequently, the output from the Michelson interferometer cannot provide unambiguous phase retrieval without further signal processing.

### 6.2.3 Interferogram recalibration

The captured reference and signal interferograms will not, in general, be ideal interferograms amenable to direct analysis. The interferometer may have experienced vibrations due to acoustic noise and electrical voltage noise on the driving signal. Additionally, stick-slip issues of the fibre stretcher mean that the captured interferogram will be far more complex than the theoretical interferograms used to develop the analysis.

Additionally, the captured interferograms are generally unlikely to have a data point occur exactly upon the zero-OPD point of the interferometer, which convolves the interferograms with the sampling interval, producing a beating function that limits resolution [38]. For polychromatic light the varying interference patterns of the different wavelengths only align at the interferometer's balance point [39].

Although the interferogram has been sampled at effectively equal time intervals by the data acquisition system, the non-linearities in scanning can be considered as non-uniformities in the sampling time interval step or time base,  $\tau_{\text{exp}}(t)$ , of the 'true' interferograms. The non-uniformities are assumed to be equal in both signal and reference interferograms, which is the case in the experiments undertaken for signal and reference data captured on a single detector.

By correcting the reference signal to remove the non-linearities in the time base, it would be possible to correct a more complicated signal with the same non-linearities. The correction of the reference interferogram's time base is the method by which the time base non-linearities are removed from the arbitrary FBG signal interferograms captured.

The reference interferogram is assumed to have originated from a high-stability, high-coherence telecomms laser [6], or a reference FBG [9]. The spectrum of the laser is considered to be a Dirac  $\delta$ -function centred on wavelength  $\lambda_{\text{laser}}$ . The inverse Fourier transform of this idealised spectrum should be a uniformly undulating interferogram with a linear phase angle  $\varphi(t)$ . The ideal time base,  $\tau_{\text{uniform}}$ , is

$$\tau_{\text{uniform}} = \frac{\lambda_{\text{laser}}}{2\pi c} \varphi(t); \quad \Delta\tau_{\text{uniform}} = \text{const.} \quad (6.11)$$

where  $c$  is the speed of light, and  $\Delta\tau_{\text{uniform}}$  is independent of time, i.e. uniform step size.

The transformation of  $\tau_{\text{exp}} \rightarrow \tau_{\text{uniform}}$  can be achieved by resampling the captured interferograms using the  $\tau_{\text{uniform}}$  time base. In this work the resampling is achieved by linear interpolation of the interferogram between the datapoints at  $\tau_{\text{exp}}$  and evaluating the interpolated function at  $\tau_{\text{uniform}}$ . The Matlab function used to interpolate the interferograms was `interp1q`.

Spline interpolation was found to introduce noise with increasing amplitude toward the higher frequencies. This can be understood as the spline fitting function attempting to minimise the difference between the fit and the noise, thus, re-introducing high-frequency components into the spectrum.

The Fourier transform of the recalibrated or synthesised reference interferogram should return a Dirac  $\delta$ -function type spectrum centred on  $\lambda_{\text{laser}}$ . In reality, the resampling will not be perfect. The linear interpolation will have deviated from the real interferogram, and introduce spectral artefacts. However, the improvement

achieved using  $\tau_{\text{uniform}}$  instead of  $\tau_{\text{exp}}$  substantially improves the spectrum obtained. Experimental examples of the improvement are shown in figures 6.13 and 6.14 (page V.I - 284).

### 6.2.4 Hilbert Transform technique

In the present work two interferograms are captured:  $V_{\text{ref}}^{\Re}(t)$  and  $V_{\text{sig}}^{\Re}(t)$ , the reference and signal interferograms respectively<sup>11</sup>. The reference interferogram contains the high-stability high-coherence telecomms laser signal only, from which  $V_{\text{ref}}(t)$  is obtained. The signal interferogram contains the telecomms laser and FBG signals. By windowing the spectrum of  $V_{\text{sig}}^{\Re}(t)$  to isolate the individual FBGs,  $V_{\text{FBG}_1}(t)$  and  $V_{\text{FBG}_2}(t)$  are obtained. The respective unwrapped phase angles  $\varphi_{\text{FBG}_1}(t)$  and  $\varphi_{\text{FBG}_2}(t)$  are calculated.

The ratio

$$\frac{\varphi_{\text{FBG}_i}(t)}{\varphi_{\text{ref}}(t)} = \frac{\Phi_{\text{FBG}_i}(t) - \overline{\omega_{\text{FBG}_i}}t}{\Phi_{\text{ref}}(t) - \overline{\omega_{\text{ref}}}t}; \quad i = 1, 2 \quad (6.12)$$

can be rearranged to give [6]

$$\varphi_{\text{FBG}_i}(t) = \frac{\overline{\omega_{\text{FBG}_i}}}{\overline{\omega_{\text{ref}}}} (\varphi_{\text{ref}}(t) - \Phi_{\text{ref}}(t)) + \Phi_{\text{FBG}_i}(t) \quad (6.13)$$

The ratio of the optical frequencies:

$$\frac{\overline{\omega_{\text{FBG}_i}}}{\overline{\omega_{\text{ref}}}} = \frac{\overline{\lambda_{\text{ref}}}}{\overline{\lambda_{\text{FBG}_i}}} \quad (6.14)$$

is equal to

$$\frac{d\varphi_{\text{FBG}_i}}{d\varphi_{\text{ref}}} = \eta_i \quad (6.15)$$

that is, the gradient of the graph of  $\varphi_{\text{FBG}_i}(t)$  to  $\varphi_{\text{ref}}(t)$  [6, 7].

Thus, if  $\overline{\lambda_{\text{ref}}}$  is stationary during the capture of  $V_{\text{ref}}^{\Re}(t)$  and  $V_{\text{sig}}^{\Re}(t)$ , and its value is known, the mean value of  $\overline{\lambda_{\text{FBG}_i}}$  can be calculated as

$$\overline{\lambda_{\text{FBG}_i}} = \frac{\overline{\lambda_{\text{ref}}}}{\eta_i}. \quad (6.16)$$

The gradient  $\eta_i$  will not normally be a single value due to the presence of noise and small departures from linearity in the values of  $\varphi_{\text{FBG}_i}(t)$  and  $\varphi_{\text{ref}}(t)$ . An experimental example of these departures is shown in figure 6.12 (page V.I - 283). To return a single representative value for  $\eta_i$ , a linear least-squares fit is made to the experimental data and the slope of the linear fit is taken as  $\eta_i$ . The norm of the

<sup>11</sup>See Appendix C (page V.II C-1) for a discussion of the analytic signal and the notation used.

residuals<sup>12</sup> to the linear fit gives the scale of the measurement uncertainty.

### 6.3 Experimental apparatus/setup

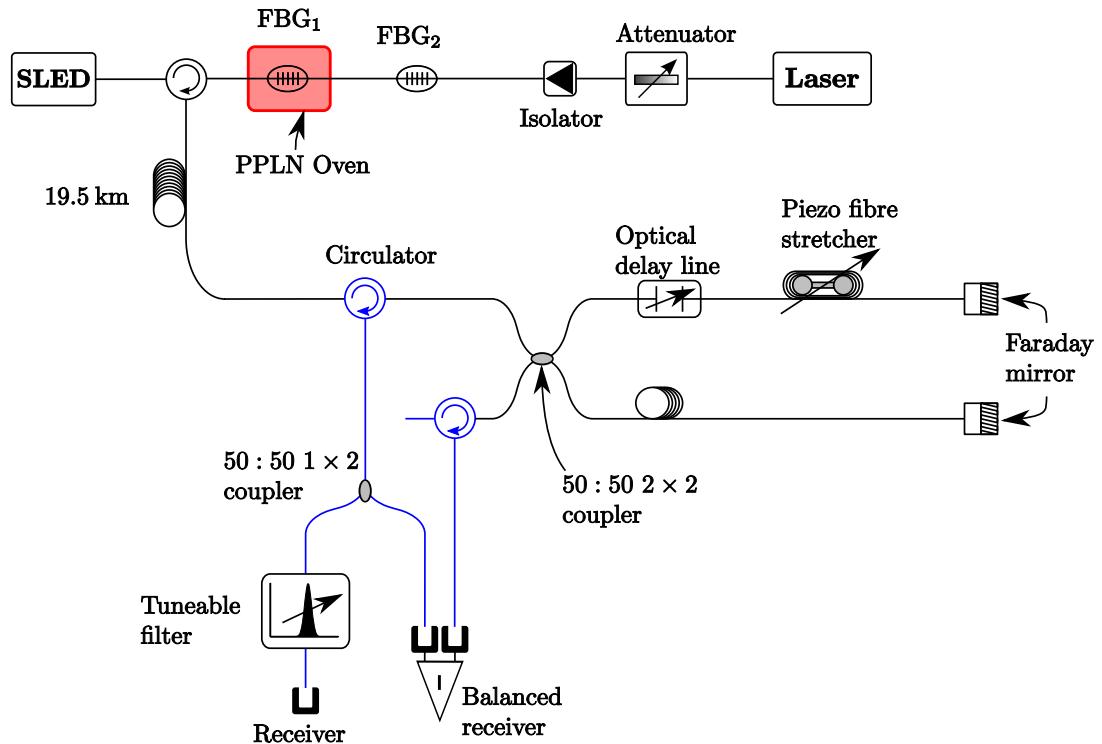


**Figure 6.3:** Schematic arrangement of  $\pi$ -shift apparatus. One FBG is placed in a Thorlabs PV40 PPLN oven where the temperature is changed to provide a changing signal. The FBGs are illuminated by a SLED, and the reflected FBG signals are passed with a high-coherence signal from a Thorlabs telecomms laser through  $\sim 20$  km of Corning dispersion-shifted fibre. The signals are demodulated by an all-fibre interferometer based upon a Sifam  $2 \times 2$  50:50 coupler. A CIRC piezo-electric unit provides the changing optical path length in the scanning arm. The zero-OPD, balance point, of the interferometer is adjusted as necessary by an Oz Optics ODL650MC optical delay line. Newport Faraday mirrors compensate for birefringence induced difference in path length by reflecting light into the orthogonal state. The two-output or  $\pi$ -shifted interferograms are captured by a NewFocus balanced receiver<sup>a</sup>. The high-coherence reference signal is isolated by an Oz Optics tuneable filter or a JDS Uniphase (JDSU) bandpass filter and captured by a NewFocus receiver.

<sup>a</sup>A receiver is a packaged combination of detector and amplifier.

The experimental apparatus is shown schematically in figure 6.3. Light from an *Exalos ESL1505-2100 Super Luminescent diode*, SLED, passed through a cir-

<sup>12</sup>The Euclidean length of the Residuals vector.

culator to illuminate two *Laser2000* isotropic FBGs, at nominal peak wavelengths of 1559.9 nm and 1565.68 nm. One FBG was placed in a modified *Thorlabs* PV40 PPLN oven (as described in section §4.3.12 (page V.I - 195) and illustrated in figure 4.20 (page V.I - 196)) with which the temperature changes were applied. The other FBG was placed beside the oven just above the optical bench as a temperature reference, to monitor the ambient temperature into which heat from the PV40 oven would escape to as the temperature gradient increased.

### 6.3.1 Apparatus

A *Thorlabs* WDM telecomms laser, tuneable over a 2 nm range, with centre wavelength 1550.52 nm, was connected to the end of the FBGs by a 60 dB fibre isolator. The telecomms laser was stable to  $\pm 1$  pm over twenty four hours which provided a high-coherence reference signal of  $< 10$  MHz ( $< 0.1$  pm). The reflected FBG signals and the laser signal pass via the circulator into 19.5 km of *Corning Dispersion shifted fibre*. This was the longest section of continuous fibre available over which the reflected FBGs could be detected by any receiver available, so that the Rayleigh scattering would be mostly from intrinsic fibre inhomogeneities.

The fibre, at the power levels used, would not have experienced any significant non-linear effects. The reference laser could have been equivalently placed at the free first port on the interferometer's output arm for signal demodulation, but was placed in series with the FBG reflections to provide forward Rayleigh scattering noise by transmission over the  $\sim 20$  km of fibre.

The length of fibre was chosen so that the FBGs were just visible using the two-output  $\pi$ -shifted technique. The FBGs were not reliably retrievable using single-output interferometry, as the FBG reflected peaks were at or below the noise level. The length of fibre provided both attenuation and phase noise via scattering, to test the limits of the technique.

The light intensity, and thus the noise level, introduced by the laser was controlled by the use of an *Agilent* 8156A optical attenuator at the output of the laser. The noise level could be increased above the FBG signal strength or decreased below it as required. In the work reported here, the noise level was set so as to exceed the FBG signal when using single-output interferometry, such as the configuration schematically shown in figure 6.4. The single-output apparatus is equivalent to that already described, except for the capturing of a single interferogram from the output port of the  $2 \times 2$  coupler [9, 40].

The FBG and laser signals passed through an *Oz Optics* circulator to the interferometer. The Michelson interferometer consisted of a *Sifam*  $2 \times 2$  50:50 coupler which split the light into two paths. The reference arm consisted of a length of

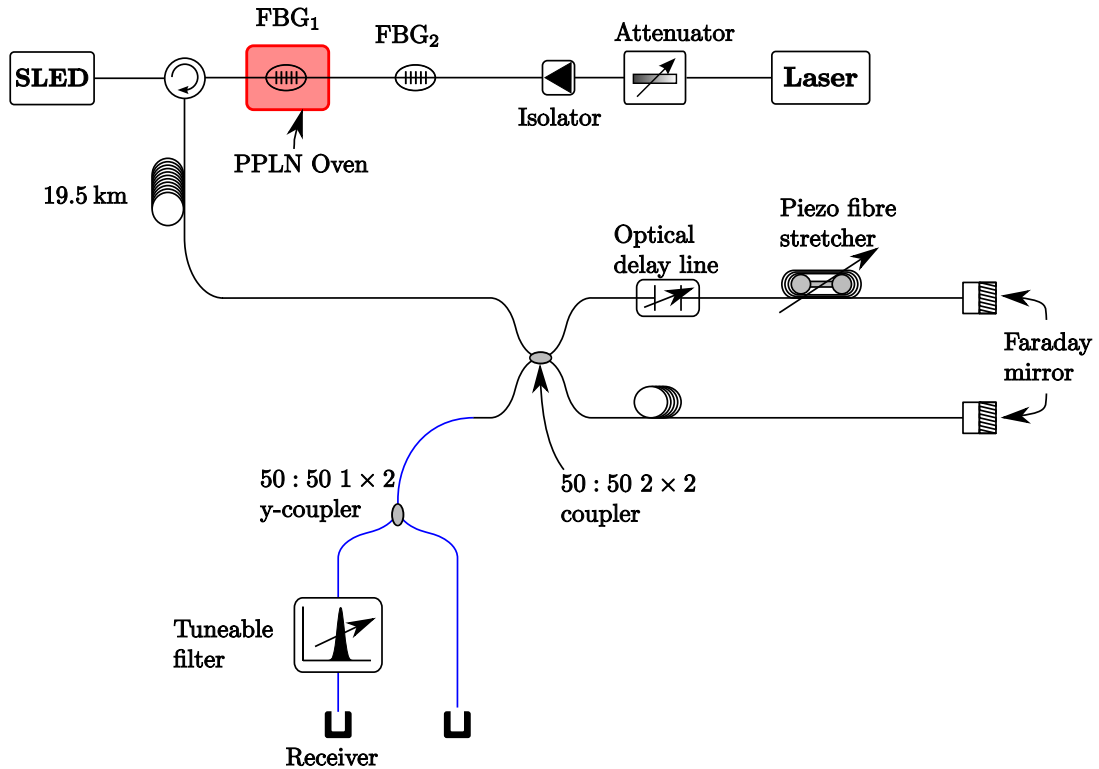


**Figure 6.4:** Schematic arrangement of single receiver apparatus. The apparatus is identical to that shown in figure 6.3 except that the  $\pi$ -shifted interferograms are not captured, instead only a single interferogram is captured by a NewFocus receiver.

SMF28 fibre  $\sim 27$  m long. The scanning arm consisted of an Oz Optics ODL650MC optical delay line, ODL, and a *Canadian Instrumentation & Research limited*, CIRL, 916 piezo-electric fibre stretcher, with maximum  $\sim 4$  mm stretch, and 10 Hz limit to achieve the maximum stretch, before the frequency response falls off linearly towards 1 kHz. The 916 was driven at 4 Hz for the experiments reported here, so the full fibre stretch was obtained to give an optical path difference, OPD, of  $< 8$  mm. The reference arm length was chosen to match the length of the scanning arm when the ODL and the stretcher were at their mid-points. Newport Faraday mirrors were placed at the end of both interferometer arms.

The ODL was used to position the stretcher balance point without the need to manually balance the interferometer arms [9] and to correct for laboratory temperature changes which moved the balance point from day to day [41, 42].

The light from the interferometer passed along both the input and output arms of the interferometer, through the circulators and onto the *NewFocus* 2117 balanced receiver which captured the difference between the  $\pi$ -shifted interferograms. A 50:50  $1 \times 2$  y-coupler<sup>13</sup> was used with either a *Santec OTF-300* tuneable filter or

<sup>13</sup>A  $2 \times 2$  coupler with one port truncated within the packaging.

*JDS Uniphase WD1551-CSW2* bandpass filter to obtain the high-coherence interferogram, which was captured by the *NewFocus 2053* receiver at a sampling rate of 30 kHz. All the fibre components were fixed to the optical bench.

### 6.3.2 Fibre stretcher driving voltage

The 916 fibre stretcher was driven by a CIRL 914-2 controller. A sine or triangular sawtooth waveform generated by a *GFG-2D* signal generator (Good Will instruments Co. Ltd) was sent to the 914-2 controller. The maximum voltage accepted by the 914-2 controller was 5 V. The full-scale range of supplied voltage to the 914-2 was 0–4.8 V. When 5 V was supplied<sup>14</sup>, the controller clipped the voltage at  $\sim 4.9$  V. By using the 0–4.8 V range, a repeatable maximum extension of the fibre stretcher was achieved at the desired temporal frequency.

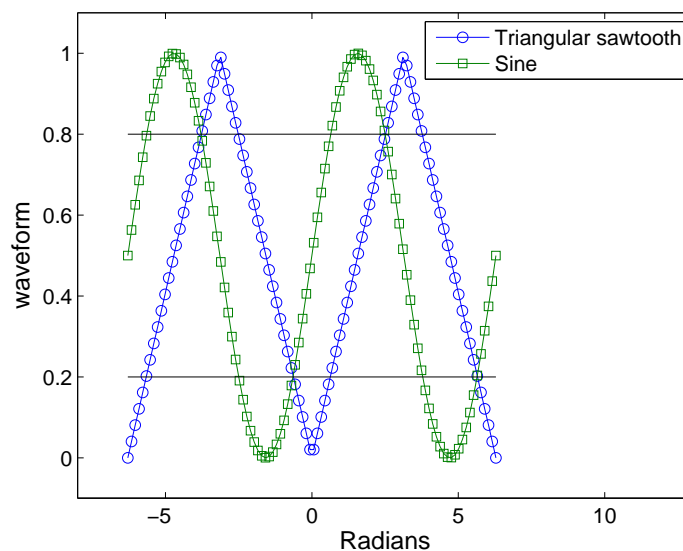


**Figure 6.5:** Sine and triangular waveforms, with limit lines at 20% and at 80%.

In the experiments reported here, the frequency of the driving signal was  $\sim 4$  Hz. Both sine and triangular sawtooth waveforms were evaluated. The advantage of the sine waveform is the gradual change from positive to negative slope, when compared to the sawtooth triangular waveform. The disadvantage is that the more linear part of the sine waveform, shown in figure 6.5, e.g. between (20 – 80%) of the maximum amplitude, is not densely populated. The slope is greater than for the sawtooth waveform. Taking the (20 – 80%) range as being the linear part of the sine waveform, more data points are sampled outside this range (58%) than within (42%). This requires faster data capture for a given resolution, with 58% of data recorded not used in the eventual analysis. The triangular sawtooth waveform has

<sup>14</sup>As measured on both an oscilloscope and digital multimeter.

60% of the captured data in the (20 – 80%) range. The quintile data sampling rates for the sine and sawtooth waveforms are shown in figure 6.6. To sample the interferogram produced using the sine waveform at a given density requires  $\sim 1.4$  times the scan rate of the sawtooth waveform.

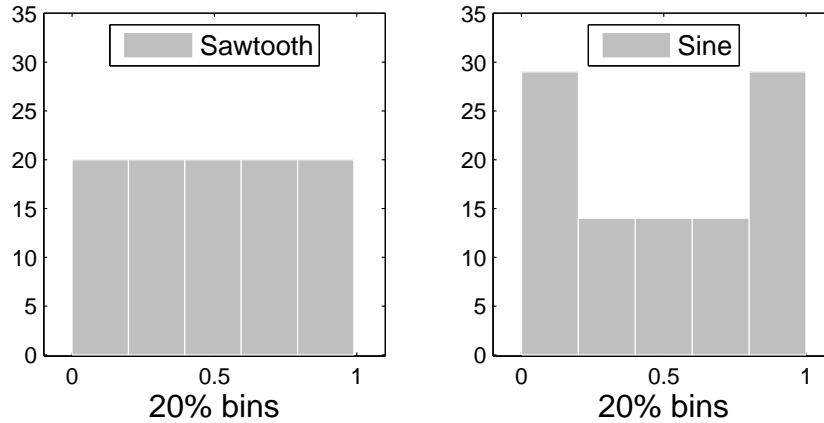


**Figure 6.6:** Quintile histogram of waveforms shown in figure 6.5.

The computer hardware and software used for data capture separately buffered the captured data and then wrote it to disk, which limited the data capture rate of the experiment, and so a triangular sawtooth waveform was used in preference to the sine waveform.  $3 \times 10^5$  samples were captured per experimental dataset, at a rate of  $3 \times 10^4$  Hz. A custom *LabVIEW* program was used to control a National Instruments PCI-6221 DAQ card, used to capture and buffer the data<sup>15</sup>, then write it to file on disk. Three channels were captured: the driving waveform, the  $\pi$ -shifted interferogram and the single-output reference interferogram.

### 6.3.3 Temperature experiment

The experiment involved the detection and successful demodulation of reflected FBG signals using the  $\pi$ -shift interferometry approach with the Hilbert transform technique. Temperature changes were the measurand chosen to be detected, which were applied with the PV40 oven using the *Thorlabs TC200* oven controller.

The experimental approach began by taking a reading with the temperature controller turned on, but not applying current to the heater. The temperature sensor would then provide a recording of the ambient temperature. The stability of this reading provided an indication of how long a temperature change might take to reach stability. If the temperature value recorded changed frequently, then the oven,

<sup>15</sup>Without buffering the writing of the data would be a blocking operation on the program, i.e. the program would wait until the data were written before proceeding. The writing to disk was dependent upon the asynchronous I/O of the computer used, and could therefore not be presumed to be constant.

at a low temperature, would take longer to reach a wide-sense-stationary thermal stability, which would produce greater uncertainty in its measurement.

The oven temperature was then increased in steps of 3 °C over the range 30 – 90 °C. The set temperature,  $\theta_{\text{set}}$ , and the actual TC200 recorded temperature,  $\theta_{\text{act}}$ , were not equal. The temperature steps recorded were of 2.8 °C over the range 27.8 – 84.7 °C. The TC200 had PID control loop offset which was likely responsible for this discrepancy, but as the increments were uniform and their slope linear, the controller’s PID settings were not changed. The linearity of  $\theta_{\text{act}}$  was such that the ratio of the actual to  $\theta_{\text{set}}$  was 1.0483, and so the  $\theta_{\text{act}}$  was used as the temperature experienced by the FBG in the oven.

At each temperature step, the oven was allowed to reach thermal equilibrium. The time taken to reach thermal stability decreased as the temperature increased, as would be expected. However, the measurement precision [43] was to 0.1° C, which made determination at lower temperatures (where the temperature difference between the ambient room temperature and the oven is small) of thermal stability difficult and more likely to have lower measurement accuracy [43] than at higher temperature settings.

After  $\theta_{\text{act}}$  had stabilised, the interferograms were recorded. Five datasets were recorded per temperature step, each containing at most six separate interferograms for the rising and falling 916 driving voltage. To compare the efficiency of the two-output,  $\pi$ -shifted approach to single-output interferometry, one of the balanced receiver detectors was blocked, and five datasets recorded. The balanced receiver operating in this manner is equivalent to a single receiver.

### 6.3.4 NewFocus receiver configuration

The photodiode in the 2053 single receiver failed during the experimental work, and was replaced with a GAP500 photodiode, as described in appendix Q.1 (page V.II Q-1). All the data in this chapter were captured with the replaced photodiode, except for the single-output plot in figure 6.19 (page V.I - 290) and the data in figure 6.38 (page V.I - 310), which were captured weeks before the diode failed.

The two NewFocus receivers were set to operate at the same parameters to provide as close to identical responses as possible. For both the 2117 and 2053 the pass band was 10 Hz–10 kHz, and the gain was switched to ‘ $\times 3$ ’ and the dial to the maximum ‘ $10^4$ ’, as shown in figure Q.2 (page V.II Q-2), in appendix §Q.2 (page V.II Q-1).

## 6.4 Results and Discussion

The results are presented for the centroid and ratio of fits to the unwrapped phases first. The discussion will follow.

### 6.4.1 Results

Five datasets were captured per temperature step. Each dataset had four to six complete interferogram rising and falling voltage pairs depending upon where the file started recording data during the fibre stretcher's cycle. Both the rising and falling signal voltage applied to the fibre stretcher produced an interferogram; however, the rising-signal-voltage interferogram's duration was longer than the falling-signal-voltage interferogram's. This may be due to slight asymmetry of the driving voltage or, as the tension on the fibre windings was released, increasing the rate at which the fibre stretcher returned to rest.

The rising signal voltage interferograms were used for the analysis. The datasets were loaded into Matlab for processing. Figure 6.7 shows the number of signal interferograms retrieved at each temperature step by an automated process undertaken in Matlab. The outlier at 50°C occurred as the dataset capture began just after the start of an interferogram cycle. There is a matching reference interferogram for every signal interferogram.

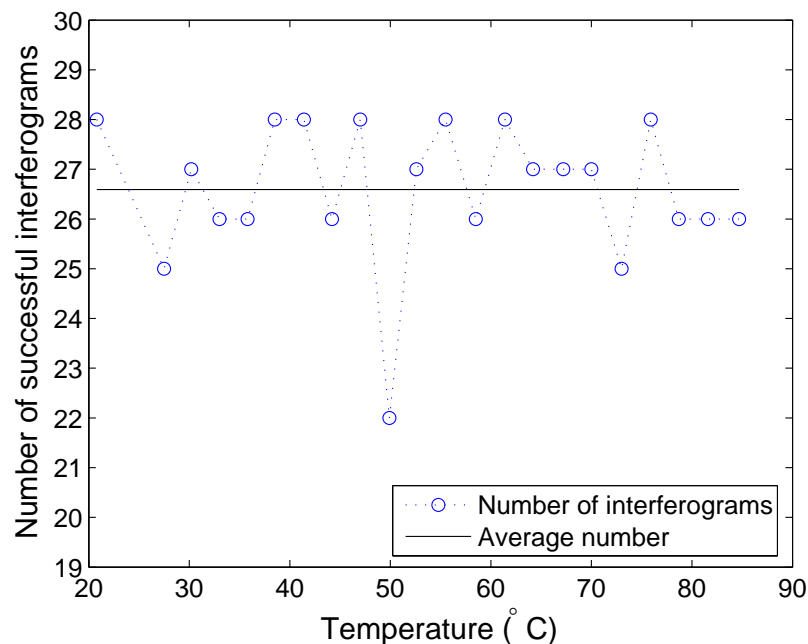


**Figure 6.7:** Number of successfully retrieved separate interferograms for each temperature step.

### 6.4.2 Analysis of interferograms

The spectrum to be recovered, as captured by an Ando AQ6317B OSA over a fibre down-lead length of 10m, is shown in figure 6.8. The FBG signals are approximately 6% and 3% of the intensity of the high-coherence reference laser signal.

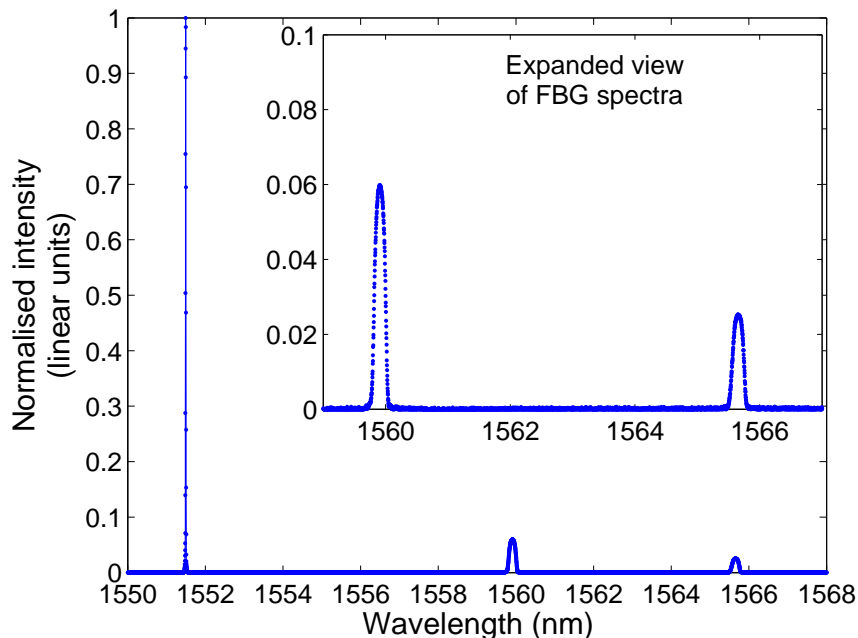


**Figure 6.8:** The spectra to be recovered, captured by an Ando AQ6317B OSA over 10 m of SMF-28 fibre. This spectrum was captured by an Ando AQ6317B optical spectrum analyser over 10 m of fibre, using 100 averages. Inset is an expanded view of the FBG spectra.

The data analysis began by windowing (multiplying) the interferograms,  $V^{\Re}(t)$  with a Hamming window equal to the length of the interferogram, giving  $V_{\text{windowed}}^{\Re}(t)$ . This was achieved by creating an array of equal length to the interferogram using the `hamming` function<sup>16</sup>. The steps of this process are represented in figure 6.9.

The FFT of the reference interferogram was taken, and the DC and low frequency components removed by zeroing the first ten elements of the FFT. The negative frequencies were zeroed and the spectrum multiplied by two to retrieve the FFT of the analytic signal. The analytic signal was retrieved by taking the inverse FFT,

$$V_{\text{analytic}}(t) = \mathcal{F}^{-1} \left( 2u(\nu) \mathcal{F} [V_{\text{windowed}}^{\Re}(t)] \right) \quad (6.17)$$

<sup>16</sup>The FFT of the Hamming windowed interferogram after the DC level has been removed differs from the FFT of the Hamming windowed interferogram containing the DC level by one part in  $10^{11}$ .

where  $\mathcal{F}$  is the Fourier transform and  $u(\nu)$  is the modified<sup>17</sup> Heavyside step function

$$u(x) \begin{cases} = 1 & x > 0 \\ = 0 & x \leq 0 \end{cases} \quad (6.18)$$

The phase angle in radians of  $V_{\text{analytic}}$  was calculated and unwrapped. The time base,  $\tau$ , of the analytic signal was computed from the unwrapped phase of the reference interferogram,  $\Phi_{\text{ref}}$ ,

$$\tau = \frac{\lambda_{\text{laser}}}{2\pi c} \Phi_{\text{ref}} \quad (6.19)$$

The steps of the HTT process are represented in figure 6.10.

The unwrapped time base illustrates the non-uniformities of the scanned interferogram. A sample time base is shown in figure 6.11 with a linear fit. Ideally the time base would be uniformly spaced for Fourier analysis. As is shown by the residual difference between  $\tau$  and the ideal linear timebase in figure 6.12, the recovered  $\tau$  is not uniform.

The interferogram was corrected using a resampled time base. A new, linear time base was created and the signal and reference interferograms resampled using linear interpolation with the new time base. This removed the non-linearities present in the recorded spectrum introduced by the non-ideal interferometer, and produced a synthesised interferogram (spectrum) closer to that from an ideal interferometer.

The recorded and recalibrated spectra are shown in figures 6.13 and 6.14 (page V.I - 284), respectively. The narrow bandwidth of the laser is recovered by using the high-coherence, i.e. narrow bandwidth, and highly-stable telecomms laser, the non-uniformities of the interferometer can be removed and the single laser peak retrieved. The  $\pi$ -shifted interferogram containing the FBG reflected peaks experiences the same interferometer introduced non-uniformities, and is similarly corrected by recalibration.

Figure 6.15 (page V.I - 285) shows magnified detail of the recalibrated spectrum of the FBG sensors with the reference laser and side structure colocated with the FBGs, from this example interferogram<sup>18</sup>. Side-peaks are indicated, which appear symmetrically located about the main peak of the reference laser<sup>19</sup>. These side-peaks are not present in the self-recalibrated reference spectrum. The intensities differ for

---

<sup>17</sup>The usual Heavyside function has  $u(x) = 1/2$  for  $x = 0$ . The modified Heavyside function used here has  $u(x) = 0$  for  $x = 0$ .

<sup>18</sup>Not all interferograms exhibited the peaks occurring at the FBG locations. This example is used to indicate their presence and how their impact was mitigated. However, the relative location of the side-peaks did not alter with changing interferogram length.

<sup>19</sup>Note that the side-peaks are unlikely to originate in the laser spectrum, but to arise in the course of the signal-processing undertaken.

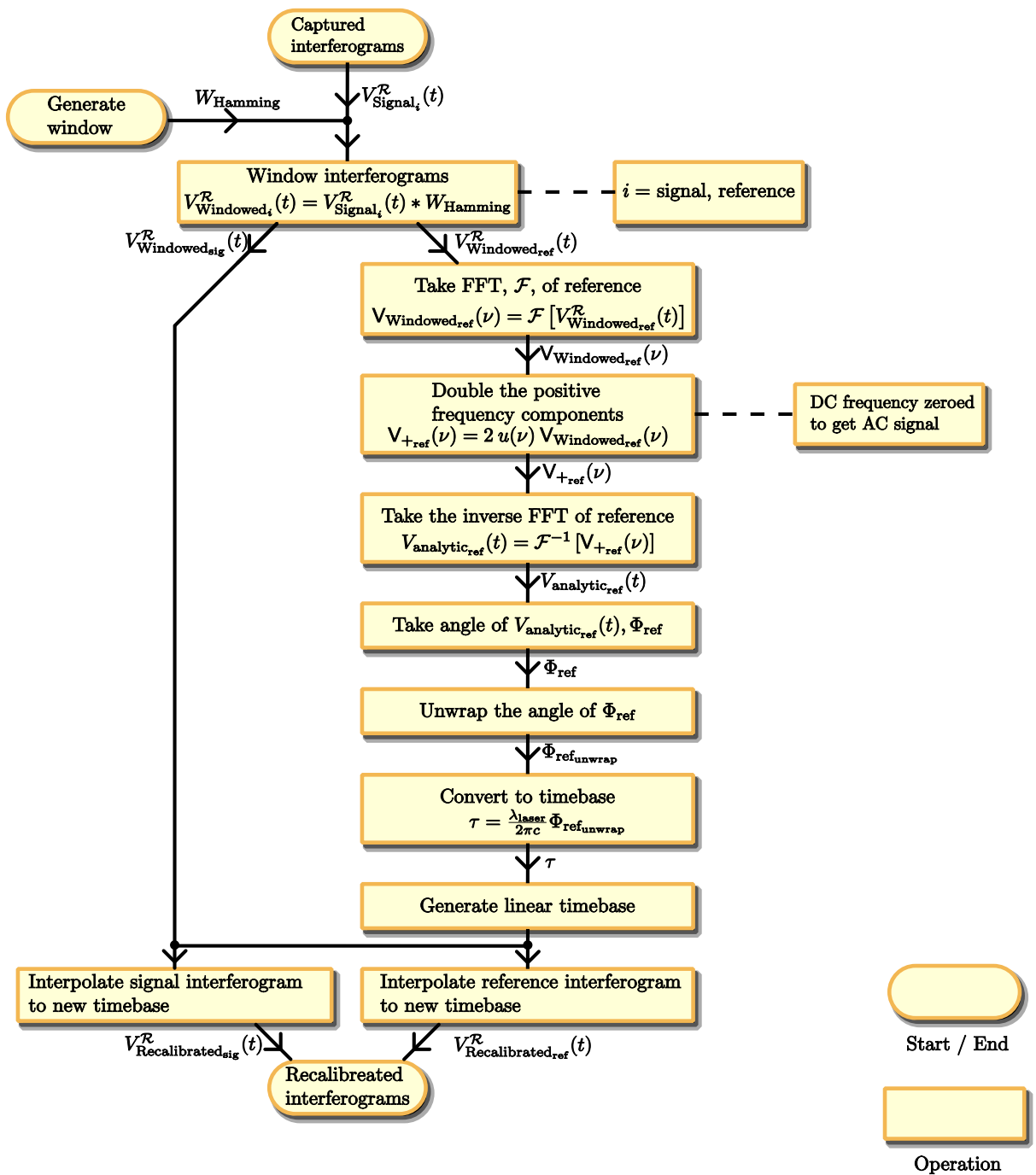


Figure 6.9: Flowchart of the interferogram recalibration process.

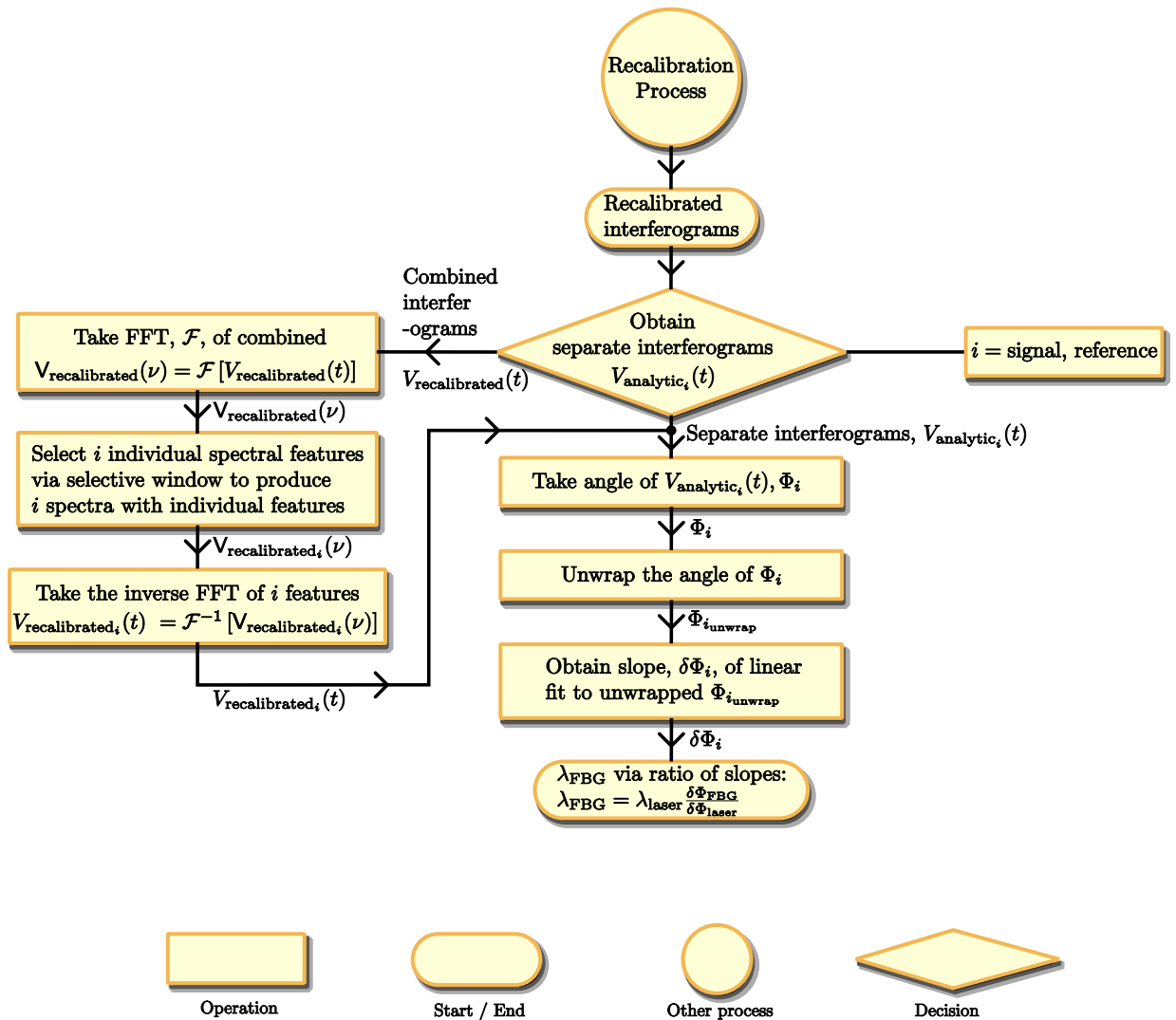
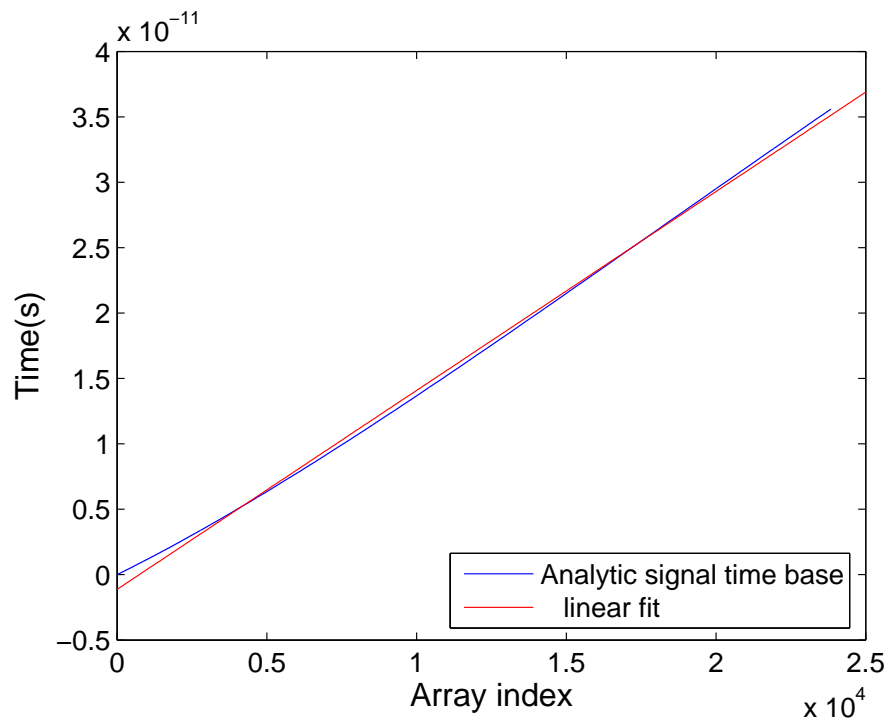
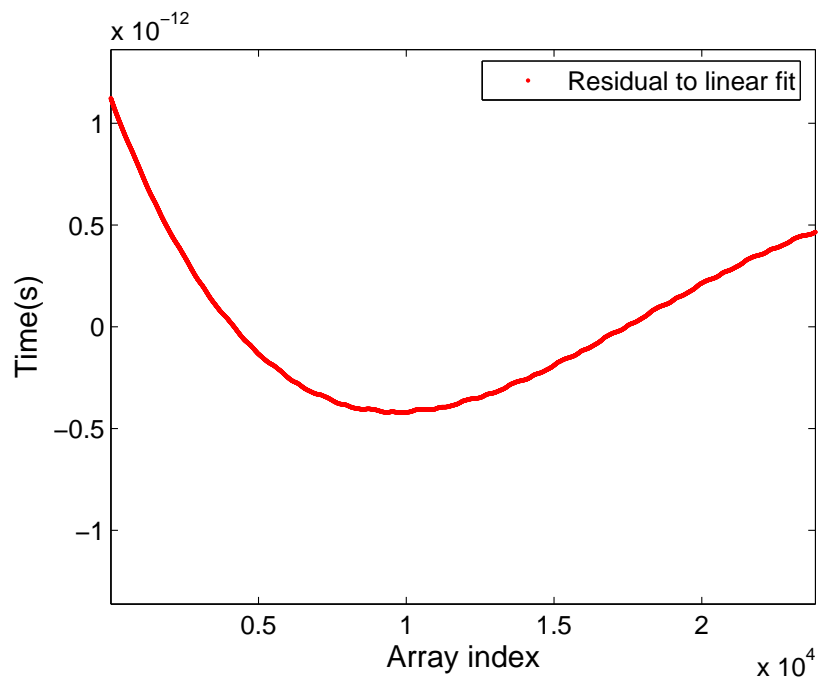


Figure 6.10: Flowchart of the Hilbert transform technique.



**Figure 6.11:** The time base of a sample analytic signal with a linear fit.



**Figure 6.12:** Residual to the linear fit to the sample interferogram's analytic signal.

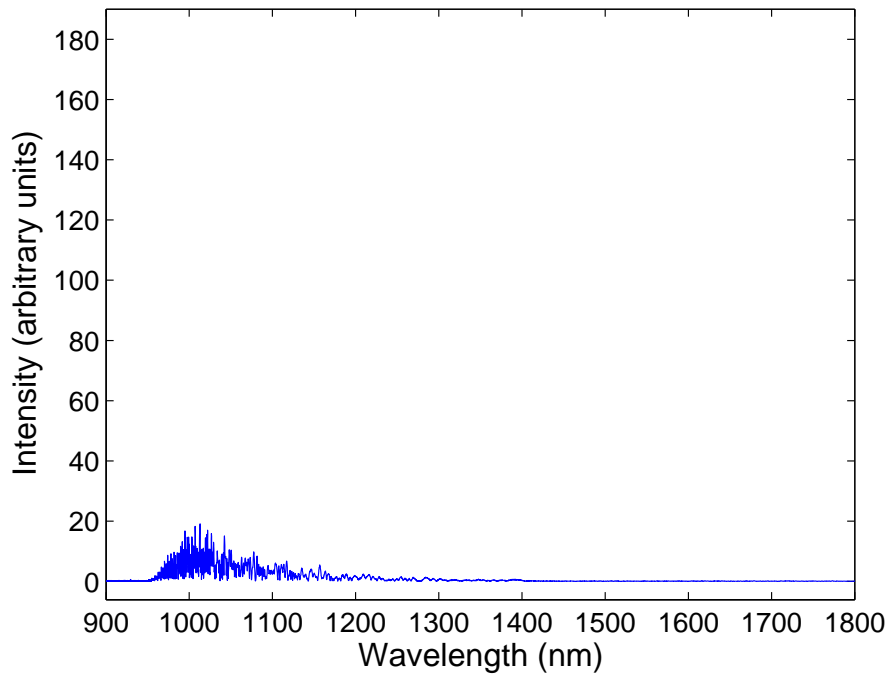


**Figure 6.13:** The spectrum of the captured reference interferogram. The non-linear sampling of the interferogram spreads the signal over several wavelengths.

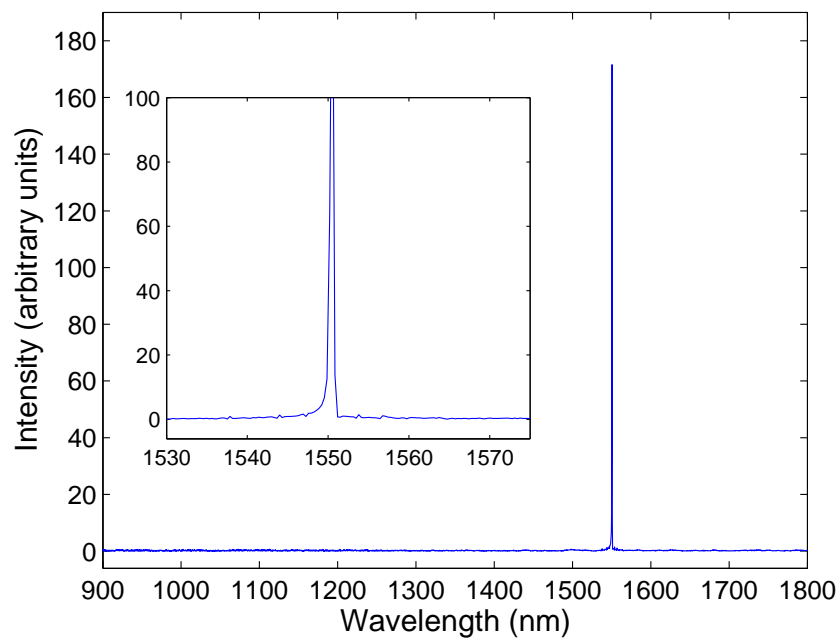


**Figure 6.14:** The recalibrated reference spectrum, which restores the spectral profile of the laser. The linear time base used permits the recalibration of the signal interferogram. Inset shows detail of laser base.

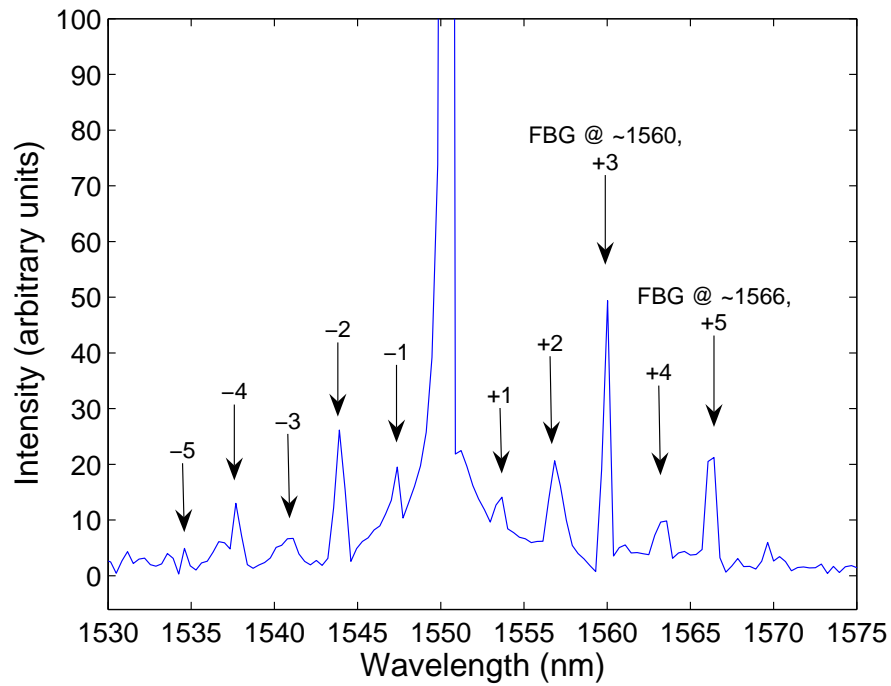


**Figure 6.15:** Magnified view of the spectrum of the recalibrated signal spectrum of the FBG sensors. Side-peaks are to be observed symmetrically about the laser peak. The FBG signals locations are +3 and +5.

peak	$\lambda_{\text{peaks}}$ (nm)	$\Delta\lambda_{\text{peaks}}$ (nm)	relative peak differences (nm)
-5	1534.8	-15.7	-2.9
-4	1537.7	-12.8	-3.2
-3	1540.9	-9.6	-3.2
-2	1544.1	-6.4	-3.3
-1	1547.4	-3.1	-3.1
+1	1553.8	3.3	3.1
+2	1557.0	6.5	3.3
+3	1560.0	9.5	3.2
+4	1563.5	13.0	3.5
+5	1566.3	15.8	2.8

**Table 6.1:** The peak location of side-peaks shown in figure 6.15; The differences of these peaks from 1550 nm, ' $\Delta\lambda_{\text{peaks}}$ '; and the relative difference of each peak from its neighbouring peak, 'peak differences'.

the  $\pm 3$  and  $\pm 5$  peaks, possibly from the presence of the FBG at this wavelength. The relative magnitude, position and profile of the side structure differed between interferograms. The side-peaks are discussed further in section §6.4.10 (page V.I - 309).

In a test case using the reference laser only, the  $\pi$ -shifted balanced receiver and the reference receiver roles were reversed. The two-input balanced receiver provided the recalibration interferogram for the reference interferogram. Again the self-recalibrated interferogram did not have side-peaks, and the cross-recalibrated interferogram did have side-peaks.

Table 6.1 contains the peak locations, their differences from 1550 nm,  $\Delta\lambda_{\text{peaks}}$ , and the relative peak differences, which results in a mean offset difference between side-peaks of  $3.15 \pm 0.21$  nm, to one standard deviation. The positions of the side-peaks did not change with interferogram length. The FBG spectra, convolved with these side-peaks modify the symmetry of peaks +3 and +5. The remaining peaks are more symmetrical. The test case conducted without the FBGs produced more symmetrical +3 and +5 side-peaks.

The presence of the side-peaks presented two problems with the use of the system for demodulation in the experiment. The first is that the unwanted structure complicates peak location, and the second is that the FBG's profile is potentially altered.

Due to the symmetry about the reference laser peak, one investigated approach was to use the shorter wavelength side-peaks to recalibrate and reduce the longer wavelength side-peaks from the FBG spectra<sup>20</sup>. The symmetry of the side-peaks' offsets and profiles about the laser wavelength suggests that the changes that generated the shorter wavelength peaks might also generate the longer wavelength peaks, in the same manner as  $g(\mu)$  is offset in equation (C.10) (page V.II C-3). Figure 6.18 shows the flowchart for this side-peak suppression. The process implemented used the resampling approach outlined above, but using the recalibrated sensor spectrum data range of 1504 – 1558.5 nm in place of the reference interferogram. The data range 1504 – 1558.5 nm is shown in figure 6.16. Figure 6.17 shows the resulting spectrum using the same view as for figure 6.15. The FBG signals at +3 and +5 are more prominent than in figure 6.15. Further iterations did not produce any consistent improvement in side-peak suppression, nor should further iterations improve the recalibration if the time base was properly corrected.

---

<sup>20</sup>The rationale for this decision, is that the spectrum,  $I(\lambda)$ , can be equivalently described by a pseudo wavelength  $I(\lambda') = I(\lambda - \lambda_{\text{laser}})$ , where the laser is centred at  $\lambda_{\text{laser}}$ . In terms of  $\lambda'$ , the spectrum is centred about zero, and the symmetrical  $\pm n$  terms contain redundant information. Consequently, the lower frequency ( $-n$  terms) can be used to deconvolve the higher frequency terms ( $+n$  terms) from the spectrum. The approach used here is to treat the lower frequency terms as if they were equivalent to interferometer non-linearities, and recalibrate the spectrum accordingly.

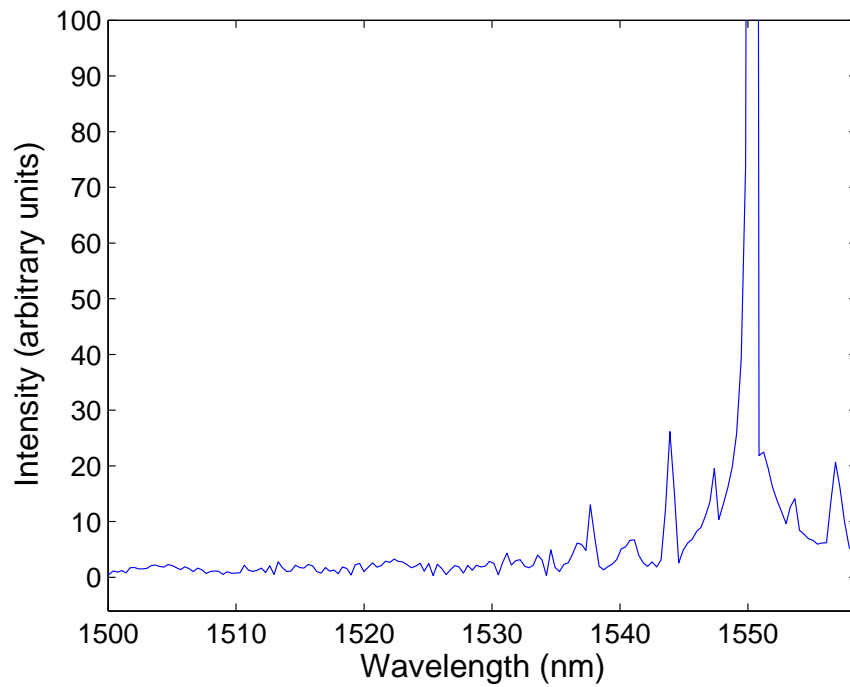


**Figure 6.16:** Subset of the recalibrated spectrum used to suppress side-peaks.

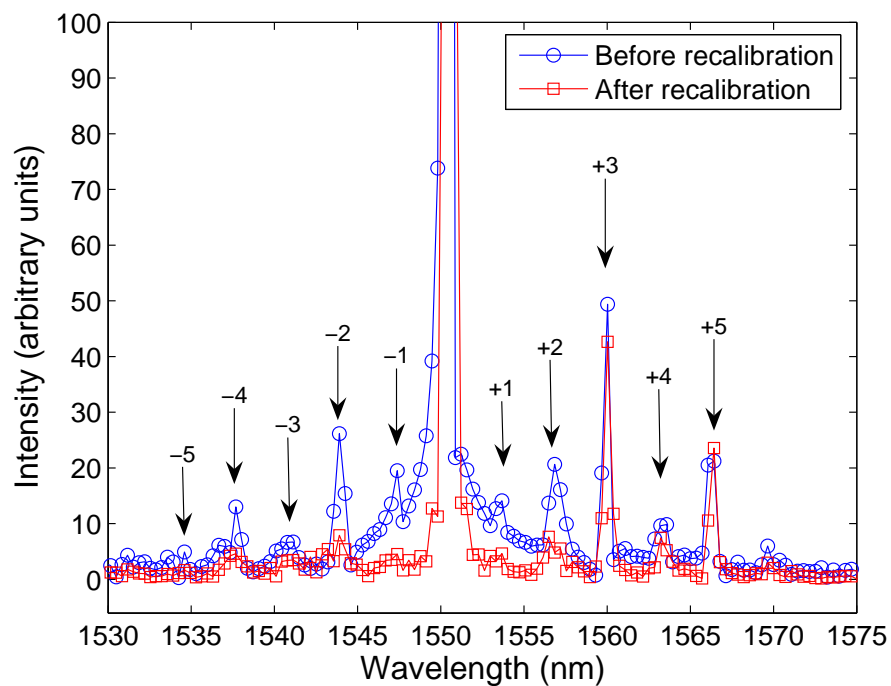


**Figure 6.17:** Recalibrated FBG sensor spectrum to suppress side-peak structure. The same view as shown in figure 6.15, with the same markers in place.

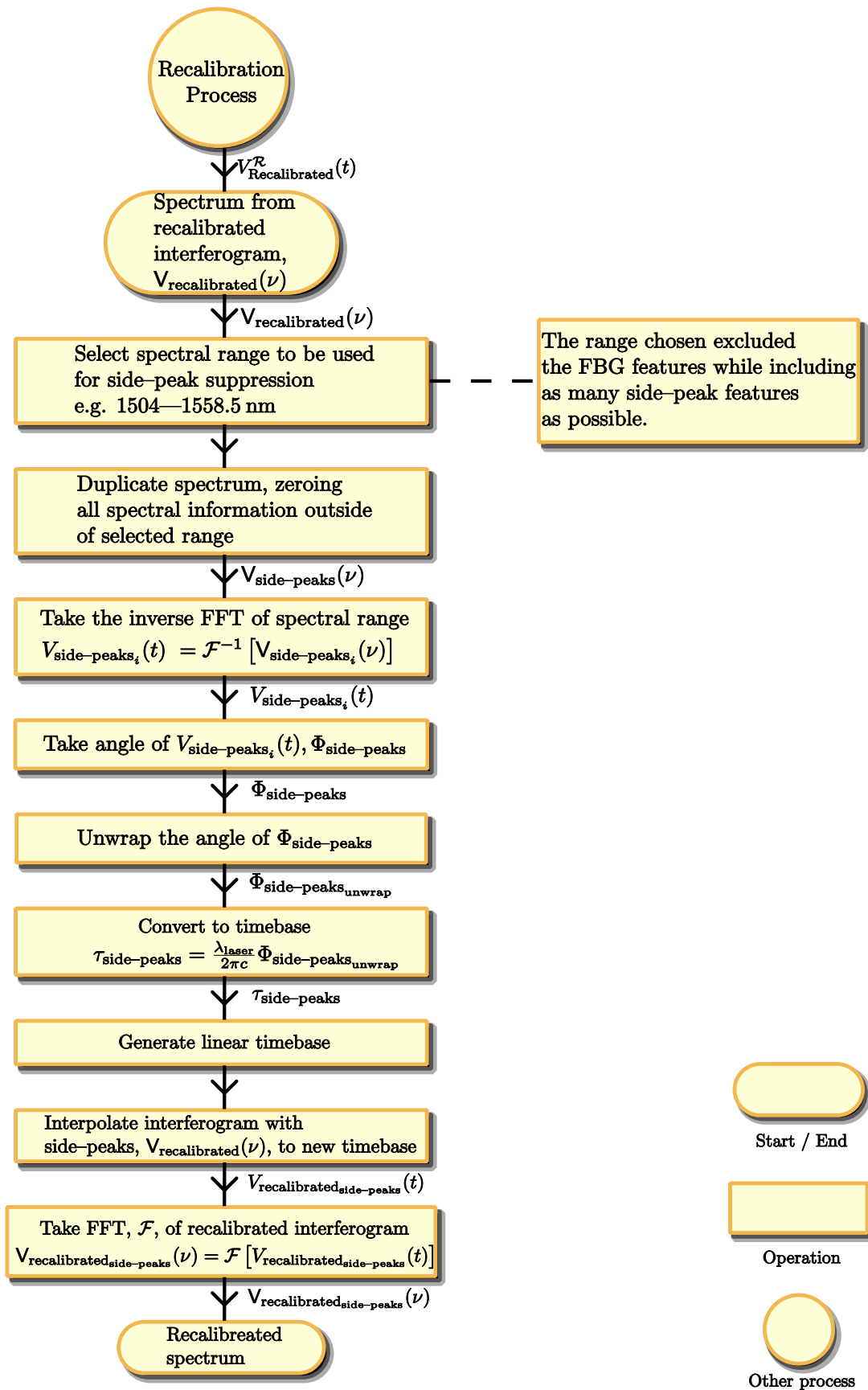


Figure 6.18: Flowchart of the spectral side-peak suppression process.

Figure 6.19 (page V.I - 290) shows the recovered spectra for both single-output and two-output,  $\pi$ -shifted interferograms, using recalibration. The figure is similar to figure 6.8 (page V.I - 279), except in the bandwidth. This is due in part to the limited resolution of the recovered spectrum, and the inherent broadening introduced by the windowing procedure, e.g. apodization.

	$\pi$ -shifted	Single-output
Laser (%)	$100 \pm 8.39$	$100 \pm 0.35$
Temp. FBG (%)	$3.28 \pm 0.55$	$0.19 \pm 0.04$
Ref. FBG (%)	$5.32 \pm 0.80$	$0.47 \pm 0.37$
noise <sub>total</sub> (%)	$0.18 \pm 0.03$	$0.53 \pm 0.23$
noise <sub>ra</sub> (%)	$0.05 \pm 0.01$	$(1053 \pm 4) \times 10^{-4}$

**Table 6.2:** Average and standard deviation of captured linear power levels, as a percentage of the laser power, for the  $\pi$ -shifted and single-output interferograms. The scaled total averaged noise level, noise<sub>total</sub>, and run-averaged noise level, noise<sub>ra</sub>, are presented, for comparison.

		$\pi$ -shifted	Single-output
noise <sub>total</sub> (dB)	{ Temp. FBG	12.49	-4.57
	{ Ref. FBG	14.60	-0.59
noise <sub>ra</sub> (dB)	{ Temp. FBG	17.98	2.47
	{ Ref. FBG	20.09	6.45

**Table 6.3:** Difference in power levels (dB) between the FBG peak levels and the total noise level, noise<sub>total</sub>, and run-averaged noise level, noise<sub>ra</sub>, for the  $\pi$ -shifted and single-output interferograms.

The tables 6.2 and 6.3 contain the averaged values of the single-output and two-output  $\pi$ -shifted peak levels. In table 6.2, the linear values of the FBG peaks and both the total average noise level and a five point run-averaged noise level<sup>21</sup> are presented as a percentage of the laser peak level.

Table 6.3 represents the same data but in terms of the FBG peaks (in dB) above the total and run-averaged noise levels. Both tables show the improvement of the two-output  $\pi$ -shifted signal recovery over the single-output approach, when the signal to be recovered is at or just above the background noise level.

The single-output spectrum is inadequate to retrieve a wavelength for the FBG. The example spectra shown in figure 6.19 are indicative of the quality of recovered spectra over the 585 total interferograms analysed in the experiment. For some single-output spectra, the FBG signal at 1560nm was slightly larger than indicated,

<sup>21</sup>The total noise level includes the side structure, whereas the five point run-averaged noise level represents the noise level likely at the FBG features. Both are included as the noise at the side structures is not likely to be symmetrical. Note the total average has been scaled so as not to overlay the data, and are not the numerical average values.

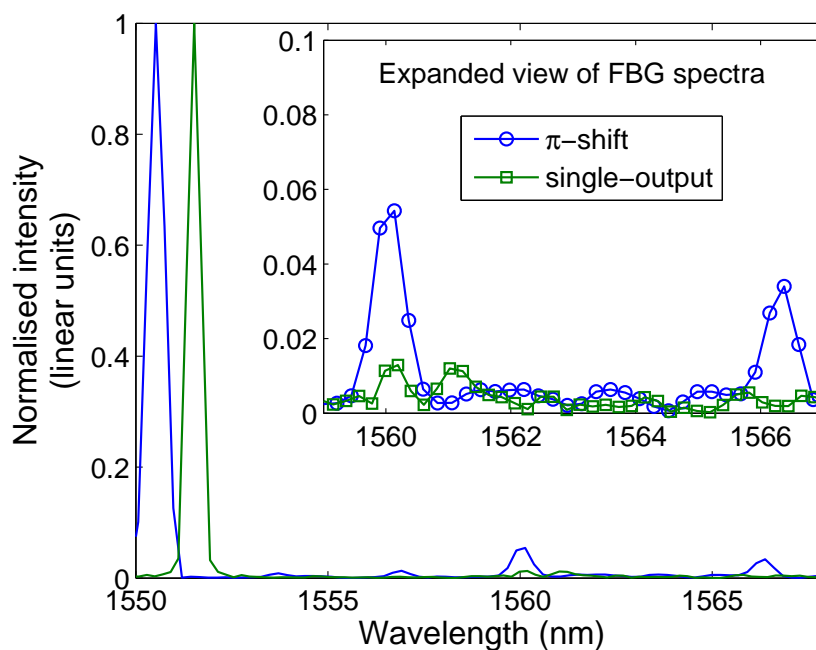


**Figure 6.19:** The recovered FBG spectra, using the two-output,  $\pi$ -shifted interferogram and the single-output interferogram, (compare to figure 6.8 (page V.I - 279)).

but a detectable profile was not consistently obtained at any temperature step. The  $\pi$ -shifted interferograms were consistently able to provide a spectrum that could be determined automatically, using Matlab.

### 6.4.3 Peak Wavelength determination using centroid

The purpose of the experiment was to demonstrate the use of the Hilbert Transform technique, HTT, with two-output,  $\pi$ -shifted interferograms, to demodulate the signals of FBG sensors, where single-output interferograms failed. The successful test would recover the temperature changes applied to the FBGs.

For comparison purposes, the centroid<sup>22</sup> data processing approach was used to recover the sensor FBG wavelength locations. The centroid equation is a weighted sum:

$$\lambda_c = \frac{\sum_{i=1}^N I_i \lambda_i}{\sum_{i=1}^N I_i} \quad (3.19)$$

where  $\lambda_c$  is the centroid wavelength, and  $I_i$  is the spectral intensity at wavelength  $\lambda_i$ . The centroid approach used in this work was to identify the laser and FBG peaks, then use a rectangular window (also termed a Boxcar window) to select the

<sup>22</sup>The centroid function is discussed in section §3.19 (page V.I - 133).

array of  $\pm(2n_w + 1)$  points about the peak location for the centroid calculation.

The determination of the optimum value for  $n_w$  is discussed in appendix §R.1 (page V.II R-1). The variable length interferograms were windowed with the smaller values of  $n_w$  as they were found to be more consistent than larger values, which admitted more noise.

	Temp. FBG ( $\times 10^{-6} \text{ }^\circ\text{C}^{-1}$ )	Ref. FBG ( $\times 10^{-6} \text{ }^\circ\text{C}^{-1}$ )
	2	5.45(68)
$n_w$	3	5.53(75)
	4	5.68(86)
		-0.005(47)
		-0.051(56)
		-0.107(65)

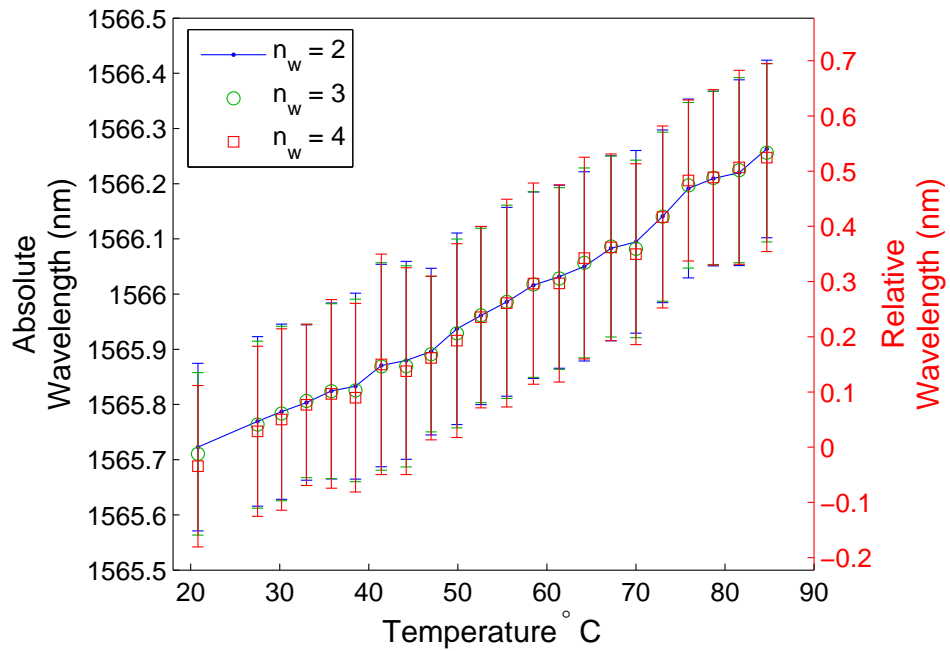
**Table 6.4:** Table of normalised FBG thermal responses,  $\frac{1}{\lambda_B} \frac{\delta\lambda_B}{\delta T}$ , for centroid windows of width  $= 2n_w + 1$ , with  $n_w = 2, 3, 4$  and respective norm of residuals (pm) of linear fit for the temperature and reference FBGs shown in parentheses.

Figure 6.20 shows the changes in average centroid calculated position for the temperature signal FBG, using ranges  $2n_w + 1$ , with  $n_w = 2, 3, 4$ . Figure 6.21 shows the corresponding reference FBG centroid calculations.

Table 6.4 lists the normalised temperature responses obtained from linear least-squares fits to the slope and the respective norms to the residuals of the fits, for  $n_w = 2, 3, 4$ . It was not appropriate to use a Hamming window (or other weighted filter) on the range of values taken for each centroid calculation. Such filters adjust the weights of the centroid sum, and this adjustment depends upon the sampling of the data, so the uniformly weighted rectangular window was used. The corresponding response of the reference FBG is shown in figure 6.21. The changes in response are small compared to the common trend, and using linear fits to the three centroid sets give normalised FBG thermal responses [41].

The sensor FBG's response is improved by subtracting the reference FBG's response from it. This should not be the case if the PV40 oven's insulation was effective at isolating environmental temperature changes over the data capture time, and may be a processing artefact introduced by the relative difference in the position of the FBG profiles being approximately constant. The normalised thermal response of the sensor FBG, when adjusted, is  $5.52 \times 10^{-6} \text{ }^\circ\text{C}^{-1}$ , which is lower than the published value of  $6.67 \times 10^{-6} \text{ }^\circ\text{C}^{-1}$  [41].

As would be expected, the wider the window, the more noise would be admitted to the centroid's weighted sum [38]. Consequently, the spread of the calculated wavelength values increases, as indicated by the norm of the residuals. A window too narrow does not admit enough of the signal and hence, adjusts the weighting towards the central data point value. An optimum width is possible; however, achieving this width is complicated by the changing noise level, interferogram length and would require *a priori* knowledge of FBG wavelength as a convergence criterion.



**Figure 6.20:** Centroid calculated wavelengths for the temperature signal FBG, using windows  $2n_w + 1$  wide, for  $n_w = 2, 3, 4$ .

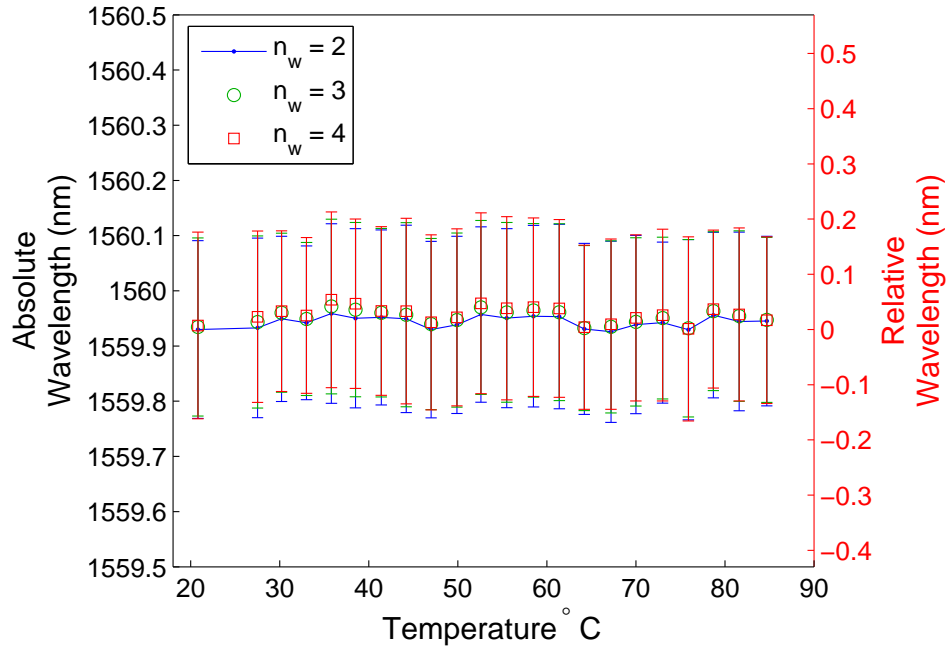


**Figure 6.21:** Centroid calculated wavelengths for the reference sensor FBG, using windows  $2n_w + 1$  wide, for  $n_w = 2, 3, 4$ .

The approach taken to determine the best width is discussed in appendix §R.1 (page V.II R-1).

For the purposes of minimising the error achievable by using the centroid function, and reporting the most conservative normalised thermal response, the value of  $n = 2$  was chosen.

The sensor's response is shown in figure 6.22, with linear and quadratic fits to the data. Also shown is the thermal response value found in the literature [41]. Figure 6.23 shows the residuals to the linear and quadratic fits, with the respective norms being 0.096 nm and 0.057 nm, indicating a slight improvement in using the quadratic fit [44]<sup>23</sup>.

As the FBGs are standard telecomms FBGs, the thermal expansion value of polyimide is not sufficient to account for the observed discrepancy. Polyimide coated fibres have been used for fibre sensing up to 200 °C without introducing changes to the thermal response [46]. The value of the thermal expansion coefficient for polyimide is approximately  $0.5 \times 10^{-6} \text{ C}^{-1}$  [47] which does not differ, within the quoted accuracy, from that of FBGs,  $0.5 \times 10^{-6} \text{ C}^{-1}$  [48].

The calculated value is approximately 82% of the quoted literature value. This discrepancy might be explained by the temperature values provided by the PV40 oven being too large, e.g. the inbuilt thermistor being incorrectly read. If the temperature step was  $2.36 \pm 1.25 \text{ }^\circ\text{C}$  over the range 19.6 – 71.3 °C instead of  $3.05 \pm 0.89 \text{ }^\circ\text{C}$  over the range 20.8 – 84.7 °C, then the thermal response reported in the literature would be obtained.

Alternatively, the sensor FBG may not have been in contact with the PV40 oven surface, although, its relative position should not have moved during the experiment. If an air gap had existed, it is possible that the FBG did not experience the same temperature as the PV40's PT100 thermistor. The oven plate, visible in figure 4.19 (page V.I - 195), contained raised fixing points for PPLN crystals and so the Thermoflex insulation foam used may not have kept the FBG in contact with the plate.

The objective of the experiment was to demonstrate the recovery of a usable signal by use of the two-output,  $\pi$ -shifted interferometry, where single-output interferometry could not. Consequently, the exact determination of the discrepancy is not as important as when characterising an FBG.

The centroid function can be used to obtain the wavelength shift recovered by the Hilbert transform when using the two-output,  $\pi$ -shifted interferograms. The uncertainty for each measurement is large: 0.345nm, equivalent to  $\sim 36^\circ\text{C}$ . As stated, the experiment was deliberately operated at the limit of the  $\pi$ -shift interferometer, so that the ability of the approach to recover signals that single-output interferometry

---

<sup>23</sup>These results were presented at the OFS-20 conference in a poster [45]

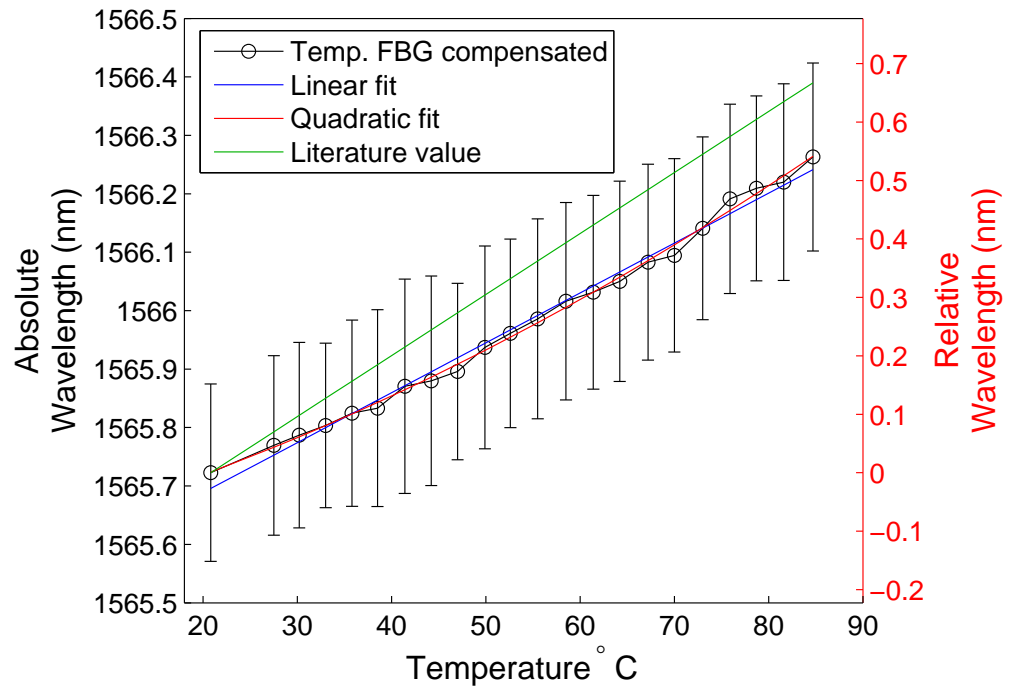


**Figure 6.22:** Temperature response of the sensor FBG, corrected against the reference FBG, to one standard deviation from centroid calculations. A linear and a quadratic fit are shown. Also plotted are the values obtained from using the literature value of  $6.67 \times 10^{-6} \text{ }^\circ\text{C}^{-1}$  [41].

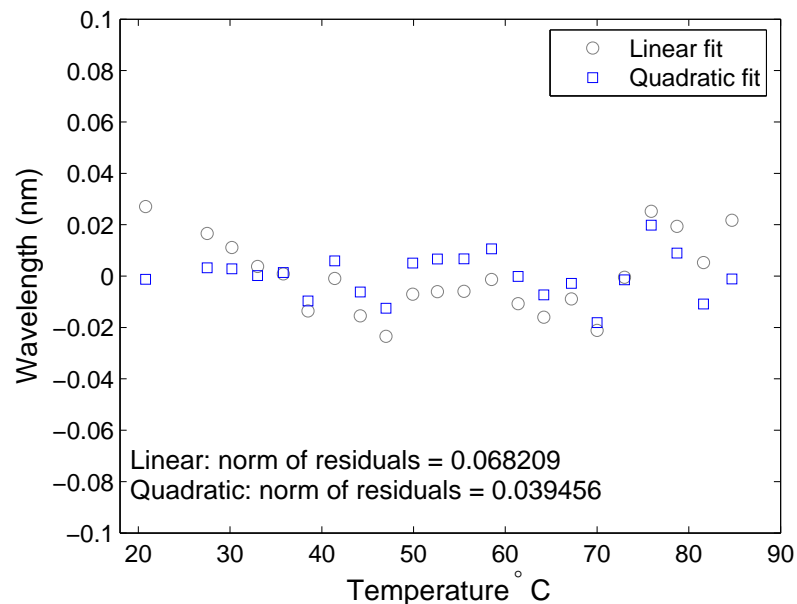


**Figure 6.23:** Plot of residuals to the fits to the data.

failed to recover would be demonstrated. It is unlikely that an operational system would be deliberately designed to operate at the limit of the systems detection. However, it is desirable to minimise the uncertainty on these measurements, where possible.

#### 6.4.4 Peak Wavelength determination using HTT

Determining the wavelength from the ratio of the slopes of the linear fits to the phase, the Hilbert transform technique (HTT), has been demonstrated to provide increased resolution [6,7] over other approaches, such as the centroid, in conditions of real-world noisy signals. The FBG wavelength is determined using:

$$\lambda_{\text{FBG}} = \lambda_{\text{laser}} \frac{\delta\Phi_{\text{FBG}}}{\delta\Phi_{\text{laser}}} \quad (6.16)$$

where  $\lambda_{\text{laser}}$  is the reference laser's wavelength,  $\delta\Phi_{\text{FBG}}$  and  $\delta\Phi_{\text{laser}}$  are the linear slopes of the unwrapped phases of the laser and FBG, respectively [6].

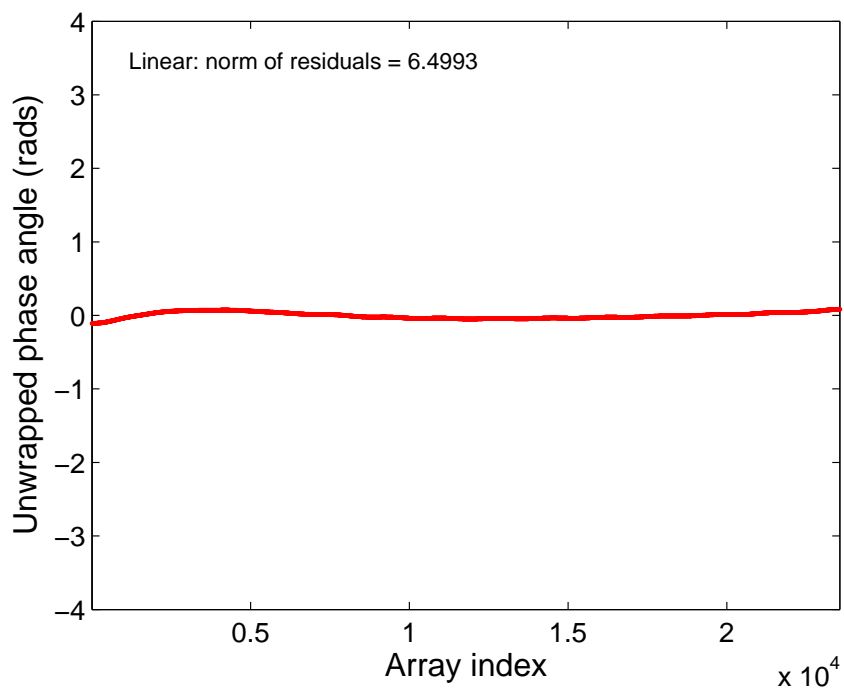
To obtain the phases of the FBGs and laser, the peaks are identified as for the centroid approach, and a Hamming window of  $2n_w + 1$  is used to separately isolate the laser and FBGs. The determination of the optimum value for  $n_w$  is discussed in appendix §R.2 (page V.II R-7).

As shown in figure 6.12 (page V.I - 283), the unwrapped phase (from which the displayed time base is calculated) is not linear. The recalibration procedure improves the linearity; however, the recalibrated unwrapped phase is not perfectly linear (the range of the residual to the fit is  $10^{-5}$  that of the uncorrected data). The residual to the fit of the corrected data is shown in figures 6.24 and 6.25 for the laser and sensor FBG, respectively.

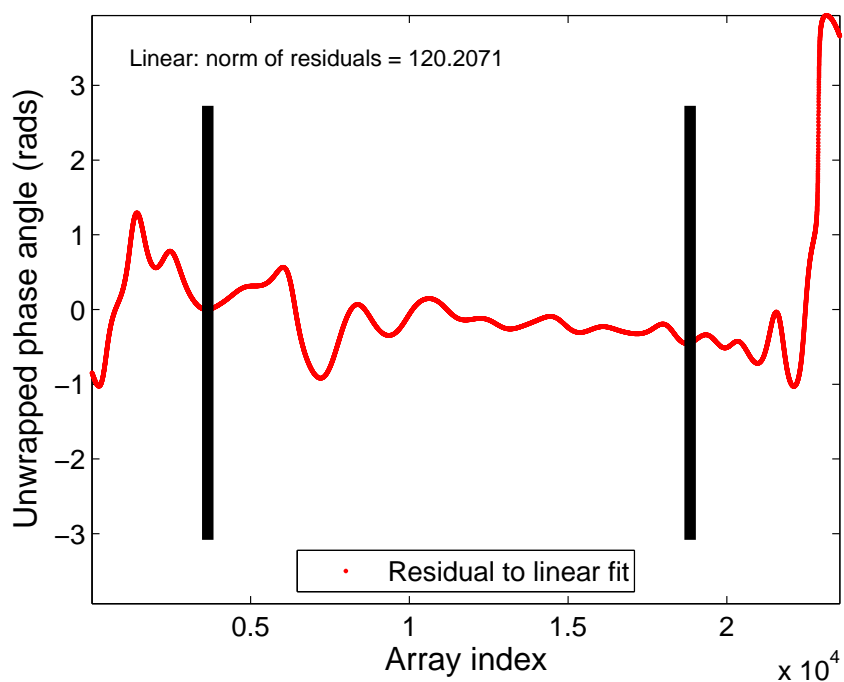
By taking the slope of linear fit to the unwrapped phase, effectively averaged values for  $\delta\Phi_{\text{FBG}}$  and  $\delta\Phi_{\text{laser}}$  can be obtained. Knowing the set value of the high-coherence reference laser, 1550.52 nm to an operational stability of  $\pm 2$  pm, the wavelength can be calculated with equation (6.16) (page V.I - 271).

Figure 6.26 (page V.I - 297) shows the temperature response obtained by using the HTT of the sensor FBG, with figure 6.27 (page V.I - 297) showing the corresponding residuals. The normalised thermal response of the sensor FBG is  $5.42 \times 10^{-6} \text{ }^\circ\text{C}^{-1}$ . This value is lower than the literature value for FBGs. Using the literature value of  $6.67 \times 10^{-6} \text{ }^\circ\text{C}^{-1}$  [41], the HTT approach wavelengths correspond to a temperature step of  $2.4 \pm 1.44 \text{ }^\circ\text{C}$  over the range  $18.2 - 70.0 \text{ }^\circ\text{C}$  instead of  $3.05 \pm 0.89 \text{ }^\circ\text{C}$  over the range  $20.8 - 84.7 \text{ }^\circ\text{C}$ .

Figures 6.22 and 6.26 are plotted to the same scale. It is immediately apparent that the uncertainty (standard deviations) associated with the HTT is less (20 pm) than for the centroid approach (164 pm), as in figure 6.22. This reduction in uncer-



**Figure 6.24:** Residual to the linear fit of the unwrapped phase of the high-coherence reference laser.



**Figure 6.25:** Residual to the linear fit of the unwrapped phase of the sensor FBG. The black lines delimit a central part of the residuals, say 10% – 80%, which has the smallest deviation from linearity

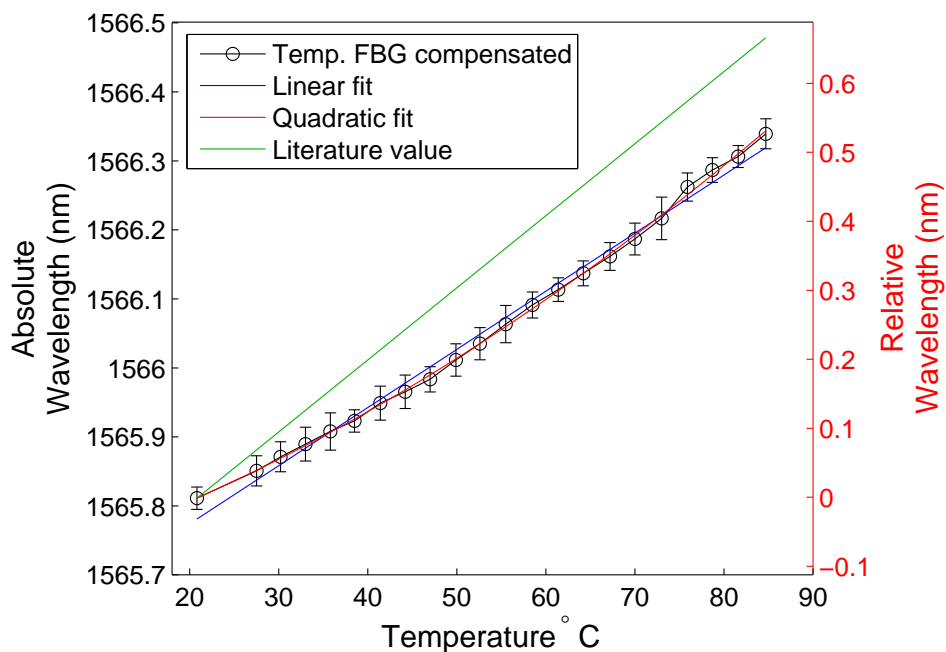


**Figure 6.26:** Temperature response of the sensor FBG, to one standard deviation, with windows  $2n_w + 1$  wide, for  $n_w = 4, 5, 6$ . A linear and a quadratic fit are shown. Also plotted are the values obtained from using the literature value of  $6.67 \times 10^{-6} \text{ }^\circ\text{C}^{-1}$  [41].

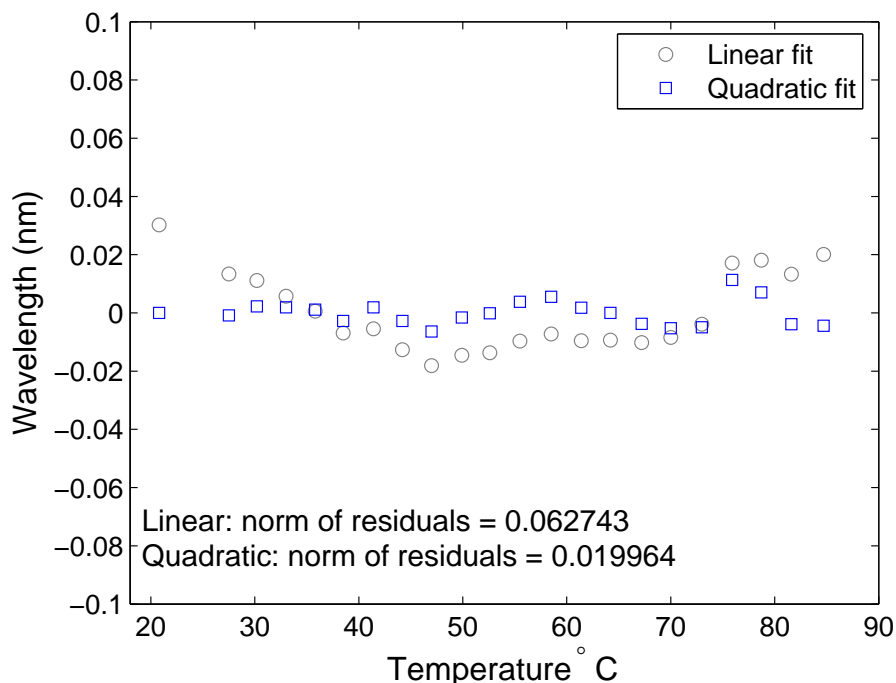


**Figure 6.27:** Residual of the HTT of the sensor FBG for data in figure 6.26.

tainty occurs for the same data as the difference is only the centroid approach and the HTT approach. The mean uncertainty is 25 pm, with maximum uncertainty = 35 pm. This is  $\sim 5 - 6$  times smaller than when using the centroid algorithm (mean uncertainty = 164 pm, maximum uncertainty = 183 pm), to calculate the wavelength shift for both FBGs.

	Temp. FBG ( $\times 10^{-6} \text{ } ^\circ\text{C}^{-1}$ )	Ref. FBG ( $\times 10^{-6} \text{ } ^\circ\text{C}^{-1}$ )
$n_w$ 6	5.37(93)	-0.005(120)
$n_w$ 7	5.36(75)	-0.051(81)

**Table 6.5:** Table of HTT approach FBG thermal responses,  $\frac{1}{\lambda_B} \frac{\delta\lambda_B}{\delta T}$ , for Hamming windows of width =  $2n_w + 1$ , with  $n_w = 2, 3, 4$  and respective norm of residuals (pm) of linear fit for the temperature and reference FBGs.

#### 6.4.4.1 Refinement of HTT calculated values

The residuals to the linear fits shown in figures 6.24 and 6.25 are flatter in the central part, and deviate most from the linear fit at the beginning and end of the datasets. By taking a central portion, say 10% – 80% of the length, indicated by the black lines on figure 6.25, the relative linearity is improved.

By calculating the linear fit to this central part of the phase angles and taking the ratio of the slopes, a further reduction in the uncertainty is obtained, as shown in figure 6.28, plotted to the same scale as figures 6.22 (page V.I - 294) and 6.26 (page V.I - 297). Figure 6.29 (page V.I - 299) shows the residuals to the plot.

The mean uncertainty is reduced to 20pm, with a maximum uncertainty of 28pm. Henceforth, the central part of the slope is used for quoted HTT calculated values.

#### 6.4.5 Effect of window length upon recovered values

The previously reported values were obtained from varying interferogram lengths but with fixed window length. The rationale for this was that the longer interferograms would provide an increase in resolution over the shorter interferograms. The shorter interferograms would not admit unnecessary noise at the edges of the interferograms and would set the minimum resolution. The longer interferograms would therefore not increase the calculated uncertainty of the measurement.

However, as the interferograms varied in length, the spectral range windowed varied as  $n_w(0.7 \pm 0.03)$  nm. To determine if the varying effective spectral window adversely affected the calculated values, the interferograms were re-examined with fixed lengths. The effect of the variable length is discussed in detail in appendix R (page V.II R-1), sections §R.4 (page V.II R-30) and §R.3 (page V.II R-13) for the centroid and HTT approaches, respectively.

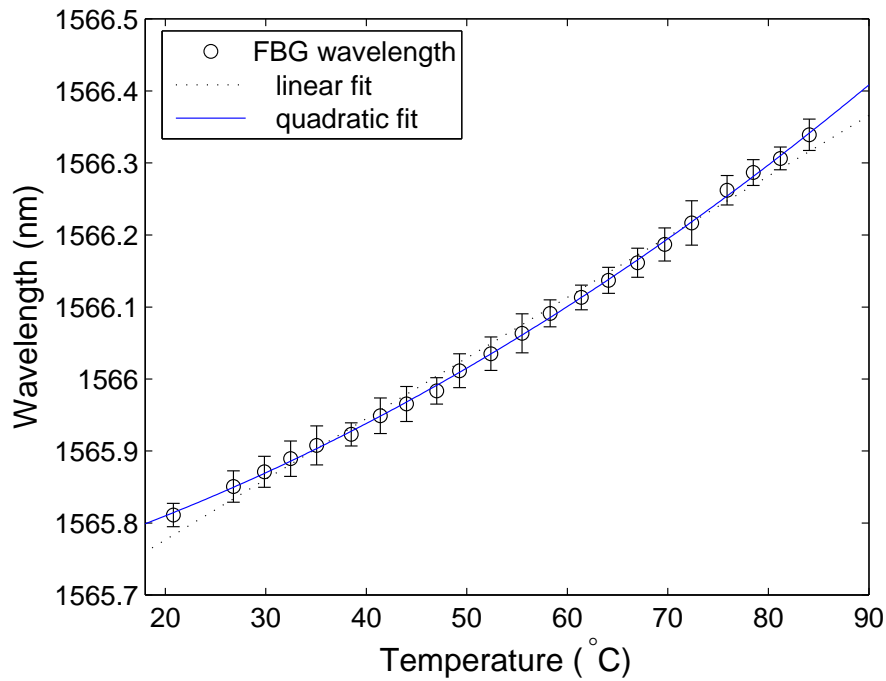


**Figure 6.28:** Temperature response of the sensor FBG, to one standard deviation, using the HTT of the central portion of the unwrapped phases.

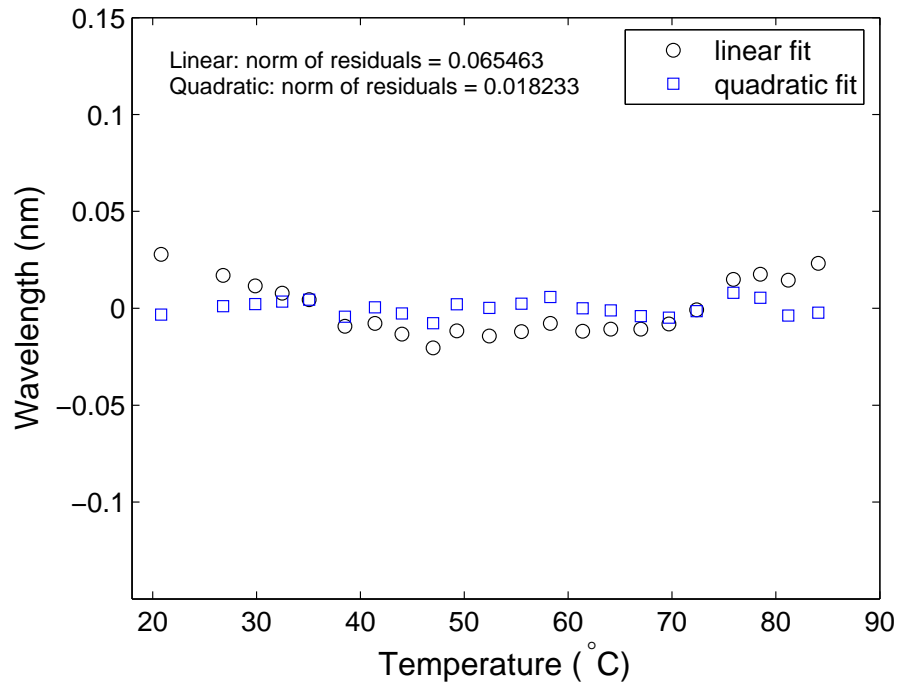


**Figure 6.29:** Residual of the ratio of the HTT of the central portion of the unwrapped phases of the sensor FBG for data in figure 6.28.

The main result of varying the fixed length over the range  $n_i = 1 \dots 16$  is that the values of the temperature response slope vary/oscillate between a maximum and a minimum, (see figures R.31 (page V.II R-24) to R.33 (page V.II R-25) for the centroid approach and figures R.49 (page V.II R-41) to R.52 (page V.II R-42) for the HTT approach). For the data analysed, the slope value obtained depended upon the interferogram length  $n_i$  chosen. By using the variable length interferograms, the resulting values reported in §6.4.3 (page V.I - 290) and §6.4.4 (page V.I - 295) have an increased uncertainty arising from this variation/oscillation, and the temperature response slope value depends upon the averaged contribution of the sampling of the variation/oscillation.

### 6.4.6 Centroid approach, different fixed lengths

This section contains a summary of the changing interferogram length,  $n_i$ , and window length,  $n_w$ , work in §R.3 (page V.II R-13) from appendix R (page V.II R-1).

In addition to the optimum window length,  $n_w$ , an optimum interferogram length,  $n_i$ , was sought. Instead of a converging value (i.e. a minimally different value), an oscillating temperature response slope was observed with changes in  $n_i$ . The values are listed in table R.6 (page V.II R-27), in appendix R (page V.II R-1).

Determining the optimum value of  $n_w$  followed the approach used in the variable interferogram length discussion, §R.1 (page V.II R-1). As for the variable length interferograms, the optimum values were  $n_w = 2, 3, 4$ .

The maximum interferogram length,  $n_i$ , should, in principle, contain the most spectral information, facilitating a more accurate determination of the peak wavelength value. Determining an optimum  $n_i$  was not as apparent as for the determination of optimum  $n_w$ . The differences in peak wavelength for changes with  $n'_i$  showed a decline with  $n'_i$ , but not a convergence.

Alternative visualisations of the data were examined. The slope of the linear fit to the temperature response was calculated for the different  $n_w$  and  $n_i$ . The optimum value for  $n_w$  was again  $n_w = 2, 3, 4$ . However, the values of the slope of the linear fit to the temperature response oscillate with  $n_i$ .

As such, the temperature response slope value, as determined by a linear fit, depended upon the length of the interferogram chosen for the determination of the value, as tabulated in table R.6 (page V.II R-27).

The origin of this oscillation is unknown. It was observed for both the centroid and HTT calculations (see §6.4.7 (page V.I - 304)). The changes with  $n_w$  are of greater size, and scale than the changes with  $n_i$ . Given its presence for both the centroid and HTT approach, a possible origin would be in the recalibration process.

The linear interpolation between the unwrapped data points may not be the most appropriate interpolation.

However, the linear fits to the temperature response slopes are calculated from the averages of  $\sim 26$  individual wavelength calculations per data point. The changes in slope would, therefore, need to exceed any preserved noise and be, even if only on average, consistently applied across the  $\sim 26$  interferograms contributing to the datapoints so that smoothing from the averaging would not hide the oscillation.

To facilitate a comparison with the variable interferogram length result, the  $n_i = 5$  value was chosen, as the value that exhibited the smallest difference from the average value (across  $n_w = 2, 3, 4$ ). Figures 6.30 and 6.31 show the changes in centroid position for the temperature signal and reference FBGs, respectively. These can be compared to figures 6.20 and 6.21 (page V.I - 292) for the variable interferogram length case. The standard deviations of the  $n_w = 2, 3, 4$  are reduced ( $\sim 50$  pm) compared to the variable interferogram length ( $\sim 160$  pm), for both the temperature signal and reference FBGs. The origin of the difference can be seen in the movement of the average position.

Table 6.6 contains the slope and norm of the residuals of the linear fits for  $n_w = 2, 3, 4$ . This can be compared to table 6.4 (page V.I - 291), for the variable interferogram length case. The norms to the residuals of the linear fits are 2.5 – 4 and 3.8 – 5.5 times that of the variable interferogram length norm values, for the temperature signal and reference FBGs, respectively.

Figure 6.32 shows the reference FBG values subtracted from the temperature signal values, which provides a slight improvement in the linearity. The literature value slope is also plotted, for comparison. Figure 6.33 shows the residuals to the linear fit in figure 6.32.

	Temp. FBG ( $\times 10^{-6} \text{ }^\circ\text{C}^{-1}$ )	Ref. FBG ( $\times 10^{-6} \text{ }^\circ\text{C}^{-1}$ )
	1	5.43(170)
$n_w$	2	5.22(281)
	3	5.50(352)
		0.11(183)
		-0.27(294)
		-0.41(355)

**Table 6.6:** Table of centroid approach FBG thermal responses,  $\frac{1}{\lambda_B} \frac{\delta\lambda_B}{\delta T}$ , for rectangular windows of width  $= 2n_w + 1$ , with  $n_w = 2, 3, 4$  and respective norm of residuals (pm) of linear fit for the temperature and reference FBGs.

The improvement in the temperature response fits achieved via the subtraction of the reference FBG wavelengths from the temperature signal FBG wavelengths, may have originated in the reduction of the magnitude of the oscillation experienced as the varying length centroid values traversed the different  $n_i$ .

The slope value is smaller than the literature value of  $6.67 \times 10^{-6} \text{ }^\circ\text{C}^{-1}$  [41]. As for the variable interferogram length case, the smaller value may be explained by

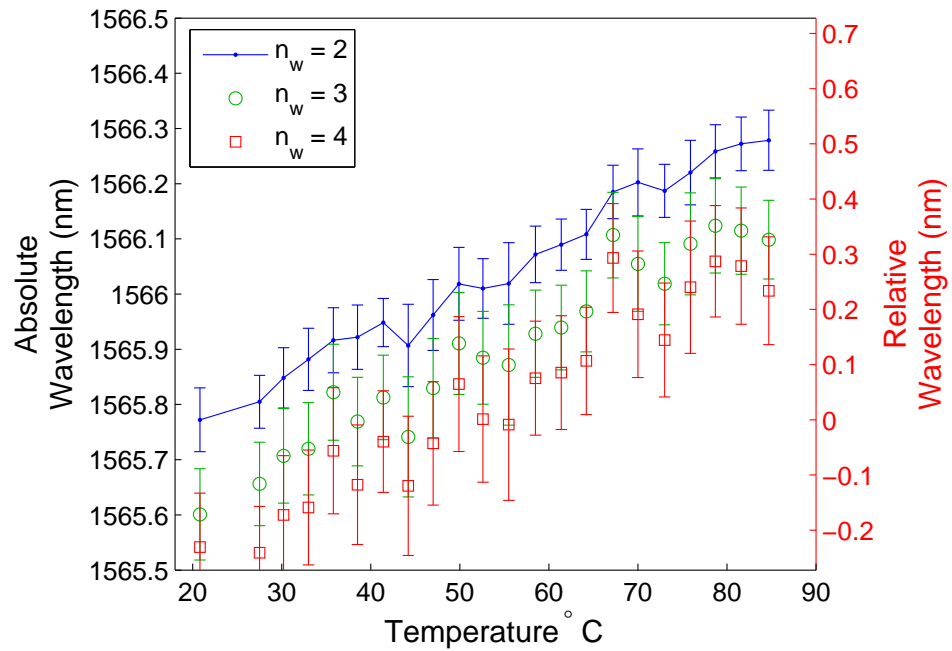


**Figure 6.30:** Centroid calculated wavelengths for the temperature signal FBG, using windows  $2n_w + 1$  wide, for  $n_w = 2, 3, 4$ .

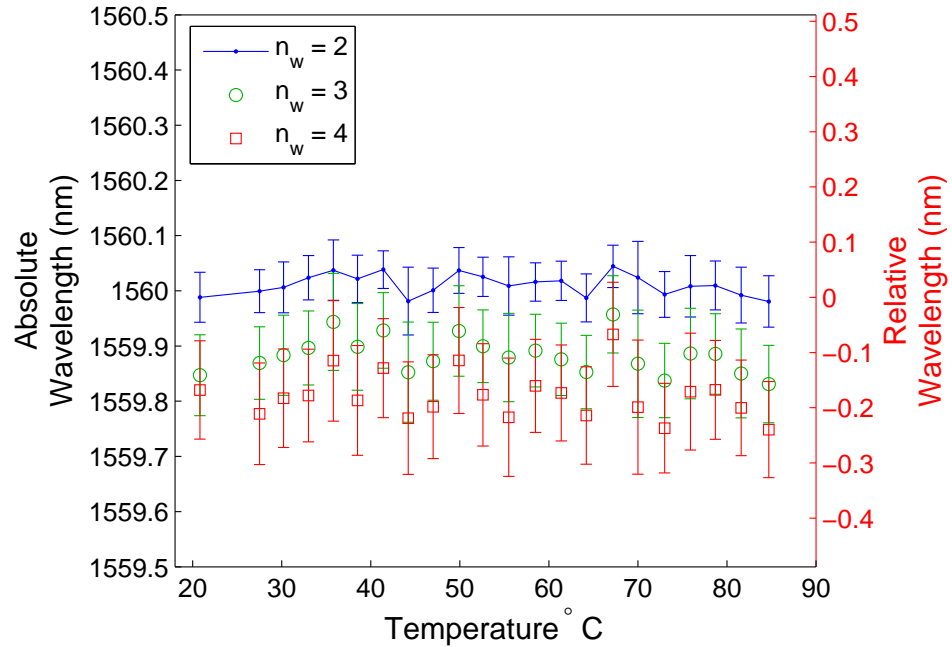


**Figure 6.31:** Centroid calculated wavelengths for the reference sensor FBG, using windows  $2n_w + 1$  wide, for  $n_w = 2, 3, 4$ .

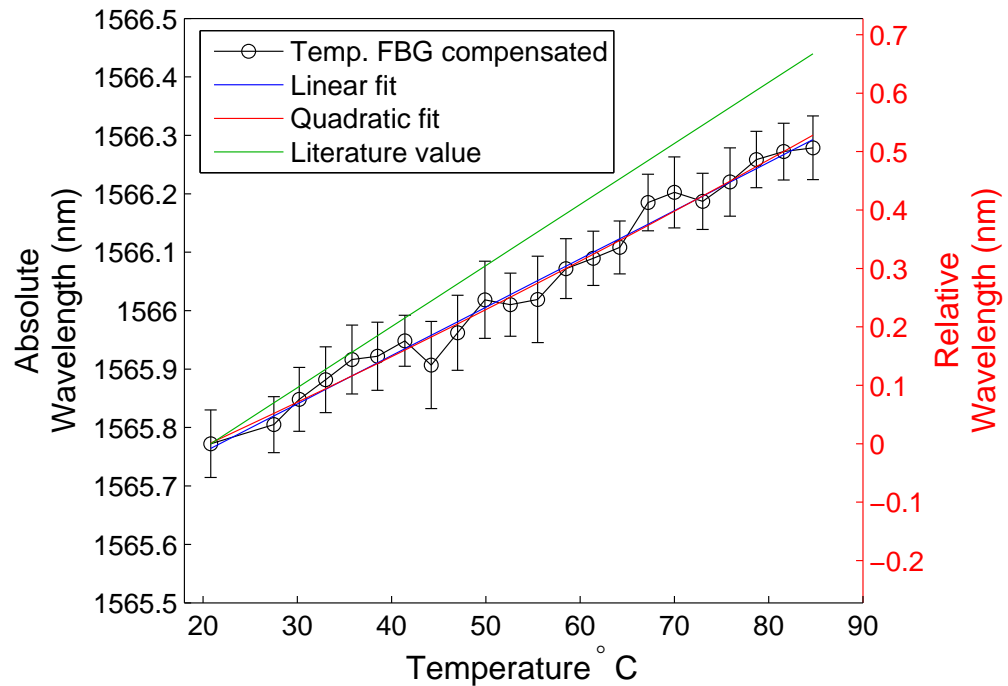


**Figure 6.32:** Temperature response of the sensor FBG, corrected against the reference FBG, to one standard deviation from centroid calculations. A linear and a quadratic fit are shown. Also plotted are the values obtained from using the literature value of  $6.67 \times 10^{-6} \text{ }^\circ\text{C}^{-1}$  [41].

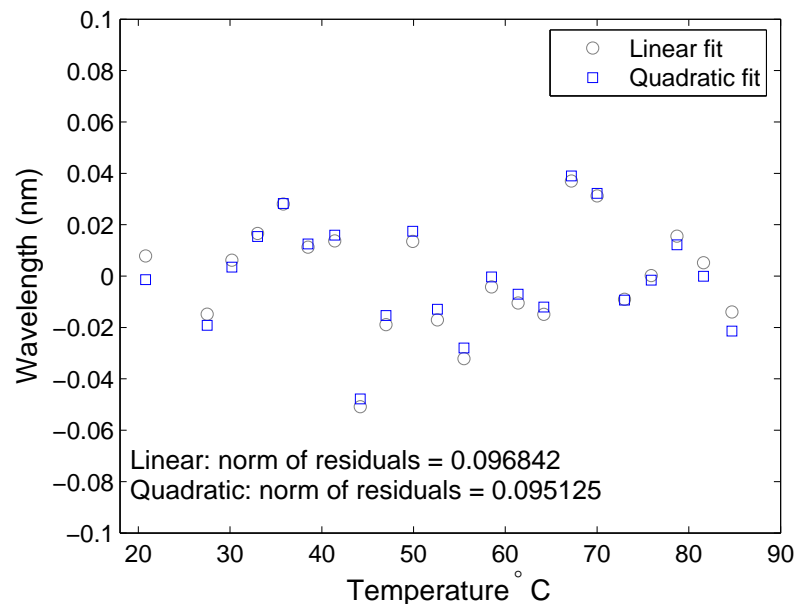


**Figure 6.33:** Plot of residuals to the fits to the data.

incorrect oven temperatures being set or reported by the oven controller. The values of the average temperature step size, the beginning and end of the temperature range are tabulated in table 6.7, for  $n_w = 2, 3, 4$ , which would return the literature value, given the calculated wavelengths. The recorded temperature step was  $3.05 \pm 0.89^\circ\text{C}$

	Avg. step( $^\circ\text{C}$ )	Start( $^\circ\text{C}$ )	End( $^\circ\text{C}$ )
	2	$2.36 \pm 1.17$	20.27
$n_w$	3	$2.30 \pm 2.07$	20.02
	4	$2.41 \pm 1.83$	20.53

**Table 6.7:** Table of temperature step size, beginning and final temperature (i.e. temperature range) which would return the centroid approach calculated FBG  $\lambda_B$  values using the literature value of the normalised temperature response slope,  $\frac{1}{\lambda_B} \frac{\delta\lambda_B}{\delta T} = 6.67 (\times 10^{-6} \text{ }^\circ\text{C}^{-1})$ , for  $n_w = 2, 3, 4$ .

over the range  $20.8 - 84.7^\circ\text{C}$ , and the corresponding variable interferogram length values are  $2.36 \pm 1.25^\circ\text{C}$  over the range  $19.6 - 71.3^\circ\text{C}$ .

#### 6.4.7 Hilbert transform technique, different fixed lengths

As for the centroid approach, this section contains a summary of the changing interferogram length,  $n_i$ , and window length,  $n_w$ , work in appendix §R.4 (page V.II R-30).

The HTT approach was evaluated for the different  $n_i = 1 \dots 16$  and  $n_w = 1 \dots 20$ . The optimum value of  $n_w$  was determined using the same approach as for the optimum  $n_w$  in the variable interferogram length case, §R.1 (page V.II R-1).

The optimum  $n_w$  was easier to determine than for the variable interferogram length case. The differences in mean HTT determined peak wavelengths,  $\Delta_w \lambda_B$  on figure R.11 (page V.II R-9), exhibited a convergence at  $n_w = 13, 14, 15$ , prior to the introduction of the neighbouring FBG into the calculation. On the basis of the improvement in determination of the optimum  $n_w$ , the fixed interferogram length approach improves upon the variable length approach, figure R.11 (page V.II R-9).

Again, the determination of an optimum  $n_i$  presented difficulties. Using the differences approach that provided the optimum  $n_w$  did not suggest an optimum  $n_i$ , as can be seen in figure R.41 (page V.II R-35). The alternative visualisation of plotting the slope of the linear fit to the temperature response slope for each combination of  $n_w$  and  $n_i$ , figures R.45 (page V.II R-37) and R.46 (page V.II R-37), demonstrated most clearly the oscillation with  $n_i$ , particularly at small values of  $n_w$ . The slope values are tabulated in table R.11 (page V.II R-39).

Again, to facilitate a comparison with the variable interferogram length result, the  $n_i = 4$  value was chosen, as the value that exhibited the smallest difference from

the average value (across  $n_w = 13, 14, 15$ ). Figures 6.34 and 6.35 show the changes in peak wavelength obtained by the HTT approach for the temperature signal and reference FBGs, respectively, to the same scales as the centroid figures 6.20, 6.21 (page V.I - 292), 6.30 and 6.31 (page V.I - 302). As can be seen, the individual data points do not exhibit the differences with  $n_w$  that the centroid values do, as would be expected from the convergence shown in figure R.11 (page V.II R-9).

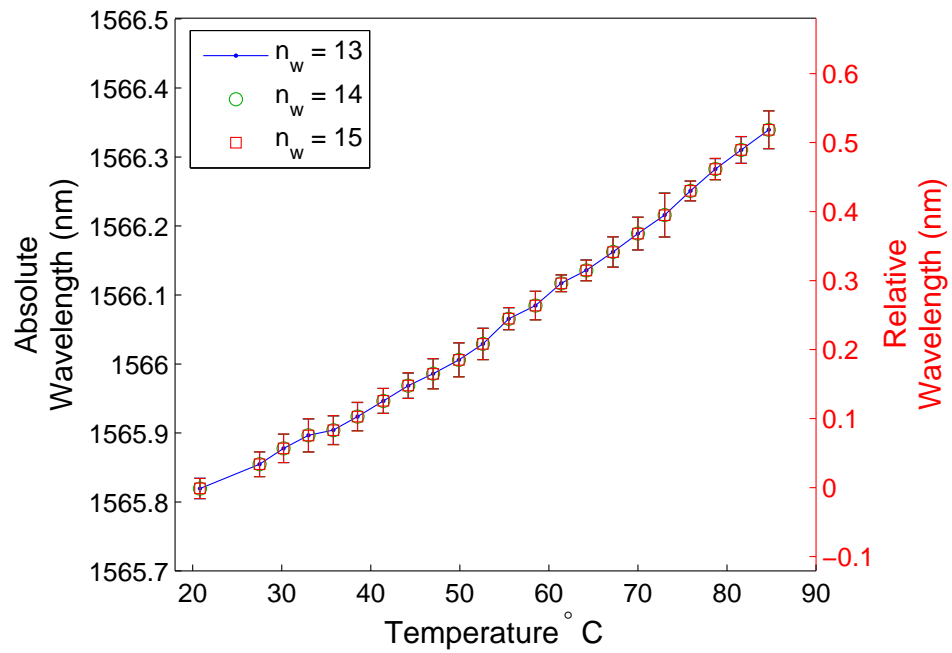
Figures 6.36 and 6.37 (page V.I - 307) show the linear and the quadratic fits to the temperature response slope, and the corresponding residuals to the fits, respectively. The literature value slope is also plotted for comparison. Figure 6.36 is not significantly different from figure 6.26 (page V.I - 297). The standard deviations of the  $n_w = 13, 14, 15$  are approximately the same,  $\sim 21$  pm for the variable interferogram length case and  $\sim 20$  pm for  $n_i = 4$ . The relative lack of improvement, compared to the centroid approach, can be understood in terms of the more rapid convergence achieved with the HTT approach with changes in  $n_w$ . The magnitude of the standard deviation is influenced more by changes in  $n_w$  than by  $n_i$ .

Table 6.8 contains the slope and norm of the residuals of the linear fits for  $n_w = 13, 14, 15$ . This can be compared to table 6.5 (page V.I - 298), for the variable interferogram length case. The norms of the residuals show a small improvement, 0.75 – 0.94 the value of the variable length temperature signal FBG values.

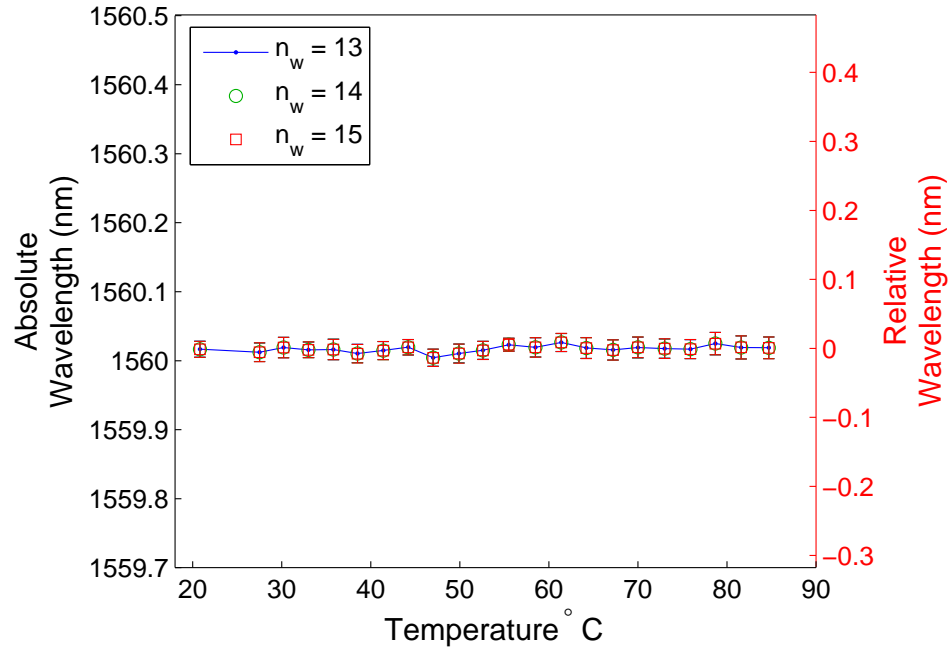
Again, the slope values are smaller than the literature value. The values for  $n_i = 4$  are also smaller than for the variable interferogram length case,  $\sim 5.37 \times 10^{-6} \text{ } ^\circ\text{C}^{-1}$ . This may, again, be a result of the improved convergence shown in figure R.11 (page V.II R-9).

Table 6.9 lists the average temperature step size and the beginning and end of the temperature range, for  $n_w = 13, 14, 15$ . The recorded temperature step was  $3.05 \pm 0.89^\circ\text{C}$  over the range  $20.8 - 84.7^\circ\text{C}$ , and the corresponding variable interferogram length results are  $2.4 \pm 1.44^\circ\text{C}$  over the range  $18.2 - 70.0^\circ\text{C}$ .

Although the temperature response slope values change with  $n_i$  for both the centroid (max: $6.2 \times 10^{-6} \text{ } ^\circ\text{C}^{-1}$  min: $5.35 \times 10^{-6} \text{ } ^\circ\text{C}^{-1}$ ) and HTT (max: $5.34 \times 10^{-6} \text{ } ^\circ\text{C}^{-1}$  min: $5.29 \times 10^{-6} \text{ } ^\circ\text{C}^{-1}$ ) approaches, the consistently lower temperature response slope values, with respect to the literature value of  $6.67 \times 10^{-6} \text{ } ^\circ\text{C}^{-1}$ , indicates that either the oven did not maintain a consistent temperature at the oven sensor and at the temperature signal FBG, or the returned values of the oven controller were scaled incorrectly. In either case, the changes in slope value observed with changes in  $n_i$  would occur.



**Figure 6.34:** Centroid calculated wavelengths for the temperature signal FBG, using windows  $2n_w + 1$  wide, for interferogram length  $n_i = 4$ .



**Figure 6.35:** Centroid calculated wavelengths for the reference sensor FBG, using windows  $2n_w + 1$  wide, for interferogram length  $n_i = 4$ .

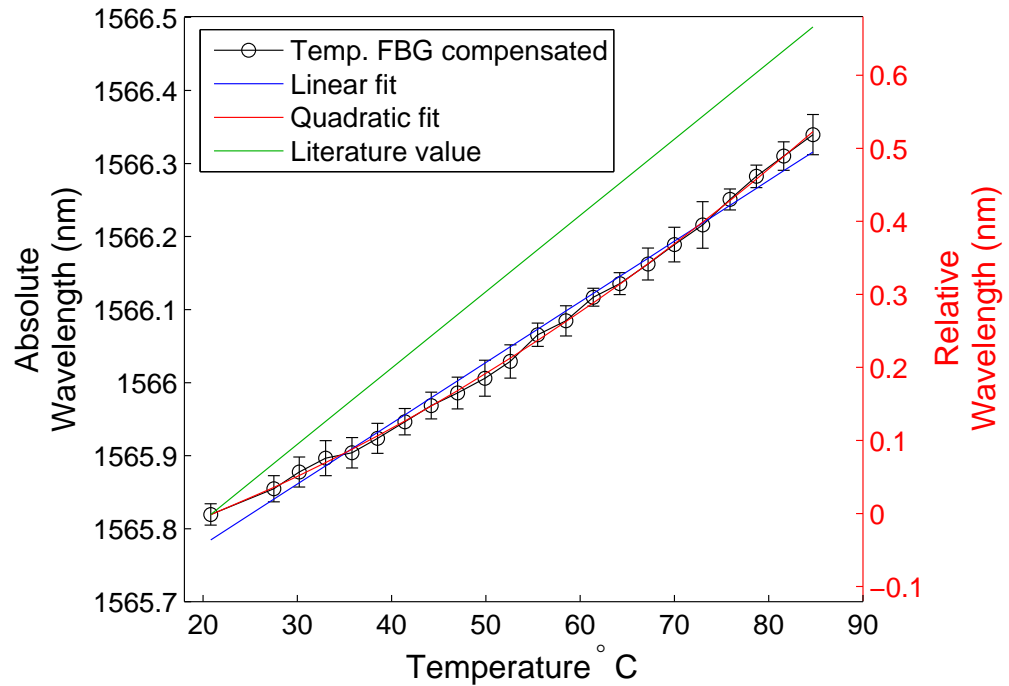


**Figure 6.36:** Temperature response of the sensor FBG, corrected against the reference FBG, to one standard deviation from centroid calculations. A linear and a quadratic fit are shown. Also plotted are the values obtained from using the literature value of  $6.67 \times 10^{-6} \text{ }^\circ\text{C}^{-1}$  [41].

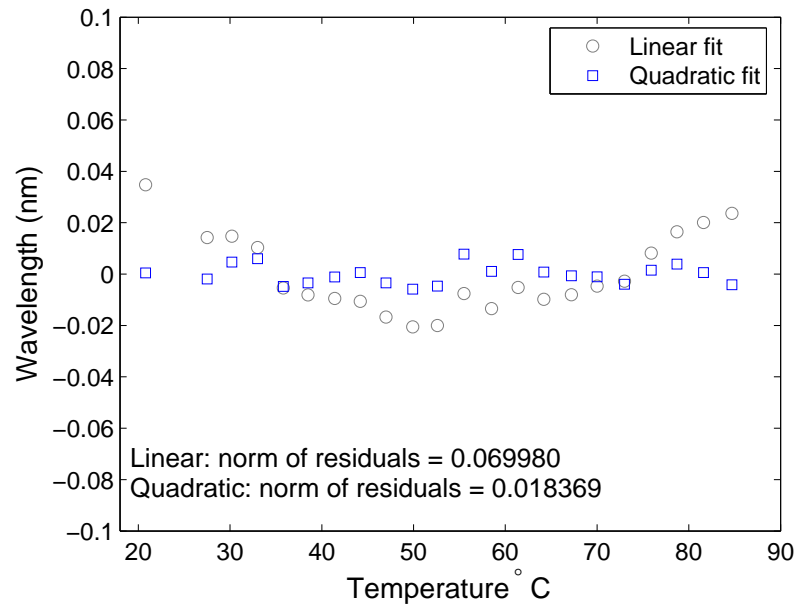


**Figure 6.37:** Plot of residuals to the fits to the data.

	Temp. FBG ( $\times 10^{-6} \text{ }^\circ\text{C}^{-1}$ )	Ref. FBG ( $\times 10^{-6} \text{ }^\circ\text{C}^{-1}$ )
	13	5.31(70)
$n_w$	14	5.31(70)
	15	5.31(70)

**Table 6.8:** Table of HTT approach FBG thermal responses,  $\frac{1}{\lambda_B} \frac{\delta\lambda_B}{\delta T}$ , for Hamming windows of width  $= 2n_w + 1$ , with  $n_w = 13, 14, 15$  and respective norm of residuals (pm) of linear fit for the temperature and reference FBGs.

	Avg. step( $^\circ\text{C}$ )	Start( $^\circ\text{C}$ )	End( $^\circ\text{C}$ )
	13	$2.32 \pm 0.66$	19.88
$n_w$	14	$2.32 \pm 0.66$	19.88
	15	$2.32 \pm 0.66$	19.88

**Table 6.9:** Table of temperature step size, beginning and final temperature (i.e. temperature range) which would give the HTT approach calculated FBG  $\lambda_B$  values using the literature value of the normalised temperature response slope,  $\frac{1}{\lambda_B} \frac{\delta\lambda_B}{\delta T} = 6.67 (\times 10^{-6} \text{ }^\circ\text{C}^{-1})$ , for  $n_w = 13, 14, 15$ .

### 6.4.8 Discussion

The ideal experiment would have been to have a two-output,  $\pi$ -shifted reference interferogram for each two-output,  $\pi$ -shifted signal interferogram. However, with only one tuneable filter and one balanced receiver, this was not possible. Consequently, common-mode noise that is rejected by the balanced receiver will be captured by the single-output reference interferogram and potentially incorporated into the recalibrated signal interferogram.

Recalibrating again using the signal spectrum would still be necessary to remove any artefacts introduced. To achieve the best results the HTT should be performed using spectra from the same detector. This would remove any sampling timing errors between receivers and data channels. Any artefacts which are introduced will increase the window necessary to isolate the laser or FBG for the ratio of the linear fits to the phase angle, potentially incorporating any remaining spectral noise. The first recalibration can be considered as regularising the spectrum sufficiently to allow recalibration from within the single spectrum.

The resolution of the interferograms was limited by the resources of the computer used for capture. Larger datasets obtained by increased scan rate or longer capture time, necessitated a reboot of the machine after recording a single dataset. Thus, the ability to get wide sense stationary conditions limited the dataset length that could be captured and, hence, the resolution of the interferograms.

The fibre stretcher was driven by a signal, passed via copper co-axial cable, to the CIRL 914-2 controller. The controller then passed the signal to the 916 stretcher

over *FCC68 6-core cable*. However, after the 6-core connector, unshielded wires attach directly to the piezo-electric stack. Electrical AC signals, such as the mains 50Hz, will be picked up over the unshielded wires at the very least, adding systematic and random noise to the driving voltage.

These noise sources should be removed by the two-step recalibration procedure as the second recalibration step uses the signal interferogram only.

### 6.4.9 Tuneable-filter and bandpass filter

The experiment was initially carried out with the Santec OTF-300 tuneable-filter. The OTF-300 presented two problems that made it unsuitable for the experiment. The OTF-300 is a thin-film based tuneable filter. When the telecomms laser was connected directly to the OTF-300 which was configured to have the centre of filter at the laser wavelength, a modulation of the laser signal was observed. Moving the centre filter wavelength to locate the laser wavelength at the  $-3$  dB point ( $\sim 50\%$  of maximum signal) removed the modulation. The modulation was visible until just before the  $-3$  dB point, but with decreasing magnitude. It is likely that as the laser's linewidth was narrower than the thin-film bandpass, a resonant cavity was established. Tuning the filter to the  $-3$  dB point suppressed the resonant condition, removing the modulation. If this is correct, a narrower laser linewidth would have required the filter to be configured below the  $-3$  dB point. The OTF-300 was successfully used with reference FBGs in [9] without this modulation being noticed.

In configuring the OTF-300 at one of the  $-3$  dB points, an asymmetry for noise about the laser wavelength is introduced. Assuming symmetrical noise about the laser wavelength, the OTF-300 filtering will pass more noise at the side nearest to the filter mean wavelength and suppress noise on the other side. This asymmetry will be evident in noise in the recalibrated spectrum, which is not corrected for this asymmetry.

The OTF-300 also displayed losses in excess of those specified in the OTF-300 manual. The losses were substantial when combined with the  $-3$  dB point arrangement, to the extent that the OTF-300 was not suitable.

A JDS Uniphase WD1551-CSW2 bandpass filter was used in preference to the OTF-300. The bandpass filter had a  $\sim 10$  nm window centred at 1551 nm, which suppressed the FBG signals ( $> 1560$  nm), but passed the laser noise. The losses were also lower, which provided for a better reference interferogram.

### 6.4.10 Side-peak structure

The side-peaks of figure 6.15 (page V.I - 285) are a significant source of measurand uncertainty by resolution impairment in the experiment. Their presence requires

further signal processing to suppress their influence, and their remaining presence after signal processing (or the signal processing itself) may alter the shape of the FBG spectrum.

Previous work undertaken in this laboratory, using a different all-fibre interferometer arrangement obtained the same side-peaks [9] using the same 1550 nm high-coherence telecomms laser, but due to the FBG signal being much stronger their presence was not noted. Additionally a bulk optic interferometer [40,49] which used a 632 nm HeNe laser reference coupled into the fibre also displayed these side structures.

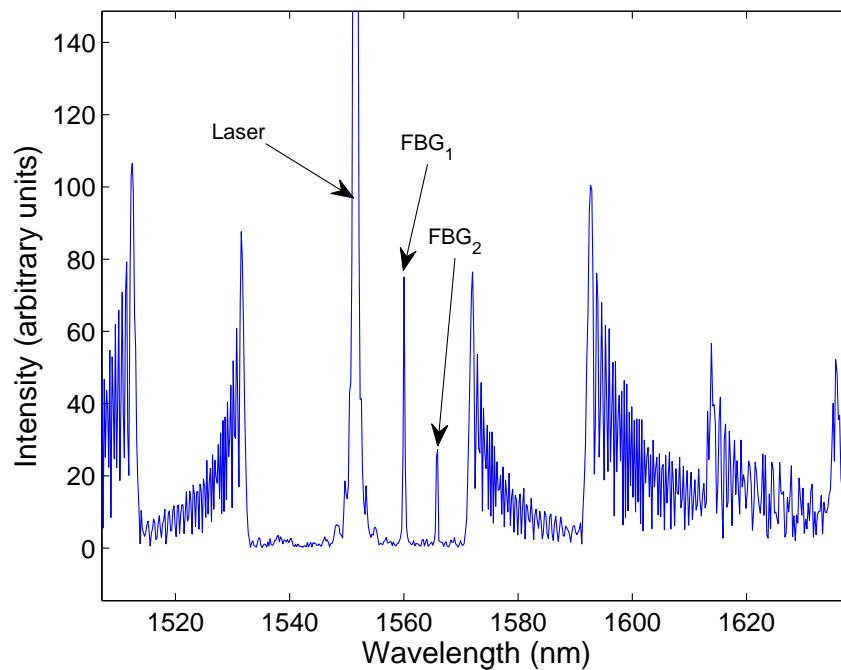


**Figure 6.38:** Side-peak structure using different fibre stretcher scan rate (4 Hz as opposed to 10 Hz for data reported). Telecomms laser at 1551.52 nm. Side-peaks have not had second pass to reduce their magnitude in this plot.

Figure 6.38 shows the effect of changing the fibre stretcher scan rate (the change in the side-peaks location also changed for different data capture rates). The FBGs lie between the laser and the first side-peak. The noise is larger here as this was taken with the ODL-300 tuneable filter. The side-peaks were observed using a bulk optic interferometer with a HeNe 632 nm and the telecomms 1550 nm, but no FBGs. Two different scan rates were analysed and, as shown in figure 6.39, there are different side-peaks present. The  $v_2$  spectrum is offset with respect to  $v_1$  to enhance clarity of presentation. The larger of the side-peaks occur at the same wavelengths in both spectra. The extra detail present in the  $v_2$  spectrum may be due to the higher scan rate.

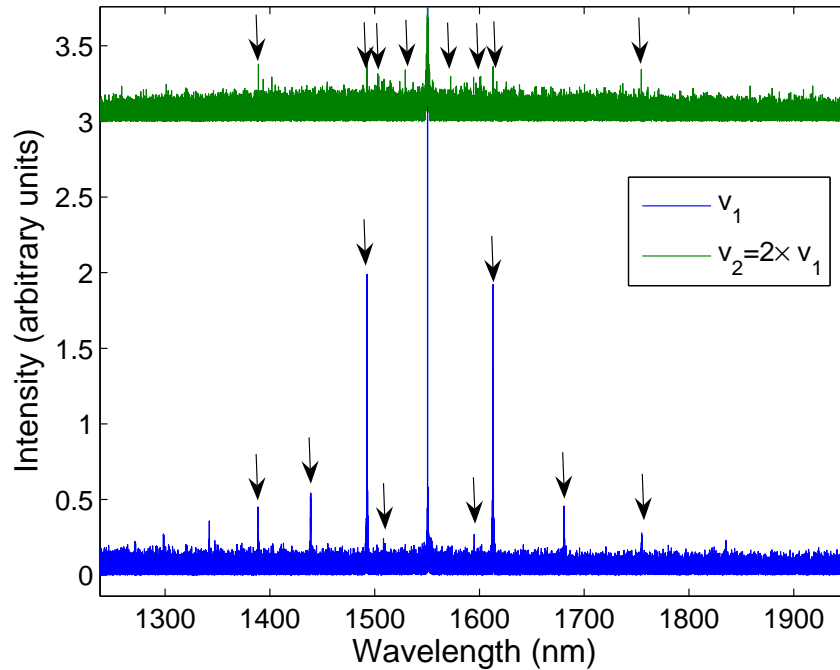


**Figure 6.39:** Side-peaks obtained from a bulk interferometer (after O’Mahoney [9]) using a HeNe 632 nm and the telecomms 1550 nm onto a single receiver. The scan rate  $v_1$  was 10 kHz, and  $v_2$  was 20 kHz.

Possible sources of these side-peaks are instrument ‘ghosts’ [25] or high-coherence ‘noise’ from the components of the interferometer instrument [50]. The ghosts are analogous to the spectral ghosts observed in diffraction grating spectrographs using ruled diffraction gratings, which are discussed in section §3.2.1.5 (page V.I - 127). It is unlikely that the side-peaks are laser relaxation oscillations or side-modes [51], given the range they extend to and that they do not appear on the OSA spectrum.

A full investigation of the source(s) of these side-peaks was not possible in the time available for this work. In a working system the FBGs would not be arranged so as to be just above noise level, and the impact of these structures would be lessened.

The greater importance of the side structure is their influence on the determination of the FBG peak wavelengths. Even at greater FBG signal strength the side-peaks will still affect high precision measurements by their presence. Centroid calculations will add their contribution, and the HTT, although less sensitive to their presence, will have their effects added along the unwrapped phase.

### 6.4.11 Optical Delay line

The Oz Optics reflector style ODL650MC optical delay line, ODL, is quoted to have a return loss of 60 dB. It is unlikely that internal reflections from the components of the ODL establish a Fabry–Perot interferometer. However, the ODL is very sensitive

to vibrations, as observed in figure 5.16 (page V.I - 242).

The ODL permits quick adjustment of the interferometer's balance point, which more than compensates for the disadvantage of acoustic noise, by providing an optical path distance change. When the 916 fibre stretcher is operated at higher driving voltage frequencies, the maximum stretched length is reduced, as the piezo reverses direction before reaching the maximum length. The ODL allows for the balance point to be moved to achieve the best interferogram for a given path length change. Additionally, it allows for changing between single and double-sided interferograms.

### 6.4.12 Long patch lead of fibre

There were three sufficiently attenuating lengths of fibre available for this experiment; 100 km of *Corning LEAF* fibre,  $\sim 20$  km of *Corning Dispersion Shifted* fibre<sup>24</sup>, DSF, and  $\sim 4$  km of Corning SMF-28e fibre. A fibre attenuator could have been used to provide tuneable signal attenuation. However, it would not have provided Rayleigh scattering noise as a long section of fibre would.

The 100 km of LEAF fibre was tested first, but did not produce a signal from the FBGs that was large enough to be detected. The DSF fibre was tested next in a double pass arrangement, where the DSF was placed between the first circulator's second port and the FBGs of figure 6.3 (page V.I - 272). Again the FBG signal was not detected, so the DSF fibre was installed as shown in figure 6.3, between the first circulator's third port and the demodulating interferometer, in a single-pass arrangement. A low, usable signal<sup>25</sup> was detected and this configuration was used. The span of SMF-28e fibre, being shorter, was discounted.

### 6.4.13 PPLN Oven

The construction of the modified PPLN oven is covered in section §4.3.12 (page V.I - 195). Thermoflex was used in place of the end faces and inside the PPLN oven, as shown in figure 4.20 (page V.I - 196).

The FBG in the oven should not have experienced ambient temperature changes. However, the oven and the ambient conditions form a temperature gradient through the apertures for the fibre. Changes in ambient air temperature would be of greater influence at the lower oven temperatures, as the temperature gradient is lower, and so more sensitive to changes of an end point.

---

<sup>24</sup>The DSF available was of unknown specification. The labelling stated OFS Corning DSF. It is likely that this fibre is either ITU-T G.653 or G.654 compliant. The fibre parameters are similar to the G.652 specification. G.653 fibre will have the additional issue of non-linearity generated noise near 1550 nm.

<sup>25</sup>The signal was usable after the signal processing discussed.

The function of the Thermoflex inside the oven was to reduce the volume of air within the oven and the susceptibility of the oven to spurious temperature changes by exchange of this air with air from outside the oven. This experimental work was undertaken in a different laboratory to the work in the previous chapters. This laboratory did not have the same thermal stability exhibited by the previous laboratory, even with the use of air-conditioning. For this reason the temperature reference was a requirement to ensure that the apparatus as a whole did not experience temperature changes that would invalidate the experiment.

The ambient temperature was checked at the start and end of the series of experiments and found not to have changed. There was more variation within the experiment, as evidenced by the uncertainty of the different temperatures being larger in the mid-range of temperatures, despite the temperature gradient between the ambient temperature and the oven increasing. The days on which the experiments were conducted, one temperature run per day, were warm days with varying cloud cover. The cloud had the effect of slightly cooling the laboratory, which may explain the discrepancy. Towards the end of the day and the data, the spread of results decreases compared to the middle of the day and data, as shown in figure 6.28 (page V.I - 299). In addition to the oven operating at a higher temperature and establishing a steeper temperature gradient with the ambient temperature, the cloud cover became more consistent, and the uncertainty reduces for the final data points in comparison to the earlier data points.

## 6.5 Conclusion

The use of the Hilbert transform technique, HTT, with two-output,  $\pi$ -shift interferometry to demodulate fibre Bragg grating, FBG, signals is reported. The FBG signals traversed a 19.5 km length of fibre. FBG signals were successfully demodulated where use of single-output interferometry did not recover the same signal, as it was obscured by background-noise.

The signal had significant noise from Rayleigh scattering and the amplification required to obtain a signal. Two-step recalibration provided a signal that retained the relative FBG to reference laser intensity ratios, as obtained by an OSA over a short ( $\sim 10$  m) patch lead.

The centroid and HTT methods of determining the mean wavelength of the FBG were examined. As expected, the centroid calculation was very sensitive to the noise level, whereas the sensitivity of the HTT could be optimised by adjusting the length of the unwrapped phase used in the linear regression fit. The limits to the HTT discussed in [38] might not strictly apply, as the interferogram used was synthesised, rather than obtained by zero-OPD triggering.

In a working sensor system, the FBG signals would not deliberately be at or around the noise level, and therefore both the centroid and HTT would not be as affected by noise. The two-output  $\pi$ -shift approach gave better SNR and elimination of Rayleigh scattering induced phase noise when using two-beam interferometers, such as the Michelson or Mach-Zehnder. The most significant limitation in this work was the presence of side-peaks near the FBG spectra.

The side-peak structure may have been generated by spurious reflections or phase modulation in the fibre components, or be instrument 'ghosts'. The same type of structure was observed in a bulk interferometer using HeNe 632 nm and the telecomms 1550 nm laser. The impact of the side-peaks was minimised by judicious resampling of the signal interferogram, based upon the apparent symmetry of the side-peak structure.

The recovered temperature response of the sensor FBG, was examined for variable and different fixed interferogram lengths. The variable interferogram length temperature response was  $5.42 \times 10^{-6} \text{ }^\circ\text{C}^{-1}$ , with an uncertainty of 32 pm and for the fixed interferogram length case was  $5.31 \times 10^{-6} \text{ }^\circ\text{C}^{-1}$ , with an uncertainty of 70 pm for the HTT. These values are lower than the published results [41], and may be due to different actual temperatures being experienced by the FBG and thermistor sensor of the oven, or incorrect thermistor values reported by the oven controller.

However, a dependence of the temperature response value on the length of the interferogram chosen was observed. This led to the optimum interferogram length,  $n_i$ , being ambiguous and the temperature response value changing between a minimum of  $5.29 \times 10^{-6} \text{ }^\circ\text{C}^{-1}$  and a maximum of  $5.34 \times 10^{-6} \text{ }^\circ\text{C}^{-1}$ . The value in the previous paragraph was from  $n_i = 4$ , the closest value to the average temperature response.

These changes in value were observed for both the centroid and HTT approaches, and were likely introduced during the recalibration process. It should be noted that the changes are not the same for the centroid and HTT approaches; however, neither is the subsequent processing of the data.

The successful use of FBG sensor demodulation using the HTT approach is shown for low SNR signals using the complementary  $\pi$ -shifted outputs of an all-fibre interferometer. The deleterious effects of Rayleigh scattering upon phase noise, and other common-mode noises are eliminated, improving the performance of the HTT technique for demodulating long distance sensors. The HTT approach, with appropriate Hamming window length, allows the effects of the changes in  $n_i$  to be mitigated, such that the changes are below the accuracy presented.

---

## 6.6 References

- [1] H. C. van de Hulst. *Light Scattering by Small Particles*, chapter 1, pages 3–10. Structure of Matter Series. Dover Publications, Inc., New York, 1981. ISBN: 0486642283.
- [2] I. Jacobs. *Optical fibers communication technology and systems overview*, volume 4 of *Handbook of Optics: Fiber Optics & Nonlinear Optics*, chapter 2. McGraw-Hill, New York, 2nd edition, 2001. ISBN: 0071364560.
- [3] K. Iizuka. *Elements of Photonics*, volume 2, chapter 11, pages 692–796. John Wiley & Sons, Inc., New York, 2002. ISBN: 0471408158.
- [4] M. E. Lines. *Interaction of light with matter: theoretical overview*, volume 30 of *Handbook of infrared Optical Materials*, chapter 2, pages 71–132. Marcel Dekker, Inc., New York, 1991. ISBN: 0824784685.
- [5] X. F. Meng, L. Z. Cai, Y. R. Wang, X. L. Yang, X. F. Xu, G. Y. Dong, X. X. Shen, and X. C. Cheng. Wavefront reconstruction by two-step generalized phase-shifting interferometry. *Opt. Commun.*, 281(23):5701–5705, 2008.
- [6] D. A. Flavin, R. McBride, and J. D. C. Jones. Short optical path scan interferometric interrogation of a fibre Bragg grating embedded in a composite. *Electron. Lett.*, 33(4):319–321, 1997.
- [7] D. A. Flavin, R. McBride, and J. D. C. Jones. Short-scan interferometric interrogation and multiplexing of fibre Bragg grating sensors. *Opt. Commun.*, 170(4-6):347 – 353, November 1999.
- [8] K. B. Rochford and S. D. Dyer. Demultiplexing of interferometrically interrogated fiber Bragg grating sensors using Hilbert transform processing. *J. Light-wave Technol.*, 17(5):831–836, 1999.
- [9] K. T. O’Mahoney. *Fourier Transform Spectroscopic Demodulation of Fibre Bragg Grating arrays*. PhD thesis, School of Science, Waterford Institute of Technology, Ireland., July 2007.
- [10] G. Chartier. *Introduction to Optics*, chapter Annex 12.B, pages 553–554. Advanced Texts in Physics. Springer Science+Business Media, Inc., New York, 2005. ISBN: 0387403469.
- [11] R. Hui and M. O’Sullivan. *Fiber Optic Measurement Techniques*, chapter 1, pages 1–128. Academic Press, New York, 2009. ISBN: 0123738652.
- [12] ITU-T. Series G. Supplement 39: Optical system design and engineering considerations, 2008.
- [13] ITU-T Manual. Optical Fibres, cables and systems, 2010. [http://www.itu.int/dms\\_pub/itu-t/opb/hdb/T-HDB-OUT.10-2009-1-PDF-E.pdf](http://www.itu.int/dms_pub/itu-t/opb/hdb/T-HDB-OUT.10-2009-1-PDF-E.pdf).
- [14] G. A. Thomas, B. I. Shraiman, P. F. Glodis, and M. J. Stephen. Towards the clarity limit in optical fibre. *Nature*, 404(6775):262–264, March 2000.

- 
- [15] R. Lingle Jr., D. W. Peckham, K. H. Chang, and A. McCurdy. *Single-mode fibers for communications*, chapter 5. Specialty Optical Fibers Handbook. Academic Press, Inc., Amsterdam, 2007. ISBN: 012369406X.
- [16] T. G. Brown. *Optical fibers and fiber-optic communications*, volume 4 of *Handbook of Optics: Fiber Optics & Nonlinear Optics*, chapter 1. McGraw-Hill, New York, 2nd edition, 2001. ISBN: 0071364560.
- [17] A. Shirley. Improved materials for low-water peak fiber manufacture. In *Optical Fiber Communication Conference and Exposition and The National Fiber Optic Engineers Conference*, page JWA61. Optical Society of America, 2005.
- [18] D. Homa, B. Childers, J. Crusse, S. Zerwekh, and S. Poland. High temperature exposure to Deuterium of optical fibers with Bragg gratings. In *Optical Fiber Sensors*, page TuE92. Optical Society of America, 2006.
- [19] T. Horiguchi, A. Rogers, W. C. Michie, G. Stewart, and B. Culshaw. *Distributed sensors: Recent developments*, volume 4 of *Optical Fiber Sensors: Applications, Analysis and Future Trends*, chapter 14. Artech House, Inc., Boston, 1997. ISBN: 0890069409.
- [20] A. Miller. *Fundamental optical properties of solids*, volume 1 of *Handbook of Optics: Fiber Optics & Nonlinear Optics*, chapter 9. McGraw-Hill, New York, 2nd edition, 2001. ISBN: 0071364560.
- [21] V. Twersky. Rayleigh scattering. *Appl. Opt.*, 3(10):1150–1150, 1964.
- [22] F. Chiaraluce. *Single-mode optical fibers and devices*, chapter 2. Single-Mode Optical Fiber Measurement: Characterization and Sensing. Artech House, Inc., Boston, 1993. ISBN: 0890066027.
- [23] J. Schroeder. *Light Scattering of Glass*, volume 12 of *Treatise on Materials Science and Technology.*, chapter 5, pages 158–222. Academic Press, Inc., New York, 1977. ISBN: 0123418127.
- [24] H. A. Gebbie. Fourier transform versus grating spectroscopy. *Appl. Opt.*, 8(3):501, 1969.
- [25] S. Davis, M. C. Abrams, and J. W. Brault. *Fourier Transform Spectrometry*, chapter 8, pages 119–141. Academic Press, San Diego, 2001. ISBN: 9780120425105.
- [26] E. Voigtman and J. D. Winefordner. The multiplex disadvantage and excess low-frequency noise. *Appl. Spectrosc.*, 41(7):1182–1184, September 1987.
- [27] E. Wolf. *Introduction to the Theory of Coherence and Polarization of Light*, chapter 5, pages 79–110. Cambridge University Press, Cambridge, 2007. ISBN: 9780521822114.
- [28] G. A. Cranch, A. Dandridge, and C. K. Kirkendall. Suppression of double Rayleigh scattering-induced excess noise in remotely interrogated fiber-optic interferometric sensors. *IEEE Photonic. Tech. L.*, 15:1582–1584, November 2003.
-

- 
- [29] S. Wu, A. Yariv, H. Blauvelt, and N. Kwong. Theoretical and experimental investigation of conversion of phase noise to intensity noise by Rayleigh scattering in optical fibers. *Appl. Phys. Lett.*, 59(10):1156–1158, 1991.
- [30] A. Yariv, H. Blauvelt, and S. W. Wu. A reduction of interferometric phase-to-intensity conversion noise in fiber links by large index phase modulation of the optical beam. *J. Lightwave Technol.*, 10(7):978–981, 1992.
- [31] M. Born and E. Wolf. *Principles of Optics: Electromagnetic Theory of Propagation, Interference and Diffraction of Light*, chapter 10, pages 554–632. Cambridge University Press, Cambridge, 7th edition, 1999. ISBN: 0521642221.
- [32] C. Brosseau. *Fundamentals of Polarized Light: A Statistical Optics Approach*, chapter 3.1, pages 69–122. John Wiley & Sons, Inc., New York, 1998. ISBN: 0471143022.
- [33] Z. Zalevsky and D. Mendlovic. *Optical Superresolution*, chapter 2, pages 9–20. Optical Sciences. Springer-Verlag New York, Inc., New York, 2004. ISBN: 0387005919.
- [34] K. Creath. *Temporal phase measurement methods*, chapter 4. Interferogram Analysis: Digital Fringe Pattern Measurement Techniques. IOP Publishing, Ltd., Bristol, 1993. ISBN: 075030197X.
- [35] V. A. Henderek. *Single mode optical fiber sensors*, chapter 3. Optical Fiber Sensor Technology: Fundamentals. Kluwer Academic Publishers, Dordrecht, 2000. ISBN: 0792378520.
- [36] M. D. Todd, G. A. Johnson, and B. L. Althouse. A novel Bragg grating sensor interrogation system utilizing a scanning filter, a Mach-Zehnder interferometer and a 3 x 3 coupler. *Meas. Sci. Technol.*, 12(7):771–777, 2001.
- [37] P. Carre. Installation et utilisation du comparateur photoélectrique et interférentiel du Bureau International des Poids et Mesures. *Metrologia*, 2(1):13–23, 1966.
- [38] S. D. Dyer, P. A. Williams, R. J. Espejo, J. D. Kofler, and S. M. Etzel. Fundamental limits in fiber Bragg grating peak wavelength measurements. In *Proceedings of the 17th International Conference on Optical Fibre Sensors*, volume 5855, pages 88–93. SPIE, May 2005.
- [39] P. Hariharan. *Basics of Interferometry*, chapter 4, pages 23–30. Academic Press, Inc., New York, 2nd edition, 2007. ISBN: 0123735890.
- [40] K. T. O’Mahoney, R. P. O’Byrne, S. V. Sergeyev, L. Zhang, and I. Bennion. Short-scan fiber interferometer for high-resolution Bragg grating array interrogation. *IEEE Sens. J.*, 9(10):1277–1281, October 2009.
- [41] A. D. Kersey, M. A. Davis, H. J. Patrick, M. LeBlanc, K. P. Koo, C. G. Askins, M. A. Putnam, and E. J. Friebele. Fiber grating sensors. *J. Lightwave Technol.*, 15(8):1442–1463, August 1997.
-

- [42] D. A. Jackson, R. Priest, A. Dandridge, and A. B. Tveten. Elimination of drift in a single-mode optical fiber interferometer using a piezoelectrically stretched coiled fiber. *Appl. Opt.*, 19(17):2926–2929, 1980.
- [43] BIPM JCGM 200:2008. International vocabulary of metrology - Basic and general concepts and associated terms (VIM), 2008.
- [44] G. M. H. Flockhart, R. R. J. Maier, J. S. Barton, W. N. MacPherson, J. D. C. Jones, K. E. Chisholm, L. Zhang, I. Bennion, I. Read, and P. D. Foote. Quadratic behavior of fiber Bragg grating temperature coefficients. *Appl. Opt.*, 43(13):2744–2751, 2004.
- [45] R. O’Byrne and S. V. Sergeyev. Application of  $\pi$ -shifted short scan interferometry to remote sensing. In Julian D. C. Jones, editor, *Proc. SPIE*, volume 7503, page 75036R. SPIE, 2009.
- [46] D. Inaudi, S. Vurpillot, N. Casanova, and A. Osa-Wyser. Development and field test of deformation sensors for concrete embedding. *Smart Structures and Materials, San Diego*, pages 138–48, 1996.
- [47] E. Rivera, D. J. Thomson, and A. A. Mufti. Comparison of recoated fiber Bragg grating sensors under tension on a steel coupon. *Proc. SPIE*, 5767:163–174, May 2005.
- [48] B. Lee, Y. W. Lee, and M. Song. *Principles and status of actively researched optical fiber sensors*, chapter 26, pages 401–436. Academic Press, Amsterdam, 2005. ISBN: 012088481X.
- [49] K. T. O’Mahoney, D. A. Flavin, L. Zhang, and I. Bennion. Fourier-transform-based spectral measurements on multiplexed fibre Bragg grating arrays. In Jose M. Lopez-Higuera and Brian Culshaw, editors, *Second European Workshop on Optical Fibre Sensors*, volume 5502, pages 423–426. SPIE, 2004.
- [50] Y. Weissman. Optical Noise Coherence Effects in a Mach-Zehnder System. *J. Lightwave Technol.*, 14:888–893, May 1996.
- [51] D. M. Baney and W. V. Sorin. *High Resolution Optical Frequency Analysis*, chapter 5, pages 169–219. Fiber Optic Test and Measurement. Prentice Hall, Inc., New Jersey, 1998. ISBN: 0135343305.

# Chapter 7

## Summary and Conclusions

---

### 7.1 Overview

In this thesis progress on the development of interferometric & spectroscopic techniques for high-resolution spectral measurements of FBGs is reported. The work builds upon well established and more contemporary work using novel components and applications to achieve high resolution spectral measurements of FBG signals. The work also reports limitations to the techniques, the mitigation of which may enable further improvements to be attained.

#### 7.1.1 Chapter objectives

Chapter 3 reported work on the development of a robust high-bandwidth ( $\sim 50\text{nm}$ ), high-resolution ( $\sim 1\text{pm}$ ) and high-speed ( $\sim 0.1\text{ms}$ ) simultaneous demodulation scheme, the SpectroBragg, for the individual sensing locations of FBG sensor arrays forming sensor networks. Multiplexed sensing arrangements benefit from simultaneous interrogation of sensor array or arrays.

The aim of the SpectroBragg project was to develop a compact, custom spectrometer providing high-speed wide-bandwidth demodulation natively in the telecomms bands, using a linear InGaAs array, enabling the lower cost telecomms fibre components to be used. An additional project aim, if time and resources permitted, was to investigate approaches to extend spectral bandwidth to cover the S,C, L & U telecomms bands ( $\sim 1460\text{--}1675\text{nm}$ ), while maintaining the resolution, e.g. by temporal multiplexing.

Chapter 4 reported the strain characterisation of a novel anisotropic fibre Bragg grating inscribed in Corning SMF-28 telecomms fibre and the testing of their appli-

cability as strain sensors. A flexible apparatus was designed and built to characterise the strain response of the novel anisotropic FBGs. The comparison of these novel FBGs with standard telecomms FBGs as strain sensors and discovery of possible strain/temperature discrimination by using the distinctive response of these novel anisotropic FBGs to both strain and temperature was investigated.

The technology to produce these novel anisotropic FBGs, using a two-photon process at 264 nm, was developed by Professor David N. Nikogosyan [1, 2]. These novel FBGs should complement, as well as compete with standard FBGs. An objective was thus to determine whether the anisotropy in these novel FBGs conferred any particular advantages over nominally axially-symmetric types.

Chapter 5 reported on the effectiveness of two polarisation mitigation schemes for the SpectroBragg, a modified polarisation fixer system based upon the work of Takada *et al.* [3] and a PDL balancing system based upon the work of Dong *et al.* [4]. Both were examined in an attempt to depolarise anisotropic and isotropic FBG signals demodulated by the SpectroBragg spectrometer. A comparison was made with a traditional, but inappropriately specified Lyot depolariser.

Chapter 6 reported the use of the Hilbert transform technique to analyse two-output,  $\pi$ -shifted interferograms in order to demodulate FBG signals. The Hilbert transform technique has been demonstrated to provide higher resolution wavelength determination than Fourier transform spectroscopy using shorter interferometer scans [5–8]. The  $\pi$ -shifted interferograms facilitated the recovery and demodulation of low signal-to-noise ratio interferograms not detectable with single-output interferograms.

## 7.2 Summary of chapters

Due to the material and modal nature of fibre optics, the polarisation and coherence properties of the electromagnetic radiation must, in general, be considered when designing sensor systems. Whether the demodulation system is based upon interferometry<sup>1</sup> or not, coherence and polarisation's ability to modulate the captured intensity at a detector should be evaluated to ensure the sensor system works as intended. Wolf's unified theory of coherence and polarisation, [9] and §2.1.2.1 (page V.I - 18), provides a convenient means of discussing the interconnections of the different chapters [10].

One of the important parameters of an FBG is its bandwidth. The unified theory's use of spectral quantities in terms of the angular frequency,  $\omega$ , affords a convenient means of discussing FBGs in terms of both peak (or mean) wavelength

---

<sup>1</sup>Such as the SpectroBragg or the  $\pi$ -shifted complementary two-output Michelson interferometer of chapter 6.

and bandwidth, along with changes therein.

The generalised Mueller matrices of *polarisers*, *phase retarders*, *polarisation rotators* and *absorbers*, and hence their effects, have been reported in [11]. Table 7.1 summarises the effects of these components upon the *Spectral Density*,  $S_W(\underline{\mathbf{r}}, \omega)$ , the *spectral DOP*,  $\mathcal{P}_W(\underline{\mathbf{r}}, \omega)$ , and the *spectral DOC*,  $\eta_W(\underline{\mathbf{r}}_1, \underline{\mathbf{r}}_2, \omega)$ .

Device	Spectral Density, $S_W(\underline{\mathbf{r}}, \omega)$	DOP, $\mathcal{P}_W(\underline{\mathbf{r}}, \omega)$	DOC, $\eta_W(\underline{\mathbf{r}}_1, \underline{\mathbf{r}}_2, \omega)$
Polariser	Changes	Change <sup>2</sup>	Changes
Retarder	No change	No change	No change
Rotator	No change	No change	No change
Absorber	Changes	Changes	Changes
Focusing Mirror	Changes <sup>3</sup>	Changes	Changes
Diffraction grating <sup>4</sup>	Changes	Changes	Changes
Scattering <sup>5</sup>	Changes <sup>6</sup>	changes	Changes

**Table 7.1:** After table 1 of [13]. Indication of modification of the *spectral density*,  $S_W(\underline{\mathbf{r}}, \omega)$ , *spectral DOP*,  $\mathcal{P}_W(\underline{\mathbf{r}}, \omega)$ , and *spectral DOC*,  $\eta_W(\underline{\mathbf{r}}_1, \underline{\mathbf{r}}_2, \omega)$ , for types of devices used in this thesis, e.g. *polariser*, *retarder*, *rotator* and *absorber*<sup>7</sup>, *focusing mirror*<sup>8</sup>, *diffraction grating*<sup>9</sup>, and *scattering medium*<sup>10</sup>.

As discussed in §2.2.2.2 (page V.I - 28), the glass material used in optical fibres is a weak absorber. As a consequence, there will be slight, extensive changes to all quantities from passage through the material. The sources used in this work were fibre coupled, including an FBG as a source. Changes to the sources'  $S_W$ ,  $\mathcal{P}_W$  and  $\eta_W$ <sup>11</sup> would not be as apparent, except as extensive changes due to the fibre leads used, e.g. PDL, as discussed in §2.2.8.5 (page V.I - 56).

The bends and twists that the fibre leads will have experienced will have acted as phase retarders and polarisation rotators, which do not change the quantities reported in table 7.1. The bends and twists do alter the Stokes parameters.

<sup>2</sup>Changes the  $\mathcal{P}_W(\underline{\mathbf{r}}, \omega)$  to be = 1.

<sup>3</sup>Changes depending upon position in focal plane. Ignoring aberrations, which will increase changes.

<sup>4</sup>Changes as, in the classical mounting, the TE and TM efficiencies are not uniform.

<sup>5</sup>The Rayleigh scattering centres in the fibre may be considered as deterministic random scattering, as the positions do not fluctuate.

<sup>6</sup>The spectral changes arise from the modification of the polychromatic envelope, due to the scattering angle having a wavelength dependence [12]. The scattering process is still inelastic.

<sup>7</sup>Polariser, retarder, rotator and absorber from table 1 of [13], which summarises the results of [11].

<sup>8</sup>Focusing mirror from [10, 14, 15].

<sup>9</sup>Diffraction grating from [10, 16–18].

<sup>10</sup>Deterministic random scattering medium from [10, 12, 19].

<sup>11</sup>In establishing the guiding core mode, losses to the cladding may be treated as equivalent to an absorber.

### 7.2.1 Chapter 3, the assembly and characterisation of the SpectroBragg

The development of a custom Čzerny–Turner type spectrometer, the SpectroBragg, with native sensitivity in the telecomms bands is reported. The SpectroBragg spectrometer consists of a Hamamatsu InGaAs array, with 512 pixels, observing a  $\sim 70$  nm bandwidth centred at  $\sim 1550$  nm. The Čzerny–Turner arrangement consisted of a collimating mirror, a diffraction grating in classical mounting and a final focusing mirror [20]. As the mirrors required off–axis alignment, the Čzerny–Turner was configured to minimise coma and astigmatism using equation (3.18) (page V.I - 132).

From table 7.1 it is seen that the SpectroBragg component parts modify the  $S_W$ ,  $\mathcal{P}_W$  and  $\eta_W$  quantities. This is in addition to the, albeit minimised, aberrations introduced by the off–axis arrangement of the mirrors<sup>12</sup>.

Using a stable high–coherence telecomms laser reference source, good wavelength repeatability<sup>13</sup> was obtained. The use of the centroid algorithm enabled super–resolution beyond the averaged native resolution of  $\sim 0.13$  nm. As discussed in appendix D (page V.II D-1),  $S_W(\mathbf{r}, \omega)$  is directly presented in terms of angular position on the InGaAs array. As the  $S_W$ ,  $\mathcal{P}_W$  and  $\eta_W$  quantities are spectral quantities, the generalised Stokes parameters,  $\underline{\mathbf{S}}_{\text{gen}}$ , for the high–coherence laser and FBGs will differ.

Additionally, the position on the array will have focusing and aberration differences, as outlined in appendix §K.2 (page V.II K-5). If these changes alter  $S_W(\mathbf{r}, \omega)$  they will correspondingly alter the centroid weighting and the calculated peak position. The best system resolution that was obtained in tests using the equipment available was sub–picometre wavelength resolution,  $< 0.5$  pm. This was observed by the recovery of a periodic signal. However, the vibrational stability of the system, either the SpectroBragg itself or the sensor under test, reduced the operational resolution to  $\sim 0.9$  pm. The vibrational stability was the largest limitation to SpectroBragg performance once the functionally inadequate Lyot depolariser was removed.

The SpectroBragg design was intended to provide sub–picometre resolution using a 1024 pixel InGaAs array over a bandwidth of 50 nm. The implemented SpectroBragg design achieved sub–picometre resolution with 512 pixels, over a bandwidth of  $\sim 70$  nm. The additional pixel density of the 1024 pixel array would have improved the SNR in the centroid calculations, but would have doubled the data transmit-

<sup>12</sup>Which would strictly make the  $S_W$ ,  $\mathcal{P}_W$  and  $\eta_W$  quantities functions of spatial bands or regions, rather than points  $\mathbf{r}_1$  and  $\mathbf{r}_2$ .

<sup>13</sup>Wavelength repeatability to one standard deviation as centre = 0.28 pm and at edge = 0.21 pm

ted to the PC and increased processing time<sup>14</sup>. The extended spectral bandwidth arose, primarily, from the restriction of the components due to availability and their physical extent and location on the bench.

## 7.2.2 Chapter 4, the strain characterisation of novel anisotropic FBGs

The strain characterisation of a novel anisotropic FBG inscribed into SMF-28 fibre has been reported. These anisotropic FBGs behave as approximately spectrally colocated orthogonally polarised FBGs, with a resultant flat-top spectral profile.

Table 7.1 indicates that these FBGs<sup>15</sup> will have different spectral, coherence and polarisation properties to standard telecomms FBGs. In contrast to FBGs in PMF, the inscribed indicatrix, §2.2.4.1 (page V.I - 39), will have the same SMF-28 material response to applied strain, but will not be as spherical as standard isotropic FBGs. In terms of the  $\underline{\mathbf{S}}_{\text{gen}}$ , equation (2.26) (page V.I - 20), the responses of isotropic and anisotropic FBGs will be different, particularly for the correlations between the orthogonal components.

An adaptable apparatus for strain characterisation was developed, which enabled quasi-steady-state strain characterisation of these novel FBGs over  $0 - 700 \mu\epsilon$  using an optical spectrum analyser, and dynamic strain characterisation in steps of  $10.5 \mu\epsilon$  over the range  $0 - 265 \mu\epsilon$ , using the SpectroBragg spectrometer. The strain response of these anisotropic FBGs ( $0.75 \times 10^{-6} \mu\epsilon^{-1}$ ) was similar to standard telecomms FBGs<sup>16</sup> (from the literature [21]:  $0.78 \times 10^{-6} \mu\epsilon^{-1}$ ; from the experiment:  $0.73 \times 10^{-6} \mu\epsilon^{-1}$ ).

The preservation of spectral profile under strain suggests that the anisotropic FBGs allow strain-temperature discrimination. In the range tested, strain does not significantly alter the spectral separation of the anisotropic FBG's component peaks, whereas the temperature changes tested have a greater effect and so alter the spectral profile. In terms of the generalised Stokes parameters the  $S_{\text{gen}_2}(\mathbf{r}_1, \mathbf{r}_2, \omega)$  term will exhibit the change in the peaks with temperature with larger changes than for applied strain, in comparison to the responses for isotropic FBGs under equivalent conditions. By measuring the bandwidth, such as the full-width at half-maximum, it would appear the temperature may be inferred, allowing the discrimination of strain. The bandwidth of a standard telecomms FBG requires much greater resolution to detect temperature-induced changes in spectral bandwidth.

---

<sup>14</sup>The ease of using a general purpose PC for data readout over USB would be of limited use for high-speed data sensing applications, as the asymmetric I/O scheduling of the hardware interrupts would impair performance. The hardware interrupts are the means by which components indicate to the CPU they need attention, e.g. data to be read in.

<sup>15</sup>Acting, at least, as polarisers.

<sup>16</sup>Similar in terms of linearity, and temporal response if not in terms of absolute magnitude.

### 7.2.3 Chapter 5, examination of polarisation mitigation approaches

Given the polarisation properties of the novel anisotropic FBG, and the polarisation rotation and phase retardation that fibre bends or twists introduce, a polarisation-sensitive demodulation system will report values dependent upon the SOP changes in addition to the property to be demodulated at the time of data capture. For the SpectroBragg, a coherence and polarisation-sensitive device, this means that in addition to the changes in  $\lambda_B$ , changes in SOP, DOP or DOC will modulate the  $\lambda_B$  value determined with the centroid calculation.

Also, for interference based systems, such as the SpectroBragg or the all-fibre Michelson interferometer (chapter 6), polarisation changes can have resolution limiting effects<sup>17</sup>.

An ideal depolariser decorrelates the orthogonal components of an arbitrary SOP. The Lyot depolariser decorrelates the  $\underline{\mathbf{W}}$  matrix entries over a frequency interval  $\Delta\omega$ . The Billings depolariser decorrelates a single  $\omega$  by taking a temporal range  $\Delta\tau$ , i.e. it operates in the temporal Fourier transform of the Lyot depolariser, hence its usefulness in interferometry. The fluctuations in correlation should be statistically stationary, at least in the wide sense, over the respective intervals.

Two alternative pseudo-depolarisation approaches were examined for use with the SpectroBragg<sup>18</sup>, using both the anisotropic and isotropic FBGs. These approaches were based upon separating the orthogonal polarisation components, modifying one component and then recombining the two components to achieve a reduction in polarisation change.

The polarisation fixing approach is to make all components of  $\underline{\mathbf{W}}$ , and by implication  $\underline{\mathbf{S}}_{\text{gen}}$ , constant. In the case where the output SOP aligns with one of the axes of  $\underline{\mathbf{W}}$ , all but one diagonal component reduce to zero which remains constant, i.e. the ideal polarisation fixer would take all arbitrarily polarised input SOPs and output a single, typically linear, SOP. In terms of the generalised Stokes parameters, outlined in §2.1.2.1 (page V.I - 18), the only non-zero terms would be

$$S_{\text{gen}_0}(\underline{\mathbf{r}}_1, \underline{\mathbf{r}}_2, \omega) = S_{\text{gen}_1}(\underline{\mathbf{r}}_1, \underline{\mathbf{r}}_2, \omega) = \begin{cases} W_{xx}(\underline{\mathbf{r}}_1, \underline{\mathbf{r}}_2, \omega) & \text{SOP } \parallel \text{ to } x \\ -W_{yy}(\underline{\mathbf{r}}_1, \underline{\mathbf{r}}_2, \omega) & \text{SOP } \parallel \text{ to } y \end{cases} \quad (7.1)$$

<sup>17</sup>Polarisation fading affects the visibility of interference fringes. Circularly polarised light does not have a unique amplitude zero-crossing when interfering with elliptically or linearly polarised light. Relative phase shifts between orthogonal components in non-commutating paths can result in multiple interferometer balance points dependent upon those relative phase shifts, e.g. when mixing orthogonal paths with the Faraday mirrors in chapter 6.

<sup>18</sup>The effectiveness of the approaches will differ for different demodulation systems and these results are specific to SpectroBragg type systems.

The ideal outcome is a single output SOP, coherently added, but with zero OPD. As reported by Tateda *et al.* [22], no current passive optical device will coherently add rotated SOP components without converting the phase shift describing the ellipticity into a non-zero OPD [22]. Consequently  $W_{xx}(\mathbf{r}_1, \mathbf{r}_2, \omega)$  becomes a function of  $\Phi_{\text{pol}}$ , as  $\omega = \omega(\Phi_{\text{pol}})$ , from equation (E.5) (page V.II E-2).

Two versions of a Mach-Zehnder interferometer based approach to SOP fixing were examined, based upon the ideas in [3,22]. After splitting the incident SOP into its orthogonal components, one SOP component was rotated so as to be parallel to the other SOP component. The two versions used a Lefèvre polarisation controller and a Faraday Mirror in conjunction with a circulator to achieve the rotation of the SOP component, respectively.

An approach based upon the balancing of PDL was also examined [4]. In this approach the losses in the orthogonal SOPs are balanced so that both orientations exhibit equal amplitude by the addition of an attenuator to balance the losses in the orthogonal components.

The greatest limitation to these techniques, as investigated, was the unwanted introduction of phase noise, which dominated the signal over the polarisation noise. Unbalancing the stationary Mach-Zehnder interferometer reduces the interferometric phase noise, but requires *a priori* knowledge of the coherence length of the source to adhere most closely to stationarity requirements, i.e. the decoherence becomes a function of  $\Delta\omega$ .

By combining the introduced decoherence approach of Takada *et al.* [3] with the polarisation fixing approach of Tateda *et al.* [22], the best polarisation mitigation of the approaches tested, as measured with the SpectroBragg, was achieved for the anisotropic FBG.

The PDL balancing approach's requirement for quasi-static system PDL was limited by the method of changing SOPs, which a deterministic polarisation controller may not have necessarily introduced. However, even under laboratory conditions with most fibre taped to a bench, the necessity of connecting to or reconnecting equipment that does not share the same plane as the bench will limit the quasi-static PDL achievable. In general for fibre sensors, a vectorial quantity transduced to the fibre will not necessarily preserve the system PDL, e.g. uniaxial pressure.

#### 7.2.4 Chapter 6, the use of $\pi$ -shift interferometry with the HTT to recover weak FBG signals

Young's experiment was used by Wolf to elaborate upon the unified theory of coherence and polarisation. A fibre Michelson interferometer interrogating an FBG signal has the possibility of being an unintentional, at least partial, implementation

of Wolf's basic apparatus [23], given possible rotations and phase retardation of the SOP, and so may reveal changes in the  $S_W$ ,  $\mathcal{P}_W$  and  $\eta_W$  quantities.

The arms of the all-fibre Michelson interferometer used in chapter 6 had Faraday mirrors so that the round-trip path length of orthogonal components would be equal. This presumes that the paths commute, which may not be the case. Also, if the SOPs recombining at the beam-splitter were not the same, the interferogram would be modulated by polarisation induced fading.

For example, circularly polarised light has no unique amplitude zero-crossing. If coherently<sup>19</sup> added to linearly or elliptically polarised light, a detector will experience a reduced interference fringe visibility.

As indicated in table 7.1 (page V.I - 321), scattering modifies the  $S_W$ ,  $\mathcal{P}_W$  and  $\eta_W$  quantities. Within a fibre, Rayleigh scattering centres are equivalent to randomly distributed weak-sources. Although the scattering centres are randomly distributed, the medium is termed *deterministic* [19], as the scattering centres do not change in time intervals of interest<sup>20</sup>.

The scattered radiation must then meet the waveguiding conditions to propagate. Electromagnetic radiation lost to the cladding modes is treated as attenuation. The guided electromagnetic radiation experiences a phase delay<sup>21</sup> with respect to the unscattered radiation and so modifies the mode. The phase shift is then preserved, so that upon illuminating a detector, the interference is observed either as phase noise, as reduced fringe visibility or as a broadened spectral profile.

The use of the Hilbert transform technique, HTT, with two-output,  $\pi$ -shift interferometry to demodulate fibre Bragg grating, FBG, signals is reported. The HTT uses the ratio of the slopes of the phase of the analytic signals of a reference and unknown signal to determine the wavelength value of the unknown signal, (§6.2.4 (page V.I - 271)). The FBG signals traversed a 19.5 km length of fibre. The signal had significant noise from Rayleigh scattering and additionally from the amplification required to obtain a signal.

The experiment was intentionally performed at the limits of signal recovery to illustrate the improvement attainable. FBG signals were successfully demodulated where use of single-output interferometry did not recover the same signal, as it was obscured by background-noise. Two-step recalibration provided a signal that retained the relative FBG to reference laser intensity ratios, as obtained by an OSA over a short ( $\sim 10$  m) patch lead.

The centroid and HTT methods of determining the mean wavelength of the

---

<sup>19</sup>The orthogonal components may be correlated but will not interfere.

<sup>20</sup>Unlike turbulent air, the scattering centres are 'frozen into' the fibre upon cooling. The scattering that occurs does not change across time intervals for otherwise uniform conditions.

<sup>21</sup>Equivalent to the OPD introduced by the difference between the core refractive index and the effective index of the scattering centre.

FBG were examined and compared. As expected, the centroid calculation was very sensitive to the noise level, whereas the sensitivity of the HTT could be optimised by adjusting the length of the unwrapped phase used in the linear regression fit. The limits to the HTT discussed in [24] might not strictly apply, as the interferogram used was synthesised, rather than obtained by zero-OPD triggering.

The two-output  $\pi$ -shift approach gave better SNR and elimination of Rayleigh scattering induced phase noise when using two-beam interferometers, such as the Michelson or Mach-Zehnder. The most significant limitation in this work was the artefact of side-peaks near the FBG spectra induced by the scan recalibration technique, as shown in figure 6.15 (page V.I - 285).

The recovered temperature response of the sensor FBG, was examined for variable and different fixed interferogram lengths. The variable interferogram length temperature response was  $5.42 \times 10^{-6} \text{ }^\circ\text{C}^{-1}$ , with an uncertainty of 32 pm and for the fixed interferogram length case was  $5.31 \times 10^{-6} \text{ }^\circ\text{C}^{-1}$ , with an uncertainty of 70 pm for the HTT. These values are lower than the literature results [21], and may be due to different actual temperatures being experienced by the FBG and thermistor sensor of the oven, or incorrect thermistor values reported by the oven controller.

However, an apparent dependence of the temperature response value on the length of the interferogram chosen was observed. This led to the optimum interferogram length<sup>22</sup>,  $n_i$ , being ambiguous and the recovered temperature response value changing between a minimum of  $5.29 \times 10^{-6} \text{ }^\circ\text{C}^{-1}$  and a maximum of  $5.34 \times 10^{-6} \text{ }^\circ\text{C}^{-1}$ .

These changes in value were observed for both the centroid and HTT approaches, and were likely introduced during the recalibration process. It should be noted that the changes are not the same for the centroid and HTT approaches. However, neither is the subsequent processing of the data.

The successful use of FBG sensor demodulation using the HTT approach is shown for low SNR signals using the complementary  $\pi$ -shifted outputs of an all-fibre interferometer. The deleterious effects of Rayleigh scattering upon phase noise, and other common-mode noises are eliminated, improving the performance of the HTT technique for demodulating long distance sensors. The HTT approach, with appropriate Hamming window length, allows the effects of the changes in  $n_i$  to be mitigated, such that the changes are below the accuracy presented.

---

<sup>22</sup> $n_i = 4$ , the closest value to the average temperature response.

## 7.3 Future investigations

In performing this work the following questions arose and are outstanding:

- Chapter 3, the development of the SpectroBragg
  - The mounting of individual SpectroBragg components had superfluous degrees of freedom for the assembly of the SpectroBragg. Future work might look at the use of cheaper mounting components, which would provide only those degrees of freedom required. Also, by using shorter supports for the components, i.e. keeping the components closer to the bench, there would be less possible cantilever action, which may reduce the system sensitivity to environmental effects.
  - Commercially available diffraction gratings, such as those employed in the SpectroBragg, rely upon collimated illumination to provide the highest quality diffracted orders. The aberrations are compensated in the Čzerny–Turner by the second mirror, i.e. after the diffraction grating. Future work could attempt to remove the aberrations prior to illuminating the diffraction grating. If possible, this may also lead to a more flexible component positioning or system footprint as the restrictions of equation (3.18) (page V.I - 132) would not be needed. This could simplify the assembly of a Čzerny–Turner type system if arranged upon its own mounting board.
  - The assembly of the SpectroBragg on a movable optical bench or optical board would have been beneficial, although it may have increased vibrational sensitivity.
  - Simplifying the assembly of the SpectroBragg would be necessary if such a device were to be commercialised. Without the machining of a customised mounting, as recommended in [25], reproducible quality of assembly would require highly specialised skillful work.
  - Exploring various means to expand the spectral range of the SpectroBragg, while preserving the achieved resolution, e.g. by use of mirrored end–face prisms or by stacked diffraction gratings.
- Chapter 4, strain characterisation of novel anisotropic FBG
  - The difference between the strain response value reported here<sup>23</sup> and the isotropic FBG literature value needs to be examined, as to whether the

---

<sup>23</sup>Given that the strain responses of the examined isotropic and anisotropic FBGs primarily depends upon the material strain response of the SMF–28 fibres, the experimental strain response values would be expected to have been closer to the literature value, which also used SMF–28.

difference is intrinsic, or an artefact of the experiments performed here. The published temperature response of the novel anisotropic FBGs agrees with the literature value for isotropic FBGs. The anisotropic FBG's strain response should depend upon the material's strain response in a similar fashion to the isotropic FBGs.

- Chapter 5, polarisation mitigation approaches
  - As higher resolution results are increasingly being sought, polarisation effects can be expected to become ever more important and their mitigation or minimisation critical. Further investigation of the various issues mentioned in determining the performance limits of the different approaches is needed before a full conclusion can be arrived at. This work may be considered as an initial investigation of these approaches for use with devices such as the SpectroBragg.
  - An interesting question which arose was whether the performance of the approaches relied upon the specific area of the Poincaré sphere covered. In particular, did the improvement obtained by the Lefèvre controller approach depend upon the coverage of the sphere that was likely to be experienced? The use of a deterministic polarisation controller instead of the twisting of the FC/APC connector, and the use of a polarimeter before and after the polarisation mitigation approach, would be the ideal experimental apparatus to evaluate these schemes.
  - The construction of a 'generalised polarimeter', to measure the generalised Stokes parameters would be very useful in evaluating any polarisation mitigation scheme, as it would provide information on both the SOP, DOP and DOC of the output signal.
  - The effects of these polarisation mitigation schemes upon mixed high- and low-coherence signal, such as might occur with reference signals. In catering for the coherence length of the high-coherence source, do artefacts arise in the low-coherence signal?
- Chapter 6, HTT analysis of  $\pi$ -shifted interferograms
  - As for the strain characterisation of the anisotropic FBGs (see chapter 4) above), determining the origin of the discrepancy between the experimental temperature response of the FBGs and the literature value.
  - Determining the source of the side-bands observed during recalibration, and steps to reduce or eliminate their magnitude would simplify, and speed up, the data processing.

- Determining the source of the oscillation of the temperature response slope changes with interferogram length,  $n_i$ . If the oscillation could be minimised or modified such that an optimum  $n_i$  value became obvious, it would enable the best  $\pi$ -shifted HTT system performance.
- Investigate whether possible stiction events in the fibre stretcher impact upon the performance of the all-fibre interferometer.

## 7.4 References

- [1] A. Dragomir, D. N. Nikogosyan, K. A. Zagorulko, P. G. Kryukov, and E. M. Dianov. Inscription of fiber Bragg gratings by ultraviolet femtosecond radiation. *Opt. Lett.*, 28(22):2171–2173, 2003.
- [2] D. N. Nikogosyan. Multi-photon high-excitation-energy approach to fibre grating inscription. *Meas. Sci. Technol.*, 18(1):R1–R29, January 2007.
- [3] K. Takada, K. Okamoto, and J. Noda. New fiber-optic depolarizer. *J. Lightwave Technol.*, 4(2):213–219, February 1986.
- [4] H. Dong, J. Q. Zhou, M. Yan, P. Shum, L. Ma, Y. D. Gong, and C. Q. Wu. Quasi-monochromatic fiber depolarizer and its application to polarization-dependent loss measurement. *Opt. Lett.*, 31(7):876–878, 2006.
- [5] D. A. Flavin, R. McBride, and J. D. C. Jones. Short optical path scan interferometric interrogation of a fibre Bragg grating embedded in a composite. *Electron. Lett.*, 33(4):319–321, 1997.
- [6] D. A. Flavin, R. McBride, and J. D. C. Jones. Short-scan interferometric interrogation and multiplexing of fibre Bragg grating sensors. *Opt. Commun.*, 170(4-6):347 – 353, November 1999.
- [7] K. B. Rochford and S. D. Dyer. Demultiplexing of interferometrically interrogated fiber Bragg grating sensors using Hilbert transform processing. *J. Lightwave Technol.*, 17(5):831–836, 1999.
- [8] K. T. O’Mahoney. *Fourier Transform Spectroscopic Demodulation of Fibre Bragg Grating arrays*. PhD thesis, School of Science, Waterford Institute of Technology, Ireland., July 2007.
- [9] E. Wolf. Unified theory of coherence and polarization of random electromagnetic beams. *Phys. Lett. A*, 312(5-6):263–267, 2003.
- [10] G. Gbur and T. D. Visser. *The structure of partially coherent fields*, volume 55 of *Progress in Optics*, chapter 5, pages 285–341. Elsevier, Amsterdam, 2010. ISBN: 9780444537058.
- [11] O. Korotkova and E. Wolf. Effects of linear non-image-forming devices on spectra and on coherence and polarization properties of stochastic electromagnetic beams: part II: examples. *J. Mod. Optic.*, 52(18):2673–2685, 2005.

- 
- [12] E. Wolf, J. T. Foley, and F. Gori. Frequency shifts of spectral lines produced by scattering from spatially random media. *J. Opt. Soc. Am. A*, 6(8):1142–1149, August 1989.
- [13] E. Wolf and O. Korotkova. Generation of stochastic electromagnetic beams with prescribed coherence and polarization properties by means of random phase screens and some uses of such beams. In *Workshop on aspects of rough surface scattering and related phenomena*. June 2006.
- [14] G. Gbur, T. D. Visser, and E. Wolf. Singular behavior of the spectrum in the neighborhood of focus. *J. Opt. Soc. Am. A*, 19(8):1694–1700, August 2002.
- [15] J. J. Stamnes. *Waves in Focal Regions*, chapter 16, pages 455–500. Adam Hilger Series on Optics and Optoelectronics. Adam Hilger imprint, IOP Publishing, Ltd., Bristol, 1986. ISBN: 0852744684.
- [16] M. Francon. *Diffraction: Coherence in Optics*, chapter 5, pages 53–97. Pergamon Press Ltd., Oxford, 1966.
- [17] E. G. Loewen and E. Popov. *Diffraction Gratings and Applications*, volume 58 of *Optical Engineering*, chapter 2, pages 25–55. Marcel Dekker, Inc., New York, 1997. ISBN: 0824799232.
- [18] M. C. Hutley. *Diffraction Gratings*, chapter 2, pages 13–56. Techniques in Physics. Academic Press, Inc. Ltd., London, 1982. ISBN: 0123629802.
- [19] E. Wolf. *Introduction to the Theory of Coherence and Polarization of Light*, chapter 6, pages 111–128. Cambridge University Press, Cambridge, 2007. ISBN: 9780521822114.
- [20] E. G. Loewen and E. Popov. *Diffraction Gratings and Applications*, volume 58 of *Optical Engineering*, chapter 12, pages 437–480. Marcel Dekker, Inc., New York, 1997. ISBN: 0824799232.
- [21] A. D. Kersey, M. A. Davis, H. J. Patrick, M. LeBlanc, K. P. Koo, C. G. Askins, M. A. Putnam, and E. J. Friebele. Fiber grating sensors. *J. Lightwave Technol.*, 15(8):1442–1463, August 1997.
- [22] M. Tateda and T. Omatsu. Polarization state fixer composed of passive optical devices. *J. Opt. Soc. Am. A*, 20(2):342–346, February 2003.
- [23] E. Wolf. *Introduction to the Theory of Coherence and Polarization of Light*, chapter 9, pages 174–201. Cambridge University Press, Cambridge, 2007. ISBN: 9780521822114.
- [24] S. D. Dyer, P. A. Williams, R. J. Espejo, J. D. Kofler, and S. M. Etzel. Fundamental limits in fiber Bragg grating peak wavelength measurements. In *Proceedings of the 17th International Conference on Optical Fibre Sensors*, volume 5855, pages 88–93. SPIE, May 2005.
- [25] J. F. James. *Spectrograph Design Fundamentals*, chapter 17, pages 172–174. Cambridge University Press, Cambridge, 2007. ISBN: 0521864631.
-

# Notation

$\alpha$	Angle of reflection at mirror $M_1$ , V.I - 132
$\alpha_{sc}$	Rayleigh scattering loss coefficient, V.I - 31
$\underline{\underline{\alpha}}_{T\varepsilon\sigma}$	Linear thermal expansion coefficient, V.I - 36
$\underline{\underline{\alpha}}_T$	Thermal expansion, V.I - 35
$\alpha_t$	Coefficient of twist effect for doped silica single-mode fibre, V.I - 55
$\beta$	Angle of reflection at mirror $M_2$ , V.I - 132
$\underline{\underline{\beta}}_m$	Magnetothermal effects, V.I - 35
$\underline{\underline{\beta}}(z)$	Plane propagation constant, V.II F-4
$\beta_T$	Volume thermal expansivity, V.I - 45
$\beta_\phi$	phase difference between the centre and edge of the beam, V.I - 124
$\beta_A$	Magnification by a focusing element, V.II K-4
$\chi_{pol}$	Ellipticity of polarisation ellipse, V.II E-2
$\chi$	Longitude angle, V.I - 235
$\underline{\underline{\chi}}_{em,me}$	Magnetoelectricity ( $\underline{\underline{\chi}}_{em}$ is not necessarily equal to $\underline{\underline{\chi}}_{me}$ ), V.I - 35
$\underline{\underline{\chi}}_e$	Electric susceptibility, V.II A-2
$\underline{\underline{\chi}}_m$	Magnetic susceptibility, V.II A-2
$\delta_{OPD}$	Change in optical path difference, V.I - 224
$\underline{\underline{\epsilon}}_\sigma$	Strain, V.I - 35
$\underline{\underline{\epsilon}}_r$	Elastic deformation induced dielectric perturbation, V.I - 52
$\underline{\underline{\epsilon}}_0$	Permittivity of free space, V.II A-2
$\underline{\underline{\eta}}$	FBG mode overlap parameter, V.I - 174
$\eta_B$	Birefringence per unit length, V.I - 56
$\eta_m$	Diffraction grating efficiency, V.I - 128
$\eta_{\text{FBG}}(V)$	Fraction of integrated fundamental mode intensity contained in the core, V.II G-7

---

$\eta(\mathbf{r}_Q)$	Square root of ratio of interfering intensities, V.II B-4
$\eta_W(\mathbf{r}_1, \mathbf{r}_2, \omega)$	spectral degree of coherence, V.I - 19
$\eta_i$	Ratio of phase of FBG <sub><i>i</i></sub> to reference, V.I - 271
$\eta_{\text{creep}}$	Viscosity of material creep, V.I - 42
$\gamma(\mathbf{r}_1, \mathbf{r}_2, \tau)$	Complex degree of coherence, V.II B-3
$\underline{\underline{\Gamma}}(\mathbf{r}_1, \mathbf{r}_2, t_1, t_2)$	Cross-correlation function, mutual coherence function when $t_2 = t_1 + \tau$ , V.II B-3
$(\infty_m m \dagger)$	Cylindrical symmetry in Hermann–Mauguin notation, V.I - 28
$\underline{\underline{\kappa}}_{\text{att}}$	Attenuation index, V.II A-4
$\kappa_{\text{CM}mq}(z)$	Oscillating, “AC”, mode coupling coefficient, V.II G-6
$\underline{\underline{\kappa}}_{\varepsilon\sigma}$	Strain sensitivity of a length of fibre, V.I - 43
$\underline{\underline{\kappa}}_T$	The temperature sensitivity of the length of fibre, V.I - 46
$\Lambda$	Grating perturbation periodicity, V.I - 62
$\lambda_B$	Bragg condition wavelength, V.I - 62
$\Lambda_{\text{FBG}}$	FBG period or pitch, V.I - 174
$\underline{\underline{\lambda}}_{\text{res}}$	Resultant FBG wavelength after shift from initial position, V.I - 174
$\delta\lambda_{B\text{FWHM}}$	Full-width at half-maximum of FBG bandwidth, V.II G-8
$\lambda_{B\text{avg}}$	Average Bragg wavelength from orthogonal components, V.I - 175
$\lambda_{B\text{dif}}$	Differential Bragg wavelength from orthogonal components, V.I - 175
$\lambda_c$	Centroid wavelength, V.I - 133
$\delta\lambda_{\text{CM}}$	FBG wavelength detuning or spectral broadening, V.II G-7
$\underline{\underline{\underline{\lambda}}}_{\sigma\varepsilon}$	Elastic stiffness tensor, V.I - 36
$\underline{\underline{\underline{\lambda}}}_{\sigma\varepsilon} \left( \underline{\underline{\underline{\mathbf{c}}}}_{\sigma\varepsilon}, \underline{\underline{\underline{\mathbf{s}}}}_{\varepsilon\sigma} \right)$	Elasticity (stiffness, compliance), V.I - 35
$\Lambda_{\text{PM}}$	Pitch of phase-mask, V.I - 174
$\overline{\lambda}_{\text{ref}}$	Mean reference wavelength, V.I - 271
$\Delta\lambda_{\text{peaks}}$	Difference in side-peak wavelength positions with respect to reference laser peak, V.I - 286
$\underline{\underline{\underline{\mu}}}_0$	Permeability of free space, V.II A-2

---

---

$\mu_W(\mathbf{r}_1, \mathbf{r}_2, \omega)$	Spectral degree of coherence, V.II B-5
$\mu_{\Delta\text{SOP}}$	Mean value of polarisation changes, V.I - 247
$\mu$	Mean value of background data, V.I - 247
$\nabla^2$	The Laplacian operator, V.II A-6
$\nabla$	The gradient operator, V.II A-1
$\nu_\sigma$	Poisson's ratio, V.I - 39
$\nu$	Frequency, V.II A-5
$\omega$	Angular frequency, V.I - 18
$\bar{\omega}$	Mean angular frequency, V.II C-3
$\Omega$	Solid angle subtended at the centre of Poincaré sphere by a closed path at the surface, V.II E-7
$\otimes$	<i>Kronecker</i> or <i>Direct</i> product, V.I - 16
$\Delta\Phi_{\varepsilon\sigma}$	Phase shift for an applied strain, under constant temperature, V.I - 43
$\Phi_{GP}$	Geometric phase shift, V.II E-7
$\Delta\Phi_T$	The phase shift experienced by a path $L$ , of fibre experiencing a change in temperature, $\Delta T(\mathbf{r}, t)$ , V.I - 46
$\Phi(t)$	Temporal phase, V.II C-1
$\phi(t)$	Temporal phase function, V.I - 267
$\phi_{pr}$	Phase retardance angle, V.I - 227
$\Pi$	Electrothermal effects, V.I - 35
$\psi_{\text{pol}}$	Azimuthal angle of polarisation ellipse, V.II E-2
$\psi$	Latitude angle, V.I - 235
$\underline{\psi}$	Propagating wave equation, V.II A-3
$\rho_{\text{Int.}}$	SpectroBragg and polarimeter intensity cross-correlation coefficient, V.II N-1
$\rho_{\lambda_B}$	SpectroBragg intensity and centroid calculated $\lambda_B$ cross-correlation coefficient, V.II N-1
$\rho_{xy}(\tau)$	Normalised cross-covariance function, V.I - 246
$\underline{\rho}(\mathbf{r}, t)$	The electric charge density, V.II A-1
$\underline{\underline{\sigma}}_{P_j}$	Pauli spin matrices, V.I - 16, V.I - 55
$\sigma_{\text{FBG}}$	General "DC" mode self-coupling coefficient, V.II G-7
$\sigma_{SB}$	The Stefan-Boltzmann constant, V.I - 44

---

---

$\underline{\underline{\sigma}}_{EM}$	Specific conductivity, V.II A-3
$\sigma_{CM_{mq}}(z)$	Average, “DC”, mode coupling coefficient, V.II G-6
$\sigma_{Int.}$	Normalised standard deviation of intensity, V.II N-1
$\sigma_{bg}$	Standard deviation of background data, V.I - 247
$\underline{\underline{\sigma}}$	Stress, V.I - 35
$\sigma_{\Delta SOP}$	Standard deviation of polarisation changes, V.I - 247
$\sigma_{\lambda_B}$	Standard deviation of peak wavelength, $\lambda_B$ , V.I - 247
$\sigma_{\lambda_B}$	Normalised standard deviation of centroid calculated $\lambda_B$ , V.II N-1
$\tau_c$	Coherence time, V.II B-5
$\tau_{exp}(t)$	Interferogram sampling time interval step or time base, V.I - 270
$\theta_{FR}(\omega)$	The angle of Faraday effect rotation, V.I - 49
$\theta_{HWP}$	HWP rotation, V.I - 55
$\theta_c$	Critical angle of refraction, V.II F-1
$\theta_d$	Diffraction angle, V.I - 124
$\theta_{act}$	The recorded temperature in $\pi$ -shift experiment, V.I - 277
$\theta_{set}$	The intended temperature set in $\pi$ -shift experiment, V.I - 277
$\theta_{\Delta}$	Dihedral angle between subsequent Stokes vectors, V.I - 236
$\theta_{rot}$	Polarisation rotation angle, V.I - 240
$\varphi(t)$	Interferogram linear phase angle, V.I - 270
$\varphi_{FBG_1}(t)$	FBG <sub>1</sub> unwrapped phase angle, V.I - 271
$\varphi_{FBG_2}(t)$	FBG <sub>2</sub> unwrapped phase angle, V.I - 271
$\Delta_i \overline{\lambda_B}$	Difference in average $\lambda_B$ with $n_i$ , V.II R-18
$\Delta_i \delta_{\lambda_b}$	$i$ lambda wavelength differences centroid standard deviation, V.II R-18
$\Delta_w \overline{\lambda_B}$	Difference in average $\lambda_B$ with $n_w$ , V.II R-2
$\Delta_w \delta_{\lambda_B}$	Difference in standard deviation of $\lambda_B$ with $n_w$ , V.II R-2

---

---

$\theta_{\text{HWP}}$	Angle through which fibre coil is rotated to produce HWP rotation, V.I - 55
ADC	Analog-to-digital converter, V.I - 91
$b(\mathbf{r}, \omega)$	Amplitude of analytic signal, V.II C-1
$\mathbf{B}(\mathbf{r}, t)$	The magnetic induction, V.II A-1
$\underline{\underline{\mathbf{B}}}_\varepsilon$	<i>Reciprocal dielectric constant or impermeability</i> , V.I - 35
$B$	Birefringence, V.I - 173
$B_{\text{ind}}$	Induced birefringence, V.I - 51, V.I - 173
$B_{\text{ins}}$	Inscribed birefringence, V.I - 173
$B_{\text{PMF}}$	Birefringence of PMF, V.I - 55
$B_{f-s}$	Waveguide birefringence, V.I - 51
$C_{\infty v}$	Cylindrical symmetry in Schoenflies notation, V.I - 28
$\underline{\underline{C}}_{\mathbf{M}}^{\mathbf{E}}$	Converse magnetoelectric effect, V.I - 32
$\underline{\underline{C}}_{\underline{\underline{\varepsilon}}\sigma}^{\mathbf{E}}$	Converse piezoelectric effect, V.I - 32
$\underline{\underline{C}}_{\underline{\underline{\varepsilon}}\sigma}^{\mathbf{H}}$	Converse piezomagnetic effect, V.I - 32
$\underline{\underline{C}}_{\mathbf{P}}^{\mathbf{H}}$	Direct magnetoelectric effect, V.I - 32
$\underline{\underline{C}}_{\mathbf{P}}^{\sigma}$	Direct piezoelectric effect, V.I - 32
$\underline{\underline{C}}_{\mathbf{M}}^{\sigma}$	Direct piezomagnetic effect, V.I - 32
$\underline{\underline{C}}_S^{\mathbf{E}}$	Electrocaloric effect, V.I - 32
$\underline{\underline{C}}_S^{\mathbf{H}}$	Magnetocaloric effect, V.I - 32
$\underline{\underline{C}}_S^{\sigma}$	Piezocaloric effect, V.I - 32
$\underline{\underline{C}}_{\mathbf{P}}^T$	Pyroelectric effect, V.I - 32
$\underline{\underline{C}}_{\mathbf{M}}^T$	Pyromagnetic effect, V.I - 32
$c_{V,p}$	Specific heat (fixed volume, $V$ , or fixed pressure, $p$ ), V.I - 35

---

---

$\underline{c}$	Speed of light, V.II A-4
$C_{2v}$	Symmetry with two vertical mirror planes, in Schoenflies notation, V.I - 28
$\underline{\underline{C}}$	Coherency matrix, V.I - 16
COTS	<b>Commercial off-the-shelf</b> , V.I - 151
$C_{xy}(\tau)$	Covariance function, V.I - 246
CP modes	Circularly polarised modes, V.I - 24
CRN	<b>Continuous random network</b> , V.I - 27
$\underline{\underline{D}}(\mathbf{r}, t)$	The electric displacement, V.II A-1
$d$	Fibre core diameter, V.I - 174
$\underline{D}_{ft}$	Constant characterising the magnitude of $\Delta n_{co}(z)$ , V.I - 31
det	Determinant of a matrix, V.I - 16
$dQ$	Heat received per unit volume, V.I - 36
DSF	<b>Dispersion shifted fibre</b> , V.I - 312
$dU$	Change in internal energy per unit volume, V.I - 36
$dW$	Work done per unit volume, V.I - 36
$\underline{\underline{e}}_{\sigma \rightarrow d}$	The direct piezoelectric effect, V.I - 43
$E_{\sigma}$	Modulus of elasticity, V.I - 39
$\underline{\underline{e}}_E$	Piezoelectricity, V.I - 35
$E_H(\mathbf{r}_O, \mathbf{r}_I)$	<i>Eikonal</i> function, V.II K-2
$EH_{lm}$ or $HE_{lm}$	Hybrid modes, V.I - 24
$\underline{\underline{E}}$	Electric Field, V.I - 35
$e_b$	The emissive power, V.I - 44
EWOFS07	Third European workshop on optical fibre sensors, V.I - 190
$\mathbb{E}$	Expectation value, V.I - 240
$\underline{\underline{f}}_T$	Heat of deformation, V.I - 35
$\underline{\underline{f}}$	<i>Photoelastic</i> or <i>Pockels</i> tensor in terms $\underline{\underline{P}}$ , V.I - 36
$-\underline{\underline{f}}_T$	Thermal pressure, V.I - 35
FC/APC	<b>Fibre coupled, angle polished connector</b> or <b>FC</b> connector, <b>angled physical contact</b> , V.I - 52

---

---

FC/PC	<b>F</b> ibre coupled, <b>p</b> olished <b>c</b> onector of <b>FC</b> connector, <b>p</b> hysical <b>c</b> ontact, V.I - 82
FFT	<b>F</b> ast <b>F</b> ourier <b>t</b> ransform, V.I - 85
FBG	<b>F</b> ibre <b>B</b> ragg <b>g</b> rating, V.I - 62
$\mathcal{F}$	The Fourier transform, V.I - 279
$G_\sigma$	Shear modulus, V.I - 39
$G(x; \underline{a})$	Gaussian function, V.I - 134
$G_b(T, \underline{\mathbf{E}}, \underline{\boldsymbol{\sigma}})$	Gibbs free energy, V.I - 36
GPIB	<b>G</b> eneral <b>P</b> urpose <b>I</b> nterface <b>B</b> us, V.I - 208
<b>H</b>	Magnetic Field, V.I - 35
HWP	<b>H</b> alf- <b>w</b> ave <b>p</b> late, V.I - 54
$HE_{lm}$ or $EH_{lm}$	Hybrid modes, V.I - 24
HiBi	<b>H</b> igh <b>b</b> irefringence fibre, V.I - 55
HTT	<b>H</b> ilbert <b>t</b> ransform <b>t</b> echnique, V.II R-1
$I_\nu$	Spectral intensity as a function of $\nu$ , i.e. a spectrum, V.II D-3
$I_{tot}$	Total sum of the intensity of polarised and unpolarised components, V.II E-5
<b>I</b>	Identity matrix, V.I - 35
$I_{inf}$	Information capacity of the measured intensity, V.II D-3
$I$	Intensity, V.II A-5
$I_{pol}$	Sum of the intensity of the polarised components, V.II E-5
$J_l$	Bessel function of the first kind, V.I - 23
$\mathbf{J}(\underline{\mathbf{r}}, t)$	The electric current density, V.II A-1
$\underline{\underline{J}}_{\mathbf{a}}(x)$	Jacobian matrix, V.I - 134
$J_m$	$m^{th}$ order Bessel function, V.I - 128
$\underline{\underline{J}}_{ID}$	$2 \times 2$ Identity matrix, V.I - 222
$\underline{\underline{J}}_{LHP}$	Jones matrix for LHP SOP, V.I - 221
$\underline{\underline{J}}_{LVP}$	Jones matrix for LVP SOP, V.I - 221
$\underline{\underline{J}}_{PMF}$	Jones matrix for PMF, V.I - 55
$\underline{\underline{J}}_{SOP-f}$	Jones matrix for SOP fixer, V.I - 222
$\underline{\underline{J}}_{rot}$	Jones matrix for polarisation rotator, V.I - 222

---

---

$\underline{\underline{\mathbf{J}}}_{\text{sys}}$	Jones matrix for optical system, V.II E-12
$\underline{\underline{\mathbf{J}}}_{\text{Y-coupler}}$	Jones matrix for Y-coupler, V.I - 222
$K_{\text{NA}}$	Numerical aperture of fibre, V.I - 174
$K_l$	Bessel function of the second kind; Hankel function, V.I - 23
$\underline{\underline{\mathbf{k}}}_T$	Material thermal conductivity, V.I - 44
$\underline{\underline{\mathbf{k}}} = k\mathbf{s}$	Propagation or wave vector, V.I - 123
$K(\vartheta_{rs})$	Kirchhoff's obliquity factor, V.II B-12
$L_B$	Beat length, V.I - 51
$\underline{\underline{L}}_{\text{coh}}$	Coherence length (along orthogonal axes), V.I - 31
$L_{\text{FBG}}$	FBG gauge length, V.I - 174
$LCP$	<b>L</b> eft- <b>c</b> ircular <b>p</b> olarisation, V.I - 21
$l$	Length, V.I - 65
$l_c$	Coherence length, V.II B-6
$L_I$	Direction cosine (along with $M_I, N_I$ ), V.II K-2
$LHP$	<b>L</b> inear <b>h</b> orizontal <b>p</b> olarisation, V.I - 21
$L - 45P$	<b>L</b> inear <b>p</b> olarisation at $-45^\circ$ , V.I - 21
$L + 45P$	<b>L</b> inear <b>p</b> olarisation at $+45^\circ$ , V.I - 21
$LVP$	<b>L</b> inear <b>v</b> ertical <b>p</b> olarisation, V.I - 21
LP $_{ij}$ modes	Linearly polarised $i, j$ modes, V.I - 24
$M_1$	Mirror $M_1$ , collimating mirror, V.II K-14
$M_2$	Mirror $M_2$ , focusing mirror, V.II K-14
$\underline{\underline{\mathbf{M}}}$	Induced magnetisation, V.I - 35
$M_I$	Direction cosine (along with $L_I, N_I$ ), V.II K-2
( $mm2$ )	Orthorhombic lattice (sides $a \neq b \neq c$ ) symmetry in Hermann-Mauguin notation [mirror-mirror-rotation( $\pi$ )], V.I - 28
$\underline{\underline{\mathbf{M}}}_{\text{attenuator}}$	Mueller matrix for variable attenuator, V.I - 227
$\underline{\underline{\mathbf{M}}}_{\parallel}$	Linear Mueller matrix for parallel orientation, V.I - 226
$\underline{\underline{\mathbf{M}}}_{\perp}$	Linear Mueller matrix for perpendicular orientation, V.I - 226
$\underline{\underline{\mathbf{M}}}_{pr}$	Mueller matrix for phase retardance, V.I - 240

---

---

$\underline{\underline{\mathbf{M}}}_{\text{SOP-f}}$	Mueller matrix for SOP fixer, V.I - 222
$\underline{\underline{\mathbf{M}}}_{\text{rot}}$	Mueller matrix for polarisation rotator, V.I - 240
$\underline{\underline{\mathbf{M}}}_{\text{sys}}$	Mueller matrix for optical system, V.II E-10
$\underline{\underline{\mathbf{M}}}_{\text{TE}}$	Mueller matrix for transverse electric orientation, V.I - 239
$\underline{\underline{\mathbf{M}}}_{\text{TM}}$	Mueller matrix for transverse magnetic orientation, V.I - 239
$\underline{\underline{\mathbf{M}}}_{\text{J}}$	Mueller–Jones matrix, V.I - 18
$\underline{n}_{cl}$	Optical fibre cladding refractive index, V.I - 25
$\underline{n}_{co}$	Optical fibre core refractive index, V.I - 25
$N$	Number of data points in digitised signal, V.I - 91
$\underline{n}_{\text{eff}}$	Effective refractive index, V.I - 25
$\overline{\Delta n}$	Mean FBG refractive index, V.I - 174
$\Delta \underline{n}_{\text{FBG}}$	Induced FBG refractive index modulation, V.I - 174
$\underline{n}_g$	Group refractive index, V.I - 25
$n_i$	Non–negative integers used in incremental interferometer length, V.I - 298
$\overline{\Delta n}_{\text{eff}}(z)$	Average effective refractive index, V.II G-6
$n_{\text{avg}}$	Average fibre core refractive index, V.I - 177
$n_{\text{dif}}$	Modulation of fibre core refractive index, V.I - 177
$\underline{\underline{n}}$	Absolute refractive index matrix (including Bianisotropy), V.II A-4
$n_w$	Non–negative integers used in window width, $\pm(2n_w + 1)$ , V.I - 290
NA	Numerical aperture, V.II F-2
$n_{f,s}$	Refractive index of fast and slow axes, V.II E-9
$N_I$	Direction cosine (along with $L_I, M_I$ ), V.II K-2
ODL	<b>O</b> ptical <b>d</b> elay <b>l</b> ine, V.I - 230
OPD	<b>O</b> ptical <b>p</b> ath <b>d</b> ifference, V.I - 60
OTDR	<b>O</b> ptical <b>t</b> ime <b>d</b> omain <b>r</b> eflectometry, V.I - 60

---

---

OSA	<b>O</b> ptical spectrum <b>a</b> nalyser, V.I - 129
$\mathcal{P}$	Cauchy principal value, V.II C-2
$\mathcal{P}$	Degree of polarisation, DOP, V.I - 224
$\mathcal{P}_{W_Q}(\mathbf{r}_Q, \omega)$	Spectral degree of polarisation, V.I - 20
$\underline{\underline{\mathbf{p}}}_{B\varepsilon\sigma}$	<i>Photoelastic, elasto-optic or strain-optic</i> tensor, V.I - 36
PBS	<b>P</b> olarisation <b>b</b> eam- <b>s</b> plitter, V.I - 224
PID	<b>P</b> roportional- <b>i</b> ntegral- <b>d</b> erivative controller, V.I - 277
PDG	<b>P</b> olarisation <b>d</b> ependent <b>g</b> ain, V.I - 56
PDL	<b>P</b> olarisation <b>d</b> ependent <b>l</b> oss, V.I - 56
$\underline{\mathbf{P}}$	Induced polarisation, V.I - 35
PMF	<b>P</b> olarisation <b>m</b> aintaining fibre, V.I - 55
PPLN	<b>P</b> eriodically- <b>p</b> oled <b>l</b> ithium <b>n</b> iobate, V.I - 195
$\underline{\mathbf{q}}$	Heat flux, V.I - 44
$\underline{\underline{\mathbf{q}}}_{B\varepsilon\sigma}$	Piezo-optical tensor, V.I - 42
$\underline{\underline{\mathbf{q}}}_M$	Piezomagnetism, V.I - 35
QWP	<b>Q</b> uarter- <b>w</b> aveplate, V.I - 54
$\underline{\mathbf{r}}_{co}$	Radius of fibre core, V.II F-4
$\mathcal{R}_{xy}$	Cross-correlation function, V.I - 240
$\mathcal{R}_{\text{FBG}}$	FBG reflectivity, V.I - 174
$\underline{\underline{\mathbf{r}}}$	<i>linear electro-optic tensor</i> in terms of $\underline{\mathbf{E}}$ , V.I - 36
$\underline{\mathbf{r}}$	Position vector, V.II A-1
$\mathcal{R}_{\text{Int.}}$	Temporal cross-correlation of the unfiltered and filtered SpectroBragg and the polarimeter data, V.II N-2
$R_1$	Radius of mirror $M_1$ , V.I - 132
$R_2$	Radius of mirror $M_2$ , V.I - 132
$\Re$	The real component of complex number, V.II A-6
$RCP$	<b>R</b> ight- <b>c</b> ircularly <b>p</b> olarisation, V.I - 21
RIN	<b>R</b> educed <b>i</b> ntensity <b>n</b> oise, V.I - 91

---

---

$S$	Entropy, V.I - 35
$\underline{S}_{\text{gen}}(\underline{\mathbf{r}}_1, \underline{\mathbf{r}}_2, \omega)$	Generalised Stokes parameters, V.I - 20
$\underline{S}$	Poynting vector, V.II A-5
SLED or SLD	Superluminescent light emitting diode, V.I - 86
SMF	Single-mode fibre, V.I - 27
SNR	Signal-to-noise ratio, V.I - 15
$S_{W_Q}(\underline{\mathbf{r}}_Q, \omega)$	Spectral density at point $Q$ , V.I - 19
SOP	State of polarisation, V.I - 21
$\underline{S}_{\parallel}$	SOP (Stokes vector) parallel orientation, V.I - 221
$\underline{S}_{\perp}$	SOP (Stokes vector) perpendicular orientation, V.I - 221
$\underline{S}$	Stokes vector, V.II E-5
$\underline{S}_{\text{SB}}$	Stokes vector for the SpectroBragg, V.I - 239
$SG(x; \underline{a})$	Super-Gaussian function, V.I - 134
$S_W(\underline{\mathbf{r}}, \omega)$	Power spectral density, V.II B-5
$T_f$	The <i>Fictive temperature</i> , V.I - 28
$T_g$	Glass transition temperature, V.I - 25
$\nabla T$	Spatial temperature change, V.I - 44
$t$	Twist or torsion applied to fibre, V.I - 52
TE	Transverse Electric orientation, V.I - 24
TEC	Thermoelectric cooling, V.I - 141
$T$	Temperature, V.I - 35
$T_{\text{level}}(x)$	Threshold function of quantity $x$ , V.I - 136
$t_{\text{level}}$	Threshold level, V.I - 136
$t$	Time, V.II A-1
TM	Transverse magnetic orientation, V.I - 24
TIR	Total internal reflection, V.I - 22
Tr	Trace of a matrix, V.I - 16
$U(P)$	Amplitude of field at point $P$ , V.II B-11
$\underline{V}(\underline{\mathbf{r}}, t)$	Analytic signal, V.II C-1
$\underline{V}^{\Im}(\underline{\mathbf{r}}, t)$	Imaginary part of analytic signal, V.II C-1
$\underline{V}^{\Re}(\underline{\mathbf{r}}, t)$	Real part of analytic signal, V.II C-1
$\underline{V}_{\text{cutoff}}$	Cut-off frequency, V.I - 24

---

---

$V_U$	Amplitude of incident wave, V.II B-11
$\underline{v}_g$	Group velocity, V.I - 25
$V_H$	<i>Hamiltonian</i> function, V.II K-1
$\underline{V}^2$	Normalised frequency, V.I - 24
$V_{\text{ref}}^{\mathfrak{R}}(t)$	Reference interferograms, V.I - 271
$V_{\text{sig}}^{\mathfrak{R}}(t)$	Signal interferograms, V.I - 271
$\mathcal{V}_{W_Q}(\underline{\mathbf{r}}_Q, \omega)$	Spectral visibility, V.I - 19
$\underline{v}$	Speed of propagating wave, V.II A-3
$\underline{\underline{V}}_{FR}(\omega)$	The Faraday tensor (Verdet's constant when $V_{FR11} = V_{FR22} = V_{FR33}$ ), V.I - 49
$V$	Volume, V.I - 65
$\mathcal{V}_Q(\underline{\mathbf{r}}_Q, t)$	Visibility or contrast function, V.II B-4
$W$	Optical aberration function, V.II K-3
$\underline{\underline{W}}(\underline{\mathbf{r}}_1, \underline{\mathbf{r}}_2, \omega)$	Cross-spectral density function of two points, $\underline{\mathbf{r}}_1, \underline{\mathbf{r}}_2$ , and frequency $\omega$ , V.I - 18
WDM	<b>W</b> avelength <b>d</b> ivision <b>m</b> ultiplexing, V.I - 140
$W_g = dN$	Illuminated width of diffraction grating, V.I - 125
$W_{\text{rect}}(n)$	Rectangular apodising window function, V.II P-3
$\underline{\hat{\mathbf{x}}}, \underline{\hat{\mathbf{y}}}$ and $\underline{\hat{\mathbf{z}}}$	Cartesian unit vectors, V.II A-1